

Transactions of the ASME®

Technical Editor
G. K. SEROVY

Associate Technical Editors
Advanced Energy Systems

M. J. MORAN

Environmental Control

H. E. HESKETH

Fuels and Combustion Technologies

D. W. PACER

Gas Turbine

S. A. MOSIER

Internal Combustion Engine

J. A. CATON

Nuclear Engineering

S. M. CHO

Power

R. W. PORTER

**BOARD ON
COMMUNICATIONS**
Chairman and Vice-President
R. NICKELL

Members-at-Large

W. BEGELL

T. F. CONRY

M. FRANKE

R. L. KASTOR

R. MATES

T. C. MIN

R. E. REDER

R. D. ROCKE

W. O. WINER

A. J. WENNERSTROM

B. ZIELS

President, **C. O. VELZY**

Executive Director,

D. L. BELDEN

Treasurer, **ROBERT A. BENNETT**

PUBLISHING STAFF

Mng. Dir., Publ.,

CHARLES W. BEARDSLEY

Managing Editor,

CORNELIA MONAHAN

Sr. Production Editor,

VALERIE WINTERS

Editorial Prod. Asst.,

MARISOL ANDINO

Transactions of the ASME, Journal of Turbomachinery (ISSN 0889-504X) is published quarterly (Jan., Apr., July, Oct.) for \$100 per year by The American Society of Mechanical Engineers, 345 East 47th Street, New York, NY 10017. Second-class postage paid at New York, NY and additional mailing offices. POSTMASTER: Send address change to Transactions of the ASME, Journal of Turbomachinery, c/o The

AMERICAN SOCIETY OF MECHANICAL ENGINEERS, 22 Law Drive, Box 2300, Fairfield, NJ 07007-2300.

CHANGES OF ADDRESS must be received at Society headquarters seven weeks before they are to be effective. Please send old label and new address.

PRICES: To members, \$29.00, annually; to nonmembers, \$100.00.

Add \$15.00 for postage to countries outside the United States and Canada.

STATEMENT from By-Laws. The Society shall not be responsible for statements or opinions advanced in papers or ... printed in its publications (B 7.1, para. 3).

COPYRIGHT © 1990 by the American Society of Mechanical Engineers. Reprints from this publication may be made on condition that full credit be given the TRANSACTIONS OF THE ASME—JOURNAL OF TURBOMACHINERY, and the author, and date of publication be stated.

INDEXED by Applied Mechanics Reviews and Engineering Information, Inc.

Journal of Turbomachinery

Published Quarterly by The American Society of Mechanical Engineers

VOLUME 112 • NUMBER 2 • APRIL 1990

TECHNICAL PAPERS

- 159 Design and Testing of the FT8 Gas Turbine Low-Pressure Compressor (89-GT-295)
R. J. Monhardt, J. H. Richardson, and J. M. Boettcher
- 165 A Variable-Geometry Power Turbine for Marine Gas Turbines (89-GT-282)
K. W. Karstensen and J. O. Wiggins
- 175 Surface Roughness Measurements on Gas Turbine Blades (89-GT-285)
R. P. Taylor
- 181 The Influence of Boundary Layer State on Vortex Shedding From Flat Plates and Turbine Cascades (89-GT-296)
C. H. Steverding and H. Heinemann
- 188 A Theory for Wake-Induced Transition (89-GT-57)
R. E. Mayle and K. Dullenkopf
- 196 Effects of Adverse Pressure Gradients on the Nature and Length of Boundary Layer Transition (89-GT-274)
G. J. Walker and J. P. Gostelow
- 206 Unsteady Transition in an Axial-Flow Turbine: Part 1—Measurements on the Turbine Rotor (89-GT-289)
J. S. Addison and H. P. Hodson
- 215 Unsteady Transition in an Axial-Flow Turbine: Part 2—Cascade Measurements and Modeling (89-GT-290)
J. S. Addison and H. P. Hodson
- 222 Compressor Blade Boundary Layers: Part 1—Test Facility and Measurements With No Incident Wakes (89-GT-50)
Y. Dong and N. A. Cumpsty
- 231 Compressor Blade Boundary Layers: Part 2—Measurements With Incident Wakes (89-GT-51)
Y. Dong and N. A. Cumpsty
- 241 The Measurement of Boundary Layers on a Compressor Blade in Cascade: Part 4—Flow Fields for Incidence Angles of -1.5 and -8.5 Degrees (89-GT-72)
W. C. Zierke and S. Deutsch
- 256 Viscous Flow in a Controlled Diffusion Compressor Cascade With Increasing Incidence (89-GT-131)
Y. Elazar and R. P. Shreeve
- 267 An Improved Incidence Losses Prediction Method for Turbine Airfoils (89-GT-284)
S. H. Moustapha, S. C. Kacker, and B. Tremblay
- 277 The Trailing Edge Loss of Transonic Turbine Blades (89-GT-278)
J. D. Denton and L. Xu
- 286 An Experimental Assessment of the Influence of Downstream Conditions on the Performance of a Transonic Turbine Nozzle of High Turning (89-GT-283)
U. W. Schaub, R. G. Williamson, J.-P. Huot, and S. H. Moustapha
- 294 The Use of Circumferentially Varying Stagger Guide Vanes in an Axial Flow Pump or Compressor
J. H. Horlock
- 298 Inlet Distortion Generated Periodic Aerodynamic Rotor Response (89-GT-299)
S. R. Manwaring and S. Fleeter

TECHNICAL BRIEFS

- 308 Visualization Studies in Rotating Disk Cavity Flows
J. Nordquist, S. Abrahamson, J. Wechkin, and J. Eaton

ANNOUNCEMENTS

- 310 Change of address form for subscribers

Inside back cover Information for Authors

R. J. Monhardt

J. H. Richardson

Pratt & Whitney,
Commercial Engine Business,
United Technologies Corporation,
East Hartford, CT 06108

J. M. Boettcher

Turbo Power & Marine Systems, Inc.
United Technologies Corporation,
Farmington, CT 06032

Design and Testing of the FT8 Gas Turbine Low-Pressure Compressor

This paper presents a discussion of the design and test phases of the Low-Pressure Compressor (LPC) used in the FT8 Gas Turbine. Design objectives, including efficiency, durability, and stall margin goals, are covered along with actual test results indicating successful accomplishment of these objectives. Unique features of the test program and an overview of the FT8 Gas Generator in comparison to the JT8D Aircraft Engine are also presented.

Background

The FT8 marine and industrial gas turbine is derived from the Pratt & Whitney JT8D series aircraft jet engine, which is the most widely used engine in aviation history with over 13,000 engines delivered and 285 million hours flown. Improvements in the JT8D since initial delivery in 1964 have increased the takeoff thrust from 14,000 lb to 21,000 lb. The FT8 design incorporates the combined technology of the current model JT8D-200 series engines and the latest PW commercial engine models PW2037 and PW4000. The FT8 also incorporates many features of the FT4 gas turbine, which has 28 years of successful marine and industrial operations and is still in service.

The FT8 is designed to provide high efficiency and reliable operation in marine, power generation, and mechanical drive applications. Development testing is expected to be completed in 1989, and the FT8 should be available for commercial service in 1990. The 33,000 hp size (24.8 MW) and 38.8 percent thermal efficiency of the FT8 is well suited to both naval and industrial applications worldwide. The design and development of the low-pressure compressor outlined in this paper are a principal part of the FT8 program.

General Description

The FT8 LPC has eight stages, of which the first three have variable geometry vanes. As shown in Fig. 1, this configuration results from moving the fan stage, fan ducts, and first stator forward of the 1.5 stage. In order to retain the stage numbering system of the existing JT8D-219 hardware, the new FT8 stages are designated stage 1.1 and stage 1.3. In addition, the 1.5 stage of the JT8D-219 is redesigned. The entire rotor structure from rotor 2 aft, the core static structure and stator vanes from stator 1.5 aft, and the #1 bearing compartment are existing JT8D-219 hardware. The inlet case and the outer main structure case are unique to the FT8 LPC. Drains are provided

at two locations in the outer rear case where there is a potential for water to collect. The LPC can be inspected through the inlet or at borescope ports located at S1.5 and the LPC exit.

Mechanical Design

In general, the FT8 LPC is conservatively designed. The FT8 minimum design life requirements of 100,000 hours and 15,000 Low Cycle Fatigue (LCF) cycles are exceeded throughout the LPC. The existing JT8D-219 hardware used in the FT8 LPC was designed to more severe conditions and therefore exceeds FT8 design requirements. Since the new FT8 hardware is not constrained by flight weight requirements, a simple conservative design approach has been taken that builds on the proven JT8D-219 LPC. The FT8 LPC is designed to provide a minimum surge margin of 10 percent so that surge is not encoun-

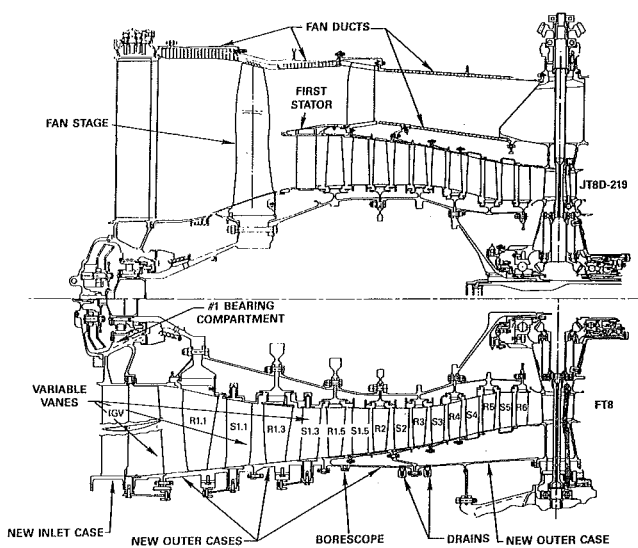


Fig. 1 Comparison of JT8D-219 and FT8 LPC

Contributed by the International Gas Turbine Institute and presented at the 34th International Gas Turbine and Aeroengine Congress and Exhibition, Toronto, Ontario, Canada, June 4-8, 1989. Manuscript received at ASME Headquarters February 14, 1989. Paper No. 89-GT-295.

tered during normal steady-state or transient operation. In the unlikely event that a surge does occur, the LPC is structurally designed to withstand high-power surge loads.

Corrosion-resistant materials are used throughout the LPC for the new FT8 hardware. Corrosion-resistant steel 17-4 PH is used for the static structure design. The blades are 6-4 titanium and the rotor disks and spacers are aluminum-coated steel. Most of the JT8D-219 hardware used in the FT8 is titanium and aluminum. There are a few steel hardware items that will be coated for corrosion protection. Aluminum coating is used for the rotating hardware and a diffused iron aluminide coating is used for the static hardware items.

The inlet case features variable position aerodynamic flaps, which are positioned behind an array of 18 rigid struts. The struts are hollow and support the #1 bearing compartment. They are designed to withstand blade loss buckling loads and provide the proper stiffness for critical speed considerations. Six of the struts are used to provide plumbing services to the #1 bearing compartment. The variable position inlet case flaps are guided by oversize bearings on both the i.d. and o.d. to provide wear resistance. Forged actuation arms attach to the flaps on the o.d. A pin through a uniball bearing in the actuation arm connects the arm to a unison ring, which slides on polyimide polymer runners attached to the case.

The stator 1.1 and stator 1.3 LPC cases support two stages of variable vanes. The cases also provide blade loss containment and abrasible rubstrips for rotor 1.1 and 1.3 blade tips. The actuation arm/unison ring and bearings for the variable vanes are similar to the inlet case design. Inner shroud assemblies contain abrasible rubber seal lands similar to the existing JT8D-219 LPC, which allow close-running clearance of rim seals.

The rear LPC cases form the main structural support between the stator 1.3 case and the intermediate case. The LPC core from S1.5 through S5 is existing JT8D-219 hardware and is supported by the rear cases at stator 2. The two rear cases are constructed of welded sheet metal and machined flanges with bosses provided for water drains and borescope ports. Our extensive JT8D-219 flight engine experience has shown that adequate inspection capability exists with access through the LPC inlet and borescope ports at the LPC exit. The FT8 features an additional access port as stator 1.5 for midcompressor stage inspection.

The actuation system for the FT8 LPC moves the Inlet Guide Vane (IGV) flap, stator 1.1, and stator 1.3 vanes to a schedule relating vane angle to LPC rotor speed. Controlled by an electronic computer control system, hydraulic cylinders move the vanes through an arrangement of vane arms, unison rings, bellcranks, and adjuster links. This system is typical of existing PW flight engine actuation systems, except the linkages and other system components have been strengthened for this non-flight application. In addition, to reduce wear and maximize vane movement accuracy, the actuator support brackets are of rugged design and connecting bolts and pins have close tolerance fits. Two hydraulic cylinders are used, one to control the IGV flap and one to control both stator 1.1 and 1.3 vanes. Schedule alterations for the IGV flap can be accommodated by changes in the electronic control software. Stator 1.1 and stator 1.3 vane schedule alterations can be made similar to the IGV with additional capability to change the proportionality between the tandem stages through an adjustable bellcrank. Rigging provisions exist in the unison ring and bellcrank to assure the proper relationship of actuator position to vane arm angle. With the actuation system positioned at 12:00 to 3:00 o'clock easy access is provided to the rigging facilities.

The FT8 LPC rotor structure is a bolted disk and spacer configuration using short tiebolts. The rotor 1.1, 1.3, and 1.5 disks are new to the FT8 LPC as are the three spacers adjacent to these disks. A flow guide attached to the front of rotor 1.1 prevents recirculation between the flowpath and the large cav-

ity behind the #1 bearing compartment. The rotor hardware is conservatively designed. Disks exceed burst margin requirements. Disks, spacers, and tiebolts exceed creep life and LCF requirements. The FT8 LPC operates at approximately 10 percent lower speed than the JT8D-219 LPC. The existing JT8D-219 rotor hardware from rotor 2 aft was designed for more severe conditions and therefore exceeds the FT8 design requirements. The FT8 rotor 1.1, 1.3, and 1.5 blades are similar to existing JT8D-219 blades. Conventional dovetail attachments are used to hold the blades in the disk rim. The attachment stress levels are consistent with successful PW experience. Blade airfoils are designed to keep resonances and flutter out of the operating range. The airfoil leading edge thickness is sized to provide resistance to foreign object damage. In addition, the outer 20 percent of the airfoil is designed to resist airfoil erosion. Rotor 1.3 and rotor 1.5 are retained in the disk with a shear-type blade lock typical of the existing JT8D-219 rotor stages. The rotor 1.1 blades use a split ring lock for blade retention. This lock is an existing JT8D-219 hardware item from the replaced fan stage. The front flow guide assures proper installation and retention of the split ring lock.

The axial gapping of the rotor to static hardware provides adequate clearance for thermal and load deflection effects during transient and steady-state operation. Further gap allowance is provided to preclude clashing of blades and vanes should an LPC surge occur. After considering the mechanical requirements of axial gapping, the cavity volume between the disk rims and stator inner shrouds has been kept to a minimum by continuing the use of rim seals found throughout the JT8D-219 LPC. The smaller cavities tend to reduce aerodynamic losses.

Aerodynamic Design

The new stages of the FT8 LPC were designed with current state-of-the-art aerodynamic methods used in the PW2037 and PW4000 flight engines and utilized the industrial experience gained from the FT4 and FT50 compressor designs. The rear stages of the LPC were retained from the JT8D-219 flight engine and are standard NACA series airfoils. The conversion of a flight engine to an industrial engine allows greater flexibility from traditional flight design rules of low weight and small frontal area to provide a truer aerodynamic optimization.

The aerodynamic design point was established based on the overall gas generator goal of 33,000 shaft horsepower. A 10 percent corrected airflow allowance for growth capability was also used as a design criterion. The design point parameters are:

Corrected speed	7130 rpm
Corrected flow	180.0 lb/sec
Pressure ratio	4.82
Adiabatic efficiency goal (excluding exit stator loss)	0.890
Exit stator total pressure loss	1.6 percent

Design constraints required that the compressor have the same surge line and proven stability characteristics of the JT8D flight engine and that the match point of the existing rear stages of the compressor correspond to a point on the flight engine operating line in order to retain optimized performance.

The match point and surge line were known from JT8D engine and test rig data and the aerodynamics throughout the JT8D compressor were derived from a two-dimensional streamline model. The new front flowpath and aerodynamics were designed to optimize performance while setting the exit velocity triangles to match those found from the streamline analysis of the JT8D. New stage aerodynamic loadings were

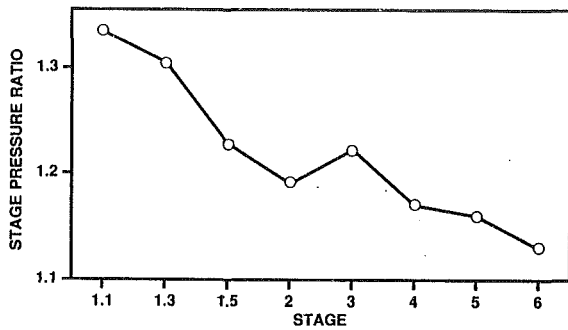


Fig. 2 FT8 LPC design

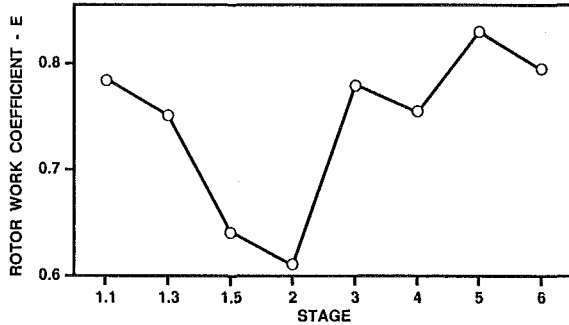


Fig. 3 FT8 LPC design

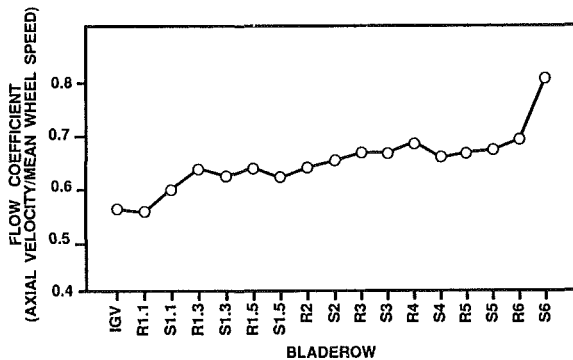


Fig. 4 FT8 LPC design

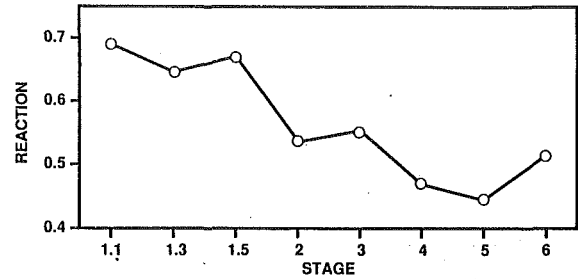


Fig. 5 FT8 LPC design

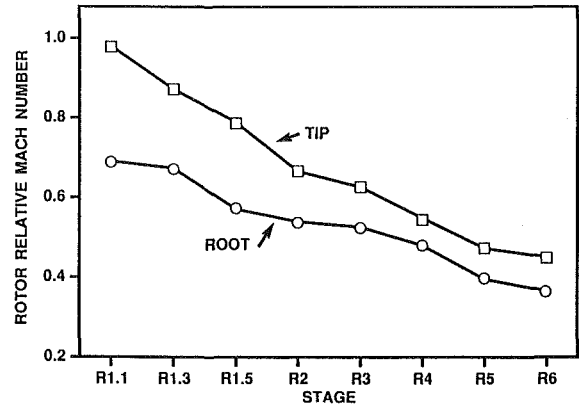


Fig. 6 FT8 LPC design

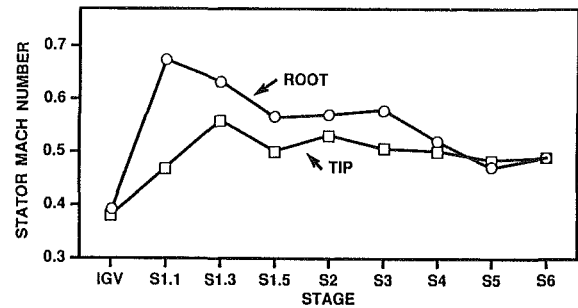


Fig. 7 FT8 LPC design

set at the design speed surge line to be lower than those of the JT8D backend to assure that the new front stages would not set the surge line at design speed. Variable stator vanes were employed to allow the new stage airfoils to be optimized for performance at high speed and closed at part speed to retain the JT8D surge line.

The goal efficiency was calculated using the Pratt & Whitney design system to set the level for the front stages while using JT8D measured data to calculate the efficiency for the existing rear stages. When the two portions were thermodynamically joined, the overall efficiency was dropped one point to make the FT8 LPC a low-risk design.

Some of the resulting design parameters are shown in Figs. 2-10. Figures 2 and 3 show the stage pressure ratio and rotor work coefficient E , where

$$E = \frac{2gJC_p\Delta T_o}{U^2}$$

U = mean rotor speed

ΔT = mean rotor total temperature rise

Figure 4 depicts the flow coefficient axial velocity normalized by mean rotor wheel speed. The reaction is displayed in Fig. 5, where

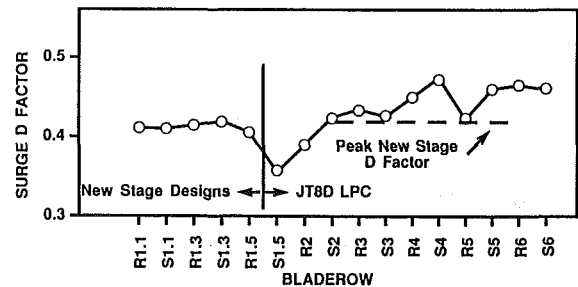


Fig. 8 FT8 LPC design

$$\text{Reaction} = \frac{\Delta P_s(\text{rotor})}{\Delta P_s(\text{stage})}$$

Rotor and stator Mach numbers at the root and tip are shown in Figs. 6 and 7. The rather high tip relative Mach numbers of the first two rotors required special attention in the airfoil design process.

Figure 8 shows the stagewise D factor at the predicted surge line. The D factor loading of the new front stages has been set lower than the level of the backend to insure that the new stages will not set surge line. Figures 9 and 10 are the solidity and aspect ratio that resulted.

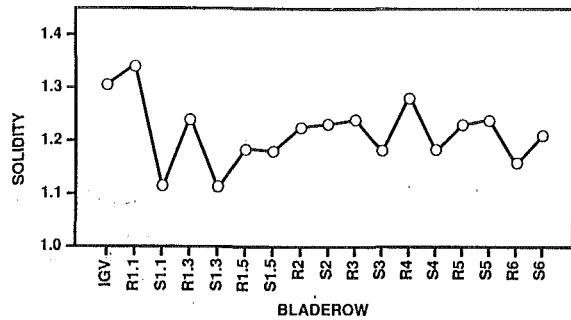


Fig. 9 FT8 LPC design

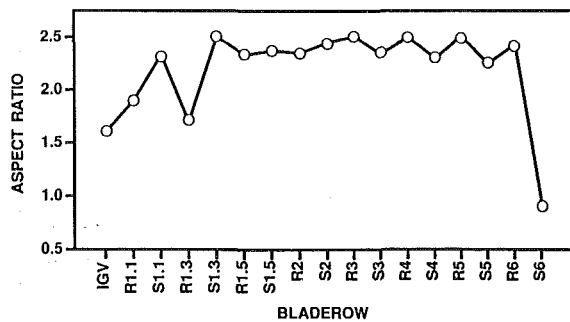


Fig. 10 FT8 LPC design

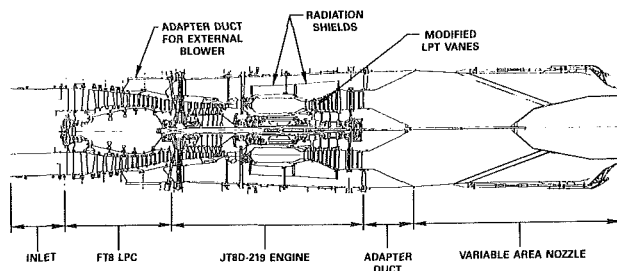


Fig. 11 FT8 LPC test engine

$$D \text{ factor} = 1 - \frac{V}{V_1} + \frac{RCu - R_1Cu_1}{\sigma V_1(R + R_1)}$$

where V = absolute velocity for stators and relative velocity for rotors; Cu = tangential component of velocity; R = radius; σ = solidity.

The airfoil sections in the existing rear of the JT8D-219 LPC are NACA 65/circular arc series or NACA 400 series. The new airfoils IGV through rotor 1.5 were designed as Controlled Diffusion Airfoils (CDA) using the methods and tools described by Caspar et al. (1980) and Hobbs and Weingold (1984). Controlled-diffusion airfoils have been used successfully at Pratt & Whitney in the PW2037 and PW4000 flight engine LPC's and HPC's. The method involves controlling the diffusion on the airfoil suction surface to avoid loss due to significant boundary layer separation. In the transonic regime, the calculation allows tailoring of the suction surface Mach number to avoid strong supersonic shock losses. The method utilizes a two-dimensional potential flow solver to predict the airfoil-to-airfoil aerodynamic properties.

Variability in the inlet was accomplished by using a fixed strut and variable flap combination. The design of the inlet vane was done based on Pratt & Whitney military experience in combination with the design methods described above.

Other aerodynamic design features of the FT8 include abrasible rim and tip seals, allowing tighter running clearance for performance and stability. Blade roots have been sealed with a rubber sealant to prevent backflow, and airfoil surface roughness has been set such that all rows are hydraulically "smooth."

LPC Test Engine

The test vehicle for the FT8 LPC is a JT8D-219 engine. The JT8D-219 represents a "known quantity," that is, an engine that has many hours of running time and provides a solid test data base. Testing the FT8 LPC in front of the known quantity minimizes the variables and unknowns encountered in component rig testing and is also cost effective.

The JT8D-219 fan and LPC was removed and replaced with the FT8 LPC, which was attached with a unique rig case; see Fig. 11. The only other change to the core engine was in the Low-Pressure Turbine (LPT) where modified second-stage vanes were used to gain a better component match. With the replacement of the JT8D-219 fan, obviously the fan airflow was eliminated, and the fan ducts in front of the intermediate case were removed.

However, the fan exhaust ducts aft of the intermediate case are structural and cannot be eliminated. These ducts are of aluminum and bonded honeycomb construction and require the cooling effects of fan airflow to survive. The outer burner case rear flange also requires cooling. This problem was solved by providing an external blower for the test engine. Sheet metal adapter ducts were attached to the forward side of the intermediate case. The blower air flows into the adapter ducts, through the hot section fan ducts, and is then dumped overboard. The blower airflow is considerably less than the actual engine fan airflow, but with the addition of convergent radiation shields it is adequate to protect the critical areas. The radiation shields are positioned between the hot section of the engine and the outer fan ducts.

A variable area nozzle was attached to the engine turbine exhaust case with rig unique adapter cases. Varying the exhaust area provides a means to change the LPC operating line and to map the LPC to the surge line.

A full complement of instrumentation was used to provide aerodynamic data, structural data, and to monitor the general health of the FT8 test engine. Pressure and temperature probes typical of test engines were installed at the LPC inlet and exit. Interstage total temperature and pressure sensors were installed on airfoil leading edges from rotor 1.1 through stator 3. All airfoils were strain gaged with the new FT8 stages receiving most of the coverage. Rotor strain gages were routed forward to a slip ring assembly mounted to the inlet case. Conventional static pressure probes were located throughout the LPC at the flowpath outer wall. In addition, high-response static pressure probes were installed at the LPC inlet, stator 1.5, and exit. Potentiometers were attached to the variable vanes to provide vane angle feedback. Case flange mounted accelerometers and hot section pressure and temperature probes typically used to monitor general engine health made up the rest of the test engine instrumentation.

The inlet of the LPC test engine is designed to accommodate a distortion screen. This screen can be installed to change inlet pressure distribution to simulate distortion typical of ground installations. Also, higher order vibratory excitations can be generated for structural evaluation of blade and vane stresses. Three separate screens are designed to provide different distortion levels and harmonic content.

LPC Test Results

A detailed test plan for the LPC test engine was written well before actual testing started in late Aug. 1988. This plan defined a program to accomplish the following objectives: (1) stress survey, (2) airflow calibration, (3) LPC performance and variable vane schedule optimization, (4) LPC surge line definition/bleed optimization, and (5) distortion effect on LPC surge line, performance, and stress.

Testing continued through Sept. and Oct. 1988 in a modified JT8D sea level test facility; see Fig. 12. The engine was tested

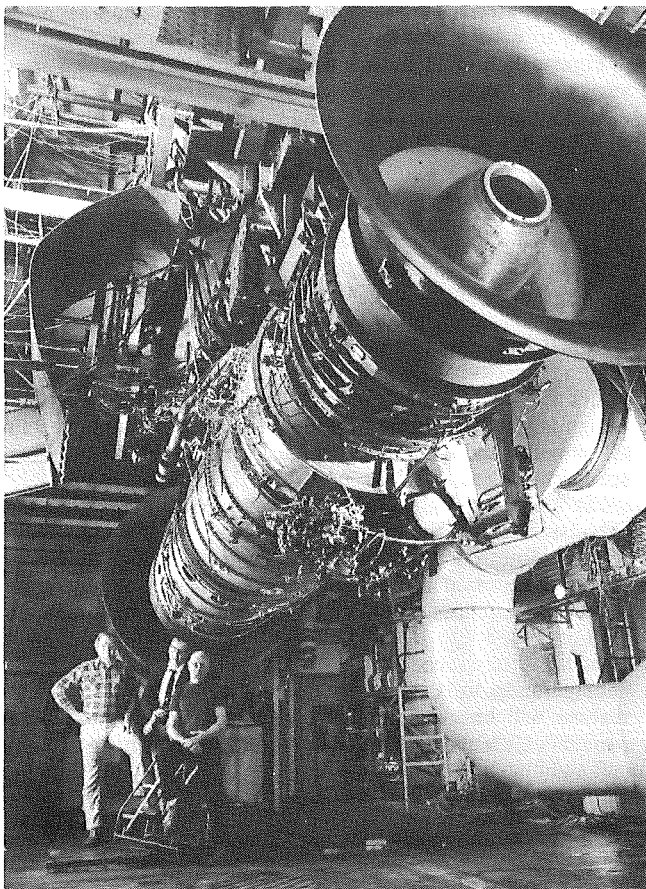


Fig. 12 FT8 LPC test engine in test facility

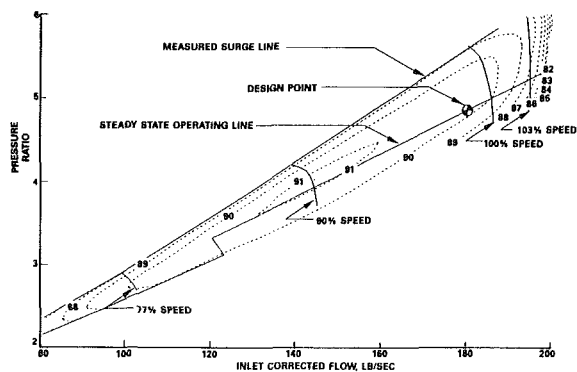


Fig. 13 FT8 LPC performance based on modified engine testing

successfully for 103 test hours covering 100 percent of the planned test program.

The efficiency of the LPC was better than the goal and very close to the maximum potential predicted by the Pratt & Whitney design system. The efficiency was still better than goal after surge line definition caused deterioration. Although the detailed analysis of the testing has not been completed at the time of this writing, it appears that the goodness came from the new front stages performing very close to their potential and the rear stages of the JT8D performing better than prior rig data indicated. A review of the JT8D rig to engine testing indicates that this conclusion is probably correct. Since the exit total pressure is measured in front of the LPC exit stator, the efficiency does not include the exit stator total pressure loss, which is estimated at 1.6 percent at the design point.

A variable vane optimization program was performed at several speeds, resulting in slight performance gains at the final

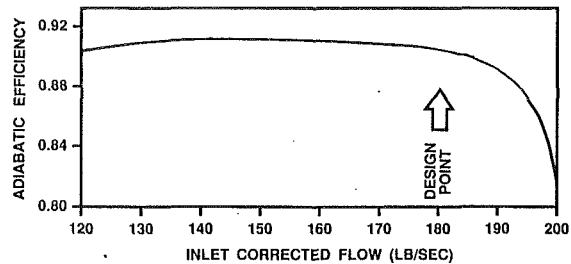


Fig. 14 FT8 LPC test performance

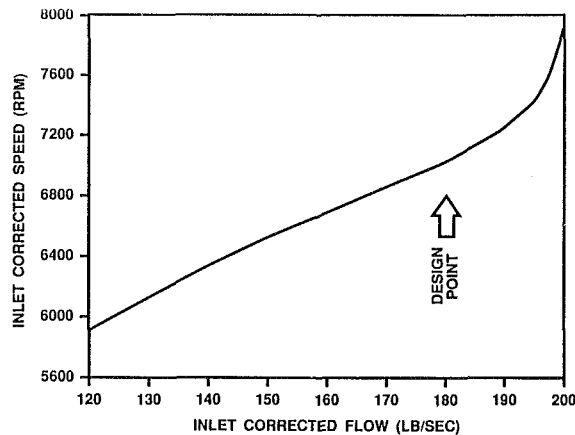


Fig. 15 FT8 LPC test performance

optimized vane schedule, which was within a few degrees of the pretest projected schedule. Checks of performance for vanes off schedule proportionally by 5 deg showed that LPC efficiency at constant corrected flow is fairly insensitive throughout the operating regime to changes in vane schedule. The flow capacity of the LPC on the optimized vane schedule was 3.2 percent higher than predicted at design speed.

Surge line was determined by running the engine at constant corrected speed while raising the operating line by opening the variable exit nozzle. Steady-state points were acquired close to the surge line and high-response instrumentation was used as the nozzle pushed the compressor into surge to determine the actual surge pressure ratio and corrected flow. The surge line defined by the efficiency optimized vane schedule was determined to be set by the portion of the LPC retained from the JT8D as intended. Testing of the LPC on vane schedules 5 deg open and closed proportionally showed that surge line was insensitive to changes of this magnitude.

Throughout this test the engine was intentionally surged many times. Stall recovery was demonstrated in every case and there was no evidence of any damage.

The variable nozzle was used to map the compressor over its entire operating region and to explore higher speed regimes for possible growth applications.

The LPC was tested to determine its tolerance to distortion. Three separate screens were designed and located in front of the compressor to create inlet pressure distortions. A 5 percent total pressure distortion over a 60-deg full-span circumferential sector was considered the worst case encountered in FT4 experience. Since Pratt & Whitney analysis determined that this level and extent of distortion should cause minimum surge line loss, a three-screen matrix was laid out to define the FT8 response to a more severe distortion, which may be encountered in the future. Based on the testing, results show that for the 5 percent, 60-deg screen, a surge margin loss of only 1 percent could be expected at 100 percent speed and above. No loss was measured at 90 percent speed and below. Airfoil stresses

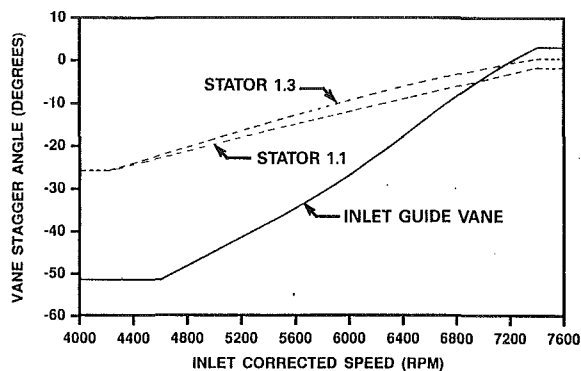


Fig. 16 FT8 LPC nominal vane schedule

recorded during the distortion testing were low and did not exceed 10 ksi.

The bleed schedule has been defined from a detailed stability audit to guarantee surge-free steady-state and transient operation when production parts variations, deterioration, stator vane rigging errors, horsepower extraction, water injection, inlet suppression, and distortion effects are accounted for. The bleed locations are the same as the existing flight engine and are located behind the LPC exit stator and in the second stage of the high-pressure compressor.

The overall performance map with postsurge efficiency levels is presented in Fig. 13. The measured surge line and steady-state operating line are shown. The drop in operating line at low speed represents the LPC exit bleed activation.

Airfoil stresses were monitored throughout the test program. With a nominal vane/bleed schedule the new FT8 airfoil vibratory stresses are well below allowable up to a redline speed of 7800 rpm. The stresses in airfoils common to the flight engine are typical of JT8D-219 experience. Airfoil stresses were also surveyed with the variable vanes ± 5 deg off schedule. No

significant stress increase was observed, indicating an insensitivity to vane schedule.

Figures 14 and 15 show how efficiency and corrected speed vary along the nominal steady-state operating line in the bleed closed regime. The variable vane schedule is shown in Fig. 16 as a function of corrected speed.

Conclusions

The FT8 industrial and marine gas generator is designed to provide efficient, reliable power at the 33,000 hp/24.8 MW rating. An integral part of the design is the low-pressure compressor, which combines the last five stages of the successful JT8D-219 flight engine with three new stages. The mechanical design is conservative, exceeding life requirements of 100,000 hours and 15,000 LCF cycles. The new stage aerodynamic design is state of the art and includes three variable vanes to allow good high-speed performance while retaining good low-speed surge line. The testing of the LPC was accomplished using a hybrid flight engine that employed a variable area exhaust nozzle for mapping the compressor up to and including its surge line. The compressor exceeded its performance goals and demonstrated a required surge line while measuring low stresses, even those measured during surge and distorted inlet testing.

In 1989, this successful LPC will be run in the FT8 engine configuration to complete engine development. The FT8 gas turbine will be available for commercial service in 1990 to provide efficient reliable power into the 21st century.

References

- Caspar, J. R., Hobbs, D. E., and Davis, R. L., 1980, "Calculation of Two-Dimensional Potential Cascade Flow Using Finite Area Methods," *AIAA Journal*, Vol. 18, No. 1, pp. 103-109.
- Hobbs, D. E., and Weingold, H. D., 1984, "Development of Controlled Diffusion Airfoils for Multistage Compressor Application," *ASME Journal of Engineering for Gas Turbines and Power*, Vol. 106, pp. 271-278.

A Variable-Geometry Power Turbine for Marine Gas Turbines

K. W. Karstensen

J. O. Wiggins

Solar Turbines Incorporated,
San Diego, CA 92101

Gas turbines have been accepted in naval surface ship applications, and considerable effort has been made to improve their fuel consumption, particularly at part-load operation. This is an important parameter for shipboard engines because both propulsion and electrical-generator engines spend most of their lives operating at off-design power. An effective way to improve part-load efficiency of recuperated gas turbines is by using a variable power turbine nozzle. This paper discusses the successful use of variable power turbine nozzles in several applications in a family of engines developed for vehicular, industrial, and marine use. These engines incorporate a variable power turbine nozzle and primary surface recuperator to yield specific fuel consumption that rivals that of medium speed diesels. The paper concentrates on the experience with the variable nozzle, tracing its derivation from an existing fixed vane nozzle and its use across a wide range of engine sizes and applications. Emphasis is placed on its potential in marine propulsion and auxiliary gas turbines.

Introduction

The 5650, a 3000/3500-shp (2237/2610-kW) gas turbine engine (shown in Figs. 1 and 2), is the product of more than 20 years of development. Solar administers an extensive field evaluation program in which nine pilot production engines have operated a total of over 190,000 hr at customer job sites.

The unique 5650 power plant combines the high thermal efficiency of diesel engines with most of the traditional advantages of the gas turbine, that is, relatively small size and weight, low vibration levels, long life, and low maintenance. The small size is a result of high thermal efficiency from the development by Caterpillar, Solar's parent company, of a primary surface recuperator of 90 percent thermal effectiveness. The small size of this recuperator allows it to be integrally mounted without the long ducting runs often associated with recuperated gas turbines in its size range.

The engine design was optimized for a 1950°F (1066°C) recuperated cycle, with a two-stage centrifugal compressor operating at a 6.5 pressure ratio. This pressure ratio has maximum thermal efficiency for a recuperated cycle at 1950°F (1066°C). The 5650 gas turbines are presently operating at 1775°F (969°C) awaiting development of a suitable cooled gas producer turbine for 1950°F (1066°C) operation.

Thermal efficiency is maintained essentially constant over the upper 40 to 50 percent of a recuperated engine's load range. This is accomplished by matching a broad range compressor to the engine cycle in combination with a variable-geometry free power turbine (Fig. 3). This paper traces the aerodynamic development of the 5650 power turbine from its origin as a

small, fixed-geometry gas producer turbine stage through its conversion to variable geometry for a heavy duty vehicle engine, to its final scale-up to the size required by the 5650. This technology is applicable not only to the experimental and limited production engines discussed here but to other two-shaft recuperated gas turbines as well.

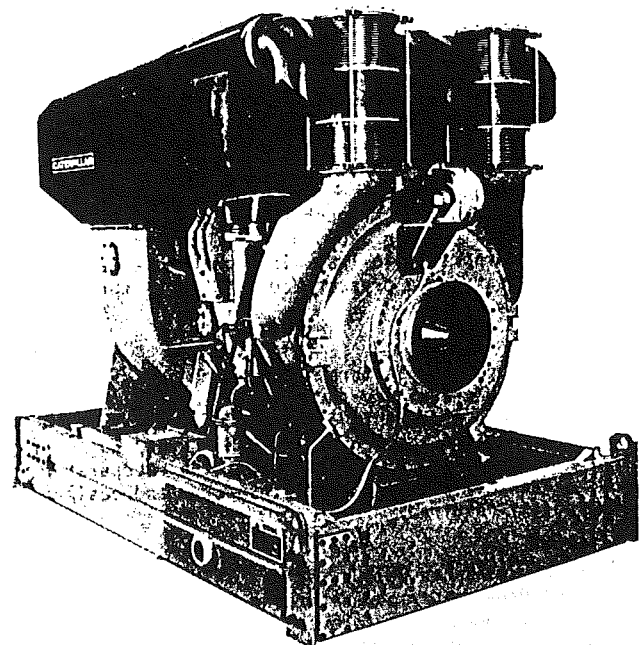


Fig. 1 Solar 5650 gas turbine

Contributed by the International Gas Turbine Institute and presented at the 34th International Gas Turbine and Aeroengine Congress and Exhibition, Toronto, Ontario, Canada, June 4-8, 1989. Manuscript received at ASME Headquarters February 1, 1989. Paper No. 89-GT-282.

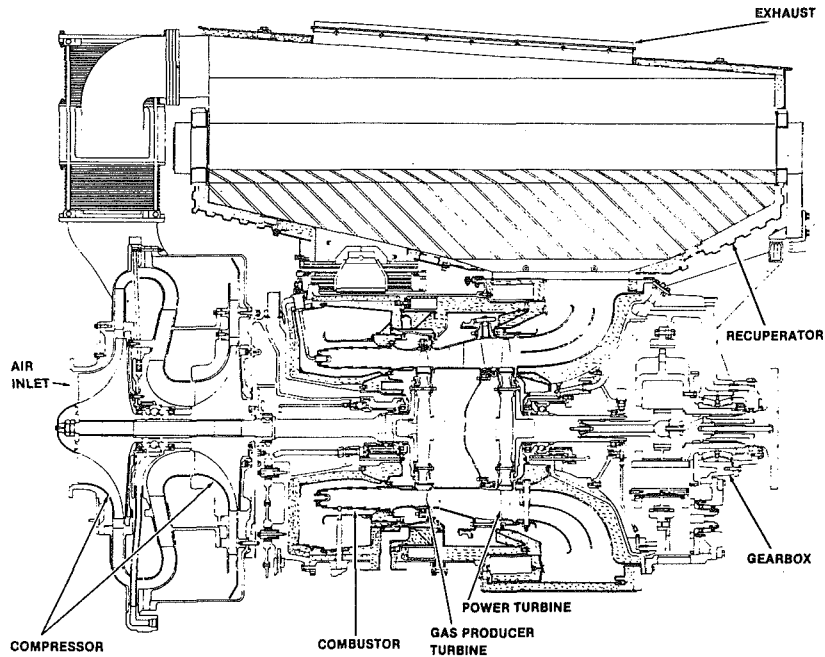


Fig. 2 5650 gas turbine cross section

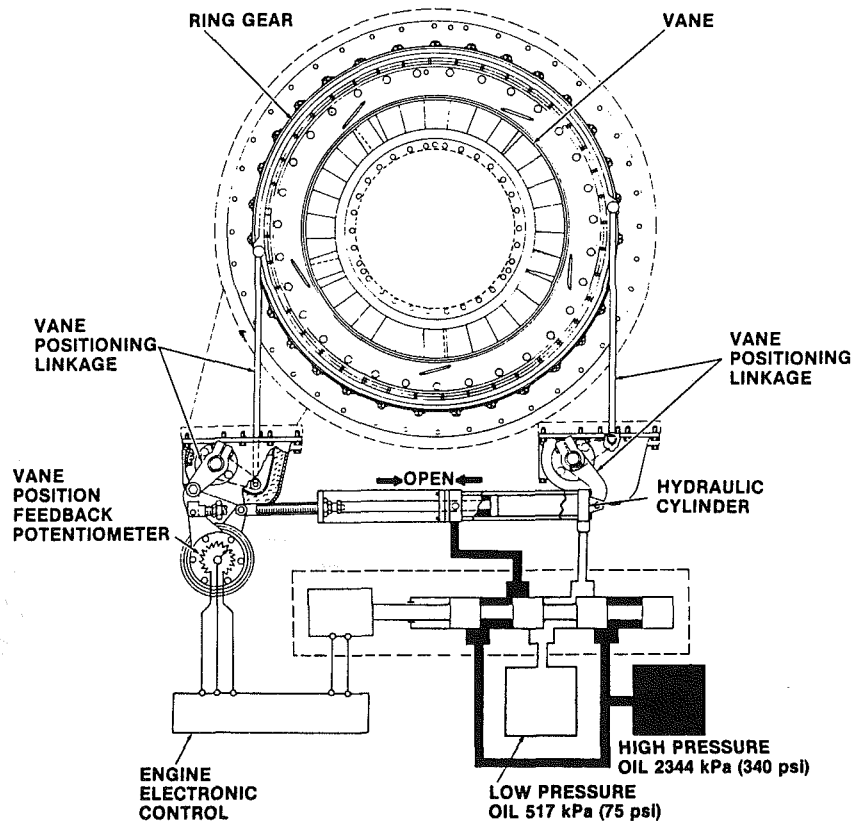


Fig. 3 Variable power turbine nozzle

5650 Background and Aerodynamic Scaling

A key element in the 5650's background at Caterpillar Inc. was a highly disciplined technique for scaling of turbomachinery components from one size to another. This technique allows engine programs of varying horsepower (air flow rate) to share the results of a single component development program. In addition, component development can be performed on test

rigs of a single scale, thereby greatly extending the payback of investment in laboratory air supply systems and other support equipment. The technique employed is geometric scaling. Engineering modifications such as a "cropping" and blade extension often follow.

Geometric scaling, as the name implies, consists of exact application of a single scale factor to all component dimensions

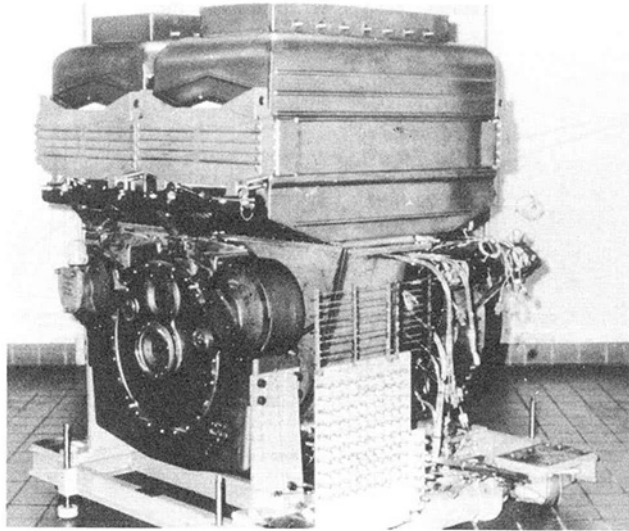


Fig. 4 Caterpillar T-700 gas turbine with primary surface recuperators

and clearances. Certain relationships are immediately apparent for an aerodynamic machine scaled in this manner and holding blade velocity (tip speed) constant:

- Rotational speed varies inversely with scale factor;
- Area and mass flow vary with the square of the scale factor;
- Volume and weight vary with the cube of the scale factor;
- Turbine power output and compressor power input vary with the square of the scale factor
- Centrifugal stresses remain constant;
- Natural frequencies of vibration remain at a constant multiple of rotational speed;
- Aerodynamic performance (efficiency) remains constant over a wide range of practical scales, varying only when extremes of downscaling produce a significant Reynolds number effect.

Geometric scaling is rigorous without regard to practical concerns such as manufacturability. These concerns are addressed either through an engineered modification or are carefully evaluated in the component test rig after the exact scaling has been certified. Wiggins and Waltz (1972) describe Caterpillar's experience in strict geometric scaling of an 8-stage axial compressor.

Several engineering modifications have been employed in meeting certain component requirements. One example is a change in the number of airfoils in an axial flow turbine. Often, larger or smaller airfoils are desired because of such concerns as trailing-edge thickness or rotor disk thickness. In this instance, a suitable airfoil is chosen and the number of airfoils and their chord length are modified such that the original airfoil pitch to chord ratio is preserved within the rescaled annulus.

The 5650 is, in general, a geometric scale-up of an earlier test bed engine designated the T-1200. The T-1200 shared a common turbine flowpath annulus size with the T-700 test bed engine shown in Fig. 4. The T-700 engine used a single-stage, 4.9-to-1 pressure ratio centrifugal compressor, which was replaced by the 6.5-to-1 two-stage compressor in the T-1200, which was later scaled up to the 5650. In addition to extensive test bed work, a vehicular arrangement of the T-700 was tested in the Caterpillar Model 992 end loader shown in Fig. 5. The T-700 engine was, in turn, a scale-up of an earlier T-375 test bed engine. The process of converting a fixed turbine stage to variable geometry took place during the design of the T-375 power turbine.



Fig. 5 Turbine-powered model 992 loader

Variable-Geometry Function

For a given pressure ratio, the thermal efficiency of simple-cycle or recuperated gas turbines is a function of the maximum cycle temperature (firing temperature). When the load on a two-shaft gas turbine is reduced below its peak efficiency rating, the engine air flow must be reduced by reducing the compressor (gas producer shaft) speed. In a fixed geometry engine, this is normally accomplished by reducing the firing temperature and, along with it, thermal efficiency. If the flow capacity of the power turbine in a recuperated two-shaft engine can be varied as load is reduced, the firing temperature, and thermal efficiency, can be maintained at a high level during part-load operation. This is accomplished by providing radial pivots for the power turbine nozzle vanes. A suitable linkage is provided to rotate the vanes in unison such that the geometric flow area at the nozzle throat is changed.

As the throat area of the power turbine nozzle is reduced, the fraction of the overall turbine pressure ratio taken across the power turbine is increased. The accompanying decrease in pressure ratio across the gas producer turbine allows a higher firing temperature for a given compressor operating point (speed, pressure ratio, and mass flow). This effect is illustrated in Fig. 6, which compares fixed and variable-geometry recuperated two-shaft gas turbines. The extent to which compressor speed (and engine load) can be reduced without a reduction in firing temperature is determined by the compressor surge characteristics. For a well-matched, broad-range compressor, the point at which firing temperature must be reduced will lie in the range of 40 to 60 percent of maximum power.

In addition to its primary mission of facilitating high part-load thermal efficiency in a recuperated gas turbine, a variable-geometry power turbine can be designed to provide the following advantages:

- Limit output shaft speed overshoot during download transients or load dumps by opening or, if required, reversing, nozzle exit flow direction during the overspeed period.
- Similarly, it can prevent overspeed damage to the power turbine if the drive train fails. This was demonstrated three times during the development. In all three instances, there was a high probability of acceleration to burst speed, for a fixed-geometry power turbine.
- Download transient response time is not set by the recuperator thermal lag time. While the recuperator metal is shedding its stored heat, the nozzle varies its angle continually as required to governed output shaft speed and scheduled firing temperature.
- Gas producer acceleration during on-load transients can be enhanced, thus limiting output shaft speed drop and time to return to governed speed.
- Dynamic engine braking can be provided in applications where load inertia is capable of driving the engine output shaft, e.g., in vehicle propulsion applications.

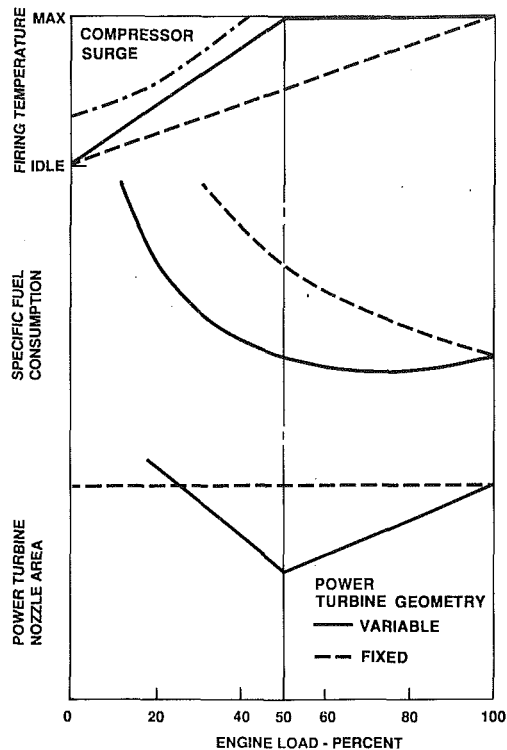


Fig. 6 Recuperated two-shaft gas turbine performance

- Engine cranking power requirements can be reduced (and/or start time reduced) by opening the nozzle to its maximum area during a start. This increases gas producer turbine torque output after light-off by increasing its share of the available cycle expansion (pressure) ratio.

Turbine Stage Evolution

The evolution of the 5650 power turbine, from the original prototype aerodynamic design through the two test bed engines to its present configuration, is shown in Table 1.

An inventory of existing turbine stages showed the best candidate power turbine for the proposed T-375 test bed engine to be the second stage of a small two-stage gas producer turbine. Analytical evaluation indicated that this stage would produce the desired 88 to 91 percent efficiency when scaled into the speed, flow, and pressure ratio of a T-375 power turbine. The required scale factor was calculated to be 1.796.

The prototype stage used relatively few large-chord airfoils in both the stator and rotor. A simple geometric scale-up produced a stage that occupied excessive axial engine length and required a rotor disk of excessive thickness and mass. This problem of unsatisfactory proportion was solved by applying the annulus scale factor to the number of airfoils rather than to their basic size, or chord. The desired axial engine length and rotor disk proportions thus were attained while preserving the original pitch/chord ratio of the prototype airfoil cascades. Fortunately, this procedure yielded an odd prime number of stator vanes and an even number of rotor blades, i.e.,

$$\text{No. of stator vanes} = (17)(1.796) = 30.53 = 31$$

$$\text{No. of rotor blades} = (32)(1.796) = 57.47 = 58$$

This relationship between vane and blade count is the easiest for the mechanical designer when considering blade vibration and rotor balance.

The T-375 vehicle engine power turbine hardware was incorporated into a cold turbine test rig. Both fixed and variable nozzles were made. Tests with the fixed nozzle (zero vane-to-shroud clearance) provided a base line for studies of the effect

Table 1 5650 power turbine evolution

	DIESEL COMPOUND TURBINE	PROTOTYPE	T375 ENGINE AND COLD RIG	T700/T1200 ENGINES	5650 INDUSTRIAL AND MARINE TURBINE
HUB DIAMETER, IN.	3.13	4.62	8.30	11.05	18.45
TIP DIAMETER, IN.	4.69	6.79	12.20	16.23	27.10
RELATIVE AERODYNAMIC SCALE FACTORS	0.68	1.000	1.796	1.331	2.391
			1.000	1.000	1.670
NO. OF NOZZLE VANES	17	17	31	31	31
NO. OF ROTOR BLADES	20	32	58	58	74
NOZZLE	FIXED	FIXED	FIXED & VARIABLE	VARIABLE	VARIABLE
INLET SWIRL ANGLE	0°	0°	0°	0°	-45°

of vane end clearance in the variable nozzle upon turbine stage performance. This rig was used for all power turbine development for the T-700 test bed vehicle engine as well as for the 5650. The larger engine components were simply scaled to T-375 (rig) size. This permitted continued use of existing compressed air supply and dynamometer.

The entire aerodynamic layout, including the power turbine of the T-700 engine, was a strict geometric scale-up of the T-375 engine. As shown in Table 1, the scale factor was 1.331 or 2.390 relative to the original prototype. The T-1200 version required a restagger of the rotor blades in order to operate at the higher air flow and pressure ratio provided by the two-stage compressor.

Power turbine requirements for the 3000/3500-shp (2237/2610-kW) 5650 engine dictated a scale factor of 1.670 relative to the T-700/T-1200 vehicle engine pair (2.223 relative to the cold rig and 3.991 relative to the original prototype). Disk thickness and mass considerations required another increase in the number of rotor blades. The number of rotor blades, 74, in combination with a partial scale-up produced a blade chord dimension that allowed the power turbine to share a common disk contour with the gas producer turbine (see Fig. 2). The relationship between annulus and airfoil scale factors is:

$$\begin{aligned} \text{Annulus scale factor} &= 1.670 \\ \text{Ratio of number of blades} &= 74/58 = 1.276 \\ \text{Airfoil scale factor} &= 1.670/1.276 = 1.309 \end{aligned}$$

Thus rotor solidity of the original prototype was again preserved.

The number of stator vanes in the 5650 was maintained at 31. The required 1.67 scale factor applied to the vane airfoil would have resulted in an undesirable axial length. Axial length was reduced as the vane chord was shortened by another method and for another reason as illustrated in Fig. 7. The exit flow from the turbines situated upstream from the prototype and the two vehicle engine power turbines was very nearly axial in the direction (zero-degree swirl angle). Exit flow from the rotor selected for the 5650 gas producer stage was calculated to have an average swirl angle of -45 deg. (Negative swirl angles denote swirl in a direction opposite turbine rotation.) This swirl would have resulted in an unacceptable incidence loss at the leading edge of the scaled-up T-700 airfoil. The airfoil was reshaped, as shown in Fig. 7, to align its leading-edge angle with the calculated swirl. The accompanying reduction to the airfoil chord also results in a more desirable axial flowpath length.

Finally, the left column of Table 1 shows the latest and smallest turbine stage to evolve from the prototype that pro-

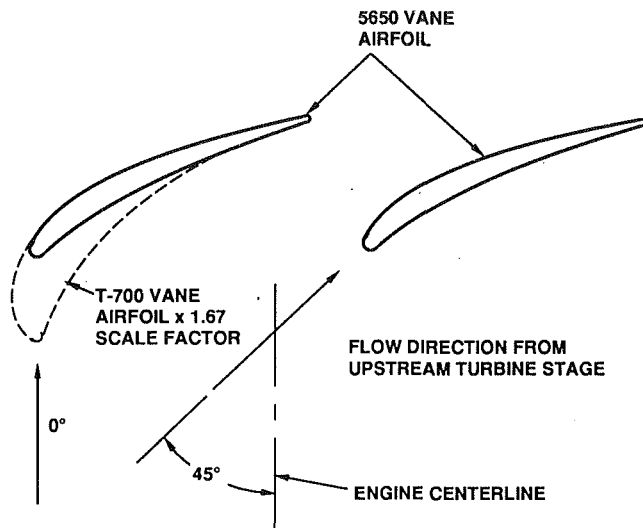


Fig. 7 Development of 5650 power turbine vane airfoil

duced the 5650 power turbine. The original turbine annulus was scaled down by a factor of 0.68 to obtain an appropriately sized stage for an experimental diesel-compounding turbine. The number of blades was reduced from 32 to 20 to avoid excessively thin trailing edges in the integrally cast rotor. This downward extension of the scaling process brings the overall annulus scaling range of a single turbine stage to 5.87:1.

Conversion From Fixed to Variable Nozzle

In approaching the problem of adding a radial axis of rotation to an existing fixed-nozzle vane, three major factors were considered:

- The axis of vane rotation should be located forward of the vane center of pressure as a safety consideration. In the event of loss of control through such mishaps as linkage failure, aerodynamic forces will tend to rotate the nozzle vanes to a more open position. This results in reduced engine temperature and speed associated reduction of load, rather than the obviously less desirable inverse progression.
- To maintain constant vane-to-shroud clearance at both ends of the vane at all angles of rotation, the nozzle shrouds must be concentric spherical zones with their center on the engine centerline. The intersection of the vane rotational axes with the engine centerline should be located axially near the plane of the vane trailing edges. This avoids a reentrant curvature of the flowpath and associated radial component to the flow approaching the rotor. The spherical zones must extend upstream far enough to enclose the entire leading-edge rotation envelope. At the nozzle exit the shroud must enclose the vane trailing edges over their normal operating range of rotation only, excluding braking excursions.
- The envelope of rotation of the vane trailing edges must, of course, clear the rotor blades during braking excursions. The axial extent of this envelope will be determined in part by the location of the vane pivot axis.

Once the prototype turbine stage was scaled up to T-375 engine size as shown in Table 1, the nozzle vane pressure loading was analytically determined. First, the total pressure load and location of the center of pressure were determined from velocity distributions for airfoil sections at several radial locations. The center of pressure for these individual sections was found to lay at approximately the same location relative to the total chord length. Integration of these data over the entire vane span produced the results shown in Fig. 8.

A single resultant pressure force F acts on the pressure sur-

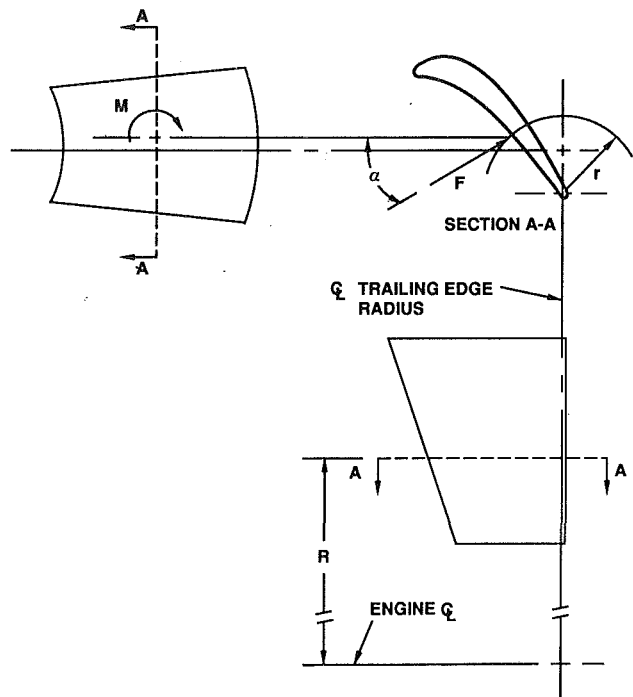


Fig. 8 Nozzle vane pressure load and center of pressure

face of the vane in a plane located a distance R from the engine centerline. The line of action of force F is inclined at an angle α with an engine centerplane and passes at a distance r from the centerline of the airfoil trailing edge radius. In addition, due to the combined effect of vane taper and twist, a small residual moment M is required to complete the aerodynamic force balance.

These results allow the location of the vane pivot axis to be selected and provide the mechanical designer with the necessary input to the calculation of bushing loads, friction, and actuation forces.

Pivot axis definition for the T-375 vehicle engine is illustrated in Fig. 9. The aerodynamic torque arm " l " was selected to ensure a positive nozzle opening torque over the normal operational range of vane angles and engine air flow rates. Factors setting an upper limit on l are total actuation force required to close the nozzle against aerodynamic forces and the axial extension of the trailing-edge rotation envelope.

The inclination angle of the vane pivot axis γ was governed by the factors previously mentioned in connection with the shape of the spherical shroud zones. It was at this point that the decision was made to scale up the number of nozzle vanes rather than their chord. The longer chord of the prototype vane required that the spherical shroud zones extend so far upstream (and radially inward) that they create difficulty in designing a satisfactory diffusion schedule into the connecting duct from the gas producer turbine.

The axis of rotation was defined for each airfoil section by coordinates x and y , relative to the existing airfoil stacking axis. A further refinement might be to convert the pivot axis to a new stacking axis, redefining the airfoil sections by projecting them onto planes perpendicular to the pivot axis. Since this would impact only nonrecurring tooling costs, it was judged not to be cost-effective and the pivot axis was allowed to remain separate from the airfoil stacking axis.

After locating the vane pivot axis to satisfy aerodynamic torque and spherical shroud requirements, it was necessary to increase the axial spacing between the nozzle and rotor to obtain clearance between the nozzle vane trailing-edge rotation envelope and the rotor blades. Past experience indicated that any significant effect of axial spacing on stage efficiency would

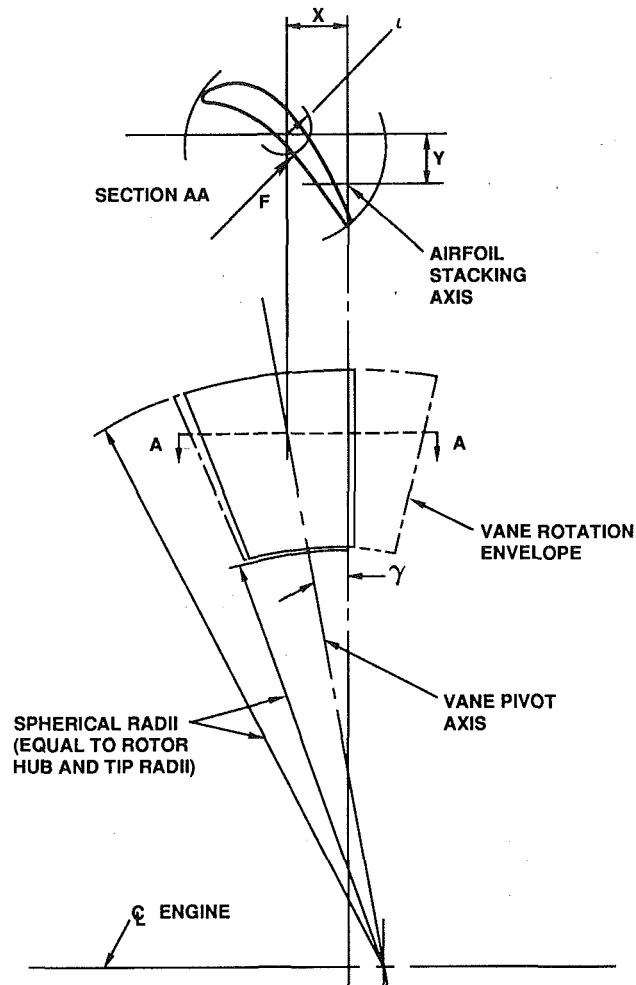


Fig. 9 Variable nozzle vane pivot axis definition

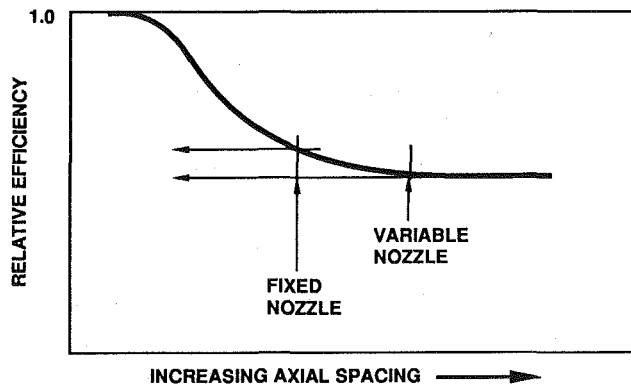


Fig. 10 Generalized relationship of turbine efficiency to axial spacing between nozzle and rotor at a constant pressure ratio

lay in the region of very close spacing, closer than in the fixed nozzle prototype (see Fig. 10).

As noted in Table 1, the T-700 engine power turbine was a total geometric scale-up of its T-375 counterpart. This scale-up was applied throughout the actuator and mechanical linkage and the aerodynamic force analysis just described for the smaller engine served the entire development program for both vehicle engines.

The reduced chord and revised leading-edge angle of the Model 5650 nozzle vane required a repetition of the vane aerodynamic force analysis as well as the process of selecting the

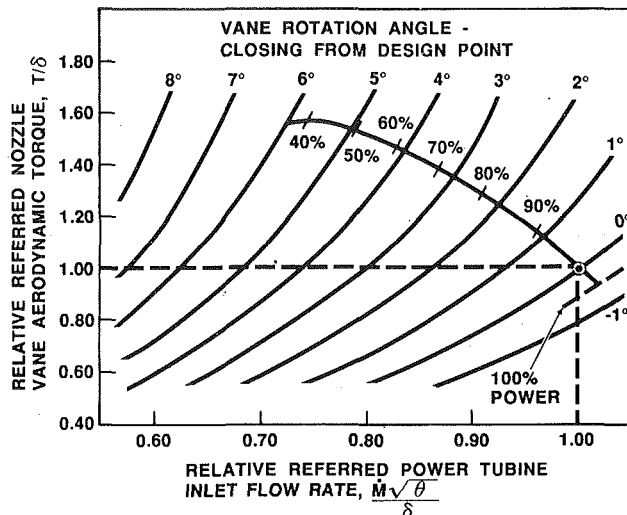


Fig. 11 Calculated 5650 power turbine vane aerodynamic torque "map" with engine operating line

pivot axis location. As in the vehicle engines, this single-point force analysis provided a starting point for the design of the nozzle actuation and control system. The continuation of the 5650 development program toward a pilot production phase permitted a more detailed analysis of nozzle vane aerodynamic forces. More extensive engine control development, especially in connection with generator set applications, also required more detailed information on actuation forces. Nozzle vane aerodynamic torque was now calculated for various combinations of vane rotation angle and power turbine inlet flow. The resulting nozzle vane torque map is shown in Fig. 11. An engine operating line plotted on this map shows the peak aerodynamic torque to occur at approximately 40 percent of maximum power where the vanes are at their most closed position. The peak torque is approximately 59 percent above that calculated for the design point angle and flow. While this torque level is within the reserve capacity designed into the actuation system, this evaluation provided some very useful insights into the dynamic behavior of the engine and its control system.

Nozzle Throat Area Variation

The rate at which turbine stage swallowing capacity varies with vane angle was a necessary input to the design of the nozzle mechanical linkage and the associated control logic. Over small variations of passage shape, passage flow coefficient remains constant. Thus swallowing capacity is directly proportional to passage area. Passage width as a function of mean stream line length was calculated for several radial sections using the BLADES computer code. Input and output parameters for BLADES are defined in Fig. 12. Throat width and location were determined for values of vane angle β . This incremental area is trapezoid of height equal to the radial distance between the boundary airfoil sections and bases equal to their respective throat widths. Total passage area is the sum of these increments plus and minus small circular segments at the shrouds. Area is a function of airfoil shape and angle only and its variation with vane angle is the same for any pivot axis location.

The variation of throat area with vane angle is shown in dimensionless form in Fig. 13. Over the normal operating range, this characteristic is identical for both the vehicle engine nozzle vanes and those in the 5650, since their contours are identical in the throat region when drawn to the same scale. As the vanes are rotated past approximately 25 deg open ($\beta = -25$ deg) a throat is no longer definable at the vane trailing edge. The nozzle passages are converging-diverging over their

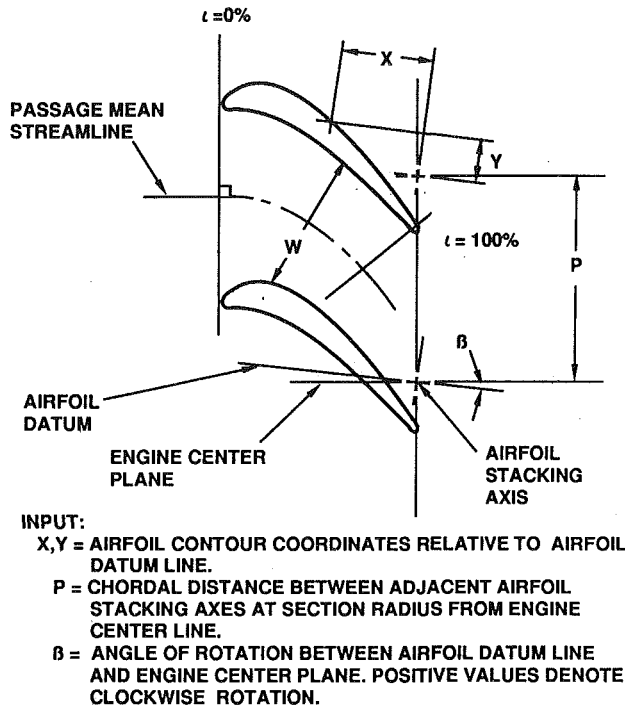


Fig. 12 "BLADES" computer code input and output

range of maximum area and become fully diverging as they are rotated further. In this region, due to its reduced camber, the 5650 vane has the larger flow area for a given angular position.

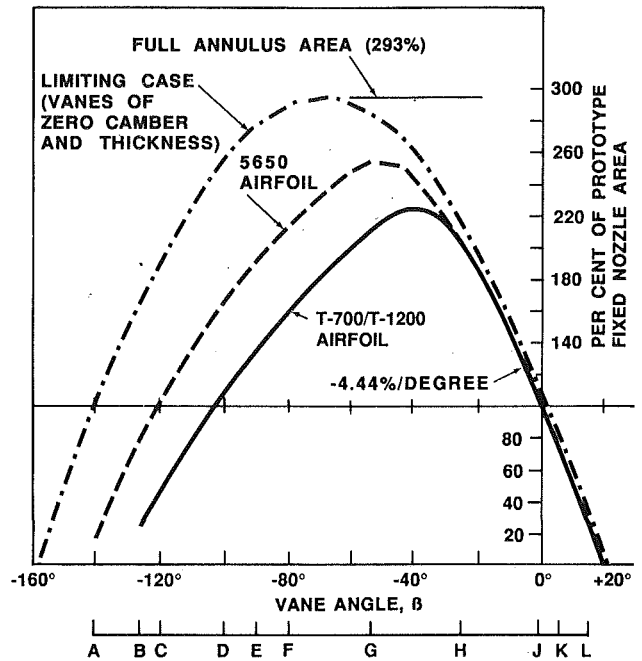
It is of academic interest to note that the area versus angle characteristic of any conceivable vane airfoil will lay within the limiting case shown in Fig. 13. This curve represents a vane of zero thickness and zero camber or, simply swirling flow in an open annulus. The limiting case is a sine curve located out-of-phase with the vane angle, β , by an angle equal to the complement of the exit angle of the real vane for which β was defined.

Data from Fig. 13 were used to determine various actuation linkage and control design parameters. The sensitivity of area to angle, 4.44 percent/deg, was used to determine various control gain levels and the required recursion (sampling) rate for the closed-loop electronic control. The commanded engine start position, $\beta = -53$ deg for the 5650, was set at the point of maximum area. The maximum travel in the braking direction was set at 120 deg for the vehicle engine allowing a 6-deg margin from vane leading-edge mechanical contact. Later engine braking tests showed that the interaction of mass flow capacity and rotor entry angle provided maximum braking effort in the region of 90 to 100 deg of opening travel. This led to the selection of $\beta = -80$ deg for the maximum retard position in the 5650. Thus, during the download transients, additional vane slewing time is not spent in obtaining a very small increment of rotor braking.

Passage shape and approximate flow configuration in the 5650 variable nozzle is shown in Fig. 14 for engine starting, full and part-load operation, and maximum rotor braking (retard) position. The position of maximum braking effort for the vehicle engine nozzle is shown in Fig. 15.

Cold Rig Testing

The power turbine components for the T-375 engine were



- A. -141° VANE LEADING EDGES CONTACT, 5650
- B. -126° VANE LEADING EDGES CONTACT, T-700/T-1200
- C. -120° MAXIMUM ACTUATOR TRAVEL, T-700/T-1200
- D. E. -100° TO -90° MAXIMUM BRAKING EFFORT, T-700/T-1200
- F. -80° MAXIMUM ACTUATOR TRAVEL, 5650
- G. -53° START POSITION, 5650
- H. -25° PASSAGE THROAT BECOMES DEFINABLE AT VANE TRAILING EDGE
- J. -1° 5650 RATED LOAD POSITION
- K. $+6^\circ$ 5650 PART LOAD POSITION
- L. $+15^\circ$ VANE TRAILING EDGES CONTACT

Fig. 13 Variable nozzle throat area as a function of vane angle

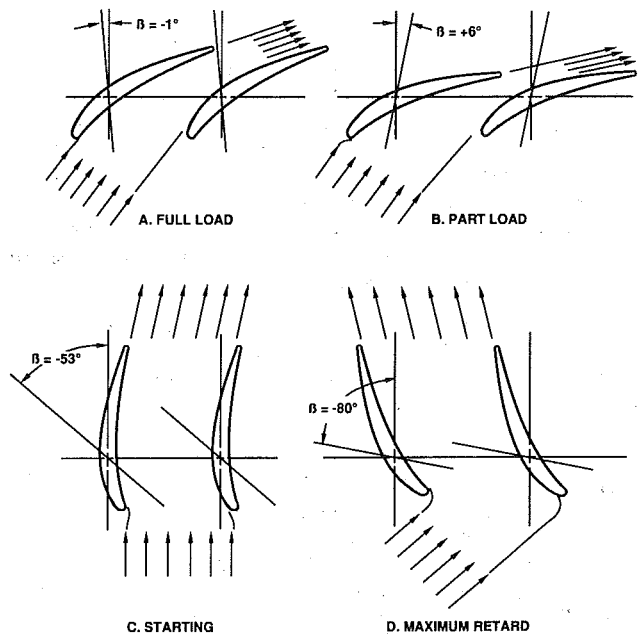


Fig. 14 5650 nozzle vane positions

built into a cold turbine test rig, as shown in Fig. 16. A conventional water brake dynamometer was driven by the power turbine through a vehicle engine reduction gearbox. Gearbox losses were previously determined in a back-to-back test of

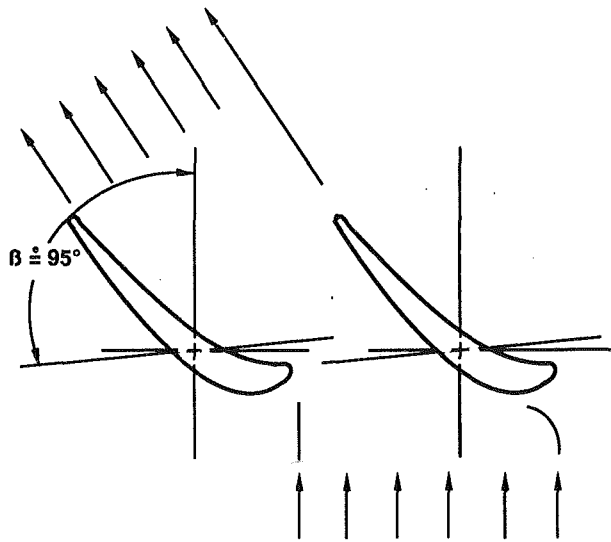


Fig. 15 T-700/T-1200 nozzle vane position at maximum braking effort

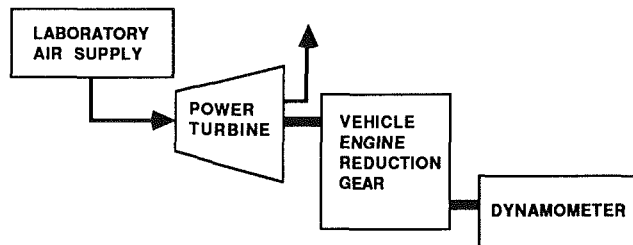


Fig. 16 Schematic of power turbine cold test rig

two boxes. This enabled the use of dynamometer readings to track aerothermal measurements of turbine work output. A locking adjustment mechanism on variable-nozzle linkage set various vane angles. In addition to the variable nozzle, the rig also had a conventional fixed nozzle to allow evaluation of losses associated with a variable nozzle, such as vane and clearance and pivot bushing leakage. All power turbine development for both vehicle engines and the 5650 was conducted using this rig. Aerodynamic components for the larger engine were used geometrically scaled back to the T-375 size for rig test. Most cold rig testing involved the development of power turbine rotor configurations for various engine matching and rating requirements. Two important tests, however, related to the variable nozzle and its application, are as follows:

- In developing the mechanical designs of the three engines with variable nozzles, vane end clearance was critical because of thermal expansion. Various mechanical designs required differing clearance values and the effect of clearance on stage efficiency was a needed input to tradeoff studies. Figure 17 shows the effect of vane end clearance determined from rig tests of the vehicle engine nozzle in comparison with predicted results based on method by Dunham and Came (1970).

2 Caterpillar modified the Navy-NASA computer code NNEP (Fishback, 1975; 1980) for use in predicting turbine engine performance from component maps. This program is especially tailored for engines using variable geometry components and requires 3-dimensional component maps that are layered according to performance at various levels of the variable parameters. In the instance of a variable-geometry turbine, the layered variable is nozzle vane angle. Using scaled components, the cold test rig was used to generate a map for the 5650 power turbine that appears as shown in Fig. 18. The program has proved quite accurate in predicting 5650 engine

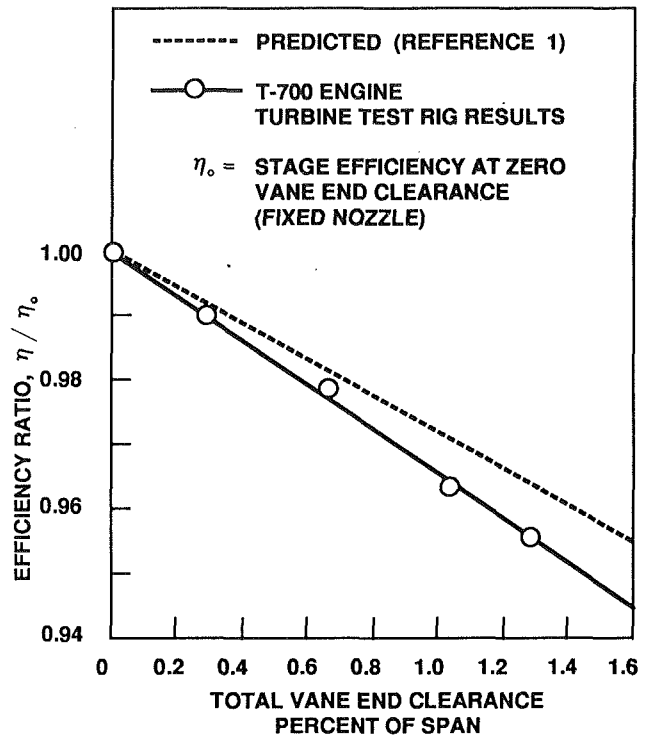


Fig. 17 Effect of variable nozzle vane end clearance on efficiency

performance. It has been used extensively in evaluating potential improvements, such as intercooling.

Engine Braking Tests

Engine braking ability was evaluated by coupling a complete T-700 vehicle engine to a motoring electric dynamometer. This combination supplied the reverse power input necessary to maintain engine output shaft speed while in the braking mode. Test results are shown in Figs. 19 and 20. Maximum braking capability was (-)42 percent of rated power output. This compares to 5 to 15 percent for a fixed-geometry two-shaft gas turbine. Precise values of negative power turbine efficiency in this test are not certain because the test engine carried only minimal turbine flowpath instrumentation.

In assessing the results of this braking test, we are not dealing with torque applied to the shaft by the turbine in the direction opposite to that of its rotation. Such a reversing turbine would require that its rotor blades also be rotated (and reshaped) such that they are pitched for opposite rotation. In a braking mode, a power turbine with a variable nozzle performs as an inefficient compressor, absorbing power from its output shaft while continuing to turn forward. The nozzle vane angle, at which maximum braking effort is obtained, is the angle that provides a combination of flow and pressure ratio requiring maximum power input to the power turbine-turned-compressor. Review of Figs. 14(D) and 15, showing nozzle passages with the vanes in a maximum braking mode, also will suggest that aerodynamic flow losses at this vane angle also contribute significantly to power absorption.

In a braking test, conducted on a fired engine, the engine compressor acts as a supercharger to the inlet of the power turbine-turned-compressor. Thus the latter's power absorption (braking effort) will be the greatest with the gas producer at idle speed where the degree of supercharge is the least.

Marine Applications

Interest in the gas turbine as a marine power plant began when the turbine demonstrated its unique abilities in aircraft

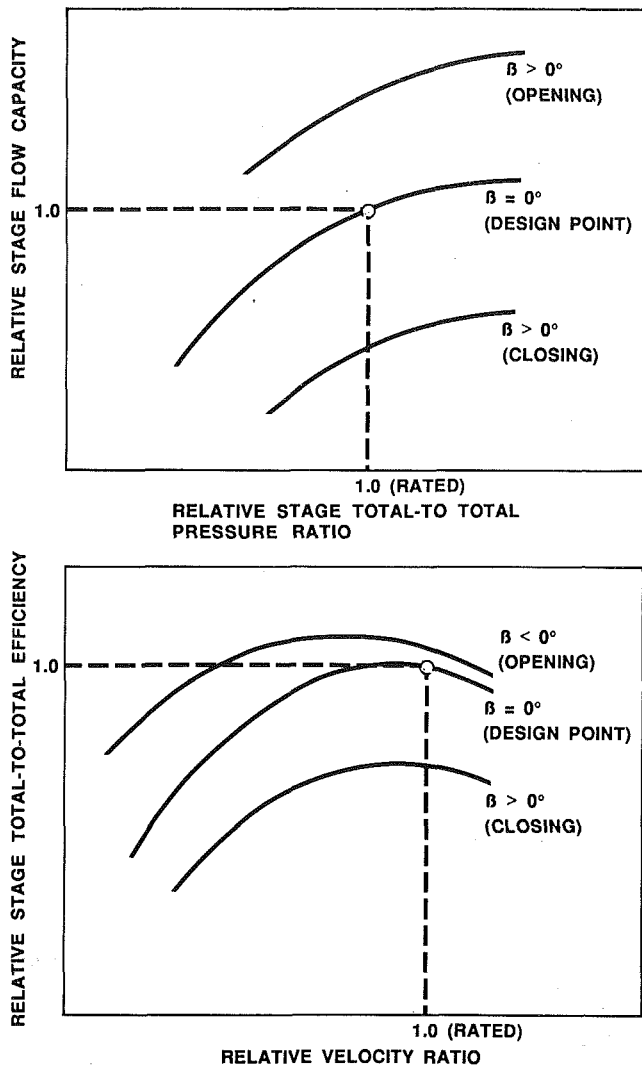


Fig. 18 Variable power turbine map

propulsion during World War II. The more important benefits of gas turbines to both the ships designers and operators include:

- Light weight;
- Small installation space;
- Low noise and vibration;
- Low maintenance;
- Little or no seawater cooling;
- Waste heat easily recovered for auxiliary use;
- Additional energy directly available as compressed air.

Most successful marine gas turbines have been simple cycle. Complex cycles have met with limited success for a variety of reasons. Early recuperator designs were bulky and their long thermal response times prevented rapid load changes. Control of these cycles was difficult before the development of solid-state electronic systems.

Simple-cycle gas turbines operate at an acceptably high thermal efficiency only at their full-load design point. Such both marine propulsion and auxiliary power plants seldom operate at full load, the advantages of gas turbine power are obtained at a high price in terms of fuel consumption.

In Solar's 5650 gas turbine, the combination of the compact primary surface recuperator with a variable-power turbine nozzle and programmable electronic control produce the results shown in Figs. 21 and 22. Normally, a two-shaft free power

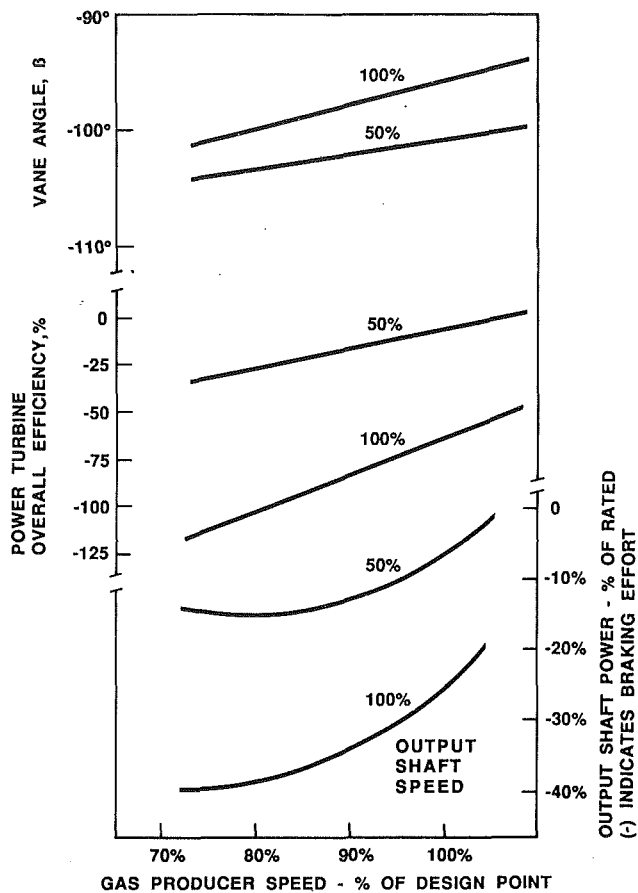


Fig. 19 T-700 engine braking test results

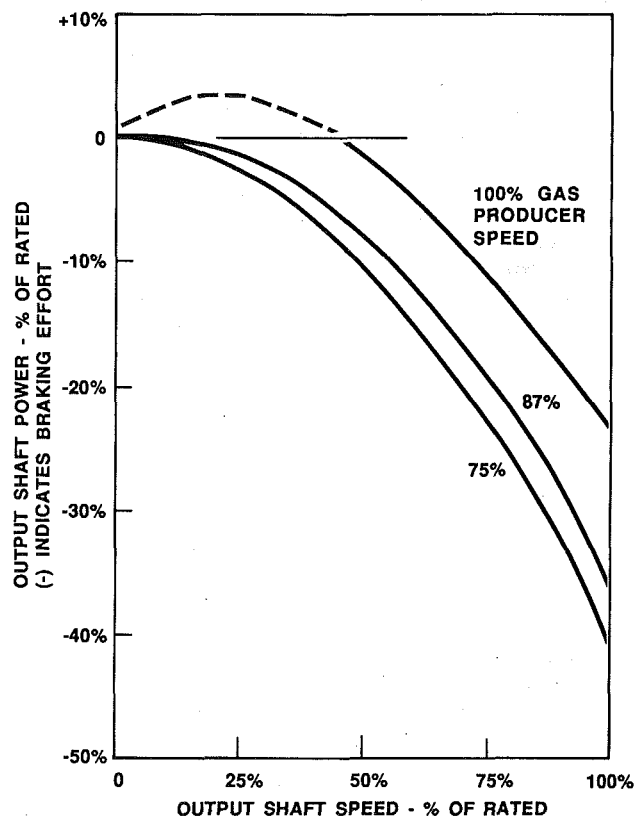


Fig. 20 T-700 engine braking effort versus output shaft speed

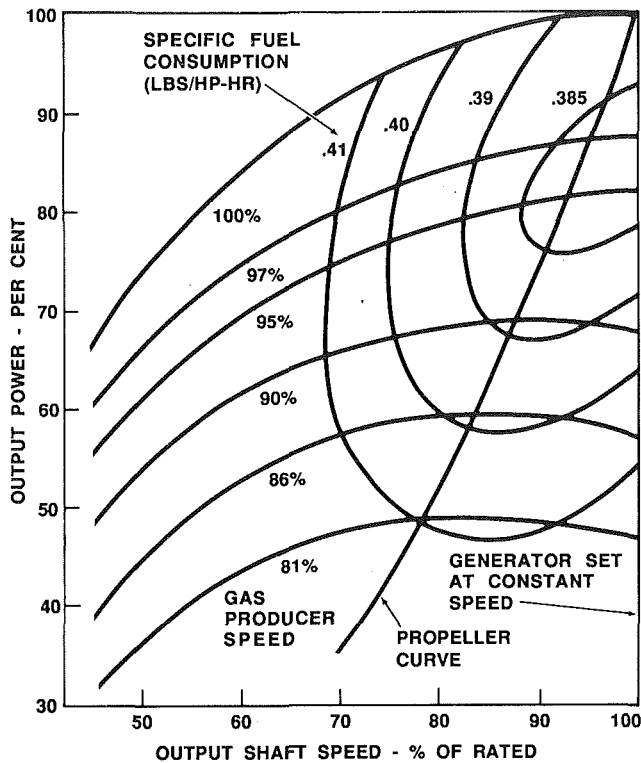


Fig. 21 5650 variable speed performance

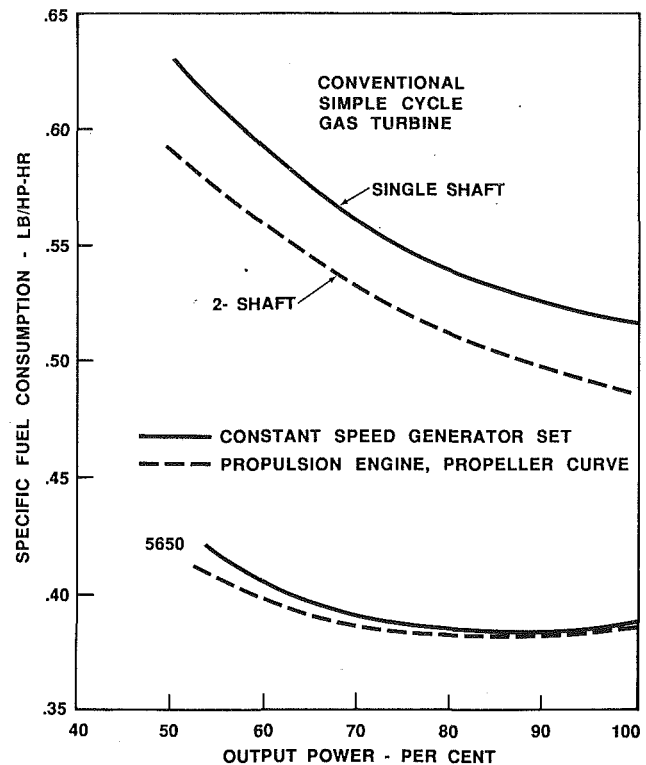


Fig. 22 Solar 5650 marine gas turbine fuel consumption

turbine engine is chosen for propulsion, and a single-shaft, constant-speed design is chosen for auxiliary (a-c) electrical power production. Typical fuel consumption curves for these two simple-cycle types are shown in Fig. 22 in comparison with those of the 5650, a single design applicable to both propulsion and auxiliary power.

The variable-power turbine nozzle is of particular importance in auxiliary power applications because it eliminates the thermal lag of a recuperator as a deterrent to rapid load changes. Additional opportunities for optimizing the electrical frequency control characteristics of the two-shaft 5650 are discussed by Mills and Karstensen (1986).

In recent studies, it was found that fuel for auxiliary electrical power is reduced 38 percent when single-shaft, simple gas turbines are replaced by 5650's. The subject of the study was a Naval combatant ship with its total power demand divided between two 2500-kW generator sets. Similar reductions in fuel usage for propulsion by 5650's can be shown for smaller vessels.

The design of the 5650 can be readily revised for conversion to an intercooled-recuperated cycle. This provides a major increase in power output, accompanied by a significant improvement in fuel economy.

Summary

The progress of a single-turbine aerodynamic design from a small, fixed-geometry stage to a variable geometry industrial engine power turbine has been traced. The process continued for well over a decade of changes to product goals and specifications driven by changing domestic and world energy and materials economics. The end result, a turbine stage almost exactly four times the diameter of the original prototype, has

validated the carefully chosen principles used in conversion to variable geometry and in rescaling the stage to match larger power requirements. The results, shown in Figs. 21 and 22, suggest that the goal of diesel performance in a gas turbine has indeed been attained.

The material in this paper is related primarily to turbine flowpath aerodynamic design. The authors plan to discuss the mechanical design of these variable-geometry power turbine nozzles, as well as the development of related control systems in subsequent papers.

Acknowledgments

The authors wish to credit the accomplishments described in this paper to a sizable team of Caterpillar design, test, and analytical engineers as well as to numerous management and support persons. In particular, major technical contributions by Messrs. E. G. Meints, D. L. Kramer, P. W. Reisdorf, B. C. Smith, and D. E. Gebhart are acknowledged.

References

- Dunham, P., and Came, P. M., 1970, "Improvements to the Airley-Mathieson Method of Turbine Performance Prediction," ASME Paper No. 70-GT-18.
- Fishbach, L. H., 1975, "NNEP—The Navy NASA Engine Program," NASA Technical Memorandum TM X-71857.
- Fishbach, L. H., 1980, "Computer Simulation of Engine Systems," NASA Technical Memorandum 7929D.
- Karstensen, K. W., 1986, "Intercooled Gas Turbine," Publication No. 86/0166, The Gas Research Institute.
- Mills, R. G., and Karstensen, K. W., 1986, "Intercooled/Recuperated Generator Drive Engine," ASME Paper No. 86-GT-70.
- Wiggins, J. O., and Waltz, G. L., 1972, "Some Experiences in the Scaling of the NASA 8-Stage Transonic Axial Flow Compressor," SAE Paper No. 720711.

Surface Roughness Measurements on Gas Turbine Blades

R. P. Taylor

Thermal & Fluid Dynamics Laboratory,
Mechanical and Nuclear Engineering
Department,
Mississippi State University,
Mississippi State, MS 39762

Results are presented from profilometer measurements of the surface roughness on in-service turbine engine blades from F-100 and TF-39 aeroengines. On each blade, one roughness profile is taken in the region of the leading edge, the midchord and the trailing edge on both the pressure and suction sides for a total of six profiles. Thirty first-stage turbine blades are measured from each engine. Statistical computations are performed on these profiles and the root mean square height, skewness and kurtosis of the roughness height distribution are presented along with the correlation length of the autocorrelation function. The purpose of this work is to provide insight into the nature of surface roughness characteristics of in-service turbine blades which can be used in the development of scaled laboratory experiments of boundary layer flow and heat transfer on turbine engine blades.

Introduction

Surface roughness can have a large effect on the skin friction and heat transfer of turbine engine blades. Some data (Rivir, 1986) indicate that rough blades can have heat transfer rates that are 100 percent greater than the rates on equivalent smooth blades. As shown by Taylor (1986), turbine engine blades, which have been in service for a few hundred cycles, can have significant roughness. Typical average roughness heights are found to be from 1 to 12 μm (50–500 microin.). Unfortunately, traditional measures of surface roughness such as average roughness height and root mean square roughness height are inadequate for the determination of the effect of surface roughness on fluid flow and heat transfer. Two surfaces with the same average roughness height can have different heat transfer rates and skin friction.

For deterministic roughness (cones or hemispheres in some known array), it is fairly straightforward to tell when surfaces are geometrically similar. Therefore, a few well-chosen experiments can be used to calibrate computational models for a broad range of deterministic surfaces. However, for randomly rough surfaces such as those which occur naturally on turbine blades, it is not obvious (and perhaps impossible) to say when two surfaces are geometrically similar. If two surfaces are randomly rough, then the most that can be said is that they are statistically equivalent.

This idea of statistical equivalence is important for both the development of computational models and for the selection of experimental test surfaces. For computational models the averages of the predicted values of skin friction and heat transfer rates for a sample of statistically equivalent surfaces should be essentially the same as the average values for the entire population of statistically equivalent surfaces. No two random surfaces have the exact same skin friction and heat transfer

rates but, by performing computations for a small sample of statistically equivalent surfaces, the mean and standard deviation of that class of surface should be obtained to a good approximation. For experimental tests, simple flows such as fully developed pipe flow or flat plate boundary layer flows will be used in the initial experiments. For these tests artificially created randomly rough surfaces will be used as test surfaces. If these tests are to be used to estimate the performance of real surfaces, then the test surfaces should have roughness which is statistically equivalent to the real surfaces.

In this paper, data are presented which give a statistical description of the surface roughness profiles on in-service turbine blades. Two military engines were selected: a TF-39 (transport plane) engine and an F-100 (fighter plane) engine. Since the major mission of our laboratory is the investigation of the effects of surface roughness on heat transfer, only first-stage turbine blades were selected.

Measurement Techniques and Statistical Computations

A random surface profile can be completely defined statistically by two characteristics—the height probability distribution function and the autocorrelation function; see Whitehouse and Archard (1970) for example. To study the character of the roughness on in-service turbine blades, the surface profile measurements and statistical computations were made as discussed next.

Surface profiles were collected using a Rank-Hobson-Taylor Surtronic III profilometer. The profilometer was set with a cutoff of 0.8 and a range of 99.9. Depending on the magnitude of the roughness, the vertical magnification was set between 200 and 1000, and the horizontal magnification was set between 40 and 100. All traces were taken near the midspan of the blade, and the direction of the traces were from the base toward the tip. All traces were approximately 1.5 cm long.

This stylus profilometer is capable, by setting the appropriate amplification ratio, of resolving surface detail between 0.1 μm and 100 μm . The major function of the instrument used in this

Contributed by the International Gas Turbine Institute and presented at the 34th International Gas Turbine and Aeroengine Congress and Exhibition, Toronto, Ontario, Canada, June 4–8, 1989. Manuscript received at ASME Headquarters February 14, 1989. Paper No. 89-GT-285.

program was the $x-y$ recording ability. The instrument also has some internal computational ability and can compute the average roughness height, the maximum peak-to-valley height, and the number of peaks per unit profile length, and other similar parameters. The parameters, which are computed directly by the instrument, were developed for surface-to-surface contact analysis, and many are of limited direct use for boundary layer analysis.

Once the profile records were obtained, they were digitized and conditioned for statistical computations. The profiles were digitized with an $x-y$ digitizing device. The record was placed on the digitizer bed, the profile was followed by hand and selected points were entered into the computer as $x-y$ coordinates. The x -spacing of these points was at most $1/5$ of the major structural scale of the roughness. The $x-y$ coordinates were then converted into the physical coordinate system of the record by using the proper scaling ratios. Since the turbine blades were curved, the profilometer picked up some of the trends of the substrata. These trends must be removed for proper statistical analysis of the roughness. This trend removal was easily accomplished by least-squares fitting of a polynomial to the $x-y$ data. This trend curve was then used as the new origin of the y -coordinate. The trend removal procedure resulted in a mean surface height $\bar{y} \approx 0$.

Once the surface profile was digitized and conditioned as just discussed, the following statistical functions and parameters were computed: (1) Height distribution function; (2) Autocorrelation function and correlation length; (3) Root mean square height, skewness and kurtosis of the height distribution.

The height distribution is computed by dividing the range of surface heights into regions or bins and counting the number of occurrences in each bin. The number of bins is set based on the total number of points, N , in the record by $N_{\text{bin}} = N/20$. To decide in which bin a given point belongs, the following algorithm is followed

$$\text{Compute: } C = \frac{y_{\text{max}} - y_{\text{min}}}{N_{\text{bin}}} \quad (1a)$$

$$\text{Compute: } J = \frac{y_i - y_{\text{min}}}{C} \quad (1b)$$

The bin, index j , in which y_i falls is the integer $j = \max$ integer $< J$. The number of points, n_j , in each bin is determined by adding 1 to n_j each time j is encountered. The probability histogram is then computed by $p_j = n_j/N$ for $j = 0, 1, \dots, N_{\text{bin}} - 1$.

The autocorrelation function is computed by evaluating the integral

$$R_x(\tau) = \lim_{L \rightarrow \infty} \frac{1}{L} \int_{-L/2}^{L/2} y(x)y(x+\tau)dx \quad (2)$$

The finite sample approximation for equation (2) is

$$R_{xj} = \frac{1}{N-j} \sum_{i=1}^{N-j} y_i y_{i+j}; j=0, 1, \dots, m \quad (3)$$

where $m = N/10$.

The variance is computed by evaluating

$$V = \frac{\sum_{i=1}^N (y_i - \bar{y})^2}{N} \quad (4)$$

Here following Sachs (1982) the variance is defined based on N and not $N-1$ as is usual when the computed mean is used in equation (4). This is done for consistency when the variance is used to normalize the higher moments below. For all sample sets in this paper, $N > 100$; so, there is very little difference in the variance when N is used in place of $N-1$. The root mean square, rms, height is computed by

$$S = \sqrt{V} \quad (5)$$

The skewness is computed by evaluating

$$Sk = \left[\frac{\sum_{i=1}^N (y_i - \bar{y})^3}{N} \right] / S^3 \quad (6)$$

and kurtosis is computed by evaluating

$$Ku = \left[\frac{\sum_{i=1}^N (y_i - \bar{y})^4}{N} \right] / S^4 - 3 \quad (7)$$

Again, following Sachs (1982), the (-3) is included in equation (7) to cause $Ku = 0$ for the normal (Gaussian) distribution. Positive skewness indicates that heights above the mean tend to be larger than heights below the mean. That is, the profile tends to have more high peaks than deep valleys. Negative skewness indicates a tendency to favor deep valleys over high peaks. The kurtosis is a measure of the peakedness of the probability distribution. A positive kurtosis indicates a tendency to have relatively smooth areas with a few large peaks or valleys. This is demonstrated in the following section.

As just stated the profilometer can resolve surface detail on the order of $0.1 \mu\text{m}$. The calibration was checked by measuring the roughness on a standard surface which was supplied with the instrument. Therefore, the bias errors associated with the profile measurements were small. These biases cancel out in the computation of the mean height and the autocorrelation. However, the biases do accumulate in the computation of the higher moments (S , Sk and Ku). In any case, these biases are much smaller than the sample variations as will be seen later.

Results of the Turbine Engine Blade Measurements

Profiles were obtained for two sets of first-stage turbine blades, 30 from a TF-39 and 30 from a F-100 engine. The TF-39 blades were all from the same turbine wheel, had shower

Nomenclature

Ku = kurtosis, equation (7)	Rt = maximum peak-to-valley height	Sk = skewness, equation (6)
L = profile length	Rtm = profile mean peak-to-valley height	V = variance, equation (4)
N = number of points in a profile record	R_x = autocorrelation function, equations (2) and (3)	x = surface coordinate
N_{bin} = number of bins in the height probability histogram	S = root-mean-square profile height, equation (5)	y = profile height coordinate
p = probability		\bar{y} = mean profile height = $1/L \int_0^L y dx$
Ra = average profile height = $1/L \int_0^L y dx$		β = 10 percent correlation length

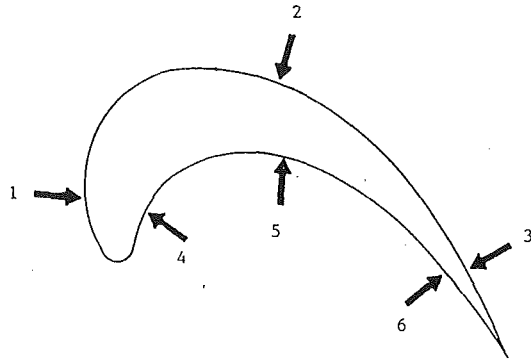


Fig. 1 Approximate trace locations

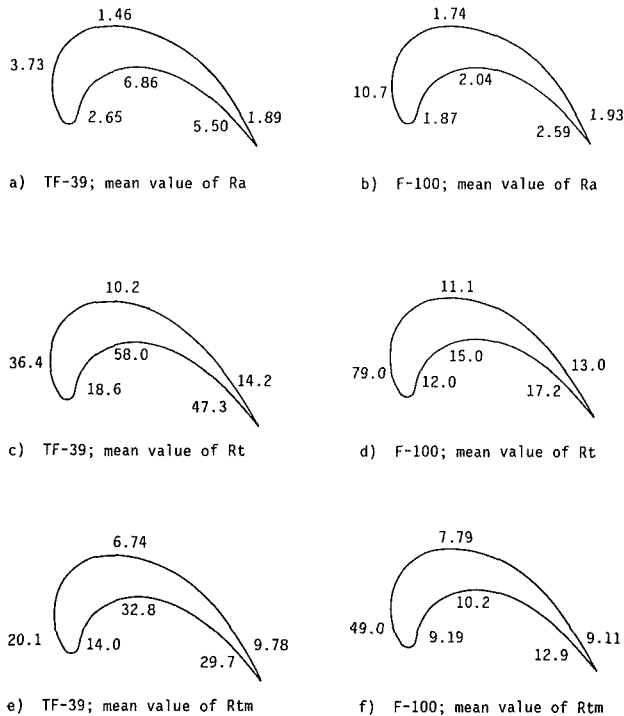


Fig. 2 Summary of the roughness parameters R_a , R_t , R_{tm} ; all values in μm

head cooling, and had a service age of 3402 h. The F-100 blades also were all from the same wheel, had shower head cooling, and had a service age of 1600–1800 cycles. Six profiles were taken on each blade for a total of 360 profiles. Profiles were taken in the region of the leading edge, the midchord, and the trailing edge on both the suction and pressure side. Figure 1 shows the approximate trace location and defines the numbering scheme used—1 for the leading edge suction, etc.

The three parameters which were obtained directly, using the profilometer, were the average roughness, R_a ; the profile maximum mean peak-to-valley height, R_t ; and the profile mean peak-to-valley height, R_{tm} . Figure 2 shows the sample mean value for each of these parameters for both engines. From the figure, it is seen that the TF-39 blades were roughest on the pressure side near the midchord and the trailing edge. The F-100 blades are roughest on the suction side near the leading edge.

In addition, the figure shows that the blades are very rough. A value of 50 μm corresponds approximately to 2000 microin. or 2 mils. The data scatter is large. Table 1 shows the summary of the standard deviation of the R_a -values for each engine.

Figure 3 shows a scattergram of Trace 5 versus Trace 6 for

Table 1 Summary of the R_a (μm) Distribution

Trace	Mean	Std. Dev
TF-39 Engine		
1	3.73	0.933
2	1.46	0.240
3	1.89	0.422
4	2.65	0.329
5	6.86	2.04
6	5.50	1.09
F-100 Engine		
1	10.7	3.04
2	1.74	0.530
3	1.93	0.468
4	1.87	0.301
5	2.04	0.360
6	2.59	0.300

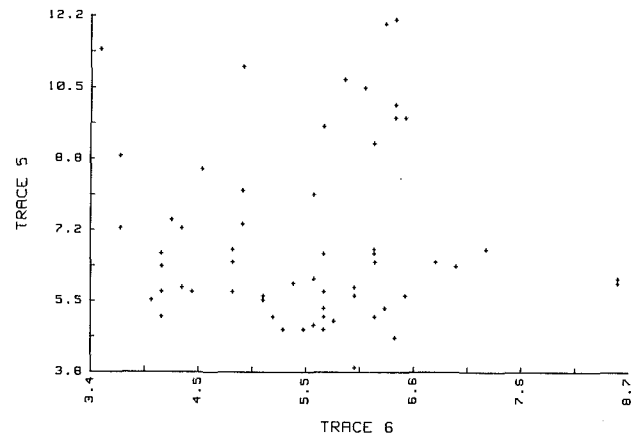


Fig. 3 Sample scattergram of the average roughness, R_a , for the TF-39 blades

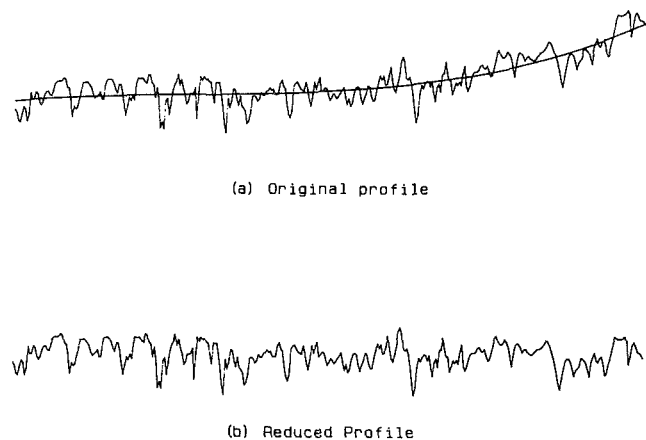


Fig. 4 Roughness profile for trace TF196

the average roughness, R_a , on the TF-39 engine. The purpose of this figure is to demonstrate that there is no correlation between the trace pairs; that is, a rougher than average value at one trace does not indicate that the values for the other traces on the same blade will be rougher than average.

Figure 4 shows a profile record for trace TF196 which is a profile taken on the suction side trailing edge of a TF-39 blade. Part (a) of the figure shows the original profile and the least-squares polynomial which was used to remove the substratum curvature. Part (b) shows the reduced profile. The figure shows that the reduction process conserves the character of the profile roughness. Figure 5 shows the probability distribution histogram and autocorrelation function for this profile. The bars in the probability plot represent the histogram of the height distribution data and the bell curve represents the expected values for a Gaussian distribution. The distribution seems to

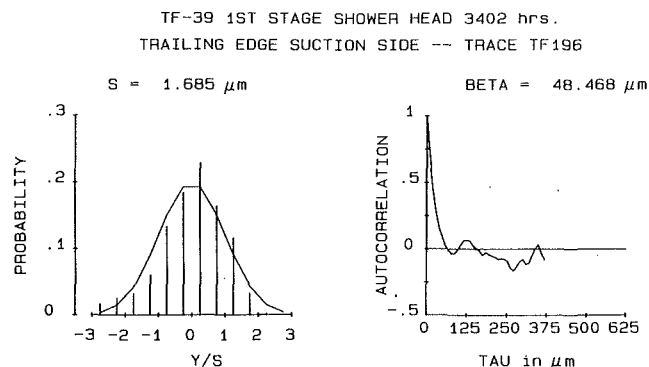


Fig. 5 Results of the statistical computations for trace TF196

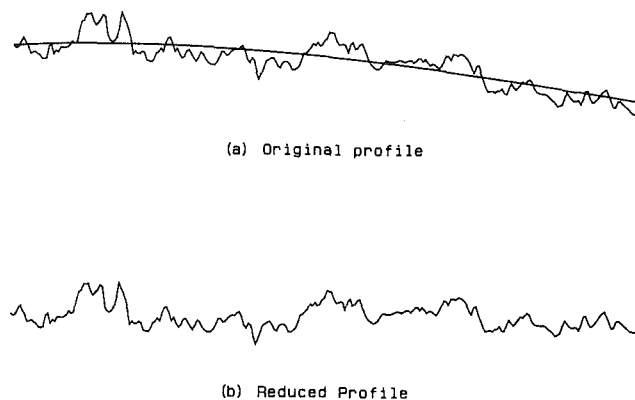


Fig. 6 Roughness profile for trace TF221

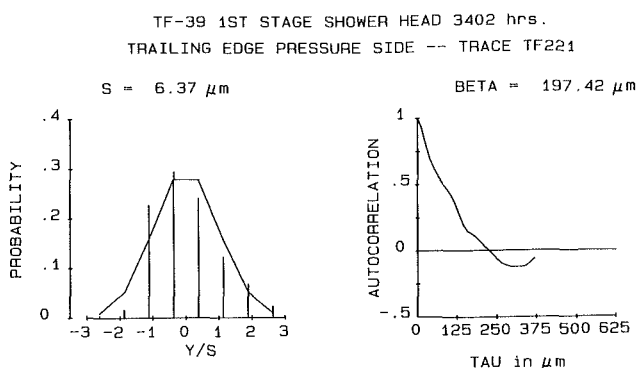


Fig. 7 Results of the statistical computations for trace TF221

loosely match the Gaussian distribution. However, it fails a chi-squared goodness of fit test at a 0.05 level of confidence. The autocorrelation function shows an exponential like decay which is typical of random data. The computed value of skewness is $Sk = -0.988$, and the value of kurtosis is $Ku = 2.86$. These values indicate a tendency to regions of smoothness and a tendency to favor valleys over peaks. Referring back to Fig. 4, we see that the profile crests have rather flat tops and the valleys are sharp and deep.

Figure 6 shows the original and reduced profiles for trace TF221 which is a profile taken on the pressure-side trailing edge of a TF-39 blade. Figure 7 shows the probability distribution histogram and autocorrelation function for this profile. This profile is chosen because of its positive skewness, $Sk = 0.602$, and almost zero kurtosis, $Ku = -0.058$. This indicates that the peaks should dominate over the valleys. Inspection of Fig. 6 shows that this is true. The peaks are moderately higher than the valleys are deep.

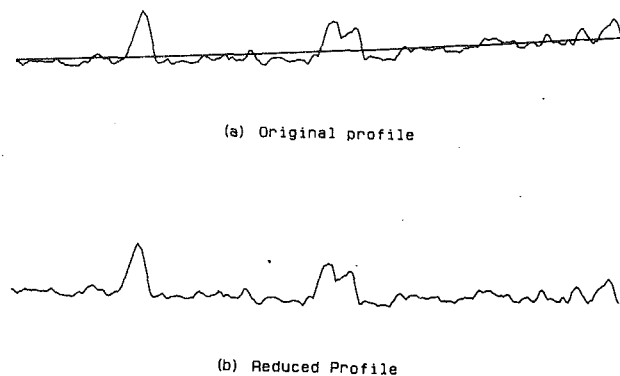


Fig. 8 Roughness profile for trace TF282

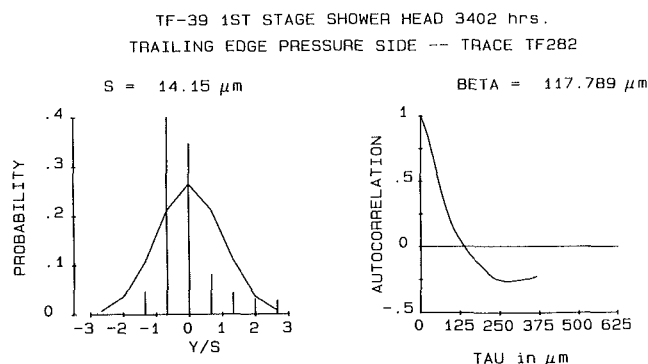


Fig. 9 Results of the statistical computations for trace TF282

Figure 8 shows the original and reduced profiles for trace TF282. This is a profile taken on the pressure-side trailing edge of a TF-39 blade. Figure 9 shows the probability distribution histogram and autocorrelation function for this profile. This profile is chosen because of its large value of kurtosis, $Ku = 5$. The skewness is $Sk = 2.13$. A large kurtosis and a positive skew indicate a relatively smooth surface with a few large peaks. Inspection of the profiles in Fig. 8 demonstrates that this is the case. The profile is comparatively smooth and has two large hills.

A paper of this nature is much too short to give the profiles, histograms, and autocorrelation functions for all 360 profiles. The data are summarized by giving the values of rms height, skewness, kurtosis, and correlation length for each profile. Figures 10-13 show plots of these values for the TF-39 engine. Figure 10 displays the rms height for each profile. The figure shows that the largest roughness magnitudes are at locations 1, 5, and 6—the leading edge on the pressure side. The figure also reveals the large scatter in the data. At trace location 5, the rms height ranges from about $7 \mu\text{m}$ to about $14 \mu\text{m}$ with outliers as large as $23 \mu\text{m}$. The figure also shows that the magnitude of the roughness varies considerably from location to location. Figure 11 shows the skewness for each profile. The figure indicates that the data has a large scatter at all trace locations. The central trend of the data shows a tendency of positive skewness at trace location 1, followed by negative skewness at locations 2 and 3. All the trace locations on the pressure side display a tendency toward positive skewness. Figure 12 gives the kurtosis for each profile. The figure shows that the kurtosis at all locations tends to be positive. The majority of the data at all trace locations lies in the band between -0.5 and 4 . Figure 13 shows the correlation length for each profile. Again, we see a wide range of values at all locations. The rms height is a measure of the height of the roughness, and the correlation length is a measure of the base dimension of a roughness element. Comparison of Figs. 10

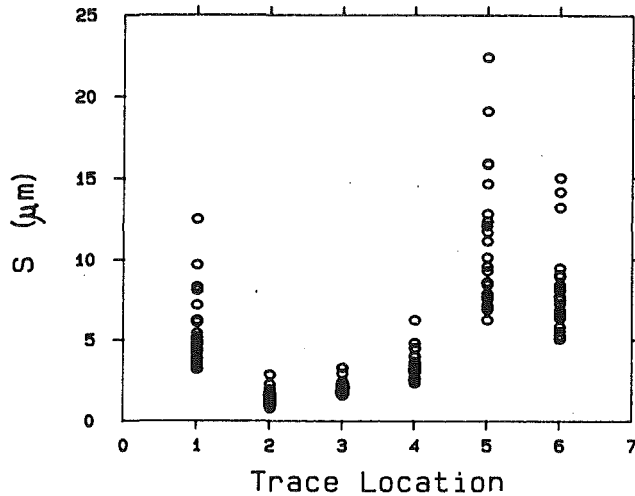


Fig. 10 Summary of the rms heights for the TF-39 engine

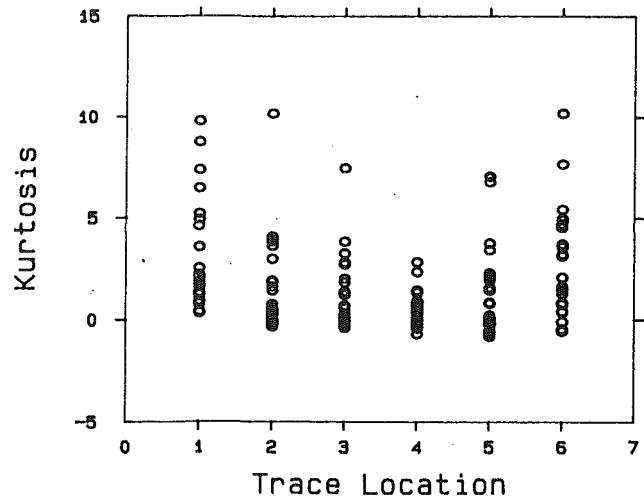


Fig. 12 Summary of the kurtosis for the TF-39 engine

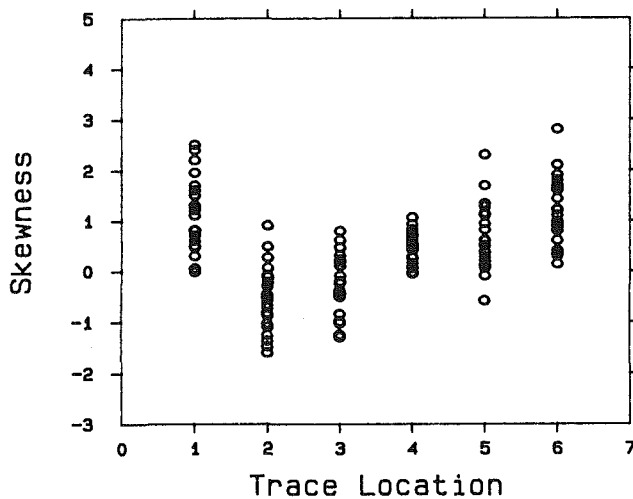


Fig. 11 Summary of the skewness for the TF-39 engine

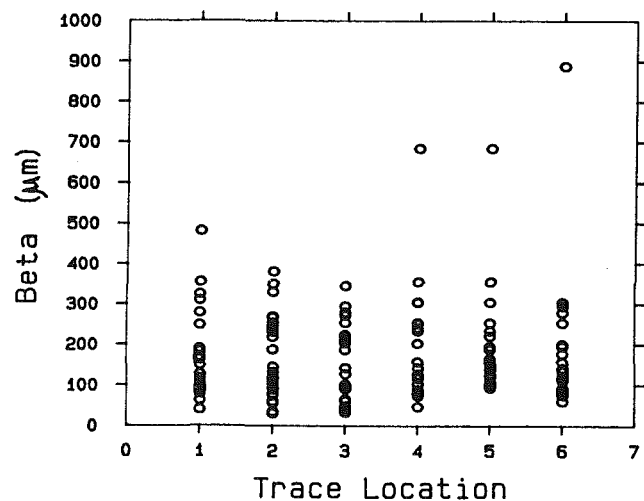


Fig. 13 Summary of the correlation length for the TF-39 engine

and 13 reveals that the roughness is characterized by roughness elements whose height to base ratio is of the order of 0.1.

Figures 14–17 give the same data for the F-100 engine. Figure 14 shows that the roughness magnitude is much greater at trace location 1 than at any of the other trace locations. Figure 15 gives the skewness of the height distribution. Comparison with Fig. 11 shows that the F-100 blades have a skewness central tendency which is more nearly zero than the TF-39 blades. A comparison of Fig. 16 and Fig. 12 shows that, while both the F-100 blades and the TF-39 blades show positive kurtosis, the F-100 blades show a very large value of kurtosis in many cases. A large positive kurtosis indicates a surface that is basically smooth but has a few tall peaks and/or deep valleys. Comparison of Figs. 17 and 14 shows that the aspect ratio (height/base) is very small for all cases except the leading edge suction side. The ratio is of the order of 0.005, and the leading edge ratio is order 0.1.

Often in engineering models of random surfaces, the assumption is made that the profile is Gaussian. Based on the data for skewness and kurtosis previously given, it seems unlikely that the Gaussian model would be appropriate. However, it is an interesting exercise to test the hypothesis that the height distribution functions are Gaussian, using the chi-squared statistic. Table 2 gives the number of profiles for which this hypothesis passes the chi-square test at the 0.05 level of confidence.

This table indicates that indeed the Gaussian distribution is most likely inappropriate for the TF-39 engine. However, for many of the trace positions on the F-100, the Gaussian assumption may be appropriate. In any case, the Gaussian assumption is clearly not appropriate for all trace locations.

Summary

The purpose of this work was to investigate the surface roughness of in-service turbine engine blades. The main ambition was to gain insights into what statistical characteristics the artificially manufactured roughness should have in laboratory flow and heat transfer experiments. The following observations are made:

1 In-service turbine engine blades can be very rough. On the F-100 blades rms heights as high as $30\ \mu\text{m}$ were common with outliers as high as $50\ \mu\text{m}$. The sample mean value of the profile maximum peak-to-valley height for the leading edge suction side of the F-100 blades was $79\ \mu\text{m}$.

2 Both the magnitude and the statistical character of the roughness vary greatly from point to point around the blade. The blade does not have a single roughness value. Therefore, heat transfer and flow experiments should investigate the effect of roughness variation.

3 The Gaussian model for the height distribution function is not universally appropriate. For the present data the Gaus-

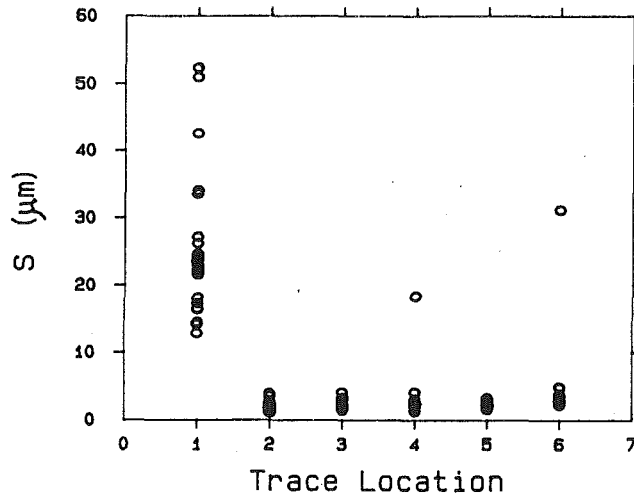


Fig. 14 Summary of the rms heights for the F-100 engine

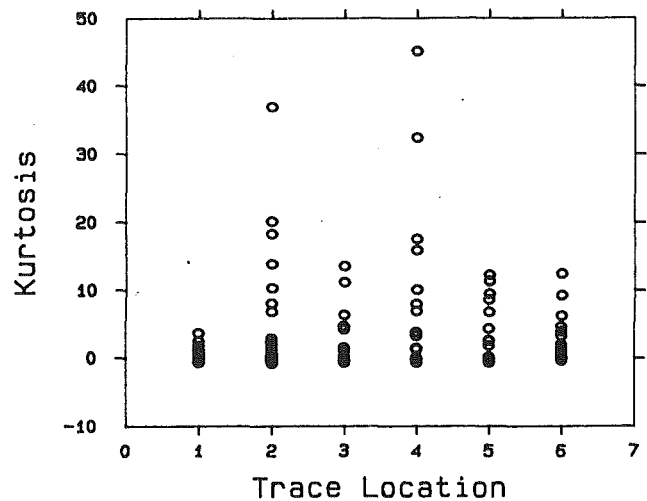


Fig. 16 Summary of the kurtosis for the F-100 engine

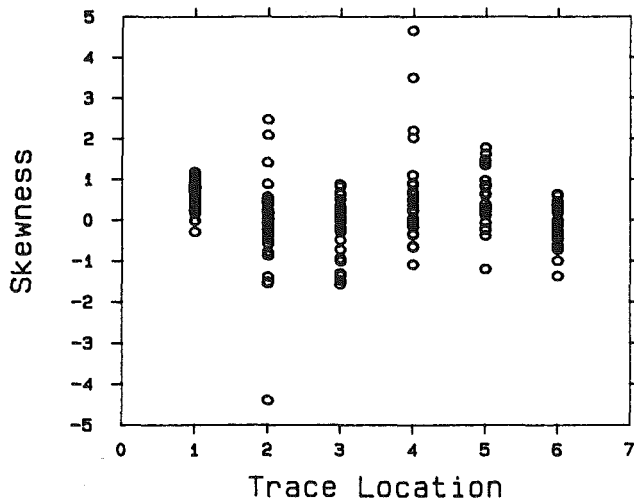


Fig. 15 Summary of the skewness for the F-100 engine

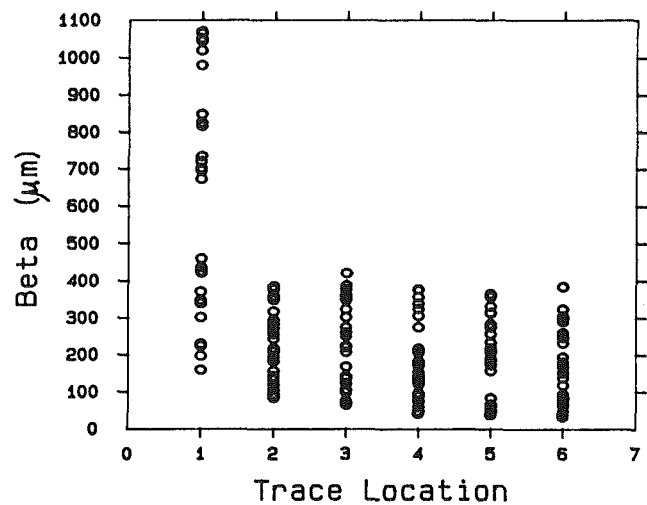


Fig. 17 Summary of the correlation length for the F-100 engine

Table 2 Fraction passing chi-squared test for Gaussian profiles

	TF-39	F-100
Trace 1	1/30	4/30
Trace 2	7/30	10/30
Trace 3	9/30	11/30
Trace 4	11/30	20/30
Trace 5	3/30	18/30
Trace 6	0/30	16/30

sian model was totally inappropriate for several of the trace locations.

Acknowledgments

This work was sponsored by the Air Force Office of Sci-

entific Services, Bolling AFB, DC. This work owes much to the efforts of Dr. Richard Rivir of the Aero-Propulsion Laboratory, Wright-Patterson AFB, OH. The author wishes to thank Dr. Rivir for his support and encouragement. Thanks also go to Mr. Weslie Thomas of Kelly AFB, TX, for his assistance in obtaining engine blades for the measurements.

References

- Rivir, R.B., 1986, Personal Communication.
- Sachs, L., 1982, *Applied Statistics*, Springer-Verlag, New York.
- Taylor, R. P., 1986, "Surface Roughness Effects on Heat Transfer and Skin Friction," Final Report 1986 Summer Faculty Research Program, Universal Energy Systems, Inc., Dayton, OH.
- Whitehouse, D. J., and Archard, J. F., 1970, "The Properties of Random Surface Roughness of Significance in Their Contact," *Proceedings of the Royal Society, London, Series A*, Vol. 316, pp. 97-121.

The Influence of Boundary Layer State on Vortex Shedding From Flat Plates and Turbine Cascades

C. H. Sieverding

von Karman Institute for Fluid Dynamics,
B-1640 Rhode Saint Genèse,
Belgium

H. Heinemann

DFVLR,
D-3400,
Göttingen, Federal Republic of Germany

The paper aims at a better understanding of the reasons for the wide range of Strouhal numbers observed on turbine blades. The investigation is restricted to the subsonic domain. First, flat plate model tests are carried out to investigate the effect of both the boundary layer state and trailing edge geometry on the vortex shedding frequency. A particular objective of the tests is to obtain data for the very common case of a mixed laminar-turbulent separation from turbine blades. These basic tests are followed by three cascade tests with blades of very different suction side velocity distributions. Based on the experience gained from the flat plate test program, an attempt is made to interpret the Strouhal number variation with Mach number and Reynolds number, and to relate the vortex frequency change to the boundary layer state on the blade surfaces.

Introduction

Vortex shedding, as excitation for acoustic resonances and structural vibrations, has been an intriguing and challenging flow problem ever since the early works of von Karman on this subject. The literature on vortex shedding from cylinders and flat plates is abundant, but the particular problem of vortex shedding from turbomachinery bladings has, to date, received only limited attention. However, the continuous trend to bigger blades with decreasing stiffness increases the probability that vortex shedding may become a non-negligible excitation generator. Furthermore, the modeling of trailing edge flows containing large-scale periodic fluctuations poses a severe problem to all those viscous flow computer codes which ignore the existence of this type of unsteadiness. As both the base pressure and the wake mixing are affected by the vortex shedding, it is indeed unlikely that the solution of the steady-state Navier-Stokes equations, with current turbulence models for the closure conditions, can result in correct blade loss predictions.

One of the first researchers to report on vortex shedding from turbomachinery bladings was Parker (1967), who found that sounds emitted from a single-stage compressor were due to a series of acoustic resonances, excited by periodic wakes shed from the rotor blades. Sauer (1979) measured the losses and vortex frequencies of a compressor cascade over a wide range of incidences. It was found that the increase of losses at both positive and negative incidence angles was accompanied by a drop in the vortex frequency. In an attempt to provide data to assess the adequacy of viscous calculation procedures for compressor blade trailing edge flows, Patterson and Weingold (1982, 1984) set up a low speed flat plate experiment, with

trailing edge boundary conditions representative of typical supercritical airfoil designs. The boundary layers were turbulent on both sides of the plate. The Strouhal number of the trailing edge vortex sheet was 0.18, which is in close agreement with Strouhal numbers for flows past circular cylinders. Differences in the boundary layer thicknesses on the two sides of the plate apparently did not affect the vortex shedding. Based on LDV measurements across the wake, the authors concluded that lateral velocities were large compared to both mean lateral velocity components and turbulent velocity fluctuations. The suppression of the vortices by splitter blades on the mean centerline increased considerably the base pressure. Similar observations had already been made by Roshko (1954) on circular cylinders. Whether these lateral velocity fluctuations can be strong enough to induce a significant fluctuation in the base pressure is not known. In a turbine blade experiment with a Kulite pressure transducer mounted in the trailing edge, Sieverding (1976) did not find any measurable pressure variation related to the vortex shedding.

The most systematic trailing edge vortex measurements on turbomachinery bladings were undertaken at the DFVLR by Lawaczek, Heinemann and Buetefisch (1976a, 1976b, 1978), who investigated 10 subsonic and transonic turbine cascades. The Strouhal numbers varied over a range $0.2 \leq S \leq 0.4$ for a Reynolds number range, based on trailing edge thickness and downstream velocity, of $0.3 \times 10^4 \leq Re_d \leq 1.6 \times 10^5$. The authors did not give any explanation for the differences compared to Strouhal numbers from cylinders, for which S varies between 0.21 and 0.19 over the same range of Re numbers. Lawaczek et al. (1976b) measured the vortex intensity in the two vortex rows and found a higher intensity for the pressure side than for the suction side. This observation was confirmed in a smoke visualization study on a 21-in. chord turbine blade by Han and Cox (1982), who found much sharper and more well-defined

Contributed by the International Gas Turbine Institute and presented at the 34th International Gas Turbine and Aeroengine Congress and Exhibition, Toronto, Ontario, Canada, June 4-8, 1989. Manuscript received at ASME Headquarters February 14, 1989. Paper No. 89-GT-296.

vortex contours on the pressure side, and concluded that this implied stronger vortex shedding from the pressure side. Bryanston-Cross and Camus (1982) investigated, in the Mach number range $0.4 \leq M_2 \leq 1.2$, two high turning gas turbine blades with different degrees of rear suction side curvature. The Strouhal number, based on trailing edge thickness and downstream velocity, was nearly the same for both blades, $S \approx 0.35$, in the Mach range $0.4 \leq M_2 \leq 1.0$. The authors did not comment on the state of the boundary layers at the trailing edge, but Schlieren photographs for the blade with the high rear SS curvature suggest laminar or transitional boundary layers. It is worth noting that there was no apparent relation between the Strouhal number and the base pressure coefficient. For equal Strouhal numbers on both blades, the authors measured differences in the base pressure of 20 percent and more.

The foregoing studies indicated that a simple flat plate experiment would be most useful, by enabling a systematic investigation of the effect of the boundary layer state on the vortex shedding. The following conditions were studied:

- Laminar flows on both sides of the trailing edge;
- Laminar flow on one side, turbulent flow on the other side;
- Turbulent flows on both sides.

Both rounded and squared trailing edges were used, the latter having the advantage of fixed separation points.

If possible, the results of the model tests should be corroborated by some cascade experiments.

Model Tests

Model Geometry. The model consisted of a 150-mm-long, 50-mm-wide, and 4-mm-thick flat plate, placed in a highly convergent channel with 250-mm inlet and 57-mm outlet height, Fig. 1.

The 55-mm-long nose section was shaped according to

$$Y = 2 \left(\frac{4}{55} x - \frac{2}{55^2} x^2 \right)$$

The model was used both with a circular and squared trailing edge. The latter was obtained by cutting off the circular TE.

The combination of the high channel convergence and the carefully shaped nose provided a continuous smooth acceleration of the flow along the plate.

Instrumentation. The plate was equipped with closely spaced pressure tappings, including one tapping in the TE base region. The boundary layer profile was measured by a flattened pitot tube of 0.12 mm thickness positioned at 3.6 mm upstream of the beginning of the TE circle. The vortex shedding frequency was measured with a Kulite pressure probe placed in the wake of the plate.

Flow Conditions. All tests were carried out at low speed. The isentropic Mach number before separation at the trailing

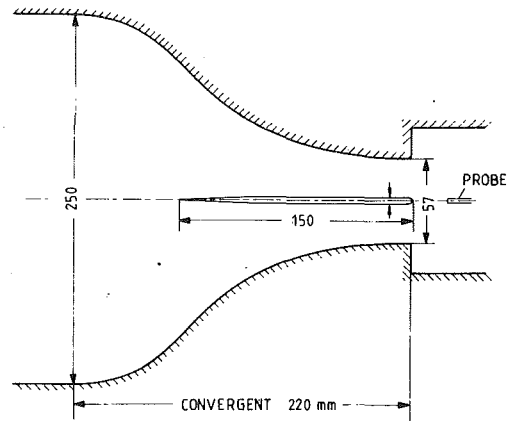


Fig. 1 Model

edge, M_{TE}^* , was varied over the range $0.1 \leq M_{TE}^* \leq 0.4$.

The overall test conditions were as follows:

- Total upstream pressure $P_{01} = 3$ to 50 mbar (gage pressure);
- Total upstream temperature $T_{01} = 275^\circ\text{K}$;
- Reynolds number : $Re_2 = (0.45-1.3) \times 10^6$;
- Turbulence intensity $Tu = 1$ percent.

Boundary layer surveys at the trailing edge showed typical laminar profiles for the previous conditions. Trip wires of 0.2-mm dia, placed at $X/C = 0.5$, were used to obtain turbulent boundary layer profiles.

Measurement Accuracy.

- Total pressure : ± 0.05 mbar;
- Wall static pressure : ± 0.1 mbar;
- Total temperature : ± 1 deg;
- Position of boundary layer probe : ± 0.01 mm.

Velocity Distributions and Boundary Layer Characteristics. Typical examples of the isentropic Mach number distributions along the flat plate are presented in Fig. 2(a). The convergent duct imposes a continuous acceleration. The rate of acceleration decreases somewhat for $X/L > 0.7$, but a strong acceleration reappears near the trailing edge. Variations in the velocity distribution due to differences in TE shape (rounded or squared) and flow conditions (with and without trip wire) are limited to the TE region; see Fig. 2(b). Note that the velocity distributions are presented in the form $M = f(X/L)$ where L is the length of the model with rounded TE. The mechanism triggering the trailing edge acceleration can be found by considering the momentum exchange between the base flow and the free-stream flow. This causes a drop in the base pressure, which affects the upstream flow velocity distribution over an appreciable distance, through a gradual decrease of the boundary layer displacement thickness. The upstream effect extends to the distance $\Delta L \approx 2d$, measured with respect to the beginning of the TE circle or the corner of the squared TE.

Nomenclature

C = chord
 CP = pressure coefficient
 d = trailing edge thickness
 f = vortex shedding frequency
 g = pitch
 L = flat plate length
 M = Mach number
 P = pressure
 Re = Reynolds number
 S = Strouhal number
 T = temperature
 U = velocity

W = cascade relative velocity
 β_1 = inlet flow angle
 β_2 = outlet angle
 δ = boundary layer thickness
 δ^* = boundary layer displacement thickness
 ϵ = rear suction side turning angle
 θ = flow turning angle

Subscripts

0 = total
 1 = upstream

2 = downstream
 b = base
 is = isentropic
 LA = laminar
 PS = pressure side
 SS = suction side
 Tu = turbulent
 TE = trailing edge

Superscripts

C = circular trailing edge
 S = squared trailing edge

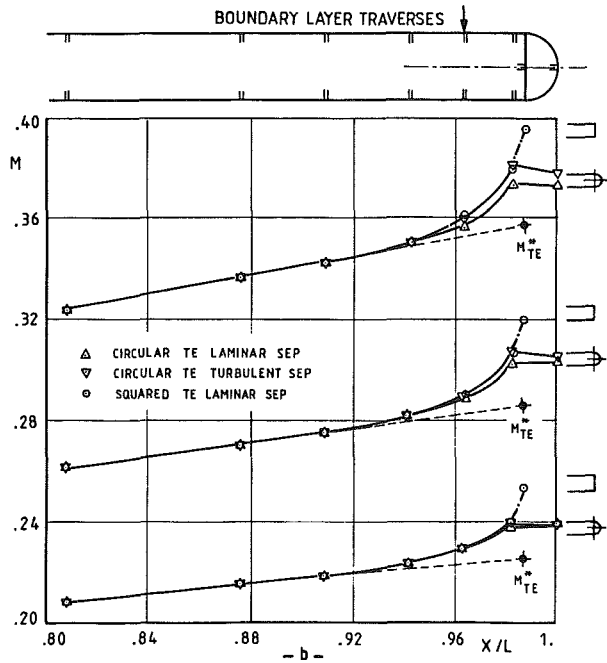
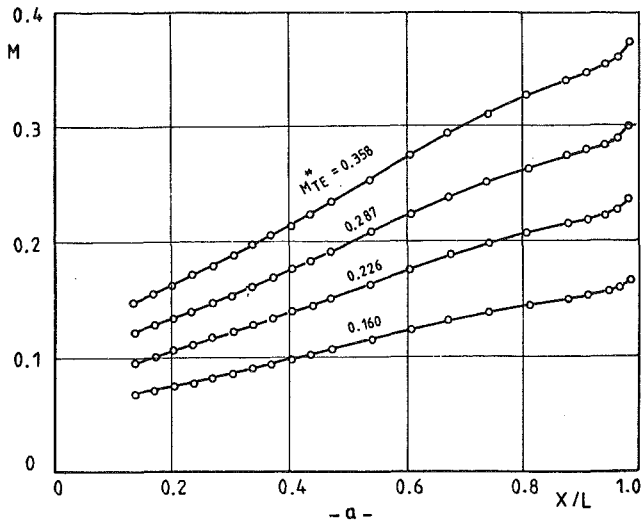


Fig. 2 Isentropic Mach number distribution along flat plate

In the absence of the TE effect, the natural evolution of the velocity distribution, under the sole influence of the external contraction of the duct, would have been most likely along the dotted lines in Fig. 2(b), which are obtained by simple extrapolation of data points situated further upstream. The endpoint of this fictitious Mach number distribution is defined as the separation Mach number M_{TE}^* . The corresponding velocity U_{TE}^* is used as the reference velocity for the definition of the Strouhal number.

Boundary layer traverses were made at $X/L = 0.963$, corresponding approximately to a distance $\Delta L = d$ from the beginning of the TE curvature. At this point, the effect of the TE expansion is still rather moderate.

Typical boundary layer profiles for tests with and without trip wire are presented in Fig. 3. The corresponding shape factors are summarized in Fig. 4. The undisturbed boundary layers exhibit clearly a laminar profile while artificially inducing transition, by use of a trip wire placed at $X/L = 0.5$, leads clearly to turbulent boundary layer profiles at the trailing edge.

Trailing Edge Vortex Shedding. The Strouhal number is calculated using the trailing edge velocity U_{TE}^* (for definition,

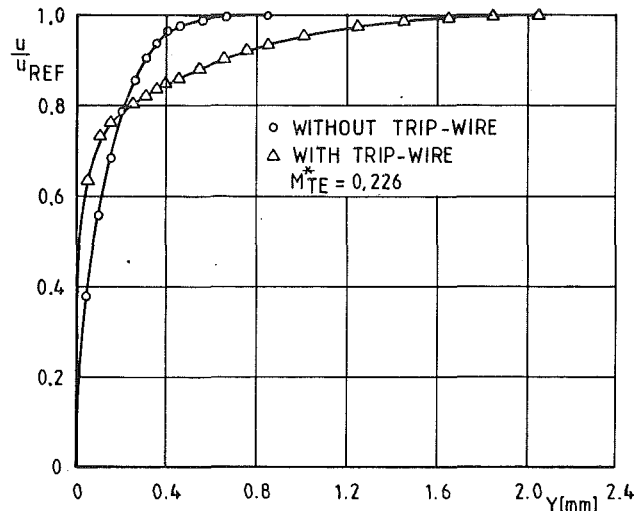


Fig. 3 Boundary layer profiles near trailing edge of flat plate

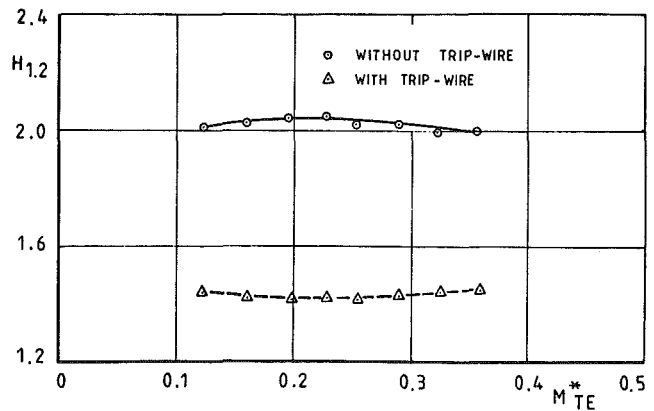


Fig. 4 Boundary layer shape factors

see previous paragraph) and the trailing edge thickness, augmented by the pressure side and suction side boundary layer displacement thicknesses

$$S = \frac{f \cdot (d + \delta_{SS}^* + \delta_{PS}^*)}{U_{TE}^*}$$

Let us first consider the case of the *flat plate with circular trailing edge*. For the case of turbulent boundary layers on both sides of the plate, Strouhal numbers of the order of $S = 0.24$ are recorded, while the values for laminar boundary layers on both sides are in the region of $S = 0.31$; see Fig. 5(a). The question arises as to whether this change is due to the difference in the nature of the boundary layers at separation, or to a difference in the position of the boundary layer separation points on the trailing edge, resulting from the different boundary layer states. Flow visualization tests by Patterson and Weingold (1982) show turbulent separation occurring at $\theta = 14$ deg of the trailing edge circle of their flat plate. Assuming for a laminar boundary layer, the extreme case of a tangential separation from the flat plate, i.e., $\theta = 0$ deg then the transition from laminar to turbulent separation results in a maximum difference for the distance between the upper and lower separation points of 3 percent. If this distance was the only factor influencing the vortex frequency, one would have expected slightly lower frequencies for the laminar separation. Since, on the contrary, the measurements show a 30 percent increase of the frequency for the laminar separation, it becomes evident that the state of the boundary layers at separation must play a predominant role in the determination of the vortex frequency.

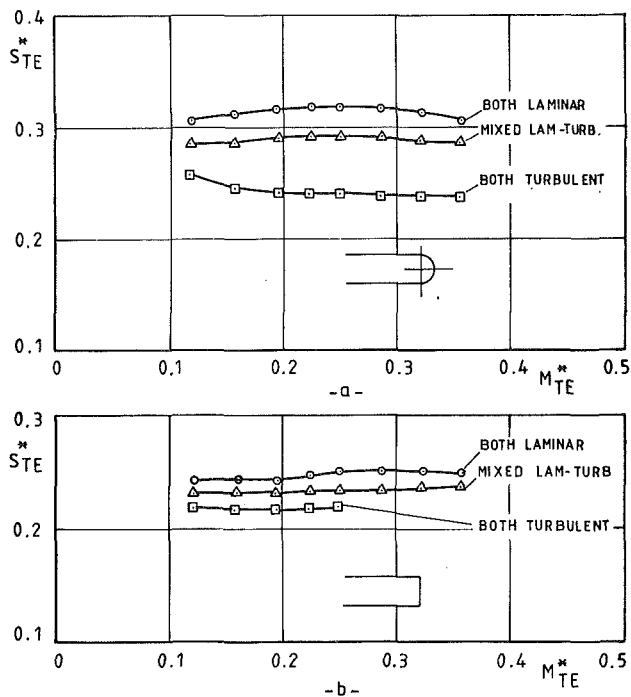


Fig. 5 Flat plate Strouhal numbers

For the configuration with the mixed laminar-turbulent separation, the Strouhal numbers lie in between those of the “all laminar” and “all turbulent” separations, but one observes a slight tendency of the data to be closer to the all laminar case.

In the case of the *flat plate with squared trailing edge*, the flow separates right at the trailing edge corner. Hence, the distance between the separation points is not affected by the boundary layer state. As for the circular trailing edge, the vortex shedding frequency increases when switching from turbulent to laminar boundary layers (Fig. 5b). However the effect of is much smaller, only 13 percent instead of 30 percent for the circular TE. This different behavior can be explained if one assumes that the shape of the trailing edge may strongly affect the evolution of the shear layer, and that it is the state of the shear layer rather than that of the boundary layer before separation which plays the most important role in the generation of the vortex street. Studying the flow behind flat plates with squared trailing edges for both laminar and turbulent boundary layers, Dymant (1978) found virtually no difference in the shear layer profiles for distances as close as half the trailing edge thickness. This suggests that a sharp corner induces early transition of the shear layers without imposing necessarily complete transition right at the corner, thus leaving some room for the influence of the Re number on the transition length. Hence, it is normal that the change in Strouhal numbers for a change in the boundary layer state is relatively small for the squared trailing edge.

Comparing the Strouhal numbers for the two TE geometries with turbulent boundary layers, one notices that the values for the circular trailing edge are about 11 percent higher than those for the squared trailing edge, i.e., $S = 0.24$ instead of 0.215. Of this difference, at a maximum, only 3 percent can be attributed to a change in the position of the separation points. The remaining difference is not explained. Remembering the importance of the state of the shear flow, it was thought that the free-stream velocity adjacent to the base flow region, $U_b = f(P_b, P_{01})$, was possibly a better reference velocity for evaluating the Strouhal number than the velocity U_{TE}^* , which is the same for both configurations. However, since U_b is higher for the squared trailing edge than for the circular trailing edge, the difference in the Strouhal numbers would be even bigger.

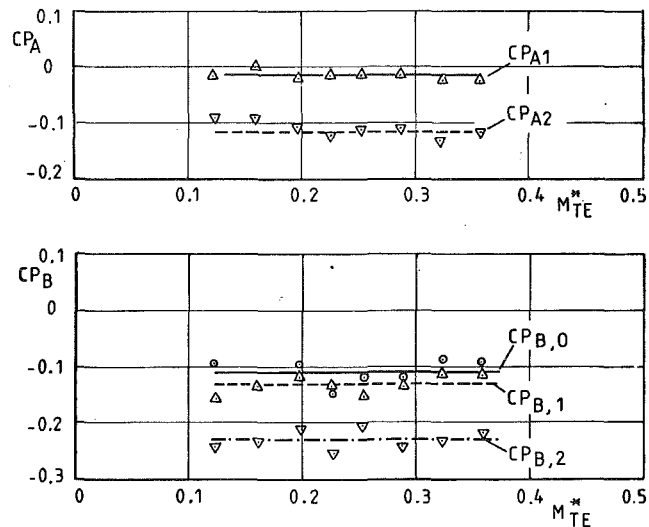


Fig. 6 Flat plate base pressure coefficients

Trailing Edge Base Pressure. The effect of the state of the boundary layers and the trailing edge shape on the base flow is presented in Figs. 6(a, b), in the form of a base pressure coefficient

$$CP = \frac{2(P_b - P_{ref})}{\rho \cdot U_{ref}^2}$$

Two different reference pressures are used:

(a) The base pressure of the plate with circular trailing edge and laminar boundary layer, $(P^C)_{b,LA}$;

(b) The trailing edge pressure P_{TE}^* defined as that pressure which would occur at the beginning of the circular trailing edge, or at the corner of the squared trailing edge, in the absence of the trailing edge acceleration; see dotted line in Fig. 2(b).

$$CP_{A1} = \frac{2[(P^C)_{b,Tu} - (P^C)_{b,LA}]}{\rho \cdot (U^C)_{b,LA}^2}$$

$$CP_{A2} = \frac{2[(P^S)_{b,LA} - (P^C)_{b,LA}]}{\rho \cdot (U^C)_{b,LA}^2}$$

$$CP_{B0} = \frac{2[(P^C)_{b,LA} - P_{TE}^*]}{\rho \cdot (U_{TE}^*)^2}$$

$$CP_{B1} = \frac{2[(P^C)_{b,Tu} - P_{TE}^*]}{\rho \cdot (U_{TE}^*)^2}$$

$$CP_{B2} = \frac{2[(P^S)_{b,LA} - P_{TE}^*]}{\rho \cdot (U_{TE}^*)^2}$$

Subscripts: TE = trailing edge, b = base, LA = laminar, Tu = turbulent;

Superscripts: C = circular TE, S = squared TE.

The coefficients CP_A compare the base pressures of the various configurations with each other, while the coefficients CP_B relate the base pressures of all configurations to the same upstream flow conditions.

The effect of the state of the boundary layer on the base pressure for the model with circular TE is small, of the order of 1.5 to 2 percent of the dynamic head; see coefficient CP_{A1} in Fig. 6(a). The large differences between the trailing edge vortex shedding for laminar and turbulent flow apparently affect the base pressure very little or not at all. The base pressure for the configuration “squared TE with turbulent boundary layer” was not measured, but it is expected that the

Table 1

Cascade	A	B	C
Inlet angle β_1	30°	0°	30°
Gaging angle β_2 (arccos $0/g$)	65°	65.1°	67.8°
Pitch to chord ratio g/c	0.75	0.72	0.71
Trailing edge thickness d/c to chord ratio	0.04	0.046	0.045
Chord length c	66	64.5	100/60*
Rear SS turning angle ϵ	0°	7°	20°

*Chord length $C = 100$ mm at VKI; $C = 60$ mm at DFVLR-Göttingen. Note: β_1 and β_2 are referred to axial direction.

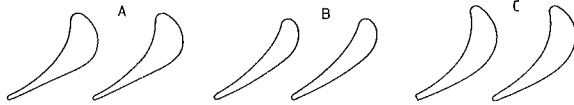


Fig. 7 Turbine cascades

difference with respect to the “squared TE with laminar boundary layer” is smaller than for the circular TE, because of the corner effect on the shear layer evolution discussed in the preceding paragraph.

The effect of the trailing edge shape on the base pressure is more significant. Compared to the circular trailing edge, the base pressure of the squared trailing edge is ~11 percent lower; see coefficient CP_{A2} in Fig. 6(a).

With respect to the upstream conditions, Fig. 6(b), the base pressure coefficients are around -12 percent for the circular trailing edge; see coefficients CP_{B0} and CP_{B1} , but almost twice as high for the squared TE; see coefficient CP_{B2} . The base pressure coefficients for the squared TE are very similar to those of Nash (1963) for a backward facing step in subsonic flow.

Cascade Tests

Description of Cascades. Vortex shedding frequency measurements are presented for three turbine cascades in the outlet Mach number range $0.2 \leq M_2 \leq 0.8$. The main geometric dimensions of the cascades are given in Table 1; see also Fig. 7.

Cascades *A* and *B* were tested at VKI. Cascade *C* was tested at DFVLR-Göttingen as well as at VKI. Preliminary results of this work were reported in 1982 (Sieverding et al., 1982).

Blades *A* and *C* were chosen because of their fundamentally different suction side design:

- Blade design *A* with a straight rear SS favoring the development of a turbulent boundary layer on the rear SS, due to a strong deceleration in the throat region, $W_{max}/W_2 = 1.53$;
- Blade design *C* with a highly curved rear SS favoring the preservation of a laminar boundary layer, by keeping the re-compression on the rear suction side very small, $W_{max}/W_2 = 1.11$. Nevertheless, it must be expected that at high Re number transition will start soon after the velocity peak.

Blade *B* is intermediate between blades *A* and *C*. Compared to blade *A*, the suction side velocity peak is greatly reduced, due to smaller changes in the surface curvature in the throat region, $W_{max}/W_2 = 1.25$. However, similar to *A* it is front-loaded, with a first velocity peak at $X/C = 0.25$ instead of $X/C = 0.55$ for the back-loaded blade *C*.

Blade Velocity Distributions and Overall Flow Conditions. Blade velocity distributions for all 3 cascades are pre-

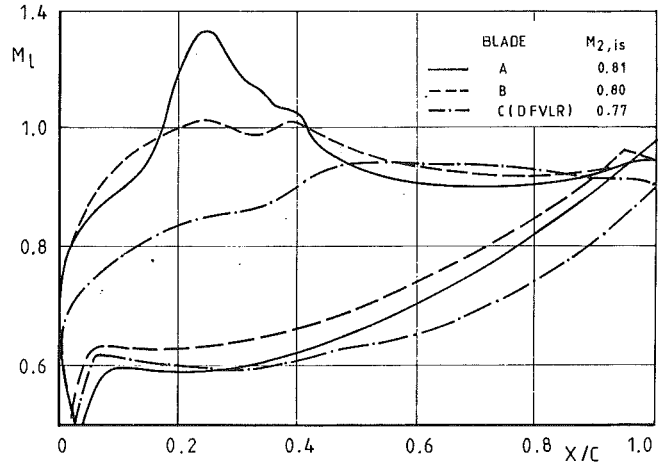


Fig. 8 Isentropic surface Mach number distributions for turbine cascades

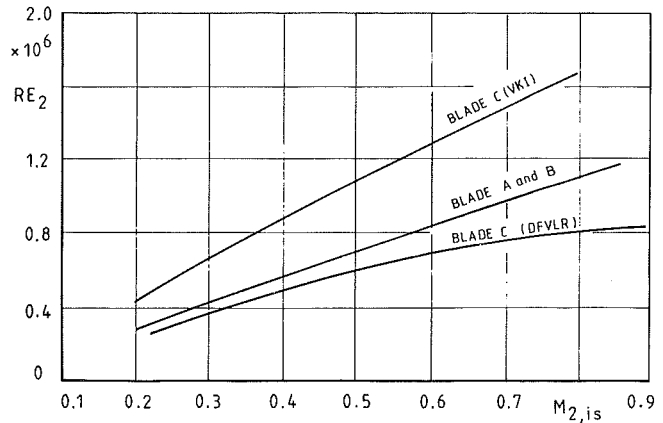


Fig. 9 Variation of Reynolds numbers in function of downstream Mach numbers

sented in Fig. 8. They illustrate clearly the different suction side design features, but there also are some noticeable differences in the pressure side velocity distributions.

For all three cascades, the increase of the outlet Mach number is accompanied by an increase in Reynolds number. The evolution of $Re_2 = f(M_{2,is})$ is presented in Fig. 9. The differences in the two Reynolds number curves for blade *C* are due to different chord lengths of the blades and different operating systems of the VKI and DFVLR cascade tunnels. The VKI cascade tunnel is of the blowdown type with exhaust at atmospheric pressure, while the tunnel of DFVLR-Göttingen is a suction-type tunnel.

Vortex Shedding Frequency Measurements. The tests were carried out using both high-speed pressure probes and optical methods. There was virtually no difference in the results obtained with both methods.

Cascade A: Two test series were performed:

- I • Forced transition on the PS, by a trip wire at 24 percent of the chord from the TE;

- natural evolution of boundary layer on suction side, with natural transition on rear suction side due to strong adverse pressure gradient in throat region;

- II natural evolution of boundary layer on both pressure and suction sides.

The trip wire used for Series I was placed relatively close to the TE, to make sure that the strong pressure side acceleration did not cause a relaminarization of the flow. The Strouhal numbers, in the form

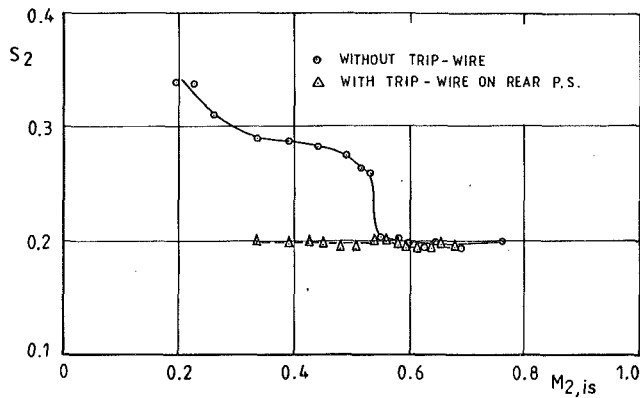


Fig. 10 Strouhal number variation with downstream Mach number for cascade A

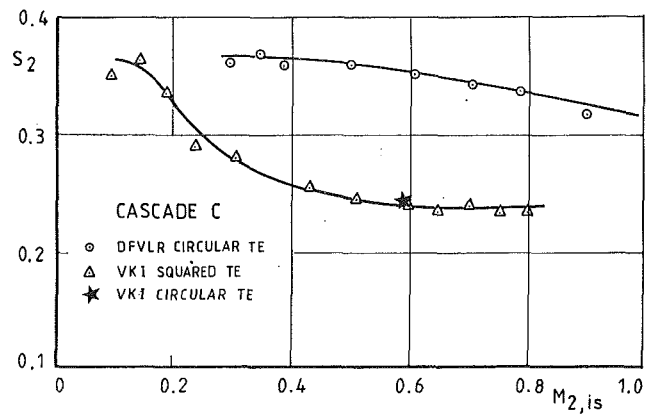


Fig. 12(a) Strouhal number variation with downstream Mach number for cascade C

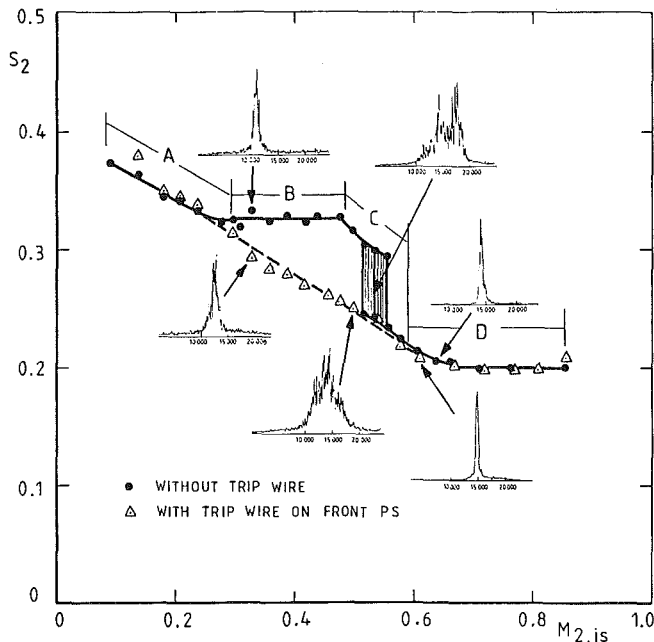


Fig. 11 Strouhal number variation with downstream Mach number for cascade B

$$S = \frac{f \cdot d}{U_{2,is}}$$

are presented in Fig. 10 for both test series. Note that, due to the lack of boundary layer measurements on the blades, the displacement thicknesses are not included, contrary to the flat plate tests.

The all turbulent Test Series I shows a nearly constant Strouhal number $S=0.195$ over the entire flow range tested. This value is about 20 percent lower than the corresponding value for the flat plate test with circular trailing edge. Most of this difference can be attributed to the fact that the boundary layer displacement thicknesses are not taken into account.

The curve for Test Series II exhibits quite different features than that of Series I. Starting from the low Mach number and Reynolds number end, the Strouhal number decreases from $S=0.34$ at $M_{2,is}=0.2$ to $S=0.26$ at $M_{2,is}=0.53$. At this point, S drops suddenly to the level of the all turbulent case of Test Series I. This sudden change obviously indicates that boundary layer transition has taken place on the pressure side. The slow decrease of S before the jump points to a progressive change from a laminar to a transitional boundary layer, due to the increase in Reynolds number.

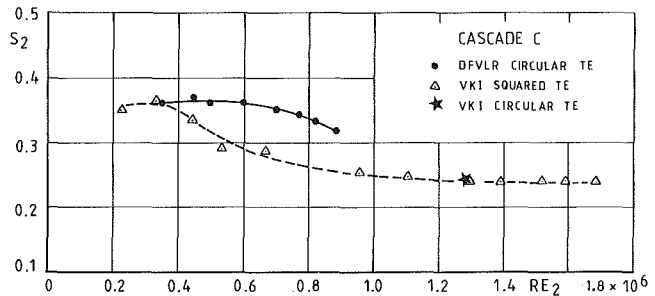


Fig. 12(b) Strouhal number variation with Reynolds number for cascade C

Cascade B: This cascade was tested as cascade A, with and without trip wire on the pressure side. But, contrary to cascade A, the wire was placed on the front part of the pressure side. The results are presented in Fig. 11.

Let us first try to interpret the data for the case without trip wire in the light of the results from the flat plate and cascade A. The curve is subdivided into 4 characteristic sections A, B, C and D. Except for Section A, Fig. 11 shows for each section typical frequency spectra, as measured by a Kulite pressure probe positioned at $6 \times d$ behind the trailing edge. Starting from the high Mach number-high Reynolds number end, Section D, the Strouhal number level of $S=0.2$ and the very narrow frequency band are indications of an all turbulent boundary layer separation from the trailing edge. In the center of Section C, the frequency spectrum is extremely wide, with a double peak which points to abrupt changes in the state of the pressure side boundary layer, flipping back and forward between a transitional and a fully turbulent state. The frequency spectra at the beginning and end of Section C are wide, but show only one predominant peak. The plateau of Section B can be interpreted as the result of a laminar pressure side boundary layer and a turbulent suction side boundary layer, the pressure side boundary layer playing a predominant role in the vortex shedding process. Decreasing further the Mach and Reynolds numbers, Section A, the Strouhal number rises again, which could be explained by a transitional state of the suction side boundary layer.

The interpretation of plateau B in Fig. 11 as being due to a laminar pressure side boundary layer is supported by the tests with the trip wire on the front pressure side. With the trip wire, plateau B disappears and the Strouhal number continues to decrease, at nearly the same rate as in Section A, until it joins the curve without trip wire at the end of Section C. The fact that the trip wire does not lead to an extension of the low Strouhal number level of Section D to lower Mach and Rey-

nolds numbers, i.e., to Section C or even beyond that, can be attributed to the strong flow acceleration for $X/C > 0.4$. This counteracts the effect of the trip wire and keeps the rear pressure side in a transitional state until the increasing Reynolds number (with increasing Mach number) causes full transition.

Cascade C. This cascade was tested with a circular trailing edge (DFVLR), as well as with a squared trailing edge (VKI), over a Mach number range $M_2 = 0.2 \rightarrow 0.9$. The two test series differed not only by their TE geometry, but also by, at constant Mach number, the higher Re number of the VKI tests; see Fig. 9. Based on the flat plate test results, one may expect that a squared trailing edge enhances the effect an increase of Re number has on the vortex shedding process. The Strouhal numbers for both test series are presented in Figs. 12(a, b) as a function of Mach number and Reynolds number, respectively.

Both the DFVLR data, for the circular TE, and the VKI data, for the squared TE, show an upper plateau for the Strouhal numbers of $S \approx 0.36$ at low Mach and Reynolds numbers. This plateau is characteristic of an all laminar trailing edge boundary layer separation. The Strouhal numbers start to decrease with increasing Re numbers, the drop of S occurring earlier at $Re \sim 0.35 \times 10^6$ for the squared trailing edge, instead of $Re = 0.6 \times 10^6$ for the circular trailing edge. At $Re \approx 1.1 \times 10^6$, the squared TE data reach a lower plateau with $S = 0.24$. Extrapolating the DFVLR data, one may expect that the curve for the circular trailing edge will join that for the squared TE at $Re \approx 1.1 \times 10^6$ (assuming that any Mach number effects are absent). To eliminate the uncertainty concerning the lower Strouhal number plateau for the circular trailing edge, one single high Re-number test was run at VKI for blade C with a circular TE. The flow conditions were chosen as: $Re = 1.27 \times 10^6$ at an outlet Mach number $M_{2, is} = 0.59$. This test is denoted in Figs. 12(a, b) by a star. It turns out that the Strouhal number falls right on top of the squared TE data; i.e., $S = 0.24$. It is believed that the lower the Strouhal number plateau characterizes an all turbulent boundary layer separation from the trailing edge. The difference with respect to cascades A and B, with the lower plateau at $S = 0.2$, is not fully understood, but could possibly be related to the differences in the rear blade suction side curvature and the trailing edge wedge angle. It also is worth noting that the all turbulent S values for the two TE geometries differ for the flat plate (the squared TE values are 10 percent lower) but not for cascade C.

Conclusions

Trailing edge vortex frequency measurements behind flat plates and turbine cascade demonstrate clearly the influence of the boundary layer state on the Strouhal number. A change from laminar to turbulent boundary layer separation, by trip-

ping the boundary layer or increasing the Reynolds number, reduces drastically the Strouhal number. The differences between S_{turb} and S_{lam} amount to about 30 percent for the flat plate, and to 80 percent and more for the cascades.

A squared trailing edge has a similar effect on the Strouhal number as a large increase in the Reynolds number. This suggests that it is the state of the free shear layer which, in the end, determines the vortex shedding process.

In the case of mixed laminar-turbulent separation, the Strouhal number takes an intermediate position between the all laminar and the all turbulent S-values.

The gradual change from a laminar to a turbulent pressure side boundary layer (with increasing Re number) is characterized by a wide spectrum for the vortex shedding frequencies. The appearance of two distinct frequency peaks for certain flow conditions (see cascade B) points to strong fluctuations in the state of the pressure side boundary layer.

The base pressure is significantly affected by the trailing edge geometry, but not by the boundary layer state (flat plate tests).

References

- Bryanston-Cross, P. J., and Camus, J. J., 1982, "Auto and Cross-Correlation Measurements in a Turbine Cascade Using a Digital Correlator," ASME Paper No. 82-GT-132.
- Dymant, A., and Gryson, P., 1978, "Etude d'écoulements turbulents subsoniques et suercriteques par visualization ultrarapide," AGARD CP 227.
- Han, L. S., and Cox, W. R., 1982, "A Visual Study of Turbine Blade Pressure Side Boundary Layers," ASME Paper No. 82-GT-47.
- Heinemann, H.-J., and Bütefisch, K. A., 1978, "Determination of the Vortex Shedding Frequency of Cascades With Different Trailing Edge Thickness," AGARD CP 227.
- Lawaczeck, O., Bütefisch, K. A. and Heinemann, H.-J., 1976, "Vortex Streets in the Wakes of Subsonic and Transonic Turbine Cascades," presented at the IUTAM Symp. on Aeroelasticity in Turbomachines, Paris.
- Lawaczeck, O., and Heinemann, H.-J., 1976, "von Karman Vortex Streets in the Wakes of Subsonic and Transonic Cascades," AGARD CP 177.
- Nash, J. F., 1963, "An Analysis of Two-Dimensional Turbulent Base Flow, Including the Effect of the Approaching Boundary Layer," ARC R&M, No. 3344.
- Parker, R., 1967, "Resonance Effects in Wake Shedding From Compressor Blades," *Journal of Sound and Vibration*, Vol. 6, No. 3.
- Patterson, R. W., and Weingold, H. D., 1984, "Experimental Investigation of a Simulated Compressor Airfoil Trailing Edge Flowfield," presented at the AIAA 22nd Aerospace Sciences Meeting, Reno, NV.
- Patterson, R. W., and Weingold, H. D., 1982, "Experimental Investigation of a Simulation Compressor Airfoil Trailing Edge Flowfield," Report FR-15859, P&W Aircraft Group, Government Products Division, Oct.
- Roshko, A., 1954, "On the Drag and Shedding Frequency of Two-Dimensional Bluff Bodies," NACA TN 3169, July.
- Sauer, H., 1979, "Investigations on Vortex Frequencies in Wakes of Cascades," *Proceedings of the 6th Conf. Fluid Machinery*, Budapest, Hungary.
- Sieverding, C. H., 1976, "Unsteady Flow Measurements in Straight Cascades," *Proceedings of Symposium on Measuring Techniques in Transonic and Supersonic Cascades and Turbomachinery*, Lausanne, Switzerland.
- Sieverding, C. H., Heinemann, H.-J., and Van Damme, 1982, "On the Influence of Boundary Layer State on Vortex Shedding From Flat Plates and Turbine Blades," EUROMECH 160, *Periodic Flow and Wake Phenomena*, Berlin, German Democratic Republic, Oct.

R. E. Mayle¹
Mem. ASME

K. Dullenkopf

Institut für Thermische
Strömungsmaschinen,
Universität Karlsruhe,
Karlsruhe,
Federal Republic of Germany

A Theory for Wake-Induced Transition

A theory for transition from laminar to turbulent flow as the result of unsteady, periodic passing of turbulent wakes in the free stream is developed using Emmons' transition model. Comparisons made to flat plate boundary layer measurements and airfoil heat transfer measurements confirm the theory.

Introduction

One of the main causes of unsteady flow in gas turbines is the wakes from upstream airfoils or obstructions as shown in Fig. 1. These wakes not only impose a free stream with a periodic, unsteady velocity, temperature and turbulence intensity on the surface boundary layer, but they also produce a convective flow either toward or away from the surface as a result of the velocity deficit associated with them. To date, even though these effects have not yet been satisfactorily investigated, the adverse influence of the unsteady wake on both the performance and life of a gas turbine is well recognized. Of particular concern is the associated increase in heat load to the turbine airfoils where, on the suction side, the wakes cause an unsteady laminar-to-turbulent transition independent of any natural transition that might occur there.

Recently, heat transfer measurements have been made using actual turbine components and facilities that model most of the engine operating conditions. This work was done by Guenette et al. (1985) and Dunn and his co-workers (1986a, 1986b, 1986c, 1988). In general, they obtained either time-resolved or time-averaged heat flux measurements on airfoil, endwall and blade tip surfaces. Dunn et al. (1986b) found that the variations in surface heat flux were large compared to the time-averaged values and that they occurred at the fundamental wake-cutting frequency. In addition, comparisons of the measured time-averaged results with current two-dimensional, boundary layer calculation programs showed that the programs fail to satisfactorily predict the heat load over an airfoil surface (Dunn et al., 1986c; Taulbee et al., 1988).

Other unsteady experiments have been conducted in large-scale, low-speed rotating facilities by Hodson (1984) and Dring et al. (1986). Hodson measured the shear stress and loss on the rotor of a single stage turbine, while Dring et al. (1986) obtained interrow aerodynamic data and time-averaged stator and rotor heat transfer data for a one-and-a-half stage turbine model. In general, both compared their rotor results to steady flow cascade measurements and found that the unsteady rotor-incident flow affected transition on the suction side. Hodson

reported that this caused a 50 percent increase in the time-averaged loss of the rotor. Dring et al. (1986) found that it doubled the time-averaged heat load in the laminar region.

The unsteady effects of passing wakes in an airfoil row have been investigated by Ashworth et al. (1985, 1987), Doorly et al. (1985), La Graff et al. (1988), and Wittig et al. (1988). In each, a rotating wheel of cylinders was used to produce the moving wakes. Doorly et al. measured large unsteady increases in the surface heat flux at the wake cutting frequency and traced the propagation and growth of turbulent regions along the suction surface. All of these investigators found that the wakes directly influenced the onset of transition on the suction side of the airfoil.

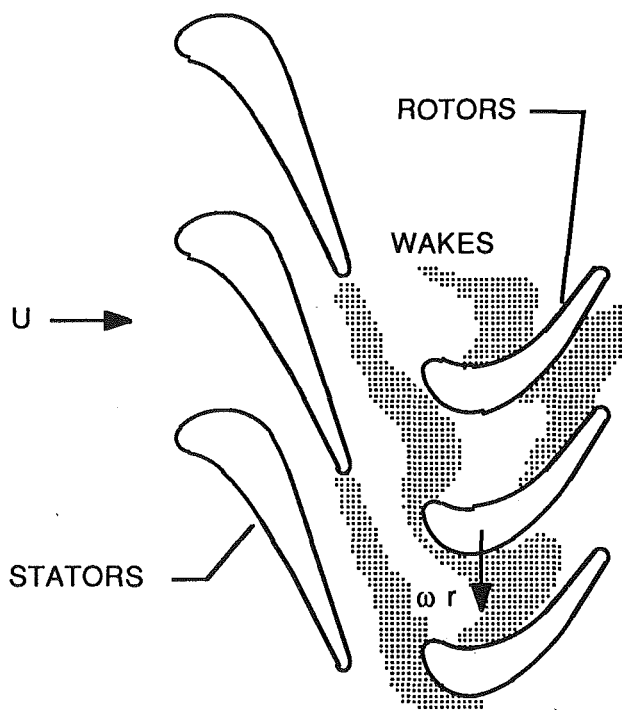


Fig. 1 Unsteady wake propagation through a rotor blade row

¹Presently, Department of Mechanical Engineering, Rensselaer Polytechnic Institute, Troy, NY 12181.

Contributed by the International Gas Turbine Institute and presented at the 34th International Gas Turbine and Aeroengine Congress and Exhibition, Toronto, Ontario, Canada, June 4-8, 1989. Manuscript received at ASME Headquarters January 4, 1989. Paper No. 89-GT-57.

In a related investigation, Pfeil and Herbst (1979) and Pfeil et al. (1983) examined the laminar-turbulent transition of a flat-plate boundary layer disturbed by passing wakes. They measured the steady and unsteady velocity components in the flow along a plate positioned downstream of a rotating cylinder of circular spokes aligned parallel to the leading edge of the plate. Besides presenting information about the time-averaged growth of the boundary layer, they showed that the wakes caused the boundary layer to become turbulent during their "impingement" on the plate. This, they pointed out, formed wake-induced transition zones, which propagated down the plate such that the time-averaged condition of the boundary layer was composed of an intermittent laminar and turbulent boundary layer. Although not formally stated, they implied that the time-averaged condition of the boundary layer may be obtained from

$$\bar{f} = (1 - \gamma)f_L + \gamma f_T \quad (1)$$

where f is a boundary layer flow-related quantity, f_L is its laminar value, f_T is its fully turbulent value, and γ , the intermittency, is the fraction of time the flow is turbulent. The latter varies between zero for laminar flow and unity for fully turbulent flow. Van Dresar and Mayle (1987) found this expression also was valid for steady flow around a cylinder with an incident wake flow providing the wake intermittency is used.

Recently, Doorly (1987) proposed an intermittency-based model for predicting the effect of a passing wake on the suction side heat flux of a gas turbine airfoil. He assumed that the high turbulence content of the wake produces a turbulent patch in an otherwise laminar boundary layer during each passing. To obtain the time-averaged heat flux, he used equation (1) and an intermittency determined by computing the temporal position of the wake adjacent to the surface. The intermittency, therefore, depended on the propagation and growth of the wake around the airfoil. A comparison to measurements showed only a qualitative agreement.

In this paper, a model similar to that proposed by Pfeil and Herbst is considered and a theory developed for wake-induced laminar-to-turbulent transition. The theory is based on Emmons' (1951) original idea of natural transition where he considered the propagation and growth of turbulent spots along a surface within a laminar boundary layer. His theory was later extended in light of new measurements by Dhawan and Narasimha (1957), who showed that the intermittency distribution through natural transition is well represented by

$$\gamma_n(x) = 1 - \exp \left[-0.412 \left(\frac{x - x_m}{x_{75} - x_{25}} \right)^2 \right] \quad (2)$$

where x is the distance along the surface, x_m is the location of natural transition, and x_{25} and x_{75} are the x -positions where $\gamma = 0.25$ and 0.75 , respectively. The quantity $x_{75} - x_{25}$ is a characteristic length for transition, which must be obtained from either experiments or a correlation.

The extension of Emmons' theory to wake-induced transition invokes the idea that the wake is a production source of turbulent spots so dense that the spots immediately form a turbulent "strip," which propagates and grows along the surface. Therefore, contrary to Doorly's model, the present model assumes that once the turbulent strip is formed by the wake its propagation and growth are independent of the wake. As a result, the theory predicts a wake-induced intermittency distribution without any need to calculate the wake position. Furthermore, it allows one to combine the effects of natural and wake-induced transition.

Theory

Consider a transitional boundary layer on an $x-z$ surface as shown in Fig. 2 where the free-stream flow is in the x -direction. The fraction of time during which the flow over a point P on a surface is turbulent was shown by Emmons to be given by

$$\gamma(P) = 1 - \exp \left[- \int_{RG} g(P_0) dV_0 \right] \quad (3)$$

where $\gamma(P)$ is the intermittency at point P , $g(P_0)$ is the rate of turbulent spot production per unit surface area at P_0 , dV_0 is an element of volume in an x, z and time t space, and R is an influence volume defined by all the points upstream in the x, z, t space that are sources of turbulent spots that will pass over P . Emmons obtained this expression by considering the propagation and growth of turbulent spots in x, z, t space as shown in Fig. 3. The source at P_0 simply produces a spot that, on the surface (Fig. 2), moves downstream and grows. The cone-like volume swept out in x, z, t space depends on the propagation and growth of the spot. The influence volume R in Fig. 3 includes all of the sources affecting point P .

Now consider a production of turbulent spots from two types of sources. In particular, consider that turbulent spots are produced both naturally (natural transition) and by the periodic passing of wakes imbedded in the free stream (wake-

Nomenclature

a = turbulent-strip production strength
 c = airfoil chord
 $F(x)$ = fractional function of x
 g = turbulent-spot production function
 h = heat transfer coefficient
 H = shape factor
 $I(x)$ = integer function of x
 n = number of rotating spokes or bars
 R = influence volume, contains all sources of turbulent spots that will pass over a point on the surface
 St = Stanton number

t = time
 U_s = local spot- or strip-propagation velocity
 U_∞ = free-stream velocity
 $U(x)$ = unit step function of x
 V = volume in x, z and t space
 x = coordinate on surface in streamwise direction
 x_t = transition position
 y = coordinate normal to the surface
 z = coordinate on surface in transverse direction
 α = one-half propagation angle of turbulent spot or strip
 γ = intermittency

$\bar{\gamma}$ = time-averaged intermittency
 $\delta(x)$ = Dirac delta function of x
 θ = momentum thickness
 ν = kinematic viscosity
 τ = wake-passing period
 τ_w = wake duration time over location x_{tw}

Subscripts

L = fully laminar
 n = quantity related to natural transition
 T = fully turbulent
 w = quantity related to wake-induced transition

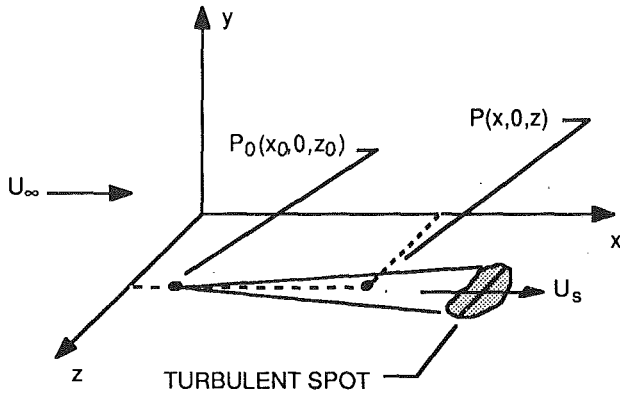


Fig. 2 Transitional boundary layer with turbulent spot on $x-z$ surface

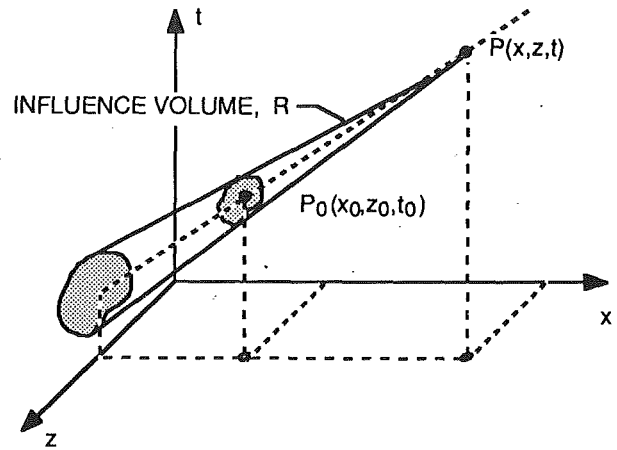


Fig. 3 Emmons' x, z, t space and influence volume R for point P

induced transition). Assuming that the production functions from each source are independent of one another, the function associated with each source can be linearly superposed such that

$$g = g_n + g_w,$$

where g_n and g_w are the individual production functions associated with natural and wake-induced transition, respectively. It is not obvious that the turbulent spot production functions are independent. In fact, Pfeil et al. (1983) indicate that a so-called "becalmed region" is formed at the trailing edge of a turbulent spot in which no other spots are produced. This would invalidate a simple superposition model unless its effect is either small or can be somehow incorporated into the production function itself. Without any further information, however, it will presently be assumed that all effects of the wake on transition can be grouped into g_w and that linear superposition provides a good approximation to transition arising from the two sources. Substituting the foregoing expression for g into equation (3) yields

$$\gamma(P) = 1 - \exp \left[- \int_{R_n} g_n dV \right] \exp \left[- \int_{R_w} g_w dV \right] \quad (4)$$

where the volumes R_n and R_w are now the influence volumes associated with the turbulent spots produced naturally and induced by the wake. These volumes can and, in general, will be different. Consistent with the idea of superposing effects, g_n will be independent of time. Obviously, g_w depends on time. If the wakes pass over the surface with a period equal to τ , the time-averaged intermittency may be obtained by averaging equation (4) over one period. This provides

$$\bar{\gamma}(x,z) = \frac{1}{\tau} \int_{t_1}^{t_1+\tau} \gamma(P) dt = 1 - [1 - \gamma_n(x,z)][1 - \bar{\gamma}_w(x,z)] \quad (5)$$

where γ_n and $\bar{\gamma}_w$ are the intermittency functions at the point P associated with the individual source functions for natural and wake-induced transition. These are

$$\gamma_n(x,z) = 1 - \exp \left[- \int_{R_n} g_n dV \right]$$

and

$$\bar{\gamma}_w(x,z) = 1 - \frac{1}{\tau} \int_{t_1}^{t_1+\tau} \exp \left[- \int_{R_w} g_w dV \right] dt. \quad (6)$$

The expression for γ_n was evaluated by Dhawan and Narasimha (1958) and the result has been given previously in equation (2). To arrive at this result, they showed that turbulent spots originate most often at a particular distance downstream on the surface, such that the function g_n is well represented by $g_n = (\text{constant}) \times \delta(x - x_{tn})$, where $\delta(x)$ is the Dirac delta function and x_{tn} is the location where the spots are most often produced (i.e., where natural transition begins). This implies for natural transition that all turbulent spots originate randomly in z and t at x_{tn} such that the only region that contains

sources in the influence volume R of x, z, t space (Fig. 3) is on the $x = x_{tn}$ plane.

For wake-induced transition, Pfeil et al., also observed a most probable location for transition, x_{tw} , and that it is in general different than x_{tn} . This implies that all wake-induced turbulent spots originate in x, z, t space on an $x = x_{tw}$ plane. Since the wake induces these spots, spots are produced only when the wake passes over this location. In this sense, the wake acts simply as a switch turning on and off the production of turbulent spots at $x = x_{tw}$. Obviously, if the wake is very weak, i.e., the velocity deficit and turbulence is small, spot production caused by the wake will be less, transition will be more natural-like, and x_{tw} will approach x_{tn} . This implies that both g_w and x_{tw} are functions of the wake strength. In addition, it seems that these quantities also may depend on the wake-passing frequency since a small but finite amount of time is required for the boundary layer to completely respond.

Now assume that the production of wake-induced spots is to intense that these spots coalesce immediately to form a transverse turbulent strip across the surface.² In x, z, t space then, a wake-induced strip will sweep out a wedgelike, rather than conelike, volume which now depends on the propagation and growth of the strip (not the wake). Furthermore, if the wake is two-dimensional, all $z = \text{constant}$ planes will be identical and the wake-induced transition problem can be solved in that $x-t$ plane as shown in Fig. 4.

To determine the wake-induced intermittency distribution $\bar{\gamma}_w$, introduce a new streamwise coordinate x^+ , defined as

$$x^+ = \int_{x_{tw}} \frac{dx}{U_s(x)} \quad (7)$$

where $U_s(x)$ is now the local strip-propagation velocity. The quantity x^+ is equivalent to a strip propagation time. If the wake indeed acts as a switch, it may be assumed that the temporal distribution of g_w will be a series of square waves, as shown in Fig. 5, where a is the turbulent strip production strength. In this figure, the wakes are passing over the position $x^+ = 0$ with a period τ and with a duration time equal to τ_w . Expressing this variation in terms of the unit step function, the production function g_w for wake-induced transition may be written as

$$g_w(P_0) = a \delta(x^+) \sum_{n=-\infty}^{\infty} [U(t_0 + \tau_w - n\tau) - U(t_0 - n\tau)] \quad (8)$$

² This requires that spots are produced with an average separation distance much less than $2U_s \tau_w \tan \alpha$, where U_s is the spot propagation velocity, τ_w is the wake duration time at $x = x_{tw}$, and α is one-half the propagation angle of the spots.

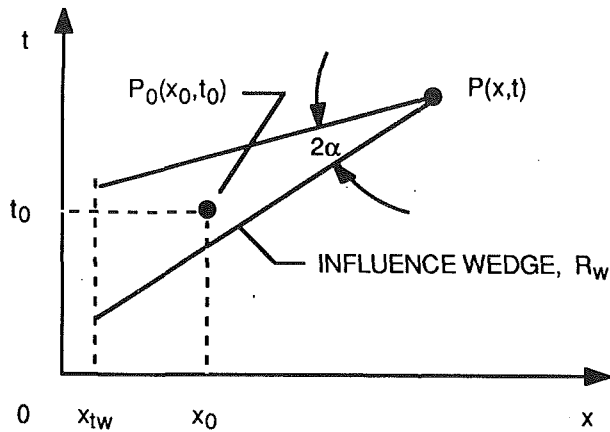


Fig. 4 Solution plane x, t for wake-induced transition and influence wedge R_w for point P

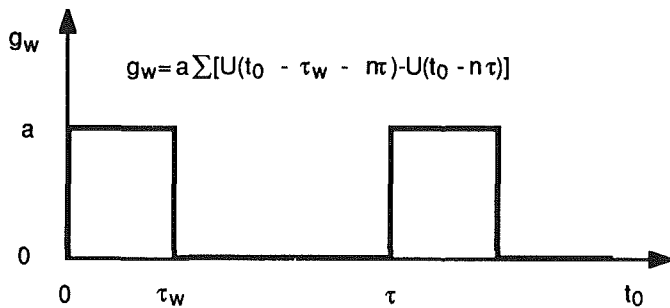


Fig. 5 Wake-induced production function for turbulent strips

where $\delta(x^+)$ is the Dirac delta function of x^+ , and $U(x)$ is the unit step function of x . Then, from equation (6), the time-averaged intermittency $\bar{\gamma}_w$ becomes

$$\bar{\gamma}_w(x) = 1 - \frac{1}{\tau} \int_{t_1}^{t_1 + \tau} \exp \left\{ -a \int_{R_w} \delta(x_0^+) \sum_{n=-\infty}^{\infty} [U(t_0 + \tau_w - n\tau) - U(t_0 - n\tau)] dV_0 \right\} dt \quad (9)$$

where a has been taken to be independent of position and time. This expression is evaluated in the Appendix and found to be equal to (see equation A4)

$$\bar{\gamma}_w(x) = 1 - \exp \left[-b \left(\frac{\tau_w}{\tau} \right) \int_{x_{tw}} \frac{dx}{U_s(x)} \right]$$

where $b = 4a \tan \alpha$ and α is one-half the propagation angle of the turbulent strip. For a constant propagation velocity U_s , $\bar{\gamma}_w$ is given by the relatively simple expression

$$\bar{\gamma}_w(x) = 1 - \exp \left[-b \left(\frac{\tau_w}{\tau} \right) \left(\frac{x - x_{tw}}{U_s} \right) \right] \quad (10)$$

A sketch of this function for several values of τ_w/τ is provided in Fig. 6. As might be expected, increasing τ_w/τ produces an earlier time-averaged transition to fully turbulent flow. A comparison between the distributions for natural transition, equation (2), and wake-induced transition is shown in the insert.

Substituting equations (2) and (10) into equation (5), yields the time-averaged intermittency (for constant U_s) accounting for both natural and wake-induced transition. This is given by

$$\bar{\gamma}(x) = 1 - e^{-0.412 \left(\frac{x - x_{tw}}{x_{ts} - x_{tw}} \right)^2} e^{-b \left(\frac{\tau_w}{\tau} \right) \left(\frac{x - x_{tw}}{U_s} \right)} \quad (11)$$

Comparisons of the aforementioned expressions for $\bar{\gamma}_w(x)$ and

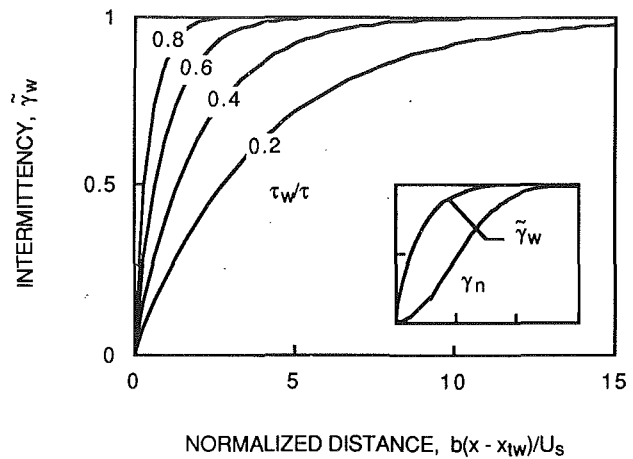


Fig. 6 Wake-induced intermittency distribution for several wake widths τ_w/τ and comparison between natural and wake-induced intermittency distributions

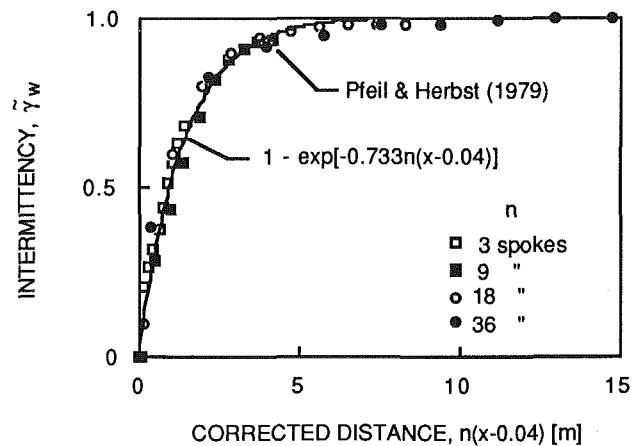


Fig. 7 Flat-plate wake-induced intermittency data of Pfeil and Herbst (1979) and comparison to theory

$\bar{\gamma}(x)$ to unsteady, wake-disturbed flat plate and airfoil experiments will now be made.

Comparisons to Experiments

The first comparison is made to the data presented by Pfeil and Herbst. They measured the time-dependent velocities in a transitional boundary layer on a flat plate positioned behind a rotating cylinder cascade. Measurements were obtained for 0, 3, 9, 18, 36 and 90 spokes in the cascade. Values of $\bar{\gamma}_w(x)$ were obtained from their reported shape factor distributions. Using equation (1)

$$\bar{\gamma}_w(x) = \frac{H - H_L}{H_T - H_L}$$

where H , H_L and H_T are the time-averaged shape factors for transitional, fully laminar and fully turbulent flow, respectively. Pfeil and Herbst's data for no spokes were used for the fully laminar shape factors, while their data for 90 spokes were used for the fully turbulent values. This is in agreement with their conclusions regarding the state of the time-averaged boundary layer. The results of these calculations are presented in Fig. 7 where $\bar{\gamma}_w$ is plotted against a modified streamwise distance $n(x - 0.04)$. Here, n is the number of rotating spokes. The data were found to collapse best for a shift in the x distance of 0.04 m, which consequently corresponds to the beginning of the wake-induced transition. The best fit of this data using equation (10) is given by

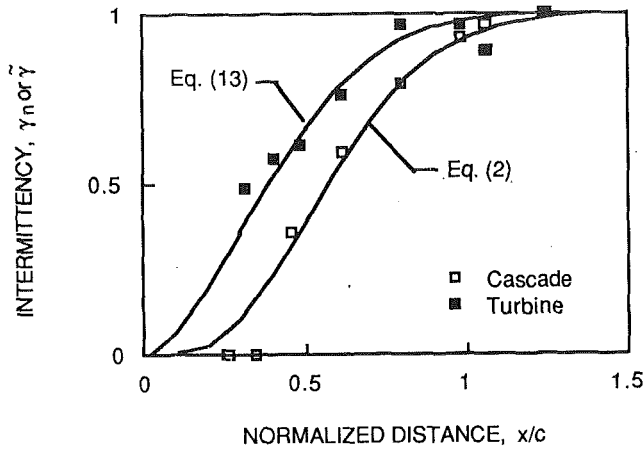


Fig. 8 Large-scale turbine intermittency data of Dring et al. (1986) and comparison to theory

$$\tilde{\gamma}_w = 1 - e^{-0.733n(x-x_{tw})} \quad (12)$$

with $x_{tw} = 0.04$ m. The agreement is excellent. Pfeil and Herbst indicate that the wakes from the individual spokes interfered with one another when $n = 90$. Hence, $\tau_w/\tau \approx n/90$. Using this and comparing the exponent in equation (12) to that in equation (10), one obtains $b/U_s = 66 \text{ m}^{-1}$. The momentum thickness Reynolds number at $x_{tw} = 0.04$ m is about 145.

Next, a comparison is made with the airfoil data of Dring et al. (1986). They obtained the time-averaged heat transfer on a first-stage rotor in a large-scale turbine facility. Heat transfer measurements on an airfoil in a steady cascade facility having the same profile also were obtained. Figure 52 in their report contains both the time-averaged and steady results plotted in the form of Stanton number against the distance along the surface of the airfoil. These results are for an airfoil with an axial chord of 161 mm and an inlet velocity of 22.8 m/s. Their figure also contains the predictions for a fully laminar and fully turbulent flow over the airfoil. Using equation (1) and the information in this figure, intermittency can be determined from

$$\gamma(x) = \frac{St - St_L}{St_T - St_L}$$

where St , St_L , and St_T are the transitional, fully laminar and fully turbulent Stanton numbers, respectively. Their predicted values of Stanton number were used for the fully laminar Stanton number St_L and fully turbulent Stanton number St_T . As pointed out by Sharma (1987), the intermittency calculated from fluid mechanic measurements does not necessarily have to correspond to that calculated from heat transfer results in flows with large pressure gradients. However, if the Pohlhausen pressure-gradient parameter $(\theta^2/\nu)(dU_\infty/dx)$ (where θ is the momentum thickness) is less than 0.005, i.e., the free-stream velocity U_∞ is nearly constant, the difference between the two is negligible. The data examined herein fall into this category.

The results are shown in Fig. 8 where the open symbols correspond to the results from the stationary cascade data and represent γ_n . The closed symbols correspond to those from the rotating turbine facility and represent $\tilde{\gamma}$. The figure shows intermittency plotted against the streamwise distance along the suction side of the airfoil divided by the airfoil's axial chord c . The data for the stationary cascade (open symbols) were used to determine the unknown quantities in equation (2) for natural transition. The best fit of equation (2) to these data provides $x_{in}/c = 0.12$ and $(x_{75} - x_{25})/c = 0.35$ and is shown in Fig. 8 marked as equation (2). Substituting these values into equation (11), the best fit to the data for the rotating turbine airfoil is given by

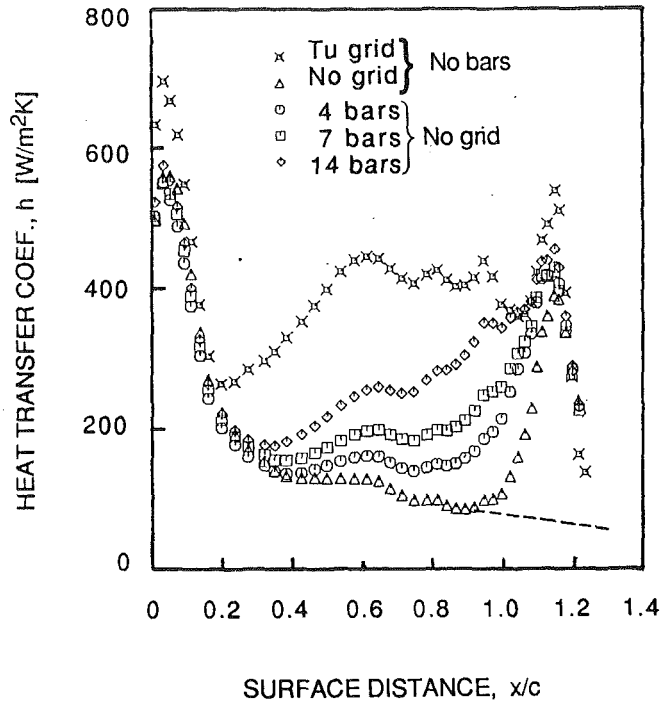


Fig. 9 Heat transfer distribution of an airfoil for different number of rods rotating at $\omega = 262$ rad/s

$$\tilde{\gamma}(x) = 1 - e^{-0.412 \left[\frac{x/c - 0.12}{0.35} \right]^2} e^{-1.62 \left[\frac{x - x_{tw}}{c} \right]} \quad (13)$$

with $x_{tw}/c = 0.05$. This distribution also is shown in Fig. 8 marked as equation (13). The agreement is good considering the scatter in the data. From Fig. 27a of Dring et al. (1989b), which provides the turbulence distribution in the wake of the upstream stator row, one finds $\tau_w/\tau \approx 0.18$. Using this and comparing the exponents in equations (11) and (13), one obtains $b/U_s = 56 \text{ m}^{-1}$, which is close to that obtained from the flat plate results. In addition, notice that x_{tw} is less than x_{in} .

The final comparison is made using data from heat transfer tests on an airfoil in a full-scale, stationary cascade with an unsteady wake generator of rotating bars placed upstream. The apparatus and experimental technique have been completely described by Wittig et al. (1988), where some preliminary results were given for wakes generated by rotating four bars. More recently, measurements of heat transfer on the same airfoil were made for no bars, 4, 7 and 14 bars. Measurements without bars also were made with a turbulence grid placed upstream to force transition to turbulent flow on the suction side of the airfoil. All of the results are shown in Fig. 9 where the distributions of heat transfer coefficient are plotted against the surface distance divided by the airfoil's chord. Each data set in the figure represents an average of four to five test runs with a scatter of less than five percent. For this series of tests, the inlet flow velocity is 80 m/s and the angular velocity of the rotating bars is 262 rad/s. The airfoil chord is 82 mm. The data shown here are just a portion of what will be reported and discussed more completely elsewhere. For the present, however, using equation (1) and the information in this figure, intermittency can be determined from

$$\gamma(x) = \frac{h - h_L}{h_T - h_L}$$

where h , h_L , and h_T are the transitional, fully laminar and fully turbulent heat transfer coefficients, respectively. The values for the fully laminar heat transfer coefficient h_L were obtained by extending the no bar results further along the

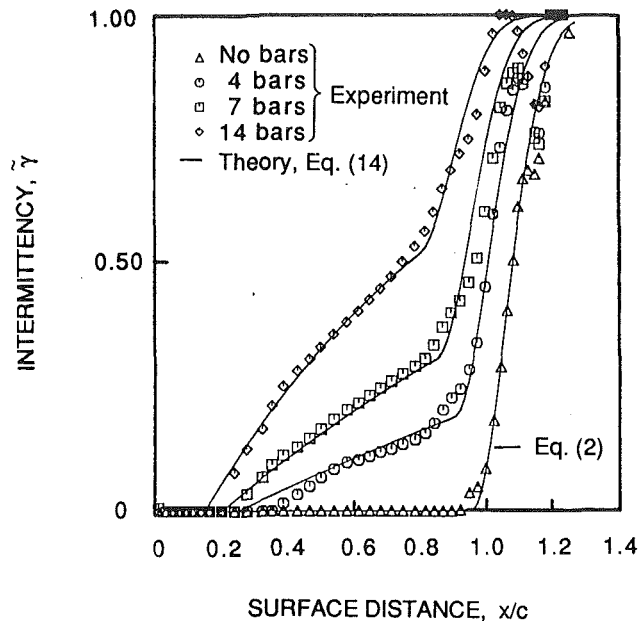


Fig. 10 Airfoil wake-induced intermittency distribution for different wake durations and comparison to theory

laminar-flow, flat-plate, heat transfer correlation (dashed line in the figure), while the results with the upstream grid were used for the fully-turbulent heat transfer coefficient h_T . The intermittency calculated in this manner is plotted in Fig. 10 for the various number of bars. The no bar case shown in this figure corresponds to the intermittency distribution caused by natural transition. The best fit of equation (2) to these data is obtained using $x_{tm}/c = 0.95$ and $(x_{75} - x_{25})/c = 0.1$ and is shown in Fig. 10 as the line marked equation (2). Substituting these values into equation (11), the best fit to the data for the rotating bars is given by

$$\tilde{\gamma}(x) = 1 - e^{-0.412 \left[\frac{x/c - 0.95}{0.1} \right]^2} e^{-0.08n \left[\frac{x - x_{tw}}{c} \right]} \quad (14)$$

This distribution is shown in Fig. 10 for the different number of bars as lines passing through the data. The agreement is remarkably good and supports the assumption of superposing natural and wake-induced transitional effects. For these tests, however it was found that both x_{tm} and x_{tw} changed slightly. The best fit was obtained when $x_{tm} - x_{tw} = 0.65c$ and $x_{tw} = 0.25c, 0.20c,$ and $0.15c$ for 4, 7, and 14 bars, respectively. From hot-wire measurements downstream of the rotating bars in the airfoil's leading edge plane, it was found that $\tau_w/\tau \approx 0.14$ for seven bars. Using this and comparing the exponents in equations (11) and (14), one obtains $b/U_s = 49 \text{ m}^{-1}$.

The values of b/U_s obtained through the aforementioned comparisons are summarized in Table 1. Since these values depend directly on the value of the wake-duration time-fraction, τ_w/τ , they are influenced by what was used to determine it and the accuracy in measuring it. In the present set of comparisons, τ_w/τ was obtained three different ways, none of which is presently known to be more correct than the other. But it is suspected that they are nearly consistent with one another such that the resulting values of b/U_s are comparable. If this is so, and until a more complete series of tests are completed, it appears that b/U_s is nearly independent of the test situation and roughly equal to 57 m^{-1} .

Conclusions

A model was described and a theory developed to predict wake-induced transition. By assuming that the wake simply

Table 1 Production strengths

	$b/U_s, \text{m}^{-1}$
Pfeil and Herbst	66
Dring et al.	56
Present work	49

increases the production of turbulent spots in a laminar boundary layer such that they merge to form a turbulent strip, the time-averaged intermittency distribution for wake-induced transition was obtained.

In contrast to natural transition where the intermittency depends exponentially on the square of the distance from the inception of transition, the intermittency for wake-induced transition depends exponentially on the distance itself. As may be expected, it also depends on the duration time of the wake in the incident flow. The important wake-induced transition parameter was found to be $\tau_w b(x - x_{tw})/\tau U_s/\tau U_s$ where b is related to the turbulent-strip production rate.

Comparing the theory to data showed very good agreement. For all of the tests considered, it appears that the quantity b/U_s is nearly independent of the test situation and roughly equal to 57 m^{-1} . For Pfeil and Herbst's data, the momentum thickness Reynolds number corresponding to the beginning of wake-induced transition x_{tw} was found to be about 145. Since it seems, however, that both b and x_{tw} depend at least on the turbulence in the wake, additional data are required before more can be said.

In addition, it was found that the effects of natural and wake-induced transition can be superposed. This provides an important relation for the gas turbine designer who must determine the time-averaged heat load or aerodynamic loss for a turbine airfoil. In either case, the local conditions on the suction side of the airfoil may be obtained from $\tilde{f} = (1 - \tilde{\gamma})f_L + \tilde{\gamma}f_T$ where \tilde{f} is the time-averaged, local boundary-layer flow related quantity (such as the heat transfer coefficient), f_L is its laminar value, f_T is its fully turbulent value, and $\tilde{\gamma}$ is the time-averaged intermittency obtained from equation (11).

Acknowledgment

One of the authors, R. E. Mayle, is truly indebted to the Alexander von Humboldt Stiftung, Federal Republic of Germany and his host Professor S. Wittig. The theory presented in this paper was developed during his tenure at the Institut für Thermische Strömungsmaschinen, Universität Karlsruhe as a recipient of the Alexander von Humboldt Award for Senior Scientist.

References

- Ashworth, D. A., LaGraff, J. E., Schultz, D. L., and Grindrod, K. J., 1985, "Unsteady Aerodynamic and Heat Transfer Processes in a Transonic Turbine Stage," *ASME Journal of Engineering for Gas Turbines and Power*, Vol. 107, No. 4, pp. 1011-1030.
- Ashworth, D. A., LaGraff, J. E., and Schultz, D. L., 1987, "Unsteady Interaction Effects on a Transitional Turbine Blade Boundary Layer," *Proceedings of the 1987 ASME-JSME Thermal Engng. Conference*, eds., P. J. Marto and I. Tanasawa, Vol. 2, pp. 603-610.
- Dhawan, S., and Narasimha, R., 1958, "Some Properties of Boundary Layer Flow During Transition from Laminar to Turbulent Motion," *Journal of Fluid Mechanics*, Vol. 3, pp. 418-436.
- Doorly, D. J., 1987, "Modeling the Unsteady Flow in a Turbine Rotor Passage," *ASME Paper No. 87-GT-197*.
- Doorly, D. J., Oldfield, M. L. G., and Scrivener, C. T. J., 1985, "Wake-Passing in a Turbine Rotor Cascade," *Heat Transfer and Cooling in Gas Turbines*, AGARD-CP-390, pp. 7-1 to 7-18.
- Dring, R. P., Blair, M. F., Joslyn, H. D., Power, G. D., and Verdon, J. M., 1986, "The Effects of Inlet Turbulence and Rotor/Stator Interactions on the Aerodynamics and Heat Transfer of a Large-Scale Rotating Turbine Model," *NASA Contractor Rept. 4079*, Vol. 1.
- Dunn, M. G., 1986a, "Heat-Flux Measurements for the Rotor of a Full-Stage Turbine: Part I—Time-Averaged Results," *ASME JOURNAL OF TURBOMACHINERY*, Vol. 108, No. 1, pp. 90-97.

Dunn, M. G., George, W. K., Rae, W. J., Woodward, S. H., Moller, J. C., and Seymour, P. J., 1986b, "Heat-Flux Measurements for the Rotor of a Full-Stage Turbine: Part II — Description of Analysis Technique and Typical Time-Resolved Measurements," *ASME JOURNAL OF TURBOMACHINERY*, Vol. 108, No. 1, pp. 98-107.

Dunn, M. G., Martin, H. L., and Stanek, M. J., 1986c, "Heat Flux and Pressure Measurements and Comparison With Prediction for a Low-Aspect-Ratio Turbine Stage," *ASME JOURNAL OF TURBOMACHINERY*, Vol. 108, No. 1, pp. 108-115.

Dunn, M. G., Seymour, P. J., Woodward, S. H., George, W. K., and Chupp, R. E., 1988, "Phase-Resolved Heat-Flux Measurements on the Blade of a Full-Scale Rotating Turbine," *ASME Paper No. 88-GT-173*.

Emmons, H. W., 1951, "The Laminar-Turbulent Transition in a Boundary Layer—Part 1," *Journal of the Aeronautical Sciences*, Vol. 18, pp. 490-498.

Guenette, G. R., Epstein, A. H., Norton, R. J. G., and Yuzhang, C., 1985, "Time Resolved Measurements of a Turbine Rotor Stationary Tip Casing Pressure and Heat Transfer Field," *AIAA Paper No. 85-1220*.

Hodson, H. P., 1984, "Boundary Layer and Loss Measurements on the Rotor of an Axial-Flow Turbine," *ASME Journal of Engineering for Gas Turbines and Power*, Vol. 106, pp. 391-399.

LaGraff, J. E., Ashworth, D. A., and Schultz, D. L., 1988, "Measurement and Modeling of the Gas Turbine Blade Transition Process as Disturbed by Wakes," *ASME Paper No. 88-GT-232*.

Pfeil, H., and Herbst, R., 1979, "Transition Procedure of Instationary Boundary Layers," *ASME Paper No. 79-GT-128*.

Pfeil, H., Herbst, R., and Schröder, T., 1983, "Investigation of the Laminar-Turbulent Transition of Boundary Layers Disturbed by Wakes," *ASME Journal of Engineering for Power*, Vol. 105, pp. 130-137.

Sharma, O., 1987, "Momentum and Thermal Boundary Layer Development on Turbine Airfoil Suction Surfaces," *AIAA Paper No. 87-1918*.

Taulbee, D. B., Tran, L., and Dunn, M. G., 1988, "Stagnation Point and Surface Heat Transfer for a Turbine Stage: Prediction and Comparison With Data," *ASME Paper No. 88-GT-30*.

Van Dresar, N. T., and Mayle, R. E., 1987, "A Quasi-Steady Approach of Wake Effects on Leading Edge Transfer Rates," *Heat Transfer in Gas Turbine Engines*, ed. D. E. Metzger, ASME Publication, HTD-Vol. 87, pp. 1-10.

Wittig, S., Schulz, A., Dullenkopf, K., and Fairbank, J., 1988, "Effects of Free-Stream Turbulence and Wake Characteristics on the Heat Transfer Along a Cooled Gas Turbine Blade," *ASME Paper No. 88-GT-179*.

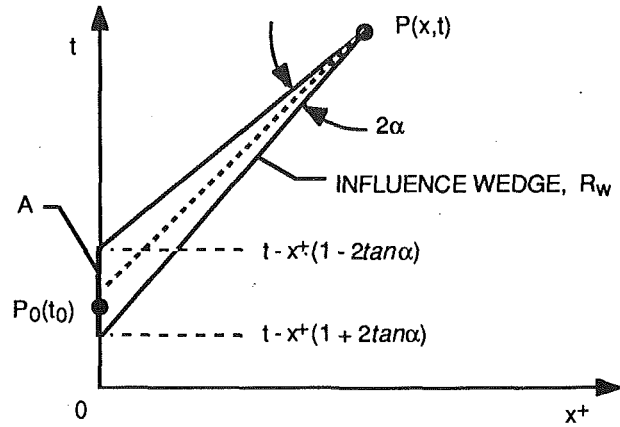


Fig. A1 Solution plane for wake-induced transition

where A is the region in R_w at $x^+ = 0$, since the only sources of turbulent strips are at $x^+ = 0$. If a turbulent strip spreads in a linear fashion with a half-angle spread of α , A lies on the t -axis between $t - x^+(1 + 2 \tan \alpha)$ and $t - x^+(1 - 2 \tan \alpha)$ for a point $P(x^+, t)$ as shown in Fig. A1. The quantity $G(x^+, t)$ can be evaluated by noting that the order of integration and summation may be interchanged since A is not a function of t_0 . This provides

$$G(x^+, t) = -a \sum_{n=-\infty}^{\infty} \int_A [U(t_0 + \tau_w - n\tau) - U(t_0 - n\tau)] dt_0. \quad (A3)$$

The integral is rather easy to evaluate since the integrand is a single square wave of width τ_w starting at $t_0 = n\tau - \tau_w$. The only time there is a contribution to the integral is when $P(x^+, t)$ is positioned such that region A contains part of this wave. Defining the integral as $G_n(x^+, t)$, one obtains

$$G_n(x^+, t) = \begin{cases} 0 & ; t \leq n\tau \\ t - n\tau & ; n\tau \leq t \leq n\tau + \{\tau_w\} \\ \{\tau_w\} & ; n\tau + \{\tau_w\} \leq t \leq n\tau + \{4x^+ \tan \alpha\} \\ \tau_w + 4x^+ \tan \alpha - (t - n\tau) & ; n\tau + \{4x^+ \tan \alpha\} \leq t \leq n\tau + x^+ 4x^+ \tan \alpha + \tau_w \\ 0 & ; t \geq n\tau + 4x^+ \tan \alpha + \tau_w \end{cases}$$

APPENDIX

The task is to evaluate the time-averaged, wake-induced intermittency given by equation (9) in the text, viz.

$$\bar{\gamma}_w(x) = 1 - \frac{1}{\tau} \int_{t_1}^{t_1 + \tau} \exp \left\{ -a \int_{R_w} \delta(x_0^+) \sum_{n=-\infty}^{\infty} [U(t_0 + \tau_w - n\tau) - U(t_0 - n\tau)] dV_0 \right\} dt. \quad (A1)$$

where $dV_0 = dx_0^+ dt_0$ for a two-dimensional source. Define the argument of the exponential function within one period τ as $G(x^+, t)$. Then, integrating with respect to x_0^+ , one obtains

$$\bar{\gamma}_w(x) = 1 - \frac{1}{\tau} \int_{t_1}^{t_1 + \tau} \exp [G(x^+, t)] dt \quad (A2)$$

with

$$G(x^+, t) = -a \int_A \sum_{n=-\infty}^{\infty} [U(t_0 + \tau_w - n\tau) - U(t_0 - n\tau)] dt_0$$

for $4x^+ \tan \alpha \leq \tau_w$. For $4x^+ \tan \alpha \geq \tau_w$, the quantities τ_w and $4x^+ \tan \alpha$ in curly braces should be exchanged. Consider first the case for $4x^+ \tan \alpha \geq \tau_w$, i.e., distances not too close to the wake-induced transition point. Substituting the foregoing expressions into equation (A3) and summing, one obtains

$$G(x^+, t) = -a \sum_{n=-\infty}^{\infty} G_n(x^+, t) = -a [\tau_w I \left(\frac{4x^+ \tan \alpha}{\tau} \right) + G_I - G_{II}]$$

where $I(x)$ is the integer function of x , i.e., $I(2.34) = 2$,

$$G_I = \begin{cases} t & ; 0 \leq t \leq \tau_w \\ \tau_w & ; \tau_w \leq t \leq \tau \end{cases}$$

and

$$G_{II} = \begin{cases} 0 & ; 0 \leq t \leq \tau F\left(\frac{4x^+ \tan \alpha}{\tau}\right) \\ t - \tau F\left(\frac{4x^+ \tan \alpha}{\tau}\right) & ; \tau F\left(\frac{4x^+ \tan \alpha}{\tau}\right) \leq t \leq \tau F\left(\frac{4x^+ \tan \alpha}{\tau}\right) + \tau_w \\ \tau_w & ; \tau F\left(\frac{4x^+ \tan \alpha}{\tau}\right) + \tau_w \leq t \leq \tau \end{cases}$$

where $F(x)$ is the fractional function of x , i.e., $F(2.34) = 0.34$. Substituting this into equation (A2) yields

$$\tilde{\gamma}_w(x) = 1 - \frac{1}{\tau} \int_{t_1}^{t_1 + \tau} e^{G(x^+, t)} dt = 1 - e^{-a\tau_w F\left(\frac{4x^+ \tan \alpha}{\tau}\right)} \frac{1}{\tau} \int_{t_1}^{t_1 + \tau} e^{-a(G_I - G_{II})} dt.$$

The integral can be evaluated quickly for $a\tau_w \ll 1$ by expanding the exponential function in a series, keeping only the first two terms, and integrating. This provides, after some manipulation

$$\tilde{\gamma}_w(x) = 1 - e^{-4a\left(\frac{\tau_w}{\tau}\right)x^+ \tan \alpha} \quad (A4)$$

Evaluating $a\tau_w$ by comparing the previous expression to experimental results (done in the text), it is found that the average $a\tau_w$ for those cases examined is about 0.3. Although not much, much smaller than unity, the error incurred in assuming so is only about 15 percent and not worth the additional complexity.

So the final result is considered to be well represented by equation (A4).

Now consider the case where $4x^+ \tan \alpha \leq \tau_w$, i.e., close to the wake-induced transition point. For $4x^+ \tan \alpha + \tau_w \leq \tau$, the only contribution to the sum

$$G(x^+, t) = -a \sum_{n=-\infty}^{\infty} G_n(x^+, t)$$

is from one of the terms, say the $n = 0$ terms, since G_n is zero outside the period $0 \leq t \leq \tau$. Thus $G(x^+, t) = -aG_0(x^+, t)$. If $a\tau_w \ll 1$, then the maximum of a $G_0(x^+, t) = a(4x^+ \tan \alpha) \ll 1$, and the exponential function of $G(x^+, t)$ in equation (A2) may again be expanded in a series. Integration of this series, keeping only the first two terms, yields the expanded form of equation (A4), i.e., result for small distances. Providing $a\tau_w \ll 1$, the same result is obtained for the remaining case where $4x^+ \tan \alpha \leq \tau_w$, $4x^+ \tan \alpha + \tau_w \geq \tau$. Therefore, equation (A4) provides an expression for the time-averaged wake-induced intermittency for all possible cases.

Effects of Adverse Pressure Gradients on the Nature and Length of Boundary Layer Transition

G. J. Walker

University of Tasmania,
Hobart, Australia

J. P. Gostelow

University of Technology,
Sydney, Australia

Existing transition models are surveyed and deficiencies in previous predictions, which seriously overestimate transition length under an adverse pressure gradient, are discussed. A new model for transition in an adverse pressure gradient situation is proposed and experimental results are provided that confirm its validity. A correlation for transition length is advanced that incorporates both Reynolds number and pressure gradient effects. Under low free-stream turbulence conditions the basic mechanism of transition is laminar instability. There are, however, physical differences between zero and adverse pressure gradients. In the former case, transition occurs randomly, due to the breakdown of laminar instability waves in sets. For an adverse pressure gradient, the Tollmien-Schlichting waves appear more regularly with a well-defined spectral peak. As the adverse pressure gradient is increased from zero to the separation value the flow evolves continuously from random to periodic behavior and the dimensionless transition length progressively decreases.

Introduction

Turbomachinery designers have become reliant on advanced computational methods to predict flows over blading. An essential requirement of these codes is their ability to predict the state of the boundary layer on the blade surface. Difficulties have often been encountered due to inadequacies in existing boundary layer transition prediction procedures. It has been necessary to resort to crude, and often unrealistic, assumptions for the codes to run. This is especially so of the adverse (or positive) pressure gradient regimes encountered by compressor blading. The problems arise because the existing experimental transition data for adverse pressure gradient flows are inadequate.

Transition on the blades of axial turbomachines may evenuate from a variety of causes including two-dimensional viscous instability, centrifugal instability on concave surfaces, surface roughness, and the diffusion of free-stream turbulence into the boundary layer. Laminar instability processes can be significantly influenced by external disturbances such as acoustic forcing, wake passing and free-stream turbulence fluctuations.

The basic mechanism may be considered to be laminar instability, which is, however, subject to being "bypassed" and therefore masked by turbulence and other effects. For this reason a series of experiments was undertaken in a relatively

clean flow environment to elucidate the influence of pressure gradient on laminar instability processes before addressing other real-flow attributes of turbomachines, such as free-stream turbulence.

The present investigation is concerned with the physics of transition under adverse pressure gradients and in the absence of interference from bypass mechanisms. The emphasis is on differences in transition modes between flows with and without an adverse streamwise pressure gradient. A new model for transition under these conditions is proposed and experimental results are presented in an attempt to validate the model.

One result of this work is a new correlation for transition length, which is broadly supported by the limited data available. The new model and correlation differ substantially from existing procedures. They offer a basis for more accurate transition modeling, which should be capable of describing laminar separation effects and can be extended to other influences on transition, such as free-stream turbulence effects.

Transition Resulting From Two-Dimensional Viscous Instability

Transition arising from two-dimensional viscous instability was the dominant mechanism leading to the onset of turbulence in the present investigation. The sequence of events involved in this type of transition is as follows:

(a) **Instability to Two-Dimensional Disturbances.** Above a critical Reynolds number, the laminar boundary layer becomes unstable to two-dimensional disturbances. Subsequent ampli-

Contributed by the International Gas Turbine Institute and presented at the 34th International Gas Turbine and Aeroengine Congress and Exhibition, Toronto, Ontario, Canada, June 4-8, 1989. Manuscript received at ASME Headquarters February 1, 1989. Paper No. 89-GT-274.

fication leads to the formation of Tollmien-Schlichting (T-S) waves. The onset of instability and the initial growth of T-S waves are well described by linearized theory and solutions to the resulting Orr-Sommerfeld equation. The shape of the neutral stability curve depends on the laminar velocity profile, which is determined principally by the streamwise pressure gradient. The range of frequencies receiving amplification varies with the boundary layer Reynolds number.

(b) Three-Dimensional Instability and Nonlinear Amplification. After sufficient amplification of the two-dimensional disturbances, a regular spanwise flow distortion becomes apparent. This three-dimensionality introduces streamwise vorticity and causes a rapid nonlinear amplification of the spanwise waves into vortex loops (also referred to as vortex trusses, hairpin eddies and lambda vortices). The vortex loops may be arranged either in streamwise rows or in a staggered ("thatched") pattern as shown in Fig. 1. The staggered pattern repeats itself at streamwise intervals of $2\Lambda_x$, where Λ_x is the wavelength of the primary instability wave, and thus introduces subharmonics at half the T-S wave frequency.

Saric and Thomas (1983) identified two types of staggered pattern having characteristically different ratios of spanwise to streamwise wavelength, Λ_z/Λ_x . The type of three-dimensionality observed was found to depend on the amplitude of the primary disturbance. For disturbance levels less than $0.002U$ at Branch II (the upper branch) of the neutral stability curve, the two-dimensional disturbances decayed without any three-dimensionality appearing. At amplitudes around $0.003U$, a C-type system of staggered vortices with Λ_z/Λ_x about 1.5 was obtained. This system, which was investigated theoretically by Craik (1971), is produced by resonant interactions among a triad of one normal and two oblique T-S waves. At amplitudes between 0.003 and $0.006U$, an H-type staggered system having a Λ_z/Λ_x of about 0.7 was observed. The latter pattern is explained by instability to three-dimensional disturbances of a basic state comprising laminar flow and a two-dimensional T-S disturbance as described by Herbert (1983).

For amplitudes greater than $0.006U$, Saric and Thomas (1983) observed a K-type array of vortices aligned in streamwise rows having a Λ_z/Λ_x of about 0.5 . This is the pattern that was observed in the early studies of three-dimensional instability carried out by Klebanoff et al. (1962). More recent experimental studies of events in the nonlinear region have been reported by Kegelman and Mueller (1986).

(c) Breakdown. The initiation of turbulent spots (or "breakdown") occurs through the appearance of high-fre-

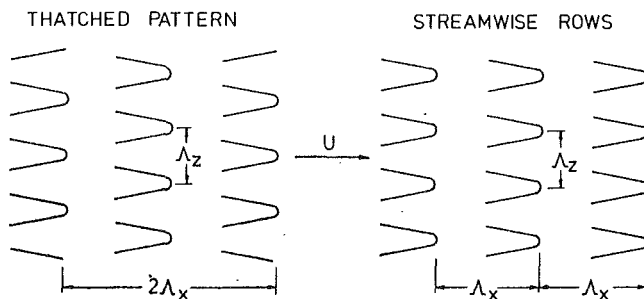


Fig. 1 Vortex loop patterns prior to breakdown

quency fluctuations near the heads of the vortex loops. The influence of streamwise pressure gradient on this process has been investigated by Knapp and Roache (1968) and by Arnal et al. (1979a, 1979b).

Knapp and Roache found natural transition in zero pressure gradient flows to be characterized by the breakdown of laminar instability waves in sets. These sets translated several wavelengths of the basic T-S wave during amplification, distortion and breakdown. They were interspersed by a significant laminar region following breakdown. The vortex loops resulting from the breakdown of wave sets were usually arranged in a staggered pattern. The "intermittency" frequency with which wave sets appeared was about one tenth of the basic T-S wave frequency.

For natural transition in an adverse pressure gradient, Knapp and Roache observed similar behavior, except that the phenomena became more exaggerated. The formation of wave sets occurred at a higher frequency, and transition approached a continuous process with much shorter intervals between the breakdown of sets. In the nonlinear region, the tendency for vortex loops to be staggered was reduced and a greater proportion appeared in streamwise rows. The work of Arnal et al. (1979b) supports the observation of the more continuous transition process, intermittency becoming more difficult to determine in these circumstances.

In forced transition produced by the introduction of sound waves, with frequencies close to those of the naturally occurring T-S waves, Knapp and Roache found the frequency of all wave regions became locked in to the sound frequency. There was a continuous breakdown of individual instability waves and the vortex loops tended to appear in rows for both zero and adverse pressure gradients.

(d) Merging of Turbulent Spots. The final stage of tran-

Nomenclature

C_p = static pressure coefficient	t = time	ν = kinematic viscosity
c_f = skin-friction coefficient	U = free-stream velocity	ξ = dimensionless distance = $(x - x_i)/\lambda$
H = form factor = δ^*/θ	u = local velocity	σ = turbulent spot-dependence area parameter
L_T = transition length = $(x_T - x_i)$	x = streamwise distance from leading edge	ρ = density
N = nondimensional spot for- mation rate = $n\sigma\theta_i^3/\nu$	y = normal distance from wall	ω = circular frequency, rad/s
n = spot formation rate	δ = absolute thickness	Λ = instability wavelength
R_t = transition inception Rey- nolds number	δ^* = displacement thickness	
R_x = length Reynolds number	γ = intermittency factor	Subscripts
R_{δ^*} = displacement thickness Rey- nolds number	η = dimensionless distance = $(x - x_S)/(x_T - x_S)$	S = start of transition ($\gamma = 0.01$)
R_{θ} = momentum thickness Rey- nolds number	θ = momentum thickness	T = end of transition ($\gamma = 0.99$)
T = turbulence level, percent	λ = distance from 0.25 to 0.75 intermittency	t = start of transition (Nara- simha method)
	λ_{θ} = pressure gradient parameter = $(\theta^2/\nu) \cdot (dU/dx)$	x = streamwise component
		z = spanwise component

sition involves a zone of intermittently turbulent flow in which adjacent turbulent spots merge through both streamwise and lateral spreading to form a continuously turbulent flow. Numerous studies of turbulent spot spreading have been reported since the earliest investigation by Schubauer and Klebanoff (1956) of an isolated spot developing in zero pressure gradient.

An isolated spot resembles a downstream-pointing arrowhead in planform. Schubauer and Klebanoff found the growth envelope to approximate a wedge of 22 deg included angle. The convection rates of the spot leading and trailing edges were $0.88U$ and $0.5U$, respectively. These values can be taken as typical, although they are known to vary slightly with Reynolds number and pressure gradient.

Transitional Flow Length

Zero Pressure Gradient. Experimental work by Narasimha and others for constant pressure boundary layers has indicated a universal distribution of turbulent intermittency regardless of the agency causing transition. This distribution is described by

$$\gamma = 1 - \exp[-0.412 \xi^2]. \quad (1)$$

Narasimha (1957) showed that this result could be derived from the turbulent spot theory of Emmons (1951) on the assumption that spots form randomly in time and cross-stream position at a preferred streamwise location lying close to the upstream end of the transition region x_t . The development of this model is described in a recent comprehensive review of transitional flow behavior by Narasimha (1985).

It also is useful to have an overall measure of transitional flow length. Defining the downstream limit of the transition zone to be the 99 percent intermittency location, the foregoing intermittency distribution gives

$$L_T = (x_T - x_t) = 3.36\lambda. \quad (2)$$

Empirical correlations for the length of the transition zone in constant pressure flows have been given by various workers in the form

$$R_\lambda = A R_t^B \quad (A, B \text{ const}). \quad (3)$$

Dhawan and Narasimha (1958) originally proposed

$$R_\lambda = 5 R_t^{0.8} \quad (4)$$

as an average fit to their available data, which showed a considerable amount of scatter. Narasimha (1978) later revised this correlation to give

$$R_\lambda = 9 R_t^{0.75} \quad (5)$$

which is still consistent with the Dhawan and Narasimha data and implies a turbulent spot breakdown rate dependent on local boundary layer thickness.

Arbitrary Pressure Gradient. Chen and Thyson (1971) modeled the transition zone for flows in a pressure gradient by assuming that:

- (i) Spot propagation velocities at any given station are proportional to the local external velocity $U(x)$;
- (ii) The spot grows at a constant angle to the local external streamline; and
- (iii) the hypothesis of concentrated breakdown at x_t remains valid.

In accordance with this model Cebeci and Smith (1974) proposed the intermittency distribution

$$\gamma = 1 - \exp[-G(x - x_t) \int_{x_t}^x dx/U] \quad (6)$$

where

$$G = (1/1200) \cdot (U^3/\nu^2) R_t^{-1.34}. \quad (7)$$

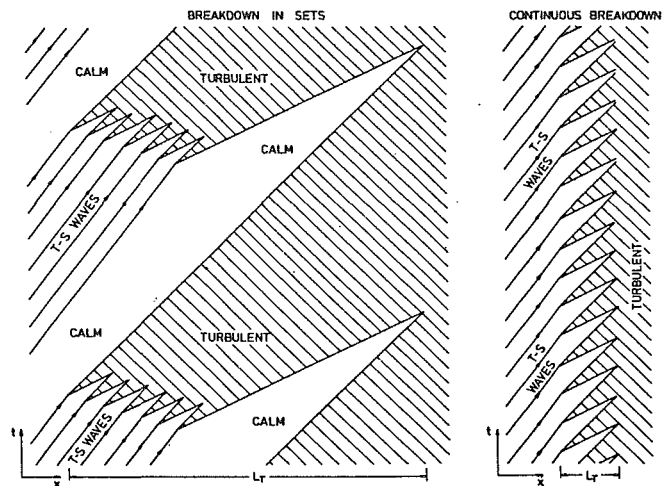


Fig. 2 Time-space distributions of the transition process

The Chen-Thyson model only allows for the effect of pressure gradient on local spot convection velocities and does not encompass any influence of pressure gradient on the mechanics of breakdown. For the case of zero pressure gradient, equations (6) and (7) lead to

$$R_\lambda = 22 R_t^{0.67} \quad (8)$$

which gives similar results to equation (4) due to compensating variations in the constants used. The model has essentially been calibrated against constant pressure flow data.

Minimum Transition Length. Difficulties experienced by users of computational routines in calculating the boundary layer development on the suction surface of airfoils operating at low Reynolds number have drawn attention to the inadequacies of approaches such as the Chen-Thyson model for the case of a strong adverse pressure gradient. A recent example is given in the computations of Subroto (1987) using the Cebeci-Smith (1974) formulation. On the suction surface of airfoils and compressor blades transition is much more rapid than in constant pressure flows and equations (6) and (7) seriously overpredict the transition length. This can lead to failure of low Reynolds number calculations due to the bursting of laminar separation bubbles in the computed flow (Walker et al., 1988).

These problems can be explained in terms of the influence of pressure gradient on the breakdown mechanism, which was not taken into account in the Chen-Thyson model. The effect of pressure gradient is illustrated by Fig. 2, which shows time-space distributions of laminar and turbulent flow through transition for two characteristically different breakdown mechanisms. The diagrams have been constructed using typical values of U , $U/2$, $U/3$, respectively, for the leading and trailing edge spot convection rates and the T-S wave velocity. The breakdown of instability waves in sets, with an intervening calming period, is seen to produce transitional flow lengths several times greater than in a forced transition situation, where breakdown occurs continuously every cycle of the basic T-S wave. Following Knapp and Roache, transition inception in a strong adverse pressure gradient is expected to result from behavior of the continuous breakdown kind; for constant pressure flows, on the other hand, transition inception is expected to result from breakdown in sets.

In an attempt to estimate the transition length in strongly decelerating flow and to place limits on the possible range of transitional flow lengths, Walker (1987) developed a minimum transition length model based on the continuous breakdown hypothesis. An equispaced spanwise array of turbulent spots was assumed to originate from x_t once each cycle of the basic

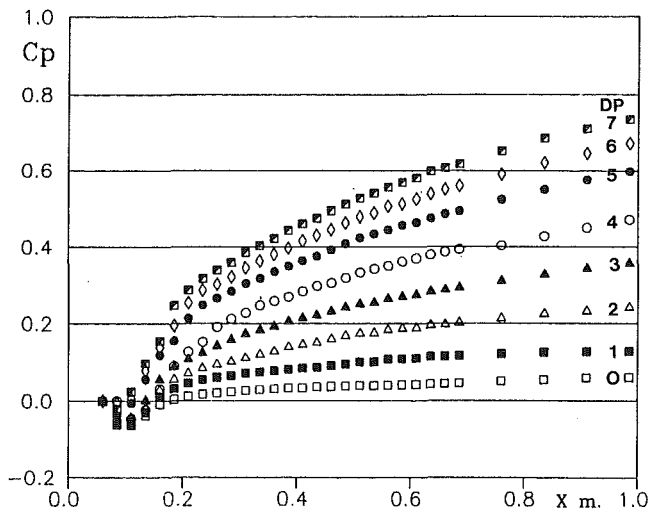


Fig. 3 Streamwise static pressure distributions for different levels of adverse pressure gradient

T-S wave. McCormick's (1968) model of an idealized triangular spot spreading at the convection velocities observed by Schubauer and Klebanoff (1956) was then applied to determine the streamwise distance required for adjacent spots to touch through either lateral or longitudinal spreading.

From the stability characteristics of Falkner-Skan boundary layers calculated by Obremski et al. (1969), the locus of maximum disturbance amplification rate was correlated by

$$(\omega\nu/U^2) = 3.2 R_{\delta^*}^{-3/2} \quad (9)$$

This was assumed to approximate the dimensionless frequency of disturbances having the maximum amplification ratio. Adopting this frequency for the spot inception rate, and assuming a spanwise spot spacing equal to the basic T-S wavelength, the streamwise spreading was found to be the limiting factor in determining minimum transition length. The corresponding transition length was given by

$$R_{L_T} = 2.3 R_{\delta^*}^{3/2} \quad (10)$$

which for zero pressure gradient flow, can be written as

$$R_{L_T} = 5.2 R_i^{3/4} \quad (11)$$

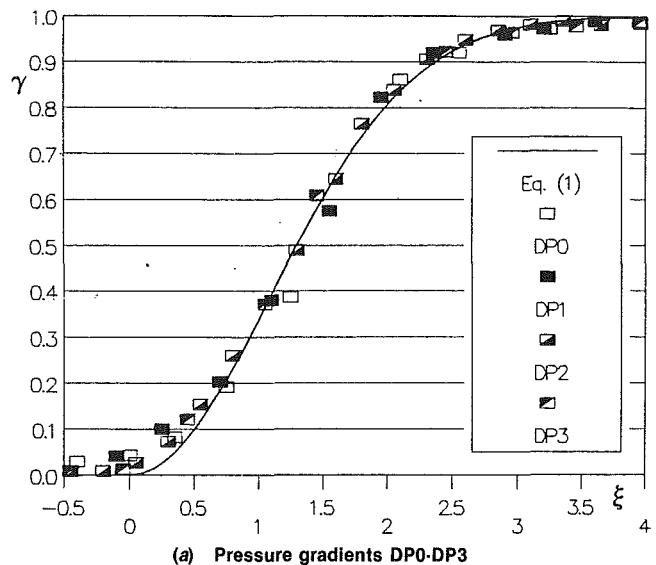
This shows the same functional dependence on Reynolds number as Narasimha's (1978) correlation, equation (7), and also gives a reasonable estimate of transition length for a forced transition case reported by Schubauer and Skramstad (1948).

An Arbitrary Pressure Gradient Transition Model. In arbitrary pressure gradient situations with low free-stream disturbance levels, the transitional flow length might be expected to vary between values predicted by zero pressure gradient correlations and those obtained from the minimum length model just outlined. This will be due to a number of pressure gradient related factors such as turbulent breakdown mechanisms and spot spreading rates. It therefore seems reasonable to attempt a correlation of the ratio of actual transition length to that given by the aforementioned minimum length model in terms of some suitable pressure gradient parameter.

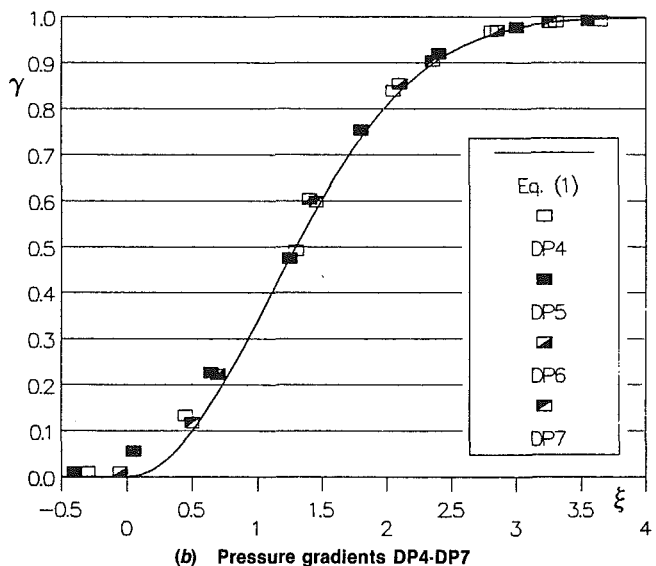
This possibility will be explored in the following discussion using data of the present investigators and other workers. Besides providing further information about the influence of pressure gradient on transition, the analysis will assist in calibrating the minimum transition length model itself.

Experimental Results and Data Analysis

Experimental investigations were undertaken in the low-speed wind tunnel described by Gostelow and Blunden (1988). The



(a) Pressure gradients DP0-DP3



(b) Pressure gradients DP4-DP7

Fig. 4 Intermittency distributions for the range of pressure gradients, plotted on a similarity basis

previous investigations were undertaken with turbulence grids present upstream of the working section, giving free-stream turbulence levels between 1 and 5 percent. For the subject experiments no such grid was present and the average free-stream turbulence level at inlet was 0.3 percent. Intermittency measurements were made using a single hot-wire probe and a DISA constant temperature anemometer. For most boundary layer velocity traverses, a flattened head pitot tube was used.

Adverse pressure gradients, of varying strength, were imposed by a fairing mounted above the flat plate. This could be rotated incrementally about an axis located 20 mm upstream of the leading edge of the flat plate. Static pressure gradients in a streamwise direction could be measured using both centerline pressure taps and velocity measurements in the free stream. Figure 3 presents the streamwise distributions of static pressure, measured using the static taps, for the different fairing settings used. There was no evidence of separation from the fairing in the region of interest. The pressure gradients were designated DP0-DP7, commencing with zero and in increasing order of adverse pressure gradient.

Intermittency values were determined on-line using a meter developed by Alt (1987). With this meter, sampling times up

to 100 s were possible. The setting of threshold levels needed particular attention for these measurements, especially under strong adverse pressure gradients where strong periodic signals were observed both before and after turbulent breakdown.

The intermittency distributions obtained for the various pressure gradients are presented in Fig. 4. These are presented in the similarity form advocated by Narasimha (1957). All intermittency data were plotted in terms of the variable

$$F(\gamma) = [-\ln(1 - \gamma)]^{1/2} \quad (12)$$

and from the resulting plots the effective transition inception x_t , obtained by linear extrapolation to the η -axis, and effective transition length, λ , were determined. The rescaled intermittency distributions were then plotted in comparison with Narasimha's universal intermittency function given in equation (1).

Agreement with the universal function is seen to be reasonable. The Narasimha procedure clearly provides a viable basis for representation of the transition region. Although data were obtained for a range of intermittencies, including 1 percent as a notional transition inception value, data consistency is maximized by designation of the "t" intercept as the start of transition.

Boundary layer velocity profiles were derived in the form of dimensionless velocity as a function of dimensionless traverse height. The form of these was generally in accordance with the plots of Gostelow and Blunden although full traverses were carried out for fewer intermittency values than in the previous study.

The resulting velocity distributions were integrated to provide integral parameters at the start and end of transition and for some intermediate locations. The results for R_x and also for R_θ appear in Fig. 5; the values for both transition inception and completion are plotted against $\lambda_{\theta t}$ in this figure.

The general shape of the R_x and R_θ plots is in accordance with the results presented in Gostelow and Blunden for a 1.7 percent turbulence level. Transition inception occurs at a value of $R_{\theta t}$ that declines mildly with increasing adverse pressure gradient. This decline levels off to a fairly constant value of $R_{\theta t}$ under moderately strong adverse pressure gradients. The completion of transition, on the other hand, occurs very much sooner as an increasingly adverse pressure gradient is imposed. As with the previous results, the tendency for the transition zone to become shorter is strong and consistent. The change is most marked when a zero pressure gradient is replaced by even a weak adverse one.

The data for the various adverse pressure gradient conditions have been analyzed according to the procedure of Narasimha (1985). A value of dimensionless turbulent spot formation parameter, N , has been obtained for each pressure gradient and these also are plotted as a function of $\lambda_{\theta t}$ in Fig. 5. Although the derivation of N depends upon a number of assumptions the value for zero pressure gradient is broadly in accordance with the compilation of Narasimha (1985). The trend reflects the rapidly decreasing transition length as the pressure gradient parameter becomes more adverse, N varying inversely as the square of transition length.

Hot-Wire Anemometer Signals. A principal reason for the shorter transition lengths and strong increases in turbulent spot formation rates is the different physical nature of the flow under an adverse pressure gradient. Anemometer traces have been presented in Fig. 6 that represent some of the more identifiable events. Traces have been given for the zero pressure gradient case and for cases representing $\lambda_{\theta t}$ values of -0.034 and -0.069 ; for each pressure gradient intermittency values of 10, 50 and 90 percent have been represented. The traces have identical frequency and amplitude scales and were printed from a Hewlett-Packard 5420A Digital Signal Analyzer set to a bandwidth of 3.2 kHz and digitizing to 512 points. While

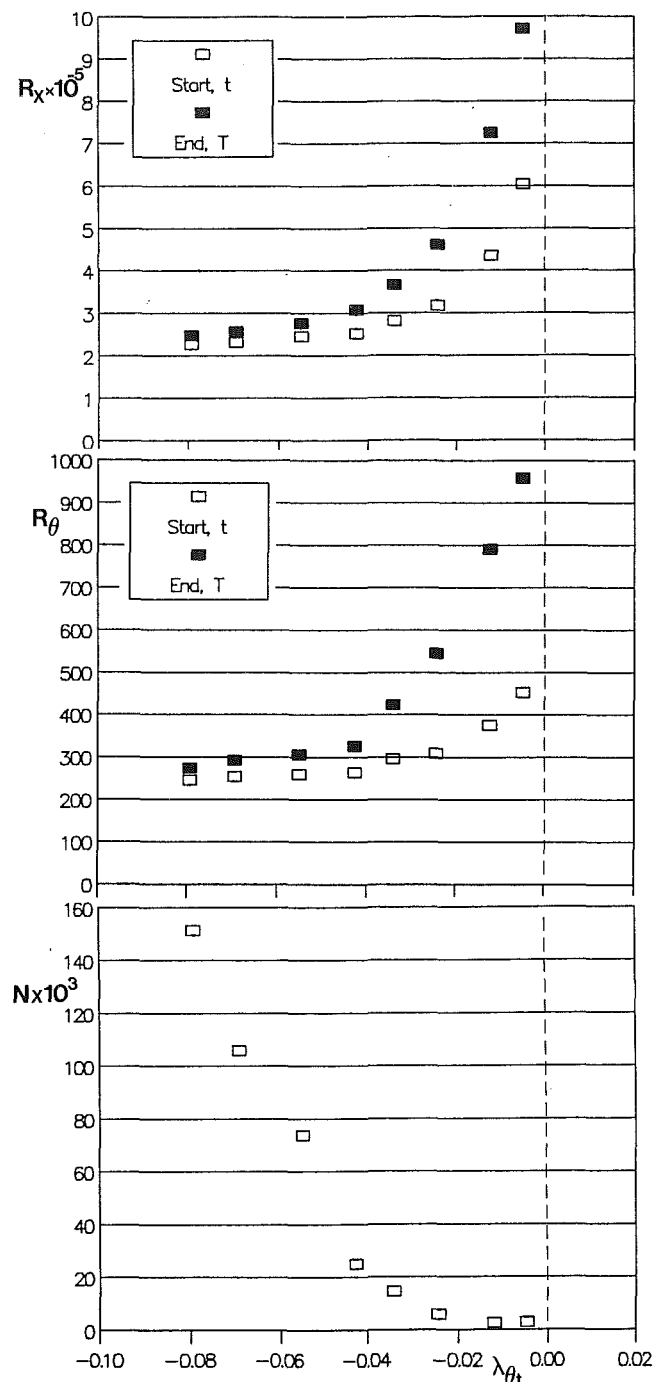


Fig. 5 Variation of R_x , R_θ and spot formation rate parameter, N , with pressure gradient parameter

these limitations have resulted in the loss of some high-frequency detail in the turbulent regions, the traces nevertheless represent the principal features of the flow.

The zero pressure gradient traces show clear evidence of T-S waves breaking down in sets with intervening calming periods. The turbulent spots are well defined making the measurement of intermittency a relatively easy task. While the intervals between spots are largely devoid of instability waves, it is nevertheless possible to discern some wave amplification and breakdown occurring at all stages of transition.

The medium pressure gradient traces still show evidence of the development of wave sets, but some T-S wave activity of lower amplitude can now be seen over most of the intervals between sets.

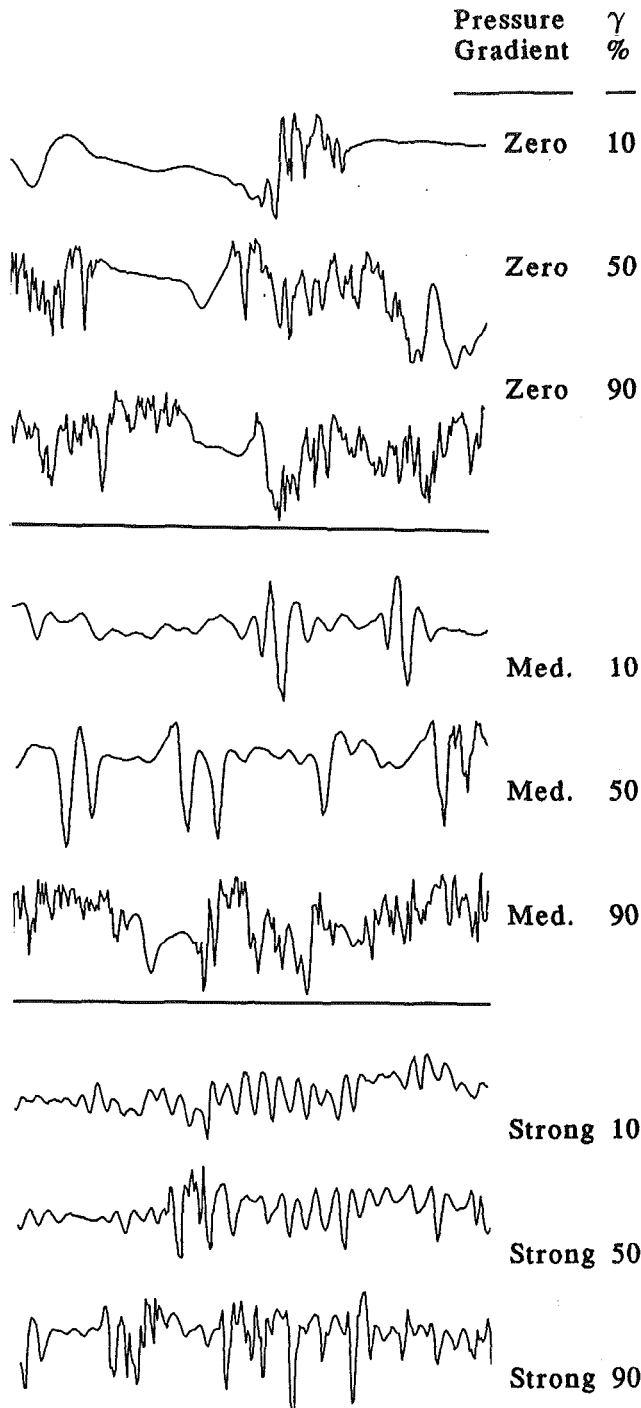


Fig. 6 Representative anemometer traces for three pressure gradients at three intermittency levels; each trace is of 40 ms duration

The high pressure gradient traces are marked by a fairly continuous appearance of instability waves, which show greater uniformity of amplitude than at the lower pressure gradients, although there is definite evidence of low-frequency amplitude modulation. The amplitude and frequency of the T-S waves under adverse pressure gradient conditions are higher than for lower pressure gradients and generally of the same order as the turbulent spots. Little information is available on turbulent spots under these conditions and especially on their spanwise structure. In essence though, whereas for weak adverse pressure gradients the T-S waves occur in packets, often associated with a single turbulent spot, for strong adverse pressure gradients the turbulent activity tends to be associated with each

T-S wave. These observations are fully consistent with the observations of Knapp and Roache (1968), and are also in agreement with the study of Arnal et al. (1979a). As noted by Arnal et al., the more progressive way in which turbulence appears during transition in an adverse pressure gradient makes the turbulent spots much more difficult to characterize. Intermittency measurements are open to greater error in this case, and the high-pass filter setting of the intermittency meter requires particular care; too low a cutoff frequency will result in an erroneously early start of transition due to triggering from well-developed instability waves, while too high a setting will indicate a delayed transition onset due to the elimination of some genuine turbulent signals.

Velocity Fluctuation Spectra. To complement the hot-wire anemometer traces, spectra of longer samples, around 70 sec, were obtained using an HP3582A analyzer. The resulting distributions are presented in Figs. 7 and 8.

Figure 7 presents spectra plotted to identical scales (8 mv full scale) for a strong adverse pressure gradient (DP6). The intermittency level increases from 1 to 90 percent and a discrete frequency of 740 Hz, corresponding to the basic T-S wave, predominates throughout.

In Fig. 8, spectra are presented for an intermittency of 10 percent for the eight values of pressure gradient tested. The spectra for the low pressure gradient cases, DP0 and DP1, are presented with a different frequency scale from the others. Each square represents 250 Hz for DP0 and DP1 and 500 Hz for the remaining pressure gradients. A continuous change in spectral shape is observed as the streamwise pressure gradient becomes more adverse. In the absence of a pressure gradient, the spectral density falls continuously with increasing frequency and there are no identifiable spectral peaks. The application of a slight adverse pressure gradient produces a peak or peaks, which build in amplitude as the pressure gradient strengthens. For strong adverse pressure gradients, in which the laminar boundary layer is approaching separation, the spectra develop a plateau at low frequencies.

Table 1 compares the observed spectral peaks with the estimated frequencies of the basic T-S instability waves obtained from equation (9), which approximates the frequency for maximum amplification rate. This should underestimate the dominant T-S wave frequency, which generally lies close to the frequency of disturbances having received the maximum amplification ratio.

Assuming the observed peak closest to the theoretical value corresponds to the basic instability wave, it is seen that equation (9) predicts the T-S wave frequency to within 30 percent. However, the theoretical value is not always an underestimate as expected, exceeding the observed frequency for low pressure gradients. This is possibly explained by the observed transition inception shape factor, H_s , having fallen below the local equilibrium value for a steady laminar boundary layer due to shear stresses generated by nonlinear wave amplification processes and incipient turbulent mixing. The observed value of H is typically 0.2–0.3 below the steady laminar value at x_s and this yields a correspondingly lower $R_{\delta_s}^*$. Using a value of $R_{\delta_s}^*$ from a steady laminar boundary layer calculation in equation (9) could therefore be expected to produce closer agreement with observed frequencies at low pressure gradients and slightly greater underestimates in strong pressure gradient conditions, with a more general tendency for the theoretical value to be low.

In any case, the estimates of frequency obtained from equation (9) are acceptably close for the intended application of transition length modeling, and surprisingly good considering the approximations involved. Even the most soundly based estimates obtained by using small disturbance theory to compute the frequencies receiving maximum amplification ratio

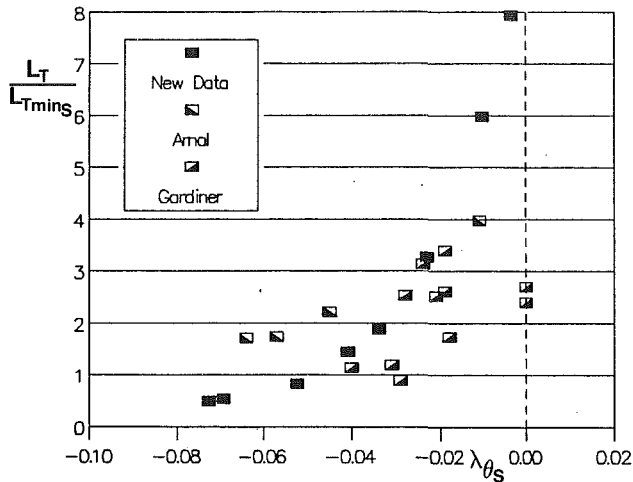


Fig. 9 Transition length data for transition inception at "S" compared with data of other authors

pressure gradient and the transition length was comparable with that predicted by equation (10). For Sharma's squared-off test configuration transition was initiated in a zero-to-mild adverse pressure gradient and the transitional flow length was about three times longer.

The data considered here all correspond to low turbulence flow situations. The present results were obtained with a free-stream turbulence level at inlet of 0.3 percent, while those of Arnal et al. were obtained with a turbulence level of 0.2 percent. Only the observations for turbulence levels of 0.3–0.4 percent have been included from the data of Gardiner.

In interpreting Fig. 9, it is important to appreciate that the limits of transitional flow in the data sets used were not all determined in exactly the same manner. Blair (1982) has previously commented on this problem and noted that transition lengths defined from velocity profile shape factor differed from those obtained from wall heat transfer data. The present results were obtained by intermittency measurement, with dimensionless velocity profile plots being used to confirm the establishment of fully turbulent flow. The present investigation, and that of Gardiner, used the 1 and 99 percent intermittency values to define the transition region. The published results of Arnal et al., however, define transition as starting when the shape factor H commences to decrease from its laminar value and finishing when H becomes essentially constant in the fully turbulent flow region. The lowest pressure gradient reading of Arnal et al. was obtained by extrapolation, necessitated by the extension of the transition region beyond the test surface.

Values of L_T/L_{Tmin} from the present investigation decrease monotonically with increasingly negative values of λ_{θ_s} . The data of Arnal et al. also show a rapid decrease but over a narrower range; the point obtained by extrapolation complicates interpretation of the Arnal results. Although the data of Gardiner are much more scattered, they also exhibit a tendency for L_T/L_{Tmin} to decrease as the pressure gradient becomes more adverse. The data envelope appears to approach a value of 1 ± 0.6 , as the transitional laminar layer approaches separation.

The observed difference between the present results and those of Arnal et al. in strong adverse pressure gradients could be due to their definition of x_T , based on a stabilization of H , overestimating the transition length. The present results indicate that H is close to the local equilibrium turbulent flow value at the 99 percent intermittency point for the zero pressure gradient case, but increasingly exceeds this value as the pressure gradient becomes more adverse. This is consistent with the observation of Clauser (1954) that a turbulent boundary layer given a sudden perturbation may take a streamwise distance of 10 to 50 boundary layer thickness to regain equilibrium.

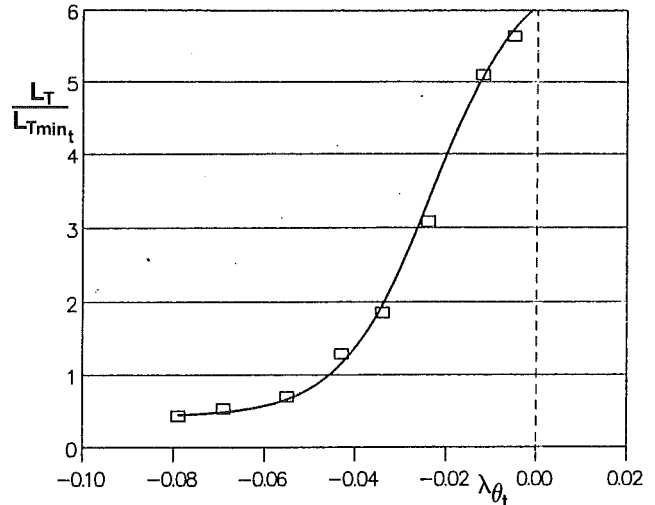


Fig. 10 Transition length data for transition inception at "I" fitted with new correlation curve, equation (13)

A transitional boundary layer is recovering from a laminar-type velocity profile with high H toward a fully turbulent profile with lower H and is in a similar situation to the perturbed turbulent layer. For the low pressure gradient data of Fig. 9, the transitional flow length is around $50\text{--}100\delta$ giving adequate time for the equilibrium turbulent profile to be achieved when the intermittency reaches 99 percent. For the strongest adverse pressure gradient cases, however, the transition length decreases to $20\text{--}30\delta$ and there is a distinct possibility that H may not have stabilized at the 99 percent intermittency point.

The data of Fig. 9 were presented on a basis of 1 percent intermittency for transition inception (the "S" basis) to provide a fair comparison with the data of other authors. Because the universal intermittency function of equation (1) provides a reasonable representation of the data for a wide range of pressure gradients, as demonstrated in Fig. 4, the use of the "I" basis for transition inception should give more consistent results. Accordingly the present data are plotted in this fashion in Fig. 10. The data have been presented in correlation form by fitting the curve

$$\frac{L_T}{L_{Tmin}} = \frac{0.14 + 20 \exp(100\lambda_{\theta_t})}{0.33 + 3 \exp(100\lambda_{\theta_t})} \quad (13)$$

This becomes asymptotic to 6.7 for favorable pressure gradients; the behavior in this regime needs to be confirmed experimentally.

Modeling Transition in an Adverse Pressure Gradient

The present investigation confirms the hypothesis of Walker (1987), which predicted a reduced transition length in decelerating flows, and the underlying physical explanation of this phenomenon. This is clearly seen from Fig. 10, which indicates about an order of magnitude reduction in transition length as the pressure gradient is increased from zero to the value producing incipient laminar separation.

This greatly reduced transition length in strong adverse pressure gradients is a fundamental prerequisite for the operation of an axial flow compressor, as indicated by Gostelow and Blunden (1988). Were the transition length not considerably shorter than indicated by flat plate correlations a turbulent boundary layer could not be developed on most compressor blades, which would consequently be incapable of sustaining the required loadings. The shorter transition lengths also are necessary for laminar separation bubbles to develop. If the

transition lengths were as great as those observed under zero pressure gradient conditions catastrophic laminar separation would be the normal flow regime.

The method of presenting transition length data for arbitrary pressure gradient by plotting L_T/L_{Tmin} against λ_{θ_i} provides a universal approach to correlating transition length. It incorporates both Reynolds number (by way of L_{Tmin}) and pressure gradient effects and also provides a rational basis for assessing existing transition criteria. The Narasimha (1978) correlation, equation (5), exhibits the same Reynolds number dependence as the minimum length model but makes no allowance for pressure gradient effects. The Chen and Thyson (1971) approach, which is basically an outgrowth of the Narasimha correlation, only allows for the influence of pressure gradient in respect of the secondary effect of changing free-stream velocity on turbulent spot convection rates; it makes no allowance for the primary influence of pressure gradient on the mechanics of instability and breakdown. On the other hand, attempts to allow for pressure gradient effects by seeking a correlation of $(R_{\theta_T} - R_{\theta_i})$ against λ_{θ_i} do not admit any influence of transition inception Reynolds number on transition length.

With regard to the minimum transition length model, it is recalled that this was expected to apply for strong adverse pressure gradient conditions. Equation (13) indicates that the observed transition length essentially stabilizes around an L_T/L_{Tmin} value of 0.44 as laminar separation, corresponding to λ_{θ_i} of -0.08 , is approached. This is significantly less than the transitional flow length ratio of unity corresponding to equation (10) and illustrates the necessity of calibrating the simple theoretical model against experimental data.

The development of the minimum transition length model incorporated the simplifying assumptions of the following:

- (a) Breakdown occurring every cycle of the primary instability wave, at a frequency approximated by equation (9);
- (b) The completion of transition at a streamwise position corresponding to the first longitudinal meeting of neighboring turbulent spots.

It is considered that the aforementioned assumptions (a) and (b) involve opposing errors, which cancel to some extent. On the one hand, the assumed spot inception frequency is mostly underestimated in strong adverse pressure gradients; this tends to increase the predicted value of L_{Tmin} by up to 30 percent. On the other hand, the development of turbulence in strong adverse pressure gradients may proceed more rapidly than indicated by the data, obtained from the spreading of isolated turbulent spots in a zero pressure gradient, used to formulate equation (10). This mechanism needs further investigation but its effect would be to decrease the predicted L_{Tmin} .

In addition to the opposing errors, resulting from assumptions (a) and (b) previously mentioned, the present experimental results may underestimate transition length by up to 20 percent due to difficulties in measuring intermittency in strong adverse pressure gradients, which were not fully appreciated during the initial observations. This would justify a transition length under strong adverse pressure gradients rather closer to the theoretical value given by equation (10) than the present experimental data would appear to indicate.

In concluding, it is emphasized that the present investigation has deliberately focused on the effects of pressure gradient and avoided any extension to account for free-stream turbulence. Free-stream disturbances can be an important consideration in turbomachinery design and performance analysis. The authors, however, believe that a proper understanding of the mechanics of pressure gradient effects in isolation is an essential prerequisite for further studies of the combined influences of pressure gradient and free-stream disturbance on transitional flow.

Conclusions

Difficulties experienced by users of computational routines in calculating boundary layer development on the suction surfaces of airfoils and compressor blades, especially those operating at low Reynolds number, have highlighted the inadequacies of existing transition models. Transition length correlations developed from constant pressure flows will seriously overestimate the transition length in an adverse pressure gradient situation. A new and more universal correlation for transition under an adverse pressure gradient, incorporating both Reynolds number and pressure gradient effects, has been proposed and confirmed. The correlation applies to flows having a low free-stream turbulence level. Although two-dimensional viscous instability is the basic transition mechanism under these conditions for both zero and adverse pressure gradient flows, the physics of transition is rather different in the two cases. In the former case, transition occurs by breakdown of the laminar instability waves in sets, producing a random time-average disturbance spectrum. For an adverse pressure gradient, the Tollmien-Schlichting waves evolve more continuously and give a distinct spectral peak. The process is akin to forced transition and is accomplished in a much shorter streamwise distance.

In the absence of a streamwise pressure gradient, transition occurs relatively slowly and the new turbulent boundary layer essentially commences from a local equilibrium condition. For an adverse pressure gradient, on the other hand, the turbulent flow develops too quickly for the mean-flow boundary layer parameters to stabilize by the end of transition. The new turbulent layer may then be expected to commence with a higher form factor than that predicted by local equilibrium theory and transition lengths inferred from velocity profile data will be too high.

As the adverse pressure gradient becomes stronger, the unsteady flow component observed over a long time interval evolves continuously from random to periodic behavior. Significant subharmonic behavior at half the primary instability wave frequency is observed in very mild adverse pressure gradients (where it is believed to arise from vortex loop thatching) and in very strong adverse pressure gradients (where it may be associated with vortex pairing mechanisms typical of separated flow). The combination of subharmonic and primary wave may produce a spectral peak at a frequency 50 percent higher than that of the basic Tollmien-Schlichting wave.

The observed strong reduction in transition length under adverse pressure gradients, with the associated rapid increase in turbulent spot formation rate, is seen to be fundamental to the loading capability of an axial flow compressor. It is also an important factor in the formation of laminar separation bubbles, which significantly influence the low Reynolds number and off-design performance characteristics of turbomachinery blading. Further work is required to examine the combined effects of pressure gradients and free-stream disturbances.

Acknowledgments

The authors wish to acknowledge the careful experimentation of Mr. A. R. Blunden, at the University of Technology, Sydney. The University of Oxford has given valued support to the second author during a period of sabbatical leave. Appreciation also is expressed for the active encouragement of Dr. P. Stow, Mr. N. T. Birch, Mr. P. Clark and Mr. D. H. Brierley of Rolls-Royce plc.

References

- Abu-Ghannam, B. J., and Shaw, R., 1980, "Natural Transition of Boundary Layers—The Effects of Turbulence, Pressure Gradient and Flow History," *Journal of Mechanical Engineering Science*, Vol. 22, No. 5, p. 213.
- Alt, P., 1987, "An Intermittency Meter for Investigating Boundary Layer

- Transition," University of Technology, Sydney, Technical Report NSWIT/ME 17.
- Arnal, D., Juillen, J.-C., and Michel, R., 1979a, "Analyse Experimentale de la Transition de la Couche Limite avec Gradient de Pression Nul ou Positif," ONERA T.P. No. 1979-8.
- Arnal, D., and Juillen, J.-C., 1979b, "Resultats Experimentaux Relatifs a l'Influence des Processus de Transition sur la Structure Initiale d'une Couche Limite Turbulente," AGARD CP-271, Turbulent Boundary Layers—Experiments, Theory and Modeling.
- Arnal, D., Habiballah, M., and Delcourt, V., 1980, "Synthese sur les Methodes de Calcul de la Transition Developpees au D.E.R.A.T.," ONERA, CERT, Rapport Technique OA No. 11/5018.
- Blair, M. F., 1982, "Influence of Free-Stream Turbulence on Boundary-Layer Transition in Favorable Pressure Gradients," *ASME Journal of Engineering for Power*, Vol. 104, pp. 743-750.
- Browand, F. K., 1966, "An Experimental Investigation of the Instability of an Incompressible, Separated Shear Layer," *Journal of Fluid Mechanics*, Vol. 26, pp. 281-307.
- Cebeci, T., and Smith, A. M. O., 1974, *Analysis of Turbulent Boundary Layers*, Academic Press, New York.
- Chen, K. K., and Thyson, N. A., 1971, "Extension of Emmons' Spot Theory to Blunt Bodies," *AIAA Journal*, Vol. 9, pp. 821-825.
- Clauser, F. H., 1956, "The Turbulent Boundary Layer," *Advances in Applied Mechanics*, Vol. IV, pp. 1-51.
- Craik, A. D. D., 1971, "Nonlinear Resonant Instability in Boundary Layers," *Journal of Fluid Mechanics*, Vol. 50, pp. 393-413.
- Dhawan, S., and Narasimha, R., 1958, "Some Properties of Boundary Layer Flow During the Transition From Laminar to Turbulent Motion," *Journal of Fluid Mechanics*, Vol. 3, pp. 418-436.
- Emmons, H. W., 1951, "The Laminar-Turbulent Transition in a Boundary Layer—Part I," *Journal of Aeronautical Sciences*, Vol. 8, pp. 490-498.
- Gardiner, I. D., 1987, "Transition in Boundary Layer Flows," PhD Thesis, College of Technology, Dundee, Scotland.
- Gostelow, J. P., and Blunden, A. R., 1988, "Investigations of Boundary Layer Transition in an Adverse Pressure Gradient," ASME Paper No. 88-GT-298.
- Gostelow, J. P., Blunden, A. R., and Blunden, W. R., 1988, "Measurements and Stochastic Analysis of Boundary Layer Transition for a Range of Free-Stream Turbulence Levels," *Proceedings 2nd International Symposium on Transport Phenomena, Dynamics and Design of Rotating Machinery*, Honolulu, HI.
- Herbert, T., 1983, "Modes of Secondary Instability in Plane Poiseuille Flow," *Proceedings IUTAM Symposium on Turbulence and Chaotic Phenomena in Fluids*, Kyoto, Japan.
- Kegelman, J. T., and Mueller, T. J., 1986, "Experimental Studies of Spontaneous and Forced Transition on an Axisymmetric Body," *AIAA Journal*, Vol. 24, pp. 397-403.
- Klebanoff, P. S., Tidstrom, K. D., and Sargent, L. H., 1962, "The Three-Dimensional Nature of Boundary Layer Instability," *Journal of Fluid Mechanics*, Vol. 12, pp. 1-34.
- Knapp, C. F., and Roache, P. J., 1968, "A Combined Visual and Hot-Wire Anemometer Investigation of Boundary Layer Transition," *AIAA Journal*, Vol. 6, pp. 29-36.
- McCormick, M. E., 1968, "An Analysis of the Formation of Turbulent Patches in the Transition Boundary Layer," *ASME Journal of Applied Mechanics*, Vol. 35, pp. 216-219.
- Narasimha, R., 1957, "On the Distribution of Intermittency in the Transition Region of a Boundary Layer," *Journal of Aero. Science*, Vol. 24, pp. 711-712.
- Narasimha, R., 1978, "A Note on Certain Turbulent Spot and Burst Frequencies," Report 78FM10, Dept. Aero. Eng., Indian Institute of Science.
- Narasimha, R., 1985, "The Laminar-Turbulent Transition Zone in the Boundary Layer," *Prog. in Aerospace Sci.*, Vol. 22, pp. 29-80.
- Obrenski, H. J., Morkovin, M. V., and Landahl, M., 1969, "A Portfolio of Stability Characteristics of Incompressible Boundary Layers," AGARDograph 134.
- Saric, W. S., and Thomas, A. S. W., 1983, "Experiments on the Subharmonic Route to Turbulence in Boundary Layers," *Proceedings IUTAM Symposium on Turbulence and Chaotic Phenomena in Fluids*, Kyoto, Japan.
- Schubauer, G. B., and Klebanoff, P. S., 1956, "Contributions on the Mechanism of Boundary Layer Transition," NACA Report 1289.
- Schubauer, G. B., and Skramstad, H. K., 1948, "Laminar Boundary Layer Oscillations and Transition on a Flat Plate," NACA Report 909.
- Sharma, O. P., Wells, R. A., Schlinker, R. H., and Bailey, D. A., 1982, "Boundary Layer Development on Turbine Airfoil Suction Surfaces," *ASME Journal of Engineering for Power*, Vol. 104, pp. 698-706.
- Subroto, P. H., 1987, "Viscous/Inviscid Interaction Analysis of the Aerodynamic Performance of the NACA 65-213 Airfoil," Master's Thesis, Naval Postgraduate School, Monterey, CA.
- Walker, G. J., 1987, "Transitional Flow on Axial Turbomachine Blading," AIAA Paper No. 87-0010.
- Walker, G. J., Subroto, P. H., and Platzter, M. F., 1988, "Transition Modeling Effects on Viscous/Inviscid Interaction Analysis of Low Reynolds Number Airfoil Flows Involving Laminar Separation Bubbles," ASME Paper No. 88-GT-32.

Unsteady Transition in an Axial-Flow Turbine: Part 1—Measurements on the Turbine Rotor

J. S. Addison

H. P. Hodson

Whittle Laboratory,
Cambridge University,
Cambridge CB3 0DY, United Kingdom

Previously published measurements in a low-speed, single-stage, axial-flow turbine have been reanalyzed in the light of more recent understanding. The measurements include time-resolved hot-wire traverses and surface hot film gage measurements at the midspan of the rotor suction surface with three different rotor-stator spacings. Part 1 investigates the suction surface boundary layer transition process, using surface-distance time plots and boundary layer cross sections to demonstrate the unsteady and two-dimensional nature of the process. Part 2 of the paper will describe the results of supporting experiments carried out in a linear cascade together with a simple transition model, which explains the features seen in the turbine.

Introduction

The relative motion of adjacent blade rows in axial turbomachines gives rise to a variety of unsteady flow interactions. The potential influence of a blade extends both upstream and downstream and decays exponentially with a length scale typically of the order of the chord or pitch. In contrast, the wakes are convected downstream of the blade row and their rate of decay is much less than that of the potential influence. The wake effect will therefore persist even where the blade rows are spaced far apart. In transonic stages, further interactions arise as the direct result of the impingement of the trailing shock waves on the downstream blade row (e.g., Doorly and Oldfield, 1985) while Binder (1985) has shown that in low aspect ratio turbines, the unsteadiness caused by the secondary flow vortices of upstream blade rows also is significant.

The majority of research concerned with the impact of wake interactions on blade surface boundary layers, whether in a turbomachine (e.g., Walker, 1974; Hodson, 1983a) or in a laboratory simulation (e.g., Doorly, 1987; Dong, 1988), has concluded that the most significant effect of this interaction is the periodic forcing of transition of the boundary layers. Published data (e.g., Pfeil et al., 1982; Doorly and Oldfield, 1985; LaGraff et al., 1988) show the front of a turbulent patch induced by the wake traveling with the leading edge of the wake at approximately the free-stream velocity while the rear travels at a slower rate, which is more typical of that observed at the rear of turbulent spots formed by natural transition. As a consequence of the differing velocities, the turbulent patches induced by successive wakes merge to form a turbulent boundary layer.

The present paper is particularly concerned with this process of boundary layer transition. It describes an investigation into the effects of wake-generated unsteadiness on the suction surface boundary layers of the rotor of a large-scale, low-speed, single-stage, axial-flow turbine. Part 1 of the paper reanalyzes the experimental data (much of which has already been reported in the publications referenced here) while Part 2 presents the results of a supporting linear cascade investigation and a model for the unsteady transition process, which draws on the conclusions of the experimental work. The pressure surface boundary layers are not discussed since it has already been shown that they do not undergo transition under normal operating conditions (Hodson and Addison, 1988).

Experimental Details

Research Turbine. The single-stage axial-flow turbine has been described in more detail by Hunter (1982) and Hodson (1983a, 1984). It was a free-vortex design with zero inlet and exit swirl and 50 percent reaction at midspan. The 36 stator blades and 51 rotor blades had aspect ratios of 1.5 and 2.0, respectively, and a hub-tip ratio of 0.7. The present study is concerned specifically with the rotor midspan blade section, which was designed for relative inlet and exit angles of 0 deg and -65 deg, respectively, corresponding to a flow coefficient (U_x/U_b) of 0.49. The flow at rotor midspan was essentially two-dimensional and free from the influences of tip leakage and secondary flows (Hodson and Addison, 1988). The operating (i.e., design) conditions are summarized in Table 1.

Experimental data have been obtained at three stator-rotor axial gaps corresponding to 50, 75, and 143 percent C_{xs} (stator axial chord). The different clearances were obtained by the use of spacer rings. Figure 1 shows the stage configured at the smallest axial gap.

Contributed by the International Gas Turbine Institute and presented at the 34th International Gas Turbine and Aeroengine Congress and Exhibition, Toronto, Ontario, Canada, June 4-8, 1989. Manuscript received at ASME Headquarters February 14, 1989. Paper No. 89-GT-289.

Table 1 Turbine midspan section—design conditions

	Stator	Rotor
Flow Coefficient U_x/U_b		0.49
Stage Loading ($\Delta h_0/U_x^2$)		1.0
Reynolds Number (Re)	4.2×10^5	3.15×10^5
Rotational Speed (rpm)	—	530.
Inlet Axial Velocity (m/s)	17.95	—
Inlet free-stream turbulence intensity	0.25%	—
Blade Inlet Flow Angle (from axial)	0.0°	0.0°
Blade Exit Flow Angle (from axial)	65.0°	-65.0°
Chord (mm)	152.4	114.3
Pitch-Chord Ratio	0.742	0.698
Aspect Ratio	1.5	2.0
Number of Blades	36	51
Mean Radius (m)	0.647	0.647

Surface-Mounted Hot-Film Gages. Surface-mounted hot-film gages have been used to investigate the boundary layer behavior of the rotor suction surface at the three axial spacings. The hot-film data were acquired in two different ways.

(a) *Axial Spacings of 75 percent C_{xs} and 143 percent C_{xs} :* Hodson (1984) used a single, calibrated hot-film gage, which was positioned at several locations along the blade surface, the data being logged at the rate of 10 samples per wake passing cycle and averaged over 100 revolutions. Here the output has been converted to shear stress $\tau_w(t)$. The rms measurements are presented as the ratio of the ensemble rms to the ensemble mean since it can be shown that

$$\frac{\sqrt{\langle \tau_w(t)^2 \rangle}}{\langle \tau_w(t) \rangle} \approx \frac{\sqrt{\langle u(t)^2 \rangle}}{\langle u(t) \rangle} \quad (1)$$

i.e., the local turbulence intensity near the wall for a single-state boundary layer.

(b) *Axial Spacing of 50 percent C_{xs} :* Hodson and Addison (1988) used a sheet of gages and presented the data as ratios of the measured voltage $E(t)$ to the zero-flow voltage E_0 of the individual sensors, thus allowing a comparison to be made between the outputs of the different sensors without calibration. In these experiments, 256 samples were logged over 6 blade passing periods and averaged over 64 revolutions.

Hot-Wire Boundary Layer Traverses. Experimental details of the hot-wire traverses and some of the results were originally reported by Hodson (1983a). Those presented here were carried out with axial gaps of 75 and 143 percent C_{xs} , using a single

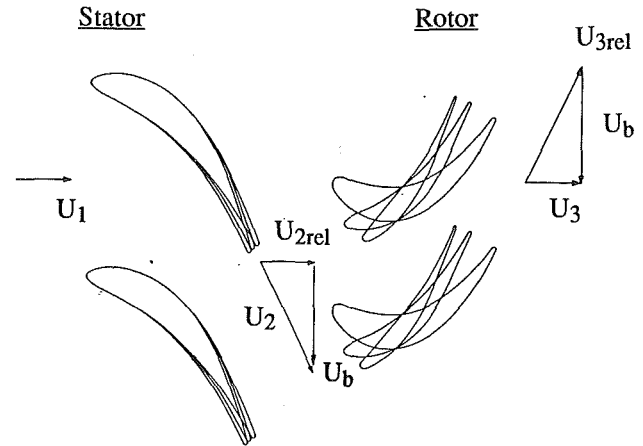


Fig. 1 Hub, mean and tip section profiles and velocity triangles for the turbine stage

hot wire aligned perpendicular to the mean flow and parallel to the surface. Data were again logged at the rate of 10 samples per wake passing cycle and averaged over 100 revolutions. For presentation, data from 12 consecutive wake passing cycles have been superimposed, effectively forming phase-locked averages based on 1200 wake passing cycles.

Results and Discussion

Steady-State Predictions and Time-Averaged Measurements. The rotor midspan surface velocity distribution predicted by the method of Whitehead (1980) is shown in Fig. 2, together with the velocity data obtained in an equivalent linear cascade (see Part 2). The profile is moderately aft-loaded with little suction surface diffusion and large areas of favorable pressure gradients. Peak suction occurs near 45 percent s^* on the suction surface, where s^* is the nondimensional suction surface distance measured from the geometric leading edge.

The predicted velocity distribution was used as input for the boundary layer prediction scheme of Cebeci and Carr (1978). Predictions of the Reynolds number based on momentum thickness (Re_θ) and shape factor ($H = \delta^*/\theta$) for the suction surface boundary layer are shown in Fig. 2. The turbulent prediction was obtained by specifying transition when Re_θ reached a value of 163 (q.v.). The time-averaged values of the measured Re_θ and shape factor for the 75 and 143 percent C_{xs} axial gaps also are plotted, together with the values measured in the linear cascade.

The experimental data of Fig. 2—originally reported by

Nomenclature

E = hot-film output voltage

C_{xs} = stator axial chord

H = shape factor = δ^*/θ

h_0 = stagnation enthalpy

Re = Reynolds number

Re_θ = Reynolds number based on momentum thickness

s = suction surface distance

s^* = fractional surface distance = s/s_{max}

T = blade passing period

t^* = dimensionless time = t/T

Tu = turbulence (or rms) intensity

U = velocity

u = streamwise velocity within the boundary layer

y = surface normal distance

y^* = nondimensional surface normal distance = y/s_{max}

δ_{95} = boundary layer thickness

δ^* = boundary layer displacement thickness

ν = kinematic viscosity

θ = boundary layer momentum thickness

τ_w = wall shear stress

Subscripts

b = blade

e = edge of boundary layer

max = maximum value

min = minimum value

x = axial

0 = zero flow

Time Mean

$$\overline{x(t)} \equiv \frac{1}{T} \int_0^T \left[\frac{1}{N} \sum_{n=1}^N x(t, n) \right] dt$$

Ensemble Mean

$$\langle x(t) \rangle \equiv \frac{1}{N} \sum_{n=1}^N x(t, n)$$

Ensemble Variance

$$\langle \langle x(t)^2 \rangle \rangle \equiv \frac{1}{N} \sum_{n=1}^N (x(t, n) - \langle x(t) \rangle)^2$$

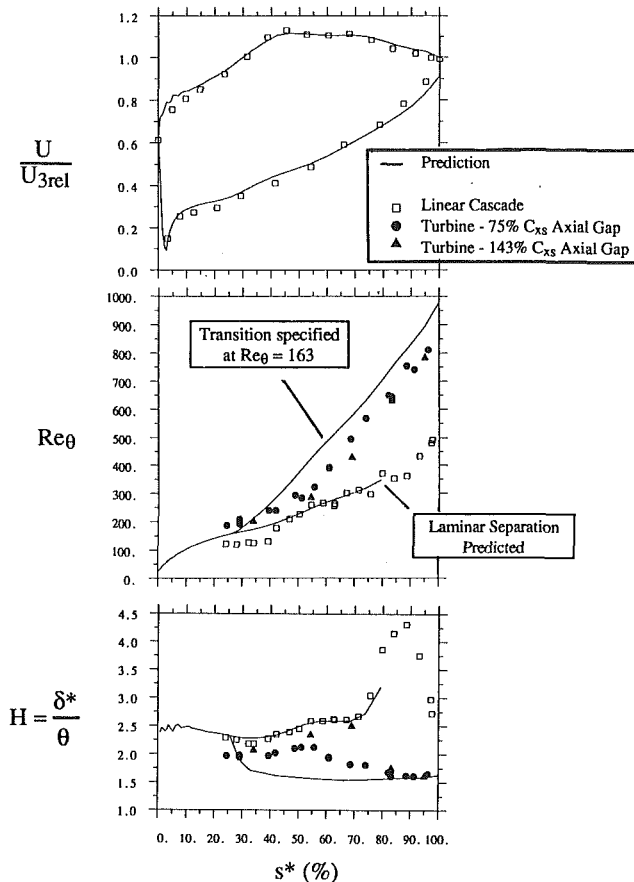


Fig. 2 Steady-state predictions and time-averaged measurements

Hodson (1983a)—show that the boundary layer does not become typical of a turbulent profile until very late. For the 75 percent C_{xs} gap, time-mean transition, as indicated by a fall in the shape factor, appears to commence just after peak suction at about 55 percent s^* . In the case of the largest axial gap, transition is just before the location at which laminar separation would otherwise occur (78 percent s^*). Upstream of the time-mean transition point, the boundary layers have a greater momentum thickness and, consequently, lower shape factor than the equivalent laminar profiles.

Surface-Mounted Hot-Film Gages. Examples of the hot-film data obtained at the design Reynolds number and the smallest axial gap (50 percent C_{xs}) are shown in Fig. 3, which was originally published by Hodson and Addison (1988). In each box the fluctuating component of the raw signal and the ensemble mean are shown together with the ensemble rms from one hot film (the scales for all plots being the same). The three traces complement each other; the raw signal contains information about individual occurrences, both random and phase-locked; the ensemble mean contains only that information that is phase-locked to the blade passing frequency, while the ensemble rms contains the information on how the random content of the signal varies as a function of rotor position measured in terms of dimensionless time t^* .

The results of Fig. 3 show that there are three distinct regions of flow on the suction surface. The first, which will later be identified as the laminar region, ends before 45 percent s^* . In this region, only relatively low amplitude, low frequency random information is present in addition to the phase-locked periodic unsteadiness. The cyclic variation of the ensemble mean is in phase with that of the random unsteadiness (rms). This implies that, although this is essentially a laminar region of flow, there is some momentum transfer due to the turbulence

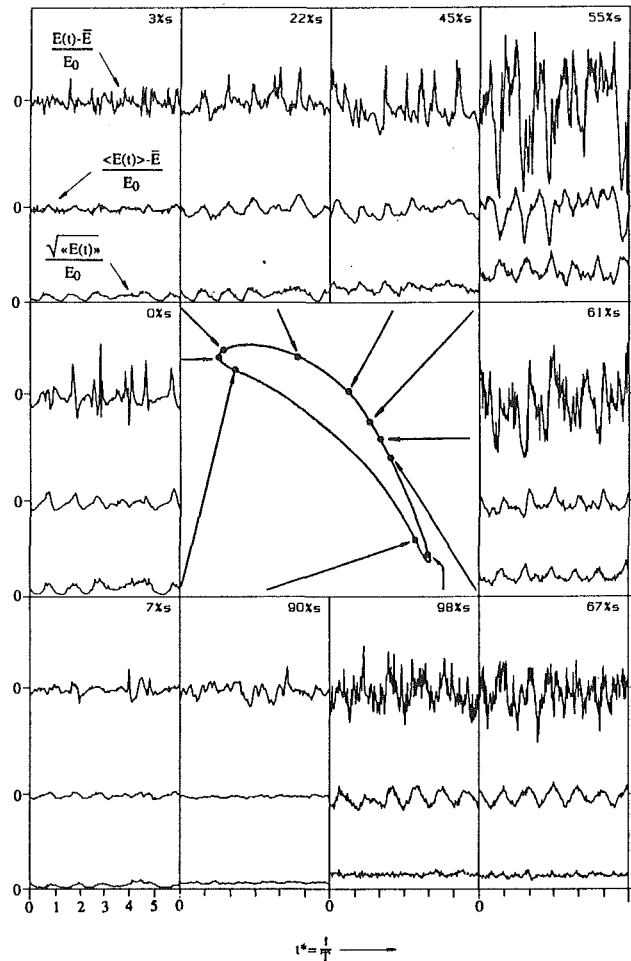


Fig. 3 Rotor midspan hot-film results obtained at design conditions and 50 percent C_{xs} axial gap (Hodson and Addison, 1988)

in the wake, which results in a periodic increase in wall shear stress and, therefore, an increase in mean momentum thickness above the laminar value. This is consistent with the experimental data of Fig. 2. It also is noted that the velocity and turbulence are not in phase (q.v.).

The second or transitional region begins near 45 percent s^* . At this location, the raw signal in Fig. 3 contains rapid periodic increases in shear stress followed by short periods of high frequency fluctuations and then a decay back to the less disturbed state. The rms traces indicate that there are no truly quiescent periods. Such traces are typical of those observed in boundary layers starting to undergo forced transition as a result of the passage of wakes over the blade surface. The rapid and relatively large increases of shear stress, indicated by the raw signals, signify the commencement of changes of state within the boundary layer, that is, from laminar to turbulent flow. The higher frequency fluctuations that follow this increase represent the first occurrences of turbulent flow. The relatively quiescent regions between the turbulent patches therefore correspond to the regions of laminar flow between the wakes. As the flow develops further on the suction surface, transition progresses so that by 55 percent s^* , the rms no longer approaches zero for any part of the wake passing cycle and the regions of higher frequency fluctuations are greater in extent. It also is noted that once the transition process is well established (e.g., 61 percent s^*), the highest levels of random unsteadiness (rms) appear to correspond to the short intervals of lower shear stress. It will be shown below that this occurs

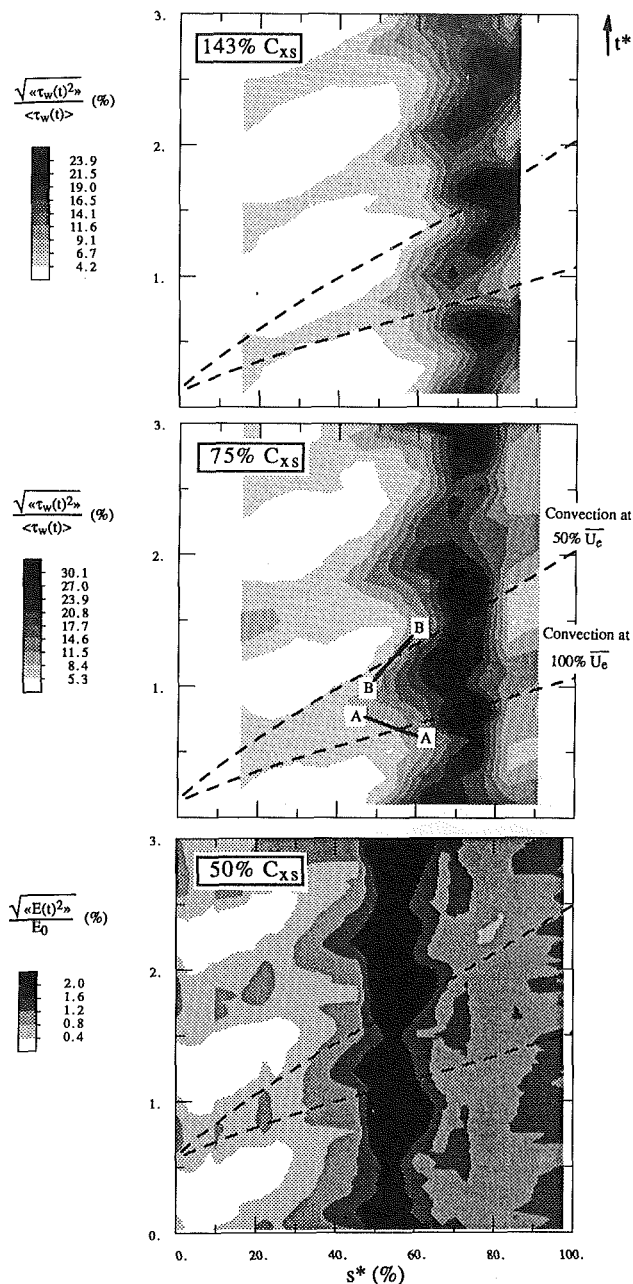


Fig. 4 Distance-time plots of suction surface random unsteadiness derived from hot-film data; rotor-stator axial spacings (a) 143 percent C_{xs} , (b) 75 percent C_{xs} , (c) 50 percent C_{xs}

where the merging of turbulent patches, caused by adjacent wakes, takes place.

By approximately 67 percent s^* , the third or turbulent phase of boundary layer development appears to have begun. In this region, the random and periodic components of the signal are of similar magnitude. The mean level of the rms traces is reduced when compared with those within the transition region. The variation in the rms is also negligible in the turbulent region suggesting that the levels of free-stream turbulence encountered during the passage of the wakes above the surface have a relatively small effect on the innermost parts of a turbulent boundary layer.

The changes of state are particularly characterized by the rms data. Three surface distance-time plots of the suction surface data, which correspond to the axial spacings of 50, 75, and 143 percent C_{xs} , are presented in Fig. 4. The contours show the development of the random unsteadiness indicated by the

rms of the hot-film signals. Figure 4 also shows the predicted trajectories of quantities convected with the free stream (100 percent \bar{U}_e) and at half that rate (50 percent \bar{U}_e). The higher quality of the data at the larger axial gaps is due to the larger number of samples taken at each point.

Figure 4 confirms that the development of the suction surface boundary layer consists of the three distinct regions of flow at each axial gap. Over the initial part of the surface, which has been identified as the laminar region, there are almost parallel tracks of random unsteadiness traveling at a velocity approximately equal to the free-stream value. These parallel tracks cover the longest surface distance at the largest axial gap (Fig. 4a), indicating that transition occurs latest in that configuration. It is particularly important to note that in these laminar regions, there is no evidence of spreading in the manner associated with the turbulent spots of Shubauer and Klebanoff (1955), Obremski and Fejer (1967), etc., where the spreading was due to the trailing edge of the spot lagging behind the leading edge, which propagated at a velocity close to that of the free stream. If these parallel tracks were to represent turbulent patches, it would imply relaminarization of the fluid near the wall at the rear of the wake. However, with the exception of the first few percent of surface distance, the acceleration parameter

$$\frac{\nu}{U_e^2} \frac{\partial U_e}{\partial s} \quad (2)$$

is less than the minimum value (3×10^{-6}) that most studies consider necessary for relaminarization (e.g., Narasimha and Sreenivasan, 1979). Any relaminarization also would be too gradual to explain this feature. Inspection of a raw hot-film signal from that region of the blade (Fig. 3) also shows that the disturbances are principally confined to low frequencies. The parallel tracks therefore seem to represent the results of disturbances from passing wake segments diffusing through the boundary layer. This is consistent with the results of the hot-wire traverses (q.v.). A feature similar to this, although not remarked on at the time, can be seen in the $s-t$ plot presented by LaGraff et al. (1988), where the tracks of the disturbed region run parallel from the leading edge to about 20 percent s^* ; a higher Reynolds number resulting in earlier transition. Many transition correlations (e.g., van Driest and Blumer, 1963; Abu-Ghannan and Shaw, 1980) suggest that if Re_θ is less than a minimum value (163 in the case of the latter) then transition will not begin. For this reason, the turbulent prediction shown in Fig. 2 was started at this value. The fact that Re_θ does not exceed the foregoing limit until about 30 percent s^* means that transition will not be predicted to begin until after that location whatever the level of free-stream turbulence. Thus it is not surprising that turbulent spots do not form immediately when the wakes impact on the boundary layer and it is necessary that models of unsteady transition do not presume that this is the case. The data of Pfeil et al. (1982) and Walker (1974) also support this viewpoint and further discussion can be found in Part 2 of the present paper.

In each case the parallel tracks of Fig. 4 are terminated by rising wedges of random unsteadiness. These denote the onset of unsteady transition. The areas are, to some extent, reminiscent of the spot spreading described by other workers (e.g., Obremski and Fejer, 1967). However, if the spreading in Fig. 4 represents a single spot developing underneath the wake as has been suggested by some authors (e.g., LaGraff et al., 1988) then the angle of the line A-A in Fig. 4(b) would imply a *negative* propagation velocity, i.e., upstream propagation for the spot leading edge. Many studies have shown that the leading edge velocity lies between 80 and 100 percent \bar{U}_e , although the $s-t$ plot of Doorly and Oldfield (1985) does show a phenomenon similar to that noted in Fig. 4. Nor do the lines parallel to A-A correspond to the small amount of upstream propagation

of the wave packets resulting from the breakdown of Tollmein-Schlichting waves noted by Obremski and Fejer (1967). Here, the high levels of disturbances mean that the linear amplification stage will be bypassed. The answer to this problem is suggested by inspection of the raw hot-film traces from the transitional region; for example, at 55 percent s^* in Fig. 3. During the sections that obviously correspond to the passage of wake segments, there is some suggestion that there are several bursts of higher frequency disturbances buried within the disturbed regions. These individual bursts correspond to the turbulent spots of natural transition. When the primary instabilities, here provided by disturbances from the wake and in natural transition by Tollmein-Schlichting waves, are amplified beyond a critical level, higher frequency disturbances are created. This results in the turbulent bursts or spots. The Tollmein-Schlichting frequency, which here is of the order of 3 kHz, i.e., $10 \times$ blade passing frequency, can be used as an estimate of the rate at which this happens (e.g., Walker, 1987). Thus we might expect to see up to five turbulent bursts in a wake-induced turbulent patch lasting for 50 percent of the wake-passing period.

It is now possible to explain the reasons for the negative slope of the lines such as A-A in the s - t plot of Fig. 4(b). The result is a consequence of ensemble-averaging. Transition commences with the formation of the first turbulent spot. The results of Fig. 4 show that this is most likely to occur near the centerline of the wake, where the turbulence is greatest. (The locations indicated by the results of Fig. 4 represent an average over many cycles.) However, as the disturbed laminar part of the boundary layer develops beyond this point on the surface, it becomes capable of undergoing transition at the lower levels of free-stream turbulence that are to be found away from the centerline of the wakes. Simultaneously, the wake itself travels at a faster rate than the leading edge of a single spot. Thus further spots can form ahead of the zone of influence of the initial single spot, the effects combining to make the inclination of the line A-A negative in Fig. 4(b). In the case of the "trailing edge" of the wedge (line B-B), these effects tend to cancel so that the slope corresponds more closely to that associated with a single spot. Nevertheless, the results still indicate the formation of additional spots behind the zone of influence of the initial spot. At the smallest axial gap (Fig. 4c), the wakes will be at their narrowest so that the inclinations of the leading and trailing edges of the transitional wedge correspond more closely to the values associated with a turbulent spot. A further discussion regarding the modeling of such features can be found in Part 2.

An alternative view of the boundary layer development is given by Fig. 5. It shows the surface distribution of the maximum and minimum limits of the ensemble rms, normalized in the same manner as in Fig. 4. In effect, the figure shows the envelopes of the surfaces contoured in Fig. 4. Over the first part of the blade, the relatively low levels of the maximum values indicate the significance of the relatively low frequency (i.e., large scale) disturbances in the disturbed laminar boundary layer. Any small (high frequency) eddies are rapidly dissipated. At the rear of the surface, where the boundary layer is turbulent, the values are greater than during the laminar phase. It should be noted that some of the energy in the turbulent boundary layers occurs at frequencies beyond the cutoff frequency of the instrumentation and so the values are artificially low in this region. However, this does not explain the variation through the transitional regions where the curves, shown in Fig. 5, reach their maximum values at about the same location as the time-averaged results of Fig. 2, indicating that the boundary layers are halfway through the transition process. If the transition to turbulent flow were to take place in a phase-locked, periodic manner whether by way of the formation of a single spot or multiple spots then the curves, shown in Fig. 5, would rise monotonically to the turbulent values during

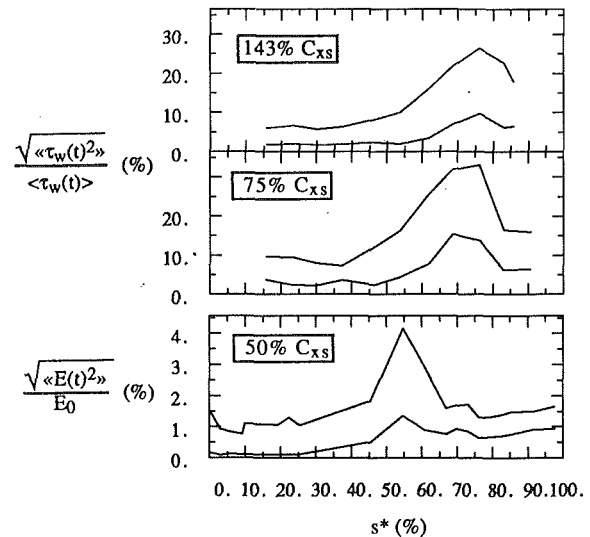


Fig. 5 Maximum and minimum values of suction surface random unsteadiness derived from surface hot-film data

transition. The fact that they do not indicates that the formation of individual spots, which grow to form the transition wedges, occurs stochastically so that the rms represents the sum of the unsteadiness due to the stochastic formation of the spots and the turbulence within the spots themselves. The relatively large values of the peaks are consistent with the fact that much larger changes of heat transfer rate result from a change of state than from the fluctuations observed in turbulent boundary layers. A similar though less pronounced feature also can be seen in the time-averaged results of Pfeil et al. (1982).

Figure 5 has indicated that the process of spot formation is stochastic. If it is assumed that the individual spots are physically identical, then the rise in rms above the turbulent level can be taken as an indicator of the rate at which the spots form. An examination of the s - t plots of Fig. 4 shows that at each axial spacing and for a given surface location, the height of the transition wedge is greatest near its bisector during the early part of the process. However, the peak values (two per wedge) are not to be found along the bisector but nearer the edges of the wedge. It also is noted that at the smallest axial gap, Fig. 4(c), the gradient along the forward part of the wedge is steeper than at the larger axial gaps indicating a more rapid change between the low interwake and high wake-peak turbulence intensities. This is a consequence of the narrower incident wakes at the smaller spacings. It is noted that the values along the bisector of the wedge rise above the subsequent turbulent values thus indicating that, at all locations, the process of spot formation is not simply periodic. Once the turbulent wedges, shown in Fig. 4, have merged, the rms falls indicating a rapid conclusion to the process of transition. The location of the end of transition indicated by the hot films is consistent with the traverse results of Fig. 2.

Hot-Wire Boundary Layer Traverses. Time-averaged integral parameters derived from the hot-wire traverses of the suction surface boundary layers have already been presented in Fig. 2. This section describes some of the unsteady data acquired at the intermediate axial gap (75 percent C_{xs}).

Figure 6 shows the time-mean velocity and rms profiles at different suction surface locations. The velocity profiles show that growth of the boundary layer is continuous, with the most significant changes occurring as the boundary layer undergoes transition. The rms profiles show that even when the boundary layer is essentially laminar, appreciable levels of random un-

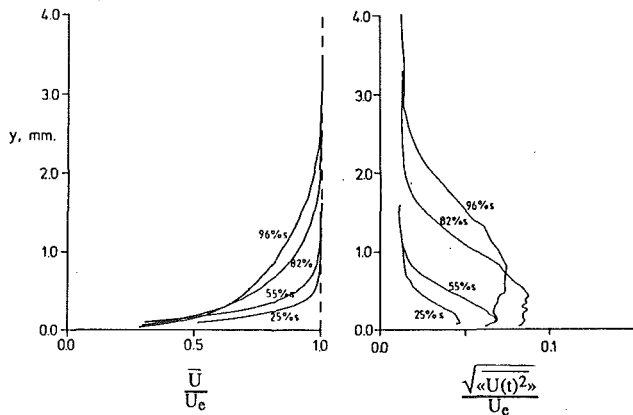


Fig. 6 Time-mean velocity and rms profiles for the suction surface boundary layer—75 percent $C_{x,s}$ axial gap (Hodson, 1983)

steadiness exist near the surface. Within the turbulent boundary layer close to the trailing edge (96 percent s^*), the rms levels are slightly lower than are normally found in turbulent boundary layers. This result can be attributed to the effects of a relatively low instrumentation cutoff frequency. It will be shown below that the higher levels of random unsteadiness at 82 percent s^* are indicative of transition.

Figure 7 shows a series of instantaneous cross sections through the boundary layer at equal intervals during a single wake-passing cycle. The abscissa is the surface normal distance normalized with respect to the suction surface distance ($y^* = y/s_{max}$). It should be noted that the s^* and y^* scales are heavily distorted. The dashed lines show where the ensemble velocity is equal to 95 percent of the value in the free stream, i.e., $y = \langle \delta_{95} \rangle$ where $\langle u(t) \rangle = 0.95 \langle U_e \rangle$. These lines can therefore be used as a guide to boundary layer thickness. The thick, solid lines drawn over the contours show where the unsteady velocity ($\langle u(t) \rangle - \bar{u}$) is zero and $\partial \langle u(t) \rangle / \partial t$ is negative. Following Hodson (1985) who showed that the wakes behave as negative jets, these lines can be taken to indicate the approximate location of the centerline of each wake. The sequence of plots shows that the wake centerlines convect across the region (26 to 96 percent s^*) at an approximately constant rate. Within the boundary layer, the wake centerlines lag behind the free stream and the edge of the boundary layer can be identified by where the lag begins.

The shaded contours in Fig. 7 are of the quantity

$$Tu = \sqrt{\langle \langle u(t)^2 \rangle \rangle} / \bar{U}_e \quad (3)$$

which would normally be referred to as an ensemble turbulence intensity. However, as the hot-film data have demonstrated (e.g., Fig. 5), the rms quantities represent the combined unsteadiness associated with stochastic processes such as spot formation as well as with the turbulence. This quantity will therefore be referred to as the "rms intensity" when both effects are present. It also should be noted that the time-mean free-stream velocity \bar{U}_e , although not constant, varies by less than 25 percent over the surface length traversed with the hot wires (see Fig. 2) so that the data trends will not be unduly affected by normalizing in this way.

The plots in Fig. 7 show the convection of alternate regions of high (wake) and low (undisturbed free-stream) turbulence across the blade surface above the boundary layer. There is a periodic variation of the rms intensity nearest the surface that is in sympathy with, though lagging behind, the turbulence intensity in the wakes. In the inner half of the boundary layer, the variation in rms intensity is particularly evident between 50 and 90 percent s^* , which is where transition is known to occur (Fig. 2). The maximum turbulence intensity within the wake, approximately 2 percent, can be seen to lag significantly

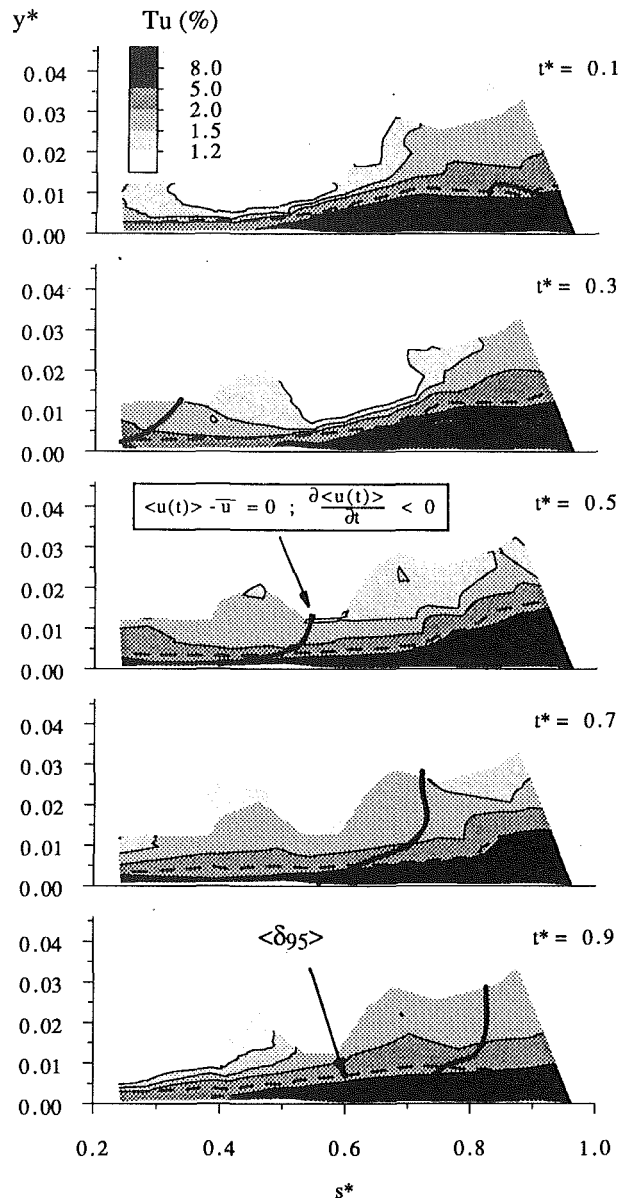


Fig. 7 Instantaneous rms intensity and velocity in the suction surface boundary layer—75 percent $C_{x,s}$ axial gap

behind the centerline indicated by the velocity field although the reasons for this are not yet understood. Since it will be shown that the turbulence in the wake is responsible for the transition process, the wakes will continue to be identified by the turbulence and not by the ensemble velocity field. As a result of these differences, the transition process will be triggered in a region of relatively slowly varying velocities.

One of the more striking features of Fig. 7 is that, over the initial part of the blade surface and in the absence of the wakes, the rms intensity does not fall below 2.5 percent near the surface even though the hot-film data of Fig. 4(b) indicate the presence of essentially laminar boundary layers. Pessimistic estimates suggest that a combination of probe vibration and the relatively high velocity gradients near the wall could have resulted in an apparent turbulence/rms intensity of 3 percent. However, as was pointed out previously, the ratio of rms to mean for the hot films gives an estimate of the near-wall turbulence intensity, and comparison with Fig. 4(b) shows that the hot-wire observations are consistent with these levels. This suggests that the levels observed by the hot wire are not unduly affected by vibration of the probe. In fact, these relatively high levels

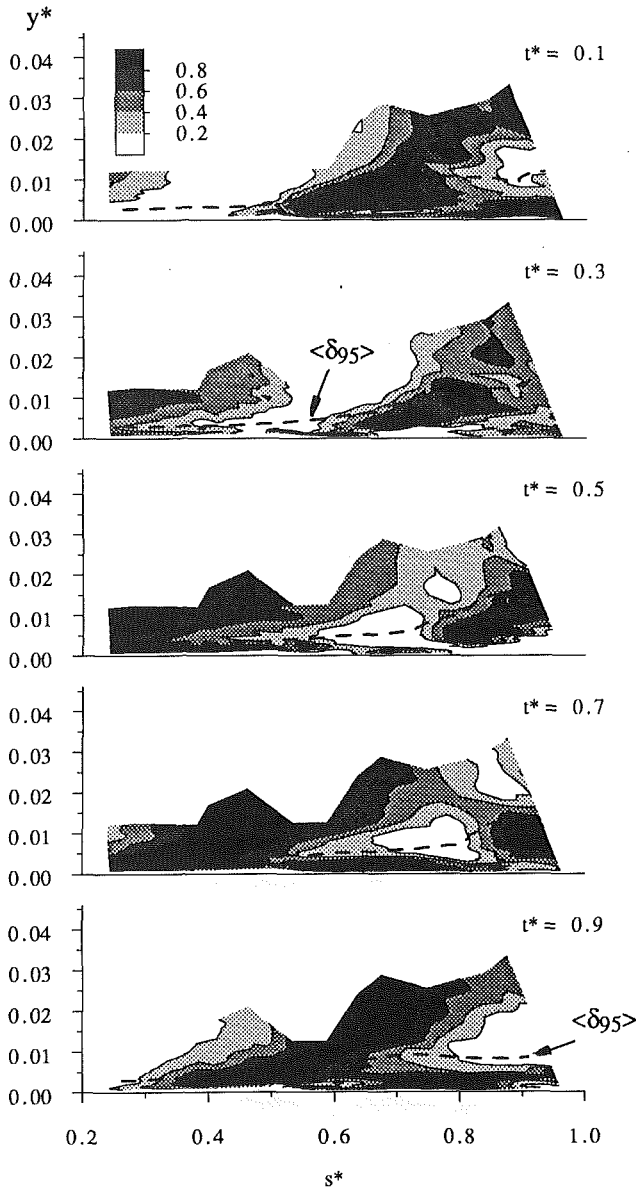


Fig. 8 Fractional increase in rms intensity during a wake passing cycle, equation (4), for the 75 percent C_{x0} axial gap

(equivalent to the maximum value in the wake) arise over the first part of the blade because the disturbances in the boundary layer are more slowly dissipated than in the free stream due to the more favorable production-dissipation balance. In addition, diffusion within the boundary layer normal to the surface exposes the disturbances to a wide range of convection velocities. Further downstream, therefore, the boundary layer contains a much more uniform background level of low frequency disturbances to which is added the periodic component by diffusion from the wake segment overhead. The persistence of disturbances in the laminar boundary layers of linear cascades is well known (e.g., Hodson, 1983b) but not often reported although Hart (1985) documented "turbulence intensities" of up to 10 percent without transition being observed. This feature will be examined in more detail in Part 2.

The background level just noted and the response of the boundary layer to the turbulence of the wake vary both along the surface and across the boundary layer. For this reason, Fig. 8 also presents a series of instantaneous cross sections through the boundary layer but, in order to view the interaction more clearly, the shaded contours are of the quantity

The effect of transition on the rms intensity through a boundary layer (after Pfeil and Herbst, 1979)

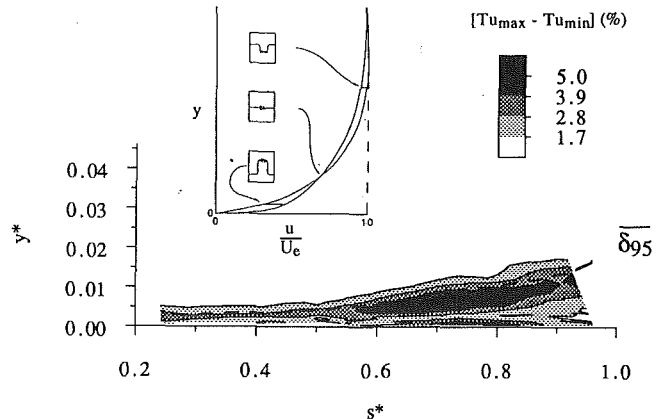


Fig. 9 Peak-to-peak variation of rms intensity $[\sqrt{\langle\langle u^2 \rangle\rangle}/U_a]$

$$\frac{Tu(s, y, t) - Tu_{min}(s, y)}{Tu_{max}(s, y) - Tu_{min}(s, y)} \quad (4)$$

which represents the normalized variation of the ensemble rms with respect to the minimum value.

In the first plot of Fig. 8 ($t^* = 0.1$), the unshaded area indicates the separation that exists between the wakes and in the free stream; the peak turbulence that marks the center of a wake is to be found near 75 percent s^* . Even though a new wake can be seen in the free stream near the start of the traverse domain, the inner part of the boundary layer has yet to be disturbed due to a time lag resulting from diffusion across the boundary layer. This lag is relatively small as can be seen from the laminar distance-time plots, which show parallel traces in the laminar boundary layer at very nearly the free-stream convection velocity. Once transition begins, the patch beneath the wake is not simply due to diffusion. The trailing edges of the spots move slower than the wake segment and give a false picture of the magnitude of the lag.

Care must be taken when interpreting these data since as Fig. 4(b) shows, the peak rms intensities correspond to the regions of highest intermittency and these are found not near the wake centerline but nearer the edges of the wakes once transition is well established. This phenomenon is responsible for the high levels of normalized rms intensity that appear very near to the surface between 60 and 80 percent s^* in the plot corresponding to time $t^* = 0.7$. Using this location in time and space as a starting point, it is relatively easy to trace the history of this feature and to see that it arises because the turbulent patch associated with a later wake catches up with that due to the preceding wake. Although the turbulent patches appear to merge near the surface ($y/\langle \delta_{95} \rangle \leq 0.5$), the contours in Fig. 8 imply that, in the outer part of the boundary layer and the free stream, the turbulent patches remain separate within the traverse domain. The main conclusion to be drawn from the data of Fig. 8 is that the transition process is undoubtedly initiated by the turbulence in the wake.

Figure 9 shows the variation in the denominator of equation (4) throughout the boundary layer. The time mean value of δ_{95} is shown by the dashed line. This figure presents data similar to those of Fig. 5 but across the entire boundary layer rather than just at the surface. During the laminar phases, the greatest changes in the ensemble rms are near the middle of the boundary layer. At the rear of the surface, the largest variation is near 75 percent δ_{95} . However, the maximum variation occurs near 70 percent s^* since the rms intensity represents the combined unsteadiness associated with stochastic processes such

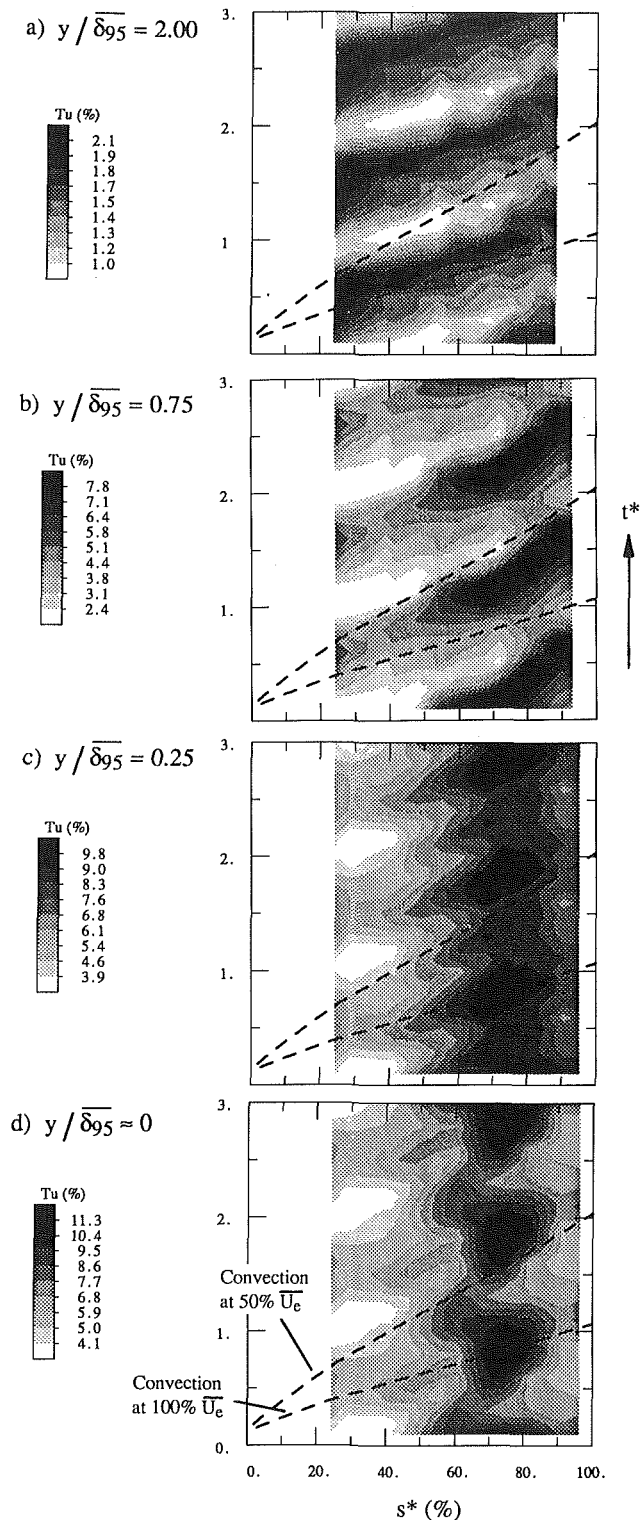


Fig. 10 Distance-time plots of rms intensity within the boundary layer at varying surface-normal distances

as spot formation as well as with the turbulence. As Pfeil and Herbst (1979) have shown (see inset), in the transition region the velocity variation associated with a change of state will not be constant across the boundary layer. For these reasons, there is a saddle point between two peaks near 70 percent s^* . This also explains why the interaction of the wake with the boundary layer does not appear as a continuous ridge in the contour maps of Fig. 7.

The hot-wire data also have been combined to produce dis-

tance-time plots of the random unsteadiness. Figure 10 contains a series of these plots at different heights (y/δ_{95}) through the suction surface boundary layer. The shaded contours are of the rms intensity defined in equation (3). Figure 10, therefore, presents the data of Fig. 7 in another format.

Figure 10(a) is a distance-time plot of the turbulence intensity outside the boundary layer ($y/\delta_{95} = 2$). Typically, the peak turbulence intensity within the wakes is of the order of 2 percent and it passes over the surface at the predicted free-stream convection velocity \bar{U}_e . When the wakes are viewed in this way, it also is apparent that there is very little growth in the fraction of the cycle time that is occupied by the wake. This is despite the fact that turbulent mixing (diffusion) and the wake-jet effect (convection) will tend to increase the time interval occupied by the wake. A simple model presented in Part 2 of the present paper examines the importance of these mechanisms and shows that the turbulent mixing is not large, that the spreading due to the blowing action of the wake jet is larger but still of the same order and that their combined effect will not cause the wakes to merge inside the rotor passage. Figure 8 also showed that this was the case.

Within the boundary layer, there are parallel tracks of higher rms intensity up to approximately 40 percent s^* , after which the peak values rise to form the V-shaped wedges associated with transition. The angle of the wedges is least and the start of transition furthest along the surface in the outer portions of the boundary layer ($y/\delta_{95} = 0.75$), Fig. 10(b). In Fig. 10(b), the ridge of the V-shaped wedge continues to the end of the traverse domain. Again, the data suggest that full transition does not occur in the outer part of the boundary layer.

Nearer the surface (Figs. 10c and 10d), the areas of highest random unsteadiness correspond to those noted in Fig. 8, which were associated with the merging of adjacent turbulent patches. Beyond the transition zone, tracks indicating the effects of the wakes upon the turbulent flow also can be seen. The similar form of the data in Figs. 4(b) and 10(c, d) implies that in the inner part of the boundary layer, transition appears to take place at the same instant at each spatial location. The boundary layer cross sections (Fig. 8) also appear to suggest that once the wakes have merged very near the surface, diffusion normal to the surface speeds up the transition process in the middle of the boundary layer. These observations are not true of the entire boundary layer so that the location of transition depends on the height within the boundary layer. This supports the earlier work of Doorly and Oldfield (1985) who produced an s - t plot that showed that the development of a turbulent patch as indicated by surface-mounted thin-film gages lagged behind the position of the wake in the free stream as indicated by Schlieren photographs.

At the surface (Fig. 4b), the hot-film data show that transition is virtually complete by 82 percent s^* , but the hot-wire traverses (Figs. 7-10) indicate later completion in the outer regions of the boundary layer. Because of these differences, the merging of adjacent turbulent patches cannot be regarded as a two-dimensional (surface distance and time) process since diffusion from the free stream and normal to the surface plays a part. However, the data do suggest that in the inner half of the boundary layer, the process may be regarded as two dimensional. In addition, the changes in the integral parameters of the boundary layer (Fig. 2) are consistent with the hot-film and near-surface hot-wire data. Since it may be argued that the outer part of the boundary layer contributes relatively little to the overall aerodynamic and thermodynamic properties of the boundary layer, the use of two-dimensional models is justified.

Conclusions

The existence of disturbed laminar, transitional and tur-

bulent flow on a turbine blade has been demonstrated. The start of the transition is unsteady and dominated by stator wake turbulence, but does not begin immediately when the wake impacts on the boundary layer. The transition process is characterized by the appearance of high frequency bursts above the lower frequency background disturbances. Several bursts exist for a single wake segment and their formation is stochastic rather than phase-locked. Although the transition location varies with distance from the surface, behavior near the surface is very similar to that in the center of the boundary layer justifying the use of hot-film gages in this application.

References

- Abu-Ghannam, B. J., and Shaw, R., 1980, "Natural Transition of Boundary Layers—the Effects of Turbulence, Pressure Gradient and Flow History," *Journal of Mechanical Engineering Science*, Vol. 22, No. 5, pp. 213–228.
- Binder, A., 1985, "Turbulence Production Due to Secondary Vortex Cutting in a Turbine Rotor," *ASME Journal of Engineering for Gas Turbines and Power*, Vol. 107, pp. 1039–1046.
- Cebeci, T., and Carr, L. W., 1978, "A Computer Program for Calculating Laminar and Turbulent Boundary Layers for Two-Dimensional Time-Dependent Flows," NASA TM 78470.
- Dong, Y., 1988, "Boundary Layers on Compressor Blades," PhD Thesis, Cambridge University, United Kingdom.
- Doorly, D. J., and Oldfield, M. L. G., 1985, "Simulation of the Effects of Shock Wave Passing on a Turbine Rotor Blade," ASME Paper No. 85-GT-112.
- Doorly, D. J., 1987, "Modeling the Unsteady Flow in a Turbine Rotor Passage," ASME Paper No. 87-GT-197.
- Hart, M., 1985, "Boundary Layers on Turbine Blades," PhD Thesis, Cambridge University, United Kingdom.
- Hodson, H. P., 1983a, "The Development of Unsteady Boundary Layers on the Rotor of an Axial-Flow Turbine," *AGARD Conference on Viscous Effects in Turbomachines*, AGARD CP-351, Copenhagen, Denmark.
- Hodson, H. P., 1983b, "The Detection of Boundary Layer Transition and Separation in High Speed Turbine Cascades," *Proceedings of the 7th Symposium on Measurement Techniques for Transonic and Supersonic Flow in Cascades and Turbomachinery*, Aachen, Federal Republic of Germany.
- Hodson, H. P., 1984, "Boundary Layer and Loss Measurements on the Rotor of an Axial Flow Turbine," *ASME Journal of Engineering for Gas Turbines and Power*, Vol. 106, pp. 391–399.
- Hodson, H. P., 1985, "Measurements of Wake-Generated Unsteadiness in the Rotor Passages of Axial Flow Turbines," *ASME Journal of Engineering for Gas Turbines and Power*, Vol. 107.
- Hodson, H. P., and Addison, J. S., 1988, "Wake-Boundary Layer Interactions in an Axial-Flow Turbine at Off-Design Conditions," ASME Paper No. 88-GT-233.
- Hunter, I. H., 1982, "Endwall Boundary Layer Flows and Losses in Axial Turbine Stage," *ASME Journal of Engineering for Power*, Vol. 104.
- LaGraff, J. E., Ashworth, D. A., and Schultz, D. L., 1988, "Measurement and Modeling of the Gas Turbine Blade Transition Process as Disturbed by Wakes," ASME Paper No. 88-GT-232.
- Narasimha, R., and Sreenivasan, K. R., 1979, "Relaminarization of Fluid Flows," *Advances in Applied Mechanics*, Vol. 19, pp. 221–309.
- Obremski, H. J., and Fejer, A. A., 1967, "Transition in Oscillating Boundary Layer Flows," *Journal of Fluid Mechanics*, Vol. 29, pp. 93–111.
- Pfeil, H., and Herbst, R., 1979, "Transition Procedure of Instationary Boundary Layers," ASME Paper No. 79-GT-128.
- Pfeil, H., Herbst, R., and Schroder, T., 1982, "Investigation of Laminar-Turbulent Transition of Boundary Layers Disturbed by Wakes," ASME Paper No. 82-GT-124.
- Schubauer, G. B., and Klebanoff, P. S., 1955, "Contributions on the Mechanics of Boundary Layer Transition," NACA TN 3489.
- van Driest, E. R., and Blumer, C. B., 1963, "Boundary Layer Transition: Free-Stream Turbulence and Pressure Gradient Effects," *AIAA Journal*, Vol. 1, pp. 1303–1306.
- Walker, G. J., 1974, "The Unsteady Nature of Boundary Layer Transition on an Axial-Flow Compressor Blade," ASME Paper No. 74-GT-135.
- Walker, G. J., 1987, "Transitional Flow on Axial Turbomachinery Blading," AIAA Paper No. 87-0010.
- Whitehead, D. S., 1980, "The Calculation of Steady and Unsteady Transonic Flow in Cascades," Cambridge University Engineering Department Report A-Turbo/TR98.

J. S. Addison

H. P. Hodson

Whittle Laboratory,
Cambridge University,
Cambridge CB3 0DY United Kingdom

Unsteady Transition in an Axial-Flow Turbine: Part 2—Cascade Measurements and Modeling

Part 1 of this paper reanalyzed previously published measurements from the rotor of a low-speed, single-stage, axial-flow turbine, which highlighted the unsteady nature of the suction surface transition process. Part 2 investigates the significance of the wake jet and the unsteady frequency parameter. Supporting experiments carried out in a linear cascade with varying inlet turbulence are described, together with a simple unsteady transition model explaining the features seen in the turbine.

Introduction

Traditionally, turbomachinery components have been tested in cascades using stationary inflow, sometimes using a grid to produce a turbulence intensity thought to be representative of the levels in a real machine. Similarly, designers make use of steady-state correlations based on many years experience of testing cascades and real machines and, again, assume a turbulence level thought to be representative. However, it has been shown by many studies (e.g., Hodson, 1984; Doorly and Oldfield, 1985; Walker, 1974), that the actual boundary layers are unsteady and that the passage of wakes from upstream blade rows allied to a high degree of inlet free-stream turbulence results in behavior that cannot be predicted satisfactorily by conventional methods.

Part 1 of the paper described experiments into this subject. The turbine used for the work was a large, low-speed, single-stage, axial-flow machine designed as a free-vortex stage with zero inlet and exit swirl and 50 percent reaction at midspan. The 36 stator blades and 51 rotor blades had aspect ratios of 1.5 and 2.0, respectively, and a hub-tip ratio of 0.7. This paper is concerned specifically with the rotor midspan blade section where the flow is known to be two dimensional (Hodson and Addison, 1988). Experimental data were obtained at three stator-rotor axial gaps corresponding to 50, 75, and 143 percent C_{xs} (stator axial chord).

Previously published measurements, including time-resolved hot-wire traverses and surface hot-film gage measurements, were reassessed in the light of more recent findings. It was shown that the passage of wake segments over the blade surface boundary layer was dominated by the wake turbulence but it did not cause immediate transition. When transition occurred, it was characterized by the stochastic appearance of turbulent spots. The spreading of the wake segment in the free stream was small and the interaction of the wakes with the laminar boundary layers shown to be quasi-steady. Although transition

location varied with distance from the surface, behavior near the surface was very similar to that in the center of the boundary layer justifying the use of hot-film gages.

In this part of the paper, the action of the wake jet, and the significance of the unsteady frequency parameter are considered. The results of a linear cascade investigation and computer predictions of wake behavior are presented and analysis of the data leads to the formulation of a simple model for the start of transition. It will be shown that this can explain many of the features highlighted by the results of Part 1.

Role of the Wake Jet in Unsteady Transition

Wakes are characterized by their turbulence and velocity profiles. The effect of the turbulence on boundary layer transition will be investigated in the cascade tests to be reported later. The effect of the wake jet can be quantified by considering the work of Obremski and Fejer (1975). They studied transition on a flat plate in nonreversing periodic flow and showed that the mechanism of transition had a strong dependence on a nonsteady Reynolds number

$$Re_{ns} = \frac{(\Delta U/U_0)}{(\omega\nu/U_0^2)} \quad (1)$$

which they related to the degree to which disturbances were amplified during one cycle. A low value ($Re_{ns} \ll 26,000$ for zero pressure gradient) resulted in aperiodic formation of turbulent spots with the unsteady flow merely playing a role in encouraging or discouraging natural spot formation at certain times of the cycle. A high value resulted in periodic spot formation with the velocity perturbation assuming a dominant role. If it is assumed that ΔU is of the order of the wake-jet velocity U_j , then using the values applicable to the turbine rotor midspan gives $Re_{ns} \approx 1500$, which is significantly less than the limit of 26,000. Therefore, the velocity fluctuation resulting from the wake jet will not be strong enough to force transition in its own right.

The extrapolation of these results to turbomachinery is not strictly valid since the plate was subjected to a standing free-

Contributed by the International Gas Turbine Institute and presented at the 34th International Gas Turbine and Aeroengine Congress and Exhibition, Toronto, Ontario, Canada, June 4-8, 1989. Manuscript received at ASME Headquarters February 14, 1989. Paper No. 89-GT-290.

stream velocity wave while the passage of a wake over the blade surface results in a convected disturbance (traveling wave). However, the mode of action of the jet will be similar and we can reasonably discount the velocity fluctuation as a primary cause of transition although it will modify the environment perceived by higher frequency disturbances from the free stream and wake turbulence.

Significance of the Reduced Frequency Parameter

The surface distance-time plots of Part 1 indicated that the wake turbulence penetrated the boundary layer without a significant delay. However, the value of the reduced frequency parameter

$$\bar{\omega} = \frac{\omega x}{U} \quad (2)$$

where x and U are representative values, is typically about 3, which suggests that the boundary layers should be truly unsteady. Although equation (2) defines $\bar{\omega}$ in inviscid terms as the ratio of the convective and periodic time scales, this apparent paradox can be resolved by rewriting it as

$$\bar{\omega} = \frac{\nu}{Ux} \left\{ \frac{x}{\delta} \right\}^2 \left[\frac{\omega \delta^2}{\nu} \right] = \frac{1}{\text{Re}_x} \left\{ \frac{x}{\delta} \right\}^2 \left[\frac{\omega \delta^2}{\nu} \right] \quad (3)$$

It is noted that δ^2/ν is a diffusive (laminar) time scale and thus the final term of equation (3) represents the ratio of the time taken for information to diffuse through the boundary layer to the periodic time of the unsteady flow (or the square of the ratio of the boundary layer and Stokes' layer thicknesses). For a laminar boundary layer

$$\left\{ \frac{\delta}{x} \right\}^2 \approx \frac{25}{\text{Re}_x} \quad (4)$$

so that equation (3) reduces to

$$\bar{\omega} \approx \frac{1}{25} \left[\frac{\omega \delta^2}{\nu} \right] \quad (5)$$

Thus the reduced frequency is both an inviscid and viscous parameter. However, in the present situation, we are concerned with the time taken for wake-turbulence to diffuse into the laminar boundary layer. At the simplest level, this is more accurately represented by using an eddy viscosity ν_t rather than the kinematic viscosity ν . Since ν_t is much greater than ν ($\nu_t \sim 10\text{--}100\nu$), the diffusion time is significantly shorter, and the effective reduced frequency given by

$$\bar{\omega}' = \bar{\omega} \left\{ \frac{\nu}{\nu_t} \right\} \quad (6)$$

is significantly less than unity. This indicates that diffusion across the boundary layer is very rapid, and suggests that the interactions can be treated as quasi-steady.

Measurements in a Linear Cascade

Since the interaction of wakes with the boundary layers can be treated as quasi-steady, it is reasonable to investigate the development of the suction surface boundary layer in a linear cascade with stationary inlet turbulence and then extrapolate the results to the unsteady case.

The cascade used was a high aspect ratio linear cascade of seven epoxy blades with sections geometrically similar to the rotor midspan of the rotating turbine stage described in Part 1. A biplanar turbulence grid consisting of a square lattice of 5/16 in. dia bars at 1 1/4 in. pitch was fitted upstream of the parallel-sided inlet duct. The intensity of the free-stream turbulence at inlet to the linear cascade was varied by altering the separation between the cascade and the turbulence grid. The levels used here were $0 \leq (\text{Tu}_m)_{in} \leq 10$ percent measured at the inlet plane in the absence of the cascade. In the central blade passage, a hot-wire probe consisting of two 5 μm tungsten wires crossed at 90 deg and aligned with the wires at 45 deg to the mean flow at each point was used to measure the flow velocity and mean turbulence intensity. Oil and dye flow visualization and hot-film gages were used to determine the state of the suction surface boundary layer. Further details of the cascade and experimental methods are given by Hodson (1984) and Hall (1985).

The measured values of Tu_m corresponding to the stations nearest the suction surface were scaled for the range of inlet turbulence intensity. These were then used with the predicted boundary layer parameters (using the boundary layer code of Cebeci and Carr (1978) as in Part 1) to apply the start and end of transition correlation originally presented by Abu Ghanam and Shaw (1980). Figure 1 shows the start of transition correlation and, superimposed, the predicted values of the momentum thickness Reynolds number Re_θ and pressure gradient parameter (modified Polhausen parameter) λ_θ for this blade. The sensitivity of the critical turbulence level to Re_θ , and hence s^* , is evident as is the relative insensitivity to λ_θ in the region of interest (i.e., $\text{Tu} > 1.5$ percent).

Figure 2 shows the observed boundary layer states as deduced from the flow visualization (separation and reattachment) and hot-film gages (transitional behavior), and compares them with the predictions. Overall, the agreement with the correlation is reasonable. It can be seen that the position of the separation line is only slightly affected by the changing levels of free-stream turbulence. This indicates that the disturbances that

Nomenclature

b = wake standard deviation in the Eulerian frame
 C_{xs} = stator axial chord
 $D(s^*)$ = decay factor for cascade free-stream turbulence intensity
 L = characteristic length of a turbulent fluctuation
 Re = blade Reynolds number
 Re_{ns} = nonsteady Reynolds number
 Re_x = Reynolds number based on (surface) distance
 Re_θ = Reynolds number based on momentum thickness
 s = (suction) surface distance
 s^* = fractional surface distance = s/s_{max}

T = blade passing period
 t^* = dimensionless time = t/T
 Tu = turbulence (or rms) intensity
 U = flow velocity
 u = streamwise velocity within the boundary layer
 x = distance
 y = surface normal distance
 α = factor in transition model
 β = wake standard deviation in the time domain
 γ = factor in transition model
 δ = boundary layer thickness
 Δ = change in
 λ_θ = (modified) Polhausen parameter = $\frac{\theta^2}{\nu} \frac{\partial U_e}{\partial s}$

ν = kinematic viscosity
 ν_t = eddy viscosity
 ω = radian frequency
 $\bar{\omega}$ = reduced frequency parameter
 \sim = ...is of the order of...

Subscripts

bl = within the boundary layer
 e = edge of boundary layer
 fs = free stream
 in = inlet to blade row/cascade
 j = wake-jet
 m = mean
 max = maximum
 $'$ = fluctuation in.....
 0 = reference

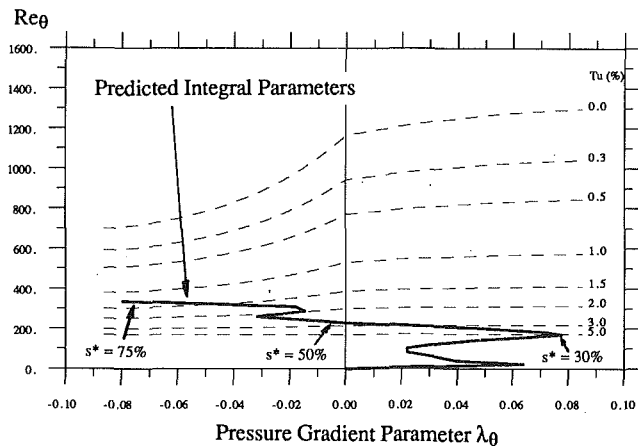


Fig. 1 Start of transition correlation of Abu Ghannam and Shaw applied to the turbine rotor suction surface

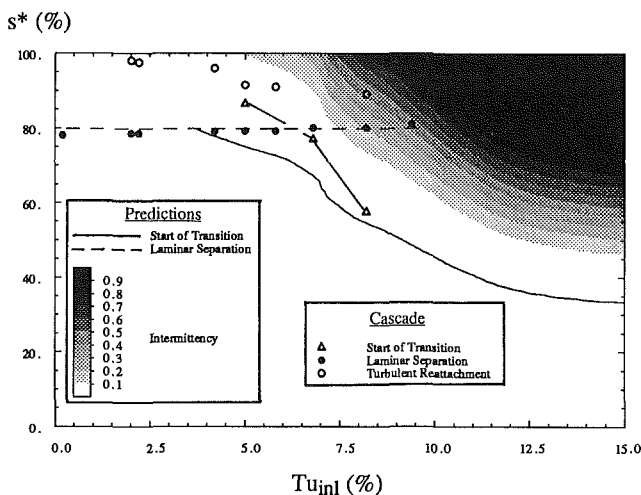


Fig. 2 Variation of suction surface boundary layer states with cascade inlet turbulence intensity

exist in the laminar boundary layer have relatively little effect on the wall shear stress. The separation line appears to move back slightly with increasing inlet turbulence due to an increase in momentum transfer. This is consistent with the results of Part 1 showing increased momentum transfer in the laminar boundary layer on the turbine rotor due to wake turbulence.

The position of the start of transition was determined from the first appearance of high-frequency disturbances in the hot-film signals. The results show that the start of transition is strongly affected by the levels of free-stream disturbances. Although the data are limited outside the separation bubble, they agree fairly well with the predictions, being between the predicted start of transition and 10 percent intermittency. An asymptotic forward limit of 36 percent s^* is predicted for the start of transition with increasing free-stream turbulence due to a minimum critical Re_θ of 163. In the research turbine, laminar separation was prevented because transition occurred forward of the liftoff line. From the cascade behavior and the predictions of the transition correlation, it is clear that the levels of inlet turbulence intensity must exceed 9 percent in order to provide levels of about 2 percent in the neighborhood of transition and it is noted that these levels did not exist in the free stream of the research turbine but only at the peak of the wakes.

Wake Spreading Due to the Wake-Jet

In Fig. 10 of Part 1, distance-time plots of hot-wire data

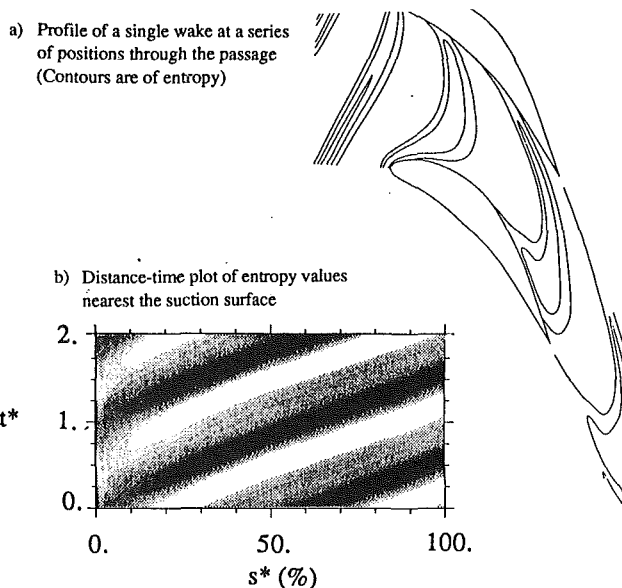


Fig. 3 Unsteady two-dimensional prediction of stator wake distortion through the turbine rotor

were presented that suggested that time domain dispersion of the wake in the free stream was minimal. One of the spreading mechanisms that operates is the wake jet and, to show this effect more clearly, an unsteady inviscid finite volume code has been run, using entropy as a convected marker [in a similar way to the earlier predictions of Hodson (1984a) and Giles (1987)]. A wake velocity defect equal to 20 percent of the inlet velocity and therefore equivalent to about twice the value measured for an axial spacing of 50 percent C_{xs} was used in order to study the effect. Details of the computational method will be given in a future publication. Figure 3(a) is a composite plot showing the shape of a single wake as it passes through the rotor passage using contours of entropy. The results agree well with the earlier predictions for the same machine by Hodson and Giles as well as the hot-wire passage measurements of Hodson (1985). There is considerable distortion caused by the differing convection velocities at the front and rear of the wake segment. But if the values of entropy nearest to the suction surface are plotted in the form of a distance-time plot (Fig. 3b), parallel traces result and it is clear that spreading in the time domain due to the wake jet is minimal.

Simple Transition Model

In order to understand the results described in Part 1 more fully, a simple model has been devised. The details are summarized in Fig. 4. The model is based on the assumption that the principal effect of the wake is the promotion of early transition of the boundary layer as a result of increased levels of disturbances. It is further assumed that the effects initiated by turbulence will be quasi-steady in nature as has been shown to be the case in the research turbine. The effect of the wake jet as a direct cause of transition has already been discounted through consideration of the nonsteady Reynolds number. Its indirect effect on transition through quasi-steady modification of the stability of the boundary layer is considered to be small when compared to the mean flow. This latter assumption is justified by recalling that the start of transition criterion of Abu Ghannam and Shaw (1980) showed that, when the levels of turbulence are greater than 1.5 percent, the influence of pressure gradient (λ_θ) is very much weaker than the influence of the boundary layer Reynolds number (Re_θ). This start of transition correlation is assumed to hold true in the quasi-

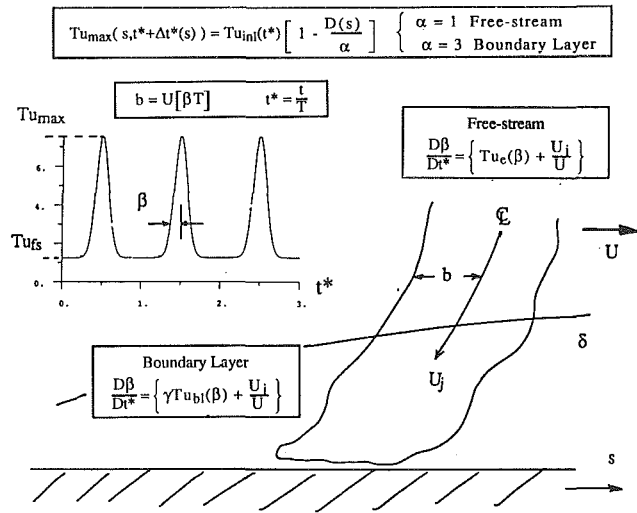


Fig. 4 Summary of the assumptions used in the unsteady transition model

Table 1 Wake parameters used in the transition model

Wake Parameter at Rotor Inlet Plane	Axial Gap (% C _{xs})		
	50	75	143
Tu _{max} Peak Turbulence (%)	9.5	7.5	4.0
Tu _{fs} Freestream Turbulence (%)	1.25	1.5	2.0
β Wake Width	0.008	0.012	0.015
U _j /U Velocity Defect (%)	10.	9.	7.5

steady case although it is noted that the transition length correlation based on a fixed start of transition location is not generally valid and most definitely cannot be used here. Boundary layer parameters predicted by the code of Cebeci and Carr (1978) are used, and the disturbances in the laminar boundary layer are assumed to be associated with low Reynolds stress and to have relatively little effect on the boundary layer parameters. The inlet turbulence profile is approximated by a periodic series of Gaussian profiles with peak value Tu_{max} and standard deviation b superimposed on a free-stream level Tu_{fs} as shown in Fig. 4. For the purposes of this model, the standard deviation (wake width) is best considered in the time domain where β is defined as the fraction of the wake passing period during which an observer on the blade surface would see turbulent flow in the free stream and therefore

$$\beta T \approx b/U \quad (7)$$

where U is the local convective velocity. The values for the three axial gaps derived from the results of Hodson (1983) are given in Table 1. This results in inlet profiles for the 3 configurations as shown in Fig. 5. Initially, only the 75 percent C_{xs} case will be considered since most data are available for this turbine configuration.

The decay of the wake turbulence intensity through the passage is assumed to be proportional to that measured in the linear cascade for the grid-generated turbulence. Thus the free-stream turbulence level at a given point in space and time is

$$Tu_e(s^*, t^* + \Delta t^*) \approx Tu_{in}(t^*) [1 - D(s^*)] \quad (8)$$

where Δt^* is the time delay due to convection, itself a function of distance s^* , and $[1 - D(s^*)]$ is the variation of turbulence intensity measured in the linear cascade.

The simplest model would assume that the wake segments are convected through the passage without spreading and that transition can simply be calculated from the free-stream turbulence at any point. This situation is shown in the distance-time plot of Fig. 6, and clearly this has not modeled the be-

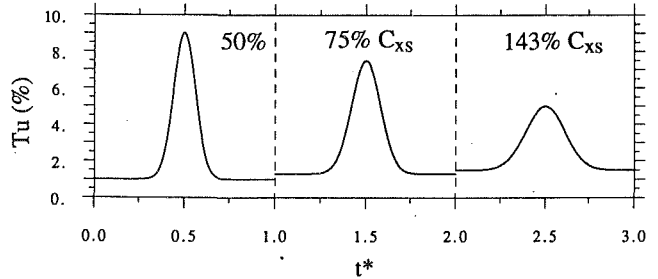


Fig. 5 Variation of wake turbulence profile at rotor inlet with rotor-stator spacing

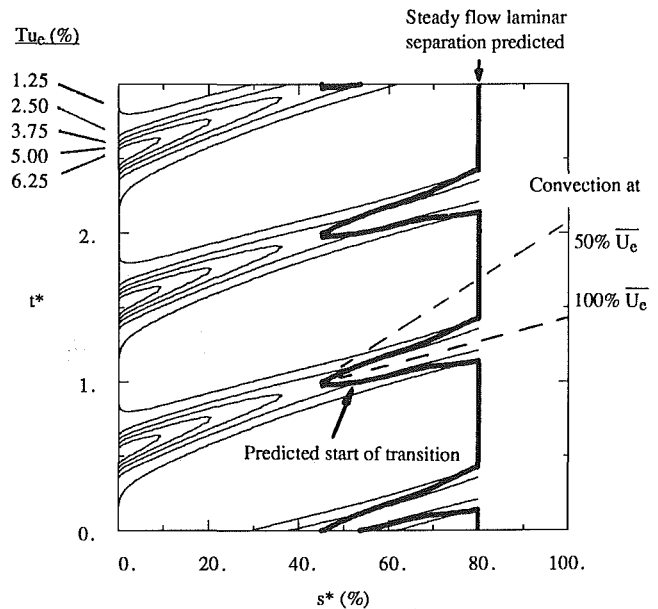


Fig. 6 Predicted start of transition — no wake spreading mechanism (75 percent C_{xs} rotor-stator axial gap)

havior measured by the hot-film gages or the hot-wire traverses. It is predicted that laminar separation will reappear between highly localized transitional regions. Even assuming that the "patches" spread with trailing edge speed 55 percent \bar{U}_e and leading edge speed 88 percent \bar{U}_e as has been shown to be typical of turbulent spots (e.g., Shubauer and Klebanoff, 1955), the separation would still occur since the wake-induced patches would not merge before the trailing edge. The cascade tests have shown that separation will only be suppressed by levels of mean inlet turbulence intensity $(Tu_m)_{in}$ greater than 7 percent, and hot-wire traverses and flow visualization (Hodson and Addison, 1988) have shown that separation does not exist on the rotor of the research turbine. Since the interwake turbulence level is ~ 1 percent, this cannot be responsible for the suppression of separation, and the implication is that the peak level is less highly localized. It is, however, reassuring to note that the decay of the peak turbulence results in earliest transition very much in line with the measured location suggesting that this combination of an approximate model for the decay of wake turbulence intensity and the start of transition correlation is valid.

We can estimate the free-stream spreading of the wake segment in the time domain by writing

$$\frac{D(U\beta)}{Dt^*} \sim u' \text{ or } \frac{D\beta}{Dt^*} \sim Tu_e(\beta) \quad (9)$$

where $Tu_e(\beta)$ is the turbulence intensity at β from the wake centerline in the free stream (Fig. 4). Additionally, there will be a spreading effect due to the wake jet, and a continuity argument suggests that

$$\frac{D(U\beta)}{Dt^*} \sim U_j \text{ or } \frac{D\beta}{Dt^*} \sim \frac{U_j}{U} \quad (10)$$

If the two effects are assumed to add, then

$$\frac{D\beta}{Dt^*} \sim Tu_e(\beta) + \frac{U_j}{U} \quad (11)$$

Using this assumption, the time behavior of the free-stream turbulence through the cycle can be determined at points downstream. The resulting boundary layer behavior (not shown) is little different to that seen for the case just described with no spreading of the wake width. This agrees with the distance-time plots resulting from the hot-wire traverses of Part 1 and predictions previously described, which showed that there was little time domain spreading of the wake turbulence in the free stream. This result is important because it shows that the unsteady effect of the free stream on the wake can be neglected in a first-order approximation.

Since transition occurs inside the boundary layer and the intensity of the fluctuations is maintained at a higher level by the more favorable production-dissipation balance, it might be expected that the spread of influence of the wake peak levels would be correspondingly more vigorous, i.e.

$$\frac{D\beta}{Dt^*} \sim Tu_{bl}(\beta) + \frac{U_j}{U} \quad (12)$$

where Tu_{bl} is a turbulence level typical of the heart of the boundary layer and the $Tu_{bl} > Tu_e$. The reduction in peak turbulence intensity is assumed to be somewhat less in the boundary layer than in the free stream such that

$$Tu_{bl}(s^*, t^* + \Delta t^*) \approx Tu_{in}(t^*) \left[1 - \frac{D(s^*)}{\alpha} \right] \quad (13)$$

where α is assumed to be a constant greater than 1. A constant value is not strictly justified given the changing pressure gradient on the blade but it is felt that it is a relatively small approximation in comparison with all the others. By trial and error, it was found that a value of $\alpha \approx 3$ gave levels of turbulence intensity typical of those measured in the disturbed laminar boundary layer of Part 1. The boundary layer level is only used to allow the increased mixing to be calculated. The value used as input for the correlation (which is based on free-stream levels) is derived from the peak value in the free stream and the wake width within the boundary layer. The results shown in Fig. 7 are very similar to the behavior previously predicted (Fig. 6) since the influence of the wake peak has still not spread far in the time domain. Similarly, the boundary layer levels have not spread as quickly as the hot film or hot-wire measurements of Fig. 4(b), Part 1 would suggest. Another effect must be dominant.

Velocity fluctuations exist in all directions. Those in the chordwise direction have already been considered and the mechanism shown to be of insufficient strength to explain the observed results. Those in the spanwise direction contribute nothing to the chordwise mixing process as long as the flow is two dimensional. However, following a mixing length argument, it is noted that a fluctuation normal to surface of typical length scale L gives rise to a streamwise fluctuation

$$u' \sim L \frac{\partial u}{\partial y} \quad (14)$$

In a boundary layer where $\partial u/\partial y$ is significant, the dispersion resulting from this effect can overwhelm the other spreading mechanisms. In order to model this in a simple way, we assume that

$$\frac{D\beta}{Dt^*} \sim \gamma Tu_{bl}(\beta) + \frac{U_j}{U} \quad (15)$$

where γ is again assumed constant for convenience. Trial and error is used to match the hypothesized boundary layer tur-

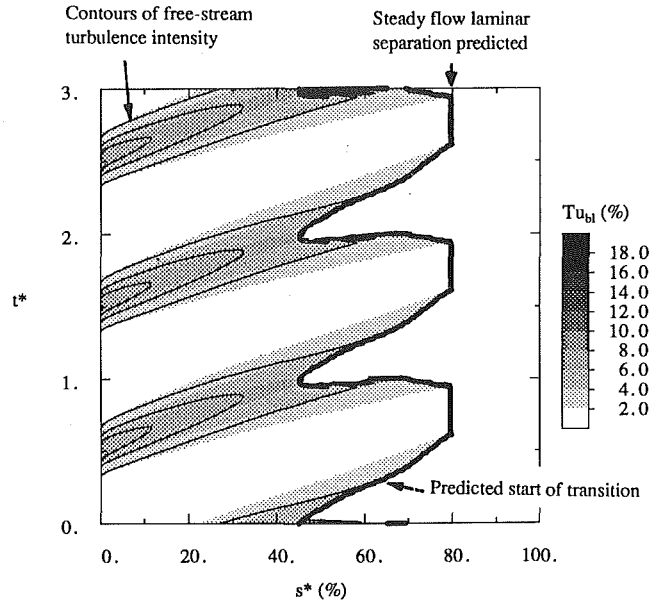


Fig. 7 Predicted start of transition — wake spreading by streamwise fluctuations and the wake jet

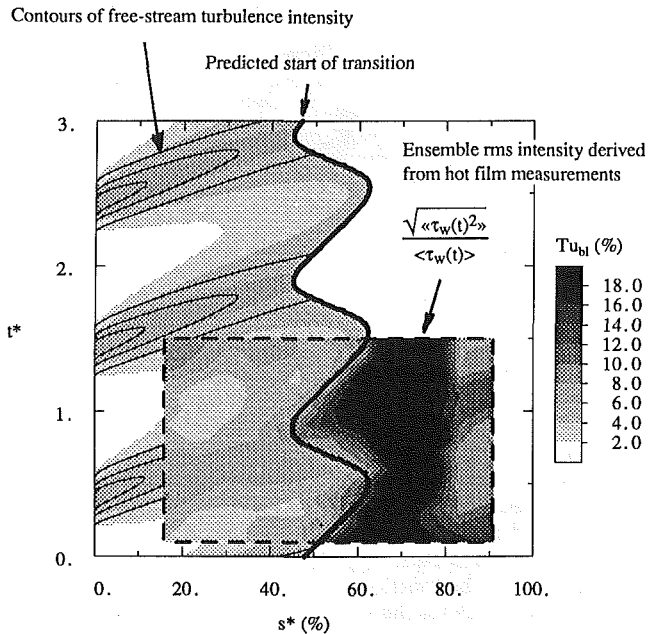


Fig. 8 Predicted boundary layer behavior compared with hot-film measurements (75 percent C_{xs} rotor-stator spacing)

bulence level to the hot-wire traverse results, and this gives the value of $\gamma \approx 8$ (using the value of $\alpha = 3$ as previously shown). For a typical value of $Tu_{bl}(s^*, t^*) \sim 2$ percent, this would imply a fluctuation length scale given by

$$L \sim \frac{u'}{\partial u/\partial y} \text{ whence } \frac{L}{\delta} \sim \frac{u'}{U_e} \left[\frac{U_e}{\delta} \right] \frac{1}{\partial u/\partial y} \quad (16a)$$

$$\frac{L}{\delta} \sim \gamma Tu_{bl}(s^*, t^*) \sim 16 \text{ percent } (\gamma = 8) \quad (16b)$$

This is not unreasonable, and is reassuringly close to the value from conventional mixing length models (e.g., $L/\delta \approx 9$ percent; Cebeci and Smith, 1974). The result of applying the approximation of equation (15) is shown in Fig. 8, where it is compared with the hot-film results of Part 1. Again, the line contours are of the free-stream wake turbulence, and the shaded

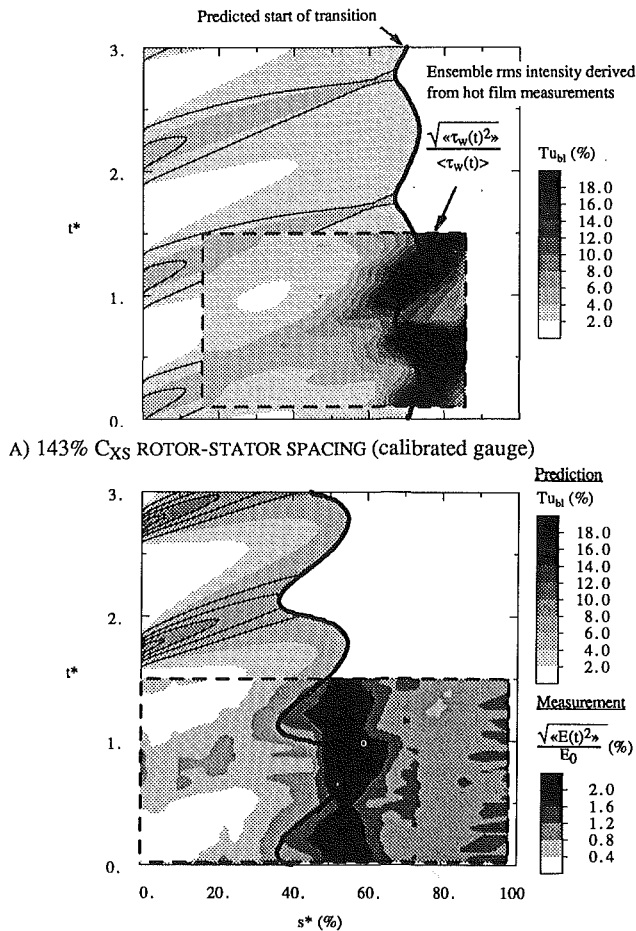


Fig. 9 Predicted boundary layer behavior compared with hot-film measurements

contours are of the boundary layer level. The shape of the predicted start of transition line follows the observed results quite closely and the spread of the predicted boundary layer turbulence intensity corresponds well with the measured values.

Given that two constants have been estimated by trial and error, the validity of the model can be judged by applying it to the two other turbine configurations reported in Part 1 with 143 percent and 50 percent C_{XS} rotor-stator spacings. These results are shown in Figs. 9(a, b), respectively. Although there is some error in the location of the transition point, it can be seen that the trends for the start of transition are well predicted showing a steepening of the "leading edge" of the wedge with reducing axial spacing, as well as the spreading of the boundary layer turbulence intensity.

Superficially, the predicted behavior and that observed on the turbine rotor are inconsistent with the results of Dooryl (1987) and LaGraff et al. (1988) in turbine cascades with simulated unsteady inflow. They showed a wake-induced patch spreading with trailing edge speed 50 percent \bar{U}_e and leading edge speed 100 percent \bar{U}_e as if it were a single turbulent spot. However, the differences can be explained. The cascades used by these workers were both run at blade Reynolds numbers of about 2.0×10^6 . This means that the boundary layer Reynolds numbers are correspondingly higher and transition occurs much earlier on the blade. Figure 10 shows the result of increasing the values of Re_θ for the turbine rotor by 3; roughly equivalent to running at the same flow coefficient but 10 times the Reynolds number (3.0×10^6) since, for a laminar boundary layer, $Re_\theta \propto Re_x^{1/2}$. The transition point moves up the blade and, with this movement, the spreading mechanisms have less time to operate. For the low Reynolds number research turbine used

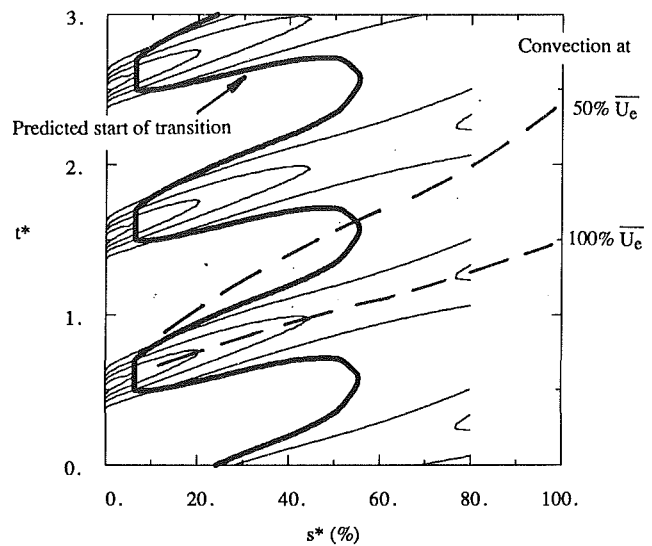


Fig. 10 Predicted start of transition for a high Reynolds number turbine blade ($Re \approx 3 \times 10^6$)

here, the shape of the inlet wakes and the magnitude of the spreading is so great that the trailing edges of the spots formed moved faster than the transition line recedes with the passing of the wake. However, in the higher Reynolds number case, the boundary layer sees larger differences between peak and interwake turbulence and this means the start of transition line moves back along the blade faster than the trailing edges of the spots formed earlier. Under these conditions, the wedge trailing edge speed becomes the same as the turbulent spots, i.e., $0.55 \bar{U}_e$ and this represents a limiting value. The leading edge steepens and would, in the limit, become 100 percent \bar{U}_e .

Further Discussion

The work reported in Parts 1 and 2 of this paper has looked at the effect of blade wakes on the boundary layers of downstream rows and, especially, the forcing of early transition. Of particular note is the fact that the wake jet seems to play a minor role. Comparison with the work of Obremski and Fejer (1967) has shown that the velocity fluctuation arising from the jet will not be a direct cause of transition. The transition correlation of Abu Ghannam and Shaw (1980) shows that, for the levels of turbulence intensity existing in a turbomachine, changes in the pressure gradient parameter λ_θ have very little effect. Finally, experimental results and computational predictions show that spreading of the wake segment by the jet action is not significant when viewed in the time domain. Therefore, we can reasonably ignore the effect of the jet when looking at wake-induced transition, and concentrate on the effect of the turbulence in the wake segment.

The incidence of the wake turbulence onto the blade boundary layer does not result in immediate transition. During the early stages of boundary layer development, the production of turbulent kinetic energy within the boundary layer is exceeded by the dissipation. There is a little transfer of momentum but the hot-wire traverses show that the integral parameters are not far from those predicted for a laminar boundary layer. After a certain point, usually characterized by a critical momentum thickness Reynolds number Re_θ , transition occurs. The start of this process is in reasonable agreement with correlations based on flat plate experiments. In the presence of disturbed laminar boundary layers, the hot films show that this is characterized by the appearance of high frequency bursts over a low frequency background. The increased momentum transfer leads to large swings in the shear stress measured at the surface by the hot films. The stochastic (as opposed to

phase-locked) nature of this process is shown up by the peak in the hot-film rms intensity in the region known to be transitional. Once the boundary layer is fully turbulent, the wakes have relatively little additional effect as shown by the small variation between maximum and minimum rms intensity measured by the hot-film gages and, consequently, steady predictions are fairly accurate.

The diffusion of the disturbances from the wake segment into the laminar boundary layer can be considered quasi-steady since $\nu_t \gg \nu$, i.e., diffusion times across the boundary layer are dominated by the short time scales of turbulent diffusion and are very much shorter than the blade passing period. The hot-wire traverses also have shown that, although transition is three dimensional (s, y, t), the differences between the surface behavior measured by the hot films and the regions of high shear in the middle of the boundary layer are small and hot films, therefore, give reasonably reliable results. In the time domain, as shown in the distance-time plots throughout this paper, the wake is not spread in the free stream to any significant degree by either the turbulence or the wake jet. However, inside the boundary layer, the higher levels of disturbances, coupled with large velocity gradients, result in a strong mixing process. For low Reynolds numbers, with the earliest transition at a reasonable distance from the leading edge, the transition "wedges" (which consist of several spots) bear little resemblance to the single spots of Obremski and Fejer (1967). However, when the blade Reynolds number is higher and transition correspondingly earlier, the turbulence has not spread as far in the boundary layer, and the wedges begin to look more like single spots.

Problems remain to be solved before we can predict the behavior of arbitrary boundary layers with confidence; chiefly, the accurate prediction of spreading within the boundary layer (a constant spreading rate as used here being too simplistic to be of general use), a general method of predicting the decay of the wake turbulence through the passage and a start of transition correlation based on disturbance intensities within the boundary layer. However, all these would seem to be within reach and a semi-empirical approach with reasonable generality should be feasible.

Conclusions

For practical applications, the wake jet has a minimal effect on the transition of blade boundary layers. The interaction of the wake turbulence with the boundary layer is quasi-steady in nature and characterized by a modified form of the reduced frequency parameter. Spreading of the wake segment in the time domain is dominated by strong mixing within the boundary layer while there is little spreading in the free stream. The

wakes have little effect on the behavior of the laminar and turbulent boundary layers but the increased level of disturbances within the boundary layer gives rise to early transition.

Acknowledgments

This research would have been impossible without the assistance of the staff and students of the Whittle Laboratory; especially Messrs. M. Hall and T. H. Rowlands who carried out the cascade tests reported in Part 2 as part of a final year undergraduate project supported by Rolls Royce plc.

References

- Abu-Ghannam, B. J., and Shaw, R., 1980, "Natural Transition of Boundary Layers — the Effects of Turbulence, Pressure Gradient and Flow History," *Journal of Mechanical Engineering Science*, Vol. 22, No. 5, pp. 213–228.
- Cebeci, T., and Carr, L. W., 1978, "A Computer Program for Calculating Laminar and Turbulent Boundary Layers for Two-Dimensional Time-Dependent Flows," NASA TM 78470.
- Cebeci, T., and Smith, A. M. O., 1974, *Analysis of Turbulent Boundary Layers*, Academic Press, New York.
- Doorly, D. J., and Oldfield, M. L. G., 1985, "Simulation of the Effects of Shock Wave Passing on a Turbine Rotor Blade," ASME Paper No. 85-GT-112.
- Doorly, D. J., 1987, "Modeling the Unsteady Flow in a Turbine Rotor Passage," ASME Paper No. 87-GT-197.
- Giles, M. B., 1987, "Calculation of Unsteady Wake/Rotor Interactions," AIAA Paper No. 87-0006.
- Hall, M., 1985, "An Investigation Into the Effect of Free-Stream Turbulence Upon the Development of Turbine Blade Boundary Layers," Internal Report, Cambridge University, United Kingdom.
- Hodson, H. P., 1983a, "The Development of Unsteady Boundary Layers on the Rotor of an Axial-Flow Turbine," *AGARD Conference on Viscous Effects in Turbomachines*, AGARD CP-351, Copenhagen, Denmark.
- Hodson, H. P., 1983b, "The Detection of Boundary Layer Transition and Separation in High Speed Turbine Cascades," *Proceedings of the 7th Symposium on Measurement Techniques for Transonic and Supersonic Flow in Cascades and Turbomachinery*, Aachen, Federal Republic of Germany.
- Hodson, H. P., 1984a, "An Inviscid Blade-to-Blade Prediction of a Wake-Generated Unsteady Flow," ASME Paper No. 84-GT-43.
- Hodson, H. P., 1984b, "Boundary Layer and Loss Measurements on the Rotor of an Axial-Flow Turbine," *ASME Journal of Engineering for Gas Turbines and Power*, Vol. 106, pp. 391–399.
- Hodson, H. P., 1985, "Measurements of Wake-Generated Unsteadiness in the Rotor Passages of Axial-Flow Turbines," *ASME Journal of Engineering for Gas Turbines and Power*, Vol. 107.
- Hodson, H. P., and Addison, J. S., 1988, "Wake-Boundary Layer Interactions in an Axial-Flow Turbine at Off-Design Conditions," ASME Paper No. 88-GT-233.
- LaGraff, J. E., Ashworth, D. A., and Schultz, D. L., 1988, "Measurement and Modeling of the Gas Turbine Blade Transition Process as Disturbed by Wakes," ASME Paper No. 88-GT-232.
- Obremski, H. J., and Fejer, A. A., 1967, "Transition in Oscillating Boundary Layer Flows," *Journal of Fluid Mechanics*, Vol. 29, pp. 93–111.
- Schubauer, G. B., and Klebanoff, P. S., 1955, "Contributions on the Mechanics of Boundary Layer Transition," NACA TN 3489.
- Walker, G. J., 1974, "The Unsteady Nature of Boundary Layer Transition on an Axial-Flow Compressor Blade," ASME Paper No. 74-GT-135.

Compressor Blade Boundary Layers: Part 1—Test Facility and Measurements With No Incident Wakes

Y. Dong¹

Gas Turbine Engineering Division,
Ruston Gas Turbines Ltd.,
Lincoln LN6 7AA, United Kingdom

N. A. Cumpsty

Department of Engineering,
Whittle Laboratory,
University of Cambridge,
Cambridge, CB3 0DY, England

The boundary layers on compressor blades are sensitive to the conditions at which transition occurs and transition can be affected by the convection of wakes from upstream blade rows. This paper and its companion, Part 2 by the same authors, describes an experiment to study the effect of the moving wakes on the boundary layer of a compressor blade. This paper describes the background and facility devised to introduce wakes together with results obtained on the blades in tests without the wakes present. Part 2 describes the measurements made with the wakes present and presents conclusions for the whole project. Further details of all aspects of the work can be found in Dong (1988).

1 Introduction

The boundary layer on the blades of an axial compressor contribute to the loss, the blockage and the breakdown into stall. The principal surface of concern is the suction surface. Until recently boundary layer calculations had not normally been part of the design process because of the poor accuracy of the predictions. Instead the blades were chosen from a limited number of families and the loss was evaluated by correlations based on an overall loading parameter, such as diffusion factor (Lieblein, 1965). The advent of the new generation of blades with prescribed velocity distributions has altered this. This type of blade is sometimes called supercritical, reflecting that the interest grew from the wish to design blades with high subsonic inlet flow and supersonic patches which avoided being terminated by shock waves. A similar design approach is applied to wholly subsonic blades and the name supercritical is often retained; another name is controlled-diffusion blading. The general design principle is that on the suction surface there is continual acceleration to a peak in the forward part of the blade. This is immediately followed by a deceleration which begins severe and is progressively reduced toward the trailing edge. The decreasing rate of deceleration is chosen because as the boundary layer thickens it is necessary to reduce the velocity gradient to avoid premature separation. This gives rise to the characteristic "ski-slope" type of distribution of pressure or velocity, steep at the beginning and progressively less steep to the rear.

The idea of allowing the pressure gradient to relax as the trailing edge is approached (at the expense of having an initial

steep gradient) is not new and was discussed by Carter (1961). The advantages for wholly subsonic operation were correctly perceived then, together with an important disadvantage. If the boundary layer is close to separation over a significant part of the blade chord (as is the case with a ski-slope type velocity distribution) and some perturbation occurs, it is likely that the flow will separate from well forward, with a catastrophic reduction in loading. On the other hand, a conventional blade with the pressure gradient tending to increase near the trailing edge tends to separate gradually with a progressive reduction in loading.

The same propensity to stall abruptly is reflected in the design itself. The desire to maximize the blade loading capability may lead to the boundary layer being chosen to be close to the verge of separation along the decelerating part of the suction surface. But it is possible that, based on incorrect prediction, the pressure gradient prescribed is in reality too strong so that on test the boundary layer separates well before the trailing edge. The most critical aspect of the boundary layer prediction is associated with transition, its position on the blade, its length and the boundary layer properties at its completion. If, for example, the boundary layer thickness is underestimated at the end of transition, a stronger pressure gradient might be specified than that actually sustainable and a radically altered flow field will be measured.

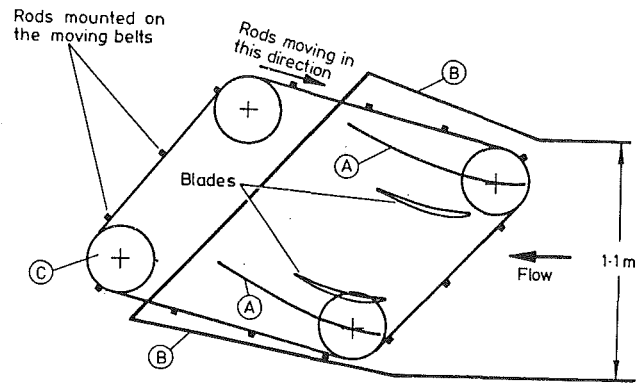
The research described in this paper (Part 1) and in its companion (Part 2) arose from a high speed rig test in which the midspan performance of a supercritical-type stator did not live up to expectation. It was suspected that the transition process had been affected by the wakes of the upstream rotors, leading to undesirable boundary layer development not predicted in the design. As transition prediction at the present time relies on empiricism, it is only natural to suspect the wakes as a possible cause, since their presence had not been properly sim-

¹Formerly, Whittle Laboratory, University of Cambridge, United Kingdom.
Contributed by the International Gas Turbine Institute and presented at the 34th International Gas Turbine and Aeroengine Congress and Exhibition, Toronto, Ontario, Canada, June 4-8, 1989. Manuscript received at ASME Headquarters January 4, 1989. Paper No. 89-GT-50.

ulated in the tests which provided the base for the existing transition models (e.g., Dunham, 1972 and Abu-Ghannam and Shaw, 1980). In the past, there have been studies carried out of transition with disturbed inlet conditions. Walker (1968, 1974) looked at the boundary layer on a C4 stator, but this was without some of the detail desirable and it was on a blade with a velocity distribution very different from that used in this work. Evans (1978) carried out a similar study but, because the effect of wakes was not separated from the three-dimensional flow influence, the results were not conclusive. Work on a turbine rotor by Hodson (1984) had shown the significant impact of wakes on the increase of profile loss compared with that in a no-wake flow. More understanding of the wake interaction with a laminar boundary layer has been gained by the results obtained in the experimental work of Pfeil, et al. (1983) on a flat plate and Doorly and Oldfield (1986) on a turbine blade. However, the pressure field is an important aspect of the transition process and no detailed study has yet been known of the impact of wake interaction on the boundary layer on a compressor blade.

Now to simulate the effect of an upstream blade row it is essential to have an upstream obstruction which moves relative to the blades under examination. To be able to study transition it is necessary to have the correct Reynolds number and to have blades large enough that the boundary layers can be accurately measured. The demands for a representative test were met with a low speed cascade tunnel having a system of two belts running on pulleys, each belt holding one end of a set of rods which passed upstream of the cascade, Fig. 1. The rods were parallel to the span of the blades and of a diameter such that the wake momentum thickness was comparable to that of a blade of the same chord as the blades under test. To correctly model the effect of a moving upstream blade row a unique rod speed is associated with each inlet flow velocity. The rods could not be driven at very high speed and the inlet velocity was limited to about 10 m/s. To get the appropriate Reynolds number the chord of the blades was large, about 450 mm in one case, 598 mm in another.

In testing linear cascades it is normal to have many blades to give adequate blade-to-blade periodicity. The object of the present tests was different; periodicity was relatively unim-



- A- sheets curved to the shape of the streamlines
- B- adjustable sides of the working section
- C- pulleys, four on each side of the tunnel, carrying belts. The belts run outside the working section.

Fig. 1 Schematic representation of the working section with the facility to simulate moving wakes, roughly to scale

portant and what mattered much more was the correct pressure distribution along the blade surfaces. With a cascade of only two blades it was possible to get the correct pressure distribution using curved plates placed about half of one pitch outside of the blades on either side, shown as A in Fig. 1. The plates, which were considerably longer in the flow direction than the blades themselves, were curved to the shape of the streamlines derived from numerical calculations at their location relative to the blades. The precise shape was adjusted prior to the boundary layer measurements until satisfactory agreement was obtained between the measured pressure distribution about the blades and that from a numerical prediction. Sidewall bleed and a suction slot were used to get the correct axial-velocity-density ratio.

The blade used for the tests described was of the so-called supercritical type, but one designed for low Mach number operation. The original design was with a solidity of 0.8 (for

Nomenclature

C = blade chord		
C_p = nondimensional surface static pressure [$C_p = (p - p_1)/(0.5\rho U_1^2)$]	Tu = free-stream turbulence level, $Tu = \sqrt{u'^2}/U_1$	δ^* = boundary layer displacement thickness, $\int_0^{\delta} \left(1 - \frac{u}{U}\right) dy$
H = boundary layer shape factor, $H = \delta^*/\theta$	u = velocity in the boundary layer	θ = boundary layer momentum thickness, $\int_0^{\delta} \left(\frac{u}{U}\left(1 - \frac{u}{U}\right)\right) dy$
p = surface static pressure	u_x = friction velocity, $\sqrt{(\tau_w/\rho)}$	λ = total length along surface of the transitional boundary layer
p_1 = static pressure of the flow at inlet	$\sqrt{u'^2}$ = root mean square (rms) turbulence velocity	μ = viscosity of air
Re_c = Reynolds number based on blade chord and inlet flow velocity, $Re_c = U_1 C/\nu$	U = free-stream velocity	τ_w = wall shear stress
Re_θ = boundary layer Reynolds number based on momentum thickness and local free-stream velocity, $Re_\theta = U\theta/\nu$	U_{l-m} = time-mean free-stream velocity	$\nu = \mu/\rho$
S = distance along blade surface measured from blade leading edge	U_1 = inlet flow velocity	ρ = air density
S_0 = total length of blade surface distance	Y = distance normal to wall, measured from wall	σ = blade solidity, defined as the ratio of blade chord to its pitch
S_{rod} = spacing between the moving rods used to generate wakes	γ = intermittency factor, the fraction of the time the flow is observed to be turbulent	ω = cycle (wake passing) frequency, Hz
	δ = boundary layer thickness, defined in measurements as distance from wall where the velocity first reaches a maximum	Ω = reduced frequency ($\Omega = \omega C/U_1$)

which the chord was 450 mm) but the first tests were with the solidity altered to 1.67 (a chord of 598 mm). The blades were tested in several ways. Each was tested with no upstream wakes as well as with the wakes present. In the no-wake configuration, the free-stream turbulence level was low, about 0.9 percent. With the smaller blade, tests also were carried out with a turbulence grid which raised the free-stream turbulence level to about 6 percent.

As the work to be described is rather lengthy, this paper has been split into two parts. The first part describes the apparatus briefly and the tests which were carried out without the moving wakes. Details of both the facilities, the instrumentation and data processing and the results have been given by Dong (1988). Part 2 describes the measurements with the moving rods and then discusses all the results and gives some conclusions.

2 The Experimental Facilities

Figure 1 provides a schematic diagram of the cascade wind tunnel used for this investigation. The desired blade surface pressure distribution was established with the help of the curved sheets (labeled as A) and the end plates (labeled as B), both of which are flexible.

The blades were designed by Rolls Royce for a flow deflection of about 20 deg with an inlet flow angle of 43.6 deg and a solidity (chord/pitch) of 0.8. Two sets of blades were used, one with a chord of 450 mm and the other with a chord of 598 mm. Only the smaller blades were used at the design solidity. The larger blades could not be accommodated with the pitch length corresponding to design solidity and were used at a solidity of 1.67.

A turbulence grid used to generate free-stream turbulence was of biplane rods 50.8 mm in diameter with 60 percent open area for the mesh. The grid was installed 5.6 blade chords (50 grid-rod diameters) upstream of cascade inlet plane. The spectrum of turbulence from high-pass filtered hot-wire signals was obtained at different spanwise and pitchwise positions near the cascade inlet plane. The turbulence generated was found to be satisfactorily homogeneous, with an rms level of 6 percent of the mean flow velocity (10 m/s). The streamwise integral length scale of the turbulent eddies, calculated from the auto-correlation function of the measured fluctuating velocity, was about 61 mm, or 13.5 percent of blade chord.

The bulk of the measurement in the experiment was made by a single sensor hot-wire (DISA 55p-15 boundary layer type) with a constant temperature anemometry. A dual sensor cross-wire (DISA 55 p63 type) was used to measure the wakes upstream of the blade leading edge. The hot-wire probe was held by a rod sliding through the blade surface on which the measurements were being made. The traverse gear mechanism was mounted in the space between a blade and the curved sheets (labeled A in Fig. 1) and was driven manually from outside the tunnel through a flexible cable.

Because of the tunnel configuration it was only practical to calibrate the hot-wire *in situ* before each traverse by using the reading in the still air and the free-stream flow with wind on. As the boundary layers on the blades were thin, the flow velocity in the local free stream could be deduced from manometer readings of inlet total pressure and local surface static pressure. The estimated errors involved in using still-air reading for calibration would be less than 1.5 percent of the velocity in the free stream. The wall-effect on the calibration was also neglected as it was difficult to include a correction, see Dong (1988). However, this was estimated to cause errors of less than 3 percent of the free-stream velocity in a region very close to the surface. These errors have a very small effect on the integral properties of the boundary layer, typically less than 2 percent for the momentum and the displacement thickness. As the same calibration technique was used in all the cases, which were used for back-to-back comparison to demonstrate the

Table 1 Experimental conditions in cases without wakes

Case Identifier	Blade Chord (mm)	Solidity σ	$Re_c \times 10^5$	Turbulence Grid	Inlet Turbulence Level (Tu)
1	450	0.8	3.1	No	0.9%
2	450	0.8	3.1	Yes	6.0%
3	598	1.67	4.0	No	0.9%

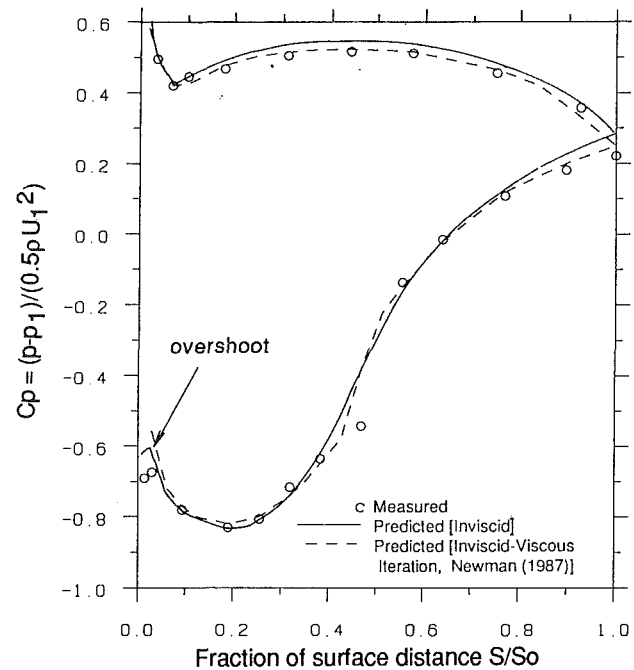


Fig. 2 Surface pressure distribution (Case 1)

effect of the wakes, such errors are not considered to significantly affect the conclusion.

The data were logged digitally and the values were stored only when the rod speed was within 1 percent of nominal rod moving speed. The sampling rate was automatically adjusted so that 320 points would always span one wake passing period. A phase-locked data-logging technique was used and 100 samples were used to derive ensemble-averaged quantities; it was found that there was little improvement in using more samples. The data acquisition facilities and the techniques were similar to those used by Hodson (1984) and were described in detail by Dong (1988).

3 Experiment Results Without Wakes

The three cases studied without wakes being present in the inflow, Cases 1, 2 and 3, as summarized in Table 1.

3-1 Case 1. $\sigma = 0.8$; $Re_c = 3.1 \times 10^5$; $Tu = 0.9$ Percent.

The measured pressure distribution on the blade surfaces is shown in Fig. 2, together with the predicted results. The abscissa S/S_0 is the fraction of the surface distance from leading edge to trailing edge. On the suction surface the predicted results using an inviscid model are very close to the measured data over about first 30 percent of the blade surface distance. The measured data suggest that there is a laminar separation bubble from about $S/S_0 = 0.3$ to 0.5, where the pressure distribution differs from that predicted. When the viscous effect was taken into the account in the prediction, by including the displacement effect of the profile boundary layers, the predicted results are seen in excellent agreement with the measured data over almost the entire suction surface. The inviscid model also predicted the pressure distribution on the pressure surface well, but again the inclusion of profile boundary layer improved the predicted results. The good agreement is the evi-

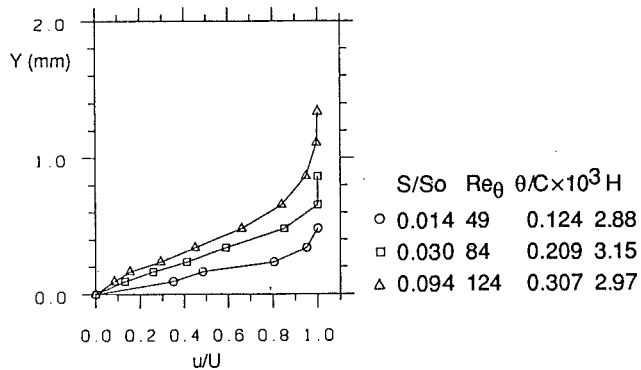


Fig. 3 Velocity profiles of suction surface boundary layer on blade front part (Case 1: $\sigma = 0.8$; $Tu = 0.9$ percent)

dence that the sidewall boundary layer effect had been effectively controlled by the sidewall suction system and the flow was two dimensional with axial velocity ratio close to unity. Further evidence for this was found by comparing velocity profiles measured at three different spanwise locations on the blade surface, which showed close similarity (Dong, 1988).

The inviscid model predicted a velocity overshoot near the leading edge of the suction surface (Fig. 2). An overshoot was indeed measured, although its value differed slightly with that predicted. It is not clear whether this discrepancy was due to discretization error inherent in the numerical analysis, or whether it was a result of errors in the manufacturing of the blade. The deceleration following the overshoot, however, did not appear to cause any boundary layer separation near the leading edge, as the measured velocity profile in that region testifies (Fig. 3). $S/S_0 = 0.014$ is where the overshoot in velocity is seen and the subsequent short deceleration ends at $S/S_0 = 0.03$. Around the leading edge the curvature is very high so the measurements of distance perpendicular to the surface may be rather inaccurate. The boundary layer was also exceedingly thin and only a few measurement points across the boundary layer were possible. Nevertheless, the results in Fig. 3 show convincingly that the velocity overshoot did not cause the laminar boundary layer to separate. The value of the shape factor $H = 2.88$ (at $S/S_0 = 0.014$) and $H = 2.97$ (at $S/S_0 = 0.094$) are higher than expected for a laminar boundary layer with local free-stream acceleration. This may be due to the inaccurate measurement in the thin boundary layer and, for the boundary layer at $S/S_0 = 0.094$, the upstream history influence.

Development of the boundary layer on the rest of the blade suction surface was similar to that known for a typical compressor blade, e.g., Evans (1971). Laminar separation was found at $S/S_0 = 0.32$, leading to transition near $S/S_0 = 0.47$ (Fig. 4). As this occurred the boundary layer began to re-attach to the surface, ending at $S/S_0 = 0.56$ as a re-attached turbulent boundary layer. Downstream of this station the value of shape factor H in the turbulent part of the boundary layer varied little, reaching 1.62 at the trailing edge.

Measurements on the pressure surface of the blade also indicated a laminar separation, but the boundary layer appeared to re-attach to the surface shortly without undergoing transition. The laminar flow was therefore seen all over the pressure surface. This was because the free-stream flow over the rear 50 percent of the pressure surface was accelerating.

At the trailing edge station, the momentum thickness and the energy loss for the boundary layer on the pressure surface only amounted to about 16 percent of that on the suction one. Excluding the mixing loss downstream of the blade trailing edge, the combined loss from both surfaces was 0.75 percent of the inlet dynamic head. When the estimated mixing loss was added, the total loss increased to about 0.83 percent of the inlet dynamic head.

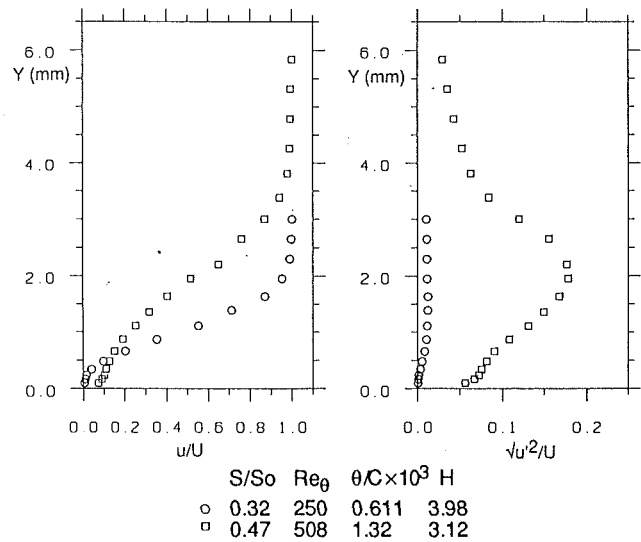


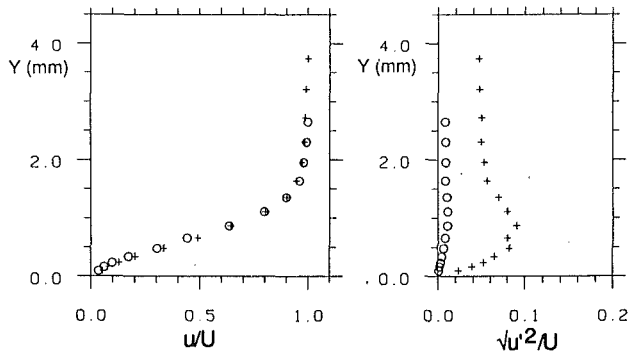
Fig. 4 Velocity profiles at the start ($S/S_0 = 0.32$) and the transition ($S/S_0 = 0.47$) point of the separation bubble (Case 1: $\sigma = 0.8$; $Tu = 0.9$ percent; Suc. Surf.)

3.2 Case 2. $\sigma = 0.8$; $Re_c = 3.1 \times 10^5$; $Tu = 6$ Percent.

Experimental conditions in this case were identical to those in Case 1 except for the level of free-stream turbulence generated by the turbulence grid described previously. Similarly good agreement between measured and predicted pressure distributions to that seen in Fig. 2 also was obtained in this case, so the similar figure was not shown here. The only important difference from the previous case was that there was no evidence of a laminar separation bubble on the suction surface. Separation did not appear in the predicted results either because, with Tu specified to be 6.0 percent, transition was predicted to occur upstream of the position where the boundary layer would otherwise separate with low level free-stream turbulence.

Particular care was taken to measure the turbulence near the leading edge as this was previously found to be much larger locally inside the boundary layer than in the free stream and thought to be able to cause early transition (Hart, 1985). In the present case, the peak value of turbulence inside the boundary layer was found to be nearly 14 percent of the inlet mean velocity at the leading edge, more than twice as large as the inlet value. Close study of the trace of instantaneous velocity showed, however, that the main component of fluctuating velocity had a very large time scale corresponding approximately to a length scale of about 80 percent blade chord. As the boundary layer was extremely thin near blade leading edge the effect on transition of fluctuations with such a large length scale (which were misleadingly included as turbulence in the estimation of RMS turbulence level) can be expected to be small. Indeed, the measured results on the suction surface showed that the boundary layer had a characteristically laminar profile from the leading edge to the point $S/S_0 = 0.26$, one measurement station upstream of the laminar separation point in Case 1. At $S/S_0 = 0.26$ the local intermittency of the flow was still below 0.1 and the velocity profile was little different from an undisturbed laminar flow such as in Case 1, see Fig. 5, even though the peak turbulence (or unsteadiness level) inside the boundary layer typically reached 10 percent of the local free-stream velocity.

The measured distributions of the intermittency factor γ on both surfaces of the blade are shown in Fig. 6. γ was obtained by measuring manually the fraction of the time the flow was turbulent from the recorded velocity traces. All methods of measuring γ would involve some arbitrariness in prescribing the threshold between the laminar and the turbulent interface.



Case (Tu)	γ	Re_{θ}	$\theta/C \times 10^3$	H
○ 1 (0.9%)	0.0	234	0.556	3.08
+ 2 (6.0%)	0.1	250	0.614	2.76

Fig. 5 Velocity profiles at $S/S_0 = 0.26$ ($\sigma = 0.8$; $Re_c = 3.1 \times 10^5$; Suc. Surf.) with and without turbulent grid

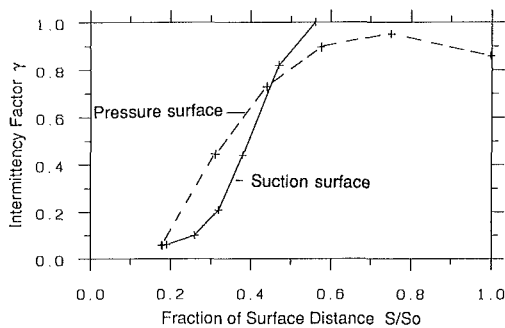


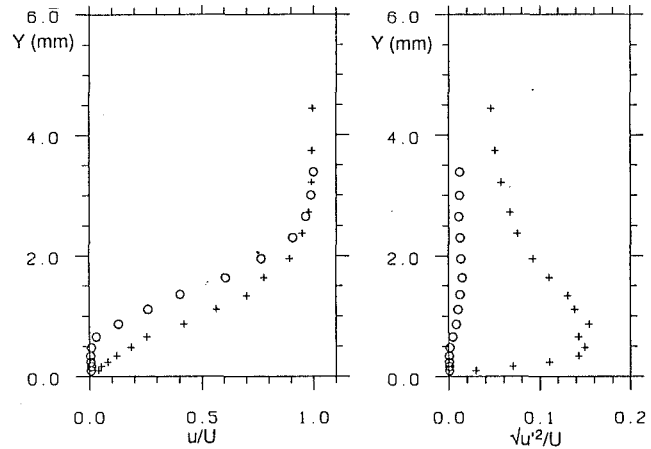
Fig. 6 Intermittency factor distribution along blade surfaces (Case 2: $\sigma = 0.8$; Tu = 6 percent)

The method chosen was simple and helped indicate the development of transition process. On the suction surface the transition started slightly before the beginning of deceleration at $S/S_0 = 0.19$, and γ exceeded 0.2 at $S/S_0 = 0.32$. The distinctive difference in the character of the boundary layer with low and high inlet turbulence was observed further downstream where transition promoted by the high level free-stream turbulence suppressed the laminar separation at the same location observed in Case 1 in Fig. 7.

Transition ended at about $S/S_0 = 0.56$ on the suction surface in Case 2. Despite different transition processes the turbulent boundary layers at this point had quite similar profiles in Cases 1 and 2, as can be seen in Fig. 8. Subsequent development of the turbulent boundary layer was also quite similar for the two cases (Fig. 9). The shape factor H is a little higher for Case 2, except at the trailing edge station where it is slightly lower: 1.48 compared with 1.62. The reduction in shape factor H for a turbulent boundary layer at an increased level of free-stream turbulence is a recognized phenomenon (e.g., Evans, 1973); what is unusual here is that it was only observed near the trailing edge.

An examination of the measured pressure distributions on the suction surface revealed slight differences between the two cases (Dong, 1988). The positive pressure gradient in the turbulent part of boundary layer for Case 2 was slightly larger than that for the Case 1 up to $S/S_0 = 0.9$, and from then on the trend was reversed. The cause of this difference is not known but it might explain the small discrepancy in shape factor.

The measured intermittency factor γ distribution on the pressure surface has also been included in Fig. 6; γ is only 0.016 at $S/S_0 = 0.18$ but rises rapidly afterward, reaching a maximum of 0.95 at $S/S_0 = 0.75$. The laminar separation on



Case (Tu)	γ	Re_{θ}	$\theta/C \times 10^3$	H
○ 1 (0.9%)	0.0	286	0.718	4.73
+ 2 (6.0%)	0.44	331	0.855	2.90

Fig. 7 Velocity profiles at $S/S_0 = 0.38$ ($\sigma = 0.8$; $Re_c = 3.1 \times 10^5$; Suc. Surf.)

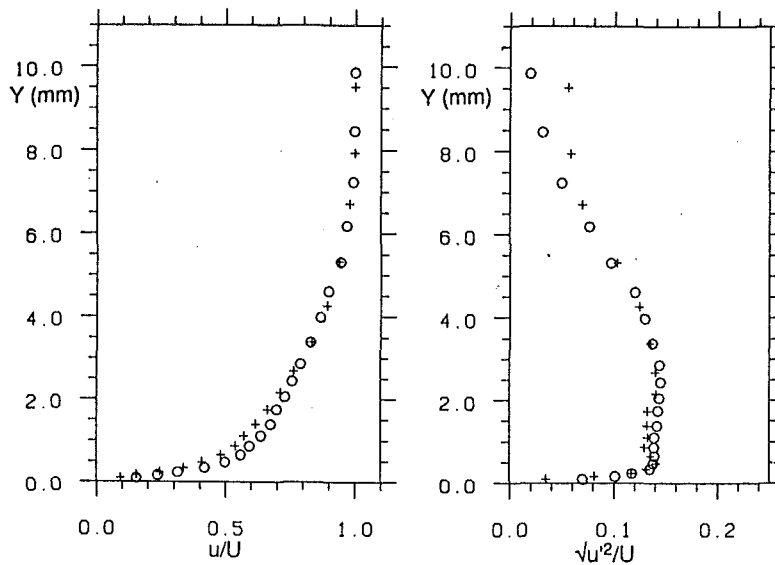
the pressure surface observed in Case 1 was also missing in Case 2 and the intermittency factor γ was higher over the first 40 percent of the blade pressure surface than on the suction one. The reason for this is that the local free-stream velocity was much lower near the pressure surface, so the turbulence level (measured as a fraction of the free-stream velocity) was much higher, and this helped promote transition more effectively. The lower free-stream velocity on the pressure surface also made a lower boundary layer Reynolds number (the maximum Re_{θ} was only 369 at $S/S_0 = 0.75$), which, with the favorable pressure gradient existing on the rear half of the pressure surface, prolonged transition process. The fall in the intermittency from $S/S_0 = 0.75$ toward trailing edge on the pressure surface appeared in the region with flow acceleration in the free stream. Jones and Launder (1972) pointed out that laminarization of a turbulent boundary layer may occur if the local value of the acceleration parameter $K (= \nu/U^2 \times dU/dS)$ exceeds 3.0×10^{-6} . The average value of K in the last 25 percent of the blade pressure surface is estimated to be 3.8×10^{-6} which exceeds the foregoing criterion, indicating that the transition process had probably been suspended or reversed because of the flow acceleration in the free stream.

The momentum and the energy loss thicknesses of the pressure surface boundary layer in Case 2 are about 38 percent greater than their counterparts in Case 1. However, they still amount to only 22 percent of those incurred to the suction surface boundary layer in the same case. The loss for both surfaces combined (excluding the mixing) was 0.78 percent of the inlet dynamic head in Case 2 compared with 0.75 percent in Case 1. The small difference was due to the increased loss on the pressure surface.

3-3 Case 3. $\sigma = 1.67$; $Re_c = 4.0 \times 10^5$; Tu = 0.9 Percent.

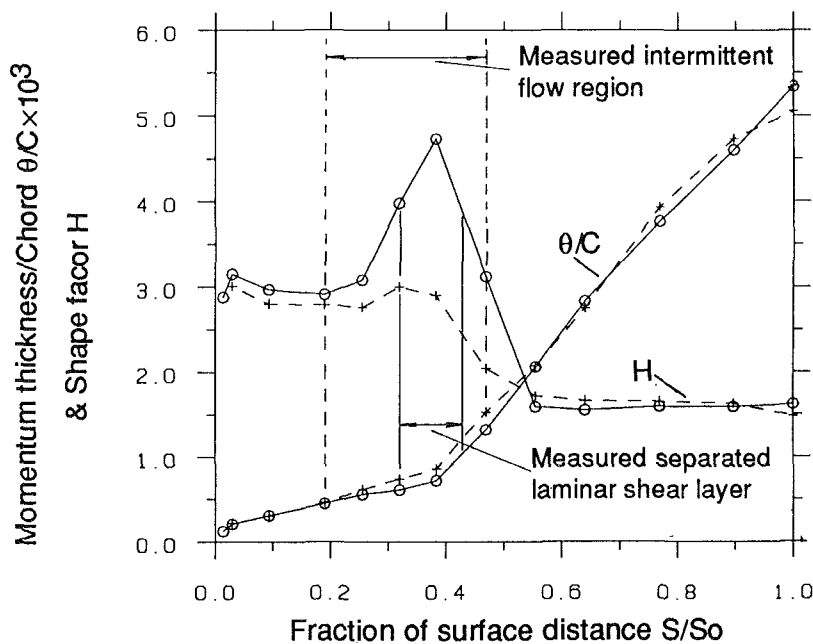
The boundary layer development on the suction surface in this high solidity, low turbulence case was found to be similar to that in Case 1 and further description is unnecessary. The pressure surface boundary layer at the trailing edge station was found to be turbulent and the momentum thickness was 42 percent of that measured at the trailing station of the suction surface. The relatively high ratio of the pressure surface momentum thickness to the suction surface one was a consequence of testing the blade at more than twice the value of the design solidity for the same profile. This resulted in strong deceleration near the leading edge on the pressure surface, as is shown in Fig. 10, where the boundary layer could have either gone through a laminar separation-turbulent re-attachment process, or natural transition.

Excluding the mixing loss (downstream of the trailing edge),



Case (Tu)	γ	Re_θ	$\theta/C \times 10^3$	H
○ 1 (0.9%)	1.0	675	2.06	1.59
+ 2 (6.0%)	1.0	678	2.07	1.72

Fig. 8 Velocity profiles at $S/S_0 = 0.56$ ($\sigma = 0.8$; $Re_c = 3.1 \times 10^5$; Suc. Surf.)



- Case 1: $\sigma = 0.8$; $Re_c = 3.1 \times 10^5$; $Tu = 0.9\%$
- + Case 2: $\sigma = 0.8$; $Re_c = 3.1 \times 10^5$; $Tu = 6.0\%$

Fig. 9 Measured integral parameters of suction surface boundary layer: Measured intermittent flow region Case 2; Measured separated laminar shear layer Case 1

the loss evaluated in this case using the measured parameters at the trailing edge plane was 1.7 percent of the inlet dynamic head. (The mixing generated loss was estimated to be about 12 percent of the unmixed loss.) This is more than twice as high as those measured in the two previous cases, primarily because the blade solidity was higher.

4 Discussion

It is recognized that the laminar boundary layer on a com-

pressor blade tested in a low turbulence at near design conditions is usually terminated by a short separation bubble (e.g., Evans, 1971). The supercritical blade tested in this program was no exception. A bubble model widely used in the prediction of boundary layer development on either a wing section or a compressor blade is that of Roberts (1980), which was based on the original Horton (1969) model.

To test the accuracy of the bubble model, predictions were made for Cases 1 and 3 using the National Gas Turbine Es-

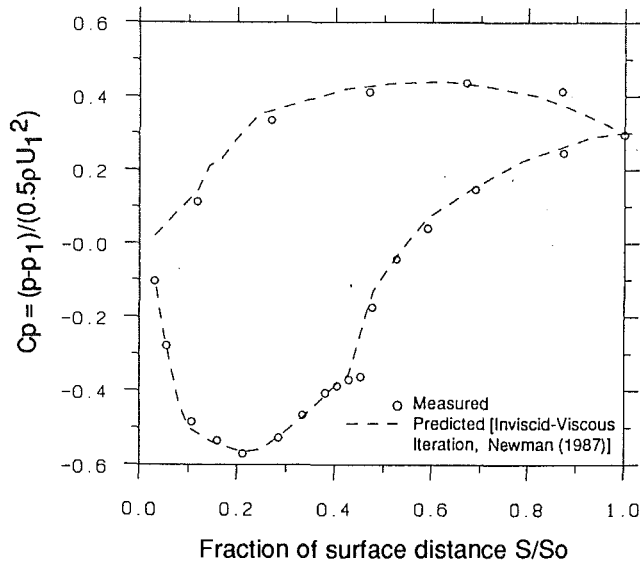


Fig. 10 Surface pressure distribution on high solidity blades (Case 3: $\sigma = 1.67$; $Re_c = 4 \times 10^5$; $Tu = 0.9$ percent)

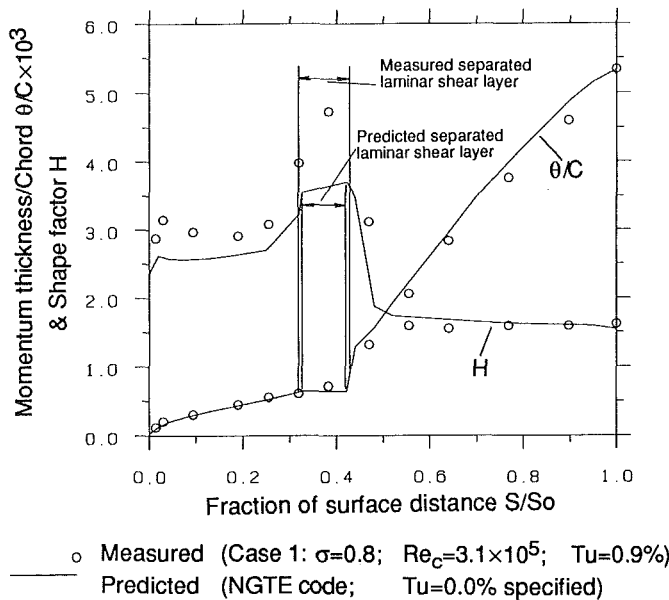


Fig. 11 Integral parameters of the suction surface boundary layer

establishment (NGTE) boundary layer method, described by Herbert and Calvert (1982), which includes in it the bubble model. The calculation method uses the lag-entrainment method for the fully turbulent boundary layer calculation — the calculation of fully turbulent boundary layers is so well developed and sufficiently good that this aspect does not deserve elaboration here. Horton's bubble model (1969) was originally used in the NGTE method, but some of its coefficients were replaced by those recommended by Roberts (1980), as they were found to give predictions matching more closely the measured results. The measured surface pressure distribution was used as input everywhere except in the bubble region, where the predicted one based on the inviscid calculation was used in accordance with the requirements of using the bubble model. In the calculation, a zero level of turbulence was specified, rather than the 0.9 percent as measured, because this gave best prediction of the bubble length for both Cases 1 and 3.

The predicted and the measured boundary layer integral parameters on the suction surface of the blade in Case 1 are compared in Fig. 11. It can be seen that the laminar part of the boundary layer, including the start of the separation, has

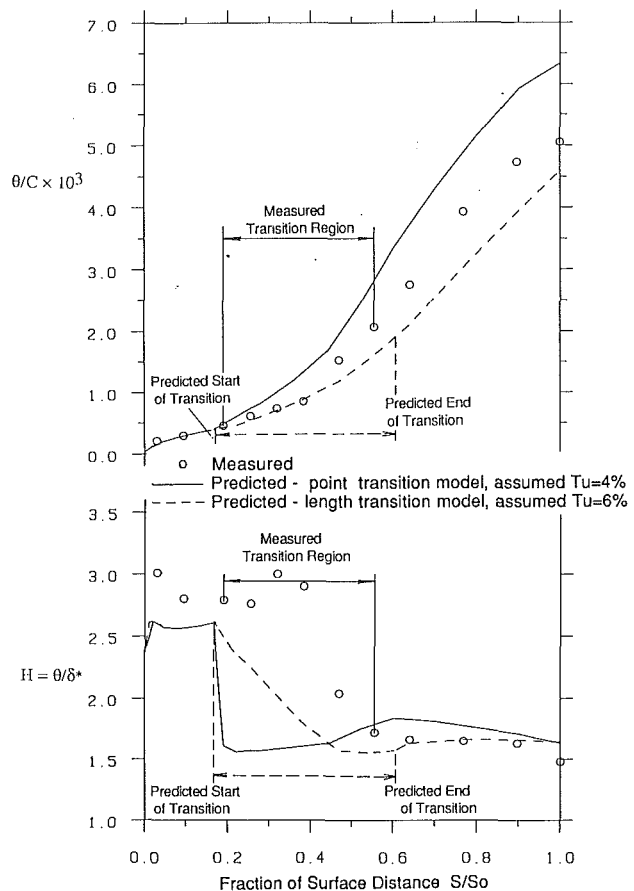


Fig. 12 Measured and predicted momentum thickness and form parameter $H = \delta^*/\theta$ along suction surface without wakes (Case 2) predictions with length and point transition

been predicted reasonably well. The momentum thickness in the separated laminar shear layer is assumed to be constant by the model, at variance with the measured results. The predicted and the measured transition location differs by less than 3 percent chord length. The measured shape factor H at the end of bubble region differs from the value predicted, but in the turbulent boundary layer the agreement is rather good. Despite these (small) discrepancies in the bubble region, the bubble model gives a reasonably accurate value of the momentum thickness θ at the re-attachment point to enable the turbulent boundary layer development to be reasonably well predicted. Similar comparison made for Case 3 showed a similar situation and the figure is therefore not included here. The performance of the bubble model is on the whole quite good and the prediction satisfactory for the low turbulence cases.

When there is relatively high level of turbulence in the free stream, as in Case 2, transition is usually promoted before laminar separation can occur. In that case, however, the modeling of transition process is more difficult, as there are more influential parameters. Models currently used in blade design are empirical and the effect of the turbulence is accounted for by correlating the Reynolds number at transition with a parameter representing the (nondimensionalized) value of RMS turbulence. Transition is either assumed to be completed at a single point, as in Dunham (1972), which is referred to here as the point transition model, or over a length, as in Abu-Ghannam and Shaw (1980), which is referred to here as length-transition model. The point transition model is physically less satisfactory in describing what is actually a rather lengthy process. The alternative length transition model, then requires a correlation to predict the end of transition. Abu-Ghannam and Shaw (1980), following the approach of Dhawan and Nar-

asimha (1958), suggested that both the length of transition and the boundary layer properties at its end can be determined by the conditions at the start and the local free-stream velocity at the end of transition. In their correlation the effect of the free-stream condition during the transition region was neglected.

The performance of both the point transition model by Dunham (1972) and the length transition model by Abu-Ghannam and Shaw (1980) has been tested against the measured data of Case 2. The point transition model was tested using the same NGTE method used previously for Cases 1 and 3, with the measured pressure distribution as the input and with a high level of turbulence specified to comply with the experimental conditions. The length transition model was tested with the results provided by Newman (1987) using a Rolls-Royce proprietary method similar to that of NGTE in its assumptions, but including a length transition model based on that of Abu-Ghannam and Shaw (1980). Newman's calculation was based on an inviscid-viscous iteration procedure where the pressure distribution was predicted with the boundary layer displacement effect taken into the account. The predicted pressure distribution was found to be in excellent agreement with the measure one (see Dong, 1988). In both calculations 6 percent free-stream turbulence was specified. The predicted and the measured integral boundary layer parameters on the suction surface of the blade are presented in Fig. 12.

The start of transition is predicted at $S/S_0 = 0.17$ with both point and length transition models, in reasonably good agreement with the measured result. With the length transition model the momentum thickness θ in the late stage of the transition region is significantly underestimated, which then affects the prediction of subsequent turbulent boundary layer. On the other hand, the point transition model results in an overestimation of the momentum thickness over nearly 80 percent of the blade surface. The predicted momentum thickness at the trailing edge is sensitive to the transition model and a difference of 38 percent of the measured value can be seen between two predictions. Large discrepancies between the predicted and the measured shape factor H are also seen in the transitional boundary layer, though not at the trailing edge.

It is probably true that the point where transition is supposed to occur and be completed can be chosen somewhere inside the transition region to match the experiment data, for example, the point where $\gamma = 0.5$ is sometimes used. This requires, however, an additional correlation to predict the distribution of the intermittency factor and in essence this is similar to a length transition model with similar difficulties.

The problem of modeling transition when there is a high level of disturbance from the upstream, such as exist in a real machine, will be discussed further in the second part of this paper, when the main results with incident wakes present are described.

5 Conclusions

A wind tunnel has been designed with a mechanism to simulate the wakes existing in a compressor. The large scale of the tunnel made it possible to study transition on a cascade with good measurement accuracy. The requirements of having a periodic and two-dimensional flow were met by using two curved sheets outside the blades, simulating local streamlines, and a system of sidewall bleed.

With no wakes introduced measurements were made of the boundary layers on a supercritical-type compressor blade at two different solidities at design incidence and representative Reynolds numbers.

With a low level of free-stream turbulence, $Tu = 0.9$ percent, a laminar separation bubble was found on the suction surface at both values of solidity. Transition occurred in the separated shear layer and the turbulent boundary layer re-attached to

the surface shortly downstream. The turbulent boundary layer remained attached to the trailing edge in both cases. On the pressure surface of the low solidity blade a laminar separation also was measured but the boundary layer re-attached without becoming turbulent.

With the high level free-stream turbulence, $Tu = 6$ percent, the laminar separations were found to have been suppressed as transition was promoted upstream of the separation location. A transitional boundary layer occupied about 36 percent of the suction surface and 82 percent of the pressure surface; on the pressure surface the transition process was eventually suspended or, possibly, reversed.

The velocity profiles of the highly disturbed laminar boundary layers were barely altered until the local intermittency factor γ of the transitional flow exceeded 0.2. Despite the differences in the transition processes in cases with low and high free-stream turbulence, the momentum and energy thickness at the trailing edge of the suction surface were similar in the two cases.

The laminar separation model originally developed by Horton (1969) and improved by Roberts (1980) gave a reasonably good prediction of the bubble length and the properties of the turbulent boundary layer at the re-attachment point. This enabled the turbulent boundary layer over the rest of the blade to be predicted reasonably accurately when the free-stream turbulence was low.

Prediction of transition in the case with a high level of free-stream turbulence was less satisfactory. Existing empirical correlations used for blade boundary layer calculation gave a poor prediction of boundary layer properties at the end of transition and, as a result, the turbulent boundary layer development was inaccurately predicted.

Acknowledgments

This project was supported throughout by Rolls Royce plc. In addition to the financial support from the Company, the authors wish to express their thanks for the help they received, particularly from Mr. C. Freeman and Ms. S. Newman. During his first three years in Cambridge, Y. Dong received a Jardine Studentship and additional support from Cambridge University; later he was supported entirely by Rolls Royce. The experimental rig was designed with the assistance of Mr. A. Timbs and built mainly by Mr. M. Scott; the assistance of both has been invaluable. The help of Mr. I. Amos in reading the manuscript is acknowledged.

References

- Abu-Ghannam, B. J., and Shaw, R., 1980, "Natural Transition of Boundary Layer—The Effects of Turbulence, Pressure Gradient and Flow History," *J. Mech. Eng. Sci.*, Vol. 22, pp. 213–228.
- Addison, J. S., and Dong, Y., 1989, "Unsteady Wake-Boundary Layer Interaction in a Compressor Cascade," presented at the 5th Symposium on the Unsteady Aerodynamics and Aerodynamics of Turbomachinery and Propellers, Beijing.
- Behlke, R. F., 1986, "The Development of a Second-Generation of Controlled Diffusion Airfoils for Multistage Compressors," *ASME JOURNAL OF TURBOMACHINERY*, Vol. 108, pp. 32–41.
- Cantwell, B., Coles, D., and Dimotakis, P., 1978, "Structure and Entrainment in the Plane of Symmetry of a Turbulent Spot," *Journal of Fluid Mechanics*, Vol. 87, Pt. 4, pp. 641–672.
- Carter, A. D. S., 1961, "Blade Profiles for Axial-Flow Fans, Pumps and Compressors," *Proceedings of the Institution of Mech Eng.*, Vol. 175, pp. 775–806.
- Dhawan, S., and Narasimha, R., 1958, "Some Properties of Boundary Layer Flow During Transition From Laminar to Turbulent Motion," *Journal of Fluid Mechanics*, Vol. 3, pp. 418–436.
- Dong, Y., Gallimore, S. J., and Hodson, H. P., 1987, "Three-Dimensional Flows and Loss Reduction in Axial Compressors," *ASME JOURNAL OF TURBOMACHINERY*, Vol. 109, July, pp. 354–361.
- Dong, Y., 1988, "Boundary Layers on Compressor Blades," PhD Thesis, University of Cambridge.
- Doorly, D. J., and Oldfield, M. L. G., 1986, "Simulation of Effects of Shock Wave Passing a Turbine Rotor Blade," *ASME Journal of Engineering for Gas Turbines and Power*, Vol. 107, pp. 998–1006.

- Doorly, D. J., 1988, "Modeling of the Unsteady Flow in a Turbine Rotor Passage," *ASME JOURNAL OF TURBOMACHINERY*, Vol. 110, pp. 27-37.
- Dunham, J., 1972, "Prediction of Boundary Layer Transition on Turbomachinery Blades," AGARD, AG-164, No. 3.
- Elder, J. W., 1960, "An Experimental Investigation of Turbulent Spots and Breakdown to Turbulence," *Journal of Fluid Mechanics*, Vol. 9, pp. 235-246.
- Evans, B. J., 1971, "Free-stream Turbulence Effects in a Compressor Cascade," PhD Dissertation, University of Cambridge.
- Evans, R. L., 1973, "Turbulent Boundary Layers on Axial-Flow Compressor Blades," PhD Thesis, University of Cambridge.
- Evans, R. L., 1978, "Boundary Layer Development on an Axial-Flow Compressor Stator Blade," *ASME Journal of Engineering for Power*, Vol. 100, Apr., pp. 287-293.
- Gaster, M., 1965, "The Role of Spatially Growing Waves in the Theory of Hydrodynamic Stability," *Progress in Aeron. Sci.*, Vol. 6, pp. 251-270.
- Gaster, M., 1969, "The Structure and Behaviour of Laminar Separation Bubbles," A.R.C., R. & M. 3595.
- Hart, M., 1985, "Boundary Layers on Turbine Blades," PhD Thesis, University of Cambridge.
- Hathaway, M. D., Gertz, J. B., Epstein, A. H., and Straziar, A. J., 1986, "Rotor Wake Characteristics of a Transonic Axial-Flow Fan," *AIAA Journal*, Vol. 24, No. 11.
- Herbert, M., and Calvert, W. J., 1982, "Description of an Integral Method for Boundary Layer Calculation in Use at NGTE, With Special Reference to Compressor Blades," National Gas Turbine Establishment Memo. M80219.
- Hobbs, D. E., and Weingold, H. D., 1984, "Development of Controlled Diffusion Airfoils for Multistage Compressor Application," *ASME Journal of Engineering for Gas Turbines and Power*, Vol. 106, pp. 271-278.
- Hodson, H. P., 1984, "Boundary Layer and Loss Measurements on the Rotor of an Axial-Flow Turbine," *ASME Journal of Engineering for Power*, Vol. 106, Apr., pp. 391-399.
- Hodson, H. P., 1985, "Measurements of Wake Generated Unsteadiness in the Rotor of an Axial-Flow Turbine," *ASME Journal of Engineering for Gas Turbines and Power*, Vol. 107, pp. 467-476.
- Horton, H. P., 1969, "A Semi-Empirical Theory for the Growth and Bursting of Laminar Separation Bubbles," A.R.C., C.P. 1073.
- Kerrebrock, J. L., and Mikolajczak, A. A., 1970, "Intra-Stator Transport of Rotor Wakes and Its Effects on Compressor Performance," *ASME Journal of Engineering Power*, Vol. 92, pp. 359-370.
- Jones, W. P., and Launder, B. E., 1972, "On the Prediction of Laminarisation With a Two-Equation Model of Turbulence," *Int. Jnl. Heat and Mass Transfer*, Vol. 15, pp. 301-314.
- Lieblein, S., 1965, "Experimental Flow in Two-Dimensional Cascades," In *Aerodynamic Design of Axial-Flow Compressors*, NASA SP - 36.
- Newman, S. P., 1987, Private Communication.
- Phell, H., Herbst, R., and Schroder, T., 1983, "Investigation of Laminar Boundary Layers Disturbed by Wakes," *ASME Journal of Engineering for Gas Turbines and Power*, Vol. 105, pp. 130-137.
- Roberts, W. B., 1980, "Calculation of Laminar Boundary Separation Bubbles and Their Effects on Airfoil Performance," *AIAA Journal*, Vol. 18, pp. 25-31.
- Walker, G. J., 1968, "The Prediction of Boundary Layer Development on Axial-Flow Turbomachinery Blades," 3rd Australasian Conf. on Hydraulics and Fluid Mechanics, Sydney.
- Walker, G. J., 1974, "The Unsteady Nature of Boundary Layer Transition on an Axial-Flow Compressor Blade," ASME Paper 74-GT-135.
- Wisler, D. S., Bauer, R. C., and Okiishi, T. H., 1987, "Secondary Flow, Turbulent Diffusion and Mixing in Axial-Flow Compressors," *ASME JOURNAL OF TURBOMACHINERY*, Vol. 109, pp. 455-482.
- Wyganski, I., Sokolov, N., and Friedman, D., 1976, "On the Turbulent 'Spot' in Laminar Boundary Layer," *Journal of Fluid Mech.*, Vol. 87, pp. 641-672.

Compressor Blade Boundary Layers: Part 2 — Measurements With Incident Wakes¹

Y. Dong²

Gas Turbine Engineering Division,
Ruston Gas Turbines Ltd.,
Lincoln LNG 7AA, United Kingdom

N. A. Cumpsty

Department of Engineering,
Whittle Laboratory,
University of Cambridge
Cambridge, CB3 0DY, United Kingdom

This paper follows directly from Part 1 by the same authors and describes measurements of the boundary layer on a supercritical-type compressor blade with wakes from a simulated moving upstream blade row convected through the passage. (The blades and the test facilities together with the background are described in Part 1). The results obtained with the wakes are compared to those with none for both low and high levels of inlet turbulence. The transition process and boundary layer development are very different in each case, though the overall momentum thickness at the trailing edge is fairly similar. None of the models for transition is satisfactory when this is initiated by moving wakes.

1 Introduction

The experimental data to be presented in this part of the paper are the main results of an investigation of wake influence on boundary layer transition on a supercritical-type compressor blade. The schematic diagram of the wind tunnel used in this work is presented in Fig. 1 of Part 1. Its design and other aspects of the experiment facilities have already been described in Part 1 and no further description will be given here. Results obtained on the same blade tested under similar conditions but without wakes also were given in Part 1 of the paper. A summary of the experimental conditions for each of the cases with wakes is given in Table 1.

The description of experiment results in this paper will start with Case 4, where the wake passing period was relatively long and the details of transition process were seen more clearly. The data were less complete for Case 4 than some others, with measurements on the suction surface only between $S/S_o = 0.26$ and 0.64 . In Case 5, which is described next, the period was shortened to half of that in Case 4 and the measurements covered the complete suction surface and part of the pressure surface. This made it possible to see how transition was initiated and developed to its completion with the presence of wakes. For the other three cases, the results are described more briefly, with attention focused on the influence of a particular parameter in addition to the wakes: high free-stream turbulence (Case 6) such as that existing in multistage compressors, lower Reynolds number (Case 7) and increased solidity (Case 8).

Following this, a discussion will be given on the implications of these results for design and prediction.

Before proceeding to describe the main results, however, the measured characteristics of the wakes generated by rods will be shown first.

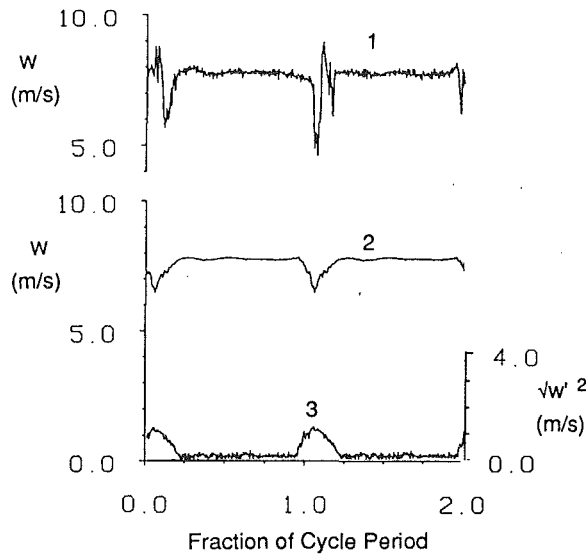
2 Experimental Results

2.1 Measured Characteristics of the Wakes. The inlet flow with incident wakes was measured using a cross hot-wire probe at three stations 8, 15 and 24 percent of blade chord downstream of the plane in which the rods move, the blade leading edge being 28 percent chord downstream. The periodic temporal variation of the velocity measured can be regarded as the periodic spatial distribution of the velocity in the frame moving with the rods, if the effect of the potential field due to the presence of the downstream blade row is small. This was found to be the case and only the results obtained at the station closest to the blade leading edge are shown in Fig. 1. Measured velocity distributions at the three stations were qualitatively similar to those found behind a rotor blade of a compressor by Wisler et al. (1987).

On the raw trace, shown in Fig. 1(a), the sign of the velocity overshoot (the streamwise component) seen in the wake region suggests the presence of some vortex shedding. This is well known for a cylinder, but recent work has revealed that it also appears in the wakes of blades of a transonic compressor rotor (Hathaway et al., 1986). The wakes generated by rods are symmetrical, unlike those usually found in a compressor, but this does not make the simulation unrepresentative. As far as the transition and the boundary layer development are concerned the major effect of the wakes is the high level turbulence they contain, rather than the unsteadiness associated with the ensemble-mean velocity variation. The velocity deficit of the wake observed in this relative frame after ensemble averaging

¹Part 1 by the same authors contains not only the description of the facilities and the results with no wakes but also the Background, Nomenclature, References and Acknowledgments.

²Formerly, Whittle Laboratory, University of Cambridge, United Kingdom. Contributed by the International Gas Turbine Institute and presented at the 34th International Gas Turbine and Aeroengine Congress and Exhibition, Toronto, Ontario, Canada, June 4-8, 1989. Manuscript received at ASME Headquarters January 4, 1989. Paper No. 89-GT-51.



- 1 : Raw Velocity Trace
- 2 : Ensemble-Averaged Velocity Trace
- 3 : Ensemble-Averaged Turbulence Trace

Fig. 1 (a) Measured inlet flow velocity in the relative frame (streamwise component)

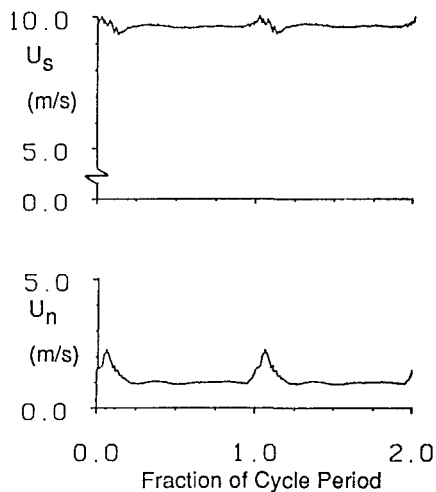


Fig. 1 (b) Velocity-time trace seen in a stationary frame at 24 percent blade chord downstream of rods traveling plane

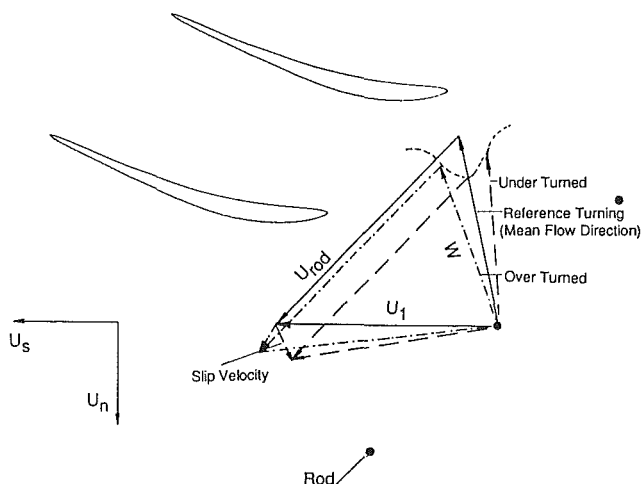


Fig. 1 (c) An illustration of direction and magnitude of the velocity within a wake in the inlet flow in a stationary frame (underturning and overturning exaggerated for clarity)

Table 1 Experimental conditions in the cases with incident wakes

Case	Chord (mm)	Solidity σ	Rod spacing S_{rod} (mm)	$Re_c \times 10^5$	Reduced Freq. $\Omega = \omega C/U_1$	Turbulence Grid
4	450	0.8	720	3.1	0.74	No
5	450	0.8	360	3.1	1.5	No
6	450	0.8	360	3.1	1.5	Yes
7	450	0.8	720	1.5	1.5	No
8	598	1.67	360	4.0	2.0	No

is about 18 percent at this measurement station. The peak level of the turbulence is also 18 percent, a magnitude similar to that found by Wisler et al. (1987) in a compressor representative of a modern machine.

The distribution of the ensemble-averaged velocity in the wake region appears rather different in a system whose axes s and n are parallel and perpendicular to the mean flow in the stationary frame at the inlet (Fig. 1(b)). First, there is an overshoot in the s component, followed by an undershoot relative to the free-stream flow as a wake passed by a measurement station. The cause of this observation is explained graphically in Fig. 1(c). Inside the wake flow is over- and underturned relative to the direction of the mean flow in the relative frame. As a result in the stationary frame the overturned part of flow has a resultant velocity higher than that in the free stream, while the underturned part has a lower one. A probe fixed in the stationary frame at the inlet therefore sees the overturned part of the wake flow before it sees the underturned part and as a consequence the temporal distributions of the velocity components, when projected to the s and n -direction, look like those shown in Fig. 1(b). The illustration also indicates that inside the wake region U_n is higher than that in the free stream and is in a direction to form a so-called "negative jet" (see Hodson, 1985), drawing the fluid away from the blade suction surface toward the pressure one. The negative jet produces an induced vortical motion inside a blade row; see, for example, Kerrebrock and Mikolajczak (1970). Evidence of this will be shown shortly when the measured results in the boundary layers on blade surfaces are presented.

The time-mean rms level of the total fluctuation at the measurement station nearest to the leading edge is 7.8 percent of the mean inlet velocity. The contributions to it by turbulence and by unsteady periodic fluctuation are 7.2 percent and 3.0 percent, respectively. The contribution by the unsteady periodic fluctuation is relatively small, partly because of the nature of the velocity triangle and partly because of the turbulent mixing effect inside the wake.

2.2 Case 4: $\sigma = 0.8$; $S_{rod}/C = 1.6$; $Re_c = 3.1 \times 10^5$; $\Omega = 0.74$; No Turbulence Grid. Before measurements of boundary layers began in each case care was always taken to make the pressure distribution on blade surface as close to its corresponding case in no-wake flow as possible. The measured surface pressure distribution is compared in Fig. 2 with that predicted using an inviscid calculation method, and with that measured in Case 1. The agreement is in general very good, except in the region between $S/S_0 = 0.33$ to $S/S_0 = 0.64$. This was where a separation bubble appeared in Case 1 (see Part 1), and measurements of the boundary layer in Case 4 were restricted to around this region.

Wake Interaction With a Laminar Boundary Layer. At three measurement stations, $S/S_0 = 0.26, 0.32$ and 0.38 , the patterns of velocity-time ($v-t$) traces acquired at similar locations across the boundary layer were found to be quite similar. A sample of them at $S/S_0 = 0.38$ is presented in Fig. 3. In the free stream, the signature of the convected wake confirms the presence of the negative-jet effect; the velocity shows first a reduction relative to its mean value followed then by an

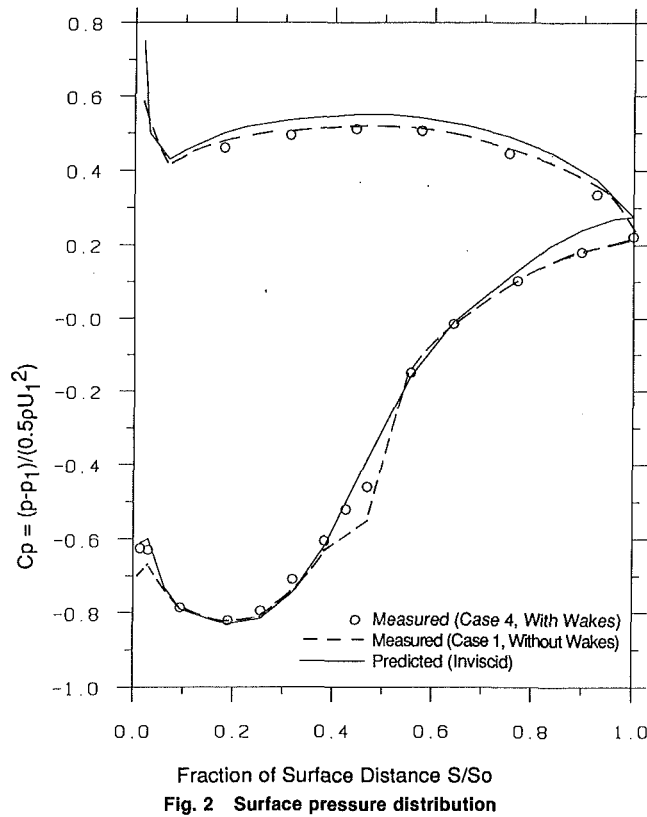


Fig. 2 Surface pressure distribution

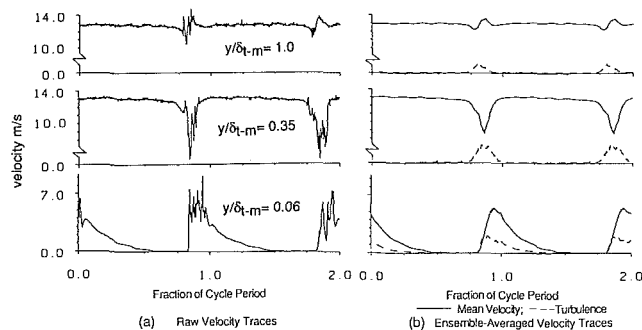


Fig. 3 Velocity-time traces at different locations across the suction surface boundary layer at $S/S_0 = 0.38$ (Case 4)

overshoot as a wake passes by the station. The major impact of the wake is seen, however, in the dramatic change of the velocity inside the boundary layer.

There is an isolated region within an otherwise laminar flow in Fig. 3 where velocity fluctuations characteristic of turbulence appear. This isolated region, as it will be shown later, has many of the characteristic properties of a turbulent spot observed in a boundary layer; see, for example, Wygnanski et al. (1976) or Cantwell et al. (1978). It will therefore be referred to as turbulent spot throughout this paper. As a spot arrives at the measurement station the flow accelerates abruptly near the wall but decelerates in the outer part of the boundary layer. After the spot has passed over the measurement station, however, the flow begins to return to its predisturbed state. Near the wall the deceleration occurs at a rate much slower than that at which the flow was accelerated as the spot approached.

It can be seen by comparing Figs. 3(a) and 3(b) that some ensemble-averaged turbulence appears on the trace where the flow is actually laminar, for example, in the region immediately following the turbulent spot. This was caused by the ensemble-averaging technique, which identifies any difference between an individual sample (raw trace) and its periodic component

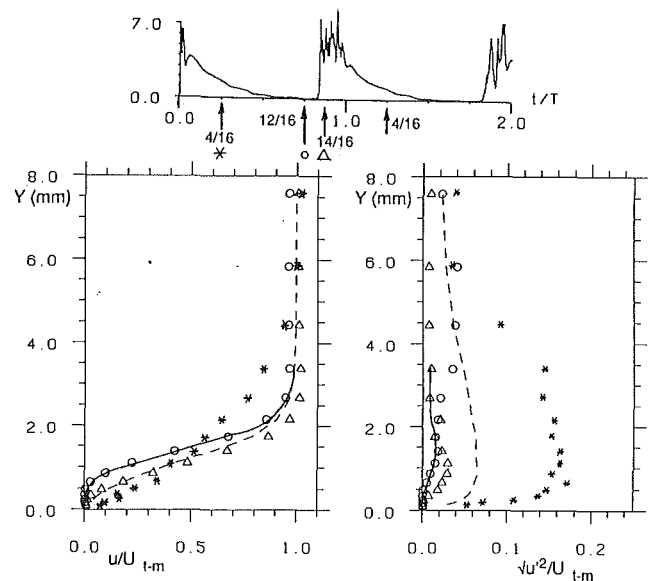


Fig. 4 Ensemble average velocity and turbulence profiles on suction surface at $S/S_0 = 0.38$ at different instants of a cycle for Case 4, time-mean values shown with broken line. For comparison Case 1 (no wakes) shown with solid lines.

as turbulence; it is not turbulence but is due to the low frequency, cycle-to-cycle variations.

The appearance of a turbulent spot brings about dramatic changes in the local overall boundary layer velocity distribution and integral quantities, such as its displacement thickness δ^* , momentum thickness θ and shape factor H . This can be seen in Fig. 4 at $S/S_0 = 0.38$. The velocity profile before the arrival of a turbulent spot (at $t/T = 12/16$) indicates a separated laminar boundary layer similar to that in the corresponding no-wake flow, Case 1. When a turbulent spot arrives, as at $t/T = 14/16$, the profile in the inner region becomes much fuller, whereas in the outer part of the layer the velocity decreases because of the thickening of the boundary layer in the spot. At this time, the level of the ensemble-averaged turbulence reaches about 16 percent of the time-mean free-stream velocity U_{1-m} over a large part of the boundary layer. The boundary layer thickens sufficiently that the measurements in this case do not reach the boundary layer edge in terms of the instantaneous velocity profile. Compared with $t/T = 12/16$, the momentum thickness θ almost triples, whereas the shape factor H drops from 5.16 to 2.12. Separation, seen in the laminar boundary layer, is momentarily suppressed. All these changes are the result of the boundary layer changing from laminar to turbulent before subsequently reverting to the laminar state. The laminar boundary layer behind the turbulent spot has a much fuller velocity profile than the one before the arrival of the turbulent spot, an effect noticed in the slow restoration process to the predisturbed state seen in the $v-t$ trace near the wall shown in Fig. 3 and documented for spots in two-dimensional boundary layers by Wygnanski et al. (1976) and others.

For a turbulent spot on a flat plate, the experimental evidence shows that its leading and trailing edges travel downstream at about 0.85 and 0.5 times of the free-stream velocity, respectively (Cantwell et al., 1978). A spot moves downstream more slowly than the free stream and grows linearly with the distance it travels. The designation of the edges for a turbulent spot in the present work was based on an ensemble-averaged $v-t$ trace near the wall. The criterion used by Doorly and Oldfield (1986) has been adopted in the present work, with the leading edge and the trailing edge of a spot defined to be where the velocity shown on the velocity-time trace is halfway between the minimum (laminar) level and the maximum (turbulent) level attained at the measurement station. The spot leading edge was found to travel at 0.76, and the trailing edge at 0.57, of the

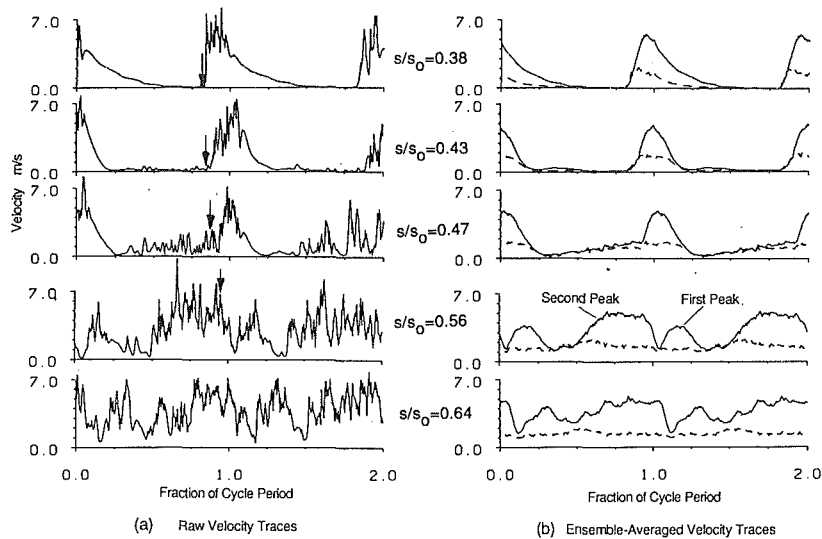


Fig. 5 Velocity-time traces at 5 different stations along the suction surface; measurements close to surface, $y = 0.48$ mm (Case 4)

time-mean local free-stream velocity, although small variations existed from station to station. (The leading edge of the turbulent spot in the work of Doorly and Oldfield, 1986, did not travel at a constant fraction of the local free-stream velocity but the trailing did at about 0.5.) On the other hand, the wake was found to travel at roughly the same speed as the local mean flow in the free stream. The turbulent spot created as a result of wake interaction with the laminar boundary layer in the present case is therefore akin to a self-sustaining turbulent spot found to exist in a transitional boundary layer on a flat plate, although the former is statistically two-dimensional while the latter is three-dimensional. The same conclusion was drawn by Doorly and Oldfield (1986) in their study of the wake interaction with the boundary layer on a turbine blade.

The sizes of the wake and the turbulent spot it created varied as they traveled downstream. Typically, the wake occupied 20 percent of the blade surface distance; for comparison at the measurement station 4.2 percent chord ahead of the blade leading edge the wake occupied a distance equal to about 18 percent of surface distance. The turbulent spot grew from about 12 to 20 percent of S_0 between $S/S_0 = 0.26$ to 0.64 , the measurement region for Case 4. The velocity time traces at different stations are shown in Fig. 5. On this figure, the turbulent spot initiated by the wake is most obvious at the more upstream stations; at $S/S_0 = 0.56$ and 0.64 , the turbulence and disturbance of the wake-induced spots is overshadowed by turbulence arising from a breakdown of the separated laminar flow between these spots. This is discussed further below. Also shown on Fig. 5 are the positions of the wake center (shown at each position by a downward vertical arrow) which can be detected at the boundary layer edge. Very clearly the slower moving turbulent spot gets left behind by the wake, which convects at the free-stream velocity.

The Behavior of the Flow in the Quiescent Region. At the time, just before the arrival of a turbulent spot ($t/T = 12/16$), the velocity profiles shown in Fig. 4 indicate that the local boundary layer has returned to a state similar to that in the no-wake flow (Case 1), which is separated and thus very unstable. The instability begins to manifest itself on the $v-t$ traces obtained near the wall at the measurement stations further downstream, as can be seen in Fig. 5. Whereas at $S/S_0 = 0.38$ the velocity was almost disturbance-free during the period with very low mean velocity, the trace at $S/S_0 = 0.43$ exhibits small sinusoidal fluctuations during similar times in the cycle. These sinusoidal fluctuations are Tollmien-Schlichting (T-S) instability waves, which are known to be prone to form on

separated shear layers. Based on the measured instantaneous of velocity profile, the instability waves were estimated, according to Gaster's (1969) formula, to have a frequency around 440 Hz, which agrees well with the value of 430 Hz measured. These waves grow rapidly further downstream and at $S/S_0 = 0.56$ have begun to break down into turbulence. The transition thus initiated has resulted in significant increase in the velocity near the wall in the previously separated flow and a second peak then emerges on the ensemble-averaged $v-t$ trace near the wall.

The flow first became fully turbulent in the corresponding no-wake flow cases (Cases 1 and 2) at $S/S_0 = 0.56$. It can be seen in Fig. 5, however, that at this position in Case 4 turbulence has not spread over the complete cycle, and transition has not yet been completed. The ensemble-averaged velocity profiles were examined on an inner region log-law plot (Dong, 1988). The velocity distribution within the first peak (associated with the wake-created turbulent spot) was found to be transitional in the sense that there was at most a very short region where the velocity profile followed logarithmic law of the wall. In contrast, the flow within the second peak, which resulted from transition initiated by T-S wave breakdown, did possess a substantial logarithmic law of the wall region, as did the boundary layer in Cases 1 and 2 at the same location. Between $t/T = 4/16$ and $8/16$, the nonturbulent region for Case 4 at $S/S_0 = 0.56$, the flow showed no logarithmic region whatsoever, but instead a profile corresponding to the linear viscous sublayer form

$$u/u_\tau = \text{const} \times (Yu_\tau/\nu),$$

extending most of the way across the boundary layer. This strange behavior in the calmed region after the spot is not understood, but also was found in Case 5. In trying to understand the behavior of the spots formed on the blades, one is aware of the difficulty associated with understanding turbulent spots even in flat plate boundary layers and the lack of knowledge about the mechanism in the calmed region that follows them.

Some period of laminar flow was still observed at $S/S_0 = 0.64$, the most downstream station used for the measurement in this Case 4. The time-mean value of the momentum thickness θ in Case 4 at $S/S_0 = 0.64$ is about 12 percent larger than in Case 1, despite the fact that the flow at this station was still intermittent, whereas in Case 1 it was fully turbulent from $S/S_0 = 0.56$. The average value of θ in Case 4 is larger because the low value in the laminar region is more than outweighed by

the high value in the turbulent region initiated by the wake, which has been turbulent from well upstream (Fig. 6).

Velocity Contour Pictures. The response of the boundary layer along the blade suction surface to the wake interaction can be seen more clearly by plotting out the "snapshots" of velocity contours made of ensemble-averaged quantities in the

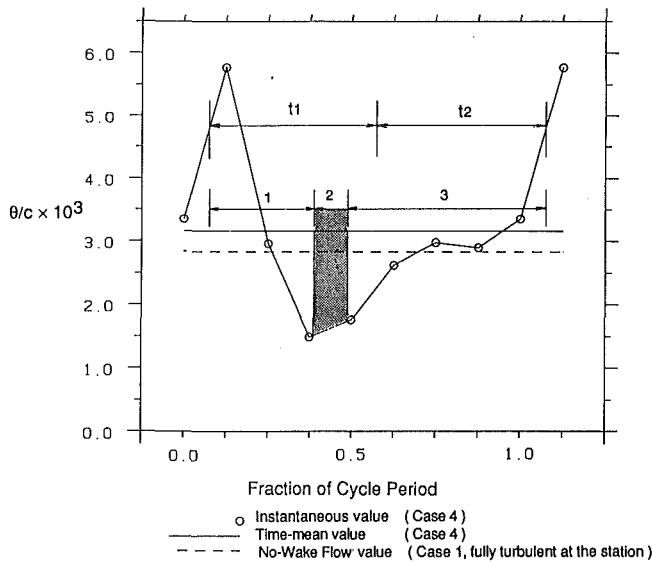


Fig. 6 Variation with time of ensemble-average momentum thickness on suction surface at $S/S_0 = 0.64$: (1) region of spot formed upstream by wake; (2) laminar region; (3) turbulent region induced by transition of separated flow (Case 4: $\sigma = 0.8$, $S_{rod}/C = 1.6$)

way used by Gaster (1965) in his study of laminar separation. Shown in Fig. 7 are snapshots at 4 of 16 instants with equal intervals during a cycle period T . The solid lines represent the contours of the ensemble-averaged velocity normalized by the time mean velocity in the local free stream u/U_{t-m} . The dotted lines represent the contours of the normalized ensemble-averaged turbulence velocity $\sqrt{u'^2}/U_{t-m}$. Qualitatively, variation of the vertical location of u/U_{t-m} lines reflects the change of boundary layer extent, for example, thickening or thinning. High values of $\sqrt{u'^2}/U_{t-m}$ indicate the traveling wake and the turbulent spot it creates, as well as the turbulent boundary layer.

Figure 7(a) shows the arrival of a wake and the turbulent spot it creates just ahead of the separation bubble, which is represented by a lump formed by the line $u/U_{t-m} = 0.05$. The separated flow re-attaches to the surface at about $S/S_0 = 0.47$, after which the dotted lines indicate that the boundary layer is turbulent. It should be noted that the vertical coordinate is stretched by a factor of 20 in relation to the horizontal one and the vertical dimension of the bubble is very small compared with the blade chord. In Fig. 7(b), the separation bubble is seen to be partially suppressed as the turbulent spot arrives at the position occupied by the bubble. The bubble is completely suppressed at the instant shown in Fig. 7(c), as the region is now covered by the turbulent spot in which velocity remains relatively high near the wall. The local thickening of the boundary layer, as it undergoes transition, is clearly visible. Finally, Fig. 7(d) shows the re-emergence of the separation bubble some time after the turbulent spot has passed by. The 5 percent turbulence contour line upstream of $S/S_0 = 0.5$ in this figure does not really indicate turbulence, but rather the high $\sqrt{u'^2}/U_{t-m}$ is the result of the ensemble-averaging technique on cycle-to-cycle variation (noted earlier). It can be seen that the raw

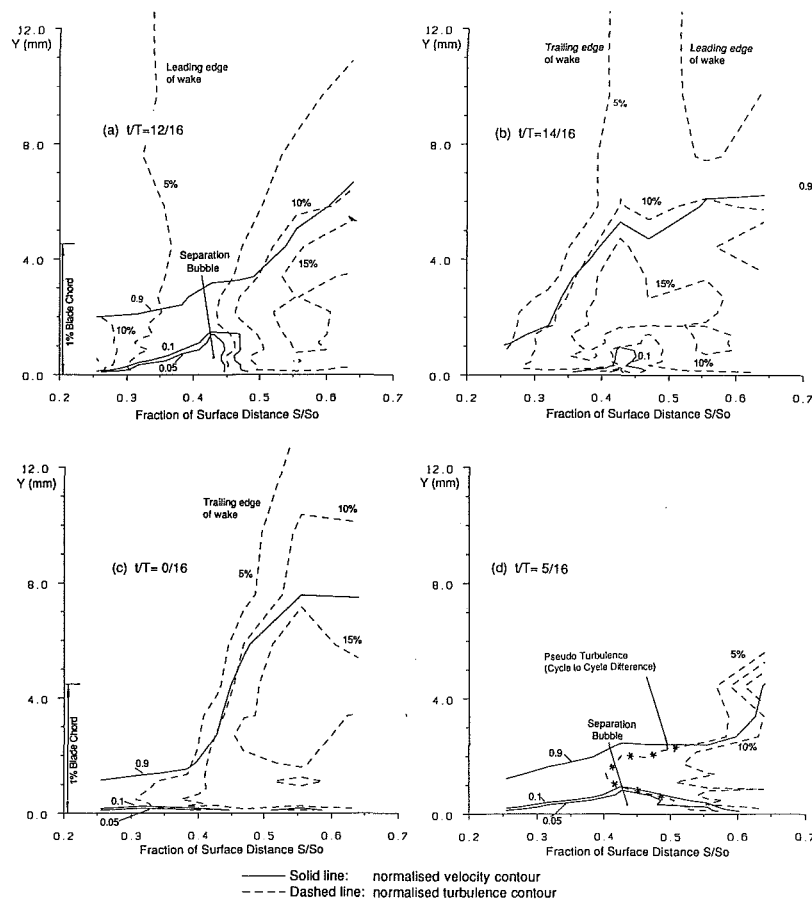


Fig. 7 Contours of ensemble-averaged velocity and turbulence in suction surface boundary layer (Case 4: $\sigma = 0.8$, $S_{rod}/C = 1.6$)

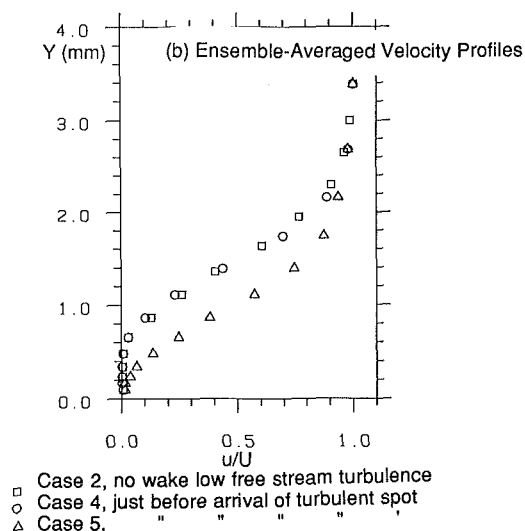
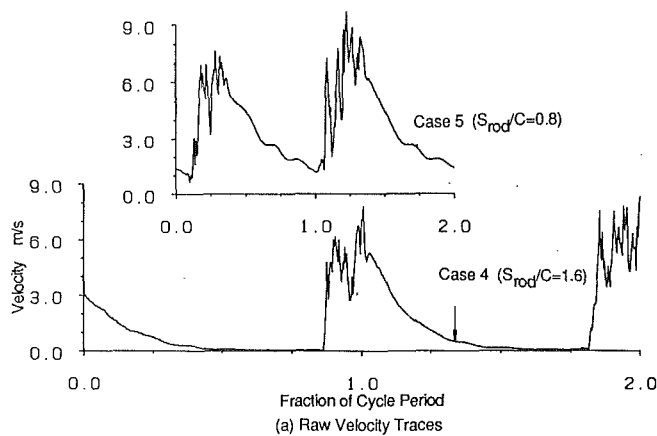


Fig. 8 Instantaneous velocities near suction surface (raw signals) and ensemble-averaged velocity profiles for different cycle period (wake spacing); $S/S_0 = 0.38$

velocity traces presented in Fig. 5 show that the flow at this moment was laminar at least up to $S/S_0 = 0.56$.

2.3 Case 5: $\sigma = 0.8$; $S_{rod}/C = 0.8$; $Re_c = 3.1 \times 10^5$; $\Omega = 1.5$; No Turbulence Grid. The experimental conditions in this case were identical to those in Case 4 except that the spacing between the rods, and therefore the cycle period, was half of that in Case 4. The surface pressure distribution was found to be in good agreement with that predicted, as in Case 4. Measurements were made at 13 different stations on the suction surface and three on the pressure surface of the blade.

The measured results at the leading edge of the blade showed that the turbulent spot was formed in the boundary layer where the wake impinged on it. Initially this turbulent spot was just the signature of the wake and it is not clear whether it was self-sustaining. The first sign of the spot developing into the self-sustaining pattern was found at $S/S_0 = 0.094$, where it began to lag behind the wake. As the cycle period in this case was shorter than in Case 4, some difference in the subsequent stage of transition was observed.

The Effect of Cycle Period. Figure 8(a) shows two $v-t$ traces near the wall at $S/S_0 = 0.38$ for Cases 4 and 5; Fig. 8(b) shows the corresponding ensemble average velocity profiles at the instant just before the arrival of a turbulent spot in the two cases as well as that for the corresponding no-wake flow, Case 1. In Case 4 there is sufficient time for the boundary layer to revert to the separated state of Case 1, but with the

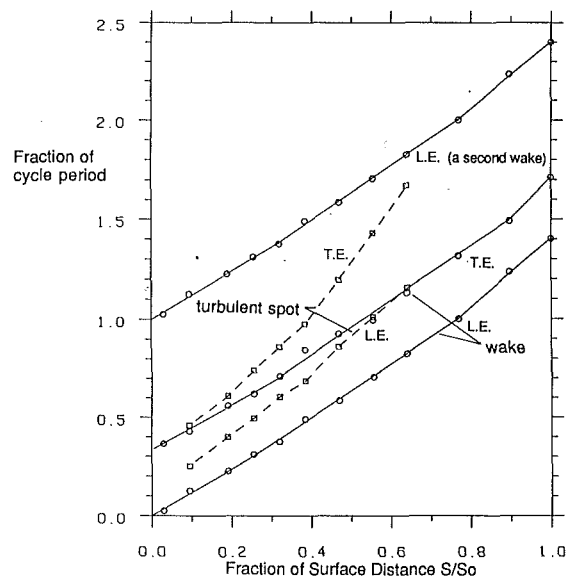


Fig. 9 Regions of suction surface occupied by wake and turbulent spot (Case 5)

shorter cycle period in Case 5 another turbulent spot arrives before this can occur. The velocity profile just before the arrival of a turbulent spot in Case 5 therefore looks much fuller than those in Cases 1 and 4. Although not shown here, velocity contour pictures similar to those shown in Fig. 7 did indicate that not only was the bubble extent smaller in Case 5 than in Cases 4 and 1, but also its location was further downstream (Dong, 1988).

At $S/S_0 = 0.64$ (the most downstream station used for measurement in Case 4) the intermittency factor was about 0.85 in Case 5 and 0.92 in Case 4. It was higher in Case 4 because the flow behind the calmed region of a spot underwent a separation-bubble induced transition (giving the second peak in Fig. 5) and this increased the fraction of cycle period for which the flow was turbulent. At the same location, the time-mean value of the momentum thickness θ was about 6 percent higher in Case 5 than in Case 4. To explain the higher values of θ one needs to look again at Fig. 6 for Case 4. The cycle period in Fig. 6 has been divided into two equal parts, each having a length the same as the cycle period in Case 5. In the first part (marked as t_1), where the turbulent spot created by the wake is located, the $v-t$ trace has a form almost identical to that in Case 5, which implies that the mean level of θ over this time is similar in the two cases. In Case 4, the mean level of θ over t_1 is clearly higher than that over t_2 , where the turbulent boundary layer begins by transition in the otherwise quiescent flow behind a turbulent spot. As the cycle period in Case 5 is only half of that in Case 4, the second part t_2 of the trace in Fig. 6 is replaced by another complete cycle identical to the first part. Hence, compared with Case 4, the average value θ over the complete cycle in Case 5 is raised.

Completion of Transition Process. The convection of the wake in the free stream and the turbulent spot it created inside the boundary layer along the blade suction surface is described in Fig. 9. The abscissa in the figure denotes the fraction of the surface distance, while the ordinate denotes the instant of the time during a cycle. A horizontal cut marks the leading and the trailing edge of either a wake or a spot on the surface at a particular time. The boundaries of the wake are defined in terms of the ensemble-averaged turbulence velocity of the boundary layer edge, which has a distinctively higher level within the wake region. The definitions for the edges of the turbulent spot are the same as the ones described in Case 4. The wake occupies typically 20 percent of the blade surface distance in the front part of the blade reducing to about 15

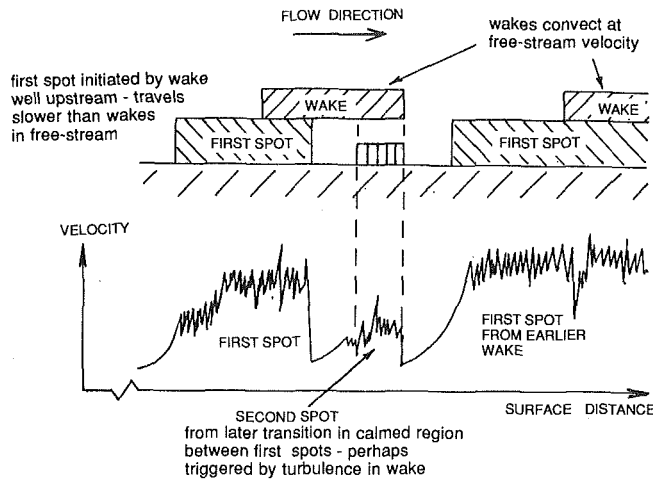


Fig. 10 Schematic description in the quiescent or calmed region between spots

percent near the blade trailing edge. The decrease occurs because the wake leading edge is always at a downstream station where the local flow has a lower mean velocity in a decelerating flow.

The edges of the spot in the first 10 percent of the blade surface are not marked in the figure because it was not possible to use the same criteria to define a spot that was insufficiently developed. Downstream of $S/S_0 = 0.64$, on the other hand, the boundary layer was nearly fully turbulent and the edges of a spot became blurred on the $v-t$ traces near wall. Between $S/S_0 = 0.094$ and $S/S_0 = 0.64$, however, the turbulent spot inside the boundary layer had grown from 12 to 20 percent of the total suction surface distance, as a result of differences in the traveling speeds of its leading and trailing edges.

A fully turbulent boundary layer occurs just downstream of $S/S_0 = 0.64$, which is significantly well upstream of where two successive turbulent spots would merge. This indicates that completion of transition in Case 5 has been caused by transition in the quiescent region of the flow, like that found in Case 4. Although the separation bubble in Case 5 is smaller than in Case 4, the shear layer profile associated with it is still unstable and any disturbance in the free stream can trigger transition. Second, as the wake in the free stream leads the turbulent spot inside the boundary layer, its high turbulence level can help to promote transition in the quiescent region ahead of a turbulent spot in the way illustrated schematically in Fig. 10. For reduced frequencies below about 2.0, the wake in the free stream cannot catch the trailing edge of a previous spot before $S/S_0 = 0.50$. This far downstream any remaining laminar boundary layer between two successive spots is fairly unstable, because of the adverse pressure gradient, so that the disturbances carried by the wake may spread down and initiate transition. In Case 5, the wake-spot merging position is around $S/S_0 = 0.7$, which is also the most upstream position where the flow was seen to be fully turbulent. It should be recalled, however, that on the blade tested the laminar separation bubble is upstream of this and it is impossible to properly isolate the effects of the strong pressure gradient, the presence of a small transient separation bubble and the free-stream wake.

The overall effect of wakes on the suction surface boundary layer was to increase the time-mean θ at the blade trailing edge by about 7 percent in Case 5 compared with the corresponding flow without wakes (Case 1), surprisingly little in view of the dramatic differences in the transition process in the two cases.

The Pressure Surface Results. The $v-t$ traces obtained at the first measurement station, $S/S_0 = 0.31$, on the pressure surface were found to be quite similar to those on the suction surface shown in Fig. 3, except near the free stream where the

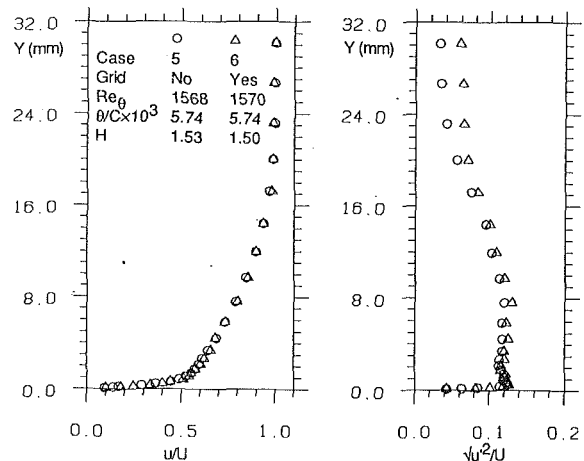


Fig. 11 Time-mean velocity and turbulence profiles at the trailing edge of suction surface, both cases with wakes; Case 5 without; Case 6 with turbulence grid

velocity variation sequence was reversed compared with that on the suction surface (Dong, 1988). This would be expected since the wake-induced motions near two surfaces were in opposite directions; the "negative jet" in the wake was drawing fluid away from the suction surface giving a "positive jet" toward the pressure surface. However, the turbulent spots on both surfaces are similar in their characteristics, which is evidence that it is the high level turbulence contained inside the impinging wake that is the main mechanism creating the turbulent spot observed, forcing the boundary layer to undergo transition at a very early location on the blade. The role played by the unsteadiness associated with the variation of the mean velocity of the wake, i.e., the effect of the negative jet on the suction surface or the positive one on the pressure surface, is relatively insignificant and may have no effect whatsoever.

Compared with Case 1 (without wakes or grid-generated turbulence) the presence of wakes has increased the time-mean momentum thickness at the pressure surface trailing edge by about 44 percent. This large difference is because in Case 1 the boundary layer on the pressure surface was laminar over the entire blade surface. The value of θ at the pressure surface trailing edge in Case 5 is, however, only 4.4 percent greater than that in Case 2 (without wakes but with 6 percent grid-generated turbulence) for which the pressure surface also had a long transitional region.

2.4 Case 6: $\sigma = 0.8$; $S_{rod}/C = 0.8$; $Re_c = 3.1 \times 10^5$; $\Omega = 1.5$; With Turbulence Grid. The experimental conditions in this case were identical to those in Case 5 but for the addition of the turbulence grid to give a mean free-stream turbulence level in the region outside the rod wakes equal to about 6 percent of the inlet time-mean velocity. Measurements made at three stations on the suction surface, $S/S_0 = 0.38, 0.64$ and 1.0 , indicated that the time-mean character of the boundary layer was quite similar to Case 5. Transition was found to be just completed at $S/S_0 = 0.64$, not far from where transition ended in Case 5. Because of the similarity, only a comparison of the results at the trailing edge station has been shown in Fig. 11 where the time-mean velocity profiles are almost identical.

The extra free-stream turbulence might be expected to affect the boundary layer development by promoting transition in the quiescent region, thereby shortening the transition process. The explanation seems to be that, with the relatively close spacing of wakes in Cases 5 or 6, the calmed period after a spot generated by one wake is terminated by the spot generated by the next wake until about $S/S_0 = 0.64$. The flow is sufficiently stable in the calmed region after the spot that free-stream turbulence does not initiate transition. The velocity-time traces showed that despite the presence of high level free-

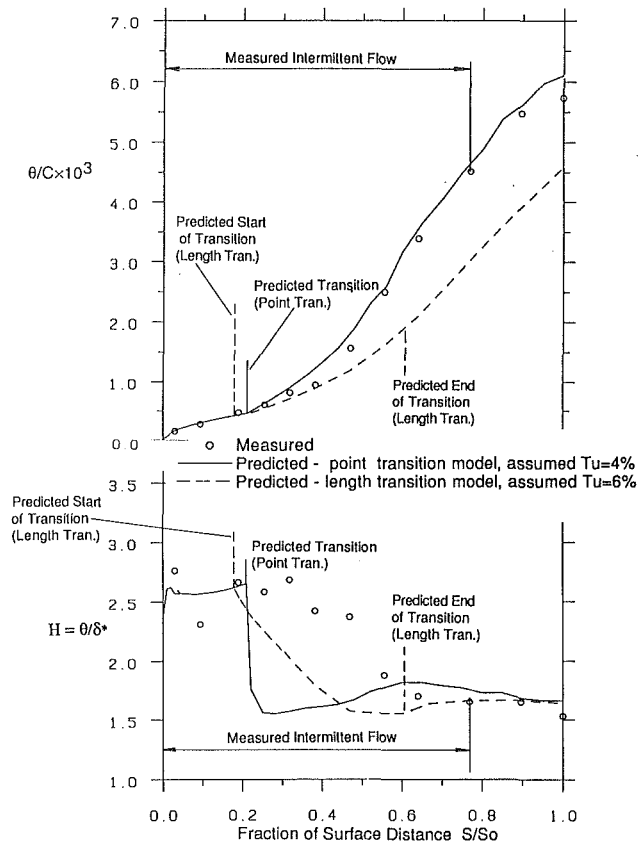


Fig. 12 Measured and predicted time-mean momentum thickness and form parameter $H = \delta^*/\theta$ along suction surface with wakes (Case 5) predictions with length and point transition

stream turbulence in Case 6 the flow outside the wake-created turbulent spot was still predominantly laminar at $S/S_0 = 0.38$ (Dong, 1988). In Case 2, without the wakes present but with the turbulence grid, the high level of free-stream turbulence resulted in a transitional flow with an intermittency factor of 0.44 at $S/S_0 = 0.38$.

The foregoing explanation also offers a clue to the paradox observed by Doorly (1988). Doorly found that on a turbine blade tested with grid-generated turbulence of only 5 percent, the mean heat transfer rate in the region between $S/S_0 = 0.10$ to 0.35 was higher than that in the case with both wakes and the same 5 percent grid-generated turbulence present. For the turbine blade, where the representative Reynolds number was much higher, the 5 percent grid turbulence alone was found to be sufficient to make the boundary layer fully turbulent at $S/S_0 = 0.35$. The wake-created turbulent spot would be followed by the calmed region in which the flow would have been more resistant to transition, thereby prolonging transition process and reducing the mean heat transfer rate compared with the case with only grid turbulence present.

2.5 Case 7: $\sigma = 0.8$; $S_{rod}/C = 1.6$; $Re_c = 1.5 \times 10^5$; $\Omega = 1.5$; No Turbulence Grid, Lower Reynolds Number. This test, reported by Addison and Dong (1989), was conducted with the inlet velocity (and consequently the chord-based Reynolds number Re_c) reduced to half of that in the previous cases. The speed of the moving rods also was reduced proportionally to maintain the design-condition velocity triangle at the cascade inlet. The experimental conditions in this case were otherwise identical to those in Case 4.

The measured results, obtained between $S/S_0 = 0.19$ and $S/S_0 = 0.64$, indicated that the pattern of the wake-boundary layer interaction at this lower Reynolds number was basically similar to those in Case 4 described earlier, see Dong (1988). The principal difference was in the greater size of the separation

bubble at the lower Reynolds number. The vertical extension of the corresponding velocity contour lines scaled well with $Re_c^{-1/2}$, as expected of a laminar boundary layer. The stream-wise extent of the bubble, however, did not appear to be as large as would be expected using Horton's bubble model (1969) in a quasi-steady way. In spite of the lower Reynolds number, the bubble was suppressed as the spot created by the wake arrived, and re-established afterward, very much in the way it responded in the higher Reynolds number flow of Case 4 (Fig. 7).

2.6 Case 8: $\sigma = 1.67$; $S_{rod}/C = 0.6$; $Re_c = 4.0 \times 10^5$; $\Omega = 0.8$; No Turbulence Grid, Higher Blade Solidity. The solidity of the blade tested in this case was more than double the value of the previous one. The longer blade used also resulted in a higher value of the reduced frequency, so the wakes were now packed more closely relative to the blade length. Basically, the observed phenomena of wake interaction with the boundary layer were similar to those on the lower solidity blade. The exception was that the separation bubble, which was seen in the corresponding no-wake flow (Case 3), did not appear. The time-mean value of the suction surface momentum thickness at the trailing edge station was slightly below the value in Case 3. However, as Dong (1988) pointed out, the measured results at the last two stations in Case 3 seem to be in error. The boundary layer calculations for Case 1, a flow with low levels of free-stream turbulence, were found to be accurate. A reasonable comparison can therefore be made of the *measured* results of Case 8 with the *predicted* ones of Case 3. If this is done, the time-mean value of the momentum thickness in Case 8 is about 4 percent higher than that of Case 3, similar to the difference found for the lower solidity blade with wakes (Cases 1 and 5). The overall effect of the wakes on the boundary layer (and the loss in the flow) on this higher solidity blade also seems to be small.

3 Discussion

The experimental results previously described have shown that transition process in the presence of wakes is very different from that seen in cases without wakes described in Part 1. A concern of this investigation is the validity of existing empirical transition models [e.g., Dunham (1972) and Abu-Ghannam and Shaw (1980)], which were built on experimental data obtained without moving wakes present, and the discussion will focus on the significance of transition modeling in relation to predicting boundary layer development.

The first question of interest is the definition of the start of transition, since a turbulent spot appeared in the boundary layer at the leading edge when a wake impinged on the blade. One of the most important characteristics of the turbulence observed in a turbulent boundary layer is that it is self-sustaining and it seems reasonable to choose this as a criterion. According to this, transition has occurred at least as early as $S/S_0 = 0.09$, since by then the wake had begun to move past the spot. At $S/S_0 = 0.09$, however, the measured results in Case 1 indicate that the laminar boundary layer had a boundary layer Reynolds number $Re_\theta = 124$, which is still below the minimum transition Reynolds number (163) assumed in both the models of Dunham (1972) and Abu-Ghannam and Shaw (1980). However, it has been observed that transition can be forced to occur in a boundary layer with lower Reynolds number: Elder (1960) showed in an experiment that a small scale, large amplitude disturbance (≈ 0.2 of the free-stream velocity) instantly triggered a self-sustaining turbulent spot where the local Re_θ was far below the minimum instability limit of 163 for a flat plate. The correlations of Dunham and Abu-Ghannam and Shaw cannot be expected to be adequate in describing transition in the presence of wakes that contain very high level turbulence, since the grid-generated turbulence used in the tests

to obtain data for such correlations is not representative of the influence of wakes.

However, the mean velocity profile and the integral properties of a boundary layer will remain close to those of a corresponding undisturbed laminar flow as long as the local value of the intermittency factor remains below about 0.2. The error in the prediction of the boundary layer development from the presence of small turbulent spots created by large amplitude disturbances is likely to be small, provided the predicted location of the start of transition lies within, or not too far downstream of, the region where the local intermittency factor of the flow is below about 0.2. If the transitional boundary layer extends over a substantial part of the blade surface, then the boundary layer development and all aspects of its prediction do depend strongly on the early stages of the transition.

To assess the capability of an existing boundary layer method in predicting the boundary layer development on the suction surface of a compressor blade some calculations have been made for comparison with those measured in Cases 5 and 8. (Data are available up to the trailing edge for these two cases.) For each case, two predictions were made, each using a different transition model. In one of them, the National Gas Turbine Establishment (NGTE) boundary layer method was used, which employs Dunham's (1972) point-transition model; i.e., transition is assumed to be completed at a single point. For this, the measured pressure distribution was used as the input and a level of 4 percent free-stream turbulence was specified. (This choice of 4 percent turbulence is in accordance with the practice adopted for the use of the method in compressors.) The other calculation method, provided by Newman (1987), used the correlation of Abu-Ghannan and Shaw (1980), called the length-transition model for convenience. (In other respects, the boundary layer method supplied by Newman was similar to the NGTE one). For this 6 percent free-stream turbulence was specified in Case 5 and 4 percent in Case 8. The surface pressure distribution for this was from a coupled inviscid calculation, which gave excellent prediction compared with the measured data (Dong, 1988).

The comparison of calculated and measured momentum thickness and form parameter for Case 5 is shown in Fig. 12. It can be seen that transition is predicted to occur at $S/S_0 = 0.21$ with the point-transition model and to begin at $S/S_0 = 0.18$ with the length-transition model. Up to the predicted location of transition the agreement with the measured results is good, which is not surprising since the measured intermittency factor in Case 5 was still less than 0.2 at $S/S_0 = 0.21$ and the flow therefore predominantly laminar. Downstream of this point, the length transition model underestimates the growth of the boundary layer, resulting in an 20 percent error in the momentum thickness at the trailing edge.

In contrast, the use of a point transition model gives a good prediction of momentum thickness over most of the blade surface, despite the fact that such a crude model does not describe the physical process of transition at all properly. The assumption of a "point" transition has allowed the calculation to overestimate the rate of momentum thickness growth in the initial part of the measured transition region after the predicted location of transition. The measured mean value of θ was only held down by the laminar flow in the quiescent region and the momentum thickness growth rate rose sharply as soon as transition occurred in the quiescent region of the flow. The gap between the predicted and the measured results is therefore narrowed between about $S/S_0 = 0.4$ to $S/S_0 = 0.56$ when the boundary layer was approaching the end of transition; since the measured θ does not differ too much from the predicted value at that station, good agreement between the measured and the predicted results is obtained in the rest turbulent boundary layer.

The predicted H is much lower than the measured value from the predicted location of transition until about

$S/S_0 = 0.56$, that is throughout the transition region, with either the point- or the length-transition models. Once in the turbulent flow region the agreement becomes better. The same comparison made for Case 8 showed a very similar situation (Dong, 1988).

The fact that a crude point transition model can produce good prediction for the overall boundary layer development on the present supercritical compressor blade is of some significance. One would like to know how generally this is applicable and, in particular, whether significant underestimation of boundary layer growth may still be possible, using such a transition model. Since the prediction of wholly laminar or fully turbulent boundary layers in two dimensions is generally accurate the question can be narrowed to whether transition can end significantly further upstream of where it did in the present work.

The location of a laminar separation bubble (at low free-stream turbulence) on a supercritical-type blade is more or less fixed around 30 percent to 40 percent chord. Thus the only way for serious underestimation of boundary layer growth to occur in the design process would be if the wakes were very closely packed so that the merging of the leading edge of a downstream wake with the trailing edge of a previous turbulent spot occurs much nearer the blade leading edge (see the illustration in Fig. 10). A measure of the closeness of the wakes is the reduced frequency Ω , which is defined as the ratio of time a particle takes to travel through a blade row (with the speed of inlet velocity) to the wake passing period. A reasonable approximation for the average speed of the wake over the blade is the inlet velocity; as an approximation the leading edge and the trailing edge of a turbulent spot travel at 0.75 and 0.55 of this inlet flow velocity. With these approximations it was found that until the value of Ω exceeds 2.5, the location of the spot merging (and the end of transition) will lie downstream of about 40 percent blade surface distance from blade leading edge; beyond 40 percent the transition is caused by the separation bubble. The possibility of underestimating boundary layer growth therefore remains open for cases with Ω substantially greater than 2.5. That transition models based on blade test data obtained without wakes being modeled properly are able to predict the overall development of the boundary layer reasonably well in the presence of wakes is largely due to the fact that the overall effect of the wakes are relatively small for the supercritical-type compressor blade. Even without wakes, such as in Cases 1 and 2, the laminar boundary layer on the blade suction surface cannot last for long before it is terminated by either a separation bubble, or transition promoted by the free-stream turbulence. It is true that the presence of wakes will initiate a much earlier start of transition, but the transition process then is also much longer (typically 60 percent of blade surface distance in Case 5, compared with less than 5 percent in Case 1 and 40 percent in Case 2). The mechanism responsible for this is the calmed region forming the laminar boundary layer immediately behind a turbulent spot initiated either by the wake or by high levels of free-stream turbulence; in the calmed region, there is unusual stability with increased resistance to undergoing transition. The prolonged existence of some laminar flow on a blade offsets the increase in loss resulting from some early turbulent flow due to the wake interaction (see Fig. 6).

The overall effect of the wakes on the boundary layer development on the suction surface on the compressor blade is very different from that on the pressure surface, which is more like the case of a turbine; see Hodson (1984). In the case of a turbine the laminar boundary layer can exist over the entire blade surface in the absence of wakes, even with high free-stream turbulence. Wakes incident on the suction surface of a turbine blade (or the pressure surface of the compressor blade tested here) result in a long region of transitional boundary layer and as a result the loss increases dramatically: 44 percent

on the pressure surface in Case 5 here compared with Case 1; 50 percent for the turbine rotor suction surface tested by Hodson (1984). For a compressor blade, the dominant profile loss comes from the *suction* surface boundary layer, so the large proportional increase in loss on the pressure side translates into only a small increase in the overall loss.

The effect of wakes on the overall boundary layer development was studied earlier by Walker (1968, 1974). In the later paper, Walker argued that the relatively small effect of wakes was a result of delay in the start of transition by the stabilizing effect associated with the periodic unsteady effect of a wake, but the evidence presented in this paper has shown that this explanation is not correct. The present results also seem to contradict those reported by Evans (1978), in which the loss was found to be significantly higher in the midspan region of a stator than that in a cascade of blades with similar profile. Evans used stator blades with twice the chord of the rotor, so the reduced frequency was high. Furthermore, Evans' stator was twisted in the wrong direction so that the sections were mis-staggered at all the spanwise positions other than the midspan. The comparison also was made at a 3.5 deg incidence at midspan which, together with the mis-staggering, would have certainly enhanced three-dimensional effects. In fact, his measured pressure distributions on the blades in the cascade and in the machine indicated quite significant differences: There was evidence of a turbulent separation on the stator, which was not seen in the cascade, so almost certainly there would have been separation of the flow in the corners of the stator suction surface and endwalls. This separation would cause significant displacement of the surface boundary layer toward the midspan region; see Dong et al. (1987).

The present work leads to the conclusion that the rotor wakes could not have caused the measured loss at midspan for a supercritical-type stator blade to be much higher than anticipated, as discussed in the introduction to Part 1. Results published some time after this present work was started (e.g., Behlke, 1986) have shown that the use of supercritical-type blade in a compressor could result in worsening of flow near endwall regions compared with a more conventional blade row. The main reason for this is that the supercritical blade is usually designed with much higher loading (or lower solidity), since cascade tests such as those reported by Hobbs and Weingold (1984) demonstrated that they have such loading capability. But whereas this can be achieved in a highly controlled cascade, it may not be obtainable in the endwall regions of a compressor where it is the endwall boundary layer that limits the performance for blades with low solidity. This could result in strong endwall boundary layer separation with the blade surface boundary layer migrating toward the midspan region.

The evidence that the wakes have a relatively small effect on the overall boundary layer development does mean that blade can probably be designed according to some existing empirical loading criterion derived from tests in quite different environment, for example, the Stratford criterion (1959). Indeed, the blade tested was designed with a conservative loading (H near 1.6 on the suction surface downstream of the velocity peak), and the measured results did show reasonable agreement with the prediction near the trailing edge, though not over much of the surface where the measurements showed the flow to remain transitional. As pointed out previously, if the value of the reduced frequency is not higher than about 2.5, the boundary layer can be predicted reasonably accurately using a transition model like the one by Dunham (1972) plus 4 percent

turbulence. A designer should always bear in mind, however, that this does not mean that the existing transition model is capable of describing the detail of the flow on a blade. It is wise, therefore, to allow certain margin, especially when a velocity distribution radically different from those proven by tests is prescribed.

4 Conclusions

A supercritical compressor blade has been tested at design incidence in a low-speed, large-scale cascade wind tunnel with incident wakes from upstream. The wake was found to create a turbulent spot where it impinged on the blade and this spot quickly became self-sustaining, behaving very much like a turbulent spot found in a transitional boundary layer on a flat plate. The spot grew as it traveled downstream, being left behind by the wake, which was convected by the free stream. The laminar separation bubble, unlike that observed in a cascade test without wakes present, was a periodically unsteady phenomenon when wakes were present; the bubble disappeared momentarily if the wake initiated turbulent flow before the laminar flow could separate. In spite of causing very early transition on the blade, however, the wake interaction with the boundary layer also resulted in a stabilizing effect on the laminar boundary layer behind a turbulent spot. This prolonged the extent of laminar flow seen on the blade surface compared with the case without wakes. The presence of wakes therefore did not have a very significant effect on the trailing edge properties of the boundary layers, despite the differences in the details of transition and development in the two cases.

The boundary layer at the trailing edge, and therefore the loss, also seemed to be rather insensitive to the change in other parameters such as the wake passing frequency, the extra free-stream turbulence, or the blade solidity. The pattern of the wake interaction with the boundary layer observed at low Reynolds number was found to be quite similar to that observed at representative design Reynolds number.

The use of a very simple point-model for transition was shown to give predictions matching the experimental values of momentum and displacement thickness quite well over most of the blade surface, including near the trailing edge; the point model was far better than the length-transition model. Nevertheless it is clear that accurate prediction of details of the boundary layer development on a compressor blade is at present still very imperfect, even for the near-design conditions. This is because none of the available transition models is capable of describing properly the complex transition process in the presence of wakes. Even the most sophisticated numerical schemes for solving the boundary layer equations are currently incapable of modeling the unsteady behavior with wakes, such as intermittent transition and separation, which are known to occur. The agreement in overall properties, such as thicknesses at the trailing edge, must be regarded as fortunate rather than evidence of correctness and reliability.

It follows that the optimization of blade profiles, using a boundary layer method and a prescribed velocity distribution method, still has limited reliability; whenever a new profile is designed in this way caution must be exercised.

Based on the experimental evidence, it is concluded that the observation of unexpectedly high loss measured in the midspan region of a supercritical stator was more likely to be due to the influence of endwall flow existing in the compressor, rather than due to the effect of wakes.

The Measurement of Boundary Layers on a Compressor Blade in Cascade: Part 4—Flow Fields for Incidence Angles of -1.5 and -8.5 Degrees

W. C. Zierke

S. Deutsch

Applied Research Laboratory,
The Pennsylvania State University,
State College, PA 16804

Measurements, made with laser Doppler velocimetry, about a double-circular-arc compressor blade in cascade are presented for -1.5 and -8.5 deg incidence angles and a chord Reynolds number near 500,000. Comparisons between the results of the current study and those of our earlier work at a 5.0 deg incidence are made. It is found that in spite of the relative sophistication of the measurement techniques, transition on the pressure surface at the -1.5 deg incidence is dominated by a separation "bubble" too small to be detected by the laser Doppler velocimeter. The development of the boundary layers at -1.5 and 5.0 deg is found to be similar. In contrast to the flow at these two incidence angles, the leading edge separation bubble is on the pressure surface for the -8.5 deg incidence. Here, all of the measured boundary layers on the pressure surface are turbulent—but extremely thin—while on the suction surface, a laminar separation/turbulent reattachment bubble lies between roughly 35 percent and 60 percent chord. This bubble is quite thin, and some problems in interpreting the backflow data are discussed.

Introduction

For the last several years, we have been using a one-component laser Doppler velocimeter (LDV) in conjunction with pressure, five-hole probe, hot-wire, and flow visualization measurements to document, in great detail, the flow field about a double-circular-arc compressor blade in cascade. Although quite sophisticated numerical codes now exist for the prediction of turbomachinery flows, there are very few detailed experimental data, under typical flow conditions, against which to test them. Obtaining such data provides the overall rationale for the experiment. A cascade flow was chosen as it is both the simplest flow field to exhibit some of the complexities of turbomachines—that is, the blade-to-blade interactions and curvature effects—and the simplest turbomachinery flow to set up in some universal manner—that is, periodic and two-dimensional. With similar reasoning a double-circular-arc blade was chosen, not because it was typical of current blade designs, but because it was the easiest geometry over which to traverse the LDV.

We have previously reported measurements at an incidence angle of 5.0 deg (stagnation point on the pressure surface) and at a chord Reynolds number near 500,000 (see Deutsch and

Zierke, 1987, 1988a, 1988b). In Part 1 of that three-part study, we described the design and testing of a unique cascade facility necessitated by the need for LDV surveys; in Part 2, we discussed the turbulent boundary layers on the suction surface; and in Part 3, we examined the transitioning boundary layers on the pressure surface as well as the asymmetric recirculating flow field in the near wake.

From a computational point of view, one of the most fundamental changes one can envision on a compressor blade is a change in incidence angle. Over the past two years, we have, to study the effect of this variation, been acquiring detailed flow data at an incidence angle of -1.5 deg—an incidence near design—and at an incidence angle of -8.5 deg—an incidence that we believe is near the minimum loss for this geometry.

In the next two sections, we shall briefly review the configuration of the cascade tunnel, the LDV system, and the data acquisition and reduction systems. We then present data from the cascade tests and the pressure surface, suction surface, and wake measurements. These are followed by a summary and conclusion section.

The Cascade Tunnel

The cascade wind tunnel has a 0.37 m by 0.64 m test section with a maximum air speed of 35 m/sec. Over the speed range

Contributed by the International Gas Turbine Institute and presented at the 34th International Gas Turbine and Aeroengine Congress and Exhibition, Toronto, Ontario, Canada, June 4–8, 1989. Manuscript received at ASME Headquarters January 4, 1989. Paper No. 89-GT-72.

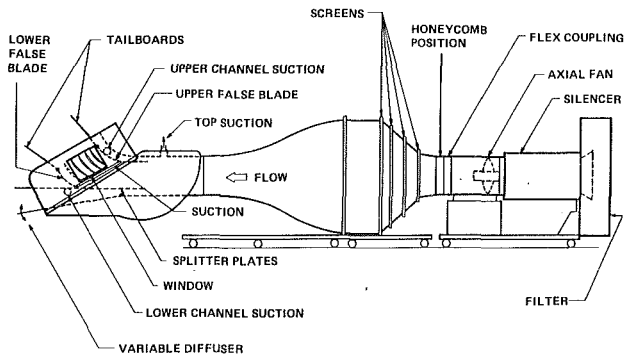


Fig. 1 Cascade wind tunnel with flow controls

Table 1 Blade geometry

c	228.6 mm
s	106.8 mm
t_{\max}	12.5 mm
r_{LE}	914.4 μm
r_{TE}	914.4 μm
σ	2.14
AR	1.61
γ	20.5°
κ_1	53.0°
κ_2	-12.0°
ϕ	65.0°

of 24–35 m/sec, the tunnel operated with a free-stream turbulence level of 0.18 percent. Figure 1 shows a schematic of the open return facility.

The blade section used in the test was a double-circular-arc

Table 2 Flow conditions

i	5.0°	-1.5°	-8.5°
β_1	58.0°	51.5°	44.5°
β_2	4.0°	2.1°	-0.6°
β_m	39.9°	32.9°	25.9°
$\frac{\epsilon}{\delta_d}$	54.0°	49.4°	45.1°
	16.0°	14.1°	11.4°
V_1	33.11 m/sec	32.88 m/sec	33.28 m/sec
V_2	17.59 m/sec	20.48 m/sec	23.74 m/sec
V_m	22.88 m/sec	24.38 m/sec	26.39 m/sec
V_x	17.55 m/sec	20.47 m/sec	23.74 m/sec
\bar{w}	0.151 ^a	0.094 ^a	0.028 ^a
	0.172 ^c	0.071 ^b	0.024 ^b
			0.018 ^c
\bar{C}_{p_2}	0.463	0.473	0.421
$\frac{C_L}{D}$	0.952	0.821	0.956
	0.658	0.555	0.452
Re_c	505,000	501,000	507,000

^a measured values

^b values computed at 131.9% chord

^c values computed at 152.6% chord

blade with 65 deg of camber and a 228.6 mm chord length. Both the leading and trailing edges were machined to a 0.914 mm radius. The blade aspect ratio was 1.61. Camber line and thickness relationships may be found in the Appendix to Part 1 of this study (Deutsch and Zierke, 1987). The cascade test section also is shown in Fig. 1. The cascade had a solidity of 2.14. The stagger angle was 20.5 deg. Table 1 summarizes the blade geometry, while Table 2 gives the flow conditions for all three incidence angles.

Two-dimensionality and periodicity are normally controlled in cascades by continuous blade pack suction but, because of the need for LDV access, this was not possible here. Details of our complicated alternative system may be found in Part 1 (Deutsch and Zierke, 1987). We found that we could create a two-dimensional flow by employing a strong suction, which was controllable in the blade-to-blade direction, just upstream

Nomenclature

AR = aspect ratio
 c = blade chord length
 C_f = skin friction coefficient
 $= \frac{\tau_w}{\frac{1}{2}\rho U_e^2}$
 C_p = static-pressure coefficient
 $= \frac{p-p_1}{\frac{1}{2}\rho V_1^2}$
 D = diffusion factor
 H_{12} = first shape factor = $\frac{\delta^*}{\theta}$
 i = incidence angle = $\beta_1 - \kappa_1$
 L_p, L_s = pressure and suction surface length scales from the point of minimum velocity to a point where the velocity defect is $\frac{1}{2}(U_e - u_{CL})$
 LDV = laser Doppler velocimeter

p = static pressure
 p_T = total or stagnation pressure
 r = radius
 Re_c = blade chord Reynolds number = $\frac{cV_1}{\nu}$
 Re_θ = momentum thickness Reynolds number = $\frac{\theta U_e}{\nu}$
 Re_{θ_s} = momentum thickness Reynolds number for onset of transition
 s = blade spacing
 t_{\max} = maximum blade thickness
 u = streamwise velocity
 u^+ = dimensionless velocity in the inner boundary layer
 $= \frac{u}{u_r}$

u_r = shear or friction velocity
 $= \sqrt{\frac{\tau_w}{\rho}}$
 U_{BF} = maximum backflow velocity
 U_e = velocity at the boundary layer or wake edge
 V = velocity
 x = streamwise coordinate
 y = coordinate normal to the blade surface or across the wake
 y^+ = dimensionless coordinate normal to the blade surface in the inner boundary layer
 $= yu_r/\nu$
 β = flow angle measured from the axial direction; Falkner-Skan streamwise pressure gradient parameter

of the blade leading edge line. Tailboards were used to control the relative exit angle of the flow. The two-dimensionality and periodicity of the flow were determined by conducting measurements of the inlet and outlet velocity profiles using five-hole probes. These surveys were referenced to a Pitot-static probe located 73 mm upstream of the blade pack leading edge line.

Cascade inlet flow profiles were documented by five-hole probe measurements approximately 36 mm upstream of and parallel to the leading edge line. Outlet flow profiles were measured parallel to the trailing edge line and 31.9 percent chord downstream of this line. Inlet velocity surveys were made after the outlet flow had been determined to be satisfactory. Inlet surveys showed some streamline bending due to the presence of the blades and the inlet values presented represent an average value of measurements over two blade spacings.

The Laser Doppler Velocimeter

All blade boundary layer and near-wake measurements were made using a single component LDV. The LDV system was described in detail in Part 2 of this study (Deutsch and Zierke, 1988a). For completeness, a brief description is included here.

For all the LDV measurements, a specially designed traversing mechanism was used that matched the arc of motion of an optics cradle to that of the blade curvature. All measurements were made in the plane of the local blade normal. Prior to the LDV measurements, a reference distance was established by focusing the LDV measurement volume on an insert, which securely fit over the blade. Repeatability in establishing a measurement reference was estimated to be ± 0.05 mm, and this uncertainty is probably the major source of scatter in the velocity data.

A five-watt, Spectra-Physics, argon-ion laser and standard TSI backscatter optical components were used for the measurements. The ellipsoidal measurement volume was reduced through the use of a (2.71:1) beam expander: The predicted measurement length in the normal to the blade direction was $33 \mu\text{m}$. Optical shifting at 5 MHz was used throughout. Note that to measure close to the blade surface, we tilted the optical cradle at an angle of roughly 1 deg. Silicon carbide particles having a mean diameter of $1.5 \mu\text{m}$ were used for laser seeding.

LDV data acquisition and reduction were accomplished by using a direct link to a VAX 11/782 computer. Mean velocity, local turbulence intensity, skewness, and kurtosis were determined by ensemble-average and monitored for every point in a profile. We have found in these boundary layers that an

ensemble size of 200 is sufficient for points at which the local turbulence intensity is less than 5 percent, 500 when less than 10 percent, and 1000 thereafter. At each chord position, profiles were defined by statistically treating the data for six individual experiments. Error bands, presented on the LDV data plots, represent 95 percent confidence levels as determined by a Student's t test.

The preliminary data analysis is automated on the VAX computer. The effect of the normal pressure gradient on the boundary layer profiles is accounted for first. Details of this technique are given by Deutsch and Zierke (1986) and follow the approach suggested by Mellor and Wood (1971) and Ball, Reid, and Schmidt (1983). Briefly the technique assumes that the profile may be represented as

$$u_{\text{meas}} = u + u_{\text{inv}} - U_e$$

so that the edge velocity, U_e , can be determined by extrapolating the outer inviscid flow, u_{inv} , to the wall (where $u_{\text{meas}} = u = 0$) in some reasonable manner.

Cascade Flow Field

Following the completion of the measurements of the flow field for a 5.0 deg incidence angle, we rotated the entire test section and established a new periodic, two-dimensional flow field. Five-hole probe measurements yielded an incidence angle of -1.5 deg and a Re_c of 501,000. The average inlet velocity of 32.88 m/sec was computed from the (gage) measurements of $p_1 = -382.0$ Pa and $p_{T1} = 269.6$ Pa. As measured with a five-hole probe 31.9 percent chord downstream of the blade trailing edge, the outlet flow yielded an axial-velocity ratio of 1.00 (on a day-to-day basis, the variation was within 3 percent) and a flow turning angle of 49.4 deg—after averaging across the three center blade passages. The deviation angle was 14.1 deg. Measurements also give a loss coefficient, $\bar{\omega}$, of 0.094 and a static-pressure rise coefficient, $(C_p)_2$, of 0.473 while calculations using the equation of Lieblein and Roudebush (1956)

$$\bar{\omega} = 2 \left(\frac{\theta}{c} \right) \frac{\sigma}{\cos(\beta_2)} \left[\frac{\cos(\beta_1)}{\cos(\beta_2)} \right]^2 \left\{ 1 - \left[\frac{\theta}{c} \right] \frac{\sigma H_{12}}{\cos(\beta_2)} \right\}^{-3} \left(\frac{2H_{12}}{3H_{12} - 1} \right)$$

give an $\bar{\omega}$ of 0.071. Our calculation of the diffusion factor of Lieblein, Schwenk, and Broderick (1953)

Nomenclature (cont.)

γ = stagger angle
 δ = boundary layer thickness
 (where $u = 0.99 U_e$)

δ^* = displacement thickness
 $= \int_0^\infty \left(1 - \frac{u}{U_e} \right) dy$

δ_{BF} = depth of backflow
 δ_D = deviation angle = $\beta_2 - \kappa_2$
 ϵ = fluid turning or deflection angle = $\beta_1 - \beta_2$

η = normalized distance across the wake

θ = momentum thickness
 $= \int_0^\infty \frac{u}{U_e} \left(1 - \frac{u}{U_e} \right) dy$

κ = blade metal angle
 ν = kinematic viscosity (0.150 cm^2/sec for air)

Π = Coles' wake parameter
 ρ = fluid density (1.205 kg/cm^3 for air)

σ = blade solidity = c/s
 τ_w = wall or surface shear stress

ϕ = camber angle = $\kappa_1 - \kappa_2$
 ω = total-pressure loss coefficient = $\frac{p_{T1} - p_{T2}}{1/2 \rho V_1^2}$

Subscripts

CL = at the wake centerline
 inv = inviscid
 LE = leading edge
 m = mean flow

meas = measured
 p = pressure surface
 s = suction surface
 TE = trailing edge
 x = axial direction
 θ = tangential direction
 1 = inlet (upstream five-hole probe measurement station)
 2 = outlet (downstream five-hole probe measurement station)

Superscripts

— = average over the blade passage

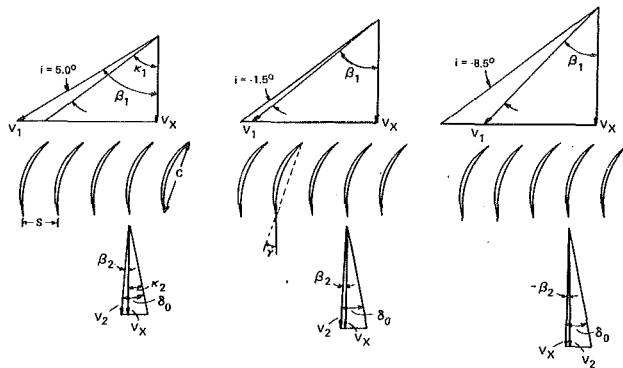


Fig. 2 Velocity triangles

$$\bar{D} = 1 - \frac{\bar{V}_2}{V_1} + \frac{V_{\theta 1} - \bar{V}_{\theta 2}}{2\sigma V_1} = 1 - \frac{\cos(\beta_1)}{\cos(\beta_2)} + \frac{\sin(\beta_1) - \cos(\beta_2)\tan(\beta_2)}{2\sigma}$$

yields $\bar{D} = 0.555$ and shows while a risk of separation still exists for $i = -1.5$ deg, the risk is not as great as for the flow field with $i = 5.0$ deg (where $\bar{D} = 0.658$). Figure 2 shows the velocity triangles for all of the inlet and outlet flow measurements.

The blade static-pressure distributions for both the 5.0 and -1.5 deg incidence angles appear in Fig. 3. The vertical lines in Fig. 3 show the locations of LDV measurements. Integrating the distribution for $i = -1.5$ deg gives a lift coefficient of 0.821. We can compare this pressure distribution with the pressure distribution corresponding to the 5.0 deg incidence angle. Although the two distributions are similar, one can notice differences that could strongly affect the boundary layers on both the pressure and suction surfaces. For the -1.5 deg incidence, the favorable streamwise pressure gradient near the leading edge of the pressure surface is much less severe and extends only to 3 percent chord. Downstream, the flow consists of a mildly adverse pressure gradient from 3 percent chord to 62 percent chord followed by an increasingly strong acceleration to the trailing edge. The initially laminar boundary layer confronts a slightly stronger adverse pressure gradient for this second incidence angle. Transition should occur in this region with a more probable chance of completion than that of the transition on the pressure surface at the 5.0 deg incidence.

As for the 5.0 deg incidence case, the very large adverse pressure gradient at the leading edge of the suction surface implies a leading edge separation. Unlike the flow for the first incidence, however, a small favorable pressure gradient exists on the suction surface from 3 percent chord to 9 percent chord. Thus the flow history of the suction surface boundary layers for the first two incidence angles differs and the boundary layers for the second incidence angle should be thinner. Moreover, although we were not able to measure the leading edge separation "bubble" for either incidence, it is likely that the separation bubble will be smaller for $i = -1.5$ deg. Both pressure distributions show a vanishing adverse pressure gradient near 80 percent chord indicating a possible separation region near the trailing edge of the suction surface.

Results from the surface flow visualization corroborate the blade static-pressure distribution results on the suction surface. With 95 percent confidence, the chemical sublimation method shows a region of low shear stress at 45.1 percent \pm 2.3 percent chord indicating that separation occurs a little earlier for the -1.5 deg incidence than for the 5.0 deg incidence. On the pressure surface, however, the surface flow visualization gave some surprising results. With the same level of confidence, a region of low shear stress was found between 14.0 percent \pm 5.5 percent chord and 38.2 percent \pm 5.2 percent chord. Thus the results indicate a separation region rather than the anticipated transition region.

As shown on the blade static-pressure distribution in Fig.

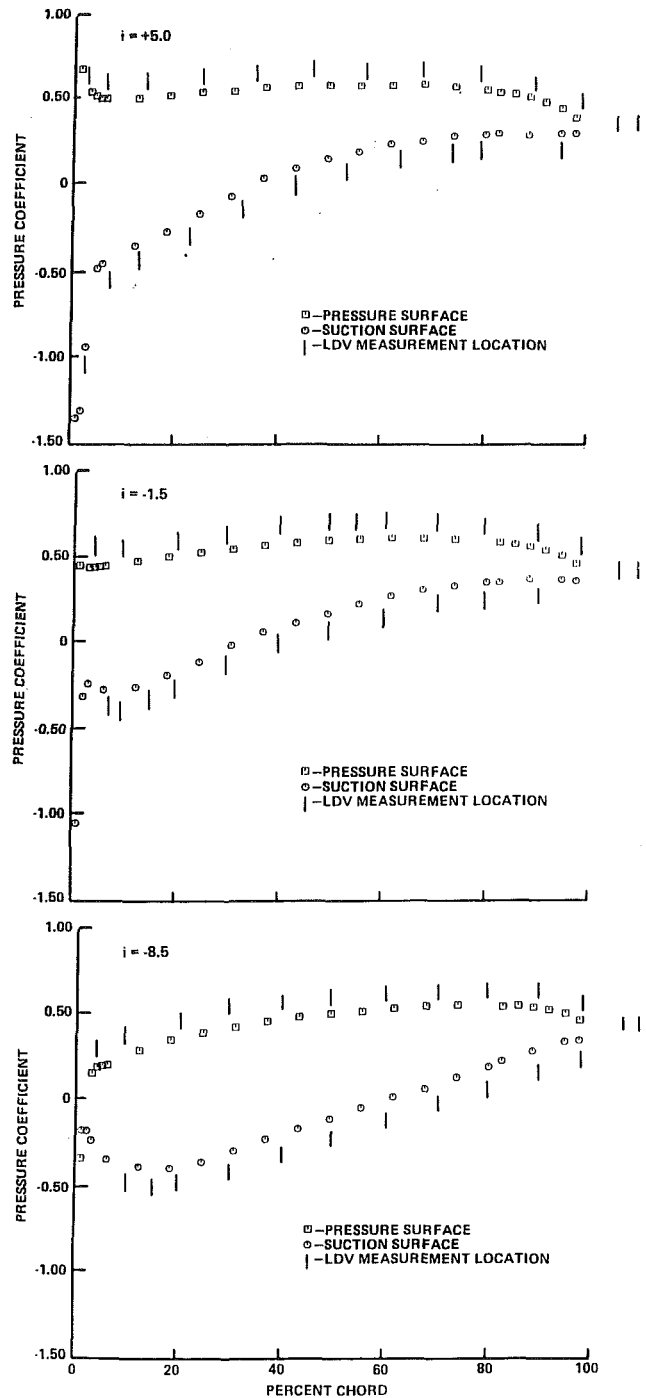


Fig. 3 Blade static-pressure distributions

3, we measured boundary layers at 12 chord locations on the pressure surface. Figure 4 shows these boundary layer profiles. At this incidence angle, the streamlines near the leading edge show less curvature than they did at the 5.0 deg incidence. Therefore, the inviscid region of the velocity profiles is quite linear. Again, the error bands give 95 percent confidence bands as determined by the Student's t test. These bands tend to represent the repeatability of measuring at the same spatial location for each of the six tests and are only visible when the boundary layer is very small and the velocity gradient is very large.

Suction surface boundary layers were measured at 11 chordwise locations. Figure 5 shows the velocity profiles and Fig. 3 shows the location of these profiles relative to the blade static-

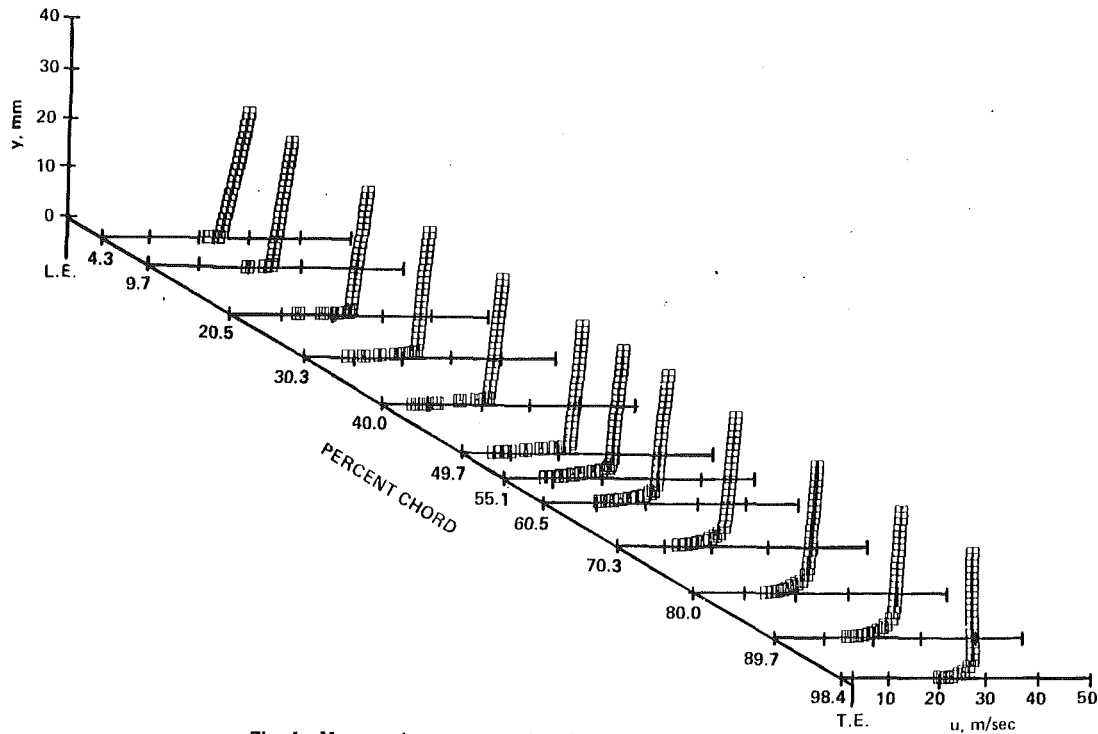


Fig. 4 Measured pressure surface boundary layers for $i = -1.5$ deg

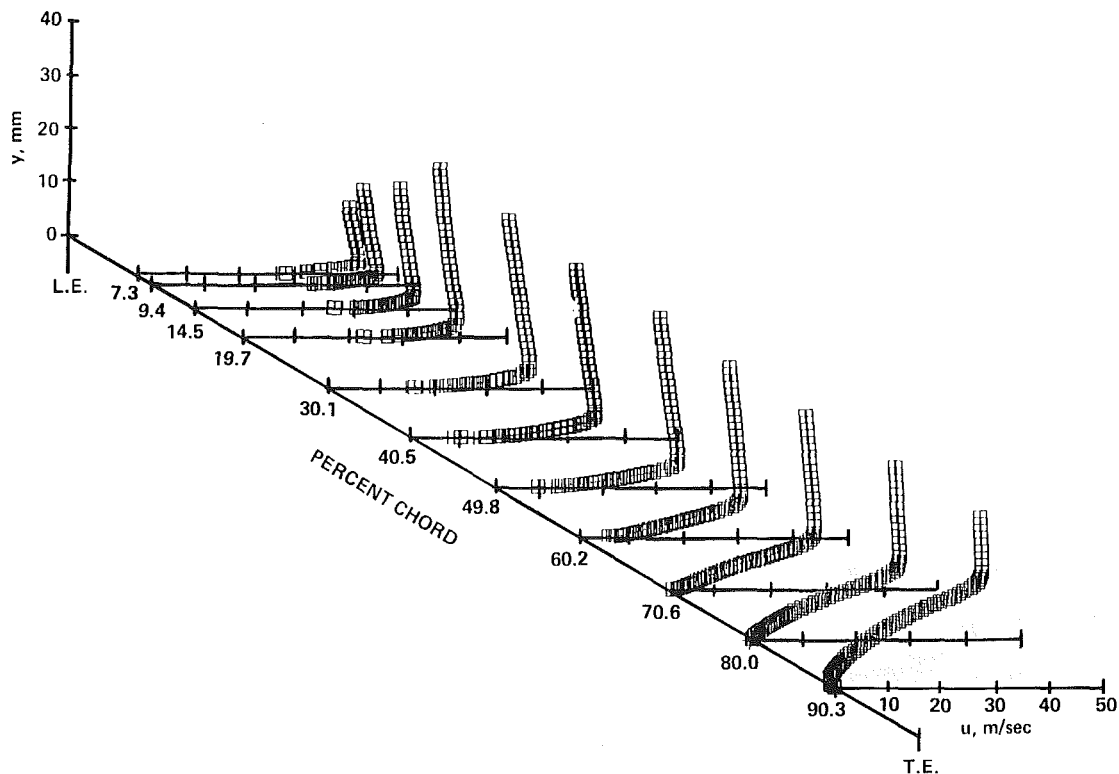


Fig. 5 Measured suction surface boundary layers for $i = -1.5$ deg

pressure distribution. Once again, a linear, normal pressure gradient is evident. As expected from the pressure distribution and the surface flow visualization, separation occurs near the trailing edge.

LDV measurements of the near wakes were made at 106.0 percent chord and 109.7 percent chord, while five-hole probe measurements of the far wake were made at 131.9 percent chord. Figure 6 shows the mean values and 95 percent con-

fidence bands for the measurements of all three wake profiles. Similarly to the 5.0 deg incidence, the near wakes are asymmetric and show negative mean velocities at the wake center. The far wake shows symmetry and a much shallower depth than the near wakes. Surprisingly, however, the width of the far wake is similar to the widths of the two near wakes.

A third periodic, two-dimensional flow field was established by once again rotating the entire test section. Inlet five-hole

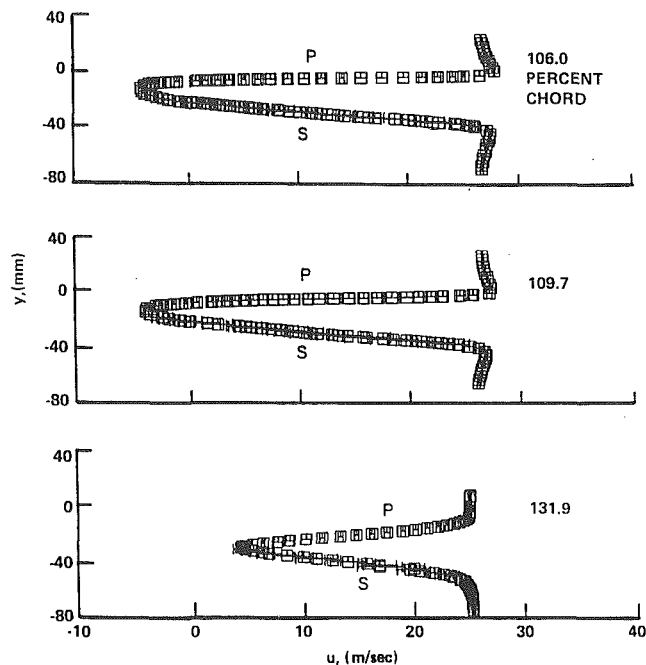


Fig. 6 Measured wakes for $i = -1.5$ deg

probe measurements yielded an incidence angle of -8.5 deg and a Re_c of 507,000. The average (gage) measurements of $p_1 = -315.8$ Pa and $p_{T1} = 351.6$ Pa result in an average inlet velocity of 33.28 m/sec. The outlet flow showed a substantially different flow field at this incidence angle than the flow fields that existed at the first two incidence angles. The periodic flow field showed very small wakes as measured with a five-hole probe 31.9 percent chord downstream of the blade trailing edge—indicating a substantially reduced region of separation, relative to the first two incidence angles.

The five-hole probe measurements give an average turning angle of 45.1 deg and a static-pressure rise coefficient, $(C_p)_2$, of 0.421. The velocity triangles are shown in Fig. 2. A deviation angle of 11.4 deg and a loss coefficient, $\bar{\omega}$, of 0.028 also indicate a reduced region of separation relative to the values from the first two incidence angles. Using the equation of Lieblein and Roudebush (1956), we computed values for $\bar{\omega}$ of 0.024 and 0.018 using the far-wake data at 131.9 percent chord and 152.6 percent chord, respectively. The diffusion factor of Lieblein, Schwenk, and Broderick (1953) gives 0.452, which also shows a reduced risk of separation (relative to $i = 5.0$ deg and $i = -1.5$ deg where \bar{D} equals 0.658 and 0.555, respectively).

The blade static-pressure distribution, for $i = -8.5$ deg, is shown in Fig. 3. Note that the chord location of maximum blade loading has moved from the leading edge (for $i = 5.0$ deg and $i = -1.5$ deg), downstream to about 21 percent chord. The large adverse streamwise pressure gradient near the leading edge has shifted from the suction surface to the pressure surface. This shift implies that a leading edge separation occurs on the pressure surface for this incidence angle. The adverse gradient on the pressure surface becomes less severe with downstream distance until near 75 percent chord, where a favorable gradient gradually becomes more pronounced toward the trailing edge. A strong acceleration of the flow exists on the first 18 percent chord of the suction surface and one would expect laminar boundary layers in this region. Either transition or separation should be expected on the aft 82 percent chord where the flow decelerates. Unlike the pressure distributions for the first two incidence angles, however, no extended region of zero streamwise pressure gradient exists near the trailing edge of the suction surface indicating no extended region of separation.

For this incidence angle, we attempted two types of surface

flow visualization: the chemical sublimation method and the oil film method. On the pressure surface, the oil film method showed oil accumulating near the leading edge, which indicated a possible separation and reattachment. On the suction surface, both methods showed some interesting results. To 95 percent confidence, the oil film method showed that the flow detached from the surface at 35.3 percent \pm 2.0 percent chord and reattached to the surface at 59.8 percent \pm 2.3 percent chord. Meanwhile, the chemical sublimation method showed transition to occur at 56.0 percent \pm 0.8 percent chord. Evidently, the appearance of a separation bubble has triggered transition from laminar to turbulent flow. The oil film method also shows a possible separation very near the trailing edge and evidence of the corner disturbances near the sidewalls. However, both surface flow visualization methods show an adequate core region of two-dimensional flow.

Figures 7 and 8 show the LDV measured velocity profiles—both mean values and 95 percent confidence bands—on the pressure and suction surfaces, respectively. The normal pressure gradients are linear as they were when $i = -1.5$ deg. Near the leading edge of the suction surface, no discernible boundary layer could be measured since the strong acceleration causes the boundary layers to be very thin.

Wakes were measured in two locations in the near-wake region and two locations in the far-wake region. Figure 9 shows the LDV measurements at 106.0 percent chord and 109.7 percent chord and the five-hole probe measurements at 131.9 percent chord and 152.6 percent chord. As one might guess, these wake profiles look quite different from the wake profiles for the other two incident angles. The near wakes are nearly symmetric and show no mean negative velocities—again indicating that no large region of separation occurs at the blade trailing edge. The symmetric far-wake profiles become much less deep but change very little in width.

Pressure Surface for a -1.5 Degree Incidence

The blade static-pressure distributions of Fig. 3 and the measured velocity profiles of Fig. 4 showed some differences between the pressure surface flow fields for $i = -1.5$ deg and $i = 5.0$ deg. After accounting for the normal pressure gradient and determining U_e and δ^* , we plotted the velocity profiles in outer variables. For the boundary layers at 4.3 percent and 9.7 percent chord, the comparisons between the data and the similarity solutions of Falkner and Skan (1931) were poor because the calculated values of δ^* used to normalize y are questionable in these extremely thin boundary layers. Comparisons at 20.5 percent and 30.3 percent chord show a continuing decrease in streamwise momentum of the measured profiles relative to the Falkner-Skan profiles: Falkner-Skan solutions could not be computed at 40.0 percent and downstream since the values of β (a streamwise pressure gradient parameter) indicated that laminar boundary layers would separate at these chord locations. The profiles at 40.0 percent and 49.7 percent chord are similar to the profiles on the suction surface at $i = 5.0$ deg where the boundary layers are recovering from a leading edge separation bubble.

At chord locations 49.7 percent chord and downstream, we successfully fit the data to the wall-wake equation. However, since the boundary layers at 49.7 percent chord and 55.1 percent chord showed negligibly small logarithmic region, transition to turbulence may not be complete. The wake region vanishes near the 80.0 percent chord location (the wake parameter of Coles (1956), P_i , becomes zero). Downstream, the values of Π become negative—corresponding to the increasingly strong favorable streamwise pressure gradient.

A review of the flow visualization results shows a region of low shear stress between 14.0 percent \pm 5.5 percent chord and 38.2 percent \pm 5.2 percent chord. These results, in conjunction with the outer variable plots, seem to indicate the presence of

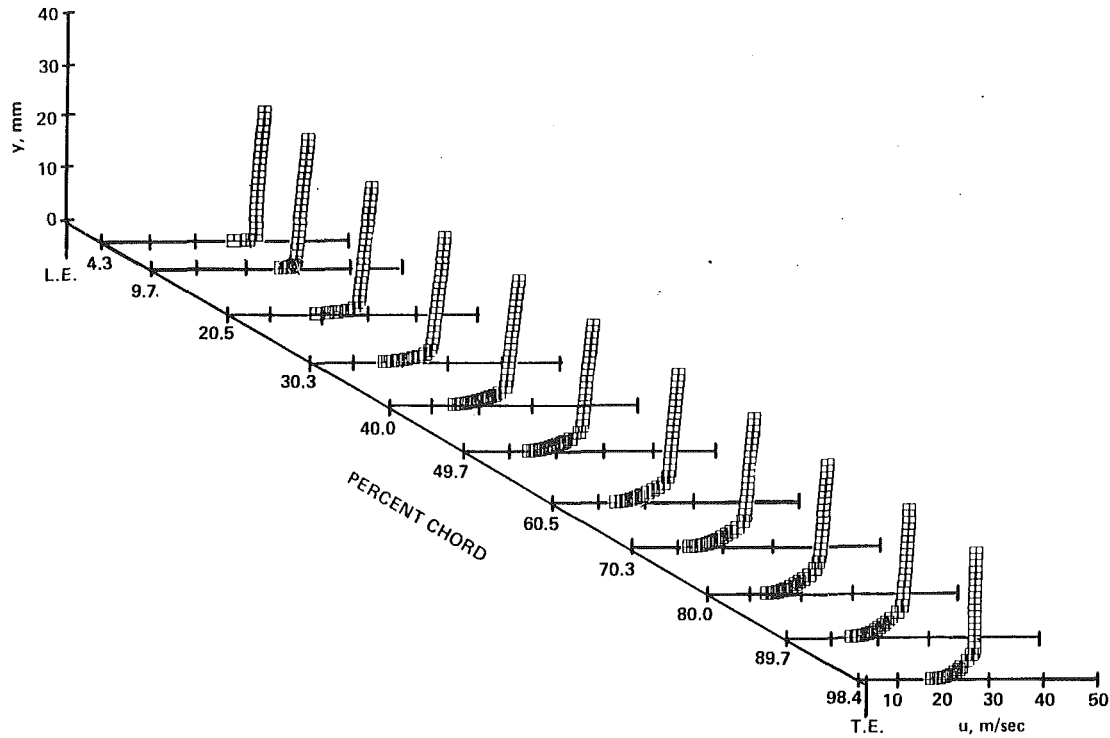


Fig. 7 Measured pressure surface boundary layers for $i = -8.5$ deg

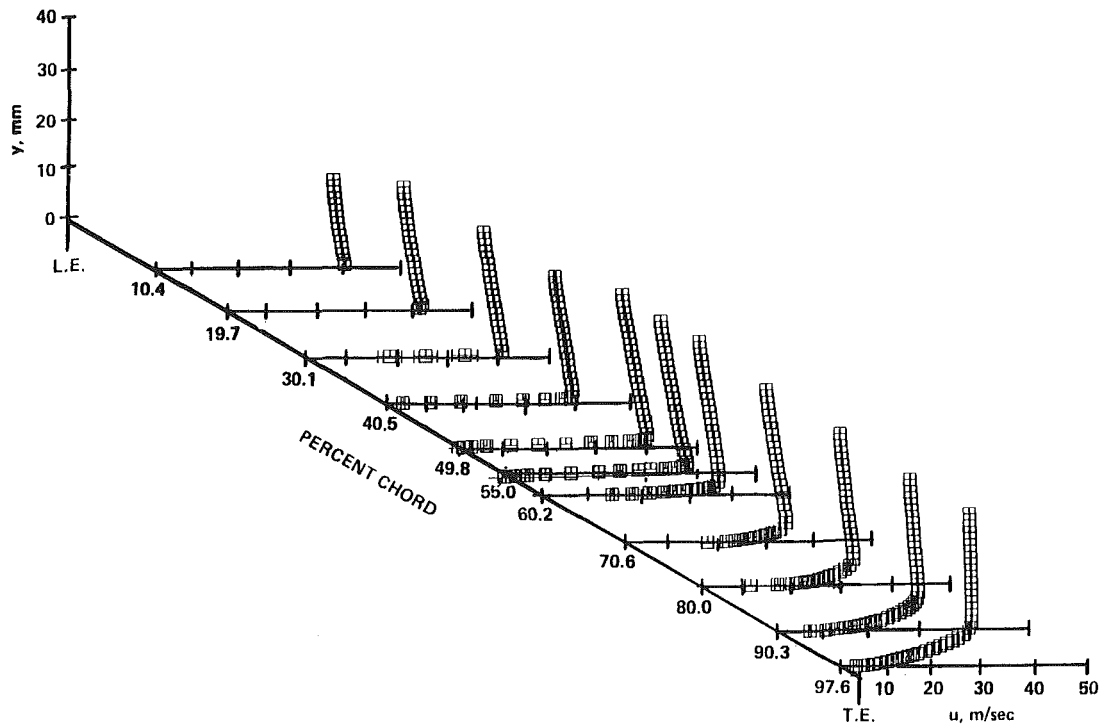


Fig. 8 Measured suction surface boundary layers for $i = -8.5$ deg

a laminar flow separation bubble with at least a partial transition to turbulence. Completion of the transition to turbulence may take place downstream of the separation bubble. This speculation may seem strange since we found no flow reversal in any of the boundary layers measured on this surface. Later results, measured on the suction surface when $i = -8.5$ deg, however, seem to indicate that we may not have penetrated the boundary layers far enough to find any backflow. The empirical relationships of Abu-Ghannam and Shaw (1980) place the onset of transition at 40.6 percent chord. This location may be in the correct vicinity, but we should ignore it since

these empirical relationships come from data of "natural" transition with no separation bubble. Transition, however, does take place. Because the transition to turbulence results in boundary layers with more streamwise momentum, a plot of mean velocity versus percent chord at a fixed distance above the blade can help determine the location of transition. Figure 10 shows this plot for $y = 0.254$. The initial decrease corresponds to boundary layer growth. A sharp rise from the 55.1 percent chord location to the 70.3 percent chord location corresponds to transitional boundary layers. The mean velocity stops increasing and begins decreasing—indicating that tran-

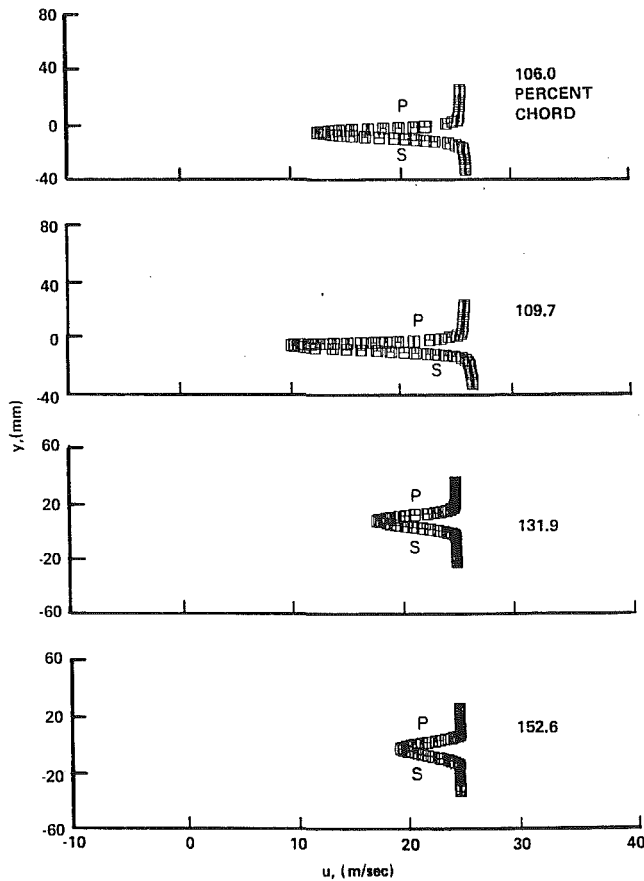


Fig. 9 Measured wakes for $i = -8.5$ deg

sition to turbulence is complete. We did not observe such a complete transition at $i = 5.0$ deg.

In order to better determine the locations of separation and transition, we computed integral parameters using spline fits of the data, Falkner-Skan solutions, a STAN5 solution, and a least-squares fit of the data to the wall-wake equation. STAN5 is a computer code developed by Crawford and Kays (1976) to numerically solve the boundary layer equations. Figure 11 shows these parameter plots as well as our best estimate of how the parameters actually vary—as determined by a complete analysis of all the data. The plots of δ^* and Re_θ in Fig. 11 give little evidence of any separation and transition. Upstream of the 40.0 percent chord location, the very thin boundary layers give questionable values of the integral thicknesses and the STAN5 solution seems to be the most reliable. At 30.4 percent chord, STAN5 computes a Re_θ of 250 and activates its transition turbulence model.¹ At 36.5 percent chord, the STAN5 solution fails to converge—indicating the onset of separation. Downstream of the 40.0 percent chord location, the calculations using both the spline fit and the wall-wake fit give similar results. Note that the boundary layers become thinner near the trailing edge as the streamwise pressure gradient becomes more favorable.

Just before the separation bubble is reached and the STAN5 solution diverges, a sharp rise in H_{12} occurs as seen in Fig. 11. Separation of a laminar boundary layer is normally indicated when H_{12} goes to 3.5 and this corresponds to 35.1 percent chord. Downstream of the peak value of H_{12} (near 37.3 percent chord where $H_{12} \approx 3.9$), the values of H_{12} do not leave the laminar regime and enter the turbulent regime until 52.0 percent chord.

¹Crawford and Kays (1976) suggest a value of Re_θ between 200 and 300 for the onset of transition.

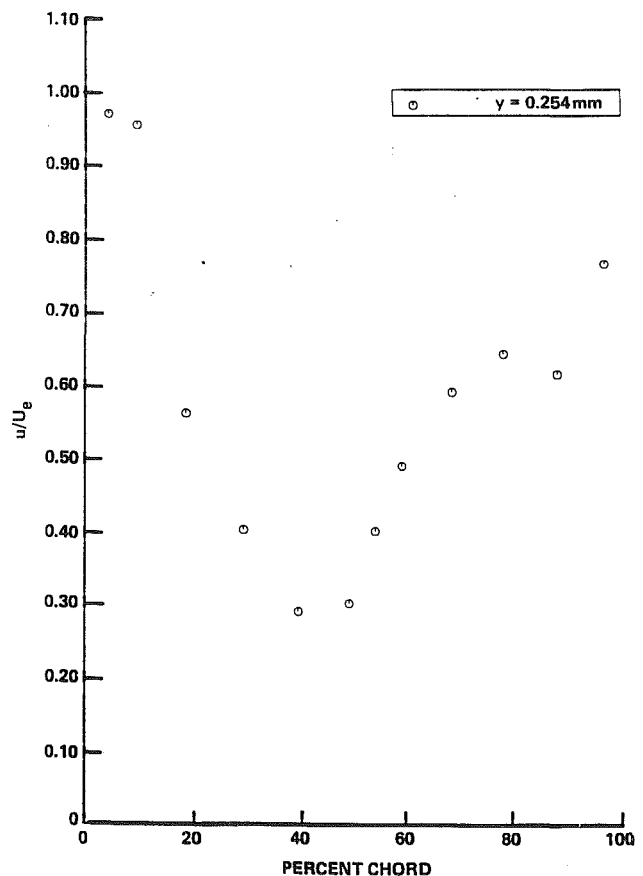


Fig. 10 Variation of mean velocity, 0.254 mm from the blade, on the pressure surface for $i = -1.5$ deg

The clearest indication that a separation bubble truly exists is shown in the plot of skin friction coefficient in Fig. 11. Observing the STAN5 solution, we see that C_f starts at infinity at the leading edge, decreases rapidly, and finally vanishes near 37.3 percent chord. Downstream, the values of C_f computed from a fit of the wall-wake equation increase rapidly as we might expect of transitional boundary layers. A further increase in C_f occurs near the trailing edge where a large favorable pressure gradient exists. Here we decided to use the values of C_f that come directly from the fit of the wall-wake equation, since the calculations using the spline fit must employ the equation of Ludwig and Tillman (1949), which may not be valid in this region.

The turbulence intensities on the pressure surface show trends similar to the turbulence intensity plots for the pressure surface boundary layers when $i = 5.0$ deg. The initial boundary layers had velocity distributions with larger standard deviations than one would deem as physically possible for laminar boundary layers. As we discussed previously (Deutsch and Zierke, 1988b), the reason for these enlarged velocity distributions is not turbulence intensity, but a combination of mean-velocity-gradient broadening and a vibration of the LDV measurement volume. From 30.3 percent chord to 60.5 percent chord, a peak in turbulence intensity, as is usual for transition, occurs away from the blade. Then, as the transition to turbulence ends, the peaks move closer to the blade surface. These peaks move to the blade surface sooner for $i = -1.5$ deg than for $i = 5.0$ deg.

Suction Surface for a -1.5 Degree Incidence

After observing the measured velocity profiles of Fig. 5, we concluded that the suction surface boundary layers for $i = -1.5$ deg and $i = 5.0$ deg were similar. Both surfaces included a leading edge separation bubble and a trailing edge separation

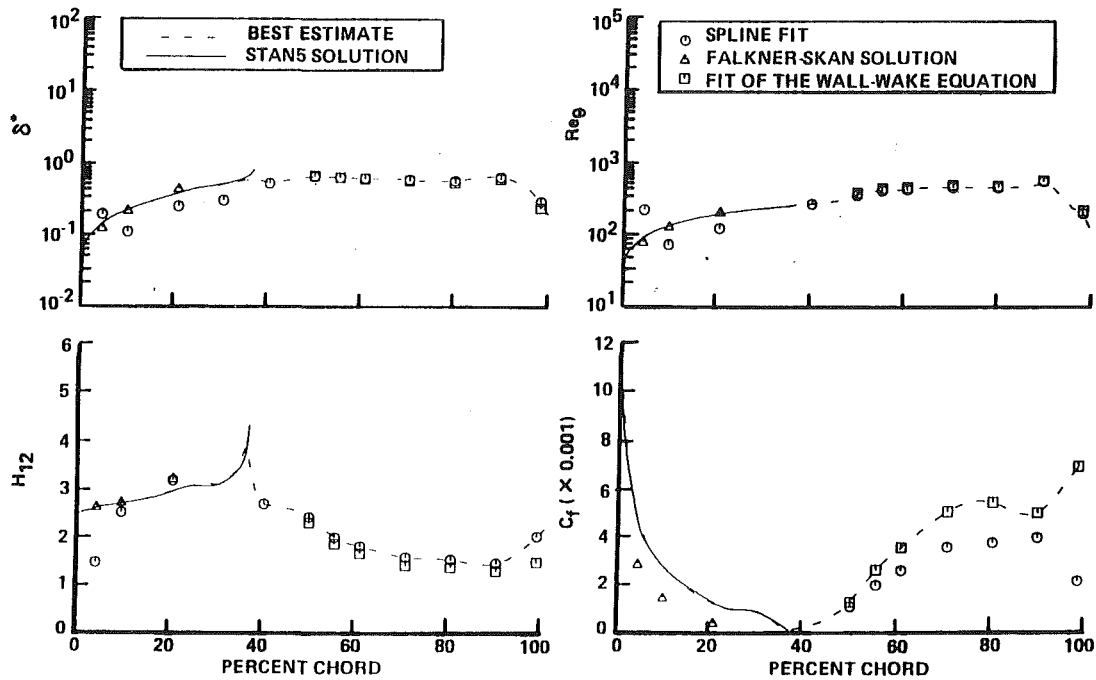


Fig. 11 Variation of displacement thickness, momentum thickness Reynolds number, first shape factor, and skin friction coefficient on the pressure surface for $i = -1.5$ deg

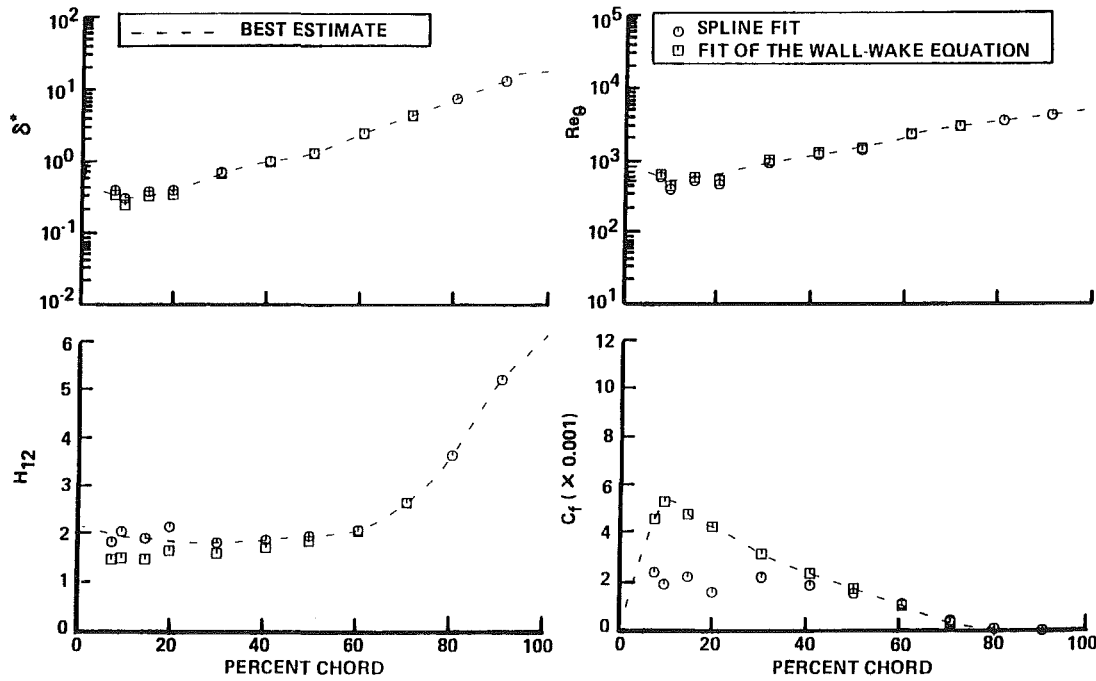


Fig. 12 Variation of displacement thickness, momentum thickness Reynolds number, first shape factor, and skin friction coefficient on the suction surface for $i = -1.5$ deg

of the turbulent boundary layer. However, the turbulent boundary layers for $i = -1.5$ deg were thinner because of both the small region, with a favorable streamwise pressure gradient, from 3 percent chord to 9 percent chord and the likelihood of a smaller leading edge separation bubble.

Since all the boundary layers on this surface were turbulent, we fit all of the profiles to both a spline and the wall-wake equation. Outer variable plots showed another difference between this flow field and the suction surface flow field for $i = 5.0$ deg. The boundary layers immediately downstream of

the leading edge separation bubble do not show signs of recovery—even though the boundary layers have clearly transitioned to turbulence. The small region of accelerated flow and the smaller leading edge separation bubble seem to have hastened the recovery process. Downstream, the boundary layer at 60.2 percent chord shows a slight inflection; the inflections become larger and finally negative mean velocities become evident at 90.3 percent chord. Another difference in the suction surface boundary layers for $i = -1.5$ deg and $i = 5.0$ deg is evident in the inner variable plots. While the wall-wake equa-

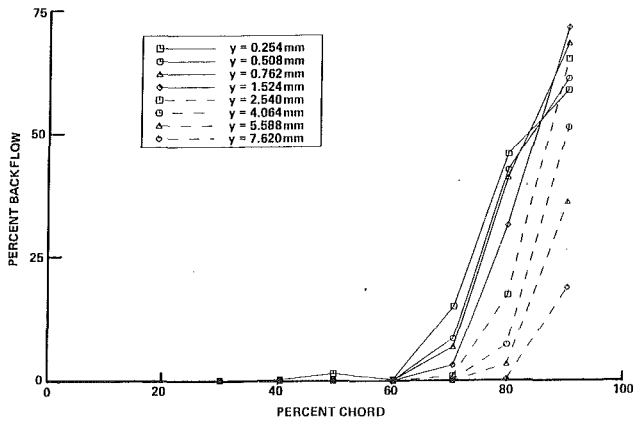


Fig. 13 Instantaneous backflow measurements on the suction surface for $i = -1.5$ deg

tion fit the data for $i = 5.0$ deg well for all the boundary layers prior to detachment, this is not the case for $i = -1.5$ deg. The boundary layers at 7.3 percent and 9.3 percent chord have a substantial logarithmic region and fit the wall-wake equation well. For 14.5 percent and 19.7 percent chord, the logarithmic region becomes quite small and the fit to the wall-wake equation worsens. While we could fit the boundary layers at 30.1 percent, 40.5 percent, and 49.8 percent chord, the fits were poor and no discernible logarithmic region is evident. Further downstream, the boundary layers at 60.2 percent and 70.6 percent chord fit the wall-wake equation well in the region just upstream of detachment.

Both the wall-wake and spline fits were used to compute various boundary layer parameters. Figure 12 shows the boundary layer growth in terms of δ^* and Re_θ . Except that the boundary layers are thinner, they grow in much the same manner as the suction surface boundary layers for $i = 5.0$ deg. The shape factors in Fig. 12 show turbulent values from the leading edge until 62.0 percent chord where the H_{12} takes on a value of 2.2—an initial indicator of turbulent separation. Using the relation of Sandborn and Kline (1961) for intermittent separation

$$H_{12} = 1 + \frac{1}{1 - \frac{\delta^*}{\delta}}$$

gives a location of 70.9 percent chord and a first shape factor of 2.73. Both of these indicators show separation for $i = -1.5$ deg to be slightly downstream of the corresponding locations for $i = 5.0$ deg. Remember that the flow visualization showed a region of low shear stress at 45.1 percent \pm 2.3 percent chord—indicating that separation for $i = -1.5$ deg is slightly upstream of separation for $i = 5.0$ deg. Because of the difficulty in finding a satisfactory run time for the flow visualization tests, we might conclude that locating separation from flow visualization is less accurate than locating separation by analyzing the LDV data.

Figure 12 shows how the skin friction coefficient changes with chord location. Similarly to the suction surface for $i = 5.0$ deg, C_f is zero at the leading edge because of the separation bubble. The values of C_f rise sharply to a peak value larger than was the case for $i = 5.0$ deg; Again, we might expect this large value of C_f because of the region of accelerated flow. The skin friction vanishes near 85.8 percent chord. Unfortunately, the calculations of C_f using the spline fit and the Ludwig-Tillman equation give smaller and more scattered values. From our experience, despite the very small logarithmic regions in many of the boundary layers, we still have more confidence in the values of C_f that come directly from fitting the data to the wall-wake equation.

Since separation of turbulent boundary layers occurs over a finite region and not just where $C_f = 0$, we can examine the entire process of separation by plotting instantaneous backflow in Fig. 13. Figure 13 shows the instantaneous backflow at each LDV measurement station for several distances from the blade. The results are very similar to the data for $i = 5.0$ deg. Using the definitions of Simpson, Chew, and Shivaprasad (1981), we can locate incipient detachment (1 percent instantaneous backflow) at 60.8 percent chord and intermittent transitory detachment (20 percent instantaneous backflow) at 72.1 percent chord. As was true at 5.0 deg incidence, the position where $H_{12} = 2.2$ seems to indicate incipient detachment while the relation of Sandborn and Kline (1961) seems to indicate intermittent transitory detachment. Also, transitory detachment (50 percent instantaneous backflow) occurs at 82.1 percent chord—very near the detachment point where $C_f = 0$.

The mean backflow data at 90.3 percent chord may be plotted nondimensionally along with the mean backflow data at 94.9 percent chord for $i = 5.0$ deg using the maximum backflow velocity as the velocity scale and the total backflow thickness as the length scale. Both sets of data show good similarity when plotted in this manner. The data collapse well with several data sets measured by Simpson, Strickland, and Barr (1977) and Simpson, Chew, and Shivaprasad (1981).

Some final physical insight can be obtained by considering the turbulence intensity profiles. With one exception, these profiles look very similar to the turbulence intensity profiles for the suction surface when $i = 5.0$ deg. Again, the small region with a favorable streamwise pressure gradient seems to have accelerated the recovery from the leading edge separation bubble. Therefore, the maximum mean-shear rate remains very close to the blade surface and the maximum turbulence intensity also will remain very close to the blade surface. Just like the turbulence intensities for $i = 5.0$ deg, the turbulence intensities for $i = -1.5$ deg track the location of maximum mean-shear rate in the turbulent separation region and the peaks move away from the blade surface. Very large 95 percent confidence bands occur at 90.3 percent chord when the mean velocities become negative.

Wakes for a -1.5 Degree Incidence

A similarity analysis of the near and far wakes give results resembling the results for $i = 5.0$ deg. The near wakes at 106.0 percent and 109.7 percent chord fail to show similarity with the Gaussian distribution of Lakshminarayana and Davino (1980)

$$\frac{U_e - u}{U_e - u_{cl}} = e^{-0.693\eta^2}$$

Similarity does hold for the far wake at 131.9 percent chord. As with the suction surface boundary layers, the difference between the wakes at the 5.0 and -1.5 deg incidence angles is the smaller shear layer thickness for $i = -1.5$ deg. Since the displacement of the free-stream fluid is smaller for $i = -1.5$ deg than for $i = 5.0$ deg, the wake is not forced to migrate as far from the extended chord line. Some strong curvature of the wake centerline is evident in the near-wake region and this indicates that some trailing edge loading does exist (as seen in the blade static-pressure distribution in Fig. 3).

Turbulence intensity profiles for the two near wakes at $i = -1.5$ deg look very similar to the near wake profiles for $i = 5.0$ deg. Both sets of profiles show asymmetric wakes with the turbulence intensity peaks displaced from the wake centerline. All of these wakes show a large scatter in turbulence intensity data in the regions of mean backflow.

Pressure Surface for a -8.5 Degree Incidence

The large adverse pressure gradient near the suction surface leading edge for the 5.0 and -1.5 deg incidence angles has

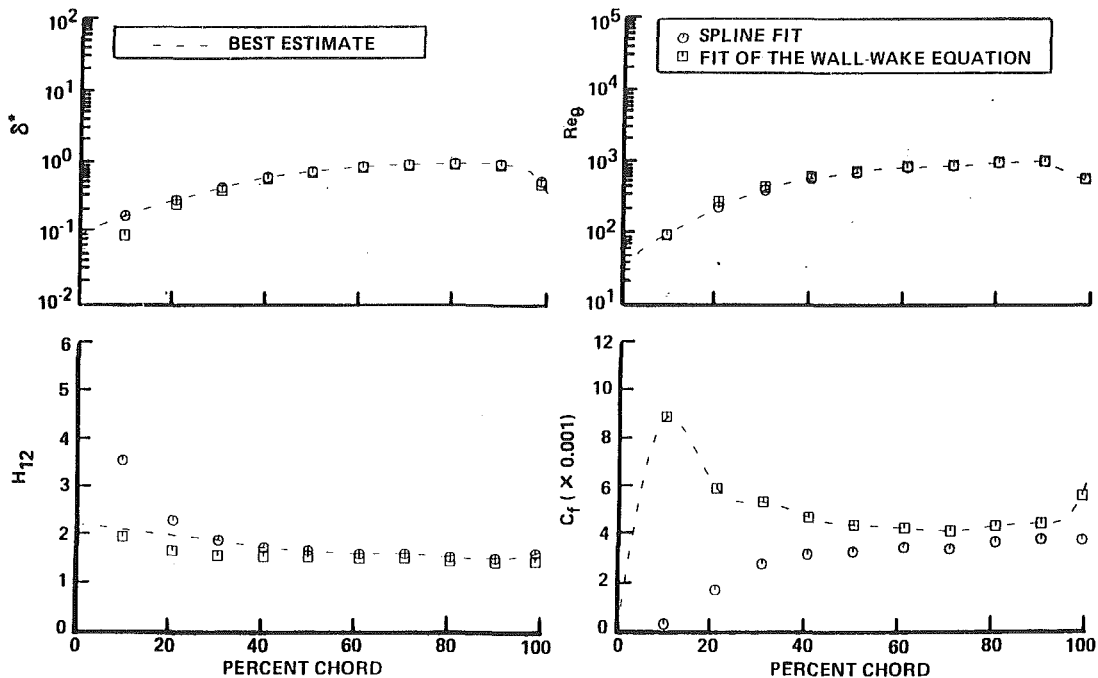


Fig. 14 Variation of displacement thickness, momentum thickness Reynolds number, first shape factor, and skin friction coefficient on the pressure surface for $i = -8.5$ deg

shifted to the pressure surface leading edge for the -8.5 incidence angle as seen in Fig. 3. Thus the separation bubble is now on the pressure surface. This separation bubble leads to an immediate transition and causes all of the measured boundary layers in Fig. 7 to be turbulent. After accounting for the normal pressure gradient, we fit each velocity profile to both a spline and the wall-wake equation. Despite the expected transition caused by the leading edge separation bubble, the first few boundary layers are very thin and only a few data points were acquired within the boundary layer. Because of these very few data points, we find it difficult to observe any evidence of a recovery from the leading edge separation bubble. Downstream, all of the profiles look like typical turbulent boundary layers. The inner variable plots also are typical of turbulent boundary layers. The wake region is quite small for all of the boundary layers—although the size of the wake region is probably distorted near the leading edge because of the very few data points.

Data fits to both a spline and the wall-wake equation were used to calculate various boundary layer parameters. Figure 14 shows the boundary layer growth in terms of δ^* and Re_θ . The boundary layers grow rapidly at first and then grow with a decreasing rate until the favorable streamwise pressure gradient near the trailing edge causes the boundary layers to become thinner. The values of Re_θ also present a dilemma. While we expect all turbulent boundary layers on this surface, the values of Re_θ for the first few boundary layers seem too small to support turbulence. Recall that Murlis, Tsai, and Bradshaw (1982) found no logarithmic region, at zero pressure gradient, for Re_θ less than 700 and Smits, Matheson, and Joubert (1983) found no logarithmic region, at favorable pressure gradients, for Re_θ less than 261. Near the leading edge, we could expect even larger minimum values of Re_θ since the streamwise pressure gradients are adverse. However, despite the limited amount of data, we did fit all of the boundary layers to the wall-wake equation even though Re_θ did not reach 700 until 49.7 percent chord.

The first shape factor plot in Fig. 14 shows another interesting development. The values of H_{12} for all of the boundary

layers lie within the turbulent regime when we use the fit to the wall-wake equation for calculating H_{12} . However, when we use the spline fit to calculate H_{12} , the boundary layers through 20.5 percent chord show values larger than 2.2. As seen in Fig. 14, differences also occur in calculating C_f when using the two types of fits. From analyzing the boundary layers on the previous surfaces and incidence angles, we have found that obtaining C_f directly from fitting the data to the wall-wake equation gives better results than obtaining C_f from the spline fit and the equation of Ludwig Tillman (1949). Since a leading edge separation bubble must exist, C_f should be zero very close to the leading edge. We assume then that C_f must rise to the value at 9.7 percent chord as obtained from the fit to the wall-wake equation—even though the values of C_f calculated this way do not imply a zero value of C_f at the leading edge. The recovery from the leading edge separation bubble may be complete before 9.7 percent chord. The values of C_f calculated from the spline fit and the Ludwig-Tillman equation do imply a zero value of C_f at the leading edge. However, these values fail to show the expected trends at other chord locations. Using the fit to the wall-wake equation, we see that C_f does decrease in the region of adverse pressure gradient, level off as the pressure gradient diminishes, and increase near the trailing edge where a favorable pressure gradient exists.

The turbulence intensity plots show typical results in the absence of transition and separation regions. The maximum value of turbulence intensity for all of these boundary layers lies very close to the blade surface. The boundary layers close to the leading edge do not show any signs of the recovery from the leading edge separation bubble.

Suction Surface for a -8.5 Degree Incidence

Recall that a strong favorable streamwise pressure gradient was found on the first 18 percent chord of the suction surface for $i = -8.5$ deg (see Fig. 3). Expecting laminar boundary layers within this region, we found that the boundary layers at 10.4 percent and 19.7 percent chord were too thin to measure. Without these measurements, we could only use our Falkner-Skan and STAN5 solutions to study the behavior of the

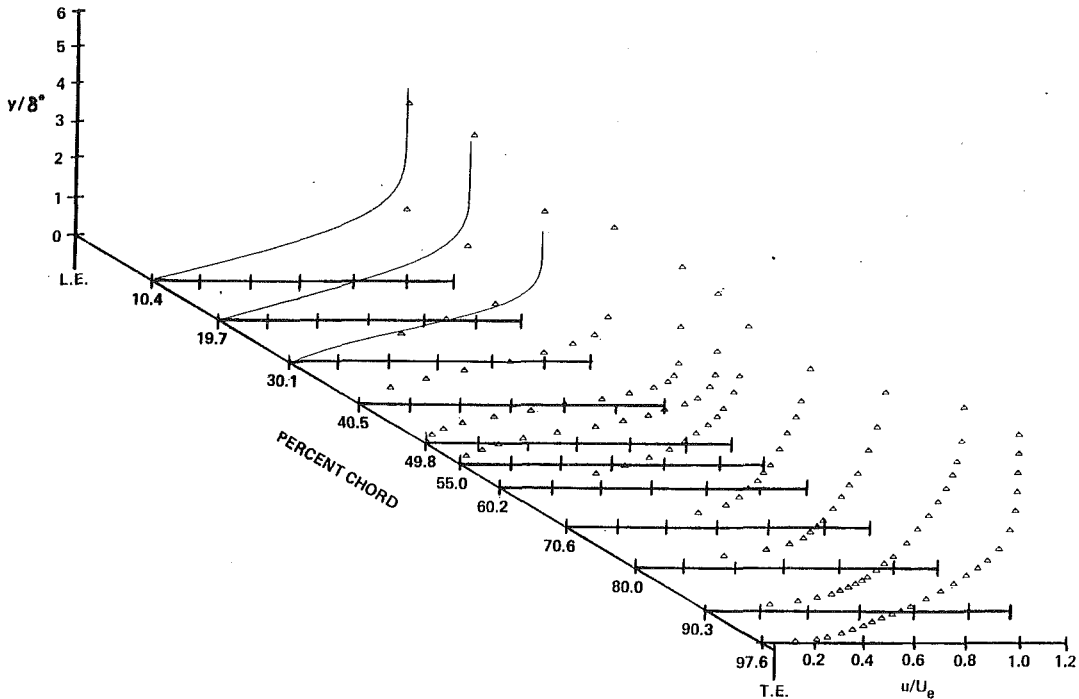


Fig. 15 Reconstructed suction surface boundary layers in outer variables with the Falkner-Skan solutions for $i = -8.5$ deg

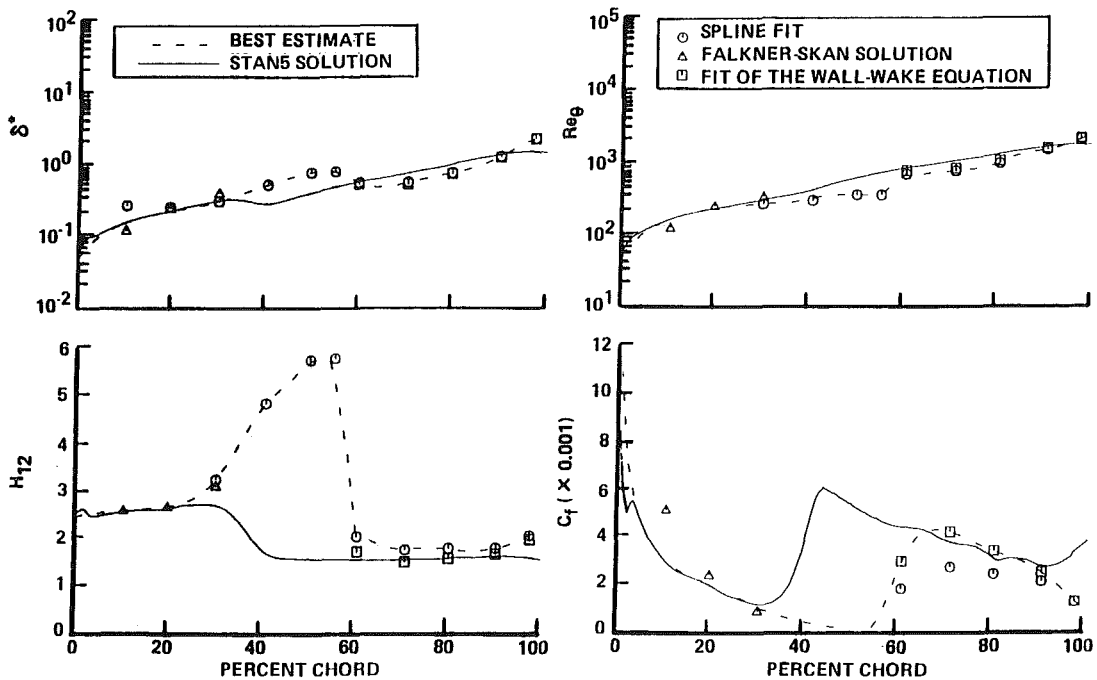


Fig. 16 Variation of displacement thickness, momentum thickness Reynolds number, first shape factor, and skin friction coefficient on the suction surface for $i = -8.5$ deg

leading edge boundary layers. For all of the remaining boundary layers of Fig. 8, we fit the data to splines (after accounting for the normal pressure gradient) and attempted to fit the data to the wall-wake equation. After this initial analysis, we plotted the velocity profiles in outer variables in Fig. 15. The data at 30.1 percent chord compare very well to the Falkner-Skan solution, which indicates the boundary layers remain laminar until this location. The Falkner-Skan solution failed at 40.5 percent chord and the outer variable plot here showed a slight point of inflection. At 49.8 percent and 55.0 percent chord, the outer variable plots showed that the boundary layers were

separated. The boundary layer seemed to have recovered by 60.2 percent chord, which signified the presence of a separation bubble. Downstream, the boundary layers appeared turbulent and eventually, the adverse pressure gradient led to a slight point of inflection in the profile at 97.6 percent chord. We were able to fit all of the boundary layers from 60.2 percent chord to 97.6 percent chord to the wall-wake equation, but only the boundary layer at 70.6 percent chord gave a convincing fit. We can conclude that the separation bubble caused the laminar boundary layer to transition to turbulence. However, the recovery from this separation bubble and the near sepa-

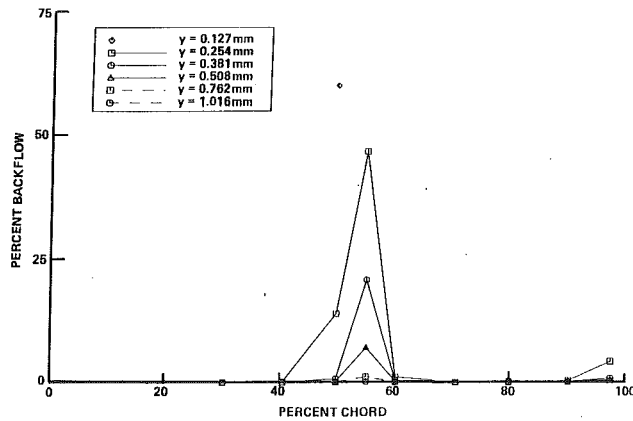


Fig. 17 Instantaneous backflow measurements on the suction surface for $i = -8.5$ deg

ration of the trailing edge turbulent boundary layer led to a very small logarithmic region for most of the turbulent boundary layers downstream of reattachment.

The boundary layer growth on this surface is dominated by the existence of a substantial separation bubble. The chordwise variation of δ^* in Fig. 16 shows a sudden rise in the boundary layer growth after the 30.1 percent chord location. The growth levels off and then suddenly δ^* decreases until just downstream of the 60.2 percent chord location. Since the separation bubble leads to a rapid transition to turbulence, we expect to see a sharp rise in Re_θ just before reattachment. Figure 16 shows this sharp rise between the 55.0 percent and 60.2 percent chord locations. The STAN5 solution fails to predict any evidence of separation. After the initially laminar boundary layer, STAN5 predicts that the adverse streamwise pressure gradient will induce a "natural" transition between 22.9 percent and 44.2 percent chord. The numerical solution predicts no bubble shape in the chordwise δ^* variation and only a gradual rise in Re_θ from the laminar region to the turbulent region.

The variation of H_{12} in Fig. 16 shows the most dramatic representation of the separation bubble. Near the leading edge, the Falkner-Skan and STAN5 solutions show values of H_{12} in the laminar regime. Calculations using the spline fit, as well as the Falkner-Skan solution, show H_{12} increasing at the 30.1 percent chord location. H_{12} continues to rapidly increase—according to the spline fit calculation—with a laminar separation value of 3.5 occurring near 31.9 percent chord. As was the case of δ^* , H_{12} peaks near 51.9 percent chord. Between the 55.0 percent and 60.2 percent, H_{12} drops very rapidly as the separation bubble induces a sudden transition to turbulence. The values of H_{12} enter the turbulent regime near 59.0 percent chord. From 70.6 percent chord through 90.3 percent chord, H_{12} remains nearly constant before rising to the turbulent separation value of 2.2 at the trailing edge. Again, STAN5 gives values of H_{12} that decrease in a region of natural transition since no separation bubble was predicted.

The STAN5 solution gives the values of C_f near the leading edge. As shown in Fig. 16, C_f decreases asymptotically from infinity at the leading edge. As with the other boundary layer parameters, however, STAN5 predicts a natural transition, which results in a sharp rise in C_f . In actuality, this sharp rise in C_f should be delayed until C_f vanishes near the peak locations of δ^* and H_{12} at 51.9 percent chord. Then, as transition takes place, C_f should rise to the values obtained from fitting the data to the wall-wake equation. After the 70.6 percent chord location, C_f decreases in the region of adverse streamwise pressure gradient and nears a value of zero as the turbulent separation process begins near the trailing edge.

On this surface, surface flow visualization tests proved especially useful in determining the location of the separation bubble as well as the location of peak transition within the

bubble. To 95 percent confidence, the oil film method placed the location of laminar detachment at 35.3 percent \pm 2.0 percent chord and turbulent reattachment at 59.8 percent \pm 2.3 percent chord. The chemical sublimation method located the peak transition at 56.0 percent \pm 0.8 percent chord, to the same level of confidence. The oil film method also showed a possible separation of the turbulent boundary layer near the trailing edge. Note that the chemical sublimation method indicated transition for the separation bubble and separation and reattachment for the very small separation bubble on the pressure surface for $i = -1.5$ deg.

Because the transition to turbulence results in boundary layers with more streamwise momentum, a plot of mean velocity versus percent chord at a fixed distance above the blade can help determine the location of transition. Most of the transition process takes place between 55.0 percent and 60.2 percent chord where a sharp increase occurs in mean velocity. Transition seems complete beyond the 70.6 percent chord location as the mean velocity decreases from this location to the trailing edge.

Besides the mean velocity data, the LDV measurements also provide information on flow reversal. Figure 17 shows the chordwise variation of percent backflow at several different distances from the blade surface. The backflow data between the 40.5 percent and 60.2 percent chord locations give the appearance of a bubble. For all distances from the blade surface, the maximum percent backflow occurs at the 55.0 percent chord location where a value of 46.7 percent can be found 0.254 mm from the blade surface. However, larger values of maximum percent backflow might occur closer to the blade surface. For only one chord location could we measure the velocity closer than 0.254 mm from the surface with the LDV. At 49.8 percent chord, the maximum percent backflow rose from 14.1 percent to 60.3 percent as we moved the LDV measurement volume from $y = 0.254$ mm to $y = 0.127$ mm. The major region of flow reversal seems to occur very close to the blade surface. This same flow phenomenon seems to account for our failure to measure any backflow on the pressure surface at $i = -1.5$ deg where a very small separation bubble almost certainly exists. Finally, as the turbulent boundary layer near the trailing edge approaches separation, we measured some backflow at 97.6 percent chord—leading to an incipient detachment point (with 1 percent instantaneous backflow) near 91.7 percent chord.

Figure 18 shows how the turbulence intensity profiles vary with chord location. Within the initial laminar boundary layers, the turbulence intensity levels are low—the problems with mean-velocity-gradient broadening and vibration (Deutsch and Zierke, 1988b) of the LDV measurement volume are not evident since we just barely penetrated these boundary layers. By 30.1 percent chord, the levels of turbulence intensity rise, with a peak value located away from the blade surface. This trend continues through 60.2 percent chord as expected in regions of transition and separation. Note the small turbulence intensity very close to the blade surface at 49.8 percent chord. This location corresponds to the point of maximum H_{12} and percent backflow, just as the separation bubble induces transition to turbulence. Beyond 60.2 percent chord, the peak in turbulence intensity lies very close to the blade surface since the boundary layers are fully turbulent. Near the trailing edge, at 97.6 percent chord, the peak once again moves away from the blade surface as intermittent separation of the turbulent boundary layers has begun.

Wakes for a -8.5 Degree Incidence

Both the near wakes at 106.0 percent and 109.7 percent and the far wakes at 131.9 percent and 152.6 percent were nearly symmetric and show good similarity with respect to the Gaussian distribution of Lakshminarayana and Davino (1980) (away

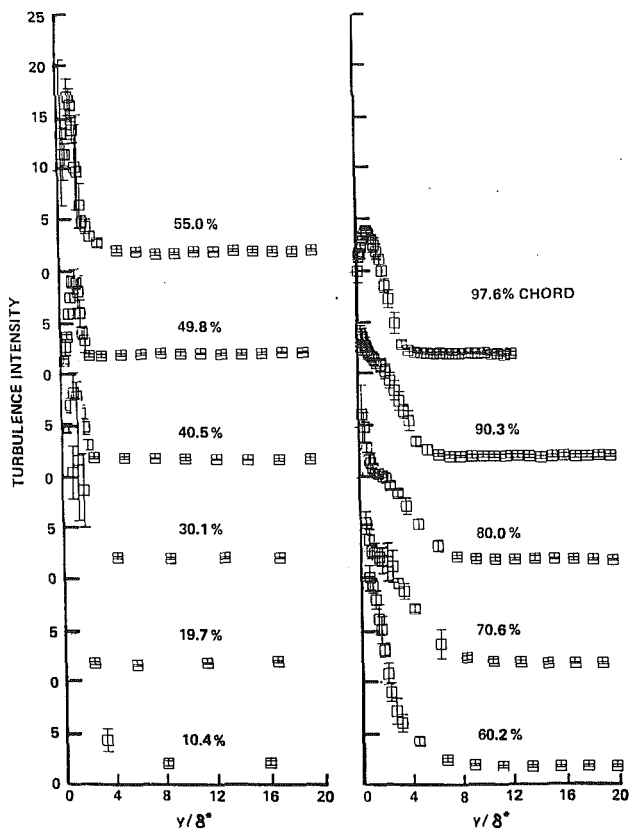


Fig. 18 Turbulence intensity on the suction surface for $i = -8.5$ deg

from the wake edge). Having near-wake similarity seems in contrast with our data from the first two incidence angles as well as the data of Hobbs, Wagner, Dannenhoffer, and Dring (1982). However, these data all showed larger regions of trailing edge separation on the suction surface than did the data for the current flow field. Evidently, the distance required for the wakes to show self-preservation is extended farther downstream as the size of the trailing edge separation region is enlarged.

The turbulence intensity profiles are quite different than the profiles for the near wakes at $i = 5.0$ deg and $i = -1.5$ deg. Although these profiles are not as symmetric as the mean-velocity profiles, they show more symmetry than the turbulence intensity profiles at the two previous incidence angles. Also, the 95 percent confidence bands on the turbulence intensity measurements are much smaller for $i = -8.5$ deg. As with all wakes, however, the peaks in turbulence intensity track the regions of large mean-velocity gradients and occur away from the wake centerline.

Conclusions

In order to use the increasing number of viscous computational codes for turbomachinery applications, we must compare the viscous solutions with detailed and precise data for various flow conditions. The physical nature of these flow fields must also be understood. Previously, we presented measurements of the boundary layers and wakes about a double-circular-arc compressor blade in cascade for an incidence angle of 5.0 deg. In the current study, we have presented measurements of the boundary layers and wakes on the same blade for an incidence angle of -1.5 deg—an incidence angle closer to the zero-degree design incidence—and an incidence angle of -8.5 deg—an incidence near minimum loss for this geometry. Because the stagnation point lay on the pressure surface for the incidence angles of both 5.0 and -1.5 deg, the

boundary layers for these two incidence angles were somewhat similar. On the other hand, the boundary layers that developed at an incidence angle of -8.5 deg were quite different.

For $i = 5.0$ deg, the initially favorable streamwise pressure gradient on the pressure surface kept the boundary layers laminar. Eventually, a natural transition took place when the pressure gradient became slightly adverse, but this transition was incomplete because of the flow acceleration near the trailing edge. In a similar manner, for $i = -1.5$ deg, laminar boundary layers were evident through at least 10 percent chord even though the pressure gradient was less favorable for this incidence. Downstream, the pressure gradient was slightly more adverse than for $i = 5.0$ deg. As a result, a very small separation bubble forms, which causes at least a partial transition to turbulence. Although we were unable to measure the backflow region of the separation bubble because of its small size, our analysis of the data showed the existence of this separation bubble.

As noted, the stagnation point lies on the pressure surface side of the leading edge for both the 5.0 and -1.5 deg incidence angles. Thus a very strong adverse streamwise pressure gradient forms near the leading edge with leads to a very small separation bubble and an immediate transition to turbulence. However, the separation bubble is probably smaller for $i = -1.5$ deg than it was for $i = 5.0$ deg. In addition, the $i = -1.5$ deg flow field has a small region of flow acceleration between 3 percent chord and 9 percent chord that was not found for the $i = 5.0$ deg case. These flow conditions give a different flow "history" for the -1.5 deg incidence angle than for the 5.0 deg incidence angle and leads to thinner boundary layers for $i = -1.5$ deg. The continuing adverse pressure gradient over most of the suction surface leads to intermittent separation near 60 percent chord and detachment near 80 percent chord for both incidence angles. These separation regions produce asymmetric near wakes with regions of strong backflow.

At $i = -8.5$ deg, the stagnation point has shifted to the suction surface side of the leading edge. Thus near the leading edge, a very strong adverse streamwise pressure gradient forms on the pressure surface and a very strong favorable streamwise pressure gradient forms on the suction surface. The resulting separation bubble near the leading edge of the pressure surface leads to an immediate transition to turbulence.

The boundary layers on the suction surface remain laminar through about 30 percent chord. In the downstream region with an adverse streamwise pressure gradient, the laminar boundary layer separates, goes through a nearly complete transition to turbulence, and reattaches. Since this separation bubble takes place over a region of about 20 percent chord, the measurements provide sufficient detail for testing computational codes for a very complex flow phenomenon. Even though this separation bubble is large relative to the ones on the other surfaces and incidence angles, the region of flow reversal is still confined to distances very close to the blade surface. Downstream of this separation bubble, the boundary layer begins the turbulent separation process near the trailing edge.

The complete set of measurements, at incidence angles of 5.0 , -1.5 , and -8.5 deg, provide an array of interesting fluid mechanical "complications," so that in spite of its geometric simplicity, quite sophisticated Navier-Stokes codes will doubtlessly be needed to calculate the complete flow field.

Acknowledgments

This study was supported under NASA Grant NSG 3264 under the supervision of Nelson Sanger at NASA Lewis Research Center. We are grateful for his encouragement and patience. Nearly a decade's worth of students have benefited and been benefited by this grant.

References

- Abu-Ghannam, B. J., and Shaw, R., 1980, "Natural Transition of Boundary Layers—The Effects of Turbulence, Pressure Gradient, and Flow History," *Journal of Mechanical Engineering Science*, Vol. 22, No. 5, pp. 213–228.
- Ball, C. L., Reid, L., and Schmidt, J. F., 1983, "End-Wall Boundary Layer Measurements in a Two Stage Fan," NASA TM 83409.
- Coles, D. E., 1956, "The Law of the Wake in the Turbulent Boundary Layer," *Journal of Fluid Mechanics*, Vol. 1, pp. 191–226.
- Crawford, M. E., and Kays, W. M., 1976, "STAN5—A Program for Numerical Computation of Two-Dimensional Internal and External Boundary Layer Flows," COSMIC Program No. LEW-13009, NASA CR-2742.
- Deutsch, S., and Zierke, W. C., 1986, "The Measurement of Boundary Layers on a Compressor Blade in Cascade at High Positive Incidence Angle: Part II—Data Report," NASA Contractor Report 179492.
- Deutsch, S., and Zierke, W. C., 1987, "The Measurement of Boundary Layers on a Compressor Blade in Cascade: Part 1—A Unique Experimental Facility," *ASME JOURNAL OF TURBOMACHINERY*, Vol. 109, pp. 520–526.
- Deutsch, S., and Zierke, W. C., 1988a, "The Measurement of Boundary Layers on a Compressor Blade in Cascade: Part 2—Suction Surface Boundary Layers," *ASME JOURNAL OF TURBOMACHINERY*, Vol. 110, pp. 138–145.
- Deutsch, S., and Zierke, W. C., 1988b, "The Measurement of Boundary Layers on a Compressor Blade in Cascade: Part 3—Pressure Surface Boundary Layers and the Near Wake," *ASME JOURNAL OF TURBOMACHINERY*, Vol. 110, pp. 146–152.
- Falkner, V. M., and Skan, S. W., 1931, "Some Approximate Solutions of the Boundary Layer Equations," *Phil. Mag.*, Vol. 12, No. 7, pp. 865–896.
- Hobbs, D. E., Wagner, J. H., Dannenhoffer, J. F., and Dring, R. P., 1982, "Experimental Investigation of Compressor Cascade Wakes," ASME Paper No. 82-GT-299.
- Lakshminarayana, B., and Davino, R., 1980, "Mean Velocity and Decay Characteristics of the Guide Vane and Stator Blade Wake of an Axial Flow Compressor," *ASME Journal of Engineering for Power*, Vol. 102, pp. 50–60.
- Lieblein, S., Schwenk, F. C., and Broderick, R. L., 1953, "Diffusion Factor for Estimating Losses and Limiting Blade Loadings in Axial-Flow-Compressor Blade Elements," NACA RM E53 D01.
- Lieblein, S., and Roudebush, W. H., 1956, "Theoretical Loss Relations for Low-Speed Two-Dimensional-Cascade Flow," NACA TN3662.
- Ludwig, H., and Tillman, W., 1949, "Untersuchungen über die Wandschubspannung in Turbulenten Reibungsschichten," *Ing.-Arch.*, Vol. 17, pp. 288–299. (English Translation, NACA TM 1285.)
- Mellor, G. L., and Wood, G. M., 1971, "An Axial Compressor End-Wall Boundary Layer Theory," *ASME Journal of Basic Engineering*, Vol. 93, Series D, No. 1, pp. 300–316.
- Murlis, J., Tsai, H. M., and Bradshaw, P., 1982, "The Structure of Turbulent Boundary Layers at Low Reynolds Numbers," *Journal of Fluid Mechanics*, Vol. 122, pp. 13–56.
- Sandborn, V. A., and Kline, S. J., 1961, "Flow Models in Boundary Layer Stall Inception," *ASME Journal of Basic Engineering*, Vol. 83, pp. 317–327.
- Simpson, R. L., Strickland, J. H., and Barr, P. W., 1977, "Features of a Separating Turbulent Boundary Layer in the Vicinity of Separation," *Journal of Fluid Mechanics*, Vol. 79, Part 3, pp. 553–594.
- Simpson, R. L., Chew, Y.-T., and Shipvapasad, B. G., 1981, "The Structure of a Separating Turbulent Boundary Layer: Part 1—Mean Flow and Reynolds Stresses," *Journal of Fluid Mechanics*, Vol. 113, pp. 23–51.
- Smits, A. J., Matheson, N., and Joubert, P. N., 1983, "Low Reynolds Number Turbulent Boundary Layers in Zero and Favorable Pressure Gradients," *Journal of Ship Research*, Vol. 27, No. 3, pp. 147–157.

References

- Abu-Ghannam, B. J., and Shaw, R., 1980, "Natural Transition of Boundary Layers—The Effects of Turbulence, Pressure Gradient, and Flow History," *Journal of Mechanical Engineering Science*, Vol. 22, No. 5, pp. 213–228.
- Ball, C. L., Reid, L., and Schmidt, J. F., 1983, "End-Wall Boundary Layer Measurements in a Two Stage Fan," NASA TM 83409.
- Coles, D. E., 1956, "The Law of the Wake in the Turbulent Boundary Layer," *Journal of Fluid Mechanics*, Vol. 1, pp. 191–226.
- Crawford, M. E., and Kays, W. M., 1976, "STAN5—A Program for Numerical Computation of Two-Dimensional Internal and External Boundary Layer Flows," COSMIC Program No. LEW-13009, NASA CR-2742.
- Deutsch, S., and Zierke, W. C., 1986, "The Measurement of Boundary Layers on a Compressor Blade in Cascade at High Positive Incidence Angle: Part II—Data Report," NASA Contractor Report 179492.
- Deutsch, S., and Zierke, W. C., 1987, "The Measurement of Boundary Layers on a Compressor Blade in Cascade: Part 1—A Unique Experimental Facility," *ASME JOURNAL OF TURBOMACHINERY*, Vol. 109, pp. 520–526.
- Deutsch, S., and Zierke, W. C., 1988a, "The Measurement of Boundary Layers on a Compressor Blade in Cascade: Part 2—Suction Surface Boundary Layers," *ASME JOURNAL OF TURBOMACHINERY*, Vol. 110, pp. 138–145.
- Deutsch, S., and Zierke, W. C., 1988b, "The Measurement of Boundary Layers on a Compressor Blade in Cascade: Part 3—Pressure Surface Boundary Layers and the Near Wake," *ASME JOURNAL OF TURBOMACHINERY*, Vol. 110, pp. 146–152.
- Falkner, V. M., and Skan, S. W., 1931, "Some Approximate Solutions of the Boundary Layer Equations," *Phil. Mag.*, Vol. 12, No. 7, pp. 865–896.
- Hobbs, D. E., Wagner, J. H., Dannenhoffer, J. F., and Dring, R. P., 1982, "Experimental Investigation of Compressor Cascade Wakes," *ASME Paper No. 82-GT-299*.
- Lakshminarayana, B., and Davino, R., 1980, "Mean Velocity and Decay Characteristics of the Guide Vane and Stator Blade Wake of an Axial Flow Compressor," *ASME Journal of Engineering for Power*, Vol. 102, pp. 50–60.
- Lieblein, S., Schwenk, F. C., and Broderick, R. L., 1953, "Diffusion Factor for Estimating Losses and Limiting Blade Loadings in Axial-Flow-Compressor Blade Elements," NACA RM E53 D01.
- Lieblein, S., and Roudebush, W. H., 1956, "Theoretical Loss Relations for Low-Speed Two-Dimensional-Cascade Flow," NACA TN3662.
- Ludwig, H., and Tillman, W., 1949, "Untersuchungen über die Wandschubspannung in Turbulenten Reibungsschichten," *Ing.-Arch.*, Vol. 17, pp. 288–299. (English Translation, NACA TM 1285.)
- Mellor, G. L., and Wood, G. M., 1971, "An Axial Compressor End-Wall Boundary Layer Theory," *ASME Journal of Basic Engineering*, Vol. 93, Series D, No. 1, pp. 300–316.
- Murlis, J., Tsai, H. M., and Bradshaw, P., 1982, "The Structure of Turbulent Boundary Layers at Low Reynolds Numbers," *Journal of Fluid Mechanics*, Vol. 122, pp. 13–56.
- Sandborn, V. A., and Kline, S. J., 1961, "Flow Models in Boundary Layer Stall Inception," *ASME Journal of Basic Engineering*, Vol. 83, pp. 317–327.
- Simpson, R. L., Strickland, J. H., and Barr, P. W., 1977, "Features of a Separating Turbulent Boundary Layer in the Vicinity of Separation," *Journal of Fluid Mechanics*, Vol. 79, Part 3, pp. 553–594.
- Simpson, R. L., Chew, Y.-T., and Shipvaprassad, B. G., 1981, "The Structure of a Separating Turbulent Boundary Layer: Part 1—Mean Flow and Reynolds Stresses," *Journal of Fluid Mechanics*, Vol. 113, pp. 23–51.
- Smits, A. J., Matheson, N., and Joubert, P. N., 1983, "Low Reynolds Number Turbulent Boundary Layers in Zero and Favorable Pressure Gradients," *Journal of Ship Research*, Vol. 27, No. 3, pp. 147–157.

DISCUSSION

N. A. Cumpsty¹ and Y. Dong²

The authors have obtained a most impressive amount of data in the four papers culminating in this one. May one ask if the measurements could be made more accessible: The presentation in Figs. 4, 5, 7, and 8 is too compact for the results to be very useful.

The main reason for writing this discussion is, at risk of being repetitive, to draw attention to the need for caution. This is based on our own measurements (Dong and Cumpsty,

1989). By introducing moving wakes into the two-dimensional flow in a cascade of supercritical (controlled-diffusion) type blades, we were able to see very substantial alterations in the suction and pressure surface boundary layers. The effects were most pronounced on the suction surface, since this boundary layer was dominated by a separation bubble in the absence of wakes or high free-stream turbulence. The wakes initiated turbulence before the separation point and temporarily prevented separation; after a wake had passed the flow reverted to laminar and a separation occurred. After the turbulent spot there was a calmed region, in which transition was delayed, and the net effect of the wakes (and of high free-stream turbulence) was to delay the completion of transition to a position further downstream. The transition, and therefore, the subsequent boundary layer development, depend on the size and frequency of the wakes and the whole process is an unsteady one.

Our measurements, therefore, bring us to offer a caveat to the assumption that the measurements by Zierke and Deutsch will represent the flow inside a compressor. Extreme caution should be exercised in the use of these data for the calibration of viscous codes intended for application to compressors. This is because the process of greatest uncertainty, transition, is probably quite different in character for this steady low-turbulence test configuration from that which will be found in the majority of blade rows in a compressor.

Authors' Closure

The authors would like to thank Professor Cumpsty and Dr. Dong for their comments. In our opinion, these comments are well taken if they prevent even one researcher from believing that matching our data "validates" his code for actual turbomachinery flows. As we tried to make clear in our publications and presentations, we acquired our data for the simplest of flows that exhibit some of the aspects of turbomachinery flow. With this in mind, we would like to see our data used in the same manner that, say, the Stanford Conference boundary layer data would be used by a researcher interested in a turbulent boundary layer with large heat addition—as a step to gain confidence in his code by using it to solve a well-documented and related, but simpler, problem.

The most surprising aspect of our work, considering its relatively simple geometry, was the prevalence and importance of separation "bubbles." Your results then, which are very interesting, are perhaps not as surprising to us as they may be to others. We could not agree with you more that the transition process on turbomachinery blades will be extremely difficult to model. Not only does the periodic unsteadiness in a turbomachine change the character of this transition process, but the three-dimensionality of the flow in a turbomachine also can affect transition. Moreover, it appears likely to us that the current turbulence models, which are after all derived from steady flow experiments, also will prove to be inadequate. Researchers must take great care in moving from the calculation of our simple flow field to the calculation of the flow in actual turbomachines. In spite of this, we hope that our data set will be useful as one step in understanding the physics of and developing models for these complicated flows.

In answer to your question about the accessibility of the results, we are happy to say that the data for all three incidence angles are available in tabulated form in the NASA Contractor Report 184118; see Zierke and Deutsch (1989). Also, COSMIC will soon make a computer tape of the data available.

Additional Reference

- Zierke, W. C., and Deutsch, S., 1989, "The Measurement of Boundary Layers on a Compressor Blade in Cascade, Volumes I and II," NASA Contractor Report 184118.

¹Department of Engineering, Whittle Laboratory, University of Cambridge, Madingley Road, Cambridge, CB3 0DY, United Kingdom.

²New Products Division, Ruston Gas Turbines Ltd., Firth Road, Lincoln, LN6 7AA, United Kingdom.

Viscous Flow in a Controlled Diffusion Compressor Cascade With Increasing Incidence

Y. Elazar

R. P. Shreeve

Turbopropulsion Laboratory,
Department of Aeronautics and Astronautics,
Naval Postgraduate School,
Monterey, CA 93943

A detailed two-component LDV mapping of the flow through a controlled diffusion compressor cascade at low Mach number (~ 0.25) and Reynolds number of about 7×10^5 , at three inlet air angles from design to near stall, is reported. It was found that the suction-side boundary layer reattached turbulent after a laminar separation bubble, and remained attached to the trailing edge even at the highest incidence, at which losses were 3 to 4 times the minimum value for the geometry. Boundary layer thickness increased to fill 20 percent of the blade passage at the highest incidence. Results for pressure-side boundary layer and near-wake also are summarized. Information sufficient to allow preliminary assessment of viscous codes is tabulated.

Introduction

Computational Fluid Dynamics (CFD) has enabled the development of rational methods for designing axial compressor blade elements. Several centers (Sanger, 1983; Hobbs and Weingold, 1984; Dunker et al., 1984, for example) have reported methods for designing "controlled-diffusion (CD)" blading. The approach is to use an inviscid flow computation (in either the direct or indirect mode) to arrive at a blade shape over the surface of which the adverse pressure distribution is such that the computed boundary layer remains attached. Experimental results have clearly demonstrated (Hobbs and Weingold, 1984; Dunker et al., 1984; Sanger and Shreeve, 1986) that the design technique works, but also have shown that the CD blade shapes can sustain a wider range of stall-free incidence than can Double Circular Arc (DCA) blade shapes designed for the equivalent design point conditions. Since stall-margin is extremely important in the design of military aircraft gas turbine engines, it is fundamentally important to be able to predict the off-design and stalling behavior of CD blading during the compressor design process. Thus efficient computational methods are required that correctly describe flows containing viscous effects such as are shown in Fig. 1. Figure 1 illustrates schematically features that may or may not all be present within a given blading at a given inlet air condition. However, whether or not there exists a leading edge separation "bubble," and where (and over what length) transition occurs in the boundary layer, will determine whether (or where) separation will occur in the adverse pressure gradient on the suction side of the blade. For a computer code to predict correctly the off-design losses and onset of stall of a given blading, the code must incorporate the ability to predict and describe separation bubbles and the process of transition. The

The purpose of the present investigation was to obtain data with which to assess the ability of emerging codes to predict the off-design behavior of (particularly) CD blading.

The work follows the earlier investigation of Sanger and Shreeve (1986) wherein the design and experimental evaluation of a particular CD stator cascade was reported. The reported experimental results included probe surveys to obtain loss coefficients, blade surface pressure distributions, and blade surface flow observations using the china-clay technique, at seven incidence angles over the useful range of the blading. Guided by the previous results, in the present study, a two-component Laser-Doppler Velocimeter (LDV) system was used to obtain a detailed mapping of the flow throughout the blading at design

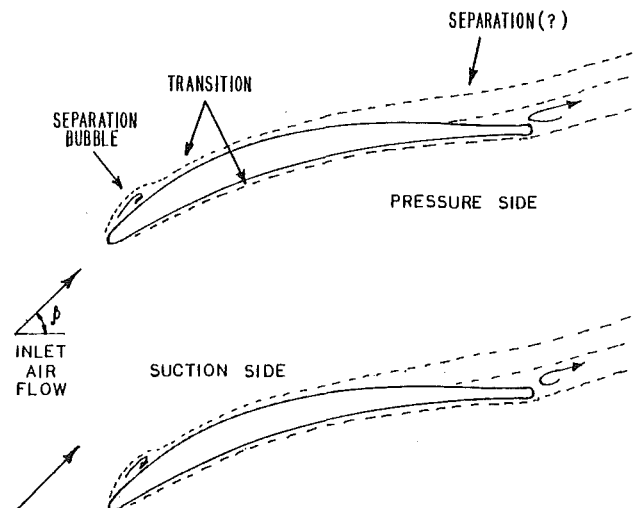


Fig. 1 Probable viscous flow features

Contributed by the International Gas Turbine Institute and presented at the 34th International Gas Turbine and Aeroengine Congress and Exhibition, Toronto, Ontario, Canada, June 4-8, 1989. Manuscript received at ASME Headquarters January 17, 1989. Paper No. 89-GT-131.

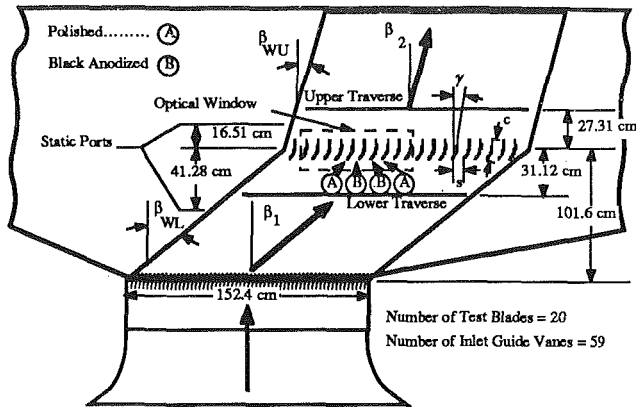


Fig. 2 Cascade wind tunnel section

and two higher incidence angles toward stall. Measurements were obtained of the outer (inviscid) flow through the blade passage, the suction- and pressure-side viscous layer growth, and the initial wake development. In the present paper, the experiment itself is described and results for the suction-side viscous behavior (which provide the most critical test of a computational description) are presented and discussed. Other results are briefly reviewed. Sufficient information is given in tables to enable a preliminary code assessment to be made by application to the geometry of the experiment. A complete account of the experiment and the results was given by Elazar (1988).

Test Facility and Instrumentation

The subsonic cascade wind tunnel at the Naval Postgraduate School was used in the present study. The configuration of the wind tunnel, the test cascade and operating instrumentation was the same as was reported by Sanger and Shreeve (1986). The geometry of the test section is shown in Fig. 2. A 0.64 cm Plexiglas window was located in the removable tunnel front sidewall in the position shown. Adjustment of the inlet air angle (β_1) required adjustment of the lower endwall (β_{WL}), upper endwall (β_{WU}) and inlet guide vanes. The test cascade, with individual blades cantilevered from a mounting plate attached to the fixed rear sidewall, moved horizontally as the endwalls were adjusted. To facilitate LDV measurements close to blade surfaces, two of the machined aluminum blades were polished and two were black-anodized. The black-anodized

Table 1 Blade coordinates, cascade geometry and test conditions

X (mm)	Y (pressure side) (mm)	Y (suction side) (mm)	
0.030	0.114	0.114	
0.056		0.213	
0.145	0.005		
0.564	0.112	0.498	
1.128	0.257	0.780	
1.692	0.394	1.024	
2.256	0.526	1.240	
2.819	0.648	1.425	
3.383	0.759	1.577	
3.947	0.838	1.684	
4.511	0.889	1.755	
5.075	0.912	1.791	
5.639	0.912	1.798	
6.203	0.894	1.781	
6.767	0.869	1.730	
7.330	0.841	1.651	
7.894	0.805	1.549	
8.458	0.765	1.430	
9.022	0.714	1.295	
9.586	0.653	1.151	
10.150	0.577	0.998	
10.714	0.485	0.843	
11.278	0.371	0.686	
11.841	0.226	0.528	
12.405	0.048	0.368	
12.510	0.010		
12.609		0.310	
12.725	0.157	0.157	

(Coordinate System as in Figure 13)

Blade Type		Controlled Diffusion
Number of Blades	20	
Blade Spacing	7.62 cm	
Chord	12.73 cm	
Solidity	1.67	
Leading Edge Radius	0.114 cm	
Trailing Edge Radius	0.157 cm	
Thickness	7%	
Setting Angle	14.2 ° ± 0.1 °	
Stagger Angle	14.4 ° ± 0.1 °	
Span	25.40 cm	

NOMINAL TEST CONDITIONS	
Reynolds No. (chord)	700,000
Inlet	
Total Temperature	294 K
Total Pressure	1.03 ATM
Mach Number	0.25
Exit	
Static Pressure	1.00 ATM

blades gave the best results and were installed as blades 7 and 8 from the left end. The surface texture, after anodizing, was estimated to be better than 1.5 microns. All measurements, at each inlet air angle, were made using the passage formed between blades 7 and 8. The cascade contained a total of 20 blades with a span of 25.4 cm across a test section measuring 1.524 m (from left to right in Fig. 2). Forty pressure taps were provided in blade 10 and six in blade 11.

Blade Cascade Geometry

The CD blade geometry, parameters for the cascade, and the nominal test conditions for the experiment, are given in Table 1. The coordinates of the cascade passage, shown in Fig. 3, can be derived using the blade coordinates (Table 1) and the setting angle (14.2°). Passage coordinates were explicitly tabulated by Elazar (1988). Figure 3 shows the measuring stations (1-19) where LDV surveys were made across the passage, and where boundary layer surveys (made normal to the blade surface) intersected the blade surfaces. As shown in Fig. 3, the passage coordinate system was defined with the center of radius of the trailing edge of the 7th blade as origin.

Nomenclature

AVDR = axial-velocity-density ratio
 c = blade chord (12.73 cm)
 C_p = pressure coefficient
 c' = cascade (axial) chord (12.33 cm)
 C = constant (for fixed cascade geometry)
 d_f = fringe spacing
 d = distance normal to the blade surface
 H = shape factor (displacement/momentum thickness)
 K = beam half-angle
 L = focal length
 M = Mach number
 P = pressure
 Re = Reynolds number
 s = blade spacing (7.62 cm)
 T = temperature
 u = velocity component parallel to blade surface

U_∞ = velocity component parallel to blade surface at the edge of the viscous layer
 v = velocity component normal to blade surface
 V = velocity
 x, X = horizontal displacement (defined in Fig. 3)
 \bar{X} = blade coordinate (defined in Fig. 13)
 y, Y = vertical displacement (defined in Fig. 3)
 \bar{Y} = blade coordinate (defined in Fig. 13)
 Y_{ac} = location as a fraction of axial chord [= (Y + 12.172)/c']
 z = spanwise displacement
 β = air angle (defined in Fig. 1)
 γ = blade setting angle (defined in Fig. 1)

δ = boundary layer thickness
 δ^* = displacement thickness
 $\Delta ()$ = uncertainty in measurement ()
 θ = momentum thickness

Subscripts

a = atmospheric
 c = chord
 i = initial LDV reading, closest to the surface
 L = lower
 ref = reference, upstream
 t = total or stagnation
 U = upper
 W = endwall
 0 = plenum
 1 = upstream
 2 = downstream

Table 2 LDV system characteristics and estimated measurement uncertainties

Item	Description	Method	Uncertainty
LASER			
Type	Argon-Ion		
Manufacturer	Lexel		
Nominal Power	1.5 watts		
WAVELENGTH			
Blue	488.0 nm		
Green	514.5 nm		
FRINGE SPACING			
Blue	4.51 μ m		
Green	4.76 μ m		
FOCAL LENGTH			
	762.0 mm		
NUMBER OF FRINGES			
	28		
HALF ANGLE			
	3.1 $^{\circ}$		
MEASURING VOLUME			
Length	2.5 mm		
diameter	133.0 μ m		
FREQUENCY SHIFT			
	2kHz - 40kHz		
Increments	1,2,5,10 MHz		
SIGNAL PROCESSOR			
Type	Counter		
Manufacturer	TSI Mod 1990		
COUNTER SETTINGS			
Filters	As Required		
Gain	As Required		
Mode	Coincident		
	Single Measure/Burst		
cycle / burst	8		
Comparison	4%		
X	Blade-toBlade (Passage)	Milling Machine Elec. Readout	0.25 mm
x	Distance from Blade Surface	Milling Machine Elec. Readout	0.05 mm
Y	Vertical	Milling Machine Scale	0.25 mm
y	Distance from Blade Surface	Milling Machine Scale	0.05 mm
z	Spanwise	Milling Machine Elec. Readout	1.25 mm
	Pitch, Roll, Yaw of LDV System	Electronic Level Sperry Model 45	0.1 $^{\circ}$
P ₁	Plenum Pressure	Water Manometer	25 Pa
p	Pressure	Scanivalve Transducer	12 Pa
P _{atm}	Atm. Pressure	Mercury Barometer	35 Pa
T ₁	Plenum Temp.	Iron Constantan Thermocouple	0.14 $^{\circ}$ C
	LDV Counter Clock		1 n-sec
K	Beam Half Angle		20 arcsec (0.2%)
L	Focal Length		7.60 mm (1%)
λ	Wavelength		0.1%
d _f	Fringe Spacing		0.3%
V	Particle Velocity		0.33% @ 10 m/s 0.65% @ 100 m/s

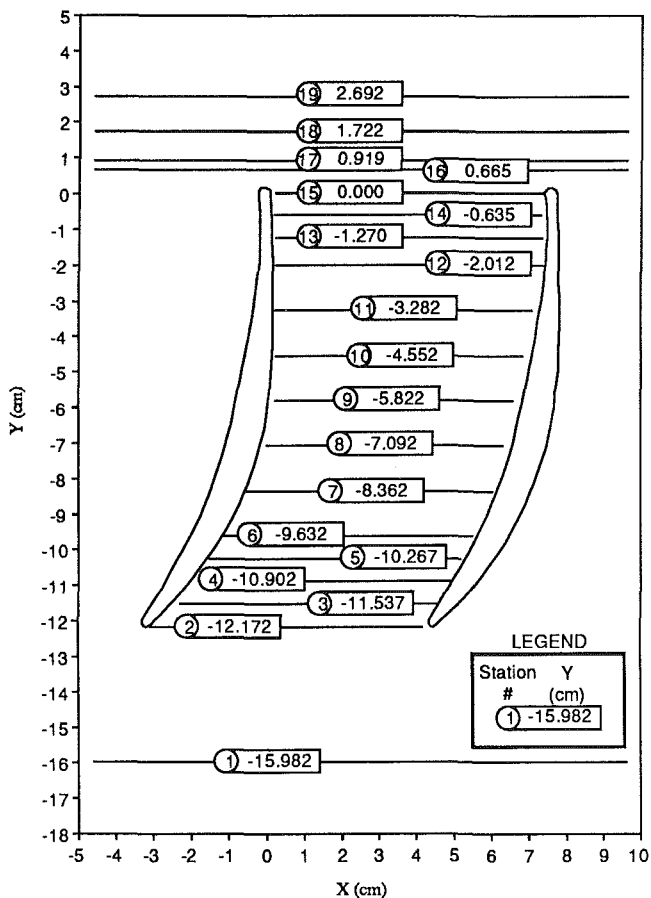


Fig. 3 Cascade passage geometry and LDV survey stations

Laser Velocimeter System

Optics and Data Acquisition. A four-beam, two color TSI Model 9100-7 LDV system was used. The system operated in the backscatter mode. Characteristics of the system are given

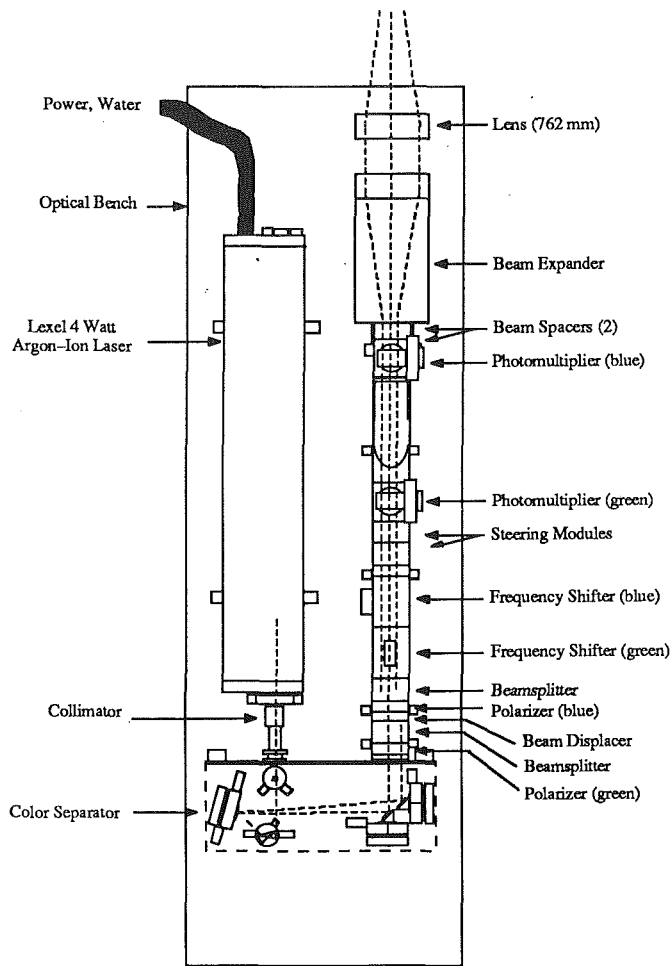


Fig. 4 Components of the LDV system

in Table 2. The components of the system are shown in Fig. 4. The laser was a Lexel, 4-watt argon-ion laser. A prism and mirror system separated the two colors from which two beams of each color were generated, equidistant from an optical axis. The beams, and fringe pattern in the measurement volume, were arranged vertical/horizontal or at 45 $^{\circ}$, depending on the location of the measurement. Two Bragg cells shifted the frequency of one beam in each pair to allow measurements in regions of reversed flow. After the beam expander, the final lens produced a focal measurement volume near the midspan center plane of the wind tunnel test section, 762 mm from the lens. Two photo-detectors collected light scattered by particles passing the measurement volume via the same optics. Two TSI Model 1990 counter-type signal processors received the output from the photo-detectors and produced digital voltages proportional to the Doppler frequencies of detected events. These data were transferred by way of an interface to a Hewlett-Packard Model HP 1000 computer operating with the TSI data acquisition software program DRP3.

Traverse System. The laser and optics, mounted on an optical bench, were supported on the bed of a large milling machine installed on the laboratory floor next to the wind tunnel. A view of the installation is given in Fig. 5. The mill was aligned and leveled such that the manual x, y, z traverse motions of the mill table moved the measurement volume of the LDV system horizontally (blade-to-blade), vertically (normal to the leading-edge locus), and fore-and-aft (spanwise) respectively. While the traverse was actuated manually, the x and y coordinates were indicated on digital electronic readouts, which were hand-recorded. The optical bench also could be

yawed to direct the optical axis $\pm 3.5^\circ$ with respect to the spanwise direction.

Seeding. Olive oil droplets were used. The particle generator incorporated a TS1 Model 9302 atomizer driven from a shop-air supply. Oil droplets carried by the controlled air pressure were injected by way of a 6.4 mm wand through the plenum of the wind tunnel below the inlet guide vanes (Fig. 2). Seeding only near the center plane of the flow beneath the correct pair of guide vanes resulted in a distribution of seed material across the 7th–8th blade space with no contamination of the window, and no detectable disturbance to the inlet flow. Preliminary tests were conducted to optimize the seed particle distribution. An air pressure of 40 psi was selected to obtain an average particle size of 0.9 microns with standard deviation 0.45 microns. At this setting, 95 percent of the particles were smaller than 1.8 microns. These characteristics were considered to be satisfactory by the criteria proposed by Durst et al. (1976) or Dring (1982).

Positioning. A special jig, described by Elazar (1988), was manufactured, which attached to the trailing edges of blades 7 and 8 at midspan. The jig contained six holes, each 0.033 cm in diameter, on which the measurement volume could be targeted. When the measurement volume was on target, the four beams were clearly visible on the back wall of the test section, and X, Y coordinates of the measurement point were then known to the accuracy of the jig.

Measurement Uncertainty. The estimated measurement uncertainties also are given in Table 2. The uncertainties in the parameters K, L and λ were given by the manufacturer. Fringe spacing (d_f) was calculated following Durst et al. (1976) as $d_f = \lambda / \sin K$. The particle velocity uncertainty ($\Delta V / V$) was calculated using

$$\frac{\Delta V}{V} = \frac{\Delta d_f}{d_f} + \frac{\Delta t}{t} = \frac{\Delta d_f}{d_f} + \frac{V \Delta t}{8d_f}$$

where Δt = instrument clock uncertainty (1 nanosec), and $t = 8d_f / V$ = time to cross eight fringes. Since the particles do not follow the flow precisely, the uncertainty in the velocity can be larger than the uncertainty in the particle velocity. The uncertainty in positioning the measuring volume on the blade surface, which gave an equal uncertainty in the displacement of the measurement from the surface in boundary layer surveys, was shown by experiment to be less than 0.05 mm.

Experimental Procedure

Program Overview. A preliminary experiment was conducted in which the test blading was removed from the test section and the inlet and outlet endwalls were set straight at $\beta = 40^\circ$. A flat plate was installed in the center of the test section and the boundary layer development on the flat plate was measured to verify all aspects of the LDV measurements. Good agreement of the velocity profiles with the Blasius solution was obtained where the boundary layer was laminar, and agreement with other published measurements was seen where the boundary layer was turbulent (Elazar, 1988). The CD blading was then installed and detailed measurements were obtained in turn at inlet air angles $\beta_1 = 40^\circ$ (the design condition), $\beta_1 = 43.4^\circ$ (about twice minimum loss) and $\beta_1 = 46^\circ$ (near to stall) as determined by Sanger and Shreeve (1986). At each inlet air angle, measurements were made to map specific regions of the flow; namely, the inlet flow field 0.3 chords upstream of the blade leading edge (Station 1 in Fig. 3); the passage between the 7th and 8th blades (Stations 2–15 in Fig. 3); the boundary layers on the suction and pressure sides of the 7th blade (nominally Stations 3–15 in Fig. 3); and the wake downstream of the 7th blade (Stations 16–19 in Fig. 3).

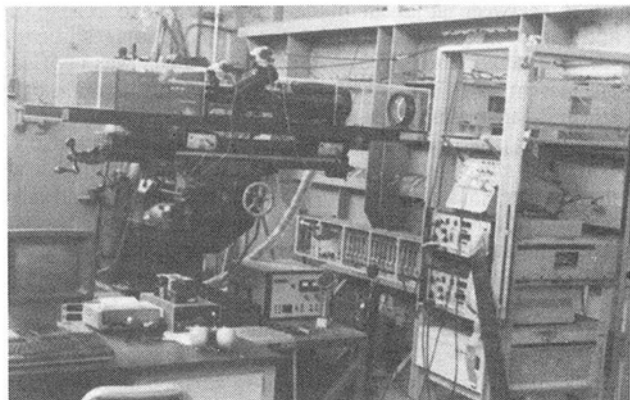


Fig. 5 LDV system installation

Setup Procedure at Each Air Angle. *Wind Tunnel Flow Verification.* At each inlet air angle, the inlet and outlet walls and inlet guide vanes were adjusted to obtain near-uniform wall static pressure (in the blade-to-blade direction) both upstream and downstream of the test cascade (Sanger and Shreeve, 1986). The blade-to-blade flow angle distribution was measured by surveys with a United Sensor Model DA-125 probe at 1.8 blade chords upstream, and by the LDV system at 0.3 chords upstream. The probe measurements provided verification of the inlet flow conditions, which were surveyed extensively in earlier studies by McGuire (1983), Koyuncu (1984) and Dreon (1986).

Probe results, spanning four blade passages at design inlet air angle, were reported by Sanger and Shreeve (1986). LDV survey results, 0.3 chord lengths upstream of the passage be-

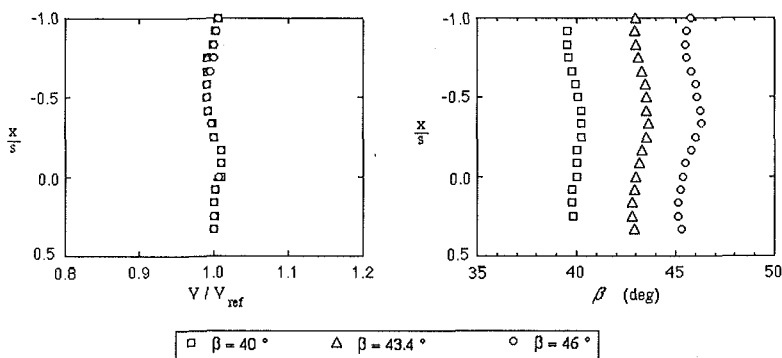


Fig. 6 Inlet flow field at Station 1

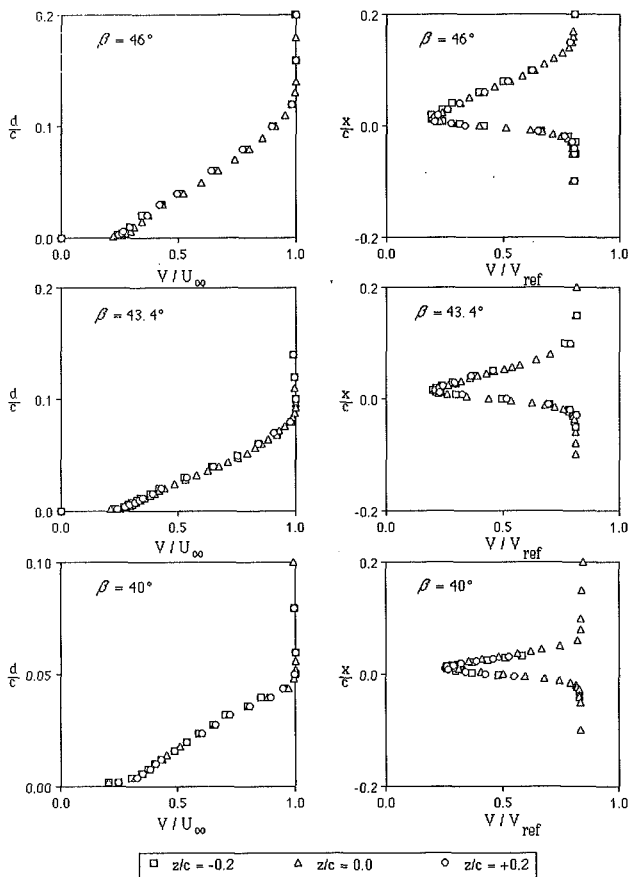


Fig. 7 Suction surface boundary layer and blade wake measurements to verify two-dimensionality

tween blades 7 and 8 (as far as the window would allow), are shown in Fig. 6.

Optical System Alignment. Proper beam crossing and fringe patterns were verified at intervals while mapping the flow at a fixed air angle. A complete optical system alignment was carried out for each inlet air angle. It was preferred to orient the crossing pairs of beams at about 45° to the flow velocity vector. Thus, at the lower stations (1–5 in Fig. 3), the pairs of beams were oriented vertical/horizontal whereas at stations 6–19, the pairs were rotated through 45° . The inlet flow and lower passage were surveyed without Bragg cells installed. The Bragg cells were installed and frequency shifting was used at all other stations.

Traverse Positioning. For inlet, passage and wake surveys, the alignment jig was attached to blades 7 and 8 and the table was adjusted to target the measurement volume on a specific target hole. When the pattern of four beams was clearly and evenly visible on the back wall of the test section, the X , Y coordinates of the target hole were entered into the digital electronic readouts. The readouts then indicated the displacement of the measuring volume in the X , Y coordinate system whose origin lay at the center of curvature of the trailing edge of the 7th blade.

For boundary layer surveys, first the optical table was yawed $\pm 3.5^\circ$ horizontally with respect to the table of the milling machine. The measuring volume was positioned at the required level (Y displacement), using the alignment jig. The measuring volume was then traversed horizontally (X displacement) until the four beams crossed on the blade surface. The crossing was observed by eye and an uncertainty of less than 0.05 mm was achieved with ease. The digital readouts were set to zero. The x and y coordinates for displacements normal to the wall were calculated from the local surface slope.

Survey Procedures at Each Air Angle. Inlet Flow and Tunnel Reference Conditions. An LDV survey was made at Station 1 (Fig. 3). The results at each inlet air angle are shown in Fig. 6. Despite the proximity of the survey to the blades, the velocity and flow angle were found to be uniform to within ± 1 percent and $\pm 0.75^\circ$, respectively. In Fig. 6, the local velocity (V) is shown normalized to a reference velocity (V_{ref}) obtained from tunnel reference parameters at the time of recording the measurement. Such referencing removes the effects of temporal variations in wind tunnel supply and ambient atmospheric conditions. It can be shown, using Appendix C of Elazar (1988), that for small variations in supply and ambient atmospheric conditions

$$V_1 = C\sqrt{T_{r0}(P_{r0} - P_a)/P_a} \quad (1)$$

where C is a constant for a fixed test geometry (inlet air angle). The value of C at each air angle was calculated as the average value of $V_1/\sqrt{T_{r0}(P_{r0} - P_a)/P_a}$ for the points in the inlet flow survey. All velocities measured thereafter were normalized with respect to the inlet flow reference velocity (V_{ref}), calculated using equation (1) with the tunnel and ambient conditions at the time of the measurement.

Passage, Boundary Layer and Wake Surveys. Passage velocities were measured at approximately 30 locations across each of the 14 stations (Fig. 3) from the leading to the trailing edge. Boundary layer surveys were made at predetermined intervals locally normal to the blade surface, beginning at Station 15 in Fig. 3 (in line with the center of curvature) and at each station toward the leading edge until the boundary became too thin. Both pressure and suction surfaces of the 7th blade were measured. Wake surveys were made at four stations downstream of the 7th blade (Stations 16–19 in Fig. 3).

Verification of Periodicity and Two-Dimensionality. In view of the unusually large number of test blades (20), periodicity between adjacent blade passages was to be expected and had been demonstrated for the central passages in earlier studies (Sanger and Shreeve, 1986). Periodicity was verified in the present study by making LDV surveys downstream of the 7th and 8th blades. The blade wakes were indistinguishable from each other (Elazar, 1988). Two-dimensionality also was examined since the wind tunnel was not equipped with wall suction. Previous studies (Sanger and Shreeve, 1988) had shown that conditions far downstream of the blade trailing edges were independent of spanwise displacement for ± 5 cm from midspan. However, conditions within the blade passage could not be examined at that time. In the present study, LDV surveys were made in the wakes and through the boundary layers at the trailing edge of the 7th blade at midspan and at ± 2.54 cm from midspan. Wake and suction surface boundary layer results are shown in Fig. 7.

Data Reduction. The LDV data were acquired using program DRP3 on the HP 1000 computer, stored on floppy disks and transferred to the mainframe IBM 370-3033 for processing. Tunnel reference measurements were recorded and entered manually. Separate computer programs were written to reduce, tabulate and plot results from passage, boundary layer and wake surveys. Blade surface pressure measurements, acquired and recorded using the HP 9845 controller, also were transferred to the mainframe for processing.

Results and Discussion

Inlet Flow. The inlet flow measurements are shown in Fig. 6. At each inlet air angle, the inlet velocity (V_{ref}) was set to approximately 85 m/s (Mach number = 0.25). The measured free-stream turbulence level, the result of the many inlet guide

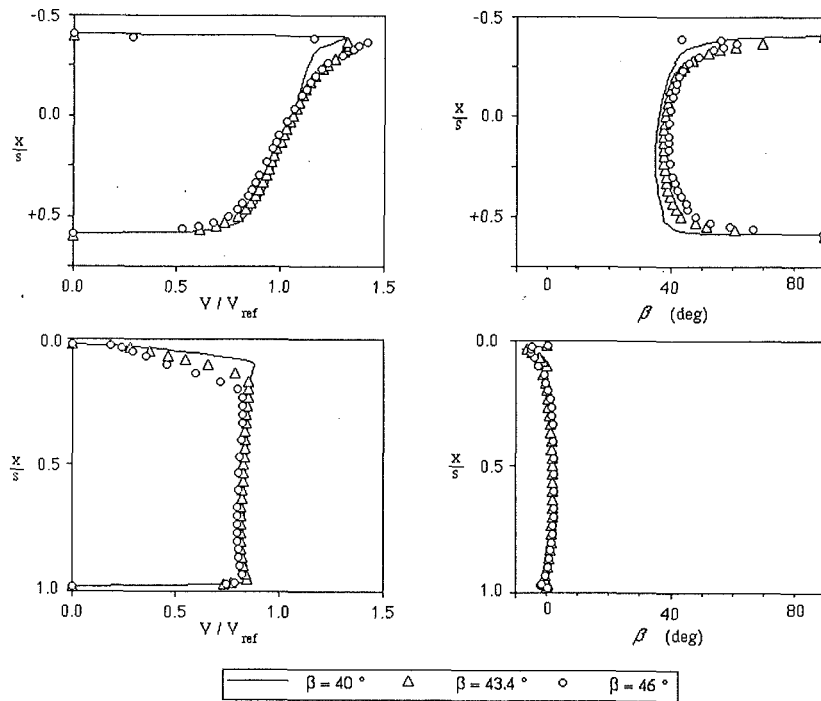


Fig. 8 Flow at the passage entrance (Station 2) and exit (Station 15)

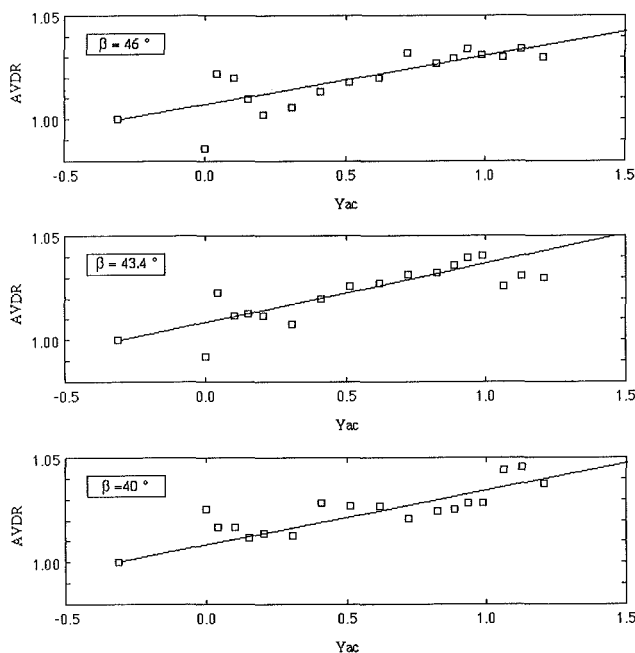


Fig. 9 Measured variation in AVDR

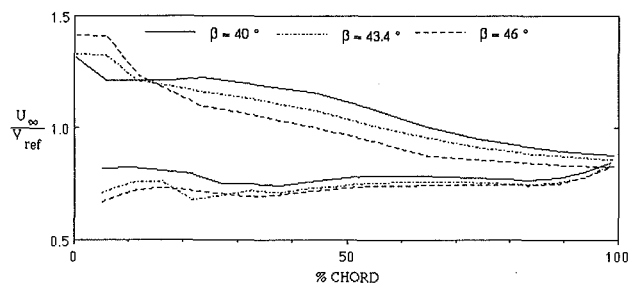


Fig. 10 Effect of inlet air angle on the edge velocity distribution

vanes (59) far upstream, was 1.4 ± 0.2 percent at all conditions. The average flow angle measured, using the LDV system 0.3 chord lengths ahead of the blading (Fig. 6), was consistent with measurements made using a pneumatic probe 1.8 chord lengths upstream; namely, 40.0, 43.4 and 46.0°. At the upstream station, the flow angle varied less than 0.1° across one blade space.

Flow Through the Passage. From blade-to-blade surveys at 14 stations, from the leading to trailing edge, the streamline paths through the passage were calculated by integrating the volume flow rate. Similarly, the local volume flow to the inlet volume flow for one passage gave the distribution of the AVDR assuming negligible effect of compressibility. It was found (Elazar, 1988) that no sudden changes occurred in the geometry of the streamlines as the incidence was increased. Rather, a progressive shift occurred away from the suction side of the passage. This orderly change in behavior is evident in Fig. 8, which shows the velocity and flow angle variations at the entrance (Station 2) and exit (Station 15) of the passage. The distribution of the AVDR from the reference inlet station to downstream of the blading is shown for the three inlet air angles in Fig. 9. The magnitude of the variation (to a maximum value of 1.05 just downstream of the blade) was consistent with previous results (Sanger and Shreeve, 1986) which gave overall values of 1.04–1.06 based on probe survey measurements well downstream (1.7 chord lengths) and well upstream (1.8 chord lengths) of the blading. Based on the results in Fig. 9, a linear variation of the AVDR from 30 percent chord upstream through the blade passage should be used for code assessment.

Also derived from the passage surveys was the velocity at the edge of the viscous layer as the suction and pressure surfaces were approached. The results are shown in Fig. 10. The edge velocity was taken either as the maximum value of the velocity (where gradients were large and the boundary layer was thin, on the suction side near the leading edge, for example) or as the velocity where the turbulence level departed from its free-stream value (where gradients were small and the boundary layer was well defined, on the pressure side near the trailing

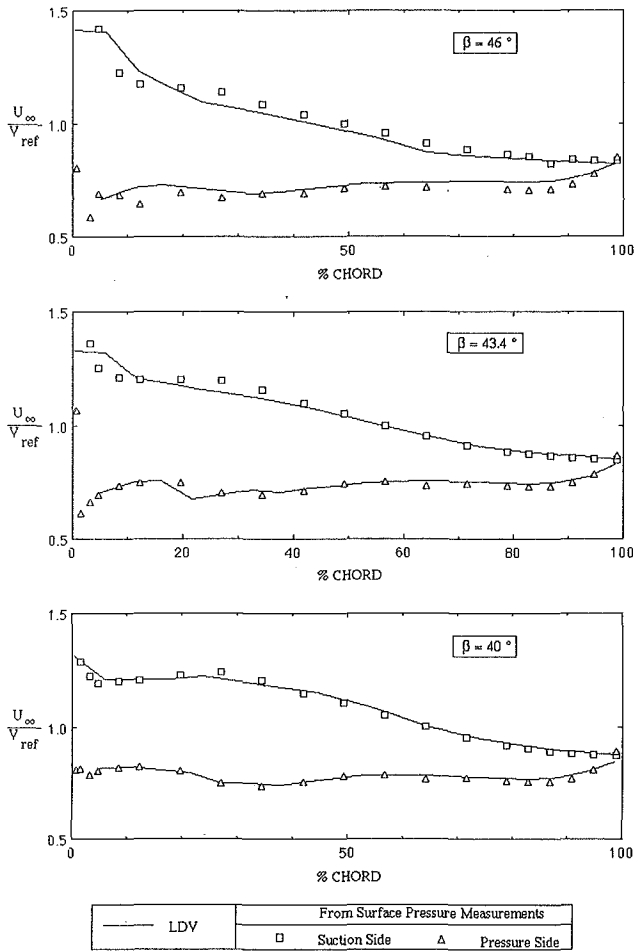


Fig. 11 Comparison with edge velocity inferred from surface pressures

edge, for example). The curves in Fig. 10 are shown without data points for clarity in comparing results at increasing incidence. Figure 11 shows, for comparison, the edge velocity derived from measurements of surface pressure, with the assumption that pressure was constant through the viscous layer and that the flow was incompressible; namely, $U_{\infty}/V_{ref} = \sqrt{1 - C_p}$.

It is clear from Fig. 11 that while the two measures of edge velocity agreed quite well at design incidence ($\beta_1 = 40^\circ$), they departed from each other as the incidence was increased, notably on the suction side of the blade. In particular, the surface pressures indicated higher peak velocities than were measured using the LDV system. Since a large transverse component of acceleration would be present locally, the ability of the seed particles to track the streamlines must be questioned. However, it also is noted that the first computations by Shamroth, using a Navier-Stokes code applied to the specified geometry and test conditions (Shamroth, 1987), also did not predict the peak suction pressures, which were measured pneumatically. As shown in Fig. 12 however, excellent agreement was obtained between the predicted and measured pressures at all incidence angles, except near the suction surface leading edge. Earlier comparisons of measured pressures with inviscid code calculations (Sanger and Shreeve, 1986) had shown disagreement toward the trailing edge, but had tended to confirm the extreme suction peaks.

Suction-Side Boundary Layer. Illustrative examples of the results of detailed boundary layer surveys are shown in Fig. 13. Equivalent results to those shown for $\beta_1 = 46^\circ$ were ob-

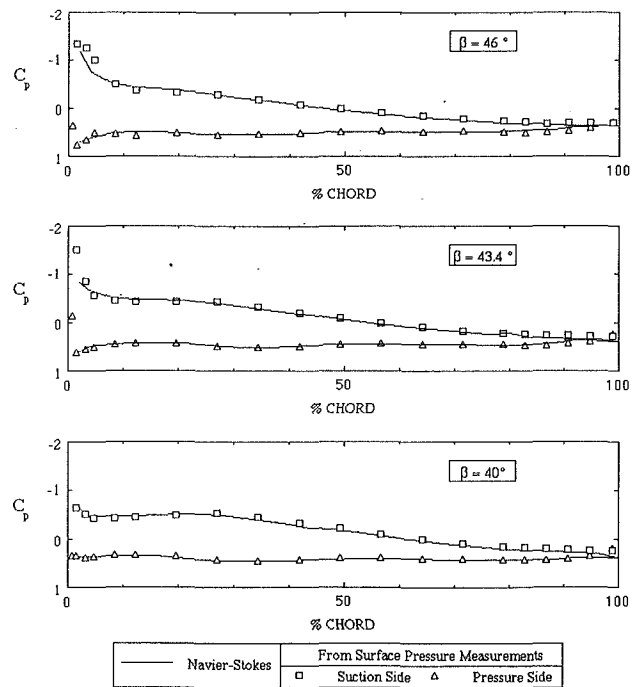


Fig. 12 Measured and calculated surface pressure distributions

tained at $\beta_1 = 40^\circ$ and $\beta_1 = 43.4^\circ$. The figure shows results for the velocity components normal (v) and parallel (u) to the surface, and the turbulence level.

The presence of a separation bubble, detected earlier using the china-clay technique (Sanger and Shreeve, 1986) was confirmed by the LDV measurements. However, no information on the flow within the separation bubble was obtained since no particles were detected within the region. The absence of data near to the wall in surveys at Stations 3 and 4 in Fig. 13 was the result of detecting no observable events. It can be seen at Station 3 that the particles were found only in the outer part of the shear layer over the bubble, consistent with the earlier suggestion that they might not follow the rapid acceleration around the leading edge of the blade. The presence of a negative component of velocity normal to the surface was consistent with the flow tending toward reattachment downstream of the bubble. If the absence of negative components of velocity normal to the wall was taken to indicate the completion of reattachment, this point moved from about 15 percent to 30 percent to 40 percent of chord as the air inlet angle was increased from 40° to 43.4° to 46° , respectively. Downstream of the completion of reattachment, the normal component of velocity was negligibly small. The peak turbulence level in the shear layer over the bubble reached over 16 percent, decreased during reattachment and became steady at 8–9 percent in the boundary layer to the trailing edge.

It was noted that the maximum turbulence level moved gradually away from the wall during reattachment to be at about 45 percent of the boundary thickness at the trailing edge. Qualitatively, similar trends to those illustrated in Fig. 13 were found in the results at $\beta_1 = 40^\circ$ and $\beta_1 = 43.4^\circ$. Thus the effect of increasing incidence was to progressively delay reattachment from the separation bubble, and to generate a progressively thicker viscous layer. However, the viscous layer remained attached all the way to the trailing edge even at the largest inlet air angle. It is probable that the appearance of separation occurring just ahead of the trailing edge, when using the china-clay technique (Sanger and Shreeve, 1986), was the result of gravitational effects on the oil mixture with which the surface was wetted, in a region of low dynamic pressures. Considerable effort was made to verify the present LDV observations, in-

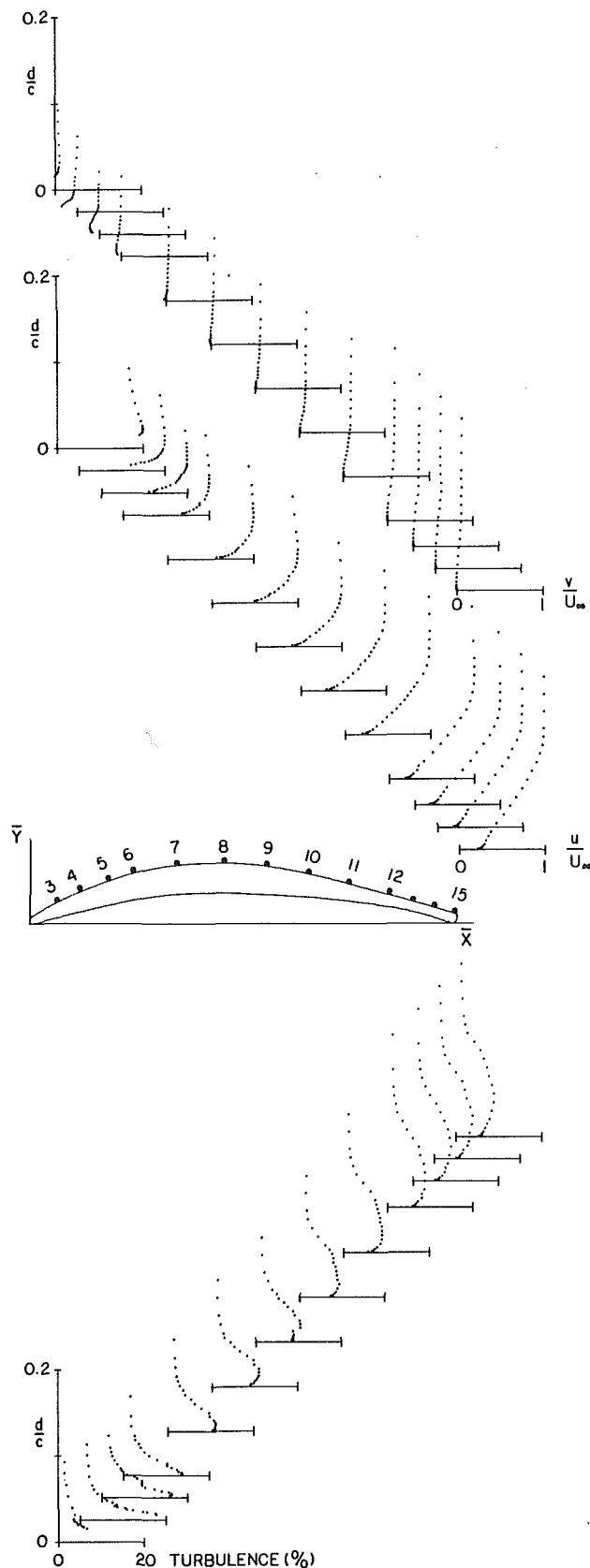


Fig. 13 Results of boundary layer surveys on the suction surface at $\beta = 46^\circ$

cluding verification of both mean velocity and fluctuation levels, by conducting redundant measurements within the blade wake with a hot-wire (Baydar, 1988). Excellent agreement be-

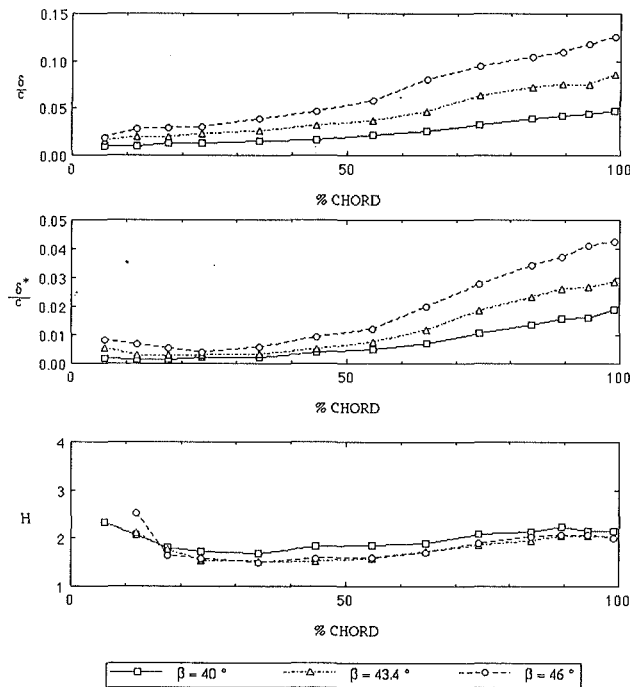


Fig. 14 Suction-side boundary layer growth

tween hot-wire and LDV was obtained. It also is noted that whereas regions of instantaneous backflow were measured in the near-wake using LDV, and a time-averaged backflow was recorded at Station 16 at $\beta = 40^\circ$, no backflow was detected at Station 15 at all three inlet air angles.

The growths in the boundary layer thickness and displacement thickness and the distribution of the shape factor on the suction side of the blade are shown in Fig. 14. The thickness was defined as the point at which the velocity component parallel to the surface reached 99 percent of the edge velocity. The displacement thickness was calculated by integration to where the edge velocity occurred. Downstream of the bubble, the layer was seen to grow steadily. Each increment in flow incidence gave approximately equal increments in boundary layer growth. At the highest incidence, the suction-side boundary layer occupied more than 20 percent of the blade passage at the trailing edge. At each incidence, the shape factor reached a minimum after reattachment and then increased to the trailing edge. The results at the design angle were different than those at the higher incidence angles, and gave larger values (closer to separation!) near the trailing edge. The largest value reached was 2.25 at Station 13, 10 percent of chord ahead of the trailing edge. At each angle, the shape factor decreased slightly from this point aft, to the trailing edge. The differences between design and off-design incidence angles suggest a non-linear behavior near the leading edge of the blade. This is supported by the measurements of the edge velocity shown in Fig. 10. Results for the integral properties at each axial measurement station are given in Table 3.

Pressure-Side Boundary Layer. Similar data were obtained for the pressure-side boundary layer velocity and turbulence profiles, thickness, and integral properties. The velocity and turbulence profiles (Elazar, 1988) indicated that the pressure-side boundary layer began laminar and became turbulent through natural transition. The pressure-side layer was much thinner, resulting in fractionally larger uncertainties in the derived integral thicknesses. Results for the integral properties are given in Table 3. (Data are included at three other stations between 6 and 9.) The boundary layer thickness, displacement

Table 3 Measured development of the blade surface boundary layers

$\beta_1 = 46^\circ$

Suction Surface						Pressure Surface								
Y_{ac}	$u_f U_{\infty}$	$(\delta^*/c) \times 100$	$(\Delta\delta^*/c) \times 100$	$(\theta/c) \times 100$	$\Delta\theta/c \times 100$	Y_{ac}	$u_f U_{\infty}$	$(\delta^*/c) \times 100$	$(\Delta\delta^*/c) \times 100$	$(\theta/c) \times 100$	$\Delta\theta/c \times 100$	H	ΔH	
0.155	0.549	0.5614	0.0292	0.3422	0.00730	1.6420	0.391	0.2087	0.0334	0.0876	0.00605	2.3960	0.55	
0.206	0.684	0.4278	0.0271	0.2713	0.00772	1.5820	0.558	0.1878	0.0292	0.0856	0.00730	2.2040	0.53	
0.309	0.573	0.6093	0.0292	0.4069	0.00730	1.5000	0.412	0.773	0.1356	0.0250	0.00772	1.9250	0.56	
0.412	0.498	0.9537	0.0313	0.6052	0.00689	1.5760	0.515	0.816	0.1336	0.0250	0.00772	2.1520	0.67	
0.515	0.420	1.2876	0.0334	0.8055	0.00626	1.5990	0.618	0.758	0.1711	0.0250	0.00772	1.8530	0.43	
0.618	0.297	2.0868	0.0355	1.2229	0.00501	1.7070	0.721	0.725	0.1878	0.0271	0.1043	0.00772	1.7990	0.39
0.721	0.209	2.8944	0.0376	1.5317	0.00376	1.8900	0.824	0.662	0.2442	0.0271	0.1482	0.00772	1.6620	0.27
0.824	0.188	3.5956	0.0376	1.7696	0.00334	2.0320	0.884	0.646	0.2796	0.0271	0.1732	0.00772	1.6150	0.23
0.884	0.174	3.8877	0.0376	1.8698	0.00313	2.0790	0.936	0.701	0.3088	0.0271	0.1899	0.00772	1.6170	0.21
0.936	0.194	4.2780	0.0376	2.0701	0.00355	2.0670	0.987	0.844	0.1440	0.0250	0.0751	0.00772	1.9510	0.54
0.987	0.220	4.4386	0.0376	2.2078	0.00396	2.0100								

$\beta_1 = 43.4^\circ$

Suction Surface						Pressure Surface								
Y_{ac}	$u_f U_{\infty}$	$(\delta^*/c) \times 100$	$(\Delta\delta^*/c) \times 100$	$(\theta/c) \times 100$	$\Delta\theta/c \times 100$	Y_{ac}	$u_f U_{\infty}$	$(\delta^*/c) \times 100$	$(\Delta\delta^*/c) \times 100$	$(\theta/c) \times 100$	$\Delta\theta/c \times 100$	H	ΔH	
0.103	0.718	0.3151	0.0271	0.1503	0.00772	2.1060	0.309	0.710	0.1774	0.0271	0.0501	0.00772	3.5210	1.08
0.155	0.724	0.2984	0.0271	0.1669	0.00772	1.7770	0.361	0.611	0.2108	0.0292	0.1043	0.00751	2.4030	0.42
0.206	0.720	0.3026	0.0271	0.1982	0.00772	1.5300	0.412	0.730	0.2108	0.0250	0.1023	0.00772	2.0780	0.40
0.309	0.640	0.3527	0.0292	0.2337	0.00772	1.5090	0.464	0.742	0.1523	0.0250	0.0772	1.9970	0.53	
0.412	0.536	0.5363	0.0313	0.3548	0.00710	1.5170	0.515	0.746	0.2045	0.0250	0.0981	0.00772	2.0710	0.42
0.515	0.438	0.7972	0.0334	0.5029	0.00647	1.5870	0.618	0.605	0.2796	0.0292	0.1669	0.00751	1.6760	0.25
0.618	0.309	1.2396	0.0355	0.7158	0.00501	1.7330	0.721	0.617	0.2380	0.0292	0.1732	0.00751	1.6660	0.24
0.721	0.172	1.9240	0.0376	1.0351	0.00313	1.8590	0.824	0.648	0.3402	0.0271	0.2003	0.00772	1.6930	0.20
0.824	0.210	2.4124	0.0376	1.2396	0.00376	1.9480	0.884	0.604	0.4048	0.0292	0.2483	0.00751	1.6380	0.17
0.884	0.139	2.7108	0.0396	1.3230	0.00271	2.0500	0.936	0.580	0.3923	0.0292	0.2483	0.00730	1.5770	0.16
0.936	0.217	2.8151	0.0376	1.3794	0.00396	2.0430	0.987	0.759	0.2838	0.0250	0.1523	0.00772	1.8500	0.26
0.987	0.210	2.9904	0.0376	1.4795	0.00376	2.0210								

$\beta_1 = 40^\circ$

Suction Surface						Pressure Surface								
Y_{ac}	$u_f U_{\infty}$	$(\delta^*/c) \times 100$	$(\Delta\delta^*/c) \times 100$	$(\theta/c) \times 100$	$\Delta\theta/c \times 100$	Y_{ac}	$u_f U_{\infty}$	$(\delta^*/c) \times 100$	$(\Delta\delta^*/c) \times 100$	$(\theta/c) \times 100$	$\Delta\theta/c \times 100$	H	ΔH	
0.103	0.766	0.1523	0.0250	0.0730	0.00772	2.0810	0.206	0.698	0.1544	0.0271	0.0459	0.00772	3.3260	0.14
0.155	0.751	0.1669	0.0250	0.0918	0.00772	1.8190	0.258	0.458	0.2421	0.0313	0.0960	0.00668	2.5280	0.50
0.206	0.674	0.2108	0.0271	0.1231	0.00772	1.7200	0.309	0.542	0.1816	0.0313	0.0793	0.00730	2.2880	0.60
0.309	0.633	0.2254	0.0292	0.1336	0.00772	1.6850	0.361	0.671	0.2087	0.0271	0.1064	0.00772	1.9570	0.40
0.412	0.601	0.4007	0.0292	0.2191	0.00751	1.8310	0.412	0.298	0.1941	0.0355	0.1169	0.00501	1.6650	0.37
0.515	0.488	0.5196	0.0313	0.2796	0.00689	1.8480	0.515	0.524	0.2337	0.0313	0.1398	0.00710	1.6520	0.30
0.618	0.403	0.7283	0.0334	0.3819	0.00626	1.9050	0.618	0.652	0.2421	0.0271	0.1419	0.00772	1.7110	0.28
0.721	0.259	1.1227	0.0355	0.5342	0.00438	2.1010	0.721	0.471	0.3694	0.0313	0.2212	0.00668	1.6770	0.19
0.824	0.267	1.4295	0.0355	0.6678	0.00459	2.1410	0.824	0.602	0.3631	0.0292	0.2212	0.00751	1.6440	0.19
0.884	0.222	1.6590	0.0376	0.7366	0.00459	2.2570	0.884	0.622	0.4257	0.0292	0.2671	0.00751	1.5990	0.15
0.936	0.261	1.6841	0.0376	0.7805	0.00438	2.1580	0.936	0.616	0.3990	0.0292	0.2650	0.00751	1.5070	0.15
0.987	0.202	1.9720	0.0376	0.9140	0.00355	2.1560	0.987	0.400	0.3694	0.0334	0.2295	0.00605	1.6130	0.19

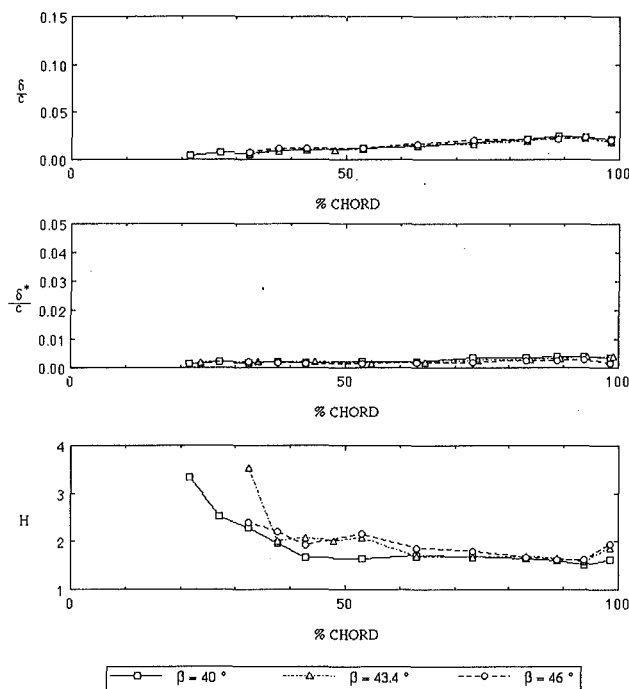


Fig. 15 Pressure-side boundary layer growth

thickness, and shape factor are shown plotted in Fig. 15. Again, a qualitative difference was noted in the results for the boundary layer shape at design incidence, although the overall thickness was not measurably different at the three angles. In contrast to the suction side, the shape factor increased toward the trailing edge over the final 5 percent of chord. This, and the behavior observed on the suction side near the trailing edge, was likely to be the upstream influence of the base and near-wake flow resulting from trailing edge bluntness.

Near-Wake. The near-wake was found to be asymmetric in both time mean and turbulence properties. Consistent with the observation that the suction surface boundary layer remained attached as incidence was increased, was the observation that the region of backflow in the wake *decreased* in size as the incidence was increased. Wake velocity and turbulence measurements were confirmed by Baydar (1988), using hot-wires, and velocity profiles compared well with multisensor pressure probe measurements by Dreon (1986). Initial attempts to derive loss coefficients, using only data obtained during LDV traverses of the near-wake, were not useful. An assumption had to be made either for the pressure to use in computing stagnation conditions (the pressure was not measured where traverses were made), or for the average angle to use in Lieblien's incompressible loss equation (equation 264 in Johnsen and Bullock, 1965). In either case, the magnitude of the uncertainty was comparable to the value of the loss. Thus the LDV measurements were consistent with earlier probe measurements of losses (Sanger and Shreeve, 1986 and Dreon, 1986) but were much less certain in magnitude.

Conclusions

Two-component laser velocimeter measurements of the flow through a CD compressor cascade at low Mach number (~ 0.25), Reynolds number of about 7×10^5 , and increasing incidence (inlet air angles of 40° , 43.4° , and 46°) have shown that the flow remained attached on the suction side of the blade, to the trailing edge, at all air angles. The suction-side boundary layer increased in thickness in approximately equal increments to fill 20 percent of the blade passage at the highest

air angle, at which losses were measured to be 3–4 times their minimum value for the cascade (Sanger and Shreeve, 1986). On the suction side of the blade, there was a laminar separation bubble with turbulent reattachment moving downstream as the air angle increased. On the pressure side, there was natural transition and little change in growth as the air angle increased. In view of the completeness of the flow mapping, with passage surveys at 19 stations and boundary layer surveys at 12 stations along two blade surfaces, the data are well suited for viscous code assessment and calibration. The present results, obtained with a CD cascade having no separation present downstream of the bubble on the suction side, are considered complimentary as a test case with earlier results for more highly loaded DCA blading with some separation present (Deutsch and Zierke, 1987, 1988).

Acknowledgment

The present study was supported by the Naval Air Systems Command as part of the Air Breathing Propulsion Research Program under George Derderian. The program also benefited from the early support and continuing interaction with Nelson Sanger at NASA Lewis Research Center. The authors would like to thank those in the CFD community who have expressed interest in computing the present configuration as a test case, and particularly Dr. Steven Shamroth who provided a complete set of results. Lt. K. D. Murray contributed significantly in the computer regeneration of important figures.

References

- Baydar, A., 1988, "Hot-Wire Measurements of Compressor Blade Wakes in a Cascade Wind Tunnel," MS Thesis, Naval Postgraduate School, Monterey, California.
- Deutsch, S., and Zierke, W. C., 1987, "The Measurement of Boundary Layers on a Compressor Blade in Cascade: Part 1—A Unique Experimental Facility," ASME JOURNAL OF TURBOMACHINERY, Vol. 109, pp. 520–526.
- Deutsch, S., and Zierke, W. C., 1988, "The Measurement of Boundary Layers on a Compressor Blade in Cascade: Part 2—Suction Surface Boundary Layers," ASME JOURNAL OF TURBOMACHINERY, Vol. 110, pp. 138–145.
- Deutsch, S., and Zierke, W. C., 1988, "The Measurement of Boundary Layers on a Compressor Blade in Cascade: Part 3—Pressure Surface Boundary Layers and the Near Wake," ASME JOURNAL OF TURBOMACHINERY, Vol. 110, pp. 146–152.
- Dreon, J. W., 1986, "Controlled Diffusion Compressor Blade Wake Measurements," MS Thesis, Naval Postgraduate School, Monterey, California.
- Dring, R. P., 1982, "Sizing Criteria for Laser Anemometry Particles," ASME JOURNAL OF FLUIDS ENGINEERING, Vol. 104, pp. 15–17.
- Dunker, R., Rechter, H., Starke, H., and Weyer, H., 1984, "Redesign and Performance Analysis of a Transonic Axial Compressor Stator and Equivalent Plane Cascades With Subsonic Controlled Diffusion Blades," ASME JOURNAL OF ENGINEERING FOR GAS TURBINES AND POWER, Vol. 106, pp. 279–287.
- Durst, F., Melling, A., and Whitelaw, J. H., 1976, *Principles and Practice of Laser Doppler Anemometry*, Academic Press, pp. 275–285.
- Elazar, Y., 1988, "A Mapping of the Viscous Flow Behavior in a Controlled Diffusion Compressor Cascade Using Laser Doppler Velocimetry and Preliminary Evaluation of Codes for the Prediction of Stall," PhD Thesis, Naval Postgraduate School, Monterey, California.
- Hobbs, D. E., and Weingold, H. D., 1984, "Development of Controlled Diffusion Airfoil for Multistage Compressor Applications," ASME JOURNAL OF ENGINEERING FOR GAS TURBINES AND POWER, Vol. 106, pp. 271–278.
- Johnsen, I. A., and Bullock, R. O., eds., 1965, "Aerodynamic Design of Axial Flow Compressors," NASA SP-36, National Aeronautics and Space Administration, Washington, D.C.
- Koyuncu, Y., 1984, "Report of Tests of a Compressor Configuration of CD Blading," MS Thesis, Naval Postgraduate School, Monterey, California.
- McGuire, A. G., 1983, "Determination of Boundary Layer Transition and Separation on Double Circular Arc Compressor Blade in a Large Subsonic Cascade," MS Thesis, Naval Postgraduate School, Monterey, California.
- Sanger, N. L., 1983, "The Use of Optimization Techniques to Design Controlled-Diffusion Compressor Blading," ASME JOURNAL OF ENGINEERING FOR POWER, Vol. 105, pp. 256–264.
- Sanger, N. L., and Shreeve, R. P., 1986, "Comparison of Calculated and Experimental Cascade Performance for Controlled Diffusion Compressor Stator Blading," ASME JOURNAL OF TURBOMACHINERY, Vol. 108, pp. 42–50.
- Shamroth, S., 1987 (Private Communication), Scientific Research Associates Inc., Glastonbury, Connecticut.

DISCUSSION

N. A. Cumpsty¹ and Y. Dong²

The authors have obtained a most impressive amount of data. We would like to offer some comments and questions about the experiment and data and to offer some cautionary observations based on our own experiments.

(1) Concerning the design of blades, we wonder why the velocity distribution has a peak near the leading edge even at design inlet angle of 40°? The conventional wisdom (see, for example, Hobbs and Weingold, 1984) is that one should have continuous acceleration up to a peak velocity quite well back on the blade, followed by a steep deceleration. The peak near the leading edge is presumably responsible for the separation bubble in the forward part. Was there a particular reason for giving results in Fig. 13 at 6° of incidence above that for design?

(2) The laser technique was unable to give measurements in the separation bubble. Would the authors care to comment on the relative advantage of boundary layer measurements on blades obtained with the laser compared with, say, a hot-wire? Were any tests done near the leading edge with an inlet angle of 46° to verify that the seeding giving most of the signal was of the correct size to follow the steep gradients without significant error?

(3) The data, as presented, are to a very small scale (Figs. 11 and 13) and for one incidence only (Fig. 13). Is there any summary conveniently available that interested persons could have with more complete and easier-to-use presentation?

(4) Our most important comments are based on our own measurements (Dong and Cumpsty, 1989), which, at risk of being repetitive, we must outline. By introducing moving wakes into the two-dimensional flow in a cascade of similar controlled-diffusion-type blades, we were able to see very substantial alterations in the suction and pressure surface boundary layers. The effects were most pronounced on the suction surface, since this boundary layer was dominated by a separation bubble in the absence of wakes or high free-stream turbulence. The wakes initiated turbulence before the separation point and temporarily prevented separation; after a wake had passed, the flow reverted to laminar and a separation occurred. After the turbulent spot there was a calmed region, in which transition was delayed, and the net effect of the wakes (and of high free-stream turbulence) was to delay the completion of transition to a position further along the chord. The transition, and therefore, the subsequent boundary layer development, depend on the size and frequency of the wakes and the whole process is an unsteady one.

Our measurements, therefore, bring us to suggest a caveat on the penultimate sentence of the Elazar and Shreeve's conclusions. Extreme caution should be exercised in the use of these data for the calibration of viscous codes intended for application to compressors. This is because the process of greatest uncertainty, transition, is probably quite different in character for this steady, low-turbulence test configuration from that which will be found in the majority of blade rows in a compressor.

Authors' Closure

In response to each of the preceding points:

(1) The reported cascade was designed somewhat before "conventional wisdom" was arrived at (Sanger, 1983). From the point of view of providing a test case for viscous analysis codes however, this may prove to be fortunate. It is useful to have data for a case in which a leading-edge separation bubble

does occur but trailing-edge separation does not, even with much increased incidence. From the point of view of blade design, the off-design behavior of the reported cascade is interesting in that downstream of reattachment, the adverse pressure gradient progressively decreases as the incidence is increased. This is not a bad characteristic if off-design performance is a critical issue.

The data at 6° above design incidence were shown as a selected example of the data obtained because the scale of the viscous effects was largest at this angle and they could therefore be seen most easily. The selection was otherwise arbitrary.

(2) Since an early goal was to obtain data corresponding to incipient stall, the intrusion of probes into the blade passages was considered to be unwise. Experience with hot-wires and LDV in the present cascade has nevertheless shown that there is no advantage whatsoever to using hot-wires over using the LDV system where optical access is available and the flow is steady. Such a conclusion might be different if an experienced LDV operator and a precision traverse (such as the milling machine table that we used) were not available, or frequency analysis of unsteady effects was required in the experiment.

The size of the seed particles was measured very carefully (Elazar, 1988) and, with reference to previous work (Dring, 1982), it was concluded that the particles would follow the streamlines very closely except, possibly, around the leading-edge curvature. Thus the observations that the surface pressure implied higher peak velocities around the leading edge than were measured for the particles in the flow in that region, and that particles were absent from the leading-edge separation bubble, which began just downstream of the leading-edge curvature (Sanger and Shreeve, 1986), were consistent with expectations.

(3) A complete listing of the LDV data will be given in a technical report (Shreeve and Elazar, 1989).

(4) The measurements and observations reported by Dong and Cumpsty (1989) are certainly interesting since most blading in a machine operates in the wakes of other blades. However, two points need to be made. First, understanding the unsteady situation requires that you first understand the steady one. From the point of view of CFD descriptions of cascade behavior, we do not have today a code that can predict with certainty a steady viscous cascade flow field if it contains transitions and separation in any form. It will be much more difficult to predict the unsteady viscous flow correctly. Our reported measurements do provide a test case for a steady flow description and can be used as a limiting test case for an unsteady code description. It would not be prudent however to interpret the results of such predictions as being totally representative of flow within a machine, but rather as being an engineering baseline from which to start.

Second, while introducing wakes, as Cumpsty and Dong have done, takes a step closer to creating the machine environment, it is nevertheless only a partial step. In multistage machines, the multiplicity of wakes present a truly complex unsteady flow to aft blade rows. However, even the second blade row in a machine sees wakes that are quite different than those produced in Cumpsty and Dong's experiments. As has been shown in the present work (Elazar, 1988), the compressor (cascade) blade wake is highly asymmetric in nature, retaining a pressure side and a suction side with different turbulence levels, and being free of the alternating vortex structure that can occur in symmetric blunt body wakes. Whether these differences are important or not can only be resolved by additional systematic experiments of the type that Cumpsty and Dong have reported.

Additional Reference

Shreeve, R. P., and Elazar, Y., 1989, "Laser Velocimeter Data From a Controlled Diffusion Compressor Cascade for Viscous Code Validation," Technical Report NPS67-89-001, Naval Postgraduate School, Monterey, California.

¹Whittle Laboratory, University Engineering Department, Madingley Road, Cambridge, CB3 0DY, United Kingdom.

²New Products Division, Ruston Gas Turbines Ltd., Firth Road, Lincoln LN6 7AA, United Kingdom.

S. H. Moustapha¹
Staff Aerodynamicist.

S. C. Kacker
Supervisor, Turbine Aerodynamics,

Pratt & Whitney Canada Inc.

B. Tremblay
Graduate Research Assistant.
Department of Mechanical and
Aeronautical Engineering,
Carleton University,
Ottawa, Ontario,
Canada K1S 5B6

An Improved Incidence Losses Prediction Method for Turbine Airfoils

The off-design performance of axial turbines is usually predicted by calculating the incidence losses using empirical correlations. Periodic review and improvement to these prediction methods, to reflect recent turbine designs and test results, are essential for the accurate assessment of losses in turbine airfoils. The purpose of the present work is to evaluate existing turbine incidence loss correlations, and present an improved prediction method for profile and secondary losses at off-design conditions which correlates better with the available experimental results. The incidence losses are shown to be a function of leading edge diameter, pitch, aspect ratio and channel convergence.

Introduction

The aerodynamic design of a turbine is usually carried out in such a manner that minimum losses occur at design point operation. This implies that the leading edges of turbine airfoils are designed to match the direction of the oncoming flow: a condition referred to as optimum or zero incidence on the airfoils. However, most of the turbines are required to operate at conditions away from their design point including engine starting, idling, variable power and speed. As a result of the off-design operating conditions, the inlet flow velocity vectors are mismatched with the leading edge angle of the blades causing additional losses, commonly referred to as incidence losses. For multistage turbines, the mismatching of the gas and blade angles may occur because the losses in an upstream component may cause the downstream stage to operate at off-design condition. Correlations to calculate the magnitude of the incidence losses are required when the off-design performance of a turbine must be predicted and performance maps generated. Turbines should be designed in a certain fashion to offer satisfactory operation over a wide range of rotational speeds and pressure ratios. Accordingly, flow and blade parameters influencing the incidence losses should be identified and their effects on losses predicted in order to enable the turbine designer to produce airfoils which are more tolerant to off-design operation. In addition, an accurate prediction of the incidence losses and the off-design characteristics of a turbine is of considerable importance for restagger and growth studies of an existing turbine design, as well as in the matching of flow conditions between a compressor and a turbine.

The methods for predicting off-design performance in turbines are usually based on empirical correlations which need

to be revised periodically to reflect recent trends in turbine design and new test results. Prediction methods at off-design condition, similar to the design case, can be divided into two categories. In the first method, overall efficiencies for families of turbines with similar characteristics, e.g., degree of reaction, aspect ratio, blade profiles, are expressed in terms of parameters such as stage loading and flow factor (Latimer, 1978). The second approach, which is commonly used, is based on incidence correlations for each loss component. Perhaps the best known and most completely documented method is due to Ainley and Mathieson (1951) who introduced a correlation for positive stalling incidence to calculate the profile losses over a wide range of incidences. Craig and Cox (1971) proposed a similar method to Ainley and Mathieson with the exception that the negative stalling incidence and minimum loss incidence have been correlated independently of the positive stalling value. Mukhtarov and Krichakin (1969) introduced the effect of leading edge diameter on profile losses and a correction for secondary losses due to incidence. The effect of the leading edge wedge angle was added by Martelli and Boretti (1987) in the stalling incidence correlation of Ainley. Chen (1987) presented a correlation for low pressure steam turbine blade sections where the incidence loss is expressed in terms of flow incidence and blade inlet angle.

The purpose of this paper is to first review in details the incidence loss correlations of Ainley and Mathieson and Mukhtarov and Krichakin, being the most comprehensive and documented methods. The correlations are then evaluated and compared with the available test results on incidence losses in turbine airfoils. A new improved prediction method for the profile and the secondary losses at off-design conditions is described.

Blade Incidence Terminology

Figure 1 shows the terminology used in this paper for in-

¹Also, Adjunct Professor, Carleton University, Ottawa, Ontario, Canada K1S 5B6.

Contributed by the International Gas Turbine Institute and presented at the 34th International Gas Turbine and Aeroengine Congress and Exhibition, Toronto, Ontario, Canada, June 4-8, 1989. Manuscript received at ASME Headquarters February 14, 1989. Paper No. 89-GT-284.

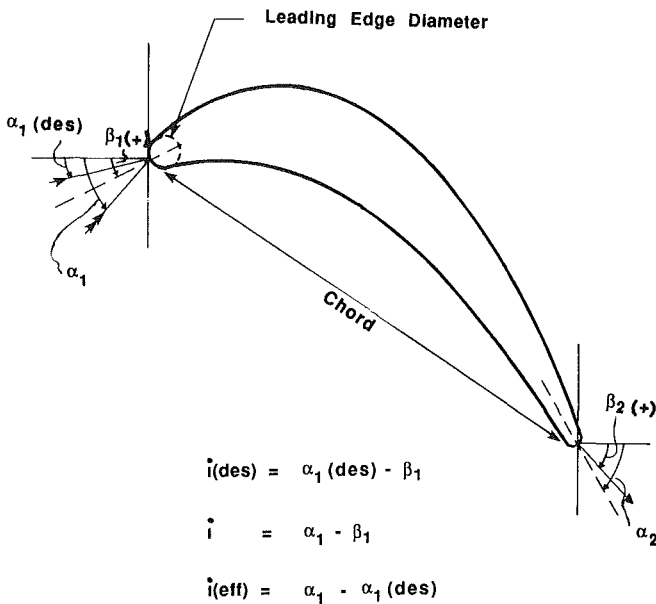
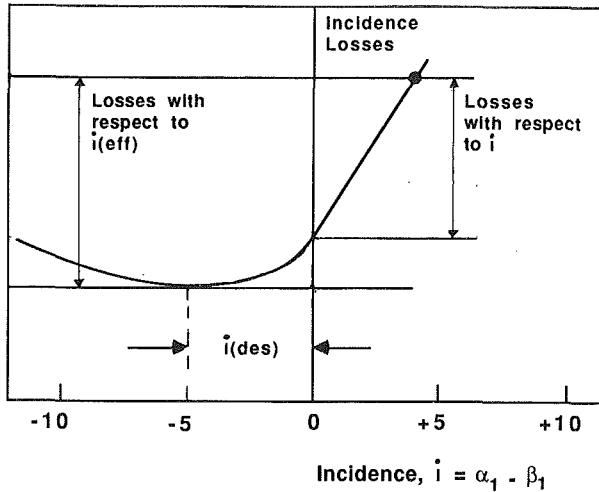


Fig. 1 Turbine blade incidence terminology

$$i(\text{des}) = \alpha_1(\text{des}) - \beta_1$$

$$i = \alpha_1 - \beta_1$$

$$i(\text{eff}) = \alpha_1 - \alpha_1(\text{des})$$

incidence on turbine airfoils. After the design inlet gas angle $\alpha_1(\text{des})$ is obtained from the calculation of velocity triangles, the turbine designer is faced with the selection of the blade inlet metal angle β_1 in order to construct the airfoil shape. The inlet metal angle or leading edge bisector is chosen in a certain

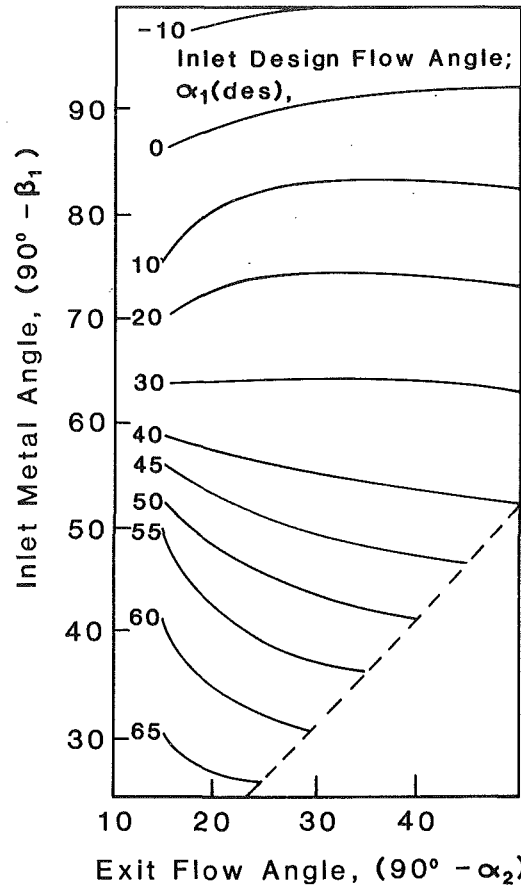


Fig. 2 Selection of inlet blade angle for typical turbine blades after Aronov and Mamaev

way to result in "minimum profile losses" at design condition: a requirement which is not easily determined prior to the definition of the airfoil geometry and the computation of the resulting surface pressure distributions and losses. Aronov and Mamaev (1971) presented a correlation (Fig. 2) to estimate the inlet metal angle during the initial phase of the airfoil geometry design. The selected inlet metal angle should be later verified once the surface velocity distribution is computed, by checking the magnitude of the leading edge overspeed. The design incidence, also referred to as induced, optimum or minimum loss incidence, is defined as the difference between the inlet design gas angle and blade angle.

The total incidence experienced by the blade at off-design conditions i , is defined as the difference between the inlet gas

Nomenclature

b_x = airfoil axial chord
 c = airfoil chord
 C_L = lift coefficient
 d = airfoil leading edge diameter
 h = airfoil height
 i = incidence (defined in Fig. 1)
 M = Mach number
 P = total pressure
 p = static pressure
 q = dynamic head = $(P-p)$
 Re = Reynolds number based on true chord and exit gas conditions

s = airfoil pitch
 t = trailing edge thickness
 t_{max} = airfoil maximum thickness
 Y = total pressure loss coefficient $\Delta P/q$ where q is (generally) taken at blade exit
 Z = airfoil Zweifel coefficient
 α = absolute/relative gas angle for vane/blade with respect to axial direction
 β = metal angle for vane or blade

γ = ratio of specific heats
 Δ = change
 ϕ^2 = kinetic energy loss coefficient = (actual gas exit velocity/ideal gas exit velocity)²

Subscripts

1,2 = inlet and exit conditions
 p = profile
 s = secondary
 m = mean

angle and the blade angle. The effective local blade incidence $i(\text{eff})$ is the deviation of the gas inlet angle with respect to the design gas inlet angle and the stalling incidence $i(\text{stall})$ is the incidence at which the loss is equal to twice the minimum loss.

The incidence losses are defined similarly (Fig. 1) depending upon whether the i or $i(\text{eff})$ is taken as datum. The incidence losses are expressed in terms of changes in total pressure loss coefficient Y or kinetic energy loss coefficient ϕ^2 .

Review of Existing Correlations

Ainley and Mathieson (1951) published a comprehensive method of predicting the design and off-design performance of axial turbines. Their method was first refined by Dunham and Came (1970) and lately by Kacker and Okapuu (1981). Improvements to Ainley and Mathieson correlation focused on revising the profile, secondary and tip clearance loss coefficients at design conditions. A full review and comparison of Ainley and Mathieson, Dunham and Came and Kacker and Okapuu correlations is given by Sieverding (1985). No serious attempt has been made in the literature to review the Ainley and Mathieson off-design correlation in light of published cascade and rig data.

In order to calculate the losses at off-design conditions, the different loss components affected by changes in inlet gas angle are first obtained at design conditions.

Profile Losses:

$$Y_{p(i=0)} =$$

$$\left\{ Y_{p(\beta_1=0)} + \left| \frac{\beta_1}{\alpha_2} \right| \left(\frac{\beta_1}{\alpha_2} \right) [Y_{p(\beta_1=\alpha_2)} - Y_{p(\beta_1=0)}] \right\} \left(\frac{t_{\max}}{c} \right)^{\frac{\beta_1}{\alpha_2}} \quad (1)$$

where $Y_{p(\beta_1=0)}$ and $Y_{p(\beta_1=\alpha_2)}$ are the profile loss coefficients of nozzle and impulse blades, respectively, and could be obtained from figures in Ainley and Mathieson (1951) and Kacker and Okapuu (1981). The foregoing equation is valid for airfoils having a trailing edge thickness to pitch ratio of 0.02, Reynolds number of 2×10^5 and Mach number less than 0.6. Corrections for other values of the previous parameters could be found in Kacker and Okapuu (1981).

Secondary Losses:

$$Y_{s(i=0)} = 0.0334 \left(\frac{c}{h} \right) \left(\frac{\cos \alpha_2}{\cos \beta_1} \right) \left(\frac{C_L}{\frac{s}{c}} \right)^2 \frac{\cos^2 \alpha_2}{\cos^3 \alpha_m} \quad (2)$$

where

$$C_L = 2 \frac{s}{c} (\tan \alpha_1 + \tan \alpha_2) \cos \alpha_m \quad (3)$$

$$\alpha_m = \tan^{-1} \left[\frac{1}{2} (\tan \alpha_1 - \tan \alpha_2) \right] \quad (4)$$

Equation (2) is valid for aspect ratio h/c greater than 2. Correction for lower aspect ratios is given by Kacker and Okapuu (1981).

Having determined the profile and secondary loss coefficients at design conditions according to equations (1) and (2), Ainley and Mathieson's correlation for off-design prediction consists of first calculating the stalling incidence. They found that the positive stalling incidence on turbine blades can be correlated satisfactorily with pitch to chord ratio (s/c), exit flow angle (α_2) and β_1/α_2 . The stalling incidence for an equivalent cascade of pitch to chord ratio (s/c) of 0.75 is determined from Fig. 3(a), the correction on exit angle for the $s/c = 0.75$ equivalent cascade being determined from Fig. 3(b). For the actual value of s/c , the stalling incidence is then obtained

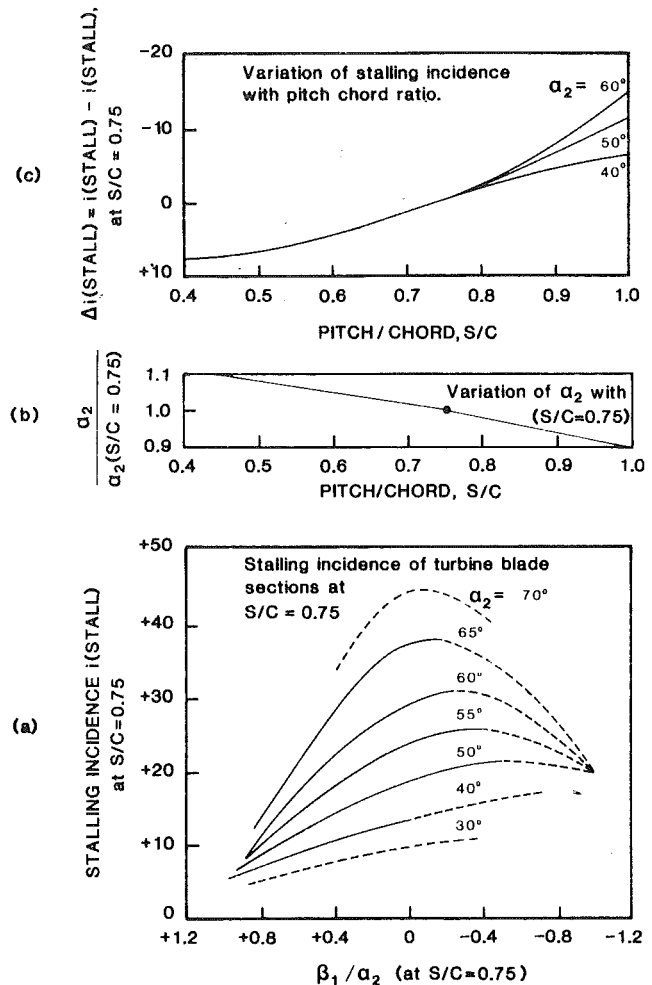


Fig. 3 Determination of stalling incidence for turbine blades after Ainley and Mathieson

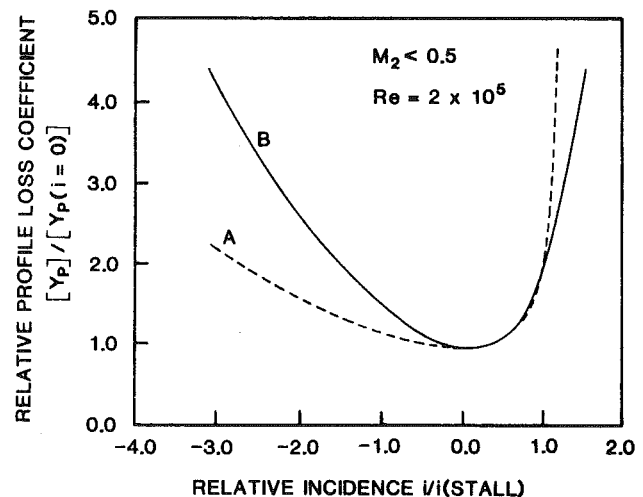


Fig. 4 Variation of profile loss with incidence for typical turbine blades after Ainley and Mathieson

from Fig. 3(c). The profile loss coefficients over a wide range of incidence can be deduced from Curve A in Fig. 4 for $Re = 2 \times 10^5$ and $M_2 < 0.5$. By using equation (2) to calculate the secondary losses at off-design conditions and curve A in Fig. 4 for the profile losses, Ainley and Mathieson found that estimates of total loss at high negative incidence are lower than

measured values. Instead of applying a correction to the secondary loss correlation, they revised the variation of profile loss with incidence as curve B in Fig. 4 in order to obtain a better match with tests. They concluded that curve B (Fig. 4) should be used to calculate the losses at incidences in the range of $-1.5 < i/i(\text{stall}) < 1.0$. For values outside this range, the secondary losses are assumed constant and equal to the values when $i/i(\text{stall})$ equal -1.5 and 1.0 , respectively.

Mukhtarov and Krichakin (1969) presented an incidence correlation for profile and secondary losses. Their procedure can be used for subsonic and transonic blade designs with optimum solidity and having geometrical parameters similar to the investigated cascades. Although the range of the blade parameters was quoted, geometric information and origin of most cascade tests were not given. The correlations are based on the kinetic energy loss coefficient.

They defined the profiles losses at any incidence as follows

$$[(1 - \phi^2) = (1 - \phi^2)_{\alpha_1} = \alpha_{1(\text{des})} + \Delta(1 - \phi^2)]_p \quad (5)$$

where $(1 - \phi^2)_{\alpha_1} = \alpha_{1(\text{des})}$ is the profile loss at the design inlet gas angle and is the summation of friction and trailing edge losses. Correlations to calculate $(1 - \phi^2)_{\alpha_1} = \alpha_{1(\text{des})}$ were given with corrections for Mach number and Reynolds number. Based on the experimental data, the profile incidence loss coefficient was found to be a function of incidence, convergence ratio, leading edge diameter and compressibility

$$\Delta(1 - \phi^2)_p = \Delta\phi_p^2$$

$$\Delta\phi_p^2 = \frac{A}{\left(\frac{d}{s}\right)^{0.67}} \left[\left(\frac{\cos \beta_2}{\cos \alpha_1}\right)^2 \left(\frac{1 + \frac{\gamma-1}{2} M_1^2}{1 + \frac{\gamma-1}{2} M_2^2}\right)^{\frac{\gamma+1}{\gamma-1}} - \left(\frac{\cos \beta_2}{\cos \alpha_{1(\text{des})}}\right)^2 \left(\frac{1 + \frac{\gamma-1}{2} M_{1(\text{des})}^2}{1 + \frac{\gamma-1}{2} M_2^2}\right)^{\frac{\gamma+1}{\gamma-1}} \right] + \frac{B}{\left(\frac{d}{s}\right)^{0.67}} \left(\frac{\cos \beta_2}{\cos \alpha_1}\right)^2 \left(\frac{1 + \frac{\gamma-1}{2} M_1^2}{1 + \frac{\gamma-1}{2} M_2^2}\right)^{\frac{\gamma+1}{\gamma-1}} \sin^2(\alpha_1 - \alpha_{1(\text{des})}) \quad (6)$$

$$\begin{aligned} \alpha_1 > \alpha_{1(\text{des})} & A = 0.024 \\ & B = 0.144 \\ \alpha_1 < \alpha_{1(\text{des})} & A = 0.0007 \\ & B = 0.206 \end{aligned} \quad (7)$$

The secondary losses at any incidence are defined similarly as

$$[(1 - \phi^2) = (1 - \phi^2)_{\alpha_1} = \alpha_{1(\text{des})} + \Delta(1 - \phi^2)]_s \quad (8)$$

where $(1 - \phi^2)_{\alpha_1} = \alpha_{1(\text{des})}$ the secondary loss at the design inlet gas angle, is defined by correlations in Mukhtarov and Krichakin (1969) as function of blade height and loading, Reynolds number and compressibility. The secondary loss correction due to incidence is obtained from the following empirical relation

$$\Delta(1 - \phi^2)_s = \Delta\phi_s^2 = (1 - \phi^2)_{\alpha_1} = \alpha_{1(\text{des})} [5.6\chi + 76\chi^2 + 400\chi^3] \quad (9)$$

where

$$\chi = \frac{\alpha_1 - \alpha_{1(\text{des})}}{180 - (\alpha_{1(\text{des})} + \beta_2)} \left(\frac{\cos \beta_2}{\cos \alpha_{1(\text{des})}}\right)^{1.5} \quad (10)$$

Equation (9) is valid for $-0.15 \leq \chi < 0.15$.

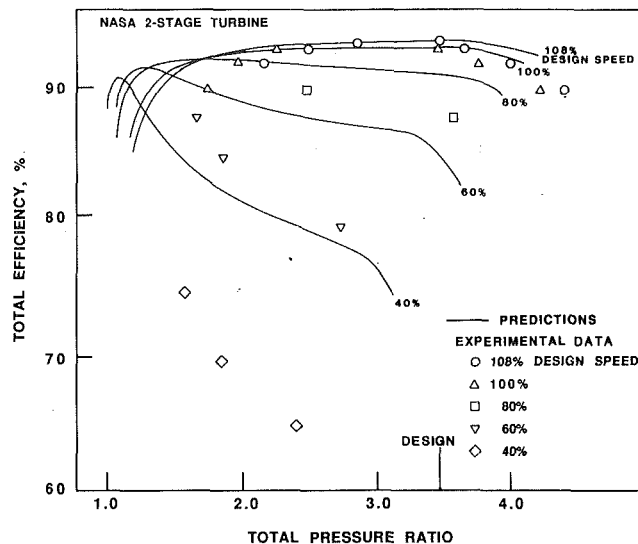


Fig. 5(a) Comparison of Ainley and Mathieson's correlation with turbine rig data (Whitney, et al.)

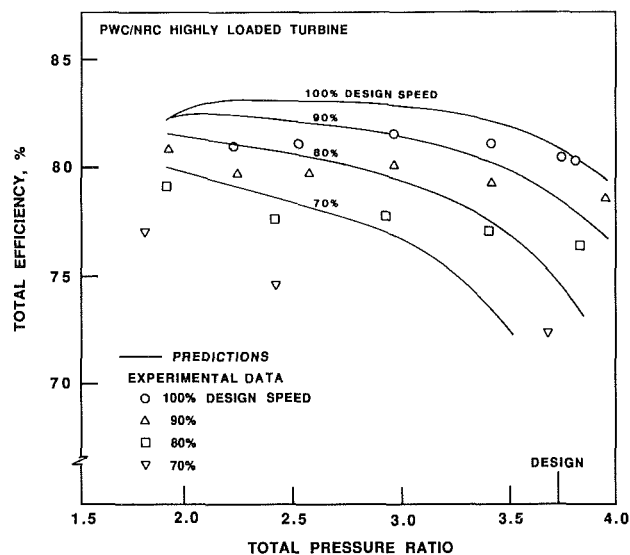


Fig. 5(b) Comparison of Ainley and Mathieson's correlation with turbine rig data (Moustapha et al.)

Incidence Loss Cascade Database

The development of an empirical loss system, either at design or at off-design conditions, is normally done in two steps. In the first step, two and three-dimensional cascade data are collected for turbine airfoils having a wide variety of geometric and flow parameters. After the "cascade database" is created, the parameters which are believed to exercise a dominant influence on the incidence losses in turbine airfoils are selected. The selection of the parameters is generally based on the availability of adequate test results related to these variables, theoretical and/or physical reasoning and a broad examination of existing statistical evidence. Once an incidence loss correlation is developed, a similar "turbine database" is built in order to test and demonstrate the ability of the prediction method to match the off-design performance of real turbines. In the process of calibrating the correlations against turbine data, corrections and loss multipliers are sometimes used to reflect the differences between the cascade and the turbine environments.

Ainley and Mathieson's correlation is one of the few methods

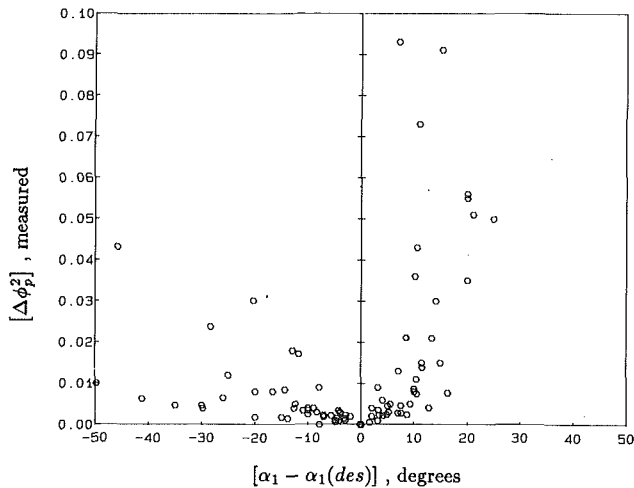


Fig. 6 Effect of incidence on profile losses

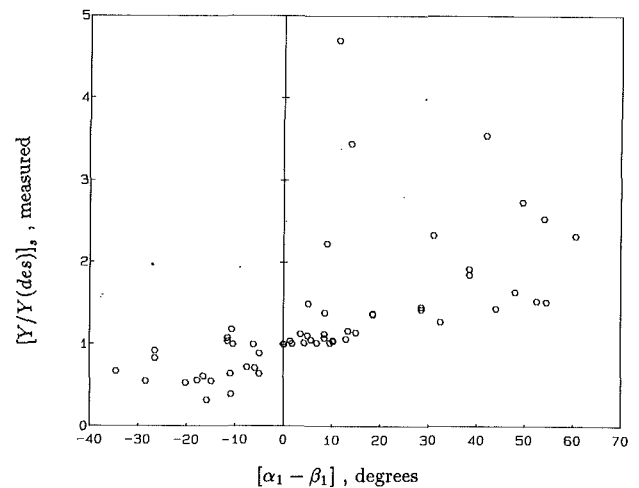


Fig. 7 Effect of incidence on secondary losses

which is widely used throughout the gas turbine industry to predict the off-design performance of turbines. Recent test results highlighted the inability of Ainley's correlation to adequately predict the change of turbine efficiency with pressure ratio and speed. Example of such cases is given in Fig. 5 for a two-stage and a single-stage transonic turbine. Due to the lack of sufficient and well-documented test results on turbines at off-design conditions, it was decided to first examine in the present paper the existing correlations against published cascade data in an attempt to explain the reason for the deviation. Cascade tests and results are well recognized to provide a satisfactory basis for estimating the losses in an actual machine. In addition to their simplicity and low cost, they offer the flexibility of investigating the separate incidence loss components (profile and secondary) as affected by varying independently each of the influencing geometric and aerodynamic parameters.

An extensive survey of published data on measured incidence losses in two and three-dimensional turbine cascades was carried out. Appendices 1 and 2 tabulate the main cascade parameters and losses as extracted from the listed references and from in-house data. The information provided in the tables formed the cascade database that has been used in the present study to evaluate the existing correlations and propose an improved prediction method.

The profile or two-dimensional losses in Appendix 1 are given in terms of changes in kinetic energy loss coefficients as most of the test results were given in this form. In addition to the design incidence and incidence with respect to the design flow angle, the geometric parameters which are believed to have a strong effect on the profile incidence losses are given; e.g., leading edge diameter, pitch and convergence ratio. The profile incidence losses are plotted in Fig. 6 as function of the effective incidence. The incidence losses are seen to be asymmetrical about the zero incidence angle with a loss that is larger for positive than for negative incidence. This is due to local separation on the suction surface at large positive incidence and the smaller area of separation at the same value of negative incidence. High convergence ratio blades such as Cascades 11 and 16 (Appendix 1) show a wider range of incidence over which the loss is low, compared to low convergence ratio blades, such as Cascades 12 and 15, respectively. The data also show that airfoils with large leading edge diameter are less sensitive to incidence.

Appendix 2, lists the various cascades and results related to secondary losses in turbine airfoils at off-design conditions. The endwall losses, expressed in terms of total pressure loss coefficient, are determined by subtracting the measured mid-

span (profile) loss from the measured full-span (total) loss. The secondary losses are plotted in Fig. 7 as a function of the incidence with respect to the inlet metal angle. Similar to the profile losses, airfoils with high acceleration such as Cascade 1 and 2 (Appendix 2) are less sensitive to incidence compared to near impulse blades such as Cascade 5 and 6. Cascade 11 with a leading edge diameter to chord ratio of 0.3 shows a modest increase of losses with incidence compared to Cascade 1 with a (d/c) of 0.04.

Profile Incidence Loss Correlation

The Ainley and Mathieson (AM) and Mukhtarov and Krichakin (MK) correlations for profile incidence losses were first examined against the available cascade data compiled in Appendix 1.

The AM correlation for profile losses, equation (1), is used after applying the corrections suggested by Kacker and Okapuu (1981) to reflect advances in aerodynamic design and analysis. Although equation (1) is given for $i = 0$, which means that the inlet flow angle is equal to the metal angle at design conditions, the curves in Fig. 4 imply that the incidence losses are with respect to the minimum profile losses. Accordingly, when applying equation (1) and using Figs. 3 and 4 (Curve B), β_1 and i are substituted with $\alpha_1(\text{des})$ and $i(\text{eff})$, respectively, to correct for the induced incidences corresponding to the cascade data in Appendix 1. After calculating the profile loss at design and at off-design conditions for the various cascades, the pressure loss coefficient (Y) is converted to kinetic energy loss coefficient by means of the following equation

$$Y = \frac{\left[1 - \frac{\gamma-1}{2} M_2^2 \left(\frac{1}{\phi^2} - 1 \right) \right]^{\frac{-\gamma}{\gamma-1} - 1}}{1 - \left(1 + \frac{\gamma-1}{2} M_2^2 \right)^{\frac{-\gamma}{\gamma-1}}} \quad (11)$$

Figure 8 compares the measured profile incidence losses with those calculated by AM correlation. Predicted losses higher than 0.1 are shown on the maximum horizontal scale. As seen, a significant number of cascades falls outside the error band and AM correlation tends to generally overpredict the incidence losses. This could be explained by the fact that Ainley and Mathieson's correlation is based on conventional airfoils design of the 50's which were less tolerant to incidence than recent blades designed with improved channel analysis procedures and advanced boundary layer computational methods. Some of the cascade losses which have been overestimated are

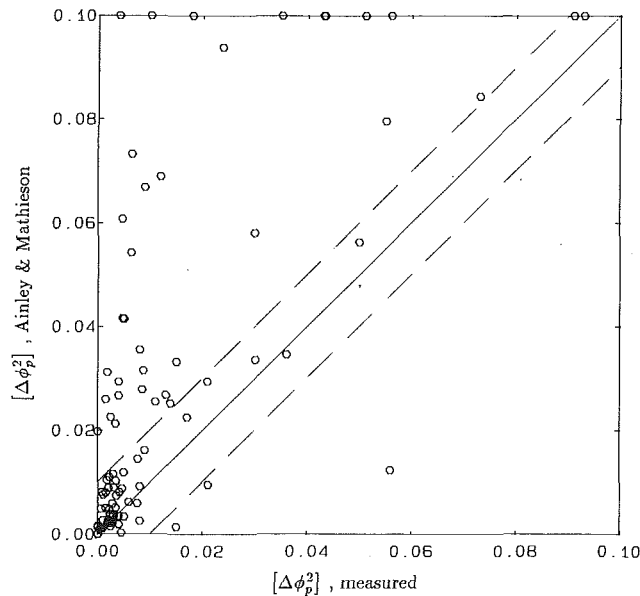


Fig. 8 Evaluation of Ainley and Mathieson profile incidence loss correlation

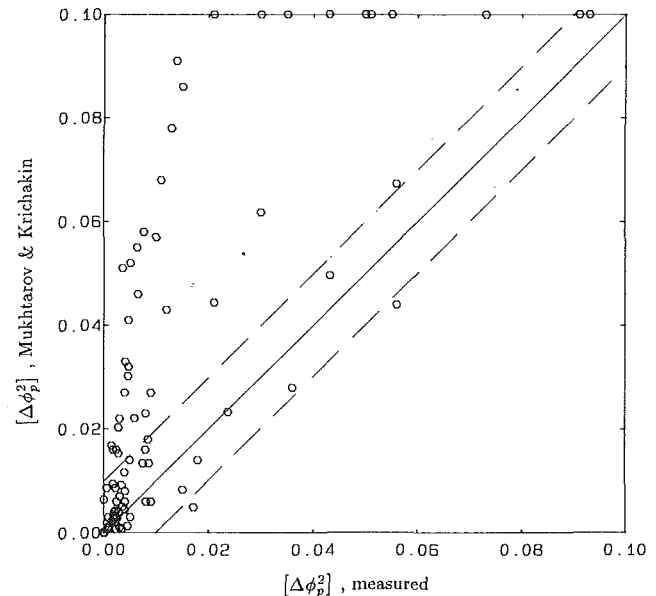


Fig. 9 Evaluation of Mukhtarov and Krichakin profile incidence loss correlation

at negative effective incidence. An example is Yamamoto and Nouse (1988), Cascade 18, who tested a turbine cascade with a design turning angle of 107 deg and a leading edge diameter to chord ratio of 0.22 over a range of negative incidence up to 60 deg and concluded that AM correlation overpredicted the measured incidence losses by a factor of almost 4. The deviation at negative incidences could be well due to the introduction of Curve B in Fig. 4, in order to account for secondary losses. As mentioned earlier, this was needed in order to match the total measured incidence losses in the lack of incidence data on secondary losses at that time.

The MK predictions are compared with the test results in Fig. 9. The compressibility effects built in the MK correlation is calculated by satisfying the continuity equation between inlet and exit and obtaining the corresponding inlet Mach number at the various gas angles. Although the leading edge diameter is an independent parameter in the MK correlation, the agreement is not satisfactory and the profile incidence losses are overpredicted by their method at positive and negative incidences.

In developing the new profile incidence loss correlation, it was decided to retain, with some modifications, the main influencing factors proposed by Mukhtarov and Krichakin. The leading edge geometry, defined as diameter pitch ratio, was shown to affect the incidence characteristics of turbine blades. This is a major shortcoming of Ainley and Mathieson's method, where the stalling incidence is independent of the leading edge shape. Stalling of a blade is due to boundary layer separation, which results from peaks in the velocity distribution in the leading edge region. The formation of these peaks is dependent, among other factors, on the leading edge geometry. Ainley's correlation is probably valid for a family of blades with similar leading edge shapes. The degree of flow acceleration in the blade passage, defined as a convergence ratio, is given with respect to the inlet metal angle as compared to the gas angle for MK correlation. After analyzing independently the effect of the aforementioned factors on incidence losses, a functional relationship was derived in order to give the correct expected trend and a good collapse of the experimental data. Figure 10 gives the improved profile incidence loss correlation and Fig. 11 shows a comparison of the experimental and predicted losses to facilitate the evaluation of the present method with previous correlations (Figs. 8 and 9). As seen from the figures, the

present correlation predicts reasonably well the incidence losses when compared to AM and MK methods. It is worth noting that some of the test results are not well predicted by any of the three correlations. This could be due to possible errors in the data or in the approximation made by the investigator in order to separate the profile from the total measured loss. The latter is particularly true if the flow is highly three-dimensional at midspan and thus deduced profile losses are exaggerated (Yamamoto and Nouse, 1988).

The improved correlation is represented according to the following equation

$$\Delta\phi_p^2 = 0.778 \times 10^{-5} \chi' + 0.56 \times 10^{-7} \chi'^2 + 0.4 \times 10^{-10} \chi'^3 + 2.054 \times 10^{-19} \chi'^6 \quad (12)$$

$800 > \chi' > 0$

$$\Delta\phi_p^2 = -5.1734 \times 10^{-6} \chi' + 7.6902 \times 10^{-9} \chi'^2 \quad (13)$$

$0 > \chi' > -800$

where

$$\chi' = \left(\frac{d}{s}\right)^{-1.6} \left(\frac{\cos \beta_1}{\cos \beta_2}\right)^{-2} [\alpha_1 - \alpha_{1(\text{des})}] \quad (13)$$

The effect of compressibility, Reynolds number and turbulence levels were neglected when developing the new prediction method. Compressibility can affect the profile losses in two ways, by causing shocks at blade leading edge and by affecting the flow acceleration within blade channels. It was felt that in the absence of incidence loss data related to the previous factors, it is sufficient to include their effects when calculating the profile losses at design conditions, using the corrections of Kacker and Okapuu (1981). The blade leading edge wedge angle and axial loading distribution are additional factors which could influence the incidence loss characteristics. A typical high pressure ratio turbine blade with high incident Mach number will probably be more sensitive to inlet gas angle change as compared to a subsonic design. Again studies and test results related to these effects have been very scarce in the open literature.

Secondary Incidence Loss Correlation

The comparison of the predicted secondary incidence losses with experimental results was carried out, using the pressure loss coefficients normalized with respect to the design condi-

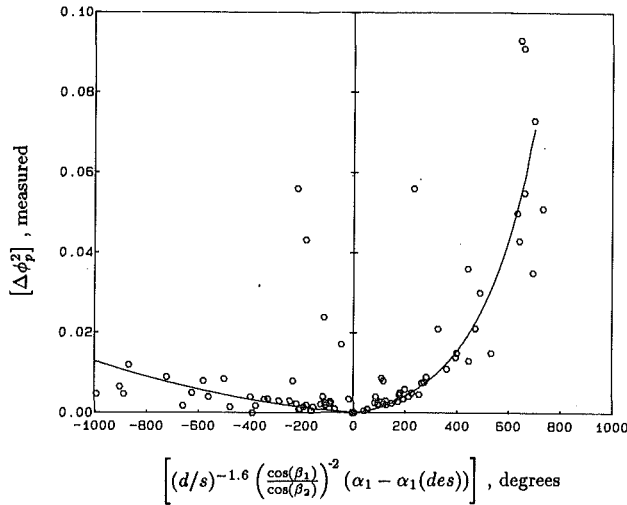


Fig. 10 Improved profile incidence loss correlation

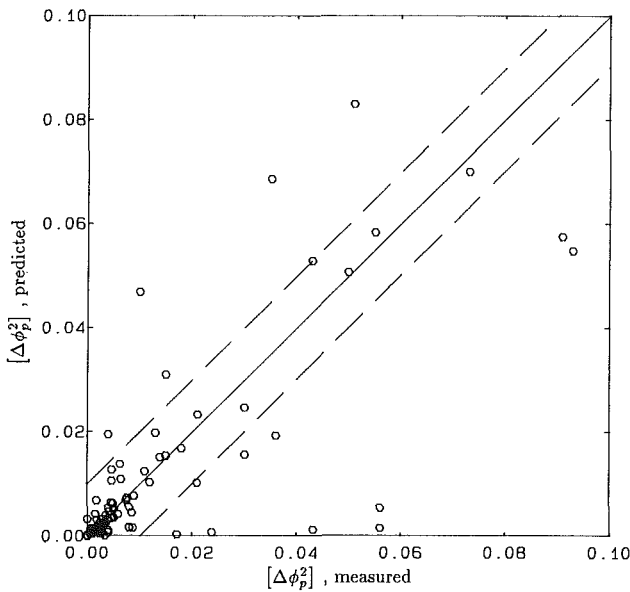


Fig. 11 Evaluation of improved profile incidence loss correlation

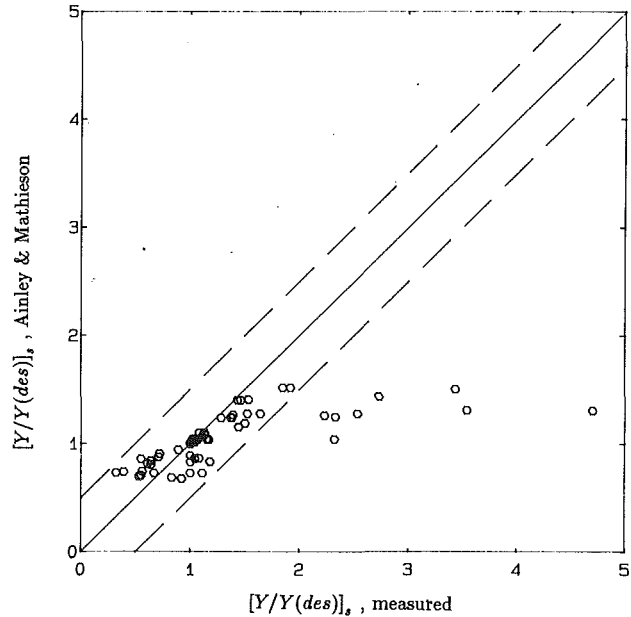


Fig. 12 Evaluation of Ainley and Mathieson secondary incidence loss correlation

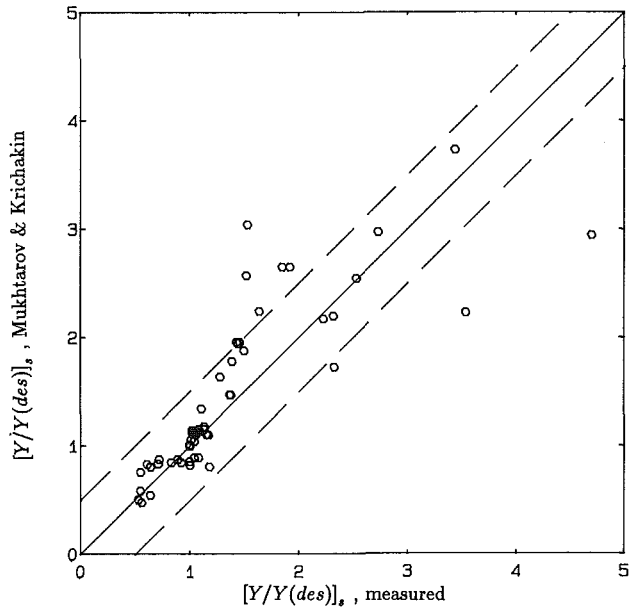


Fig. 13 Evaluation of Mukhtarov and Krichakin secondary incidence loss correlation

tions. The secondary losses at design conditions were taken at the design inlet gas angle or at the inlet metal angle depending on the data available. According to Ainley and Mathieson, there is no incidence effect on secondary losses other than those associated with increased or reduced turning in their correlation, equation (2), for positive or negative incidences, respectively. Figure 12 compares the measured losses with those obtained by AM correlation. The method underpredicts the losses for cascades having low aspect ratio when operated at large positive incidence. This is due to their assumptions of constant secondary losses for values of $i/i(\text{stall})$ greater than 1, as mentioned earlier. The MK correlation is compared in Fig. 13 with the experimental results. The data are scattered around the error band and are generally better predicted by the MK as compared to the AM correlation.

The new secondary incidence loss prediction method is mainly based on the same influencing factors as the MK correlation with the addition of the blade leading edge diameter effect. Figure 14 shows the new correlation given by the following equation

$$\left(\frac{Y}{Y_{(des)}}\right)_s = \exp(0.9 \chi'') + 13 \chi''^2 + 400 \chi''^4 \quad (14)$$

$$0.3 > \chi'' > 0$$

$$\left(\frac{Y}{Y_{(des)}}\right)_s = \exp(0.9 \chi'')$$

$$0 > \chi'' > -0.4$$

where

$$\chi'' = \frac{\alpha_1 - \beta_1}{180 - (\beta_1 + \beta_2)} \left(\frac{\cos \beta_1}{\cos \beta_2}\right)^{-1.5} \left(\frac{d}{c}\right)^{-0.3} \quad (15)$$

In Fig. 15, the improved correlation is evaluated in a manner similar to Figs. 12 and 13 for ease of comparison. The introduction of the leading edge diameter effect provided a better collapse of the data and hence a slight improvement over the

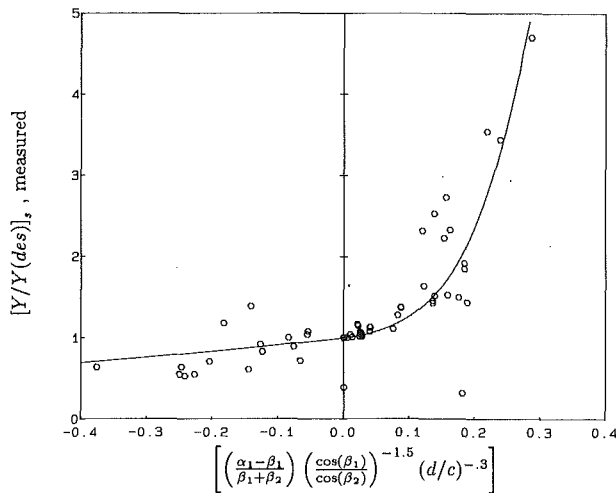


Fig. 14 Improved secondary incidence loss correlation

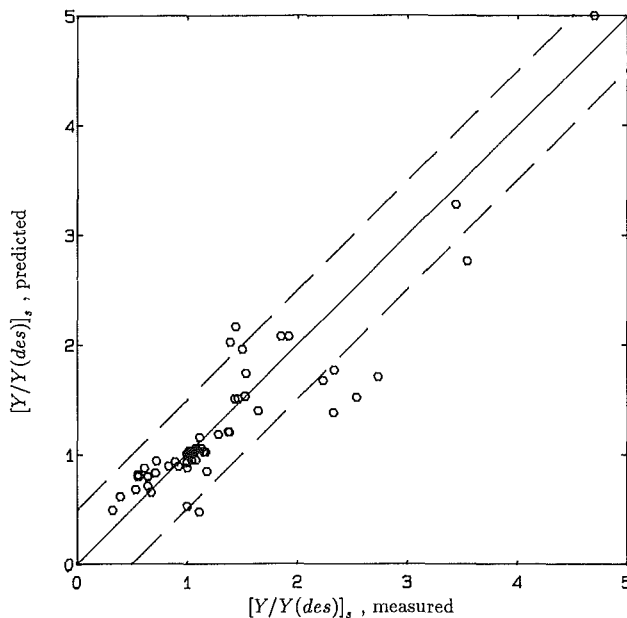


Fig. 15 Evaluation of improved secondary incidence loss correlation

MK correlation. It is felt that the leading edge diameter has an influence on the losses by affecting the developed horseshoe vortex at the leading edge.

For the secondary, as well as the profile incidence losses data, test results on the exit flow angle change with incidence were not reported and accordingly the deviation effect was neglected by assuming a metal angle at exit when using the different correlations.

Conclusions and Recommendations

The prediction methods for the off-design performance of turbines are generally based on empirical correlations which calculate the profile and secondary losses when the airfoils are operated with incidence. These correlations should be periodically reviewed and updated to reflect recent trends in turbine design and new cascade and turbine rig data.

Due to the lack of sufficient and well-documented test results on turbines at off-design conditions, it was decided, as a first step, to examine the existing correlations against recently published cascade data. Cascade tests and results have proven to

give a satisfactory basis for estimating the losses in an actual machine. An extensive survey of the literature was conducted to collect data on incidence losses in turbine cascades. Predicted losses from the correlations presented by Ainley and Mathieson and Mukhtarov and Krichakin were compared with the experimental results of 36 cascades. The correlations failed to adequately predict the measured losses.

An improved incidence losses prediction method, which correlates better the available cascade data, is presented. The losses were shown to be influenced by the airfoil leading edge diameter and the degree of acceleration in the blade channel. Additional factors likely to affect the incidence loss characteristics were addressed, however not included in the correlations due to the lack of sufficient data. The Mach number, Reynolds number, turbulence level, leading edge wedge angle, exit flow angle and axial loading distribution are examples of such factors.

The ability of the improved prediction method to match the off-design performance of turbines is still to be demonstrated. Future efforts will be directed toward establishing a data bank of measured turbine off-design maps. Compared to cascade data, reliable test results for turbines are usually scarce in the open literature, mainly due to the proprietary nature of the data. It is important to be selective in picking up the appropriate test results. The turbine selected must be a good competent design, otherwise the map gets distorted by the peculiarity of the design, such as separation or unintended incidence at design point, due to poor matching of blade and vane row. Once the turbine database is generated, the present correlations will be verified and calibrated in order to reflect the real machine environment. In this process, it is to be expected that empirical factors will be developed and applied to the proposed correlations so as to ultimately obtain a satisfactory procedure for predicting the off-design performance of axial flow turbines.

References

- Ainley, D. G., and Mathieson, G. C. R., 1951, "A Method of Performance Estimation for Axial Flow Turbines," British ARC, R&M 2974.
- Aronov, B. M., and Mamaev, B. I., 1971, "Choosing the Design Inlet Angle in Designing a Turbine Cascade," *Teploenergetika*, Vol. 18 (8), pp. 32-35.
- Aronov, B. M., Bogatyrev, A. G., Epifanov, V. M., Mamaev, B. I., and Shkurikhin, I. B., 1975, "Experimental Study of Blade Inlet Angle Influence on Profile Cascade Effectiveness," *Soviet Aeronautics*, Vol. 18, No. 3.
- Chen, S., 1987, "A Loss Model for the Transonic Flow Low-Pressure Steam Turbine Blades," Institute of Mech. Engrs. C269.
- Craig, H. R. M., and Cox, H. J. A., 1971, "Performance Estimate of Axial Flow Turbines," *Proceedings of the Institution of Mechanical Engineers*, Vol. 185, No. 32, pp. 407-424.
- Dunham, J., and Came, P. M., 1970, "Improvements to the Ainley/Mathieson Method of Turbine Performance Prediction," *ASME JOURNAL OF ENGINEERING FOR POWER*, Vol. 92, pp. 252-256.
- Goobie, S., Moustapha, S. H., and Sjolander, S. A., 1989, "An Experimental Investigation of the Effect of Incidence on the Two-Dimensional Performance of an Axial Turbine Cascade," submitted for presentation at the International Symposium on Air Breathing Engines (ISABE), Athens, September.
- Hodson, H. P., and Dominy, R. G., 1986, "The Off-Design Performance of a Low Pressure Turbine Cascade," ASME Paper No. 86-GT-188.
- Hodson, H. P., and Addison, J. S., 1988, "Wake-Boundary Layer Interactions in an Axial Flow Turbine Rotor at Off-Design Conditions," ASME Paper No. 88-GT-233.
- Kacker, S. C., and Okapuu, U., 1981, "A Mean Line Prediction Method for Axial Flow Turbine Efficiency," ASME Paper No. 81-GT-58.
- Latimer, R. J., 1978, "Off-Design Performance of Gas Turbine," Paper No. VKI Lecture Series.
- Martelli, F., and Boretti, A. A., 1987, "Transonic Profile Losses in Turbine Blading," Institute of Mech. Engrs., C266.
- Moustapha, S. H., Okapuu, U., and Williamson, R. G., 1987, "Influence of Rotor Blade Aerodynamic Loading on the Performance of a Highly Loaded Turbine Stage," *ASME Journal of Turbomachinery*, Vol. 109, Apr.
- Mukhtarov, M. Kh., and Krichakin, V. I., 1969, "Procedure of Estimating Flow Section Losses in Axial Flow Turbines When Calculating Their Characteristics," *Teploenergetika*, Vol. 16 (7), pp. 76-79.
- New, W. R., 1940, "An Investigation of Energy Losses in Steam Turbine Elements by Impact. Traverse Static Test With Air at Subacoustic Velocities," *Trans. ASME*, Vol. 62, 1940.

Patterson, D. J., and Hoeger, M., 1986, "The Effect of Reynolds Number and Velocity Distribution on LP Turbine Cascade Performance," ASME Paper No. 86-GT-271.

Scholz, N., 1954, "Secondary Flow Losses in Turbine Cascades," *Journal Aero.*, Vol. 21.

Sieverding, C. H., 1985, "Axial Turbine Performance Prediction Methods," *Thermodynamic and Fluid Mechanics of Turbomachinery*, Vol. 2, NATO ASI Series.

Todd, K. W., 1956, "Further Study of Secondary Flow," AEI Work Report Ex.

Vijayaraghavan, S. B., and Kavanagh, P., 1988, "Effect of Free-Stream Turbulence, Reynolds Number and Incidence on Axial Turbine Cascade Performance," ASME Paper No. 88-GT-15.

Whitney, W. J., Schum, H. J., and Behning, F. P., 1972, "Cold-Air Investigation of a Turbine for High-Temperature Engine Applications: Part 4—Two-Stage Turbine Performance," NASA TN-D6960.

Wolf, H., 1961, "Die Rand Verluste in Geraden Schaufelgittern," *Wissenschaftliche Zeitschrift der Technischen Hochschule, Dresden*, Vol. 10, No. 2.

Yamamoto, A., and Nouse, H., 1988, "Effects of Incidence on Three-Dimensional Flows in a Linear Turbine Cascade," ASME Paper No. 88-GT-110.

APPENDIX 1

Table 1 Profile Incidence Losses: Cascade Database

Cascade Ref.	<i>d/c</i>	<i>s/c</i>	$\frac{\cos \beta_1}{\cos \beta_2}$	<i>i</i> (des)	<i>i</i> (eff)	$\Delta\phi_p^{2*}$
1 in house	.100	.92	1.78	-5.0	10.0	.0087
1	.100	.92	1.78	-5.0	0.0	.0000
1	.100	.92	1.78	-5.0	-10.0	.0025
2 in house	.052	.75	1.68	-5.5	25.0	.0499
2	.052	.75	1.68	-5.5	10.5	.0075
2	.052	.75	1.68	-5.5	-15.0	.0018
2	.052	.75	1.68	-5.5	-35.0	.0047
2	.052	.75	1.68	-5.5	-41.2	.0063
3 in house	.052	.80	1.55	-5.5	20.0	.0550
3	.052	.80	1.55	-5.5	5.5	.0050
3	.052	.80	1.55	-5.5	-10.0	.0035
3	.052	.80	1.55	-5.5	-20.0	.0018
3	.052	.80	1.55	-5.5	-30.0	.0047
4 in house	.052	.84	1.41	-7.0	15.2	.0910
4	.052	.84	1.41	-7.0	10.2	.0360
4	.052	.84	1.41	-7.0	2.0	.0040
4	.052	.84	1.41	-7.0	-4.8	.0010
4	.052	.84	1.41	-7.0	-29.8	.0040
4	.052	.84	1.41	-7.0	-49.8	.0100
5 in house	.044	.79	1.27	-2.0	11.1	.0730
5	.044	.79	1.27	-2.0	7.1	.0130
5	.044	.79	1.27	-2.0	2.0	.0020
5	.044	.79	1.27	-2.0	-3.9	.0030
5	.044	.79	1.27	-2.0	-8.9	.0040
6 in house	.045	.82	1.07	-3.0	7.1	.0930
6	.045	.82	1.07	-3.0	3.1	.0090
6	.045	.82	1.07	-3.0	-2.0	.0020
6	.045	.82	1.07	-3.0	-7.9	.0090
6	.045	.82	1.07	-3.0	-12.9	.0180
7 Aronov et al	.072	.72	1.85	-10.0	20.0	.0560
7	.072	.72	1.85	-10.0	10.0	.0080
7	.072	.72	1.85	-10.0	0.0	.0000
7	.072	.72	1.85	-10.0	-10.0	.0040
7	.072	.72	1.85	-10.0	-20.0	.0080
8 Aronov et al	.032	.83	2.27	-5.0	15.0	.0150
8	.032	.83	2.27	-5.0	5.0	.0045
8	.032	.83	2.27	-5.0	0.0	.0000
9 Aronov and Mamaev	.054	.68	1.35	-0.8	0.0	.0000
9	.054	.68	1.35	-0.8	-2.9	.0023
9	.054	.68	1.35	-0.8	-7.0	.0023
9	.054	.68	1.35	-0.8	-10.9	.0034
9	.054	.68	1.35	-0.8	-12.6	.0040
10 Aronov and Mamaev	.054	.68	1.60	-0.2	7.6	.0028
10	.054	.68	1.60	-0.2	4.1	.0022
10	.054	.68	1.60	-0.2	0.0	.0000
10	.054	.68	1.60	-0.2	-3.9	.0028
10	.054	.68	1.60	-0.2	-5.6	.0022

*Measured losses

Table 1 (Continued)

Cascade Ref.	<i>d/c</i>	<i>s/c</i>	$\frac{\cos \beta_1}{\cos \beta_2}$	<i>i</i> (des)	<i>i</i> (eff)	$\Delta\phi_p^{2*}$
11 Aronov and Mamaev	.054	.68	1.85	0.0	16.3	.0077
11	.054	.68	1.85	0.0	12.8	.0041
11	.054	.68	1.85	0.0	8.7	.0024
11	.054	.68	1.85	0.0	4.8	.0024
11	.054	.68	1.85	0.0	3.1	.0009
12 Aronov and Mamaev	.054	.68	1.07	-4.0	4.0	.0059
12	.054	.68	1.07	-4.0	-0.1	.0000
12	.054	.68	1.07	-4.0	-4.2	.0008
12	.054	.68	1.07	-4.0	-7.8	.0000
12	.054	.68	1.07	-4.0	-12.4	.0050
13 Aronov and Mamaev	.054	.68	1.30	-4.0	11.6	.0139
13	.054	.68	1.30	-4.0	7.5	.0046
13	.054	.68	1.30	-4.0	3.4	.0023
13	.054	.68	1.30	-4.0	-0.2	.0000
13	.054	.68	1.30	-4.0	-4.8	.0006
14 Aronov and Mamaev	.054	.68	1.54	3.0	13.4	.0210
14	.054	.68	1.54	3.0	9.3	.0050
14	.054	.68	1.54	3.0	5.2	.0030
14	.054	.68	1.54	3.0	1.6	.0005
14	.054	.68	1.54	3.0	-3.0	.0010
15 in house	.053	.75	1.07	0.0	10.6	.0430
15	.053	.75	1.07	0.0	3.2	.0035
15	.053	.75	1.07	0.0	-3.2	.0015
16 in house	.053	.75	1.41	0.0	21.1	.0510
16	.053	.75	1.41	0.0	20.0	.0350
16	.053	.75	1.41	0.0	14.1	.0300
16	.053	.75	1.41	0.0	11.5	.0150
16	.053	.75	1.41	0.0	10.4	.0110
16	.053	.75	1.41	0.0	-4.5	.0015
16	.053	.75	1.41	0.0	-8.3	.0030
16	.053	.75	1.41	0.0	-13.8	.0015
16	.053	.75	1.41	0.0	-14.4	.0085
16	.053	.75	1.41	0.0	-16.7	.0080
16	.053	.75	1.41	0.0	-26.0	.0065
16	.053	.75	1.41	0.0	-25.0	.0120
17 Hodson and Dominy	.032	.56	1.33	0.0	0.0	.0000
17	.032	.56	1.33	0.0	8.6	.0211
17	.032	.56	1.33	0.0	-20.3	.0301
18 Yamamoto and Nouse	.222	.84	1.45	-6.2	0.0	.0000
18	.222	.84	1.45	-6.2	-4.2	.0034
18	.222	.84	1.45	-6.2	-11.7	.0171
18	.222	.84	1.45	-6.2	-28.3	.0238
18	.222	.84	1.45	-6.2	-45.8	.0432
18	.222	.84	1.45	-6.2	-54.2	.0560
19 Vijayaraghavan and Kavanagh	.118	1.12	1.53	-7.0	7.0	.0028
19	.118	1.12	1.53	-7.0	0.0	.0000
19	.118	1.12	1.53	-7.0	-7.0	.0019

*Measured losses

APPENDIX 2

Table 2 Secondary Incidence Losses: Cascade Database

Cascade Ref.	d/c	h/c	$\frac{\cos \beta_1}{\cos \beta_2}$	i	[Y/Y(des)] _s *
1 New	.040	1.17	3.16	0.0	1.0000
1	.040	1.17	3.16	31.0	2.3300
1	.040	1.17	3.16	42.0	3.5400
1	.040	1.17	3.60	44.0	1.4400
2 New	.285	4.00	3.33	0.0	1.0000
2	.285	4.00	3.33	32.5	1.2800
2	.285	4.00	3.33	48.0	1.6400
2	.285	4.00	2.89	49.5	2.7300
2	.285	4.00	3.33	54.0	2.5300
2	.285	4.00	4.03	60.5	2.3200
3 New	.285	2.30	3.33	54.5	1.5200
4 New	.285	1.50	2.97	52.5	1.5300
5 Todd	.120	2.50	1.58	0.0	1.0000
5	.120	2.50	1.46	-10.7	1.1800
5	.120	2.50	1.46	9.0	2.2300
5	.120	2.50	1.46	14.0	3.4400
6 Todd	.037	2.50	1.27	0.0	1.0000
6	.037	2.50	1.17	11.3	4.7000
7 Wolf	.122	4.00	2.40	8.5	1.0800
7	.122	4.00	2.40	-26.5	.8300
7	.122	4.00	2.40	-11.5	1.0800
7	.122	4.00	2.35	18.5	1.3800
8 Wolf	.122	1.00	2.35	28.5	1.4300
8	.122	1.00	2.35	38.5	1.8500
8	.122	1.00	2.40	8.5	1.1300
8	.122	1.00	2.35	-26.5	.9200
8	.122	1.00	2.35	-11.5	1.0400
8	.122	1.00	2.35	18.5	1.3700
8	.122	1.00	2.35	28.5	1.4600
8	.122	1.00	2.35	38.5	1.9200
9 Wolf	.155	2.20	1.44	3.5	1.1300
9	.155	2.20	1.88	-28.5	.5500
9	.155	2.20	1.88	-16.5	.6100
9	.155	2.20	1.88	-7.5	.7200

*Measured losses

Table 2 (Continued)

Cascade Ref.	d/c	h/c	$\frac{\cos \beta_1}{\cos \beta_2}$	i	[Y/Y(des)] _s *
10 in house	.100	2.23	1.78	5.0	1.1100
10	.100	2.23	1.78	-5.0	.8900
10	.100	2.23	1.78	-15.0	.5500
11 Patterson and Hoeger	.300	1.00	1.88	0.0	1.0000
11	.300	1.00	2.48	4.3	1.0200
11	.300	1.00	3.77	9.7	1.0200
11	.300	1.00	4.93	13.0	1.0700
12 Scholz	.300	3.00	2.04	1.4	1.0400
12	.300	3.00	2.74	5.7	1.0600
12	.300	3.00	4.02	10.3	1.0500
12	.300	3.00	5.63	13.4	1.1700
13 Scholz	.300	5.00	2.10	1.8	1.0100
13	.300	5.00	3.01	7.0	1.0200
13	.300	5.00	4.02	10.3	1.0400
13	.300	5.00	5.83	15.0	1.1500
14 in house	.044	1.00	1.27	5.1	1.5000
14	.044	1.00	1.27	0.0	1.0000
14	.044	1.00	1.27	-5.9	.7100
14	.044	1.00	1.27	-10.9	.6400
15 in house	.045	1.00	1.07	0.1	1.0000
15	.045	1.00	1.07	-5.0	.6400
15	.045	1.00	1.07	-10.9	.3900
15	.045	1.00	1.07	-15.9	.3200
16 Hodson and Dominy	.032	1.77	1.33	0.0	1.0000
16	.032	1.77	1.33	8.6	1.3900
16	.032	1.77	1.33	-20.3	.5300
17 Yamamoto and Nouse	.222	1.37	1.45	-6.2	1.0000
17	.222	1.37	1.45	-10.4	1.0000
17	.222	1.37	1.45	-17.9	.5600
17	.222	1.37	1.45	-34.5	.6700
17	.222	1.37	1.45	-52.0	1.0000
17	.222	1.37	1.45	-60.4	1.1100

*Measured losses

The Trailing Edge Loss of Transonic Turbine Blades

J. D. Denton

Whittle Laboratory,
Cambridge University
Cambridge, England CB3 0EL

L. Xu

Beijing University of Aeronautics &
Astronautics,
Beijing, China

Trailing edge loss is one of the main sources of loss for transonic turbine blades, contributing typically 1/3 of their total loss. Transonic trailing edge flow is extremely complex, the basic flow pattern is understood but methods of predicting the loss are currently based on empirical correlations for the base pressure. These correlations are of limited accuracy. Recent findings that the base pressure and loss can be reasonably well predicted by inviscid Euler calculations are justified and explained in this paper. For unstaggered choked blading, it is shown that there is a unique relationship between the back pressure and the base pressure and any calculation that conserves mass, energy and momentum should predict this relationship and the associated loss exactly. For realistic staggered blading, which operates choked but with subsonic axial velocity, there is also a unique relationship between the back pressure and the base pressure (and hence loss) but the relationship cannot be quantified without knowing a further relationship between the base pressure and the average suction surface pressure downstream of the throat. Any calculation that conserves mass, energy and momentum and also predicts this average suction surface pressure correctly will again predict the base pressure and loss. Two-dimensional Euler solutions do not predict the suction surface pressure exactly because of shock smearing but nevertheless seem to give reasonably accurate results. The effects of boundary layer thickness and trailing edge coolant ejection are considered briefly. Coolant ejection acts to reduce the mainstream loss. It is shown that suction surface curvature downstream of the throat may be highly beneficial in reducing the loss of blades with thick trailing edges operating at high subsonic or low supersonic outlet Mach numbers.

1 Introduction

In subsonic flow the trailing edge loss of turbine blades is usually small compared to the boundary layer losses and is often neglected for blades with thin trailing edges. However, it is well known that as the exit Mach number is increased toward unity the loss coefficient rises sharply and the base pressure falls. The boundary layer loss should, if anything, decrease with Mach number so the increased loss must come from the complex shock pattern formed around the trailing edge. The loss usually continues to rise with Mach number for low supersonic outflow, $M_2 < 1.2$, but may level off and even decrease at high exit Mach numbers for some types of blade. It also is known (Xu, 1985) that the trailing edge loss increases roughly linearly with trailing edge blockage and so becomes more important for the thick trailing edges that must be used on cooled blades. The trailing edge blockage may be as high as 20 percent on some such blades and the associated loss may then be the main source of loss for the turbine. In fact it is probably true to say that high trailing edge loss is the main reason for the current use of two-stage subsonic HP turbines instead of single-stage transonic turbines in modern civil aircraft engines.

The flow pattern at a supersonic trailing edge is on the whole well documented and understood (for example, Sieverding et al., 1983). The general features of the flow are illustrated in Fig. 1. The flow immediately upstream of the trailing edge will usually be supersonic on the suction surface and close to sonic on the pressure surface. Immediately behind the trailing edge is a region of relatively low velocity fluid at nearly uniform pressure, the base pressure. This base region is roughly triangular in shape at high Mach numbers and is bounded by shear layers in which the velocity rises rapidly from the low value in the base region to the supersonic flow in the free stream. The shear layers start where the flow separates from the blade surfaces close to the start of the trailing edge curvature and the resulting change in direction generates expansion waves which propagate into the main flow. In some cases, the expansion may be immediately followed by a weak shock, the lip shock, which brings the flow to the base pressure while in others the expansion may be directly to the base pressure. The flows from the suction and pressure surfaces must meet downstream of the trailing edge and this occurs in the confluence region at the downstream end of the base region. After meeting, the flows must turn to a common flow direction. In doing so they generate shock waves which again propagate into the flow. One of these shocks will propagate toward the suction surface of the adjacent blade and has a large effect upon its pressure distribution, while the other will run down-

Contributed by the International Gas Turbine Institute and presented at the 34th International Gas Turbine and Aeroengine Congress and Exhibition, Toronto, Ontario, Canada, June 4-8, 1989. Manuscript received at ASME Headquarters February 1, 1989. Paper No. 89-GT-278.

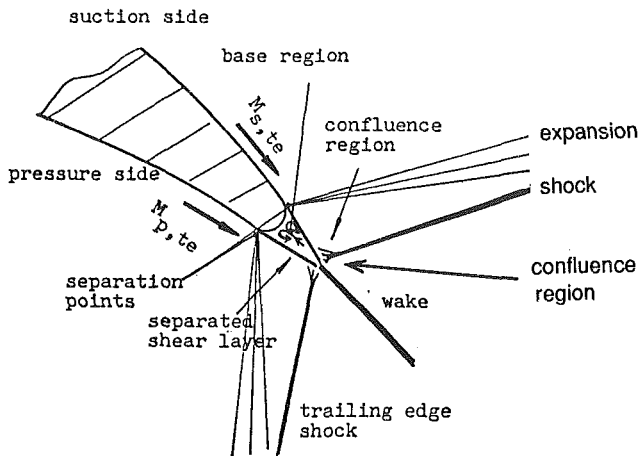


Fig. 1 Structure of supersonic trailing edge flow

stream away from the blades. Downstream of the confluence region the flow may be either subsonic or supersonic and a turbulent, unsteady blade wake is often clearly visible on schlieren photographs.

Although the basic flow pattern is well understood, the magnitude of the base pressure and hence the quantitative details of the flow are extremely difficult to predict. Once the base pressure is known the resulting inviscid flow pattern, including the shape of the base triangle can be relatively easily constructed by the method of characteristics (for example, Bosschaerts et al., 1987). The blade loss can then be obtained from a continuity, energy and momentum balance between the trailing edge plane and a mixed out uniform flow far downstream.

The flow in the base region and shear layers is undoubtedly highly viscous and that in the wake may also be unsteady. Hence, it has usually been assumed that the level of base pressure is determined by viscous effects and that quantitative predictions must rely upon empirical data or, in the long run, on solutions of the viscous flow equations. An example is Carriere's (1970) method, which uses empirical data for the amount of turning at the confluence. Most of the empirical data available have been obtained on isolated aerofoils in a supersonic free-stream flow and Xu (1985) shows that these may not be representative of the flow in turbine blades. A simpler and more practical alternative is to obtain the base pressure directly from an empirical correlation. Such a correlation has been obtained by Sieverding (1983) and predicts the base pressure as a function of back pressure, trailing edge wedge angle and suction surface curvature downstream of the throat. The trailing edge thickness, blade boundary layer thicknesses and surface Mach numbers at separation do not enter directly into the correlation.

Two-dimensional Euler solvers have been used for many years to predict the inviscid flow through turbine blade rows. For subsonic flow, they can give good predictions of the blade surface pressure distribution but for supersonic flow they usually give little detail of the complex trailing edge shock system. This is because such methods smear shock waves over several grid points and insufficient grid points are used in the trailing edge region to adequately resolve the complex shock system. The solutions obtained also depend on how the trailing edge is modeled and Singh (1984) has developed a method in which the pressure at the trailing edge is made to fit Sieverding's correlation.

Although they are nominally inviscid these Euler solutions always contain significant levels of numerical viscosity and as a result the computed flow is not exactly isentropic, even in subsonic flow. Despite this lack of entropy conservation, Euler solutions should, if correctly formulated in finite volume form, exactly conserve mass, momentum and energy throughout the flow field. It is this feature that enables them to predict the correct shock loss despite the inevitable shock smearing. The level of numerical viscosity determines the amount of shock smearing since the velocity gradients adjust themselves so that the combination of numerical viscosity and velocity derivatives generates the entropy needed to satisfy the conservation equations across shock waves; i.e. the Rankine-Hugoniot equations. If the numerical viscosity is too large the shocks will be highly smeared, if it is too low overshoots and undershoots will occur but in either case the overall loss will be correct. The idea that Euler solutions can generate the correct overall loss despite local errors in the solution is central to the theme of this paper.

Sieverding (1979) noted that the numerical loss predicted by an Euler solver was of a similar level to the measured loss for a family of high-speed steam turbine rotor tip sections and in fact ranked the sections in the correct order of loss. At the time, this was regarded as an interesting coincidence. More recently, Xu and Denton (1987a) found that an inviscid Euler solver gave better predictions of base pressure and loss than either Sieverding's correlation or a prediction based on a combination of Carriere's and Nash's methods for predicting the base pressure.

In confirmation of these findings, Fig. 2 shows a comparison of experimental data and an inviscid Euler calculation for the loss coefficient versus Mach number curve of the cascade tested by Haller (1980). The agreement at $M_2 < 0.8$ is fortuitous because in subsonic flow the calculated loss results from numerical errors, especially around the leading edge, and from incorrect prediction of the pressure acting on the trailing edge while the measured loss is due to the blade boundary layers and to subsonic base pressure drag. It is not claimed that an Euler solver can predict the latter. However, the increase of loss at exit Mach numbers around unity is due to increased trailing edge loss in both the calculations and the experiments,

Nomenclature

C = blade chord	P_s = average suction surface pressure downstream of throat	θ = boundary layer momentum thickness
C_p = specific heat capacity at constant pressure	P_b = base pressure, average pressure acting on trailing edge	
M = Mach number	V = flow velocity	Subscripts
s = blade pitch	β = stagger angle	1 = inlet flow
t = trailing edge thickness	δ = flow deviation	2 = downstream flow
0 = blade opening	δ^* = boundary layer displacement thickness	c = coolant flow
m = mass flow rate		t = at throat
T_0 = Stagnation temperature		
P_0 = stagnation pressure		

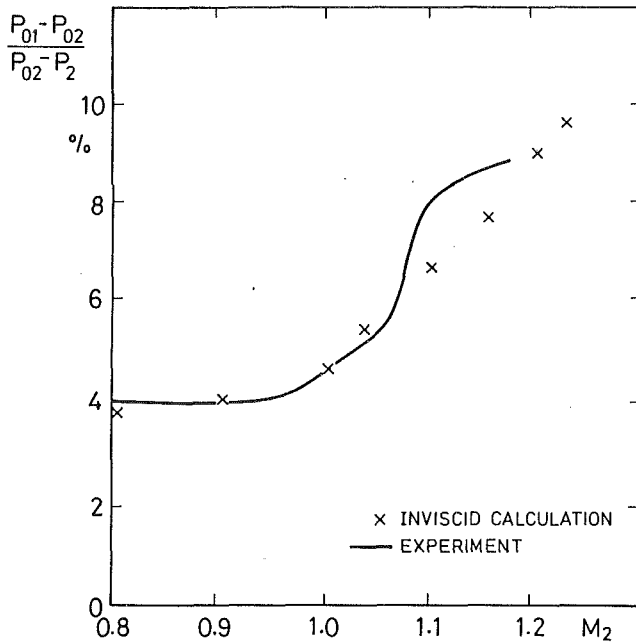


Fig. 2 Loss versus Mach number for blade rd.

and is reasonably well predicted. This is despite the fact that the grid used (48×19 points) was far too coarse to reveal details of the shock system at the trailing edge. In fact, it is not possible to say with certainty that the calculation predicted any shock waves at all. This paper is concerned with the explanation of this remarkable result.

2 Unstaggered Trailing Edge

Although a cascade of unstaggered plates with thick trailing edges is scarcely representative of a real turbine blade such a geometry serves as a useful introduction to the ideas involved. A single plate in a parallel-sided wind tunnel is representative of an infinite cascade in this case and this greatly simplifies experimental testing. As a result a single thick plate has often been tested experimentally (for example, Sieverding et al., 1983; Xu and Denton, 1987b; Motabelli, 1988), as a model of a turbine blade trailing edge on the argument that the local features around the trailing edge are not greatly affected by the neighboring blades. It does not seem to have been realized that the base pressure and loss for such a geometry are exactly predictable by simple theory.

The flow around such a model in a wind tunnel is sketched in Fig. 3, where the sequence of pictures illustrates the changes in flow as the tunnel back pressure is lowered with constant inlet stagnation conditions. At a certain back pressure, the passage between the plate and the tunnel walls will choke and at lower back pressures than this the mass flow will not change; this will occur well before the tunnel exit flow is supersonic. As the back pressure is lowered from the choking value, the trailing edge shock system will develop and move backward, as illustrated, until at a certain back pressure the normal shock will jump downstream to the exit of the wind tunnel. The axial Mach number behind the trailing edge is now supersonic and further reductions in the back pressure cannot affect the trailing edge flow. Thus there exists a range of trailing edge flows for which the passage is choked but the flow, well downstream of the trailing edge, is subsonic but only a single flow pattern can exist when the flow well behind the trailing edge is fully supersonic.

Over the range where the passage is choked, the overall loss and the base pressure can be calculated by a simple mass, momentum and energy balance between the throat and a mixed

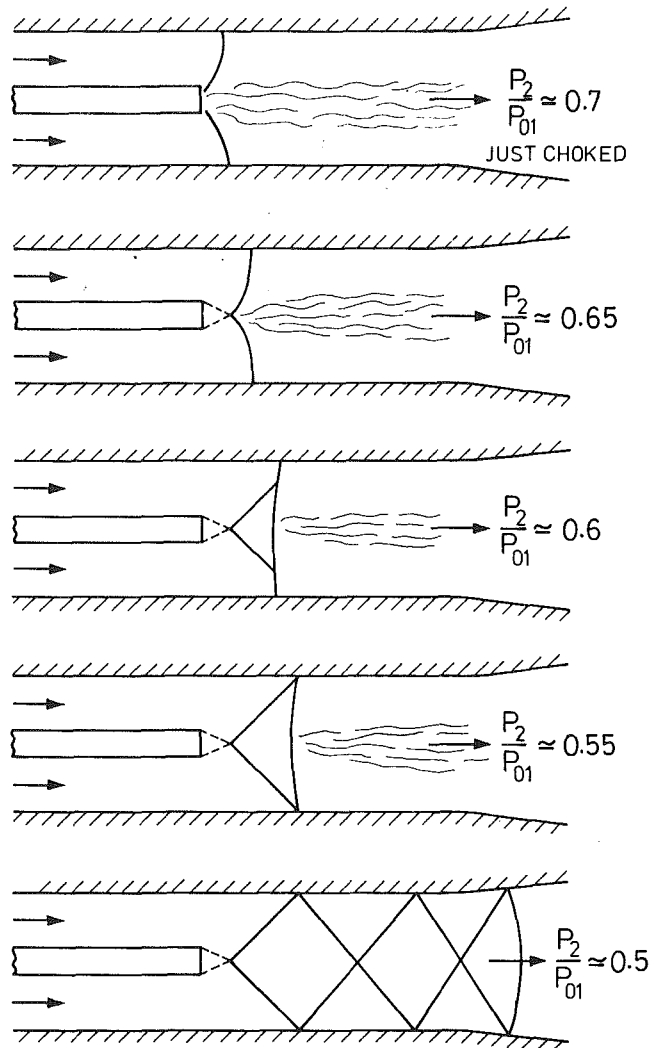


Fig. 3 Flow behind a blunt trailing edge in a wind tunnel

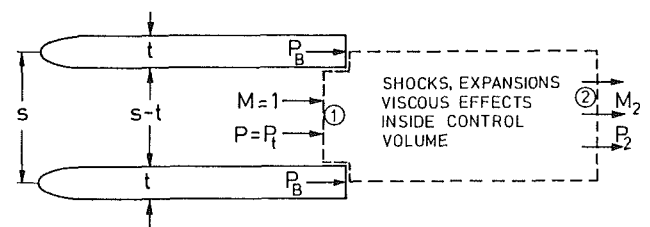


Fig. 4 Control volume analysis of an unstaggered cascade

out uniform flow far downstream. The analysis does not exclude viscous effects downstream of the trailing edge so the uniform mixed out flow will exist even if only a long way downstream.

Consider the flow through the control volume illustrated in Fig. 4. The flow in the gap between the plates is assumed to be choked and uniform, the blade surface boundary layers are neglected at this stage but are considered in Section 4. The mass flow is fixed by the choking condition at the throat area; hence

$$\frac{m\sqrt{C_p T_0}}{(s-t) P_{01}} = F(M) = \text{constant} \quad (1)$$

where $F(M)$ is the dimensionless mass flow function as a function of Mach number, M . For a given geometry and stagnation

conditions, this equation completely fixes the mass flow rate, m

Assuming adiabatic flow the stagnation temperature, T_0 will be constant throughout. If we specify the mixed out Mach number M_2 then

$$\frac{m\sqrt{C_p T_0}}{s P_{02}} = F(M_2) \quad (2)$$

Dividing equation (2) by equation (1) gives

$$\frac{P_{02}}{P_{01}} = \frac{(s-t) F(1)}{s F(M_2)}$$

Thus the mixed out stagnation pressure is completely determined once the downstream Mach number is specified. This result has been obtained from the continuity and energy equations and so far we have not used the momentum equation. The latter may now be used to obtain the base pressure. Having found P_{02} from equation (3), P_2 and V_2 can easily be found from the specified M_2 .

Applying the momentum equation to the control volume, we have

$$m V_t + P_t (s-t) + P_b t = m V_2 + P_2 s \quad (3)$$

This gives P_b , the average pressure acting on the trailing edge.

The result that the base pressure and loss can be exactly determined without involving any viscous effects seems at first sight to be contrary to common sense. However, it is not implied that viscous effects are not important in determining the detailed flow pattern, which may well be dominated by viscous or even by unsteady effects within the control volume. The viscous effects are merely a "means to an end." Their magnitude must adjust itself to satisfy the overall conservation equations and the boundary conditions. A simple analogy is provided by a hydraulic jump in the free surface flow of liquids. The flow in the jump can be seen to be highly turbulent and unsteady but the overall loss in head that it produces is determined by the depth of the liquid upstream and downstream, i.e., by the boundary conditions. In a choked turbine cascade, the analogous boundary condition is the total to static pressure ratio across the cascade and it is this that determines the loss.

Examining equations (1)–(3) shows that they are exactly the same as the normal shock equations with allowance for a change of area through the shock. The change of area permits discontinuous solutions to exist when the upstream Mach number is unity. Just as the loss in a normal shock is determined by the pressure ratio across it and is independent of the detailed flow within the shock so the loss in this case is independent of the detailed flow within the trailing edge region and is fixed by the back pressure.

Another remarkable result of the analysis is that the loss is completely independent of the trailing edge shape. A rounded trailing edge, a square trailing edge or a tapered trailing edge with the same blockage, will all produce the same mixed out loss although the detailed flow pattern around them will be very different. If we consider a long tapered trailing edge forming a one-dimensional gradually diverging passage, the loss will be entirely due to the normal shock whose strength and position in the passage is determined by the back pressure and is easily calculable.

The predictions of the aforementioned analysis are plotted against pressure ratio for plates with 10 percent and 20 percent trailing edge blockage in Fig. 5. As the back pressure is lowered from the point at which the passage first chokes, the loss will increase and the base pressure will fall. At the point at which $M_2 = 1$, the base pressure would be zero and so this condition clearly cannot be reached in practice; before this, the shock will jump to the downstream boundary and only one solution on the supersonic branch of the curve is possible. The exact

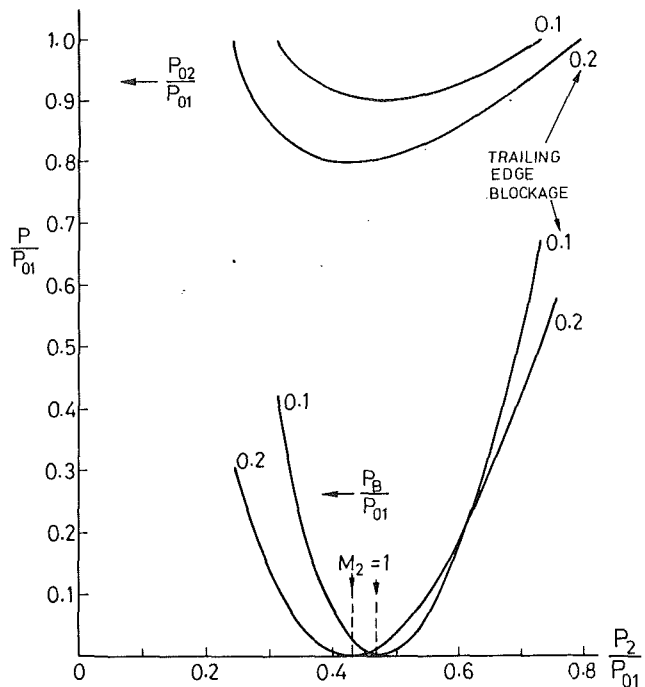


Fig. 5 Base pressure and loss of unstaggered trailing edge

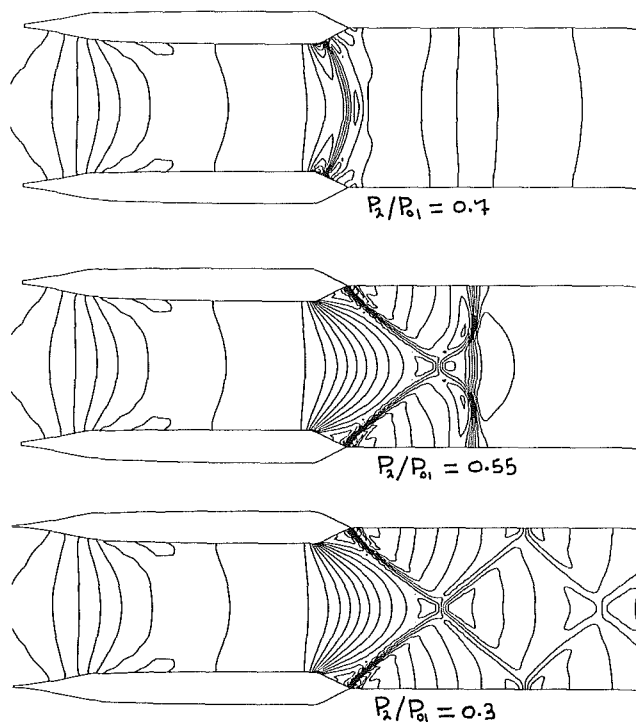


Fig. 6 Computed static pressure contours for an unstaggered thick plate cascade

point at which the jump occurs will depend on the detailed geometry and cannot be predicted by this theory.

Since, for the unstaggered cascade, the loss and base pressure follow directly from the conservation of mass, energy and momentum, any numerical scheme which satisfies the conservation equations should be able to predict these quantities. As previously discussed, finite volume Euler solutions conserve these variables exactly and so should succeed in predicting the base pressure and loss even when the details of the flow around the trailing edge are inaccurate, due to shock smearing and the neglect of viscosity. To check this conclusion the author's

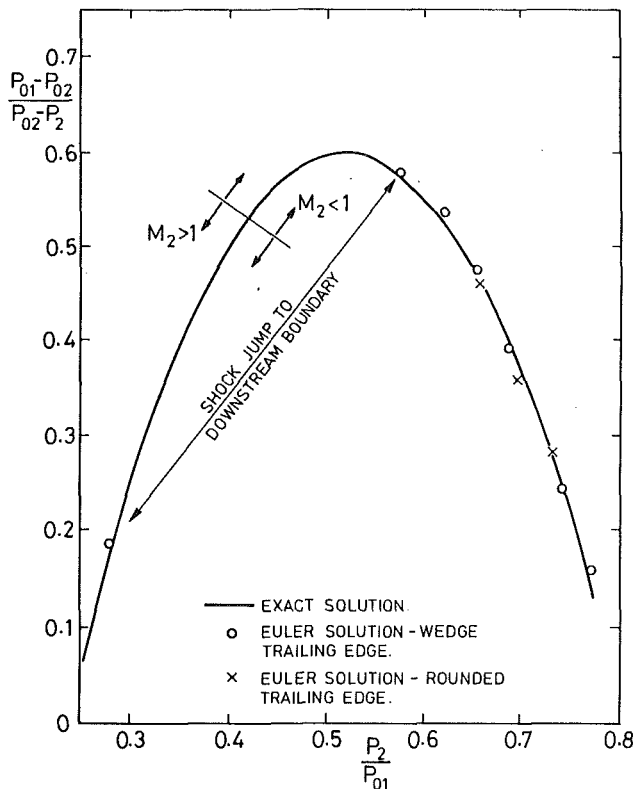


Fig. 7 Comparison of exact and Euler solutions for unstaggered cascade

method (Denton, 1982) has been applied to a wedge-shaped trailing edge with 20 percent blockage. Some of the computed flow patterns are illustrated in Fig. 6. The predicted stagnation pressure loss coefficient is compared with the analytical result in Fig. 7 where agreement is seen to be almost exact. In this case, choking first occurred at a pressure ratio around 0.75 and the jump to supersonic exit flow occurred at a pressure ratio around 0.575. Also shown on Fig. 7 are several results for a rounded trailing edge showing similar agreement and confirming that the overall mixed out loss is not dependent on the trailing edge shape.

3 Staggered Trailing Edges

A cascade of staggered thick plates, Fig. 8, can only be treated as an unstaggered one with the same throat blockage if there is no deviation between the plate surface and the downstream flow. This is not generally the case. Another important difference is that the axial Mach number is usually subsonic when the relative exit Mach number is supersonic. This means that the back pressure can affect the trailing edge flow in most practical circumstances. The single solution with supersonic axial Mach number is beyond the limit load condition and is not usually achievable in two-dimensional cascade flow although it may occur in turbines as a result of three-dimensional flow. Thus the usual operating range of transonic blade rows lies in the range where the throat is choked and the back pressure can affect the trailing edge flow; this is the range in which the theory of Section 2 gives useful results.

Consider a cascade of staggered plates as shown in Fig. 8. The stagger angle is β and the deviation angle is δ . The average pressure acting on the suction surface between the throat and the trailing edge is P_s . Plane CD is far downstream of the cascade where the flow has become uniform and lines BC and ED are periodic boundaries so that all pressures and fluxes through them cancel. The conservation equations are

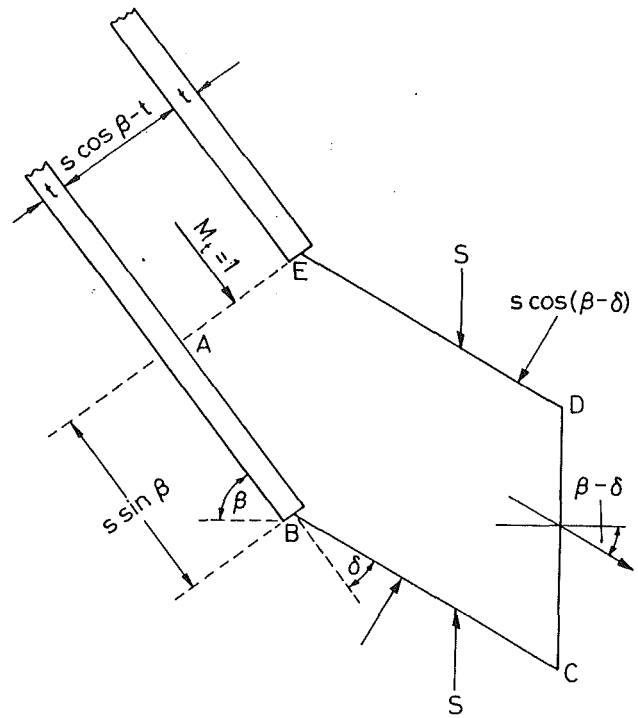


Fig. 8 Control volume for a staggered trailing edge

$$\frac{m\sqrt{C_p T_0}}{(s \cos \beta - t) P_{01}} = F(1) = \text{constant} \quad (4)$$

$$\frac{m\sqrt{C_p T_0}}{s \cos(\beta - \delta) P_{02}} = F(M_2) \quad (5)$$

Dividing these equations gives

$$\frac{P_{02}}{P_{01}} = \frac{F(1)(s \cos \beta - t)}{F(M_2) s \cos(\beta - \delta)} \quad (6)$$

Momentum Parallel to the Throat

$$P_t (s \cos \beta - t) + m V_t + P_b t = P_2 s \cos \beta + m V_2 \cos \delta \quad (7)$$

Momentum Perpendicular to the Throat

$$P_s s \sin \beta = P_2 s \sin \beta + m V_2 \sin \delta \quad (8)$$

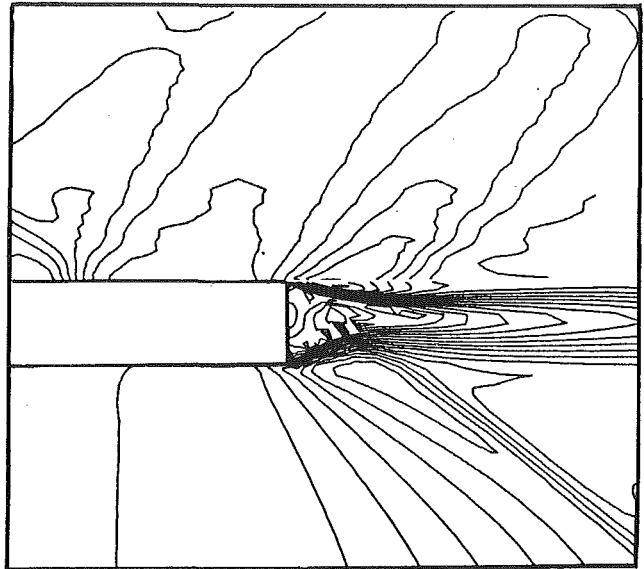
Compared to the unstaggered case, we have only one more equation, equation (8) and two more unknowns, P_s and δ , so it is clear that the equations are not themselves sufficient to close the problem. A further equation relating P_s , P_b and δ is needed for this closure.

It has generally been assumed that the closure of the problem is only possible by including details of the viscous flow in the base region. This is not yet accurately predictable so in current design methods closure is usually by a direct specification of P_b , probably from Sieverding's correlation. Comparison with the unstaggered case, however, suggests that closure of the problem may be possible even for inviscid flow.

Consider the cascade shown in Fig. 9 for which the flow outside of the base triangle is assumed to be inviscid and the flow downstream of the trailing edge is fully supersonic. The flow in the supersonic region may be calculated by the method of characteristics once the boundaries of the region, i.e., sonic line and base triangle shape, are known. The Mach number at the separation point on the pressure surfaces can be found from the turning (if any) between the sonic line and the separation point and hence may be regarded as fixed by the geometry. If the Mach number at the separation point on the

suction surface is specified and the base pressure also is specified, the base triangle can be constructed and the shock and expansion system of the flow field may be constructed by characteristics theory. This will lead to a new estimate of the separation Mach number on the suction surface. This new estimate can be used iteratively to update the flow field until convergence to a separation Mach number that is compatible with the specified base pressure and with the shock-expansion relations is obtained. Hence, we see that, in inviscid flow, characteristics theory provides a unique relationship between the base pressure and the suction surface separation Mach number. Since the whole downstream flow field is predicted by characteristics theory, both the average suction surface pressure, P_s , and the downstream pressure, P_2 , are determined by this solution. It must be remembered that the solution was obtained from a specified base pressure and, hence, for any specified base pressure, there is only one possible back pressure.

An alternative way of thinking about this result is that, in inviscid flow, the shock-expansion relations provide a unique relationship between the base pressure and the average suction surface pressure. This relationship, together with equations



MACH NUMBER CONTOURS

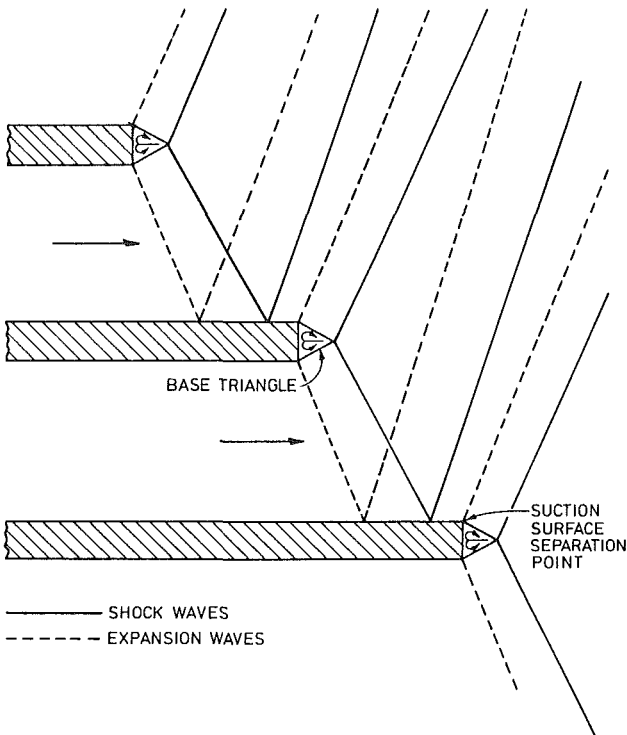
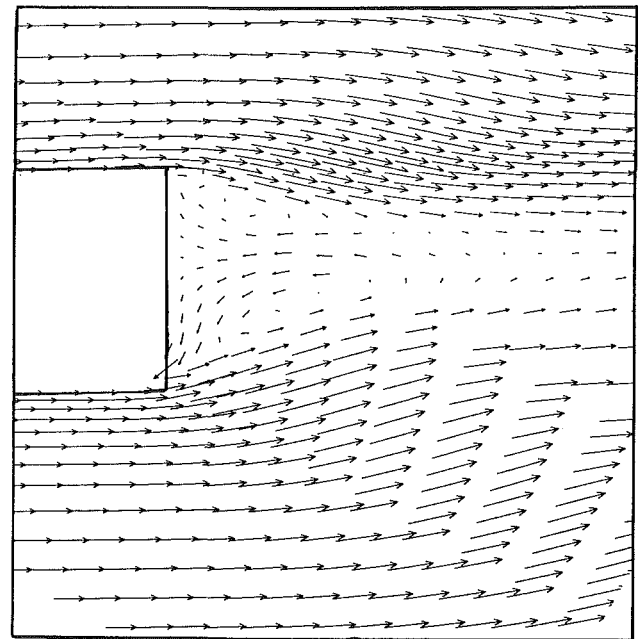


Fig. 9 Shock-expansion wave system behind a supersonic trailing edge



VELOCITY VECTORS

Fig. 11 Details of the computed trailing edge flow for a 60 deg staggered thick plate cascade

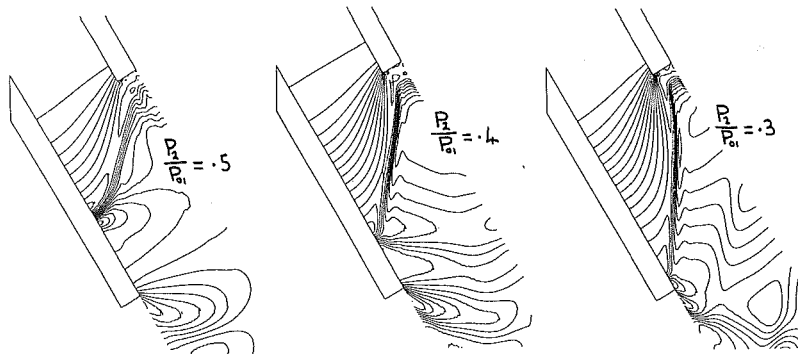


Fig. 10 Computed static pressure contours for a 60 deg staggered thick plate cascade

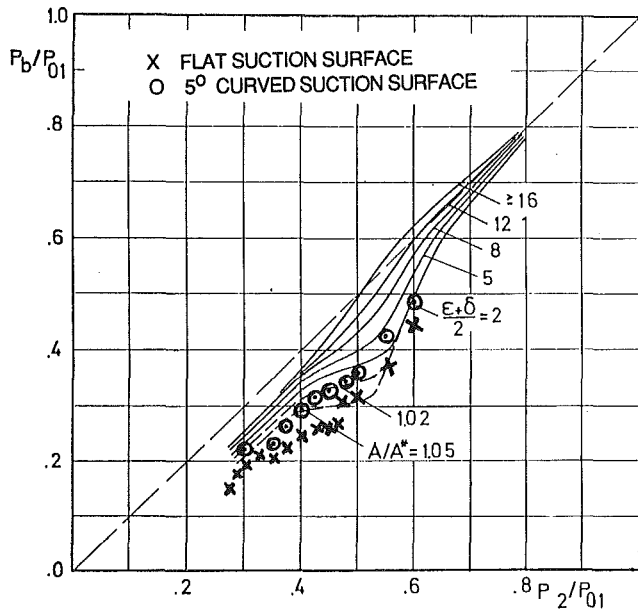


Fig. 12 Comparison of computed base pressures with Sieverding's correlation

(4)–(8) is sufficient to close the problem and to enable the base pressure and loss to be calculated for a specified back pressure.

The relationship between base pressure and suction surface pressure is not easy to obtain since it involves applying characteristics theory to a complex geometry. However a relationship may be hypothesized, such as

$$P_s = 0.5 (P_t + P_b) \quad (9)$$

and equations (4)–(8) can then be solved to obtain predictions of base pressure and loss. It turns out that the results are extremely sensitive to the value of $(P_s - P_2)$ and so such approximate relationships are not very useful. However, they do show that the loss is generally reduced when $(P_s - P_2)$ is negative. This may be thought of due to negative deviation (overturning), produced by the low value of $(P_s - P_2)$, see equation (8), increasing the value if P_{02} needed to satisfy equation (6). The implications of this result are discussed in Section 5.

The foregoing results imply that an accurate solution of the characteristic relationships should be able to predict the back pressure and loss when the base pressure is specified and when the downstream flow is fully supersonic. In current practice, the back pressure may be used to estimate the base pressure (by way of Sieverding's correlation) and then the base pressure used to construct the flow field, but no check on the compatibility of the original back pressure and that predicted by the flow field solution appears to have been made. It should be possible to adjust the base pressure iteratively until the required back pressure is obtained from the flow field solution and then to use a mixing calculation to obtain a prediction of the loss of the cascade under consideration.

In order to predict this inviscid relationship correctly, a numerical method must now not only satisfy conservation of mass, energy and momentum between the throat and downstream but it must also predict the correct relationship between the base pressure and the suction surface pressure. Euler solutions will only predict this latter relationship approximately because of shock smearing. Since the predicted base pressure and loss are very sensitive to $(P_s - P_2)$ it is not clear how accurate the results will be. However, as the mesh is refined, the accuracy of Euler solutions will become better and the predicted loss must tend to the correct inviscid value, i.e., to the value that would be obtained from a characteristics solution. The experience quoted in Section 1 suggests that rea-

sonable results may be obtained even with coarse meshes which do not accurately resolve the shock system.

The analysis neglects the effects of blade boundary layers but permits viscous effects downstream of the cascade. Blade boundary layers will affect the results in two ways. First, they will reduce the mass and momentum fluxes across the throat and, second, they will affect the pressure on the suction surface, especially at the shock wave-boundary layer interaction. The former is easily allowed for and is discussed in Section 4. The second effect is much more complex and cannot be accurately predicted, however, the shock wave-boundary layer interaction usually smears the shock wave where it interacts with the suction surface and so makes the blade surface pressure distribution more like that computed by an Euler solver. Hence, it may contribute to the agreement between Euler solvers and real flows rather than make the former less valid.

In order to test the ability of Euler solvers to predict the base pressure and loss of staggered cascades, a series of fine grid solutions have been obtained on a cascade of 60 deg staggered plates with a square trailing edge giving 20 percent throat blockage. The grid used consisted of 40 points in the pitchwise direction and 150 points in the axial direction. Some of the solutions obtained are illustrated in Fig. 10. At low back pressures, $P_2/P_{01} < 0.45$, stable solutions were obtained with flow remarkably like that found experimentally. A well-defined base triangle with two recirculating vortices was predicted, as illustrated in Fig. 11. The details of the viscous flow within the base triangle will of course not be correct but, according to the theory presented previously, the shape of the triangle is determined by inviscid effects and should be correct. At higher back pressures it was not possible to obtain steady solutions and plots of the velocity vectors showed vortices being shed from the trailing edge and convecting along the wake; again there is no reason to expect the details of these vortices to be correct but, according to the theory, the overall dissipation within them should be correct. In these cases, average values of the base pressure and loss were taken over one cycle. The predicted base pressures are compared with Sieverding's correlation in Fig. 12. Since this cascade had no suction surface curvature and no trailing edge wedge angle, there is no corresponding curve on the correlation; however, the agreement of the predictions with the correlation for low wedge angles and curvatures is reasonably good. The agreement is in fact much better than that usually found between the correlation and experimental measurements (for example, Xu and Denton, 1987). There are no experimental measurements of loss for this case but since the base pressures are reasonable the computed loss also must be in reasonable agreement with that which would be predicted using the correlation.

4 Effect of Blade Boundary Layers and Trailing Edge Ejection

Blade boundary layers are easily included in the analysis of Section 2. Their effect will be to reduce the mass flow through the throat by $\rho_1 V_1 \delta^*$ and to reduce the momentum flux through the throat by $\rho_1 V_1^2 (\delta^* + \theta)$. Thus equation (4) becomes

$$\frac{m \sqrt{C_p T_0}}{(s \cos \beta - t - \delta^*) P_{01}} = F(1) = \text{constant} \quad (10)$$

and equation (7) becomes

$$m V_t - \rho V_t^2 \theta + P_t (s \cos \beta - t) + P_b t = m V_2 \cos \delta + P_2 s \cos \beta \quad (11)$$

Dividing equation (10) by equation (5) shows that the effect of the boundary layer on P_{02} at a constant value of M_2 and δ is exactly the same as an increase of blade thickness by δ^* . The momentum thickness of the boundary layer does not directly affect the loss but as shown by equation (11) it does have an effect on the base pressure. Increases of momentum

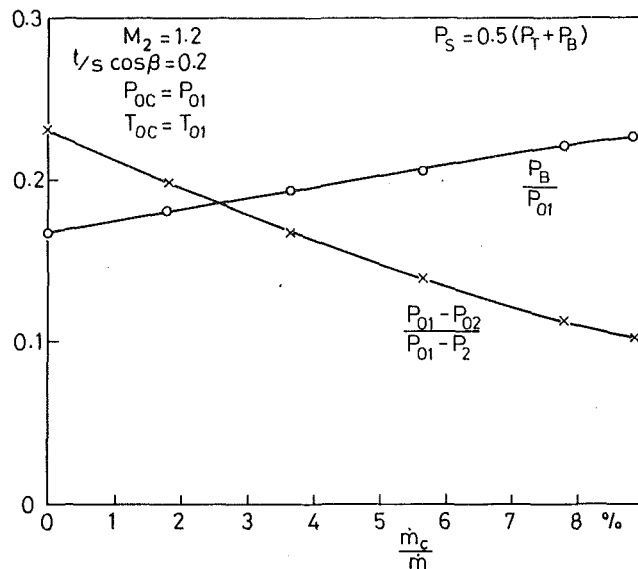


Fig. 13 Effect of trailing edge blowing on base pressure and loss

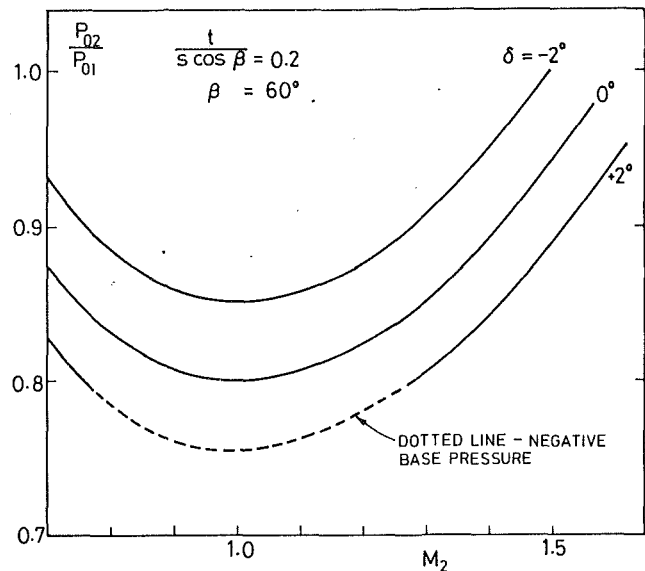


Fig. 14 Effect of deviation on loss

thickness at constant M_2 are predicted to increase the base pressure and this is in agreement with both supersonic base pressure theories and with experimental measurements.

The relative importance of the displacement and momentum thicknesses is the opposite of that in a low speed situation where θ has a much greater effect on the loss than does δ^* . It implies that a separated boundary layer with a high displacement thickness will cause a high loss in transonic flow, whereas it might not be so harmful in subsonic flow. Since the displacement thickness of the boundary layer is usually much less than the trailing edge thickness ($\delta^*/(s \cos \beta)$ is typically 0.02–0.03 while $t/(s \cos \beta)$ is typically 0.05–0.20) the boundary layer loss is usually much less important than the trailing edge loss for choked blade rows.

If coolant flow is ejected from the trailing edge, the effect is similar to a negative boundary layer thickness. The coolant flow rate is m_c and it is ejected with velocity V_c parallel to the plate surface. If the downstream flow rate remains m , the throat flow is $m - m_c$. Equation (10) becomes

$$\frac{(m - m_c) \sqrt{C_p T_{01}}}{(s \cos \beta - t) P_{01}} = F(1) = \text{constant} \quad (12)$$

and equation (7) becomes

$$(m - m_c) V_t + m_c V_c + P_t s \cos \beta + t P_b = m V_2 \cos \delta + P_2 s \cos \beta \quad (13)$$

The energy equation must now be used to obtain the mixed out temperature T_{02} , if the coolant stagnation temperature is T_{0c} this is given by

$$m T_{02} = (m - m_c) T_{01} + m_c T_{0c} \quad (14)$$

Dividing equation (12) by equation (5) now gives

$$\frac{P_{02}}{P_{01}} = \frac{F(1)}{F(M_2)} \frac{m (s \cos \beta - t)}{(m - m_c) s \cos (\beta - \delta)} \sqrt{\frac{T_{02}}{T_{01}}} \quad (15)$$

Comparison of the last equation with equation (6) shows that coolant ejection serves to reduce the trailing edge loss because of the increase in mass flow but the decrease in mixed out temperature far downstream will reduce the magnitude of the effect. This conclusion assumes that the deviation, δ , is not affected by the ejection which is unlikely to be exactly true.

The overall loss accounting with coolant flows is more complex and must include the entropy generation due to viscous effects inside the coolant passages, as well as the entropy gen-

eration due to mixing of fluids at different temperatures. However, if the mass flow, stagnation pressure and stagnation temperature of the coolant are specified, the velocity of ejection and the foregoing equations solved iteratively to obtain the loss and base pressure. As a simple example, Fig. 13 shows the effect of coolant ejection upon the base pressure and loss when the coolant is supplied at the same stagnation conditions as the main flow. This calculation assumes that the suction surface pressure in equation (8) is that given by equation (9); this assumption is not necessarily accurate but serves to illustrate the trends.

5 Effect of Suction Surface Curvature

Study of equation (6) shows that for a staggered trailing edge the loss is controlled by the deviation between the downstream flow angle and the blade angle. In general, the blade angle used in equation (6) should be that given by $\cos^{-1}(0/s)$. Figure 14 shows the predictions of equation (6) for a 60 deg blade angle with 20 percent trailing edge blockage. Within the assumptions of the model, these results are exact. They show clearly that negative deviations are very desirable for reducing the loss for this thick trailing edge. Similar results are found for thinner trailing edges but for very thin trailing edges realistic solutions of equation (6) at high Mach numbers can only be obtained for positive values of deviation. Equation (8) shows that to obtain a large negative deviation the blade must have a low average suction surface pressure downstream of the throat. As shown in Section 3 for a straight suction surface, this pressure is determined by the back pressure and cannot be varied. However, for a real blade, the pressure also is affected by the suction surface curvature. Increasing the suction surface curvature downstream of the throat will lower the average pressure on the surface and so reduce the deviation. This suggests that for thick trailing-edged blades curved suction surfaces may give less loss than flat surfaces. This conclusion contradicts conventional rules which favor a straight suction surface downstream of the throat for blades with low supersonic exit Mach numbers and which also suggest that a convergent-divergent passage is best at high outlet Mach numbers. The origin of these rules is not known but it is likely that they originated from steam turbine technology where thin trailing edges are usual. Hence, the aforementioned conclusions for thick trailing edges may not be in conflict with conventional wisdom.

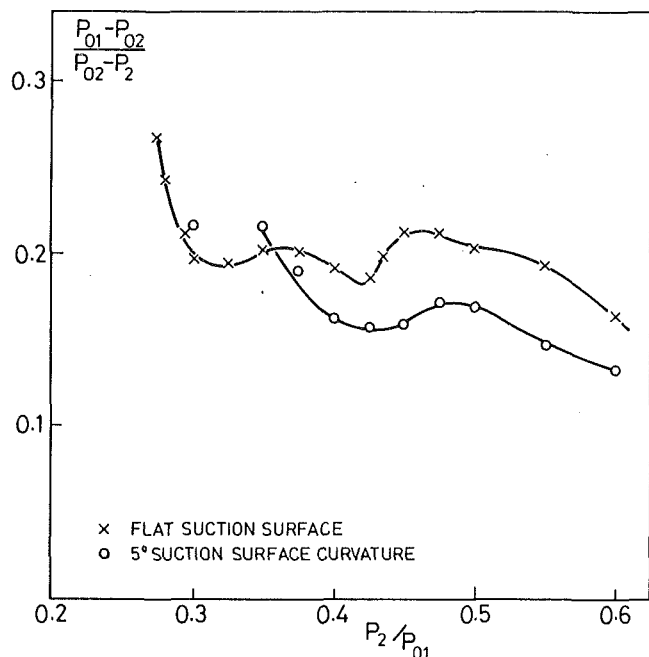


Fig. 15 Effect of suction surface curvature on loss

As a test of this conclusion Euler solutions were obtained for the same 60 deg staggered thick plate cascade as before but with the plate bent so as to give 5 deg of turning downstream of the throat. The plate thickness, measured perpendicular to its surface, was held constant and the ratio of plate thickness to throat gap also was maintained constant; this required the blade pitch to be slightly increased. The conditions were then felt to be equivalent to those for the straight staggered plate since both the mass flow and the throat blockage were both the same for each passage. The predictions for loss are compared with those for the straight blade in Fig. 15 and those for base pressure in Fig. 12. An increase in base pressure at all exit Mach numbers is convincingly demonstrated. This is consistent with the predictions of Sieverding's correlation which also suggests that trailing edge wedge angle should have a similar effect. The reduction of loss that would be expected from the increase in base pressure is only predicted to occur for high subsonic and low supersonic exit flows. In both cases, there is an increase in computed loss at low back pressures, which appears to be associated with the reflection of the downstream running shock wave from the downstream boundary of the calculation domain. Hence, it may not be a physically realistic result and in fact all the loss predictions at low back pressure should be treated with caution. Similar results for the variation of both base pressure and loss with suction surface curvature have been obtained for two other cascades, one with a different trailing edge shape and one with a different stagger angle.

As emphasized previously, the predictions of the Euler solver are not exact in this case, even for inviscid flow, because the shock smearing will affect the suction surface pressure. However, the predictions are felt to be a very good guide to what will occur in practice and suggest that curved suction surfaces should be seriously considered for thick trailing-edged blades in the high subsonic and low supersonic exit Mach number range.

Conclusions

This investigation has led to both theoretical and practical conclusions. From a theoretical point of view, it has been shown that the problem of predicting the base pressure and loss of a transonic trailing edge operating at a specified back pressure can be closed without the need to involve viscous effects. In practice viscous effects will only modify the solution by changing the pressure distribution on the suction surface downstream of the throat. An inviscid Euler solution will predict the base pressure and loss if it predicts the average suction surface pressure correctly. In practice, reasonable predictions may be obtainable despite the numerical shock smearing.

Blade surface boundary layers and trailing edge coolant ejection can be allowed for if their effect on the average suction surface pressure is known. The effect of boundary layers is to effectively thicken the trailing edge by the boundary layer displacement thickness. For choked turbine blades with realistic trailing edge thickness, the loss due to blade boundary layers is likely to be much less than that due to the trailing edge shock system, the boundary layer loss will only be dominant for blades with very thin trailing edges. Trailing edge ejection effectively thins the trailing edge and reduces the loss of the mainstream flow.

Both theory and inviscid predictions indicate that, for thick trailing-edged blades operating in the transonic regime, blades with some curvature of the suction surface downstream of the throat should have less loss than those with straight suction surfaces. This conclusion urgently needs to be tested experimentally.

It should be emphasized that all the theory and conclusions only apply to choked blade rows for which the mass flow rate is not a variable and that the loss considered is the mixed out loss far downstream of the blade row. In practice, the wake and shock system from the trailing edge may interact with a downstream blade row well before complete mixing occurs and the entropy generation in this unsteady interaction may be quite different from that calculated by either this or any other method.

References

- Bosschaerts, W. R. M., Sieverding, C. H., and Arts, T., 1987, "Comparison of Two Explicit Euler Solvers With a Hybrid Approach to Calculate Transonic Cascade Flows With Embedded Shocks," IMechE Paper No. C284/87.
- Carriere, P., 1970, "Analyse theorique du decollement et du recollement turbulent au bord d'un aubage aux vitesses supersoniques," in: *Flow Research on Blading*, L. S. Dzung, ed., Elsevier, New York.
- Denton, J. D., 1982, "An Improved Time Marching Method for Turbomachinery Flow Calculation," ASME Paper No. 82-GT-239.
- Haller, B. R., 1980, "The Effects of Film Cooling on the Aerodynamic Performance of Transonic Turbine Blades," PhD thesis, Cambridge University, United Kingdom.
- Motabelli, F., 1988, "Base Pressure in Transonic Speeds—A Comparison Between Theory and Experiment," ASME Paper No. 88-GT-132.
- Sieverding, C. H., Hautot, P., and Decuyper, R., 1979, "Investigation of Transonic Steam Turbine Tip Sections With Various Suction Side Blade Curvatures," IMechE Paper No. C195/79.
- Sieverding, C. H., Stanislas, M., and Snoek, J., 1983, "The Base Pressure Problem in Transonic Cascades," ASME Paper No. 83-GT-50.
- Singh, U. K., 1984, "Computation of Transonic Flows In and About Turbine Cascades With Viscous Effects," ASME Paper No. 84-GT-18.
- Xu, L., 1985, "The Base Pressure and Trailing Edge Loss of Transonic Turbine Blades," PhD thesis, Cambridge University, United Kingdom.
- Xu, L., and Denton, J. D., 1987a, "The Base Pressure and Loss of a Family of Four Turbine Blades," ASME Paper No. 87-GT-202.
- Xu, L., and Denton, J. D., 1987b, "Base Pressure Measurements on a Model of a Turbine Blade Trailing Edge," IMechE Paper No. C283/87.

An Experimental Assessment of the Influence of Downstream Conditions on the Performance of a Transonic Turbine Nozzle of High Turning

U. W. Schaub

Senior Research Officer.

R. G. Williamson

Assistant Director.

Division of Mechanical Engineering,
National Research Council of Canada,
Ottawa, Ontario, Canada K1A 0R6

J.-P. Huot

Senior Aerodynamicist.

S. H. Moustapha

Staff Aerodynamicist.

Pratt & Whitney Canada Inc.

The present work was conducted to extend information derived in a previous study where it was found that the performance of a transonic turbine nozzle of high turning angle was significantly affected by the design and operation of the downstream rotor and the detailed characteristics of the nozzle flow field. Measurements obtained in an operating stage environment were compared with information from simplified test arrangements. In particular, it was possible to make direct comparisons of static pressure distributions at the vane root as affected by downstream conditions. Detailed exit flow surveys indicated areas susceptible to the influence of rotor presence. Probe interaction effects also were assessed in a special series of tests conducted over a representative range of Mach numbers. Finally, experiments were performed with a perforated plate simulating rotor presence, in an attempt to determine the limitations of such simplified test arrangements in the generation of pertinent data. The results shed further light on a complex subject, and have been aimed at practical validation of test arrangements and techniques.

Introduction

Experimental assessment of the aerodynamic performance of turbine nozzles has evolved through conditions of increasing complexity. Valuable initial data were obtained in linear cascades, first at low speeds and then with exit flows up to supersonic. Three-dimensional effects were accentuated in more realistic annular geometries, and recent work has been concerned with nozzle performance under the combined influence of high Mach numbers, low hub-to-tip ratio and high flow turning angles. Such test conditions, involving significant shock systems and boundary layer interactions, in flows of high swirl and large radial and circumferential pressure gradients, pose new challenges in terms of experimental technique in order to simulate the flows actually existing in the complex stage environment. In particular, it appears that test conditions and, in some cases, instrumentation downstream of the nozzle, may significantly affect the distribution and magnitudes of the flow parameters, with appreciable influence on measured performance.

Different investigations addressed the effects of the aerodynamic interaction between the vanes and rotor blades and

emphasized the significance of the downstream conditions in affecting the radial pressure gradient at nozzle exit. Boletis and Sieverding (1984) reported some tests in a low speed annular nozzle cascade with a flow turning of 69 deg and a hub-to-tip ratio of 0.8. The nozzle was tested with and without a downstream rotor. They did not observe any fundamental modification to the nozzle exit flow field, and therefore concluded that high hub-to-tip ratio annular nozzles with moderate turning could be tested without a downstream rotor. Sjolander (1975) showed no effect on the outlet flow field behind a low turning annular nozzle when tested with and without downstream exit guide vanes. Denton (1983) and Spurr (1980) reported a new technique for testing nozzles without the complexity of providing a moving blade row. A perforated plate was used to simulate the rotor of the last stage of a steam turbine, and realistic measurements were obtained at the exit of an annular cascade of nozzle blades. Squire and Bryanston-Cross (1986) used the same technique to balance the large radial pressure gradients downstream of a low hub-to-tip ratio (0.5) annular nozzle.

The work reported here was carried out to extend information derived in a previous study (Williamson et al., 1986) where experiments were conducted on a large scale, transonic turbine nozzle with and without a representative rotor downstream. Two nozzle designs, involving the same low aspect ratio (0.6), high turning angle (76 deg), and hub-to-tip ratio

Contributed by the International Gas Turbine Institute and presented at the 34th International Gas Turbine and Aeroengine Congress and Exhibition, Toronto, Ontario, Canada, June 4-8, 1989. Manuscript received at ASME Headquarters February 1, 1989. Paper No. 89-GT-283.

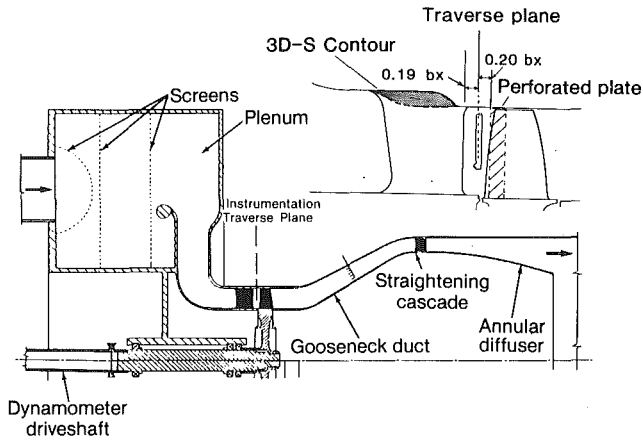


Fig. 1 Highly loaded turbine rig

(0.72), and differing only in outer wall contour, were tested over a range of exit Mach number for different rotor speeds and blade numbers. The results demonstrated that the overall and relative performances of the two nozzle designs were affected significantly by conditions downstream of the nozzle exit. In general, it appeared that low aspect ratio nozzles of high turning angle might be susceptible to hub flow separation, whose propagation could be beneficially influenced by rotor design and operation.

In the present study, a similar nozzle was operated with three different downstream conditions: nozzle alone, with a rotor, and with a perforated plate designed to simulate the rotor presence. The results are presented in the form of radial distributions of flow angle and pressure loss at the nozzle exit for the three cases. Comparisons of static pressure distributions at the vane root, as affected by downstream conditions, also are given. In addition, probe interaction effects were assessed in a special series of tests conducted over a representative range of Mach number.

Experimental Method

Test Facility. The test facility (Fig. 1), which has been described by Moustapha and Williamson (1986), was designed to accommodate single turbine stages of about 53 cm o.d. with blade heights up to 7.5 cm. Turbine power was absorbed in a water brake dynamometer with a speed range up to 10,000 rpm. Air was drawn through the rig by a large exhaustor plant. In tests involving the rotor, the inlet air was prewarmed by mixing with the output of a propane combustor to maintain stage exit temperature near cell ambient conditions. Inlet air temperature could be varied up to the design point value of

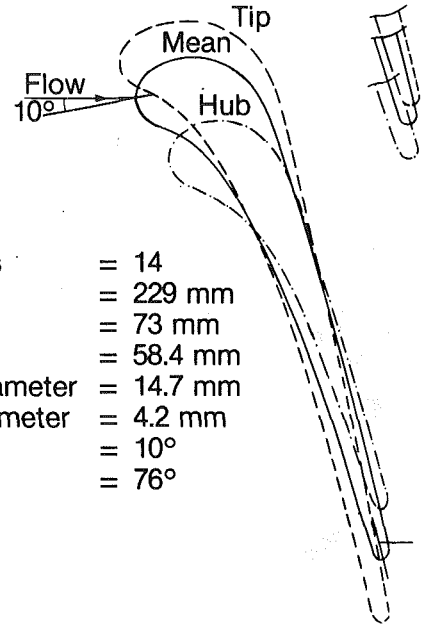


Fig. 2 Vane sections and midspan geometric parameters

Number of vanes	= 14
Mean radius	= 229 mm
Span at exit	= 73 mm
Axial chord	= 58.4 mm
Leading edge diameter	= 14.7 mm
Trailing edge diameter	= 4.2 mm
Inlet metal angle	= 10°
Exit metal angle	= 76°

near 120°C depending upon operating conditions. The pre-warming feature also was used to raise the inlet temperature in the tests without the rotor, in order to avoid freezing or condensation problems at nozzle exit.

A meridional view of the test facility in the vicinity of the nozzle is shown in Fig. 1. Tests described in this report were run with the nozzle alone, with a perforated plate simulating the rotor, and with an operating rotor. During tests with the nozzle alone, and with the perforated plate, the rotor was replaced by a dummy ring of diameter equal to that of the rotor blade hub platform.

Details of the vane section employed are presented in Fig. 2. The 14 vanes were stacked such that the trailing edge was straight and radial in meridional and axial views. Design exit Mach number at the mean section was 1.2, corresponding to a value of $Pr = 2.3$. Vane Reynolds number during the present tests was up to 1.8×10^5 , based on mean chord and inlet conditions, and up to 9×10^5 , based on exit conditions. The outer wall of the nozzle incorporated an S-shaped contour—similar to that reported by Williamson and Moustapha (1986)—which varied circumferentially from vane suction to pressure surfaces. Further information on this concept will be presented in a later report.

The rotor has been described by Moustapha et al. (1987), and was designed for subimpulse conditions at the blade root,

Nomenclature

bx = axial chord of vane
 C_{p0} = local nozzle total pressure loss coefficient
 $= (Pom_1 - Po_2) / (Pom_1 - Psm_2)$
 $\overline{C_{p0}}$ = circumferential mean of C_{p0}
 $\overline{C_{p0}}$ = area-weighted radial mean of C_{p0}
 $\overline{C_{p0h}}$ = C_{p0} evaluated over hub 50 percent of annulus height
 $\overline{C_{p0t}}$ = C_{p0} evaluated over tip 50 percent of annulus height
 N = rotational speed

N_r = $N / \sqrt{Tom_1}$ relative to design value, percent
 \overline{Mn} = Mach number
 \overline{Mn} = area weighted mean Mach number
 Po = local total pressure
 Pom = mean total pressure
 PR = stage total pressure ratio, Pom_1 / Pom_3
 Pr = nozzle total to static pressure, Pom_1 / Psm_2
 Ps = local static pressure
 Psm = mean static pressure
 Tom = mean total temperature

x = axial distance from vane leading edge
 α = local exit swirl angle (degrees from axial)
 $\overline{\alpha}$ = circumferential mean of α
 $\overline{\alpha}$ = area-weighted radial mean of $\overline{\alpha}$

Subscripts

1 = nozzle inlet plane
 2 = nozzle exit plane
 3 = rotor exit plane
 h = hub
 t = tip

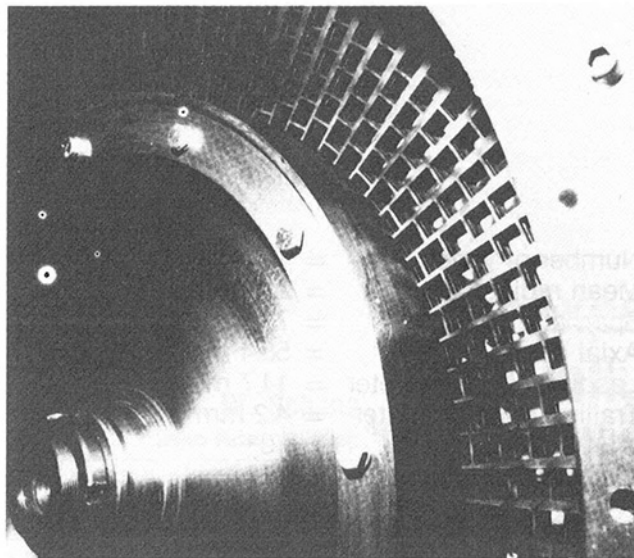


Fig. 3 Perforated plate

with a resultant large flow deflection (130 deg) and high inlet relative Mach number (0.8). The 51 blade variant was used in the present tests.

Rotor Simulator. To investigate whether the rotor could be adequately simulated with simple stationary hardware, a perforated plate was fabricated, guided by a design procedure reported by Squire (1986). This method seeks to control the radial pressure gradient in the nozzle exit plane by removing the tangential component of velocity. While Squire based the perforation detail and the effective stagnation pressures on a requirement for constant annular mass flow rate per unit area, the present design used the nozzle exit stream properties measured with the rotor operating at design conditions. In both cases, it was assumed that the flow through the holes would be fully choked. The present plate featured square holes (11 mm), as depicted in Fig. 3, which, together with a depth aspect ratio of unity, was expected to be highly effective in achieving the removal of nozzle exit swirl. The "plate" was actually comprised of a stack of identically perforated annular rings that could be displaced circumferentially relative to one another, either for modulating open area or for assisting in flow deflection. Neither of these two features was used in the present tests since the stack with aligned holes appeared to perform sufficiently well. The plate was located at the plane of the rotor leading edge, 0.39 vane axial mean chords downstream of the vane trailing edge, and about one tenth of the distance used by Squire.

The design method initially led to a requirement for open area ratios in excess of unity at the hub. Faced with a similar problem, and exacerbated by the fact that round holes were used instead of square ones, Squire employed an annular slot in the hub region. The square holes of the present design, when closely pitched, justified relaxing the assumed contraction coefficient from 0.6 (typical of isolated holes) to 0.8, thereby circumventing the problem.

Instrumentation. Instrumentation was designed to explore mean gas angles and pressures under steady-state conditions. Static pressure tappings in the large upstream plenum chamber were used to sense nozzle inlet stagnation pressure. The test facility, although designed for investigation of a complete stage, also permitted radial and circumferential traversing at nominal nozzle exit plane (Fig. 1), the actual traverse position being 11.5 mm axially downstream of the nozzle trailing edge (corresponding to 0.19 nozzle axial mean chords). Most traverses were performed using a 4.8-mm-dia wedge probe. Approach

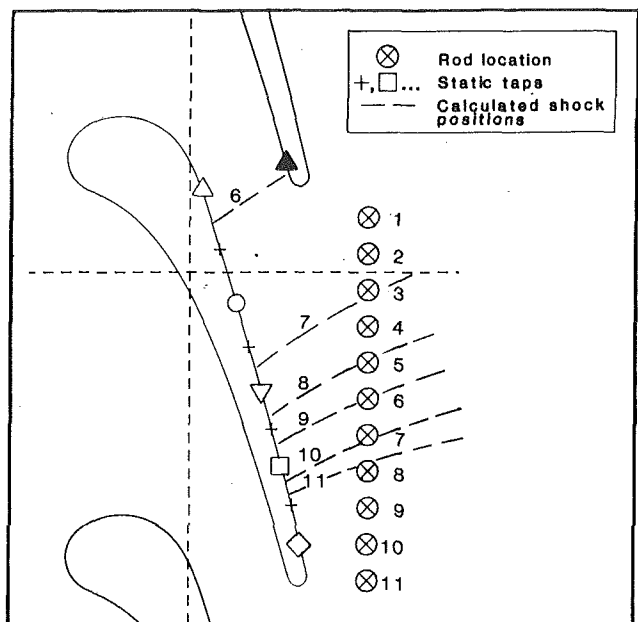


Fig. 4 Rod and static tap locations at the hub, including estimated bow shock position ($Pr = 2.3$)

of the probe to the hub was limited by contact with the wall when the total pressure port was 4.8 mm from the surface. Considerable care was taken to ensure adequate sealing of the traverse slot, and checks were made with smoke to ensure no detectable leaks were present.

The probe was operated under computer control, being automatically nulled for flow direction at each preselected point before total pressure data were recorded. For each circumferential position, data were secured at 12 radial immersions of the probe. A total of 11 circumferential increments, equispaced across a nozzle exit, was required to complete the mapping for each test condition.

Nozzle exit wall static pressures were averaged from blade to blade at hub and tip by using circumferential slits which extended over two nozzle exit passages and which connected to relatively large volume subsurface chambers, in which the static pressures were measured. A linear variation of static pressure from hub to tip was assumed to permit calculation of local probe Mach numbers for estimation of corrections to measured total pressure under supersonic flow conditions.

Earlier work by Williamson et al. (1986) had indicated that the vane root suction surface was susceptible to flow separation under some test conditions. In order to provide additional information in this area, 10 static pressure tappings were inserted in the uncovered suction surface of the vane, near the root, as detailed in Fig. 4.

Additional pressure and temperature measurements downstream of the rotor (Moustapha et al., 1987) permitted definition of overall stage operating conditions in the present tests.

Probe Blockage Experiments

A survey probe at nozzle exit typically operates in a shear flow environment, produced by wakes, boundary layers, and secondary flows. This suggests that both the survey probe measurement and the nozzle surface isentropic Mach number (based on local static and inlet total pressure) could be subject to significant experimental errors in addition to any incurred because of blockage effects. Probe readings could be degraded by falsely indicated flow alignment, while inferred surface Mach numbers would be exaggerated because actual total pressure would be less than the upstream value. Observed sudden

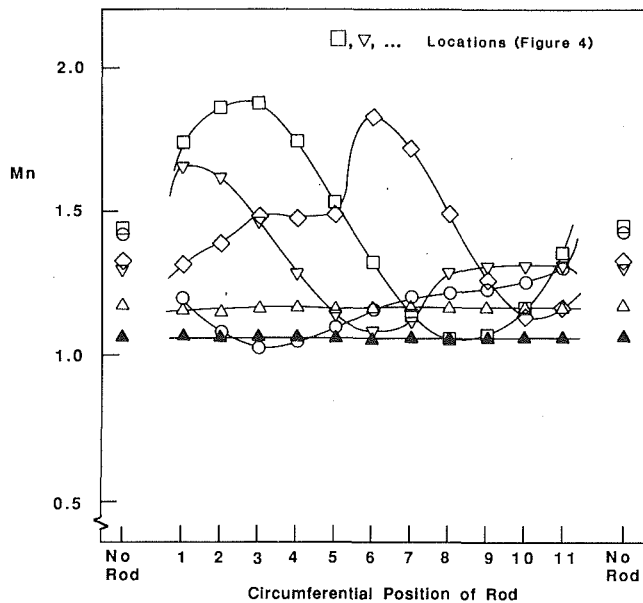


Fig. 5 Effect of cylindrical rod location on the local vane root surface Mach number at design pressure ratio ($Pr = 2.3$)

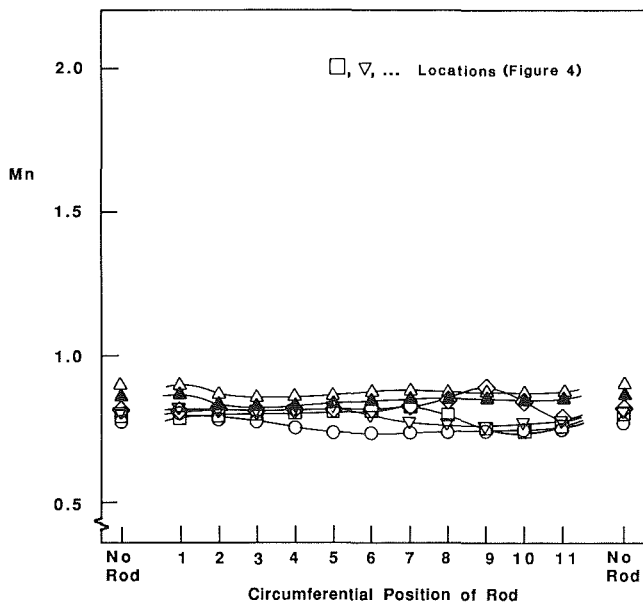


Fig. 6 Effect of cylindrical rod location on the local vane root surface Mach number at low pressure ratio ($Pr = 1.4$)

drops in streamwise Mach number are further evidence of more total pressure loss due to interactions between the boundary layer and shock system.

The first tests reported here were made to investigate whether the influence of the nozzle exit survey probe was significant with respect to the measured magnitude and distribution of flow parameters. During nozzle exit flow surveys, the probe was sequentially positioned in 11 equispaced circumferential locations covering one nozzle passage. For the present tests, the probe was replaced with a cylindrical rod of the same diameter (4.8 mm) which fully spanned the annulus space, except for a small radial clearance gap necessary for moving the rod in the circumferential direction. The rod produced a blockage ratio relative to the throat area of 0.24.

Unfortunately, measuring instrumentation to sample the stream properties nonintrusively in the probe survey plane was not available, but it was possible to infer changes in the flow

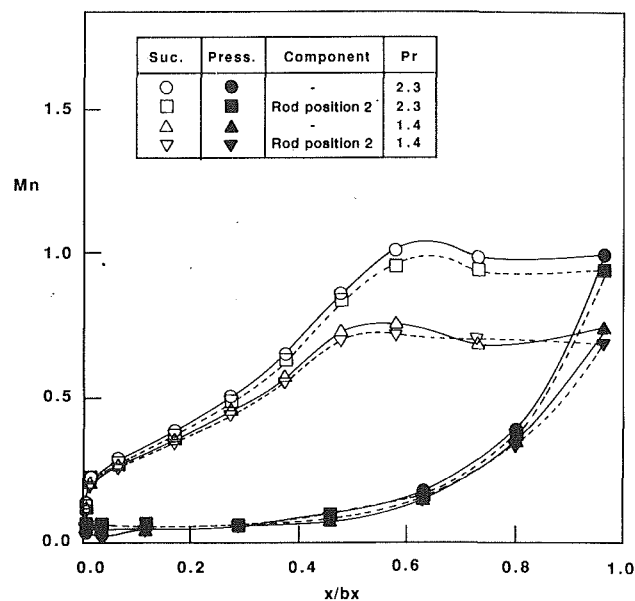


Fig. 7 Effect of cylindrical rod blockage on the vane mean radius surface Mach number distribution at pressure ratios of 2.3 and 1.4

field by measuring surface pressures on the solid boundaries of the flow. Two sets of experiments were conducted, one involving blade surface static pressure measurements near the vane root, where the Mach numbers were highest and the flow most sensitive to disturbance, the other with similar measurements at midheight, to give some indication of overall perturbations. Physical considerations necessitated separate nozzles to accommodate all the pressure tapplings. Accordingly, one nozzle passage was equipped with a chordwise distribution of ten pressure taps at a constant radius of 200 mm relative to the turbine axis near the root. A single pressure tap was located on the pressure surface near the throat, the remainder were distributed along the suction surface downstream of the throat, the first one starting orthogonally opposite the single tap on the pressure surface. Figure 4 shows the pressure tap layout.

The experiment involved stepping the rod from one position to the next, and comparing the measured static pressures with the datum (empty passage) in terms of isentropic Mach numbers for three test pressure ratios of 1.4, 1.9, and 2.3.

The probe interference hardware tested was intended to generate a maximum interference limit, simulating a fully immersed probe. Figure 4 illustrates the circumferential rod position relative to the nozzle passage surface pressure taps. Detached shock waves, computed, using Moekel's method (presented in Shapiro, 1954), tend to be located far upstream because Mach numbers are low and the rod is a relatively large and blunt body.

The influence of rod position on each pressure tap, as shown in Figs. 5 and 6, appears to be a maximum for taps alongside, or just downstream of the rod, while taps at the throat did not register any disturbance. As can be seen from these measurements, and the calculated shock waves shown in Fig. 4, the upstream influence was attenuated as the rod was moved to higher position numbers. As expected, the influence of the rod also decreased with reduction of nozzle pressure ratio (Fig. 6).

As noted earlier, a second nozzle (with a minor difference in outer wall contour) was equipped with a mean line distribution of pressure taps. As depicted in Fig. 7, the nozzle passage incorporated 12 pressure taps on the suction surface and 6 pressure taps on the pressure surface. This figure shows that the surface Mach number is depressed by up to 5 percent locally on the suction surface in the general throat region for

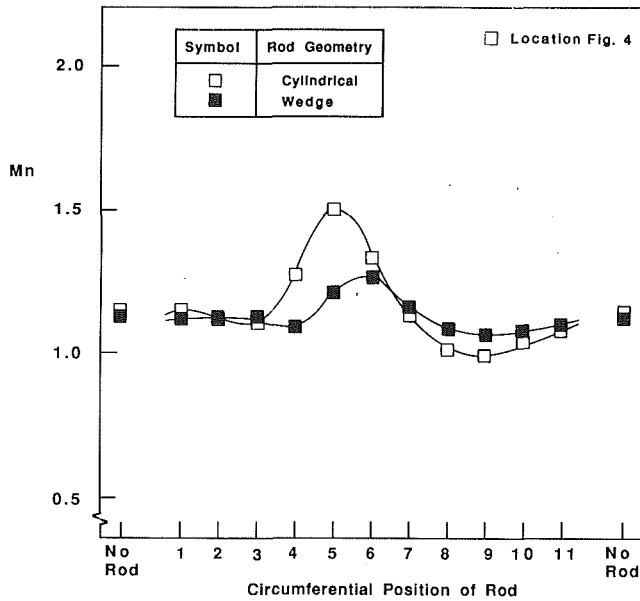


Fig. 8 Effect of rod cross section on the local vane root surface Mach number at intermediate pressure ratio ($Pr = 1.9$)

rod position No. 2, the maximum interference case. However, the inlet surfaces of the nozzle and the pressure surfaces do not show any evidence of disturbance. The visible perturbation is, therefore, attributed to subsonic flow solid wall blockage effects of the rod, i.e., displacement of streamlines, and its effects on the boundary layer in the region of minimum pressure. The invariance of surface isentropic Mach number in the inlet portion of the nozzle at pressure ratio settings of 1.4 to 2.3 (i.e., during subsonic and supersonic nozzle flows) suggests that nozzle flow rate was not affected significantly by the presence of the rod, and that the observed excursions of pressure on the downstream suction surfaces were associated with local boundary layer development with no first-order interference effect on the measured stream properties at the probe measuring location.

The aforementioned experiments were repeated for a less blunt probe support system, fabricated by milling two flat sides on a similar rod to create a sectorlike cross-sectional shape featuring an apex angle of 37 deg and a frontal width of 3 mm. This gave it the same configuration as the head of the wedge probe used in the nozzle exit flow survey (Williamson et al., 1986, 1987). As indicated in Fig. 8, the wedgelike rod, when aligned with the flow at a radius of 200 mm, offered less blockage, and consequently was found also to cause less disturbance at the pressure orifices of the nozzle. It is interesting to note that the chordwise distribution of surface Mach number, while exhibiting a noticeably weaker disturbance imprint, was nevertheless qualitatively similar to that created in the plain rod experiments.

All of these tests tended to confirm that nozzle flow rate was essentially unaffected by the simulated probe. The major evidence of interference was confined to the uncovered suction surface pressure distribution. The implication is that stream properties sensed by the probe under transonic flow conditions, i.e., under design conditions, were largely free of probe interference effect. Under subsonic flow conditions, some streamline repositioning, and hence, also minor distortion in the measured total pressure and flow angle profiles, was physically possible.

Effect of Downstream Component

With the validity of earlier nozzle exit traverses confirmed, at least to first-order, attention was turned to a further ex-

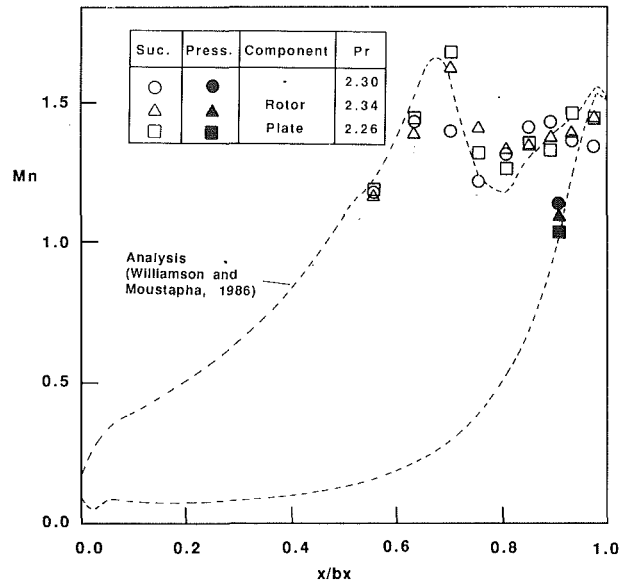


Fig. 9 Effect of downstream component on vane root surface Mach number distribution at design pressure ratio

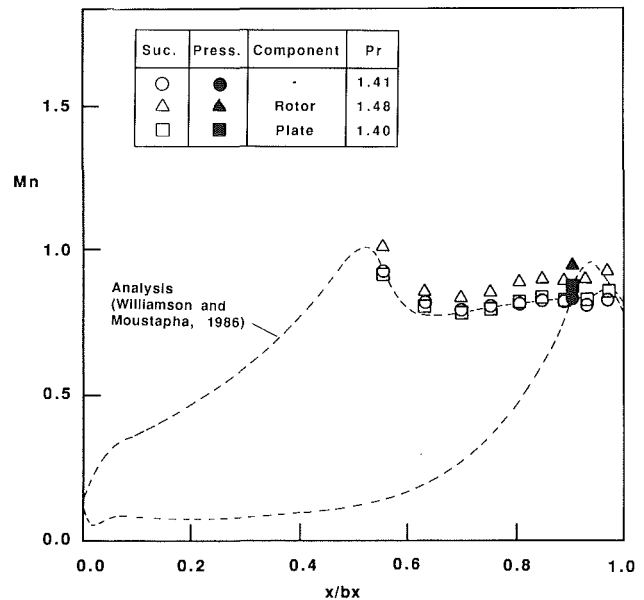


Fig. 10 Effect of downstream component on vane root surface Mach number distribution at low pressure ratio

amination of the effects of downstream components on the measured performance of the nozzle. Tests were conducted over a range of nozzle pressure ratio for three different configurations: nozzle alone, nozzle with operating rotor, and nozzle with perforated plate, as described earlier. Measurements included vane surface pressure distributions and nozzle exit flow traverses.

Vane root Mach number (at a radius of 200 mm), based on local static and inlet total pressures, is plotted in Figs. 9 and 10 for the supersonic and subsonic flow cases; i.e., $Pr = 2.3$ and 1.4. A calculated inviscid distribution, from Williamson and Moustapha (1986), also is included to help orient the limited data.

During supersonic flow, the suction surface Mach number can be seen to rise downstream of the throat up to the reflection on the uncovered surface of the shockwave of the covering blade. The Mach number then rises again toward the trailing

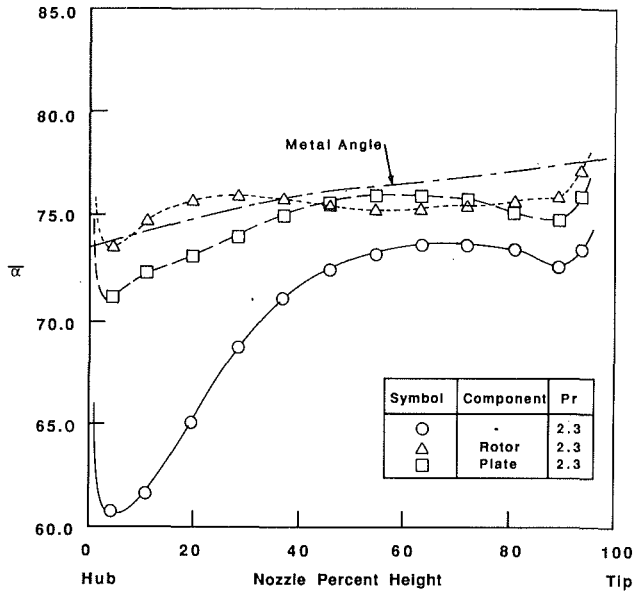


Fig. 11 Effect of downstream component on radial distribution of circumferentially averaged nozzle exit flow angle at design speed and pressure ratio ($Pr = 2.3$)

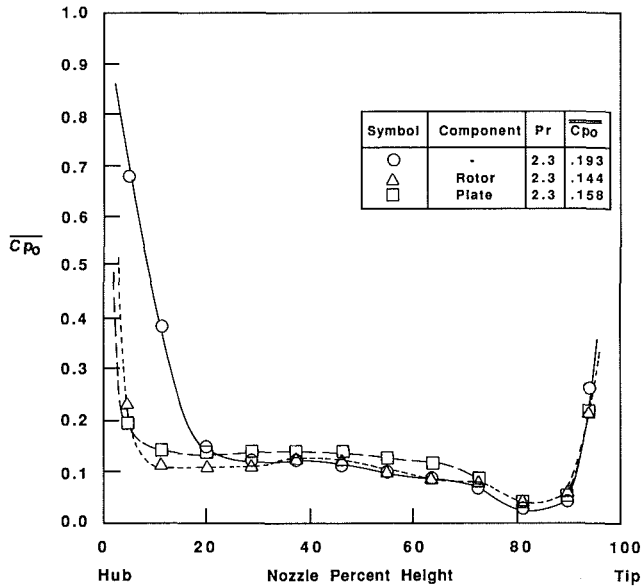


Fig. 12 Effect of downstream component on radial distribution of circumferentially averaged total pressure loss coefficient at design speed and pressure ratio ($Pr = 2.3$)

edge of the nozzle vane. The final Mach numbers, reached on both suction and pressure surfaces, were observed to be higher when either the perforated plate or the rotor was present, suggesting that the flow remained attached up to the trailing edge, and thereby, generating a Mach number distribution closer to the inviscid flow calculation.

Under subsonic flow conditions, as shown in Fig. 10, the Mach number downstream of the throat first decreased and then tended to constancy—a distribution that is consistent with initial diffusion of the core flow, followed by separation, as implied by the inviscid flow calculation. Neither the perforated plate nor the rotor appeared to alter this basic distribution. It is noted that the increased exit Mach number apparent in the "rotor" data reflects a slightly higher test pressure ratio.

Figures 11 and 12 present radial distributions of flow angle and total pressure loss measured at the nozzle exit traverse

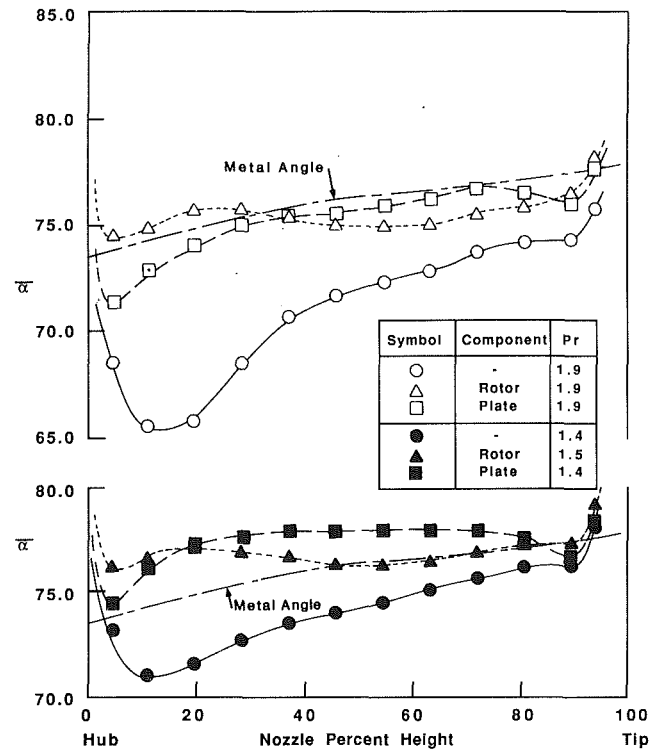


Fig. 13 Effect of downstream component on radial distribution of circumferentially averaged nozzle exit flow angle at design speed and pressure ratios of 1.9 and 1.4

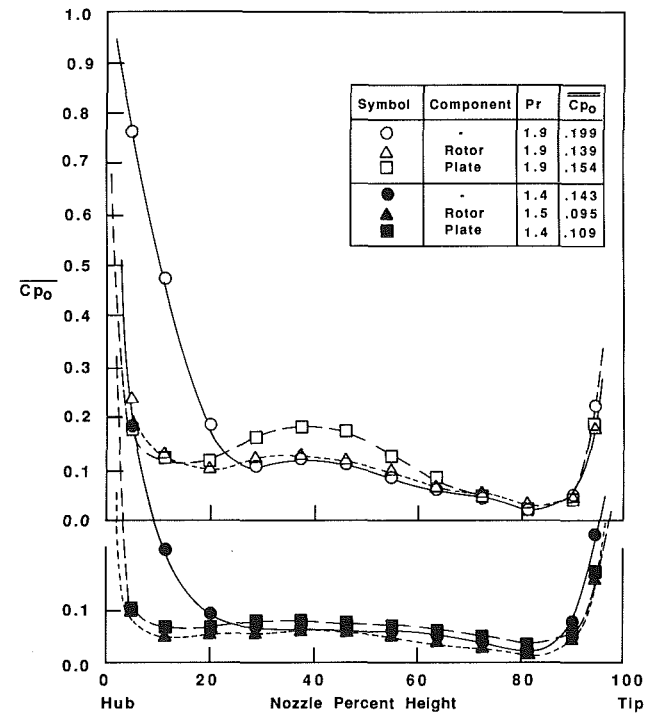


Fig. 14 Effect of downstream component on radial distribution of circumferentially averaged total pressure loss at design speed and pressure ratios of 1.9 and 1.4

plane at design pressure ratio ($Pr = 2.3$) for cases with the nozzle alone, with the perforated plate, and with the rotor operating at design speed. As found in earlier work by Williamson and Moustapha (1986), there was a considerable difference between data taken with the nozzle alone and with an

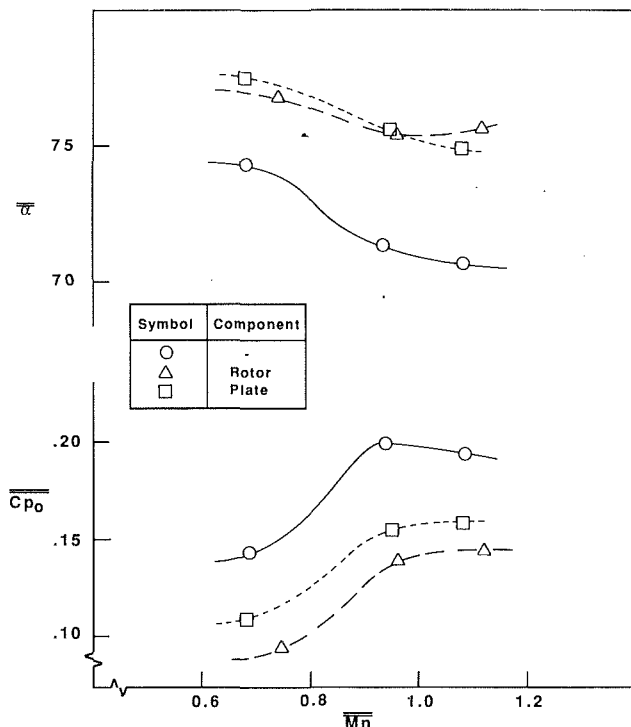


Fig. 15 Effect of stage operating conditions and downstream component on overall nozzle performance

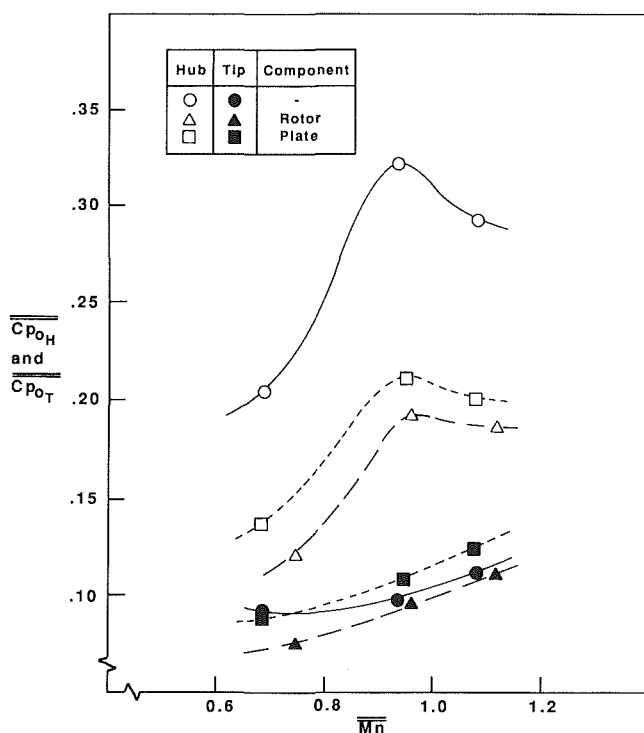


Fig. 16 Effect of stage operating conditions and downstream component on nozzle hub-and-tip loss split

operating rotor present, particularly in the vicinity of the hub. The perforated plate appeared to provide nozzle exit conditions which were a fair approximation to those obtained with an operating rotor, the match of flow angles and losses at the hub showing significant improvement. Bearing in mind the uncertainty associated with some of the traverse measurements in highly sheared and supersonic flows, and also the fact that

no attempt was made to improve the match by rotationally skewing the stack of annular rings making up the "plate," the similarity demonstrated between the data is remarkable.

Similar data, for lower nozzle pressure ratios, are presented in Figs. 13 and 14. It is evident in Fig. 13 that the slight overturning of the perforated plate data at midheight, relative to the rotor results, appears to increase as pressure ratio is reduced. Increased loss also is apparent in this region (Fig. 14). However, the overall match between perforated plate and rotor data is generally reasonable, and represents a considerable improvement on the nozzle alone performance in the hub region.

The general impression of the potential usefulness of the perforated plate in simulating an operating rotor is confirmed in Fig. 15. Overall area-weighted mean angles and total pressure losses for the three cases tested are presented in Figs. 15 and 16 as a function of mean area-weighted nozzle exit Mach number. Lines have been faired through the data following the trends established by Williamson et al. (1986). The benefit, due to the downstream component, is obvious for both angle and loss measurements. The overall averages of nozzle exit flow angle achieved by the perforated plate are seen to be quite close to those observed while testing the rotor, except at the highest pressure ratio where a difference of approximately 1 deg was measured. On the other hand, the perforated plate was generally associated with a higher nozzle pressure loss than was the rotor. It is interesting to note that the largest reduction in loss associated with either downstream component occurred at the intermediate pressure ratio (exit Mach number of 0.95), which corresponds to critical conditions, as discussed in the previous paper (Williamson et al., 1986).

The contributions of the outer and inner 50 percent of the annulus area to the measured total pressure losses is shown in Fig. 16. The substantial contribution of the plate to matching the nozzle hub losses with the operating rotor is evident, although the plate is less helpful in the tip region.

The detailed geometry of the downstream component and its axial location appear to play an important role in the observed flow redistribution. The channelling effect of the rotor, for example, is one physical phenomenon that cannot be adequately simulated by a perforated plate. The complexity of the situation suggests that improvements on the perforated plate would require considerable experimentation.

Conclusions

Experiments have been conducted to assess possible interference effects of a nozzle exit traverse probe in conditions of highly swirled transonic flow. A rod spanning the annulus in the nozzle exit traverse plane was used to simulate the measuring probe at full immersion. Under "worst case" conditions (full immersion and appropriate circumferential position), the nozzle flow rate, inferred from vane static tappings, was unaffected by the presence of the rod. Although some disturbance to the pressure distribution on the uncovered suction surface could be detected for some rod positions, it appeared likely that flow sensed at the rod itself would be largely unaffected by such perturbations. As expected, decreased Mach number and a smaller rod blockage reduced the interference. Although it was concluded that nozzle exit flow traverses were not compromised by interference effects, at least to first-order, additional experiments are planned to confirm this finding through direct comparison of probe and LDA measurements.

Further experiments related to nozzle exit conditions compared the nozzle performance when tested alone, with an operating rotor, or with a stationary perforated plate located at a position corresponding to the rotor leading edge. Distributions and overall levels of nozzle losses and mean flow angles measured with the operating rotor were matched quite well by the simpler perforated plate arrangement. In particular, the

losses and gas angles associated with an incipient nozzle hub flow separation without a downstream component were improved appreciably by the presence of the plate at all nozzle pressure ratios. Based on results presented, the perforated plate would be worth further investigation for use in the testing of transonic turbine nozzles of high turning angle.

References

- Binder, A., Forster, W., Kruse, H., and Rogge, H., 1984, "An Experimental Investigation Into the Effect of Wakes on the Unsteady Turbine Rotor Flow," ASME Paper No. 84-GT-178.
- Boletis, E., and Sieverding, C. H., 1984, "Experimental Study of the Flow Field Behind an Annular Turbine Nozzle Guide Vane With and Without Downstream Rotor," ASME Paper No. 84-GT-82.
- Denton, J. D., 1983, "A Review of Current Research Activity on the Aerodynamics of Axial Flow Turbines," VKI LS 1983-06.
- Dring, R. P., Joslyn, H. D., Hardin, L. W., and Wagner, I. H., 1982, "Turbine Rotor-Stator Interaction," ASME Paper No. 82-GT-3.
- Moustapha, S. H., Okapuu, U., and Williamson, R. G., 1987, "The Influence of Rotor Blade Aerodynamic Loading on the Performance of a Highly Loaded Turbine Stage," ASME JOURNAL OF TURBOMACHINERY, Vol.109.
- Moustapha, S. H., and Williamson, R. G., 1986, "Investigation of Two Endwall Contours on the Performance of an Annular Nozzle Cascade," *AIAA Journal*, Vol. 24.
- Shapiro, A. H., 1954, *The Dynamics and Thermodynamics of Compressible Fluid Flow*, The Ronald Press Company, Vol. II, p. 884.
- Sjolander, S. A., 1975, "The Endwall Boundary Layer in an Annular Cascade of Turbine Nozzle Guide Vanes," Carleton University, Ottawa, Report TRME/A 75-4.
- Spurr, A., 1980, "A Computational and Experimental Study of Fully 3D Transonic Flow in Turbomachinery," PhD Thesis, University of Southampton, United Kingdom.
- Squire, L.C., and Bryanston-Cross, P. I., 1986, "The Design and Testing of a Model of the Final Stage Stator of a Steam Turbine," unpublished Cambridge University Engineering Department Report.
- Williamson, R. G., and Moustapha, S. H., 1986, "Three-Dimensional Cascade Testing of Turbine Nozzles at High Exit Mach Number," *ASME Journal of Fluids Engineering*, Vol. 108.
- Williamson, R. G., Moustapha, S. H., and Huot, J. P., 1986, "The Effect of a Downstream Rotor on the Measured Performance of a Transonic Nozzle," ASME JOURNAL OF TURBOMACHINERY, Vol. 108.

The Use of Circumferentially Varying Stagger Guide Vanes in an Axial Flow Pump or Compressor

J. H. Horlock

Open University,
Milton Keynes, United Kingdom

An actuator disk analysis is given of the flow through a guide vane and rotor combination. It is shown that changes in total pressure across the rotor are in general related to circumferential variations in guide vane outlet angle. In particular known variations in inlet total pressure may be eliminated by suitable circumferential changes in guide vane stagger.

1 Introduction

Guide vanes are frequently used ahead of the first rotating row of a pump or compressor, to off-load that rotor (reducing cavitation or Mach number). The guide vane stagger (uniform round the annulus) may be varied and rotor stall may be delayed (by rotating the vanes to higher stagger).

Variation of guide vane outlet angle circumferentially around the annulus has been employed to break up rotating stall patterns in a research compressor (Horlock, 1956). It has also been proposed by Chen et al. (1987) in order to enhance the tolerance of an axial compressor to an inlet distortion. The authors suggest that by opening the guide vanes in the portion of the circumference exposed to low total pressure, and closing them in a region of high total pressure, the axial velocity distortion just ahead of the compressor can be reduced.

The author's interest in circumferentially variable guide vane stagger was recently revived by observing their use to cancel out an angle variation at inlet to a propeller disk, arising from a uniform flow entering at an angle to the axis of propeller rotation (Fig. 1). The rotor blades experience an angle of attack that varies as they move round the annulus, and this may be eliminated most effectively by use of guide vanes of variable outlet angle ahead of the rotor.

The actuator disk analysis given here, of nonaxisymmetric flows through a guide vane and rotor combination, illustrates the relation between guide vane outlet angle and stagnation pressure rise. In particular it is shown that an entering deficit in stagnation pressure may be eliminated by varying the vane outlet angle round the annulus (and hence the rotor work).

2 Analysis

We use a set of equations developed by Mokolke (1974), and used subsequently by Henderson and Shah (1982), to study the flow. For small perturbations from a uniform flow at an angle α to the axis, the following equations for axial velocity,

tangential velocity, and total pressure perturbations satisfy the continuity and Crocco equations:

$$V'_x = \sum_n (A_{1n} e^{nx} - A_{2n} e^{-nx} + A_{3n} e^{-inx}) e^{in\theta} \quad (1)$$

$$V'_\theta = \sum_n (iA_{1n} e^{nx} + iA_{2n} e^{-nx} + aA_{3n} e^{-inx}) e^{in\theta} \quad (2)$$

$$P'_T = \sum_n 2(1+a^2)A_{3n} e^{inx} e^{in\theta} \quad (3)$$

Here the perturbations are written as fractions of mean axial dynamic head ($P'_T = \bar{P}_T / \frac{1}{2} \rho \bar{V}_x^2$) or mean axial velocity ($V'_x = \bar{V}_x / \bar{V}_x$, $V'_\theta = \bar{V}_\theta / \bar{V}_x$) where the superscript ' refers to the actual perturbations.

We consider a guide vane/rotor combination (Fig. 2). There are three regions: upstream (u), between the two rows (m), and downstream (d). In any one region, three constants are required to describe the flow: A_{1u} , A_{2m} , and A_{3d} . But in the upstream area, the term involving the negative exponential ($A_{2n} e^{-nx}$) cannot be present, and similarly in the downstream flow the positive exponential ($A_{1n} e^{nx}$) cannot exist. Thus

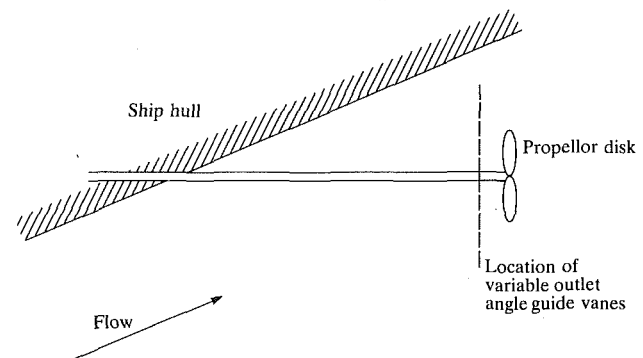


Fig. 1 Flow into propeller past inclined ship hull

Contributed by the International Gas Turbine Institute for publication in the JOURNAL OF TURBOMACHINERY. Manuscript received at ASME Headquarters October 1989.

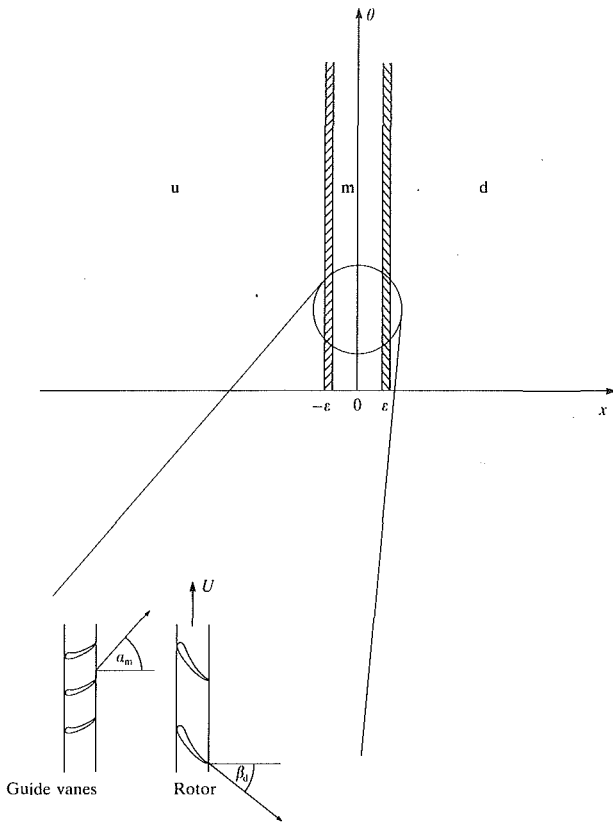


Fig. 2 Actuator disk model of flow through guide vanes and rotor

there are two constants describing the flow in each of these regions. If the flow far upstream is specified, then one of those constants is known, leaving six to be determined (one in the u area, three in the m area, and two in the d area). We shall match total pressure, axial velocity, and tangential velocity at each of the two disks to give the six equations required for solution.

We shall assume the following:

- (i) that the two disks are close together, at $x=0+\epsilon$, $x=0-\epsilon$, so that at the disks the exponential terms become unity.
- (ii) that the mean flow in the upstream region is axial ($a_u=0$), but that tangential mean velocity exists in the m and d regions produced by stator blade angles at $\bar{\alpha}_m$ to the axial flow direction, and rotor blade angles at $\bar{\beta}_d$ to the axial flow direction

$$(a_m = \tan \bar{\alpha}_m, \quad a_d = (U/\bar{V}_x) - \tan \bar{\beta}_d).$$

With these assumptions, the conditions at the disks are as follows (dropping the n subscripts and the summation signs for simplicity, i.e., for the first harmonic):

Upstream of guide vanes

$$V'_{x_u} = (A_{1_u} + A_{3_u})e^{i\theta} \quad (4)$$

$$V'_{\theta_u} = iA_{1_u}e^{i\theta} \quad (5)$$

$$P'_{T_u} = 2A_{3_u}e^{i\theta} \quad (6)$$

Between blade rows

$$V'_{x_m} = (A_{1_m} - A_{2_m} + A_{3_m})e^{i\theta} \quad (7)$$

$$V'_{\theta_m} = (iA_{1_m} + iA_{2_m} + a_m A_{3_m})e^{i\theta} \quad (8)$$

$$P'_{T_m} = 2(1 + a_m^2)A_{3_m}e^{i\theta} \quad (9)$$

Downstream of rotor

$$V'_{x_d} = (-A_{2_d} + A_{3_d})e^{i\theta} \quad (10)$$

$$V'_{\theta_d} = (iA_{2_d} + a_d A_{3_d})e^{i\theta} \quad (11)$$

$$P'_{T_d} = 2(1 + a_d^2)A_{3_d}e^{i\theta} \quad (12)$$

The simplest matching condition is in total pressure at the guide vane trailing edge (assuming no losses across the row), i.e.,

$$P'_{T_u} = P'_{T_m} \quad (13)$$

$$A_{3_u} = (1 + a_m^2)A_{3_m} \quad (14)$$

Matching of the axial velocity perturbation at the same location yields

$$V'_{x_u} = V'_{x_m} \quad (15)$$

$$A_{1_u} + A_{3_u} = A_{1_m} - A_{2_m} + A_{3_m} \quad (16)$$

The tangential velocity at the guide vane trailing edge is given by

$$\bar{V}'_{\theta_m} + \bar{V}'_{\theta_m} = (\bar{V}'_{x_m} + \bar{V}'_{x_m}) \tan(\bar{\alpha}_m + \bar{\alpha}_m) \quad (17)$$

where $\bar{\alpha}_m$ is the circumferential variation in the guide vane angle, $\bar{\alpha}_m = \alpha_0 e^{i\theta}$. Since $\bar{V}'_{\theta_m} = \bar{V}'_{x_m} \tan \bar{\alpha}_m$ it follows that

$$V'_{\theta_m} = \tan \bar{\alpha}_m V'_{x_m} + \sec^2 \bar{\alpha}_m \alpha_0 e^{i\theta} \quad (18)$$

and hence

$$iA_{1_m} + iA_{2_m} + a_m A_{3_m} = a_m [A_{1_m} - A_{2_m} + A_{3_m}] + \alpha_0 (1 + a_m^2) \quad (19)$$

For matching at the second (rotor) row, the axial velocity equation is straightforward

$$V'_{x_d} = V'_{x_m} \quad (20)$$

$$A_{1_m} - A_{2_m} + A_{3_m} = -A_{2_d} + A_{3_d} \quad (21)$$

The perturbation in tangential velocity results from the equations

$$\bar{V}'_{\theta_d} = U - \bar{V}'_{x_d} \tan \bar{\beta}_d \quad (22)$$

$$\bar{V}'_{\theta_d} + \bar{V}'_{\theta_d} = U - (\bar{V}'_{x_d} + \bar{V}'_{x_d}) \tan \bar{\beta}_d \quad (23)$$

so that

$$\bar{V}'_{\theta} = -\bar{V}'_{x_d} \tan \bar{\beta}_d \quad (24)$$

$$V'_{\theta} = -V'_{x_d} \tan \bar{\beta}_d \quad (25)$$

$$iA_{2_d} + a_d A_{3_d} = (A_{2_d} - A_{3_d}) \tan \bar{\beta}_d \quad (26)$$

Finally, for loss-free flow, the increase in total pressure across the rotor may be related to the change in tangential velocity. In the mean flow

$$\Delta \bar{P}_T = \bar{P}_{T_d} - \bar{P}_{T_m} = \rho U (\bar{V}'_{\theta_d} - \bar{V}'_{\theta_m}) \quad (27)$$

Nomenclature

a, A = constants
 P_T = total pressure
 U = blade speed
 V_x, V_θ = velocity components
 x, θ = coordinate system
 α = guide vane outlet angle

β = rotor (relative) outlet angle
 ρ = density
Subscripts
 1, 2, 3 = referring to constants at given location
 d = downstream

m = between blade rows
 u = upstream

Superscripts

$\bar{\quad}$ = undisturbed or mean flow
 \prime = perturbation
 \prime = dimensionless perturbation

In perturbed flow

$$\Delta\bar{P}_T + \Delta\bar{P}_T = \bar{P}_{T_d} + \bar{P}_{T_d} - (\bar{P}_{T_m} + \bar{P}_{T_m}) \\ = \rho U [\bar{V}_{\theta_d} + \bar{V}_{\theta_d} - (\bar{V}_{\theta_m} + \bar{V}_{\theta_m})] \quad (28)$$

so that

$$\bar{P}_{T_d} - \bar{P}_{T_m} = \rho U (\bar{V}_{\theta_d} - \bar{V}_{\theta_m}) \quad (29)$$

$$\frac{\bar{P}_{T_d} - \bar{P}_{T_m}}{\rho \bar{V}_x^2} = \frac{U}{\bar{V}_x} (V'_{\theta_d} - V'_{\theta_m}) \quad (30)$$

$$P'_{T_d} - P'_{T_m} = \frac{2}{\bar{\phi}} (V'_{\theta_d} - V'_{\theta_m}) \quad (31)$$

and

$$\bar{\phi}(1 + a_d^2)A_{3_d} - \bar{\phi}(1 + a_m^2)A_{3_m} \\ = iA_{2_d} + a_d A_{3_d} - iA_{1_m} - iA_{2_m} - a_m A_{3_m} \quad (32)$$

With A_{3_u} , $\bar{\alpha}_m$, $\bar{\beta}_d$, $\bar{\phi}$, α_0 all specified, the six equations (14), (16), (19), (21), (26), and (32) are available for solution of the six unknowns A_{1_u} , A_{1_m} , A_{2_m} , A_{3_m} , A_{2_d} , A_{3_d} . A_{3_m} is directly obtained from equation (14), and eliminated from the five remaining equations, which may then be written in matrix form

A_{1_u}	A_{1_m}	A_{2_m}	A_{2_d}	A_{3_d}	
1	-1	+1	0	0	=
0	$(i - a_m)$	$(i + a_m)$	0	0	=
0	1	-1	1	-1	=
0	0	0	$(i - \tan \bar{\beta}_d)$	$(a_d + \tan \bar{\beta}_d)$	=
0	i	i	$-i$	$\bar{\phi}(1 + a_d^2) - a_d$	=
					$A_{3_u} \left[\bar{\phi} - \frac{a_m}{1 + a_m^2} \right]$

The general solution of these equations is straightforward but involves complex expressions, and is therefore not given here. Rather we shall consider some special cases of particular interest. To this end we obtain a partial solution to the equations as follows, seeking the coefficient A_{3_d} , which describes the downstream stagnation pressure. From equation (26A)

$$A_{2_d} = A_{3_d} \frac{(a_d + \tan \bar{\beta}_d)}{(\tan \bar{\beta}_d - i)} \quad (33)$$

Elimination of A_{1_m} and A_{2_m} from equations (19A), (21A), and (32A) yields

$$A_{3_d} = \frac{(1 + a_m^2)\alpha_0 - \bar{\phi}A_{3_u}}{Pa_m - Q} \quad (34)$$

where

$$P = \frac{a_d - i}{\tan \bar{\beta}_d - i} \quad (35)$$

$$Q = \bar{\phi}(1 + a_d^2) + \frac{\tan \bar{\beta}_d (i + a_d)}{(i - \tan \bar{\beta}_d)} \quad (36)$$

Equation (34) shows that downstream total pressure variation is eliminated if

$$\alpha_0 = \frac{\bar{\phi}A_{3_u}}{(1 + a_m^2)} = \bar{\phi} \cos^2 \bar{\alpha}_m A_{3_u} \quad (37)$$

This simple result requires explanation. If $A_{3_d} = 0$, then it follows from equation (33) that $A_{2_d} = 0$. Equations (11) and (12) then show that $V'_{x_d} = V'_{\theta_d} = 0$ and the downstream flow is entirely uniform. But the axial velocity is constant through the two blade rows ($V'_{x_u} = V'_{x_m} = V'_{x_d} = 0$ from equations (15) and (20)). We may therefore study the work input by the rotor on the basis that the local axial velocity is constant (\bar{V}_x) at guide vane and rotor exit. However the work transfer is not constant but simply

$$\Delta P_T = U[U - \bar{V}_x \tan \bar{\beta}_d - \bar{V}_x \tan (\bar{\alpha}_m + \bar{\alpha})] \quad (38)$$

$$\Delta \bar{P} = -U \bar{V}_x \sec^2 \bar{\alpha}_m \alpha_0 e^{i\theta} \quad (39)$$

$$\Delta P'_T = -\frac{2}{\bar{\phi}} \sec^2 \bar{\alpha}_m \alpha_0 e^{i\theta} \quad (40)$$

For uniform downstream flow this "deficit" in work transferred from the rotor to the fluid compensates exactly for the "excess" total pressure at entry

$$\Delta P'_T + 2A_{3_u} e^{i\theta} = 0 \quad (41)$$

i.e.,

$$\alpha_0 = \bar{\phi} \cos^2 \bar{\alpha}_m A_{3_u} \quad (37)$$

is the variation in guide vane angle required to eliminate the wake, as found earlier from solution of the overall equations.

We may note that all the change in axial velocity takes place upstream of the guide vanes, between $x = -\infty$ and $x = 0$ ($A_{1_u} = -A_{3_u}$). This is the objective recommended by Chen et al. (1987).

The complete set of coefficients for this case is thus as follows:

$$-\frac{A_{3_u} a_m^2}{(1 + a_m^2)} \quad (16A)$$

$$\alpha_0(1 + a_m^2) \quad (19A)$$

$$-\frac{A_{3_u}}{(1 + a_m^2)} \quad (21A)$$

$$0 \quad (26A)$$

$$A_{3_u} \left[\bar{\phi} - \frac{a_m}{1 + a_m^2} \right] \quad (32A)$$

$$A_{1_u} = -A_{3_u} \quad (42)$$

$$A_{1_m} = -\frac{A_{3_u}}{2} \left[\frac{1}{(1 + a_m^2)} + i \left(\bar{\phi} - \frac{a_m}{1 + a_m^2} \right) \right] \quad (43)$$

$$A_{2_m} = \frac{A_{3_u}}{2} \left[\frac{1}{(1 + a_m^2)} - i \left(\bar{\phi} - \frac{a_m}{1 + a_m^2} \right) \right] \quad (44)$$

$$A_{3_m} = \frac{A_{3_u}}{(1 + a_m^2)} \quad (45)$$

$$A_{2_d} = 0 \quad (46)$$

$$A_{3_d} = 0 \quad (47)$$

(We may note that the result may be generalized for flow entering through a stator row rather than a guide vane row by writing $A_{3_u}(1 + a_u^2)$ for A_{3_u} in these expressions, where $a_u = \tan \bar{\alpha}_u$ and $\bar{\alpha}_u$ is the flow angle upstream of the stator.)

3 Discussion

There thus appears to be the opportunity for eliminating an entry variation in total pressure P_{T_u} by varying the outlet angle from the guide vane row and thus adjusting the local rotor work to compensate for P_{T_u} . This may have practical application for cases where the wavelength of the entry disturbance is several times greater than the pitch of the guide vanes, i.e., gross distortions rather than narrow entry wakes.

The case of no entry distortion in total pressure is also of interest. In this case variation of guide vane outlet angle produces a nonuniform work input from the rotor and a variation in total pressure *at outlet*

$$A_{3d} = \frac{(1 + a_m^2)\alpha_0}{Pa_m - Q}$$

This kind of situation may be produced by a rotor receiving a flow of uniform total pressure but at an angle to the axis of rotation of a rotating row (Fig. 1). The tangential velocity at entry to the rotor will vary as $e^{i\theta}$, being against rotation over half the annulus and with rotation over the other. To some extent the flow leaving the guide vane in the two-dimensional example we have considered (with $V'_{\theta u} = iA_{1u}e^{i\theta}$ in equation (6)) simulates this "inclined" entry flow with uniform stagnation pressure to a single rotor, and explains how that rotor will produce a nonuniform stagnation pressure. Indeed one way to eliminate the production of such a variation in P_{T_d} in the inclined rotor case is to put a real guide vane ahead of the isolated rotor equal and opposite to the hypothetical guide vane of the two-dimensional simulation of the "inclined" flow.

4 Conclusion

An actuator disk analysis has related circumferential perturbations in stagnation pressure (P_T) through a guide vane and rotor combination to circumferential variation in guide vane outlet angle. In particular it is shown that variations in P_T may be eliminated by suitable guide vane settings to give a particular vane outlet angle.

References

- Chen, G. T., Greitzer, E. M., and Epstein, A. H., 1987, "Enhancing Compressor Distortion Tolerance by Asymmetric Stator Control," presented at the AIAA/SAE/ASME/ASEE 23rd Joint Propulsion Conference, Paper No. AIAA-87-2093.
- Henderson, R. E., and Shah, I. C., 1982, "The Influence of Unsteady Rotor Response on a Distorted Flow Field," *ASME Journal of Engineering for Power*, Vol. 104, pp. 683-691.
- Horlock, J. H., 1956, "A Note on the Suppression of Rotating Stall," Aeronautical Research Council Report No. 17810.
- Mokelke, H., 1974, "Distortion Induced Engine Instabilities," AGARD Lecture Series, AGARD-LS-72.

Inlet Distortion Generated Periodic Aerodynamic Rotor Response

S. R. Manwaring

S. Fleeter

Thermal Sciences and Propulsion Center,
School of Mechanical Engineering,
Purdue University,
W. Lafayette, IN 47907

Fundamental inlet distortion-generated rotor blade row unsteady aerodynamics, including the effects of both the detailed aerodynamic forcing function for the first time and steady loading are experimentally investigated in an extensively instrumented axial-flow research compressor. A two-per-rev forcing function with three gust amplitude ratios is generated. On the rotor blade pressure surface, the unsteady pressure nondimensionalization compresses the magnitude data with mean flow incidence angle. This is not the case on the higher camber suction surface. These pressure surface unsteady data are primarily affected by the steady loading level, whereas the suction surface unsteady data are a function of the steady loading level and distribution as well as the gust amplitude ratio. In addition, a design inlet distortion blade surface unsteady pressure correlation is considered.

Introduction

Inlet flow distortions are generated by a variety of sources, including engine inlet designs and aircraft maneuvers. In addition to the performance degradation associated with inlet flow distortions, they also can result in detrimental aeromechanical effects. Namely, as schematically depicted in Figs. 1 and 2, inlet flow distortions represent unsteady aerodynamic forcing functions to downstream rotor blade rows due to rotor blade relative velocity and incidence angle fluctuations, thereby resulting in the possibility of significant aerodynamically induced blade vibrations. In fact, distortions are one of the most common excitation sources for aerodynamically forced response of blade rows. Distortions also affect the stability margin of rotor blade rows, as the resulting flow degradation from distortion can cause incidence angle migration that experience has shown to be generally destabilizing (Cardinale et al., 1980).

Of particular interest in this paper are distortion-generated unsteady aerodynamic blade response phenomena. In the high-speed regime, Datko and O'Hara (1987) measured the forced vibratory response of an advanced transonic compressor first-stage integrally bladed disk (a blisk) generated by seven different inlet total pressure distortion screens. The blisk was found to be susceptible to excessive resonant stresses generated by the inlet distortions, with complex inlet distortions exciting the lower natural frequencies at a number of engine orders. The harmonic content of the distortion was not always discernible from the inlet total pressure profiles. In addition, these results demonstrated that the uniform inlet flow rotor forced response characteristics may not be representative of the response when a distortion is present. They concluded that unless vibratory responses to inlet distortion can be accurately predicted, rotors, particularly blisks, should be tested to assess the resonant stresses in the presence of inlet distortions.

Contributed by the International Gas Turbine Institute and presented at the 34th International Gas Turbine and Aeroengine Congress and Exhibition, Toronto, Ontario, Canada, June 4-8, 1989. Manuscript received at ASME Headquarters February 14, 1989. Paper No. 89-GT-299.

The accurate prediction of distortion-generated blade response requires the development of a first principles based design system. On a first principles basis, inlet flow distortions represent high-energy aerodynamic excitations characterized by low to moderate values of the reduced frequency, with the distortion-generated blade row response analyzed by first defining the unsteady aerodynamic forcing function in terms of harmonics. The periodic vibratory response of the airfoil row to each harmonic of the forcing function is then assumed to be comprised of two components. One is due to the streamwise and transverse components of the harmonic forcing function, \hat{u}^+ and \hat{v}^+ , respectively, being swept past the nonresponding airfoil row, termed the streamwise and transverse gust responses. The second, the self-induced unsteady aerodynamics, arises when the aerodynamic forcing function generates a vibrational response of the airfoil row.

Unfortunately, current state-of-the-art analyses do not model the unsteady aerodynamic forcing function. Additionally, the gust and motion-induced unsteady aerodynamic models involve many physical and numerical assumptions (AGARD Manual, 1987). Therefore, experimental modeling of the fundamental inlet distortion-generated blade row periodic unsteady aerodynamic response, including both the forcing function and the blade row unsteady aerodynamics, is needed for the development, validation, and enhancement of theoretical and numerical models.

Unsteady aerodynamic gust experiments of direct interest to turbomachines have been performed in low-speed research compressors. With regard to inlet flow distortions, O'Brien et al. (1980) used six dynamic pressure transducers embedded on each rotor blade surface to measure unsteady aerodynamic response. However, the periodic rotor blade row inlet-flow field was not measured, and thus the unsteady aerodynamic gust forcing function was not quantified. Hardin et al. (1987) measured low reduced frequency oscillating airfoil aerodynamics on a rotor of a single-stage compressor and also stated

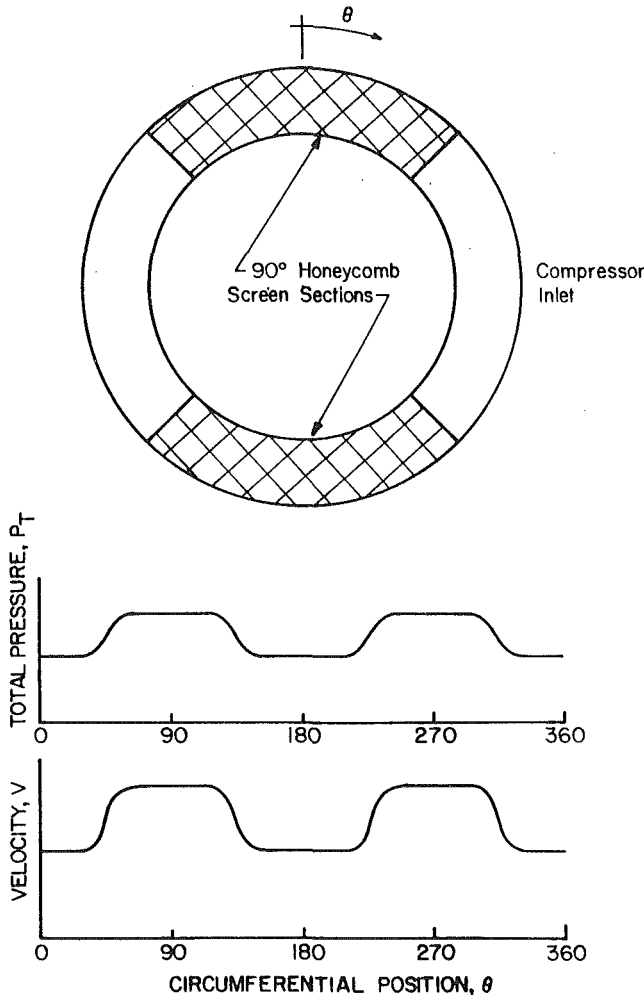


Fig. 1 Two-per-rev distortion aerodynamic forcing functions

that they had performed similar distortion experiments although they did not present these results.

In this paper, the fundamental flow physics of distortion-generated periodic rotor blade row unsteady aerodynamics, including the effects of both the detailed unsteady aerodynamic forcing function for the first time and steady loading, are experimentally investigated. This is accomplished by performing a series of experiments in an extensively instrumented axial-flow research compressor. In particular, the effects of the detailed forcing function, defined in terms of the ratio of the forcing function streamwise-to-transverse first harmonic gust components, $\hat{u}^+/\hat{\theta}^+$, as well as the steady aerodynamic loading level, characterized by the mean incidence angle, on the gust-generated unsteady aerodynamic response of a first-stage rotor blade are quantified.

In these experiments, the two-per-rev unsteady aerodynamic

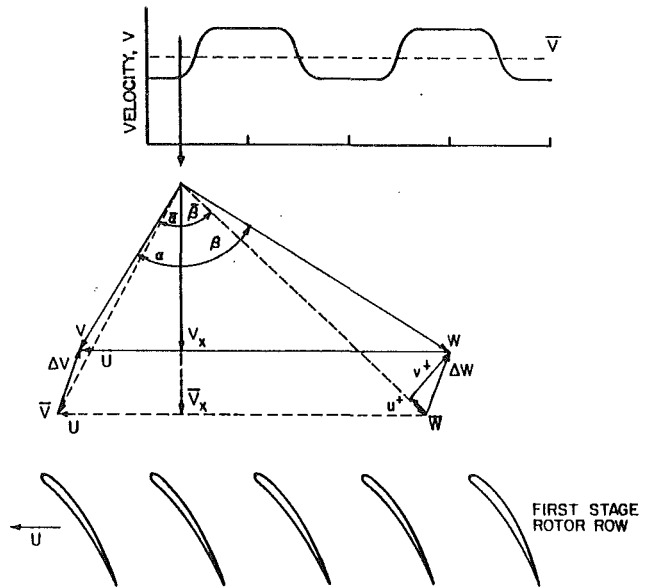


Fig. 2 Decomposition of distortion forcing function

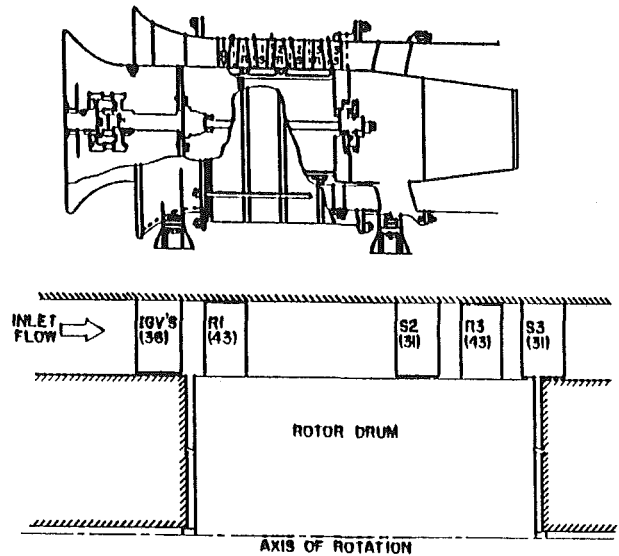


Fig. 3 Research compressor schematic

forcing function is generated by two 90 deg circumferential inlet flow distortions (Fig. 1). This distortion, measured with a rotating cross hot-wire probe, is then analyzed and decomposed into streamwise and transverse components (Fig. 2). The resulting unsteady aerodynamic gust-generated rotor blade surface unsteady pressure chordwise distributions are measured with embedded ultraminiature high response dynamic pressure transducers.

Nomenclature

b = rotor blade semichord
 \bar{C}_l = rotor blade steady loading
 $= \int_0^c (C_{p, \text{pressure}} - C_{p, \text{suction}}) dx$
 \bar{C}_p = rotor blade steady pressure coefficient
 C_p = rotor blade unsteady pressure coefficient
 $C_{\Delta p}$ = rotor blade unsteady pressure difference coefficient

\bar{i} = rotor blade mean incidence angle
 k = reduced frequency = $\omega b / \bar{V}_x$
 p = digitized ensemble-averaged unsteady pressure
 \bar{P}_s = rotor blade surface steady pressure
 \hat{p} = first harmonic complex unsteady pressure

\hat{u}^+ = streamwise gust first harmonic component
 $\hat{\theta}^+$ = transverse unsteady velocity component
 \bar{V}_x = mean axial velocity
 ΔW = total unsteady velocity
 ΔW = total first harmonic gust vector
 $\bar{\beta}$ = relative mean flow angle
 ω = two-per-rev forcing function frequency, rad

Table 1 Overall airfoil and compressor characteristics

	ROTOR	STATOR	IGV
Airfoil Type	C4	C4	C4
Number of Airfoils	43	31	36
Chord, C (mm)	30	30	30
Solidity, C/S	1.14	1.09	0.96
Camber, θ	27.95	27.70	36.9
Stagger Angle, λ	36	-36.1	18.5
Aspect Ratio	2.0	2.0	2.0
Thickness/Chord (%)	10	10	10
Design Flow Rate (kg/s)		2.03	
Design Axial Velocity (m/s)		24.4	
Rotational Speed (RPM)		2250	
Number of Stages		2	
Stage Pressure Ratio		1.003	
Inlet Tip Diameter (mm)		420	
Hub/Tip Radius Ratio		0.714	
Stage Efficiency (%)		85	

Research Compressor

The Purdue Axial Flow Research Compressor experimentally models the fundamental turbomachinery unsteady aerodynamic multistage interaction phenomena including the incidence angle, the velocity, and pressure variations, the aerodynamic forcing function, the reduced frequency, and the unsteady blade row interactions. The compressor is driven by a 15 hp d-c electric motor and is operated at a speed of 2250 rpm. Each identical stage of the baseline compressor contains 43 rotor blades and 31 stator vanes having a British C4 profile, with the first-stage rotor inlet flow field established by a row of 36 variable setting inlet guide vanes. The overall airfoil and compressor characteristics are presented in Table 1. For these experiments, the first-stage rotor blade row was extensively instrumented. To eliminate any potential flow effects on the instrumented first-stage rotor blades, the first-stage stators and second-stage rotors were removed, as schematically depicted in Fig. 3.

Instrumentation

Both steady and unsteady first-stage rotor blade row data are required. The steady data quantify the rotor mean inlet flow field and midspan steady loading distribution. The unsteady data define the periodic aerodynamic forcing function and the resulting midspan blade surface periodic pressure distributions.

The inlet flow field, both steady and unsteady, is measured with a rotating cross hot-wire probe mounted 30 percent of blade chord upstream of the rotor row. The cross hot-wire probe was calibrated and linearized for velocities from 18.3 m/s to 53.4 m/s and ± 35 deg angular variation, with the accuracy of the velocity magnitude and flow angle determined to be 4 percent and ± 1.0 deg, respectively. Centrifugal loading effects on the rotating hot-wire sensor resistances, and thus the responses, were found to be negligible.

The detailed steady aerodynamic loading on the rotor blade surfaces is measured with a chordwise distribution of 20 mid-

span static pressure taps, 10 on each surface. The static pressure at the rotor exit plane, measured with a rotor drum static tap, is used as the blade surface static pressure reference. These static pressure measurements are made using a rotor based 48 port constant speed drive Scanivalve system located in the rotor drum.

The measurement of the midspan rotor blade surface unsteady pressures is accomplished with 20 ultraminiature, high response transducers embedded in the rotor blades at the same chordwise locations as the static pressure taps. To minimize the possibility of flow disturbances associated with the inability of the transducer diaphragm to exactly maintain the surface curvature of the blade, a reverse mounting technique is utilized. The pressure surface of one blade and the suction surface of the adjacent blade are instrumented, with transducers embedded in the nonmeasurement surface and connected to the measurement surface by a static tap. The embedded dynamic transducers were both statically and dynamically calibrated. The static calibrations showed good linearity and no discernible hysteresis. The dynamic calibrations demonstrated that the frequency response, in terms of gain attenuation and phase shift, were not affected by the reverse mounting technique. The accuracy of the unsteady pressure measurements, determined from the calibrations, is ± 4 percent.

The rotor-based static pressure Scanivalve transducer, rotating cross hot-wire probe and 20 blade surface dynamic pressure transducers are interfaced to the stationary frame-of-reference through a 40-channel slip ring assembly. On-board signal conditioning of the transducer output signals is performed to maintain a good signal-to-noise ratio through the slip ring. The remaining 17 channels of the slip-ring assembly are used to provide excitation to the transducers and on/off switching to the Scanivalve d-c motor.

Data Acquisition and Analysis

Steady Data. The rotor blade surface static pressure data, measured with the rotor-based Scanivalve system, are defined by a root-mean-square error analysis of 20 samples with a 95 percent confidence interval. The reference for these midspan blade pressure measurements is the static pressure at the exit of the rotor measured on the rotor drum. Thus the blade surface and the reference static pressures are measured at different radii. Hence, a correction for the resulting difference in the radial acceleration is applied in calculating the blade surface static pressure coefficient defined as

$$\bar{C}_p = \frac{\bar{P}_s - \bar{P}_{\text{exit}}}{\frac{1}{2}\rho U_t^2} \quad (1)$$

where U_t is the rotor blade tip speed.

Periodic Data. The periodic data of interest are the harmonic components of the aerodynamic forcing function to the first-stage rotor blade row, together with the resulting rotor blade surface unsteady pressures and unsteady pressure differences. These are determined by defining a digitized ensemble-averaged periodic unsteady aerodynamic data set consisting of the rotating cross hot-wire probe and blade surface dynamic pressure transducer signals at each steady operating point. In particular, these time-variant signals are digitized with a high-speed A-D system at a rate of 20 kHz and then ensemble averaged.

The key to this averaging technique is the ability to sample data at a preset time, accomplished by an optical encoder mounted on the rotor shaft. The microsecond range step voltage signal from the encoder is the data initiation time reference and triggers the high-speed A-D multiplexer system. To significantly reduce the random fluctuations superimposed on the periodic signals of interest, 200 averages are used. A Fast Fourier Transform (FFT) algorithm is then applied to these

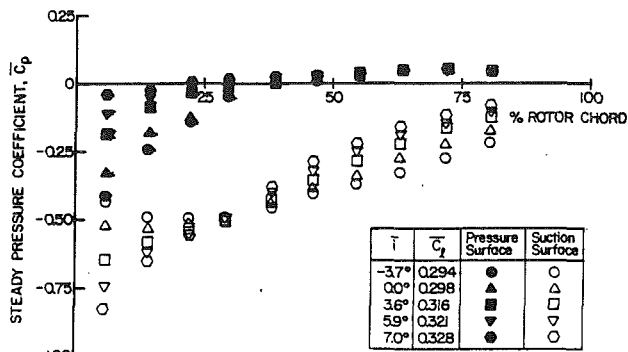


Fig. 4 Fourier decomposition of forcing function, $|\hat{u}^+/\hat{v}^+| = 0.4$

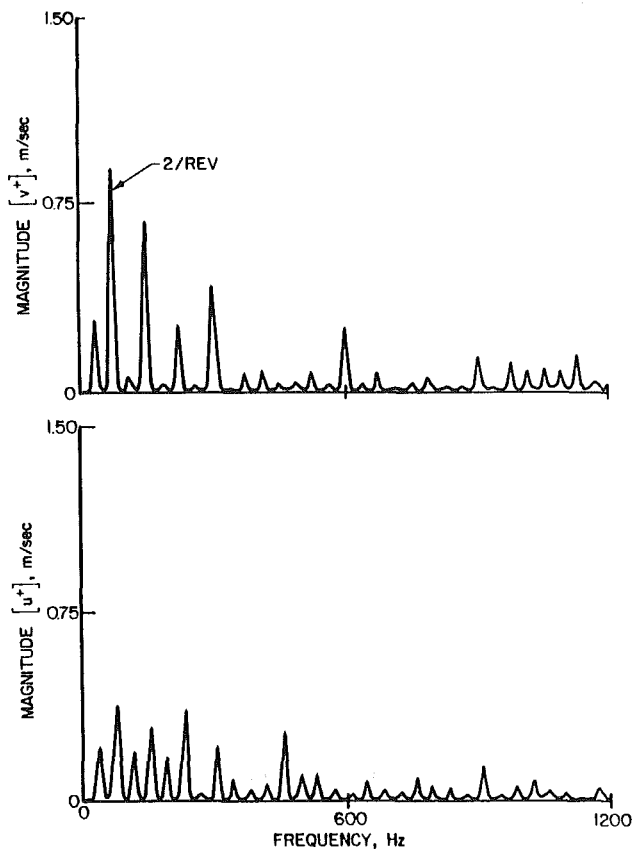


Fig. 5 Fourier decomposition of forcing function, $|\hat{u}^+/\hat{v}^+| = 0.7$

ensemble-averaged signals to determine the harmonic components of the unsteady aerodynamic forcing function and the resulting rotor blade surface harmonic unsteady pressures and pressure difference.

The unsteady inlet flow field to the rotor row is measured with the rotating cross hot-wire probe which quantifies the relative velocity and flow angle. The velocity triangle relations depicted in Fig. 2 are then used to determine the unsteady inlet flow field to the rotor, in particular, the streamwise and transverse velocity components, u^+ and v^+ , respectively. These are then Fourier decomposed to determine the first harmonic of the streamwise and transverse velocity components, termed the streamwise and transverse gust components, \hat{u}^+ and \hat{v}^+ .

The various unsteady aerodynamic gust mathematical models reference the gust-generated airfoil aerodynamic response to a transverse gust at the leading edge of the airfoil. However, in the experiments described herein, the time-variant data are referenced to the initiation of the data acquisition shaft trigger pulse. Thus, for consistency with the models, the periodic data

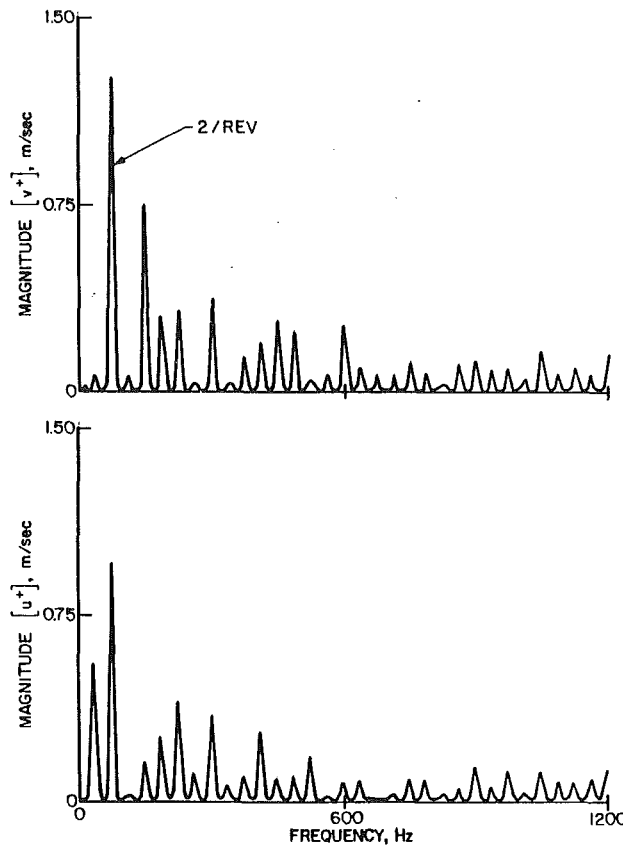


Fig. 6 Fourier decomposition of forcing function, $|\hat{u}^+/\hat{v}^+| = 0.9$

are further analyzed and referenced to a transverse gust at the leading edge of the first-stage rotor blade. This is accomplished by assuming that: (1) The aerodynamic forcing function remains fixed in the stationary reference frame; (2) The forcing function does not decay from the rotating hot-wire probe axial location to the rotor row leading edge plane.

The rotor blade surface unsteady pressure data, measured with the embedded high response pressure transducers, are analyzed to determine the harmonics of the chordwise distribution of the unsteady pressure coefficient, C_p , and the unsteady pressure difference coefficient, $C_{\Delta p}$. These are defined in equation (2) and are specified from the Fourier coefficients of the digitized ensemble-averaged dynamic pressure transducer signals.

$$C_p = \frac{\hat{p}}{\rho \bar{V}_x^2 \left(\frac{\hat{v}^+}{\bar{V}_x} \right) \bar{\beta}} \quad (2a)$$

$$C_{\Delta p} = C_{p, \text{pressure}} - C_{p, \text{suction}} \quad (2b)$$

where \hat{v}^+ is the first harmonic transverse gust component, \bar{V}_x is the mean axial velocity, and $\bar{\beta}$ is the relative mean flow angle.

The final form of the gust-generated rotor blade row unsteady aerodynamics is the chordwise distribution of the harmonic complex unsteady pressure and pressure difference coefficients. Also included as a reference, where appropriate, are predictions from the transverse gust analysis of Smith (1971). This model analyzes the unsteady aerodynamics generated on a flat plate airfoil cascade at zero incidence by a transverse gust convected with an inviscid, subsonic, compressible flow.

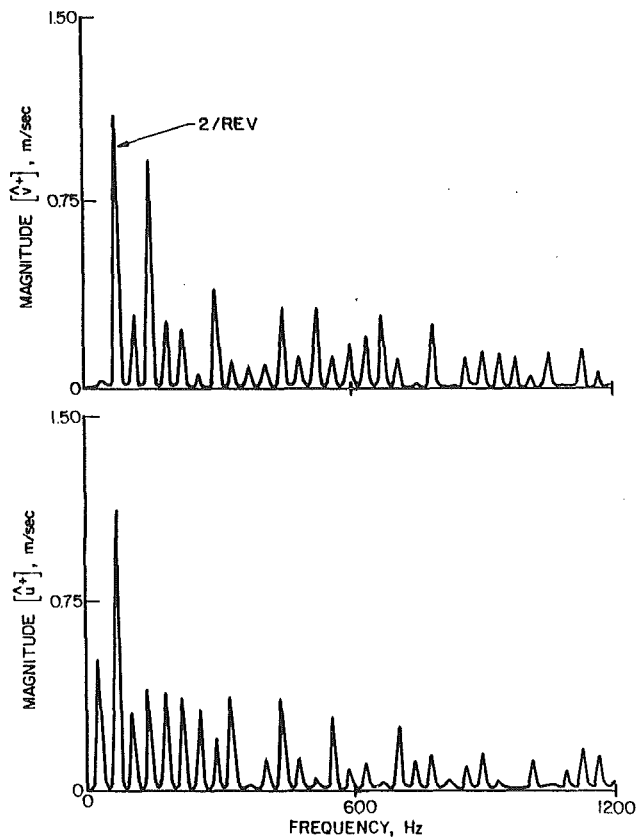


Fig. 7 Steady loading effect on surface static pressure coefficient with inlet flow distortion

Results

A series of experiments are performed to investigate and quantify the effects of the detailed inlet distortion aerodynamic forcing function, defined by the ratio of the amplitudes of the first harmonic streamwise-to-transverse gust components, $|\hat{u}^+ / \hat{v}^+|$, and the level of steady aerodynamic loading, characterized by the mean incidence angle, on the periodic gust unsteady aerodynamics of the first-stage rotor blade row. The variation in the rotor blade steady loading was obtained by holding the rotor speed constant and varying the mass flow rate, and thus, the mean flow incidence angle to the rotor blade row.

Periodic Aerodynamic Forcing Function

Three distinct two-per-revolution aerodynamic forcing functions to the first-stage rotor blade row are generated by varying the orientation of the two honeycomb sections mounted in the inlet. These are characterized by nominal first harmonic streamwise-to-transverse gust amplitude ratios of 0.4, 0.7, and 0.9. The Fourier decomposition of these inlet distortion aerodynamic forcing functions to the first-stage rotor row in terms of the streamwise and transverse gust components for these three gust amplitude ratios are presented in Figs. 4-6. The inlet distortion results in a dominant two-per-rev excitation fundamental harmonic with much smaller higher harmonics. Additionally, as the gust amplitude ratio increases, many of the higher harmonics of both gust velocity components increase in amplitude, although they do not approach that of the two-per-rev fundamental.

Blade Surface Static Pressures

The effect of steady aerodynamic loading, characterized by the mean incidence angle, on the rotor blade surface static

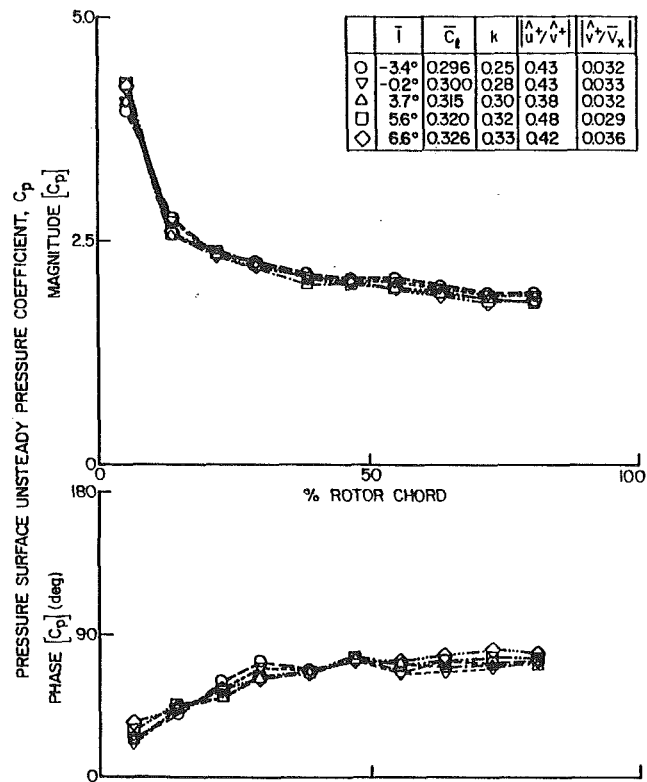


Fig. 8 Pressure surface steady loading effect on unsteady pressure, $|\hat{u}^+ / \hat{v}^+| = 0.4$

pressure coefficient with the inlet distortion is shown in Fig. 7. The level of steady loading only affects the static pressure distribution on the pressure surface over the front 40 percent of the chord. On the suction surface, the steady loading variation has a large effect on the static pressure distribution over the entire suction surface. These data also give no indication of surface flow separation. It should be noted that these surface static pressure distributions are not affected by the characteristics of the periodic unsteady aerodynamic forcing function.

Rotor Periodic Aerodynamic Response

The periodic aerodynamic response of the first-stage rotor blade row to the inlet distortion forcing function, including the effect of steady aerodynamic loading, are presented in Figs. 8-16. In particular, these figures present the chordwise distributions of the complex unsteady pressure coefficient on the individual rotor blade surfaces, as well as the corresponding complex unsteady pressure difference coefficients, generated by the two-per-rev inlet distortion forcing function.

Pressure Surface Unsteady Pressures. The effect of steady aerodynamic loading level on the distortion-generated first harmonic complex unsteady pressure distribution on the rotor blade pressure surface is shown in Figs. 8-10 for nominal streamwise-to-transverse gust amplitude ratios of 0.4, 0.7, and 0.9, respectively.

The unsteady pressure magnitude data decrease monotonically with increasing chord location, with a sharp decrease in the front region of the pressure surface and then a gradual decrease over the remainder of the chord for all steady loading levels and gust amplitude ratios. For each nominal value of the gust amplitude ratio, this form of the dimensionless unsteady pressure coefficient, equation (2a), results in the compression of these magnitude data for all mean flow incidence angle values. As the gust amplitude ratio increases, these magnitude data exhibit a small decrease in value. This is due

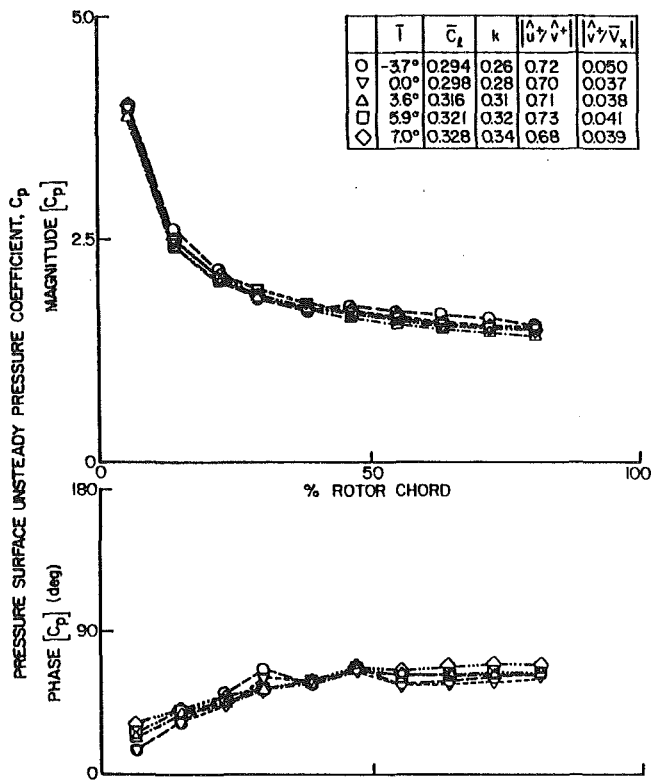


Fig. 9 Pressure surface steady loading effect on unsteady pressure, $|\hat{u}^+/\hat{v}^+| = 0.7$

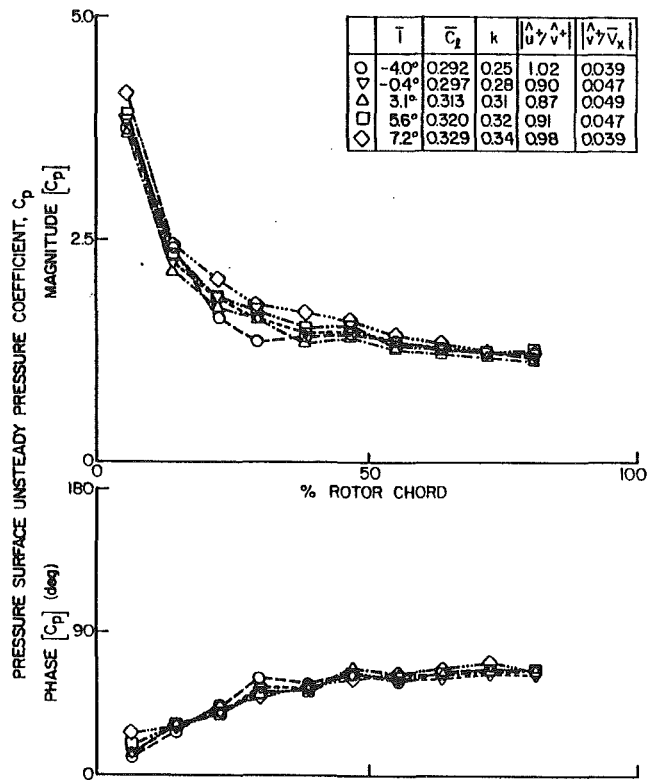


Fig. 10 Pressure surface steady loading effect on unsteady pressure, $|\hat{u}^+/\hat{v}^+| = 0.9$

to the gust vector becoming more parallel to the mean flow, and thus, less normal to the blade pressure surface. Thus the magnitude of the unsteady pressure response on the blade pressure surface, i.e., the low camber airfoil surface, is primarily due to the level of steady loading as characterized by the mean flow incidence angle.

The unsteady pressure phase data increase monotonically with chord over the front half of the blade, becoming nearly constant over the aft half for all steady loading levels and gust amplitude ratios. The steady aerodynamic loading and the gust amplitude ratio have only a very small effect on these phase data. Thus the phase of the unsteady pressure response on the low camber blade pressure surface is nearly independent of the steady loading level and the gust amplitude ratio.

Suction Surface Unsteady Pressures. The effect of steady aerodynamic loading on the distortion-generated first harmonic complex unsteady pressure on the rotor blade suction surface is shown in Figs. 11–13 for the three gust amplitude ratios.

The unsteady pressure magnitude data decrease over the front 25 percent of the chord for all steady loading levels and gust amplitude ratios. On this part of the suction surface, the magnitude data decrease in value as the gust takes on larger streamwise components. In contrast to the pressure surface, this form of the dimensionless unsteady pressure coefficient, equation 2(a), does not compress these magnitude data with mean flow incidence angle, the exception being between 13 percent and 20 percent of the chord. As the gust amplitude ratio increases, these magnitude data exhibit a relatively large decrease in value over the front half of the chord. This is due to the gust vector becoming more parallel to the mean flow, and thus, less normal to the blade pressure surface. Thus the magnitude of the unsteady pressure response on the blade suction surface, i.e., the higher camber airfoil surface, is due to both the level of steady loading as characterized by the mean

flow incidence angle and the streamwise-to-chordwise gust amplitude ratio.

The unsteady pressure phase data generally decrease monotonically with increasing chord for all gust amplitude ratios and steady loading levels. As the gust amplitude ratio increases, i.e., as the gust takes on a larger streamwise component, the phase data generally decrease in value, with the chordwise phase data variation decreasing more rapidly over the front half of the blade and more slowly over the aft half. With regard to the steady loading level, the phase data are nearly independent of the steady loading level in the neighborhood of the quarter chord. Forward and aft of the quarter chord, steady loading has different effects. In particular, aft of the quarter chord, the phase data decrease as the mean incidence angle is increased. In contrast, near the leading edge, the phase data increase with increasing mean incidence angle.

Unsteady Pressure Differences. The effect of steady loading on the first harmonic complex unsteady pressure differences across the rotor blade camberline is shown in Figs. 14–16 for streamwise-to-transverse gust amplitude ratios of 0.4, 0.7, and 0.9, respectively. Also presented as a reference are the flat plate cascade inviscid transverse gust predictions.

The unsteady pressure difference magnitude data generally decrease with increasing chord, attaining a near minimum value in the midchord region of the airfoil. As the gust amplitude ratio increases, i.e., as the gust takes on a larger streamwise component, the chordwise position of this minimum magnitude moves forward. Aft of this minimum magnitude position, the magnitude data are a function of the steady loading level. In the front chord region, increased steady loading results in an increase in the magnitude data. In the mid to aft chord region of the blade, the unsteady pressure differences are greatly decreased in magnitude, but still increase with increased mean incidence with this increase greater for higher values of the gust amplitude ratio. Additionally, the lowest gust amplitude

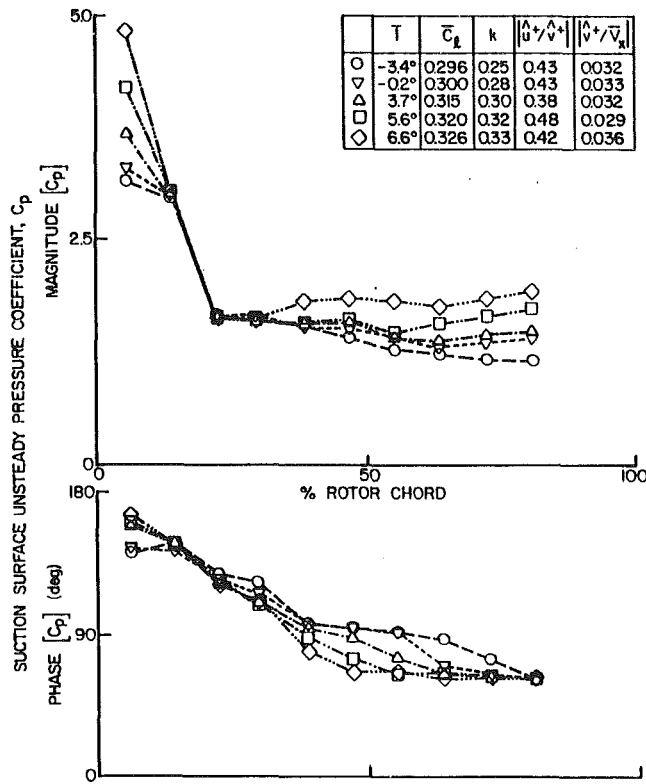


Fig. 11 Suction surface steady loading effect on unsteady pressure, $|\hat{u}^+/\hat{\theta}^+| = 0.4$

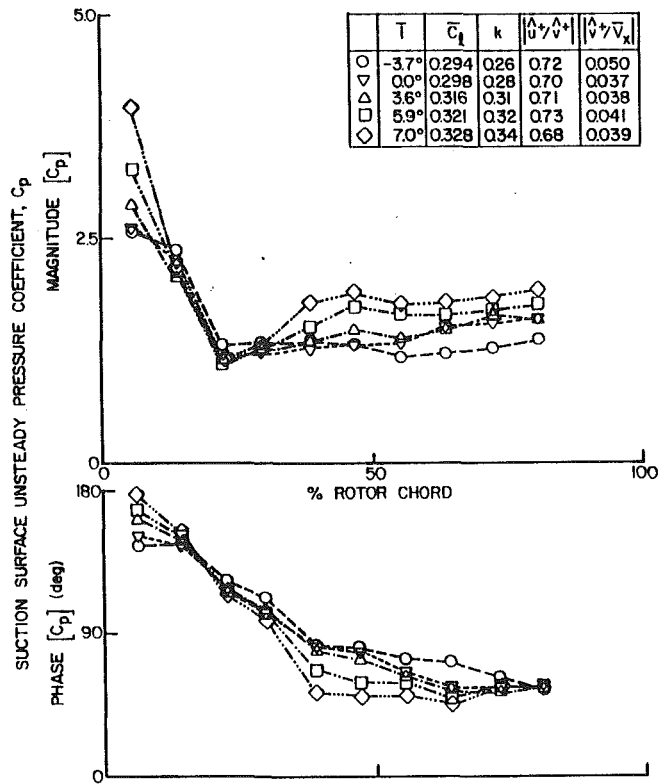


Fig. 12 Suction surface steady loading effect on unsteady pressure, $|\hat{u}^+/\hat{\theta}^+| = 0.7$

ratio value and lowest mean incidence angle data most closely approximate the transverse gust flat plate cascade model and exhibit the best correlation with the prediction.

An inviscid, incompressible flow cascade model that accounts for airfoil profile effects was used to determine the effect of variations in the mean flow incidence angle on the airfoil surface steady pressure difference distribution. Figure 17 demonstrates that the pressure difference in the front chord region increases with increasing mean flow incidence angle. Thus, for a quasi-steady harmonic gust disturbance, i.e., a low reduced frequency inlet distortion, the unsteady pressure difference magnitude will increase in the front chord region as the mean flow incidence angle is increased, for example Figs. 14-16.

The unsteady pressure difference phase data are nearly constant over the front part of the blade for all three gusts. There is a sharp increase in the phase in the quarter to midchord region of the blade. The chordwise location of the onset of this rapid increase is a function of the steady loading and the gust amplitude ratio. Aft of the chordwise location of this rapid phase increase, the phase data increase with increased steady loading.

Summary and Conclusions

The fundamental flow physics of distortion generated periodic rotor blade row unsteady aerodynamics, including the effects of both the detailed unsteady aerodynamic forcing function for the first time and steady loading, were experimentally investigated. This was accomplished through a series of experiments performed in an extensively instrumented axial-flow research compressor. A two-per-rev aerodynamic forcing function was generated by mounting two 90-deg honeycomb sections 180 deg apart circumferentially in the compressor inlet. In terms of the gust amplitude ratio, three distinct two-per-revolution aerodynamic forcing functions were considered.

The rotor blade surface steady-loading distributions were quantified with surface static pressure taps and a rotor-based

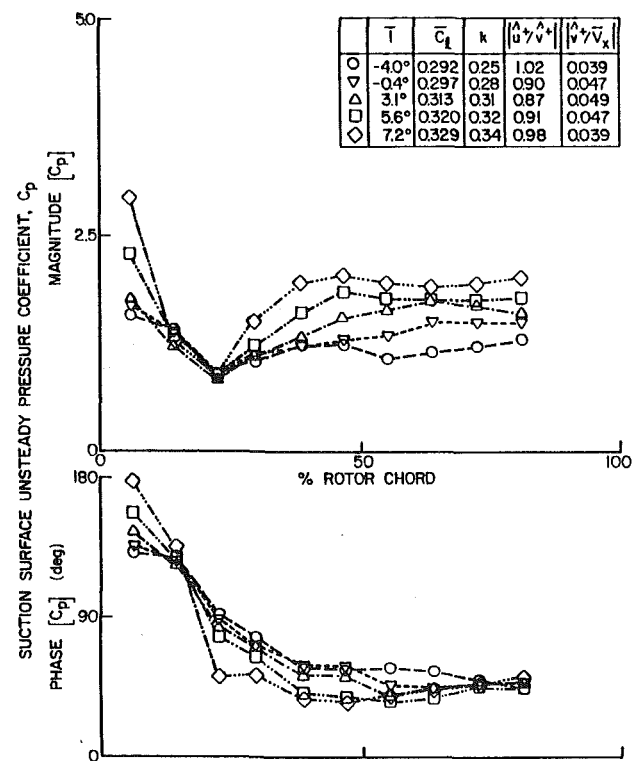


Fig. 13 Suction surface steady loading effect on unsteady pressure, $|\hat{u}^+/\hat{\theta}^+| = 0.9$

Scanivalve system. The aerodynamic forcing function to the rotor blade row was determined with a rotating cross hot-wire probe, with the aerodynamic gust-generated rotor blade surface unsteady pressure chordwise distributions measured with

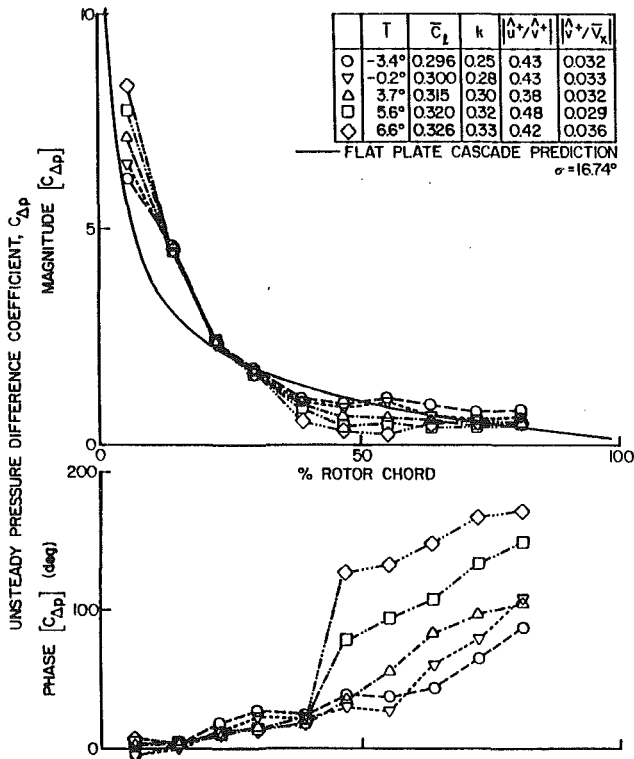


Fig. 14 Steady loading effect on unsteady pressure difference, $|\hat{u}^+/\hat{v}^+| = 0.4$

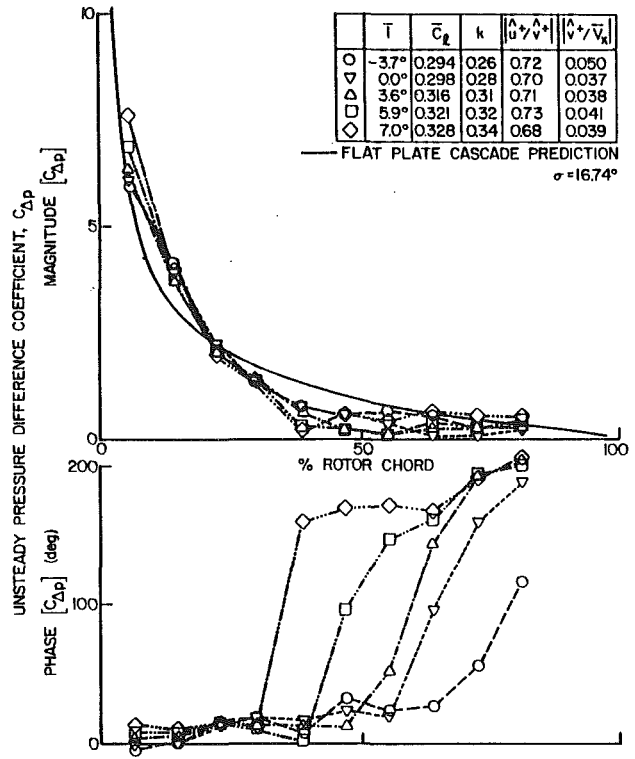


Fig. 16 Steady loading effect on unsteady pressure difference, $|\hat{u}^+/\hat{v}^+| = 0.9$

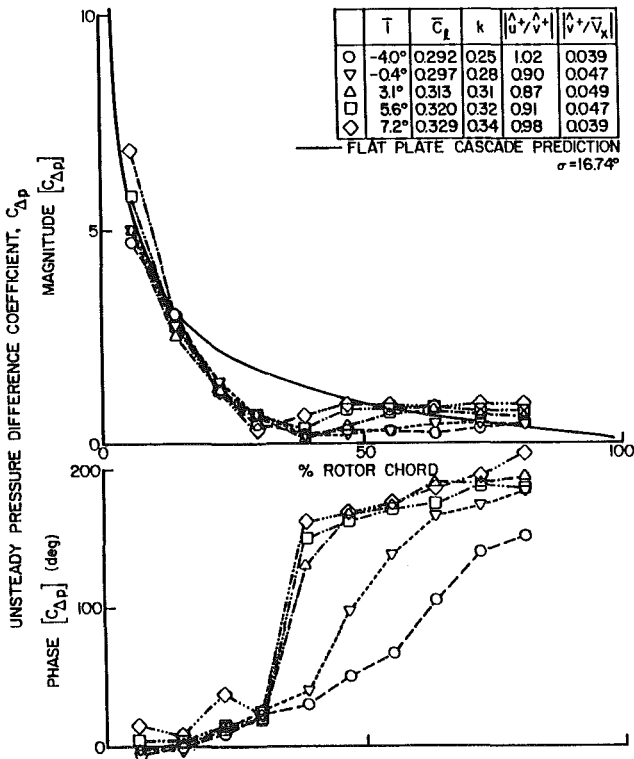


Fig. 15 Steady loading effect on unsteady pressure difference, $|\hat{u}^+/\hat{v}^+| = 0.7$

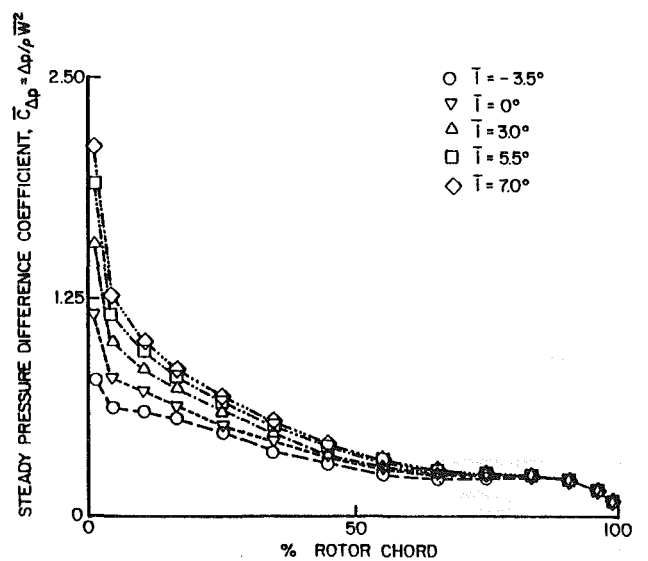


Fig. 17 Steady loading effect on prediction steady pressure difference

embedded ultraminiature high-response dynamic pressure transducers.

The detailed distortion gust-generated unsteady aerodynamic results of these experiments are summarized in the following.

Forcing Function:

- The inlet distortion forcing function shows a dominant two-per-rev, with much smaller higher harmonic content.
- As the gust streamwise-to-chordwise gust amplitude ratio increases, many of the higher harmonic amplitudes increase, although they do not approach that of the two-per-rev.

Pressure Surface:

- The unsteady pressure phase data are nearly independent of the steady loading level and the gust amplitude ratio.

- The unsteady pressure magnitude data decrease monotonically with increasing chord, with a sharp decrease in the front region.
- The selected nondimensionalization compresses the unsteady pressure magnitude data with regard to mean flow incidence angle for each gust amplitude ratio.
- Increasing gust amplitude ratio results in a small decrease in the magnitude data in the front chord region due to the gust vector becoming more parallel to the mean flow.
- The magnitude of the unsteady pressure response on the blade pressure surface, i.e., the low camber surface, is thus primarily affected by the level of steady loading as characterized by the mean flow incidence angle.

Suction Surface:

- The unsteady pressure phase data generally decrease as the gust amplitude ratio increases. As the incidence angle is increased, the phase data increase and then, aft of 25 percent chord, decrease.
- The unsteady pressure magnitude data decrease over the front 25 percent of the chord for all steady loading levels and gust amplitude ratios.
- The selected nondimensionalization does not compress these unsteady pressure magnitude data with regard to mean flow incidence angle, the exception being between 13 and 20 percent of the chord.
- Increasing gust amplitude ratio results in a large decrease in the magnitude data in the front chord region due to the gust vector becoming more parallel to the mean flow.
- The magnitude of the unsteady pressure response on the blade suction surface, i.e., the high camber surface, is thus affected by both the level of steady loading and the gust amplitude ratio.

Unsteady Pressure Difference:

- The magnitude data increase in the front chord region as the steady loading is increased. In the mid to aft chord region, the increase in these data with loading is a function of the gust amplitude ratio.
- The phase data exhibit a sharp increase in the quarter to midchord region of the blade, with this location a function of the steady loading and the gust amplitude ratio. Aft of this chordwise location, the phase data increase with increased steady loading.

Acknowledgments

Research sponsored by the Air Force Office of Scientific Research (AFSC) under Contract F49620-88-C-0022. The United States Government is authorized to reproduce and distribute reprints for governmental purposes notwithstanding any copyright notation hereon.

References

- AGARD, 1987, *Manual on Aeroelasticity in Axial-Flow Turbomachines, Vol. 1: Unsteady Turbomachinery Aerodynamics*, AGARDograph No. 298.
- Cardinale, V., Bankhead, H., and McKay, R., 1980, "Experimental Verification of Turboblading Aeromechanics," Paper No. 23, 56th Symposium of the AGARD Propulsion and Energetics Panel.
- Datko, J. T., Jr., and O'Hara, J. A., 1987, "The Aeromechanical Response of an Advanced Transonic Compressor to Inlet Distortion," ASME Paper No. 87-GT-189.
- Hardin, L. W., Carta, F. O., and Verdon, J. M., 1987, "Unsteady Aerodynamic Measurements on a Rotating Compressor Blade Row at Low Mach Number," *ASME Journal of Turbomachinery*, Vol. 109, No. 4, pp. 499-507.
- O'Brien, W. F., Cousins, W. T., and Sexton, M. R., 1980, "Unsteady Pressure Measurements and Data Analysis Techniques in Axial-Flow Compressors,"

Measurement Methods in Rotating Components of Turbomachinery, ASME, New York, pp. 195-201.

Smith, S. N., 1971, "Discrete Frequency Sound Generation in Axial-Flow Turbomachines," ARC R&M 3709.

APPENDIX

As noted, when the transverse gust is utilized in the nondimensionalization of the unsteady pressure, equation (2a), the magnitude data on both the pressure and suction surfaces decrease with increasing value of the streamwise-to-chordwise gust amplitude ratio. To provide a more advanced design tool that accounts for this effect, a semi-empirical analysis of these unsteady pressure data was considered.

The blade surface unsteady pressure response is generated by the velocity fluctuations normal to the blade surfaces. Therefore, an unsteady pressure nondimensionalization, which considers the gust component normal to each blade surface, was investigated, accomplished with the following modified complex unsteady pressure coefficient:

$$C'_p = \frac{\hat{P}}{\rho \bar{V}_x^2 \left(\frac{a_n \Delta \hat{W}}{\bar{V}_x} \right) \bar{\beta}} \quad (A1)$$

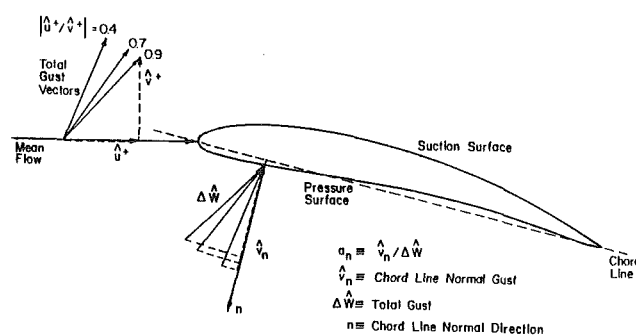


Fig. A1 Blade pressure surface gust vector orientation

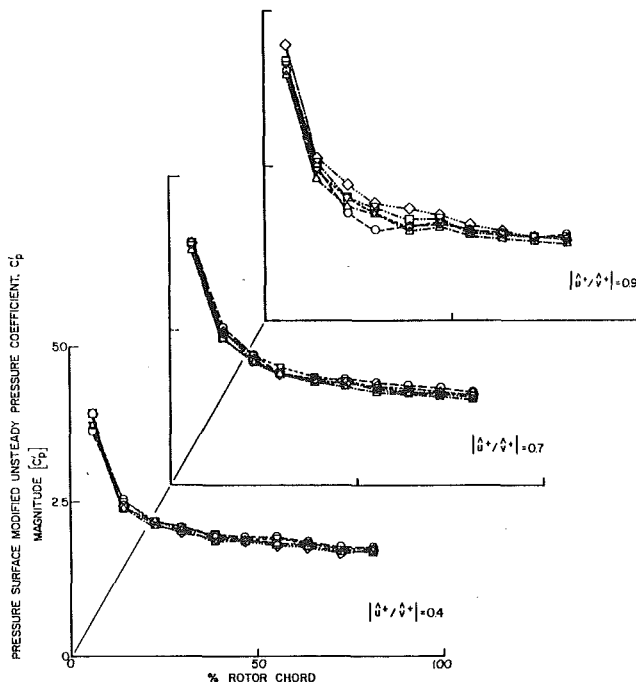


Fig. A2 Pressure surface semi-empirical correlation

$$\Delta \hat{W} = \sqrt{(\hat{v}^+)^2 + (\hat{u}^+)^2} \quad (\text{A2})$$

where a_n is the magnitude ratio of the gust component normal to the chordline and the total gust.

Figure A1 schematically depicts the blade pressure surface flow field with zero mean flow incidence. The blade surfaces are approximated by the chordline, with the normal gust component calculated from the data. On the pressure surface, the low camber airfoil surface which is well approximated by the chordline, this semi-empirical correlation is valid, with the magnitude data for the various streamwise-to-chordwise gust amplitude ratios collapsing to a single curve (Fig. A2). However, on the high camber suction surface, although this semi-empirical correlation does decrease the differences in the magnitude data for the three streamwise-to-chordwise gust amplitude ratios, there are still large differences (Fig. A3). This is most likely associated with the strong interactions between the steady and unsteady flow fields in the leading edge region and aft of midchord region. The chordline is a poor approximation to this high camber airfoil surface. It should be noted that incorporating only the total gust vector, $\Delta \hat{W}$, i.e., setting a_n to unity in equation (A1), was also considered. However, rather than a collapsing of the magnitude data with increasing streamwise-to-chordwise gust amplitude ratio, this resulted in an amplification of this effect.

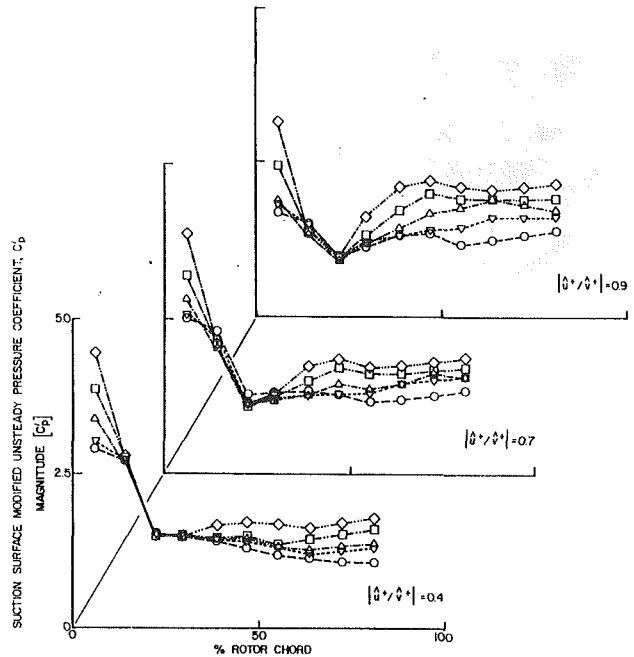


Fig. A3 Suction surface semi-empirical correlation

Visualization Studies in Rotating Disk Cavity Flows

J. Nordquist,¹ S. Abrahamson,¹ J. Wechkin,¹ and J. Eaton¹

An experimental study was performed in a simplified turbine disk cavity consisting of a single disk rotating near a stationary flat plate, bounded radially by an axial seal fixed to the plate. The disk Reynolds number was 6.2×10^5 . Cooling flow was supplied axially at a dimensionless radius of 0.33. Flow visualization showed boundary layers on both the rotating and stationary disks with the core between the layers rotating in solid body motion. At intermediate cooling flow rates, large vortical structures aligned with the disk spin axis and spanning the core were observed.

Introduction

The flow between the rotating disk and fixed shroud in a turbine disk cavity is important to the operating temperature and longevity of the disk. A disk cavity is bounded axially by the rotor and stator disks, and radially by the hub and the seal. The seal is supposed to prevent the leakage of hot gases into the cavity (called *ingress*), minimizing cooling flow requirements.

Research on turbine cavities can be divided into mathematical studies with simple cavity geometries, experimental studies of the flow structure in simple configurations, realistic cavity performance measurements, and studies of ingress into cavities. Mathematical studies assumed infinite disks with axisymmetric flow. However, experiments show strong azimuthal variations and unsteadiness (e.g., Maroti et al., 1960). No published studies observed ingress directly or measured an ingress flow rate. A maximum tolerable rate of ingress has not been defined. With no general understanding of the flow structures that occur in the cavity, the causes of ingress are unknown. The objective of the present study was to visualize a simplified cavity flow to examine the dominant features of the flow. The simplified geometry was selected so the results could be used to test both numerical models under development, and the level of apparatus complexity necessary to observe ingress.

Experimental Apparatus and Techniques

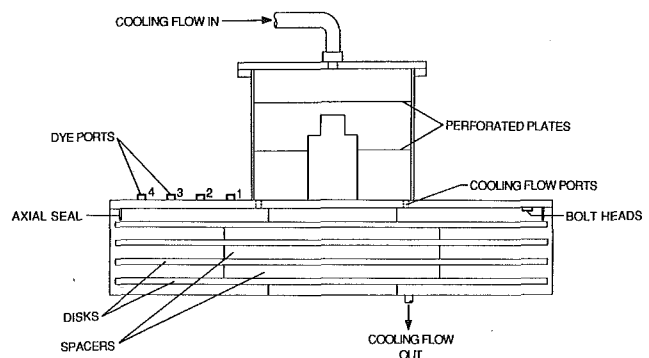
The experiments were performed in a water flow facility containing the simplified turbine disk cavity. The rotating tur-

bine disk was represented by a 112-cm-dia flat disk and the stator by the top cover plate of the facility. The facility is sketched in Fig. 1, and Table 1 gives a summary of the relevant dimensions and dimensionless parameters. The radial boundaries were the rotating hub and a simple axial seal fixed to the stator. Cooling flow was supplied to the cavity through a 35.6-cm-dia ring of 48, 1.6-cm-dia holes. The cooling flow was exhausted through the gap between the axial seal and the disk. For some of the ingress studies, simulated bolt heads, cut from a 5-cm-dia acrylic rod to a height of 0.7 cm, were attached to the stator as shown in Fig. 1.

The Reynolds number for the experiment was found using the seal radius R_s and the disk tangential speed $R_s\Omega$. The scaled cooling flow rate Q^* is defined as the ratio between the bulk radial velocity through the seal and the disk tangential speed. The disk speed was measured using a magnetic tachometer with an uncertainty of ± 1 rpm. The cooling flow rates were measured using a rotometer with a range of 370–1330 cm³/s and uncertainty of ± 20 cm³/s.

Two methods were used to visualize the flow field: injection of bromthymol-blue dye and hydrogen bubbles. Both techniques are described in detail by Abrahamson et al. (1988). The dye was injected into the flow through the dye ports labeled 1 to 4 in Fig. 1. The axial position of the injection probe was adjustable from the disk surface to 6 mm from the stationary top. To study the ingress of fluid from outside the cavity, dye was injected into the region just outside of the axial seal.

The hydrogen bubble wire was fixed along a radial line supported at the ends by probes inserted through dye ports 1 and 4. The wire height was adjustable from 2 mm above the



EXPERIMENTAL APPARATUS
Cross Section
(RESERVOIR TANK, PUMP MECHANISM, & SUPPORT STRUCTURE NOT SHOWN)

Fig. 1 Experimental apparatus: cross section (reservoir tank, pump mechanism, and support structure not shown)

¹Department of Mechanical Engineering, Stanford University, Stanford, CA 94305.

Contributed by the International Gas Turbine Institute for publication in the ASME JOURNAL OF TURBOMACHINERY. Manuscript received at ASME Headquarters September 1, 1989.

Table 1 Apparatus dimensions and dimensionless parameters

R_s	seal radius	54.6 cm
R_d	disk radius	55.9 cm
R_c	shroud radius	57.8 cm
R_b	bolt circle radius	49.7 cm
G	cavity height	3.3 cm
t	seal clearance	0.25, 0.64 cm
R_{cf}	cooling flow port radius	17.8 cm
A_{cf}	cooling flow port area	112.6 cm ²
D	cooling flow port hydraulic diameter	1.6 cm
Ω	disk rotation rate	0–6.28 rad/s (0–60 RPM)
Q	cooling flow rate	0–757 cm ³ /s
ν	kinematic viscosity	0.01cm ² /s at 20°C
Re	Reynolds' number, $\frac{R_s^2 \Omega}{\nu}$	6.2×10^5 ($\Omega = 2.09$ rad/s)
Re_{cf}	cooling flow port Re , $\frac{u D}{\nu}$	$0-10^3$ ($u = \frac{Q}{A_{cf}}$)
Q^*	$\frac{Q}{2\pi\Omega R_s^2 t}$	0–0.076

disk surface to 6 mm from the stationary surface. Illumination of the hydrogen bubbles was provided by a 2-mm-thick laser sheet. Velocities were measured by timing the travel of bubble patches with an uncertainty of approximately 10 percent.

Results

With no cooling flow, the flowfield appeared steady with no azimuthal variation. The flow structure in a plane normal to the disk is sketched in Fig. 2. Boundary layers were observed on both the disk and stator; the layer thicknesses were estimated to be on the order of 1/10 of the axial height of the cavity (about 0.3 cm). Between the boundary layers, the flow was in solid body motion with a rotation rate of approximately 0.35 Ω , agreeing with earlier works. In the disk boundary layer the flow was primarily tangential with an outward radial component. Spiral waves were observed in the disk boundary layer beginning about 0.7 R_s and traveling outward. These were presumed to be the spiral vortices associated with boundary layer transition. In the stator boundary layer the flow was primarily tangential with an inward radial component. No flow was observed to exit through the axial seal and marked disk boundary layer fluid was observed to turn upward near the seal and form into the boundary layer on the stator.

Addition of cooling flow up to $Q^* = 0.019$ did not change the basic structure. The cooling flow, which entered axially, flowed across the cavity and entered the disk boundary layer, resulting in a higher radial flow rate and slightly thicker layer. The core between the boundary layers rotated in solid body motion at approximately 0.35 Ω with little or no radial motion. Some disk boundary layer fluid exited through the axial seal and some was observed to turn upward at the seal and enter the inflowing stator boundary layer. Spiral vortices were observed in the disk boundary layer throughout this low-cooling-flow regime.

At moderate cooling flow rates ($0.019 < Q^* < 0.045$), the flow was substantially different. It was no longer axisymmetric or steady, and large vortical structures (sketched in Fig. 3) were observed in the core between the boundary layers on the disk and stator.

Typically, there were three vortices, each approximately 10 cm in diameter, evenly spaced around the circumference of a circle approximately 0.4 R_s in radius. They rotated in the same sense as the disk, and precessed at about 0.23 Ω . The vortices appeared most energetic at $Q^* = 0.041$. Maroti et al. (1960) observed a similar phenomenon in the flow between a rotating disk and a stationary plate without radial containment. Radial flow reversals observed through tuft visualization were interpreted as the stall cells sometimes found in vaneless diffusers.

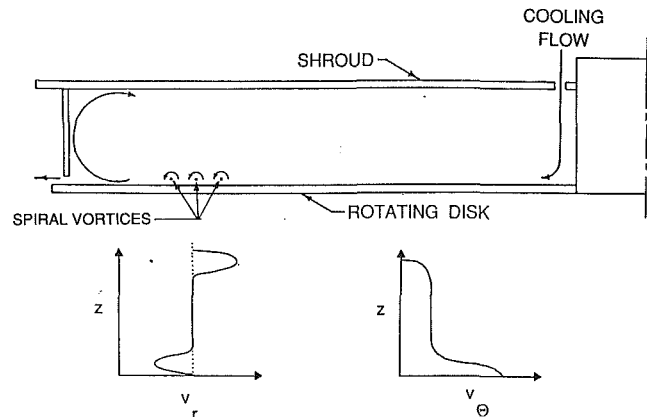


Fig. 2 Cross-sectional sketch of cavity flow (including hypothesized velocity profiles)

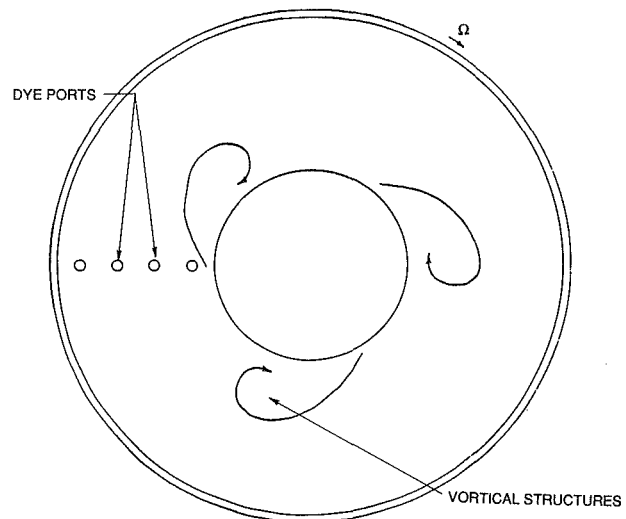


Fig. 3 Vortical structures at intermediate cooling flow rates (overhead view)

At a Reynolds number around 6×10^5 , they observed three cells. In the current experiment, the vortices caused significant radial flow reversals, which could have been misinterpreted as stall cells. One might explain the vortices as the result of a strong radial gradient in the tangential velocity produced by the interaction of the cooling flow entering the cavity with no tangential velocity, and the solid body core flow at larger radii. The gradient, unstable due to the Kelvin–Helmholtz instability, rolls up. A similar situation is observed in corotating disk flows with a fixed outer shroud (see Abrahamson et al., 1988). The velocity gradient is reversed in that case producing oppositely signed vortices.

This model does not tell the full story: At high cooling flow rates ($Q^* > 0.045$) the vortical structures disappeared, and the flowfield resembled the structure observed at the lower cooling flow rates. The disk boundary layer was thicker due to the increase in the outflow rate, spiral vortices were observed in the disk boundary layer, and core fluid precessed at about the same 0.35 Ω as previously observed. We have no explanation for this observed behavior, but it is consistent with the disappearance of the stall cells observed by Maroti et al. at sufficiently high throughflow rates.

In all these studies, ingress of fluid from the outside of the axial seal into the simulated turbine cavity was never observed. Even when the flow was unsteady and radial inflow was observed in the core fluid, the radial flow reversals did not penetrate through the seal to exchange fluid with the outside. Several modifications were made in attempts to induce ingress

including increasing the seal gap and installing simulated bolt heats on the stator. None of these modifications (which are described fully in Nordquist et al., 1988) caused any observable ingress.

Conclusions

The flow visualization studies at moderate cooling flow rates revealed the presence of energetic vortical structures in the simulated turbine disk cavity. The cause of the structures is unknown, nor is it understood why they disappear at higher cooling flow rates. It is also not known whether these structures are present in more realistic cavities so further investigation of the phenomenon is needed.

In all the studies described above, ingress of fluid from outside into the cavity was never observed. The present geometry was simplified relative to actual turbine disk cavities so the results would be useful for verification of numerical results, but the simplifications may have ruled out ingress. Potentially important differences between the present model

and realistic turbine cavities are the variation of the axial dimension with radius and the baroclinic effects due to temperature (and therefore density) variations within actual cavities.

Acknowledgments

This work was funded by grants from Garrett Turbine Engine Company and General Motors Corporation with matching funding from the National Science Foundation (Grant #MEA-83-51417).

References

- Abrahamson, S., Koga, D., and Eaton, J., 1988, "An Experimental Investigation of the Flow Between Shrouded Corotating Disks," Report MD-50, Thermosciences Division, M.E. Dept. Stanford University, Apr.
- Maroti, L. A., Deak, G., and Kreith, F., 1960, "Flow Phenomena of Partially Enclosed Rotating Disks," *ASME Journal of Basic Engineering*, Vol. 82, pp. 539-552.
- Nordquist, J. S., Abrahamson, S. D., Wechkin, J., and Eaton, J. K., 1988, "Visualization Studies in Rotating Disk Cavity Flows," Stanford University Department of Mechanical Engineering Report IL-98.